TWO-PHASE FLOW WITH HEAT TRANSFER IN HELICALLY-COILED TUBES

by

Kenji Ishida, MSc., DIC., BSc.(Marine Eng.)

A Thesis submitted for the Degree of

Doctor of Philosopy of the University of London

April, 1981

Mechanical Engineering Department

Imperial College

London S.W.7.

TO KEIKO & MONA

A B S T R A C T

This thesis describes the flow mechanisms in helically-coiled tubes with heat transfer.

It has six chapters: introduction to the present work, a review of previous work, description of the test facilities and test procedures, analysis and discussion of the experimental results, theoretical analysis and a summary of this work.

Three configurations of helically-coiled tubes were investigated: coil diameters of 260, 390 and 520mm. In all cases the tubes were of Inconel 600, 13mm inside diameter, 0.5mm tube wall thickness. The electrical resistance of the coils was such that they acted as the heat source when an electric current was passed along them.

Data were obtained in order to investigate the following phenomena:

(i) Single-phase flow with sub-cooled water and dry saturated steam:

Wall temperature profiles, pressure drops, local heat transfer coefficients.

(ii) Two-phase flow with steam-water mixtures:

As for single-phase flow with the additions of flow patterns and burnouts.

The outlines of each chapters are presented as follows:

Chapter One contains the introduction, the purpose of the study and practical application of the helically-coiled tube.

Chapter Two is a review of previously published work about flow mechanisms of bends, coiled tubes and helically-coiled tubes. It begins with summaries of work on pressure drops and heat transfer

coefficients of the laminar and turbulent singlephase flows.

The most important work described in this chapter includes the following. Dean (1) was the first to mention the laminar secondary flow in a coiled pipe. Later, using the friction factors, heat transfer coefficients of the laminar and turbulent flows were investigated by Seban and McLaughlin (22), Mori and Nakayama (5,24), Akiyama and Cheng (9,23) and Kozeki (53,80).

The different flow patterns in the two-phase flow are reported by several investigators using various fluids at different pressure. Banerjee et al (39,55) mentioned "film inversion" in which the flowing liquid film tends to build up at the inner side of the tube in the stratified and wavy flows.

Banerjee et al, Owhadi et al (47, 64) and Kozeki (53,80) investigated two-phase flow pressure drops empirically and compared their results with the Lockhart-Martinelli correlation.

The two-phase local heat transfer mechanisms were investigated by Owhadi et al at atmospheric pressure and by Kozeki at 10~30 $^{Kg}/_{cm^2}g$. From their results they concluded that the heat transfer coefficient at the outer side is the maximum, the inner side is the minimum and the average heat transfer coefficient is similar to that for a straight pipe.

Burnout was investigated by Carver et al (68), Cumo (70) and Kozeki (80) at the different pressures and mass flow rates, and they concluded that it occurred at smaller steam quality than that for the straight pipe. The incipient points of burnout were found at different positions at different pressures and mass flow rates.

Chapter Three describes the test facilities of the present work. Dry saturated steam was generated in the steam generator and sub-cooled water was also supplied from another part of the steam generator. The steam or sub-cooled water was used separately to obtain the data of the single-phase flow. The steam and sub-cooled water could be mixed in the mixer to form an annular two-phase flow artificially, and such mixtures were used for two-phase flow experiments.

Chapter Four contains the experimental results and empirical analyses of the single-phase and two-phase flows.

The wall temperature had its maximum value at the inner side in both the case of steam and of sub-cooled water flow. The buoyancy force significiantly affected the axial water flow near the water saturation temperature. Also the relationship between Rayleigh number and Reynolds number of the water flow was reported.

The ratios of the local heat transfer coefficient between the inner side and the outer side of the steam and the water flows were compared with those of Seban and McLaughlin, Owhadi et al and Kozeki.

The wall temperature in the two-phase flow was maximum at the upper side, the entire temperature profile being different from that of the single-phase flow.

It was apparent that film inversion was taking place from the wall temperature profile observed in this work.

Two-phase flow patterns are plotted on Baker's original map and on Goldmann's map. The wavy region was observed as a narrow strip between an annular region and a stratified region in the Baker's map.

Using the Lockhart-Martinelli correlation the two-phase pressure drops were compared with that for the straight tube. In the range of $X_{tt} < 0.1$ the pressure drops, ϕ_{gtt}, were greater than those for straight tubes. In this range, the main reason for the large pressure drops was a large kinetic energy loss due to the frequent entrainment and depositon of droplets between the gas core and liquid surface. Turbulent characteristics appeared in the liquid phase around $Re_f = 800 \sim 1000$. In the range of $X_{tt} > 0.1$ the two-phase pressure drop had a similar profile to that for a straight pipe.

The local heat transfer coefficients were evaluated using Chen's correlation. The upper side had the maximum heat transfer coefficient when the steam quality was ~~greater~~ smaller than 50%. Nucleate boiling heat transfer is thought to be the predominant mechanism in this range of steam quality.

In the case of $x > 50\%$, the convective heat transfer becomes more important, however both heat transfer mechanisms are present in the coil. The average heat transfer coefficient was close to Schrock-Grossman's (100) correlation.

Onset of burnout occurred successively at the upper, outer and lower and inner sides. On decreasing the water flow rate, keeping steam flow rate and heat flux constant, burnout occurred initially at a point towards the tube exit and then shifted progressively nearer to the tube entrance. The first appearance of burnout occurred at different points in all three coils and varied with different mass flow rates and pressures. Burnout was determined by the progress of transition to completely stratified flow and start of "film inversion" phenomena.

Chapter Five contains theoretical analyses of the turbulent single-phase flow and the two-phase annular flow. In the case of the

turbulent single-phase flow, the flow was divided into a central core and a laminar boundary layer. The centrifugal force was assumed to prevail over the turbulent diffusion in the central core. The local relationship between the velocity distribution and shearing stress was assumed to be similar to that for the straight tube. Thus, the velocity profile in the gas core and friction factor can be calculated. Also, the local heat transfer coefficients could be obtained theoretically using the correction factor (S_c). These theoretical results were compared with the results of other investigators and the present work.

The annular flow was divided into the central gas core, gas boundary layer and liquid film. In the gas core, the centrifugal force would prevail and develop a secondary flow similar to that in the straight tube. In the liquid film the secondary flow would be from the inner side to the outer side. This secondary flow would be controlled by the force balance in the circumferential direction. We extended the analysis of turbulent single-phase flow for use with annular flow.

In general the liquid film is affected by the pressure profiles, centrifugal force, circumferential shear stress and tube wall shear stress. The distribution of the liquid film is determined by the balance of these forces. We studied the circumferential liquid film profile theoretically using the force balance equation and several assumptions. The theoretical results were compared with the empirical results of Whalley and Williams (88), the comparison was in good agreement qualitiatively.

The main feature of the flow boiling heat transfer in helical coiled tube was thought to be convective boiling in the liquid film. The theoretical local boiling heat transfer coefficient was derived from

the liquid film thickness and liquid velocity at the film surface. The theoretical results at 2 bars and 40 bars respectively were compared with the present work and Kozeki's (80) results. The comparisons showed similar profiles, but both the results varied quantitatively with up to 20∿50% variations.

Chapter Six has the conclusions from the empirical and theoretical results for the single-phase and two-phase flows of the present work.

A C K N O W L E D G E M E N T S

I wish to thank all those who provided me with help and encouragement during the present study. First and foremost, it is my duty to thank my supervisor, Dr. El-Shirbini for providing inspiration, guidance and maintaining a good pace of research.

I am grateful to Dr. M. Kozeki, Mitsui Engineering and Shipbuilding Co. Ltd., who offered a number of suggestions and helped me both in technical and non-technical matters throughout this study.

Thanks are due to Mr. P. Gibbs who has been helpful in making various suggestions and helping my language difficulties during the course of the work. Thanks are due to Miss E.M. Archer for helping me in preparing various technical reports.

I would like to thank several people who provided help during the experimental stages of my work. The assistance provided by the steam laboratory staff in particular by Mr. N. Wood, Mr. J. Martin and Mr. J. Knight, is acknowledged. Also, thanks are due to Mr.T.Thomas and Mr. D. Bloxhalm who provided the electrical equipment for the test facilities.

I acknowledge with deep respect the encouragement provided by Professor Takeda (Kobe University of Mercantile Marine), my parents and my wife, Keiko, during my stay in England.

Finally, I would like to thank Mr. B. King for providing photographs of the apparatus and also Miss J. Davies for her excellent typing of the thesis.

Kenji Ishida

South Kensington, London

April 1981

C O N T E N T S

Abstract 3

Acknowledgements 9

Contents 10

Nomenclature 15

List of the figures and tables 27

CHAPTER ONE

Introduction 38

CHAPTER TWO

A Review of the Literature

2.1 Introduction 41

2.2 Laminar Single-phase flow 41

2.2.1 General concept and pressure drop in laminar flow 41

2.2.2 Velocity profiles in laminar flow 44

2.2.3 Temperature profile in laminar flow 45

2.2.4 Heat transfer coefficient of laminar flow 46

2.2.4.1 For axially uniform wall heat flux 46

2.2.4.2 For uniform wall temperature 49

2.3 Laminar-turbulent transition in coils 50

2.4 Turbulent flow 51

2.4.1 Pressure drop (friction factors) 51

2.4.2 Velocity and temperature profiles in turbulent flow 53

2.4.3 Heat transfer coefficient in turbulent flow 54

2.5 Two-phase flow

2.5.1 Pressure drop and hold-up in two-phase flow 65

2.5.2 Flow patterns in the helically-coiled tubes 71

2.5.3 Heat transfer coefficient in two-phase flow 75

2.5.4 Burnout 79

2.5.5 Convective heat transfer to vapour phase 81

CHAPTER THREE

Experimental Facilities

3.1 General description of the test arrangement 94

3.2 Steam circuit 95

3.2.1 Steam generator 95

3.2.2 The mixer of steam and water 96

3.2.3 Water separator 97

3.2.4 Steam circulator 97

3.3 Water circuit 98

3.4 The coils 98

3.5 Heat system 100

3.6 Instrumentation 101

3.6.1 Instruments of steam circuit 101

3.6.2 Instruments of water circuit 102

3.7 Thermocouple distribution 102

3.8 Temperature measurement 103

3.9 Test procedure 104

CHAPTER FOUR

Experimental results and analysis

4.1 Introduction 118

4.2 Results of single-phase flow 119

4.2.1 Water flow 119

4.2.1.1 Pressure drop of water flow 119

4.2.1.2 Wall temperature profile (water flow) 119

4.2.1.3 Heat transfer coefficient of water flow 124

4.2.2 Steam flow 140

4.2.2.1 Pressure drop of steam flow 140

4.2.2.2 Wall temperature profiles of steam flow 141

4.2.2.3 Heat transfer coefficient of steam flow 146

4.3 Results of Two-phase flow 156

4.3.1 Flow patterns 156

4.3.2 Pressure drop in two-phase flow 171

4.3.3 Wall temperature profile in two-phase flow 178

4.3.4 Heat transfer coefficient of flow boiling in two-phase flow 211

4.3.5 Burnout phenomena 228

4.4 Summary of the Chapter 245

CHAPTER FIVE :

Theoretical analysis of the flow in coiled tube

5.1 Theoretical analysis of single-phase flow 252

5.1.1 Analysis of friction factor 252

5.1.1.1 Velocity distributions in the core region 256

5.1.1.2 Velocity distributions and the wall shear stresses in the boundary layer 257

5.1.1.3 Friction factor 264

5.1.1.4 Discussion and comparison theoretical analysis with the empirical results 266

5.1.2 Analysis of heat transfer coefficient in single-phase flow 271

5.1.2.1 Temperature profile in the core region 273

5.1.2.2 Heat transfer in thermal boundary layer 274

5.1.2.3 Heat transfer coefficient of boundary layer 276

5.1.2.4 Heat transfer coefficient. for the uniform wall temperature in the circumferential direction 278

5.1.2.5 Heat transfer coefficient for the uniform heat flux in the circumferential direction 283

5.1.2.6 Discussion and comparison in the theoretical analysis with the empirical results 285

5.2 Theoretical analysis of two-phase flow 300

5.2.1 Introduction 300

5.2.2 Flow model and assumptions 300

5.2.3 Analysis of the gas flow 303

5.2.4 Analysis of annular liquid flow 309

5.2.4.1 Analysis for liquid film thickness 313

5.2.5 Discussion and comparison between the theoretical results and the empirical results 318

5.3 Analysis of heat transfer in annular flow 329

5.3.1 Discussion and comparison between the theoretical results and the empirical results 331

5.4 Summary of the chapter 336

CHAPTER SIX

Conclusions

6.1 Conclusions of single-phase flow 339

6.2 Conclusions of two-phase flow 340

APPENDIX 344

REFERENCES 364

N O M E N C L A T U R E

Symbol	unit	Description	Introduced in Chapter
A	m^2	tube cross-section area	2
A	-	parameter in eq . (2.41)	2
A	-	constant in eq. (5.1.10)	5
A_t	-	constant in two-phase flow, defined by eq. (5.2.3)	5
a	m	tube radius	2
a	-	coefficient used in eq. (2.78)	2
$B_{\dot{m}}$	-	parameter defined by eq. (5.1.24c)	5
B_n	-	parameter defined by eq. (5.2.33a)	5
b	-	index used in eq. (2.78)	2
b	-	constant in eq. (5.2.1), = 150	5
C	-	parameter in eq. (2.83) and defined by eq. (2.83.4)	2
C	-	coefficient = $\partial P/H\partial\theta$	5
C	Kg/m^2	static head pressure gradient, defined by eq. (2.61)	2
C_d	Kg/m^3	mass liquid concentration in the gas phase	4
C_e	Kg/m^3	droplet concentration in the gas core	4
C_t	-	coefficient in two-phase flow, defined by eq. (5.2.3)	5
C_θ	$^oC/m$	temperature gradient in θ-direction	5
C_p	$Kcal/Kg^oC$	specific heat	4
D	-	deposition rate	4
D	-	constant in single-phase flow defined by eq. (5.1.10)	5
D_t	-	constant in two-phase flow defined by eq. (5.2.2)	5
D'	-	parameter in eq. (2.59)	2

Symbol	unit	Description	Introduced in Chapter
d	m	tube diameter = 2a	2
E	-	entrainment rate	4
E	-	parameter in eq. (5.1.90)	5
F	-	convective heat transfer correlation factor in Chen (96) correlation	4
F	-	$= \{Re(\frac{a}{R})^2\}^{0.2}$	5
F_r	m/s^2	acceleration velocity in r-direction	5
F_ψ	m/s^2	acceleration velocity in ψ-direction	5
$F(\psi)$	-	parameter in eq. (5.2.50)	5
f	-	friction factor	2
f	-	coefficient of function ψ	5
f_g	-	volumetric quality defined by eq. (2.66.1)	2
f_m	-	mean value of coefficient f	5
G	Kg/m^2s	mass velocity	2
G_{dep}	Kg/m^3	mean integral flow of deposition liquid	4
G_f	Kg/m^2s	mass velocity of liquid phase alone	2
G_g	Kg/m^2s	mass velocity of gaseous phase alone	2
Gr	-	Grashof number $=\{\beta g \Delta T d^3 \rho^2/\mu^2\}$	4
g	m/s^2	acceleration due to gravity	2
g_m	$^oC, -$	temperature difference = (T_W-T)	2
g_o	-	conversion factor in eq. (2.60)	2
Δg_m	-	parameter in eq. (2.41)	2
h	$Kcal/m^2h^oC$	heat transfer coefficient	2
h_f	$Kcal/m^2h^oC$	heat transfer coefficient for liquid flow alone	2
h_{fo}	$Kcal/m^2h^oC$	heat transfer coefficient for total flow assumed liquid	2
h_m	$Kcal/m^2h^oC$	heat transfer coefficient defined by $(T_w^* - T_m^*)$	5

Symbol	unit	Description	Introdueed in Chapter
h_{mac}	$Kcal/_{m^2hd}$	macroconvective heat transfer coefficient used in eq.(4.3.17)	4
h_{mic}	$Kcal/_{m^2h^oC}$	microconvective heat transfer coefficient used in eq.(4.3.17)	4
h_o	$Kcal/_{m^2h^oC}$	heat transfer coefficient defined by $(T_w - T_o)$	5
h_{TP}	$Kcal/_{m^2h^oC}$	two-phase heat transfer coeffieient	2
h_{TpK}	$Kcal/_{m^2h^oC}$	two-phase convective heat transfer coefficient	2
h_δ	$Kcal/_{m^2h^oC}$	heat transfer coefficient defined by $(T_w^* - T_\delta^*)$	5
i_f	$J/_{Kg}$	enthalpy of saturated liquid	4
i_{fg}	$J/_{Kg}$	latent heat of vaporization	4
J	-	parameter in eq. (5.2.50)	5
j	-	index used in eq. (2.41)	2
K	-	Dean number = $Re\ (\frac{a}{R})^{\frac{1}{2}}$	2
K	-	constant in eq. (2.87)	2
K_d	$m/_s$	mass transfer coefficient for deposition	4
K_1	-	constant	5
k	$Kcal/_{mh^oC}$	thermal conductivity	2
k_c	$Kcal/_{mh^oC}$	thermal conductivity of the Coils	3
M	-	parameter in eq. (5.1.68)	5
M	-	index or coefficient = 4 or 5	2,5
m	m	film thickness used in eq. (4.3.14)	4
$m_{0.02}$, $m_{0.1}$, etc.		values of the film thickness which are exceeded for 2%, 10% etc. of time	
		absolute pressure	5

Symbol	unit	Description	Introduced in Chapter
N_u	-	Nusselt number = $2ah/k$	
Nu_{av}	-	mean value of Nu_m averaged by ψ	5
Nu_m	-	Nusselt number = 2ahc/k	5
Nu_o	-	Nusselt number = $2ah_m/k$	5
Nu_δ	-	Nusselt number = $2ah_\delta/k$	5
ΔNu	-	parameter in eq. (2.41)	2
n	-	index (= 4)	2
n	-	index in eq. (2.85)	2
P	Kg/cm^2	pressure	
P_n	Kg/cm^2	local pressures of the test facilities (n = 0·7) shown in Fig. (3.1)	3
P^*	Kg/cm^2	pressure in Chapter 5	5
P_o^*	Kg/cm^2	pressure at the tube centre	5
P_δ^*	Kg/cm^2	pressure at the surface of boundary layer	5
Pr	-	Prandtl number (= $Cp\,\mu/k$)	
ΔP_{12}	Kg/cm^2	pressure difference in the orifice shown in Fig. (3.1)	3
ΔP_{34}	Kg/cm^2	pressure difference in the venturi shown in Fig. (3.1)	3
p	-	dimensionless pressure = $P^*/\rho w^2_m$	5
p_η	-	parameter defined by eq. (5.1.18)	5
Δp_{sat}	Kg/cm^2	saturated vapour pressure difference corresponding to ΔT_{sat}	4 4
Δp_e	Kg/cm^2	saturated vapour pressure difference corresponding to ΔT_e	4
Q	-	parameter in eq. (2.18.1) = $(K^2Pr)^{1/4}$	2
Q_f	m^3/s	volumetric rate of liquid phase flow	2
Q_g	m^3/s	volumetric rate of gaseous phase flow	2
Q_o^*	Kg/ms	liquid flow rate from the outer to inner sides in the water film	5

Symbol	unit	Description	Introduced in Chapter
Q_o	-	dimensionless Q_o^*, = $Q^*/\gamma_f \cdot W_{fm} \cdot a$	5
Q_w	$Kcal/m^2h^oC$	heat flux at the tube wall to the fluid per unit area and unit time	2
q	$Kcal/m^2h$	heat flux	2
q	-	dimensionless heat flux, $= q^*/C_p \cdot \rho \cdot g \cdot W_m \cdot a \cdot C_\theta$	5
q^*	$Kcal/m^2h$	heat flux defined by eq. (5.1.46)	5
q^*_w	$Kcal/m^2h$	heat flux at tube wall	5
q^*_r	$Kcal/m^2h$	heat flux in r-direction	5
q^*_ψ	$Kcal/m^2h$	heat flux in ψ-direction	5
q^*_θ	$Kcal/m^2h$	heat flux in θ-direction	5
R	m	coil radius	2
Ra	-	Rayleigh number = Gr·Pr	4
Re	-	Reynolds number = $2aWm^*/\nu$	
Re_b	-	Reynolds number at bulk temperature	2
Re_{cri}	-	critical Reynolds number	2
Re_f	-	liquid-phase Reynolds number = $2aW_f^*/\nu_f$	5
Re_g	-	gas-phase Reynolds number = $2aUg^*/\nu_g$	5
Re_s	-	Reynolds number in the supposed straight pipe = $2as^*/\nu$	5
Re_{fs}	-	liquid-phase Reynolds number in the supposed straight pipe = $2aS^*/\nu_f$	5
Re_{gs}	-	gas-phase Reynolds number in the supposed straight pipe = $2aS^*/\nu_g$	5
R_t	Ωm	electrical resistivity	3
r	m	co-ordinate in the radial direction in the cross-section, shown in Fig.(5.1.1)	5
S	m	tube perimeter	2
S	-	suppression factor used in Chen correlation eq. (4.3.22)	4

Symbol	unit	Description	Introduced in Chapter
S^*	$^m/_s$	velocity in the supposed straight pipe	5
S	-	dimensionless velocity $= S^*/_{Wm}$	5
S_c	-	correction factor in eq. (5.1.50)	5
S_m^*	$^m/_s$	mean velocity in the supposed straight pipe	5
S_m	-	dimensionless velocity = S_m^*/w_m	5
S_r	-	dimensionless resultant velocity of w_s and v_s	5
T	^oC	temperature	
T^*	^oC	temperature defined by eq.(5.1.46)	5
T	-	dimensionless temperature = $T^*/aC\theta$	5
T^*_B	^oC	temperature at the surface of laminar sub-layer	5
Tc^*	^oC	temperature at the tube centre	5
T_m^*	^oC	mixed mean temperature	5
T_n	^oC	local temperatures of the test facilities (n=0~6) shown in Fig.(3.1)	3
Tsat	^oC	saturation temperature	2
T_w^*	^oC	tube wall temperature	5
$T\delta^*$	^oC	temperature at the surface of boundary layer	
Tsat	^oC	saturation temperature	2
ΔT	^oC	temperature difference between inside wall and fluid	4
ΔTe	^oC	effective superheat into which bubble growth	4
$\Delta Tsat$	^oC	wall superheat	4
U	$^m/_s$	velocity component in r-direction	5
U	$^m/_s$	slope of the velocity profile at specific point in the flow in eq. (2.75)	2

Symbol	unit	Description	Introduced in Chapter
U	-	dimensionless velocity in r-direction = U/W_m	5
V	m/s	velocity component in ψ-direction	5
v	m/s	mean velocity in the neutral position in Fig. (2.22)	2
v	-	dimensionless velocity in ψ-direction = V/w_m	5
v_o	m/s	superficial linear velocity	2
v_s^*	m/s	maximum value of V in the boundary layer	5
v_δ^*	m/s	velocity in ψ-direction at the surface of boundary layer	5
$v_{f\delta}^*$	m/s	velocity in ψ-direction at the liquid film surface	5
$v_{f\delta}$	-	dimensionless velocity = $v_{f\delta}^*/w_{fm}$	5
v_δ^*	m/s	velocity in ψ-direction at the surface of gas-phase boundary layer	5
$v_{g\delta}$	-	dimensionless velocity = $v_{g\delta}^*/w_{gm}$	5
W	m/s	velocity component in θ-direction	5
Wg	Kg/h	gas-phase flow rate	2
W_m	m/s	fluid mean velocity	4
w	-	dimensionless velocity in θ-direction = W/w_m	
w_m	m/s	mean velocity in θ-direction	5
w_s^*	m/s	value of W when V = v_s^* at η= ns	5
w_δ^*	m/s	velocity in θ-direction at the surface of boundary layer	5
w_{fo}	m/s	superficial liquid velocity	2
w_{go}	m/s	superficial air velocity	2
w_{fm}^*	m/s	superficial liquid-phase velocity (volumetric flow/sectional area)	5
w_{gm}^*	m/s	superficial gas-phase velocity	5

Symbol	unit	Description	Introduced in Chapter
$(w^*_{fm})_{film}$	m/s	superficial liquid velocity in θ-direction in the liquid film	5
$w^*_{f\delta}$	m/s	velocity in θ-direction at the liquid film surface	5
$w_{f\delta}$	-	dimensionless velocity = $w^*_{f\delta}/w^*_{fm}$	5
$w^*_{g\delta}$	m/s	velocity in θ-direction at the surface of gas-phase boundary layer	5
$w_{g\delta}$	-	dimensionless velocity = $w^*_{g\delta}/w^*_{gm}$	5
X_{tt}	-	Lockhart-Martinelli parameter defined by eqs. (2.55) and (2.78)	2
x	-	steam quality	2
x_{crit}	-	critical steam quality	2
Y	-	parameter in eq. (2.36) and eq. (5.1.63)	2,5
y	-	parameter in eq. (2.83.2)	2
Z	m	pipe length	2
Z	-	parameter in eqs. (2.66), (2.83) and (5.1.63)	2,5
Z_m	-	mean value of Z in eq. (5.1.63)	5
GREEK FIGURES			
α	-	void fraction	2
α	-	proportional coefficient in eq.(2.29)	2
α	m^2/s	thermal diffusivity	4
α_g	-	constant (= 0.316)	
β	$1/^oC$	coefficient of expansion	4
$\Gamma_{cent.}$	-	parameter of centrifugal force term in eq. (5.2.49)	5
$\Gamma_{iner.}$	-	parameter of the inertia term in eq. (5.2.49)	5

Symbol	unit	Description	Introduced in Chapter
γ	$Kg/_{m}3$	specific weight	5
δ	m	thickness of the velocity boundary dary layer	2
δ_t	m	thickness of the thermal boundary layer	2
δ^*	m	boundary layer thickness	5
δ	-	dimensionless boundary layer thickness = δ^*/a.	
δ_b^*	m	thickness of laminar sub-layer	5
δ_f^*	m	liquid film thickness	5
δ_g^*	m	gas-phase boundary layer thickness	5
δ_o^*	m	mean boundary layer thickness	5
	m	thermal boundary layer thickness	5
δ_{fm}^*	m	averaged film thickness by ψ	5
δ_{gm}^*	m	averaged gas boundary layer thickness by ψ	5
ε_H	m^2/s	eddy diffusivity of heat	5
ε_M	m^2/s	eddy diffusivity of momentum	5
ζ	-	thickness ratio defined by eq.(2.15)	2
H	-	= R/a	5
η	-	= 1-ξ	5
η_s	-	maximum value of η	5
θ	rad.	angle to horizontal plane	2
θ	rad.	axial co-ordinate shown in Fig.(5.1.1)	5
$\Lambda_{\delta-\delta}$	-	parameter defined by eq. (5.1.26a)	5
λ	-	liquid fraction input flow in eqs. (2.56) - (2.58)	2
λ	-	factor used in Baker flow pattern chart defined by eq.(2.71)	2

Symbol	unit	Description	Introduced in Chapter
μ	$Kg.s/m^2$	viscosity	
μ_m	$Kg.s/m^2$	mixture viscosity	2
ν	m^2/s	kinetic viscosity	4
ξ	-	$= r/a$	5
ρ	Kg/m^3	density	2.4.5
σ	N/m	surface tension	2.4.5
τ	Kg/m^2	shear stress	2
τ^*	Kg/m^2	shear stress	5
τ	-	dimensionless shear stress = $\tau^*/\rho w_m^2$	5
τ_i	Kg/m^2	interfacial shear stress	4
τ_s^*	Kg/m^2	shear stress in axial direction in the supposed straight pipe	5
τ_w^*	Kg/m^2	shear stress in θ-direction at the tube wall	5
$\tau_{r.\theta}$	Kg/m^2	shear stress in θ direction shown in Fig. (5.1.1)	5
$\tau^*_{\theta.\psi}$	Kg/m^2	shear stress in θ-ψ direction shown in Fig. (5.1.1)	5
$\tau^*_{\psi.r}$	Kg/m^2	shear stress in ψ-r direction shown in Fig. (5.1.1)	5
	rad	angle shown in Fig. (2.22)	2
ϕ_f^2	-	two-phase frictional multiplier $= (\frac{dP}{dz})_{TP}/(\frac{dP}{dz})_f$	2
ϕ_g^2	-	two phase frictional multiplier $= (\frac{dP}{dz})_{TP}/(\frac{dP}{dz})_g$	2
ϕ_{fo}^2	-	two-phase frictional multiplier based on pressure gradient for total flow assumed fliquid	2

Symbol	unit.	Description	Introduced in Chapter
ψ	-	factor used in Baker flow pattern chart defined by eq.(2.72)	2
ψ	rad	circumferential co-ordinate in cross-section shown in Fig.(5.1.1)	5
$(\frac{dP}{dz})$	$Kg/m^2.m$	pressure gradient	2,4
$(\frac{dP}{dz}_A)$	$Kg/m^2.m$	acceleration pressure drop	4
$(\frac{dP}{dz}_F)$	$Kg/m^2.m$	frictional pressure drop	4

SUBSCRIPTS AND ABBREVIATIONS

I,II	First or second approximation
0, 1, 2, 3...	referring to sections 0, 1, 2....
A	air or acceleration component
ave.	average
b	bulk or boundary layer
c	coils or helical-coiled tubes
Cr	critical
cent.	centrifugal
DNB	departure from nucleate boiling
F	friction component
f.	liquid phase or film
fH	liquid phase flow in helically coiled tube
fm	superfacial liquid phase flow
fo	total flow assumed liquid
fs	liquid phase flow in the supposed straight pipe
f_δ	liquid film surface
G	gravity component
g	gas phase
gH	gas phase in helically coiled tube
gm	superficial gas phase flow
g_δ	gas phase boundary layer

H	helically-coiled tube
h	uniform heat flux in the circumferential direction
i	interfacial
iner.	inertia
m	mean or coefficient (=4)
mac.	macroconvective
mic.	microconvective
o	tube wall inner surface
r	resultant or r-direction
s	straight pipe or supposed straight pipe
sat	saturation
TP	two-phase flow
TPF	friction component of two-phase flow
TPK	two-phase convective flow
t	turbulent flow, thermal boundary layer
	or uniform wall temperature in the ψ-direction
tt	liquid turbulent/gas turbulent
turb.	turbulent flow
vt	liquid viscous/gas turbulent
W	water
w	tube inner wall
δ	boundary layer
θ	θ-direction or temperature difference
ψ	ψ-direction

PREFIXES AND SUPERSCRIPT

d	differential
∂	partial differential
o,-	denotes average property

LISTS OF FIGURES AND TABLES

Fig. Number	Title	Introduced Section
2.1	Flow pattern of the secondary flow for small K (<17), from Dean (1).	2.2.1
2.2	Flow pattern of the secondary flow for large K, from Mori and Nakayama (5).	2.2.1
2.3	Comparison of laminar friction factors.	2.2.1
2.4	Velocity profiles in laminar flow, from Mori and Nakayama (5).	2.2.2
2.5	Stream-function contours, from Austin & Seader (18).	2.2.2
2.6	Comparison of velocity profile in horizontal plane between Akiyama & Cheng and Adler (16).	2.2.2
2.7	Temperature profiles in horizontal and vertical planes, by Mori & Nakayama (5).	2.2.3
2.8	Temperature profile in laminar flow, by Kalb & Seader (21).	2.2.3
2.9	Profile of local heat transfer coefficients in laminar flow (a) small coil ($^{R}/a$ = 16.4) (b) large coil ($^{R}/a$ = 104).	2.2.4
2.10	Comparison of heat transfer coefficients.	2.2.4
2.11a	Friction factor for turbulent flow, from Ito (25).	2.4.1

Fig. Number	Title	Introduced Section
2.11b	Comparison of friction factors Ito's results with Seban & McLaughlin's results.	2.4.1
2.12	Comparison of fully-developed axial velocity profiles along vertical and horizontal plane (a) Re = 6.8×10^4 $R/a = 25.9$ (b) Re = 2.5×10^4 $R/a = 40.0$, from Pratap (34).	2.4.2
2.13	Temperature profile in the fully-developed turbulent flow, from Mori & Nakayama (24).	2.4.2
2.14	Comparison of predicted fully-developed temperature profiles with experimental results, from Pratap (34).	2.4.2
2.15	Turbulent heat transfer coefficients (a) large coil ($R/a = 104$) (b) small coil ($R/a = 16.4$).	2.4.3
2.16	Comparison of turbulent heat transfer coefficients.	2.4.3
2.17a,b	Pressure drop in two-phase flow, from Rippel et al (41).	2.5.1
2.18	Hold-up in spiral coil compared with data from horizontal flow, from Rippel et al (41).	2.5.1
2.19	Two-phase flow pressure drops (a) Effect of coil angle (b) Effect of coil radius, from Banerjee et al (39).	2.5.1

Fig. Number	Title	Introduced Section
2.20a,b	Two-phase flow pressure drop (a) small coil ($^{R}/a = 20.0$), from Owhadi et al (47). (b) similar coil ($^{R}/a = 33.3$), from Kozeki (48).	2.5.1
2.21	Flow patterns in helically-coiled tubes (a) from Boyce et al (42) (b) from Banerjee et al (39) (c) from Kozeki et al (53) (d) from Farmer (54).	2.5.2
2.22	Film invasion phenomenon, from Banerjee (55).	2.5.2
2.23	Liquid film movement at various gas mass flow rates.	2.5.2
2.24	Local heat transfer coefficients for two-phase flow, from Owhadi et al (47).	2.5.3
2.25	Correlation of h_{TP}/h_f in helically-coiled tube, from Owhadi et al (47) (a) small coil ($^{R}/a = 20.0$) (b) large coil ($^{R}/a = 41.8$).	2.5.3
2.26	Effect of coiled tube on departure of nucleate boiling (DNB), from Carver et al (68).	2.5.4
2.27	Dryout steam qualities, from Kozeki et al (48.53).	2.5.4
3.1	Schematic diagram of the test facility.	3.1
3.2	Diagram of the steam-water mixer.	3.2.2

Fig. Number	Title	Introduced Section
3.3 a,b,c	Configurations of coils (A,B,C).	3.4
3.4a,b	Thermocouple distributions on the tube surface.	3.7
3.5	Thermocouple for measuring bulk temperature.	3.7
3.6	Arrangement of measuring devices.	3.8
4.2.1 a,b,c	Wall temperature profiles along the pipe length for water single-phase flow at 3.42×10^5 Kg/m^2h flow rate and at 934, 2102 and 3736 $Kcal/m^2h$ heat fluxes. (a)-coil A, (b)-coil B, (c)-coil C.	4.2.1.2
4.2.2 a,b,c	Wall temperature profiles along the pipe length for water single-phase flow at 1.71×10^5 Kg/m^2h flow rate and at 934, 2102 and 3736 $Kcal/m^2h$ heat fluxes (a)-coil A, (b)-coil B, (c)-coil C.	4.2.1.2
4.2.3	Secondary flow streamlines in water laminar flow.	4.2.1.2
4.2.4	Oscillating wall temperature profiles at similar condition to Fig. (4.2.1a).	4.2.1.2
4.2.5	Effect of buoyancy force, Rayleigh number - Reynolds number.	4.2.1.2
4.2.6 a,b,c	Local heat transfer coefficients in the tube cross-section of water flow at 3.42×10^5 Kg/m^2h and at 934, 2102 and 3736 $Kcal/m^2h$ heat fluxes (a)-Coil A, (b)-Coil B, (c)-Coil C.	4.2.1.3

Fig. Number	Title	Introduced Section
4.2.7 a,b,c	Local heat transfer coefficients in the tube cross-section of water flow at 1.71 x 10^5 Kg/m^2h and at 934, 2102 and 3736 $Kcal/m^2h$ (a)-Coil A, (b)-Coil B, (c)-Coil C.	4.2.1.3
4.2.8	Local heat transfer coefficient distributions in the tube cross-section. Values are obtained from Figs. (4.2.6) and (4.2.7).	4.2.1.3
4.2.9	Comparison of heat transfer coefficient of this work with Seban & McLoughlin's data.	4.2.1.3
4.2.10	Ratio of heat transfer coefficient between the outer and inner sides (water flow).	4.2.1.3
4.2.11	Pressure drops of present work for steam flow.	4.2.2.1
4.2.12 a,b,c	Wall temperature profile along the pipe length for steam single-phase flow at 1.64 x 10^5 ~ 1.84 x 10^5 Kg/m^2h flow rates and at 412, 934 and 1660 $Kcal/m^2h$ heat fluxes. (a)-Coil A, (b)-Coil B, (c)-Coil C.	4.2.2.2
4.2.13 a,b,c	Wall temperature profile along the pipe length for steam single-phase flow at 8.55 x 10^4 ~ 9.57 x 10^4 Kg/m^2h flow rates and 412, 934 and 1660 $Kcal/m^2h$ (a)-Coil A, (b)-Coil B, (c)-Coil C.	4.2.2.2

Fig. number	Title	Introduced Section
4.2.14 a,b,c	Local heat transfer coefficients in the tube cross section at $1.64 \times 10^5 \sim 1.84 \times 10^5$ Kg/m^2h steam flow rates and at 412, 934 and and 1660 $Kcal/m^2h$ heat fluxes. (a)-Coil A, (b)-Coil B, (c)-Coil C.	4.2.2.3
4.2.15 a,b,c	Local heat transfer coefficients in the tube cross section at $8.55 \times 10^4 \sim 9.57 \times 10^4$ Kg/m^2h steam flow rates and at 412, 934 and 1660 $Kcal/m^2h$ heat fluxes. (a)-Coil A, (b)-Coil B, (c)-Coil C.	4.2.2.3
4.2.16	Local heat transfer coefficients in the tube cross-section of steam single-phase flow.	4.2.2.3
4.2.17	Comparison of heat transfer coefficients of this work with Seban & McLaughlin (22).	4.2.2.3
4.2.18	Ratio of heat transfer coefficient between the outer and inner sides (steam flow).	4.2.2.3
4.3.1 a,b	Wall temperature profile at various water flow rates (a) at 16.06×10^4 Kg/m^2h, (b) at 9.91×10^4 Kg/m^2h.	4.3.1
4.3.2	Model of wall temperature profile to determine the flow patterns.	4.3.1
4.3.3 a,b,c,d	Flow patterns of the present experiment on the Baker Map (a)-Coil A, (b)-Coil B, (c)-Coil C, (d) for full scale.	4.3.1

Fig. Number	Title	Introduced Section
4.3.4 a,b,c,d	Flow patterns of the present experiment on Goldmann's Map. (a)-Coil A, (b)-Coil B, (c)-Coil C, (d) for full scale.	4.3.1
4.3.5	Comparisons of the present data of two-phase flow pressure drop with the two-phase frictional multiplier, ϕ_{gtt}.	4.3.2
4.3.6	Two-phase flow pressure drops from three investigators.	4.3.2
4.3.7 a-e	Wall temperature profiles along the pipe length for Coil A at various total flow rates and at 7399 $Kcal/m^2h$ heat flux.	4.3.3
4.3.8a f	Wall temperature profiles along the pipe length for Coil B at various total mass flow rates and at 7951 $Kcal/m^2h$ heat flux.	4.3.3
4.3.9 a g	Wall temperature profiles along the pipe length for Coil C at various total mass flow rates and at 7942 $Kcal/m^2h$ heat flux.	4.3.3
4.3.10	Wall temperature values of four positions at 1,2,3,4 and 5m from the test section entrance for four flow conditions.	4.3.3
4.3.11	Position of film flow in stratified flows, from Whalley and Wiliam (88).	4.3.3
4.3.12	Entrainment correlation, from Whalley et al (93).	4.3.3

Fig. number	Title	Introduced Section
4.3.13	Variation of deposition coefficient with surface tension, from Whalley et al (93).	4.3.3
4.3.14	Effects of secondary flow force on the liquid surface.	4.3.3
4.3.15	Twin-helix flow, from Lacey (58).	4.3.3
4.3.16	Temperature profiles for pool boiling and for convective boiling with same superheat from Chen (96).	4.3.4
4.3.17 a,b,c	Local heat transfer coefficient profiles for two-phase flow against steam quality, (a)-Coil A, (b)-Coil B, (c)-Coil C.	4.3.4
4.3.18 a,b,c	Ratio of heat transfer coefficients between two-phase flow and liquid-single-phase flow. against $(^1/X_{tt})$. (a)-Coil A, (b)-Coil B, (c)-Coil C.	4.3.4
4.3.19	Comparison of the heat transfer coefficient ratio of the present work with other investigators.	4.3.4
4.3.20 a,b,c,d	Onset of burnout in Coil A at various heat flux. (a) at $3.7 \times 10^{3Kcal}/m^2h$ (b) at $5.1 \times 10^{3Kcal}/m^2h$ (c) at $6.6 \times 10^{3Kcal}/m^2h$ (d) at $8.4 \times 10^{3Kcal}/m^2h$.	4.3.5
4.3.21 a,b,c,d	Onset of burnout in Coil B at various heat flux. Heat flux is the same as (4.3.20).	4.3.5

Fig. number	Title	Introduced Section
4.3.22 a,b,c,d	Onset of burnout in Coil C at various heat flux. Heat flux is the same as (4.3.20).	4.3.5
4.3.23	Burnout heat flux of four positions in different Coils.	4.3.5
4.3.24	Heat flux profiles at (T_{sat} + 10°C) in three coils.	4.3.5
4.3.25	Comparison of average DNB quality at 2600 psia, from Carver et al (68).	4.3.5
4.3.26 a,b,c	Positions of burnout on Baker map (a)-Coil A, (b)-Coil B, (c)-Coil C.	4.3.5
4.3.2.7	Positions of burnout at different pressures and mass flow rates.	4.3.5
5.1.1	Coordinate system for helically-coiled circular tube.	5.1.1
5.1.2	Single-phase flow model.	5.1.1
5.1.3	Comparison of single-phase pressure drop between the present theory and other works.	5.1.1
5.1.4	Mean thickness of boundary layer.	5.1.1
5.1.5	Velocity profiles in horizontal and vertical planes of the theoretical work.	5.1.1
5.1.6	Energy balance in r.ψ directions of the fluid.	5.1.2
5.1.7	Theoretical and empirical temperature profiles in the core flow.	5.1.2

Fig. number	Title	Introduced section
5.1.8	Theoretical Nusselt number ratios at S_c = 0.585 and at S_c = 1.0.	5.1.2
5.1.9	Comparison of Nusselt numbers between theory and other investigators.	5.1.2
5.1.10	Influence of Prandtl number on Nusselt numbers.	5.1.2
5.1.11 a,b,c	Comparison between the theoretical and empirical heat transfer coefficients (a)-Coil A, (b)-Coil B, (c)-Coil C.	5.1.2
5.1.12	Heat transfer coefficients at various S_c and at Re = 44040 and Re= 23940.	5.1.2
5.1.13	Temperature profiles in the coreflow at different Dean numbers, from Pratap (34).	5.1.2
5.1.14	Comparison between the theoretical average heat transfer coefficient taken from eq's (5.1.82) and (5.1.92) and empirical results at the inner and outer sides.	5.1.2
5.2.1	Model of annular two-phase flow.	5.2.2
5.2.2	Relation between $F(\psi)$ of eq. (5.2.50) and liquid film thickness.	5.2.4.1
5.2.3	Liquid film profiles from eq. (5.2.51) of air-water mixture in Coils A and C (a) high air-low water flow (b) high air-middle water flow.	5.2.5
5.2.4	Comparison of liquid film profiles from eq.(5.2.51) with results of Whalley and Wiliams (88).	5.2.5

Fig. number	Title	Introduced Section
	(a) W_{gm} = 29.3^{m}/s and W_{fm} = 0.045^{m}/s (b) W_{gm} = 48.3^{m}/s and W_{fm} = 0.045^{m}/s .	
5.2.5	Liquid film profiles at 2.713 x 10^{5} $^{Kg}/_{m^2h}$ total flow rates in Coil C (a) at 2 bars (b) at 40 bars.	5.2.5
5.2.6	Comparison of local heat transfer coefficient profiles between theoretical results from eq. (5.2.60) and empirical results. (a) the present work at about 2 bars (b) Kozeki's result (48,80) at 20 bars.	5.3.1

TABLES

Table Number	Title	Introduced Section
2.1	Coefficients in convective heat transfer equation.	2.5.3
3.1	Definitions of three helically-coiled tubes.	3.4
4.3.1	Categories of mass flow rates of steam and water.	4.3.3
4.3.2	Coefficients in convective heat transfer equation from experimental work.	4.3.4

C H A P T E R 1

INTRODUCTION

A steam generator is one of the major components of the marine engine and of both nuclear and conventional power stations, and it strongly influences their overall performance.

Helically-coiled tubes have a few disadvantages such as manufacturing and maintenance difficulties, on the other hand the advantages of the helically-coiled tubes are that it is more compact as a unit and has a larger surface area of heat exchange and better absorption of heat expansion than a straight tube. Therefore in recent years interest in the helically-coiled tube has grown. This interest has led to deeper research into the subject being needed in two areas of application in particular. Firstly, in the case of helically-coiled tube in once-through high pressure boilers for nuclear and conventional power stations, where the rate of heat transfer used is close to the limiting heat flux conditions. Secondly in the development of coiled tubular chemical reactors which make use of the very vigorous mixing of the phases.

Two-phase flows in curved ducts, bends or coiled tubes with a circular section found in many industrial applications exhibit phenomena that although experienced for a long time, have so far been understood only superficially.

Up to the present a considerable amount of information has been reported on single-phase flow characteristics in helically-coiled tubes such as pressure drop, velocity and temperature distributions, heat transfer coefficient and critical heat flux, etc. (e.g. Dean (1), Adler (2), Barua (3), Seban and McLaughlin (22), Ito (6,25) and Mori and

Nakayama (5,24)). For two-phase flow there are the same characteristics as for single-phase flow with addition of flow pattern and burnout (e.g. Carver et al (68), Banerjee et al (39), Owhadi et al (47), Lacey (58), Akagawa et al (8), Kozeki (48, 53.80) and Whalley and Wiliams (88)).

The object of the present work is not to assemble all the literature in the field, but to focus attention on the detailed flow mechanisms. The subject particularly of annular two-phase flow in helically-coiled tubes presents many difficulties both experimentally and theoretically.

In the present experiments, special attention was given to the following:

- Two-phase flow patterns,
- Wall temperature profiles along the tube length,
- Local heat transfer coefficient in flow boiling,
- Burnout phenomena

For the theoretical analysis, firstly we divided an annular flow into a central gas core, a gas boundary layer and the liquid film. In general the liquid film is affected by the pressure profile, centrifugal forces, circumferential shear stress and tube wall shear stress. The liquid film is distributed around the wall by the balance of these forces. We studied the circumferential liquid film profiles using the force balance equation and several assumptions. Secondly, the mechanism of the flow boiling heat transfer was thought to be convective boiling in the liquid film. The theoretical local boiling heat transfer coefficient was derived using the liquid film thickness and liquid velocity at the film surface.

Five years ago (1976) the author became very interested and decided to concentrate on this subject when he saw the figure of the twin-helical flow structure in a coiled tube reported by Lacey (58) and the fascinating photographs of annular films with droplets in the gas core in a vertical tube taken by Hewitt (59).

C H A P T E R 2

A Review of Literatures

2.1 Introduction

This chapter contains a review of some relevant literature on various phenomena of single and two phase flows in helically-coiled tubes.

In the present work the heat transfer coefficient of single phase flow, the flow patterns and the heat transfer coefficient of two-phase flow and dryout phenomena in the helically-coiled tubes are described by the author. The mechanisms of these flow characteristics are complex and result from a combination of many separate factors. The most important of these factors are stream characteristics, boiling characteristics, the heterogeneity of the annular film adjacent to the tube, slip between vapour and liquid, entrainment and deposition and dryout characteristics.

2.2 Laminar Single-phase flow

2.2.1 General concept and pressure drop in laminar flow

The flow in curved pipes is characterised by a secondary flow in a cross-sectional plane normal to the main flow, and the consequent double spiral flow. The increase in resistance observed in this type of flow has attracted the attention of many investigators.

The first theoretical study was done by Dean (1-1927) for fully developed laminar flow. Using a perturbation method he tried to find the deviation of a velocity profile from the Poiseuille flow pattern by solving the Navier-Stokes equations. He pointed out that a secondary flow is set up and dynamical similarity introduces a parameters

$$K = Re \cdot \left(\frac{a}{R}\right)^{\frac{1}{2}} , \qquad (2.0)$$

which is called Dean number, where Re is Reynolds number, a is the tube radius and R is the coil radius. However, his solution is applicable only in quite small Dean number regions (K < 17), the flow pattern by his analysis is shown in Fig. (2-1), and his formula for the resistance coefficient is not useful enough for practical use. The following equation for friction factor comes from his work;

$$\frac{f_c}{f_s} = 1 - (0.03058)\ 2Re\{(\frac{a}{R})^2/_{576}\}^2 + (0.01195)\{2Re\ (\frac{a}{R})^2/_{576}\}^4 \qquad (2.1)$$

where f_c is a friction factor of the coil and f_s is a friction factor of the straight tube.

Adler (2-1934) closely examined the velocity distributions by experiment, and found that a velocity profile of fully developed laminar flow differs greatly from the parabolic distribution. This led Adler (2) to consider the effect of the thin boundary layer along the wall. His formula for the resistance coefficient asymptotically approaches to the observed results for very large Dean numbers.

The same assumption of a boundary layer is employed by Barua (3-1962) and he put forward theoretical formula which he compared with Hasson's empirical result (4-1955) and concluded that the first two terms of the series were accurate.

Mori and Nakayama (5-1965) solved the governing equations by integral methods, subdividing the flow pattern into a central core and a boundary layer region. They obtained a flow pattern for the large Dean number region, as shown in Fig. (2.2).

A similar analysis was performed by Ito (6-1970).

These works resulted in the following expressions for $\frac{fc}{fs}$;

White (7-1929)

$$\frac{f_c}{f_s} = \left[1 - \{1 - (\frac{11.6}{K})^{0.45}\}^{2.22}\right]^{-1} \quad (2.2)$$

Adler (2-1934)

$$\frac{f_c}{f_s} = 0.1064K^{\frac{1}{2}} \quad (2.3)$$

Hasson (4-1955)

$$\frac{f_c}{f_s} = 0.0969K^{\frac{1}{2}} + 0.556 \quad (2.4)$$

for $30 < K < 2.000$

Barua (3-1962)

$$\frac{f_c}{f_s} = 0.09185K^{\frac{1}{2}} + 0.5093 + 1.413K^{-\frac{1}{2}} + 2.321K^{-1} + 2.012K^{-3/2} \quad (2.5)$$

Mori and Nakayama (5-1965)

$$\frac{f_c}{f_s} = \frac{0.108K^{\frac{1}{2}}}{1-3.253K^{-\frac{1}{2}}} \quad (2.6)$$

Ito (6-1970)

$$\frac{f_c}{f_s} = 0.1033K^{\frac{1}{2}}(1+3.945K^{-\frac{1}{2}}+7.782K^{-1}+9.097K^{-3/2}+5.608K^{-2}) \quad (2.7)$$

for $30 < K$

Akagawa et al (8-1971)

$$\frac{f_c}{f_s} = \left[1 - \{1 - (\frac{11.6}{K})^{0.45}\}^{2.22}\right]^{-1} \times 0.0049Re^{0.75} \quad (2.8)$$

for $2000\sim3000 < Re < Re_{critical}$

Akiyama and Cheng (9-1971) predicted the fully-developed flow by solving the finite difference equations, stream function and axial velocity. Fig. (2.3) shows their numerical analysis and the experimental and theoretical data available in the literature. Their result agrees with the experimental data of White (7) and Ito (6) from relatively small to high Dean number, while the predictions based on boundary layer approximation Adler (2), Barua (3) and Mori and Nakayama (5) led to an incorrect trend in the low Dean number region. Ito's prediction is generally acceptable for the range of Dean numbers under consideration, but has some errors in the lower parameter range.

2.2.2 Velocity profiles in laminar flow

In an investigation of the fully-developed region, the measurements were mostly made of the friction factors and overall heat transfer rates. Only in a few cases (Adler (2), Hawes (10-1932) and Mori and Nakayama (5) results shown in Fig. (2.4) have the distributions of velocity and temperature been measured.

The experimental apparatus and techniques used in these investigations have been quite similar (each using a hot wire anemometry), but the range of flow parameters such as the Reynolds number, radius ratio of the coil etc. differed in each case.

Austin (11-1971) measured the velocity using hot-film anemometry whereas Olson (12-1971) employed a pulsed-wire technique and Humphrey (13-1977) employed a laser-Doppler velocimeter.

Several theoretical attempts have been made by Dean (1, 14-1928), McConalogue and Srivastava (15-1968), Truesdell and Adler (16-1970), Akiyama and Cheng (9), Patankar et al (17-1974), Austin and Seader (18-1973) and Humphrey (13) to solve the equation of fluid motion for the case of toroidal flow. From these works velocity profiles were

obtained, with similar results except for the velocity profile in boundary layer.

The numerical stream function contours at different Dean numbers and radius ratios by Austin and Seader(18) are shown in Fig. (2.5).

A comparison of Adler's experimental data with Akiyama and Cheng's prediction is shown in Fig. (2.6). Austin and Seader concluded that the model streamline of Mori and Nakayama (5) for a Dean number of 400 and a large curvature ratio, Fig. (2.2) are seen to differ significantly from the results of numerical solution, Fig. (2.5). The agreement between the experimental data of Mori and Nakayama (5) and numerical solution of Austin and Seader (18) was in agreement with velocity profile in the horizontal plane, the numerical results for vertical plane were within their data scatter.

2.2.3 Temperature profile in laminar flow

Mori and Nakayama (5) measured the temperature profile for vertical and horizontal planes and have shown the temperature profiles at Prandtl number Pr = 0.7 and Dean number K = 632 in Fig. (2.7). They defined the difference between the wall temperature (Tw) and the mixed mean temperature (Tm) when the value at the edge of the thermal boundary layer (δ_t) is bigger than the value at the edge of the velocity boundary layer (δ), i.e. $\delta_t > \delta$.

Akiyama and Cheng (9), Dravid et al (19-1971) and Kalb and Seader (20-1972, 21-1974) have predicted the temperature profiles for the same Prandtl number (Pr = 0.7) as Mori and Nakayama (5) and higher Prandtl numbers (Pr = 1, 5 and 1600 respectively) in the fully-developed region by numerical methods. From these results, Mori and Nakayama predicted temperature profiles in case of Pr = 0.7, which varied ~~with~~ to the results of Akiyama and Cheng (9) and Kalb~~ana~~ and Seader (20, 21), Fig. (2.8) which

obtained by Kalb and Seader (21) and shows the different temperature profile in the central flow region from Fig. (2.7). The temperature profile for Prandtl numbers higher than 0.7 along the central vertical axis exhibits a saddle shape in the central region, indicating a rather dominant convective motion therein. The thermal boundary condition was found to have a significant effect on the temperature field obtained using numerical analysis. Fig. (2.8) also compares the results for K=512 and Pr = 0.7 with the corresponding temperature profiles obtained for axially uniform wall heat flux with peripherally uniform wall temperature. The most striking difference is that of the temperature profiles with a Prandtl number of 0.7. There is an increased degree of concavity in the central region of the tube for the uniform-wall-temperature case, and there is a greater spread in the local temperature derivatives at the wall from inner to outer walls for the uniform-wall-temperature boundary condition. These differences are less marked at higher Prandtl numbers than 0.7.

2.2.4 Heat transfer coefficient of laminar flow

2.2.4.1 For axially uniform wall heat flux

The definition of Nusselt number (Nu) is given by:

$$Nu = \frac{2a.q}{k(T_w - T_m)} \qquad (2.9)$$

where a is the tube radius, q is the heat flux, k is the thermal conductivity, T_w is the wall temperature and T_m is the mixed mean temperature.

The laminar Nusselt number for a straight pipe is $\frac{48}{11}$ therefore the ratio of Nusselt number for a curved pipe to that for a straight pipe is written that:

$$\frac{Nuc}{Nus} = \frac{11}{48} \cdot \frac{2a.q}{k(T_w - T_m)} \qquad (2.10)$$

where Nue and Nus are the Nusselt numbers of curved and straight pipes.

MORI and NAKAYAMA (5) have made a theoretical analysis of laminar flow heat transfer inside coils using the perturbation technique and obtained the following equations for the first and second approximations respectively;

$$\left(\frac{Nu_c}{Nu_s}\right)_I = 0.1979\ \frac{K^{\frac{1}{2}}}{\zeta} \qquad (2.11)$$

for $\delta_t > \delta$ and $\delta_t < \delta$ as the first approximation where ζ is the thickness ratio defined as eq.(2.15).

For the second approximation, for the case $\delta < \delta_t$ and $Pr > 1$, and $\delta > \delta_t$ and $Pr < 1$ respectively:

$$\left(\frac{Nu_c}{Nu_s}\right)_{II} = \left(\frac{Nu_c}{Nu_s}\right)_I \cdot \frac{1}{1+\frac{37.05}{\zeta}\left\{\frac{1}{40} - \frac{17}{120}\zeta + \left(\frac{1}{10\zeta} + \frac{13}{30}\right)\frac{1}{10Pr}\right\}^{-\frac{1}{2}}} \qquad (2.12)$$

$$\left(\frac{Nu_c}{Nu_s}\right)_{II} = \left(\frac{Nu_c}{Nu_s}\right)_I \cdot \frac{1}{1-\frac{37.05}{\zeta}\left\{\frac{2}{\pi 12} + \frac{1}{24} - \frac{1}{120\zeta}\left(\frac{4}{3}\zeta - \frac{1}{3\zeta} + \frac{1}{15\zeta^2}\right)\frac{1}{20Pr}\right\}K^{-\frac{1}{2}}} \qquad (2.13)$$

where the ratio of the thermal and velocity boundary layer thickness, ζ is given by the following two equations:

$$\zeta = \frac{2}{11}\left\{1 + \left(1 + \frac{77}{4Pr^4}\right)^{\frac{1}{2}}\right\} \qquad (2.14)$$

since $\zeta \leq 1$, $Pr \geq 1$

and

$$\zeta = \frac{1}{5}\left[2 + \left\{\left(\frac{10}{Pr^2}\right) - 1\right\}^{\frac{1}{2}}\right] \qquad (2.15)$$

since $\zeta \geq 1$, $Pr \leq 1$.

Seaban and McLaughlin (22-1963) attempted to measure local heat transfer coefficient in the thermal entrance region of helically coiled tubes as a function of circumferential and axial positions on the tube wall. Fig. (2.9) shows the profiles of local heat transfer coefficients for small and large coils. They have reported the following equation from Fig. (2.9a).

$$Nu_c = 0.023\ Re^{0.85} Pr^{0.4} \tag{2.16}$$

Dravid et al (19) recommended the following empirical correlation for the fully developed Nusselt number:

$$Nu_c = (0.65K^{\frac{1}{2}} + 0.76) \cdot Pr^{0.175} \tag{2.17}$$

for $50 \leq K \leq 200$ and $5 \leq Pr \leq 175$.

Akiyama and Cheng (23-1972) obtained the Nusselt number by considering either the wall-velocity and temperature gradients, or the overall force and energy balances.

$$\frac{Nu_c}{Nu_s} = 0.27\ Q\ (1 - \frac{1.48}{Q} + \frac{23.2}{Q^2} - \frac{120}{Q^3} + \frac{212}{Q^4}) \tag{2.18}$$

where $$Q = (K^2 Pr)^{1/4} \tag{2.18.1}$$

As the Nusselt number is a function of Q, this equation shows the influence of Prandtl number on fully developed laminar forced convection in a curved pipe.

Kalb and Seader (20) have obtained the following Nusselt numbers in the low-Prandtl-number range by the numerical method:

$$Nu_c = 3.31 \cdot K^{0.115}\ Pr^{0.0108} \tag{2.19}$$

for $20 < K < 1200$, and $0.005 \leq Pr < 0.05$.

$$Nu_c = 0.913 \cdot K^{0.476}\ Pr^{0.200} \tag{2.20}$$

for $80 < K < 1200$, and $0.7 < Pr < 5$.

These equations (2.16), (2.17), (2.18), (2.19) and (2.20) are shown in Fig. (2.10).

2.2.4.2 For uniform wall temperature

Mori and Nakayama (24-1967) correlated the following equation from the experimental results of their report (5) and the empirical resistance formula of Ito (25-1959):

$$Nu_c = \frac{0.864}{\zeta} K^{\frac{1}{2}} (1+2.35K^{-\frac{1}{2}}), \qquad (2.21)$$

where ζ is obtained from equations (2.14) and (2.15).

Akiyama and Cheng (23) have deduced the approximate equation using the parameter K^2Pr:

$$\frac{Nu_c}{Nu_s} = 0.1810 \left(1 - \frac{0.839}{Q} + \frac{35.4}{Q^2} - \frac{207}{Q^3} + \frac{4.9}{Q^4}\right), \qquad (2.22)$$

for $Q = (K^2Pr)^{1/4} \gtrsim 3.5$ and $Pr \gtrsim 1$.

A correlation of the numerically calculated fully-developed Nusselt numbers by Kalb and Seader (21) is:

$$Nu_c = 0.836K^{\frac{1}{2}}Pr^{1/10} \qquad (2.23)$$

for $80 \lesssim K$, and $0.7 \lesssim Pr \lesssim 5$.

The Dean number exponent of $\frac{1}{2}$ in equation (2.23) is in agreement with the prediction of Mori and Nakayama (24) at high Dean numbers.

The Prandtl number exponent of 1/10 is less than the values reported under boundary conditions of axially uniform wall heat flux with peripherally uniform wall temperature.

2.3 Laminar-Turbulent Transition in Coils

This is more difficult to define for a coil than for a straight pipe, because the transition point is identified as a change in slope of the friction factor-Reynolds number curve, rather than by a discontinuity.

The critical Reynolds number (Re_{cr}) is greater for coils than for straight pipes, and its value has been proposed by several workers. Some of the recent and probably more reliable are:

(1) Ito (25)

$$Re_{cr} = 2 \left(\frac{a}{R}\right)^{0.32} x10^4 \qquad (2.24)$$

for $0.00116 \leq \frac{a}{R} \leq 0.0667$.

(2) Kutateladze and Borishanski (26-1966)

$$Re_{cr} = 2300 + 12930 \left(\frac{a}{R}\right)^{\frac{1}{2}} \qquad (2.25)$$

for $0.0417 \leq \frac{a}{R} \leq 0.167$

(3) Schmidt (27-1967)

$$Re_{cr} = 2300 \left\{ 1+8.6 \left(\frac{a}{R}\right)^{0.45} \right\} \qquad (2.26)$$

(4) Mori and Nakayama (24)

$$Re_{cr} = 6.5 \left(\frac{a}{R}\right)^{\frac{1}{2}} x\ 10^5 \qquad (2.27)$$

for $0.00588 \leq \frac{a}{R}$

(5) Srinivasan et al (28-1968)

$$Re_{cr} = 2100 \left\{ 1+12 \left(\frac{a}{R}\right)^{\frac{1}{2}} \right\} \qquad (2.28)$$

It can be seen that Schmidt (27) and Srinivasan et al (28) approach the value for a straight tube as the radius of curvature becomes very large.

2.4 Turbulent Flow

2.4.1 Pressure drop (friction factors)

For turbulent flow in straight tubes, the friction factor is empirically related to the Reynolds number by an equation of the following form:

$$f_s = \alpha Re^{-\frac{1}{m}} \qquad (2.29)$$

The commonly used values of m are 4 and 5. When m is taken as 4, the value of α is 0.316 after Blasius resistance formula which is valid for Reynolds numbers less than 10^5. When m is taken as 5, the value of α is 0.184.

Mori and Nakayama (24) have made an analysis of turbulent flow in coils and have proposed the following formula for f_c when the values of m are 4 and 5.

$$f_c \left(\frac{a}{R}\right)^{-\frac{1}{2}}_{m=4} = 0.300 \left\{ Re \left(\frac{a}{R}\right)^2 \right\}^{\frac{-1}{5}} \times \left[1 + 0.112 \left\{ Re \left(\frac{a}{R}\right)^2 \right\}^{\frac{-1}{5}} \right] \qquad (2.30)$$

$$f_c \left(\frac{a}{R}\right)^{-\frac{1}{2}}_{m=5} = 0.192 \left\{ Re \left(\frac{a}{R}\right)^{2.4} \right\}^{\frac{-1}{5}} \times \left[1 + 0.068 \left\{ Re \left(\frac{a}{R}\right)^{2.5} \right\}^{\frac{-1}{6}} \right] \qquad (2.31)$$

The dimensionless factor, $Re \left(\frac{a}{R}\right)^2$, has been defined for the turbulent flow by Ito (25) instead of Dean number, $Re \left(\frac{a}{R}\right)^{\frac{1}{2}}$, for the laminar flow.

The formula (2.30) agrees with the empirical formula of Ito (25) which is the following:

(i) $$f_c \left(\frac{a}{R}\right)^{-\frac{1}{2}} = 0.029 + 0.304 \left\{ Re \left(\frac{a}{R}\right)^2 \right\}^{\frac{-1}{4}} \qquad (2.32)$$

for $0.034 < Re \left(\frac{a}{R}\right)^2 < 300$.

He also made the analysis using the one-seventh power law, and has recommended the following three empirical equations:

$$f_c \left(\frac{a}{R}\right)^{-\frac{1}{2}} = 0.316 \left\{Re \left(\frac{a}{R}\right)^2\right\}^{-\frac{1}{5}} \qquad (2.33)$$

for $Re \left(\frac{a}{R}\right)^2 > 6.$

By making use of Blasius formula

$$f_c = 0.316\ Re^{-\frac{1}{4}} \qquad (2.34)$$

Equations (2.32)-(2.34) are plotted in Fig. (2.11a). Eq. (2.34) may be expressed in an alternative form,

$$\frac{f_c}{f_s} = \left\{Re \left(\frac{a}{R}\right)^2\right\}^{\frac{1}{20}} \qquad (2.35)$$

where

$$\frac{f_s}{8} = 0.023\ Re^{-\frac{1}{5}} \qquad (2.35.1)$$

(ii) $$f_c \left(\frac{a}{R}\right)^{-\frac{1}{2}} = 0.0323 + 1.6 \left\{Y^2 \left(\frac{a}{R}\right)^{\frac{1}{2}}\right\}^{-1.27} \qquad (2.36)$$

for $Y^2 \left(\frac{a}{R}\right)^{\frac{1}{2}} < 12$

where $Y^2 \exp Y = Re \left(\frac{a}{R}\right)^{\frac{1}{2}}$ (2.37)

(iii) $$f_c = 1.186 Y^{-2} \qquad (2.38)$$

for $Y^2 \left(\frac{a}{R}\right)^{\frac{1}{2}} > 5.3.$

Friction factors for isothermal and nonisothermal conditions were obtained from both the large, $\frac{R}{a} = 104$, and small $\frac{R}{a} = 17$, coils by Seban and McLaughlin (22) and these results are shown in Fig. (2.11b). They are compared to experimental results (eq. (2.35)) for coils of similar ratio of helix to tube diameter. They concluded from this Fig. (2.11b) that the equation (2.35) is only 6% low.

The results of Seban and McLaughlin (22) for the large coil also agree with Ito's critical Reynolds number,(eq. (2.24))but those for the small coil do verify the predicted transition point.

The effect of coil curvature on the friction factor is substantially less in turbulent flow than in laminar flow.

2.4.2 Velocity and Temperature profiles in turbulent flow

The velocity profiles in the fully-developed flow field have been measured by Adler (2), Mori and Nakayama (24) and Hogg (29-1968), the latter two authors also provide temperature profile in fully-developed thermal field for uniform heat-flux boundary conditions.

In the developing region of a turbulent flow field, Hawthorne (30-1951) presents the contours of stagnation pressure at several axial positions in a 180^{o} bend. The inlet velocity distribution for these experiments varied linearly from zero at the bottom of the pipe to a maximum in the region close to the top wall.

Further measurements in the developing flow region have been reported by Detra (31-1953) and by Rowe (32-1966).

Patankar et al (33-1975) and Pratap (34-1975) compare their numerical prediction of the fully-developed axial-velocity profiles with experimental data of Rowe (32), Hogg (29) and Mori and Nakayama (24), Figs. (2.12a) and (2.12b) display the comparison of fully-developed axial-velocity profiles along vertical and horizontal diameters with experimental data of Hogg (29) and Mori and Nakayama (24).

The predicted velocity profiles agreed with experimental data. The fully-developed secondary velocities along the vertical diameter are compared with the experimental data of Hogg (29), the results are very close for both the Reynolds numbers.

Temperature profile in the fully-developed turbulent flow field has been measured by Mori and Nakayama (24) and Hogg (29).

Fig. (2.13) shows the profile obtained by Mori and Nakayama. Fig.(2.14) shows the computed temperature profiles (non-dimensionalised with inside wall temperature) in coils by Patankar et al (33) and Pratap (34) with radius ratio ($\frac{R}{a}$) of 25.9 and comparison with experimental data of Hogg. The agreement is satisfactory in the inside region but discrepancies exist in the outside region.

2.4.3 Heat transfer coefficient in turbulent flow

Mori and Nakayama (24) have made a rather lengthy analysis of turbulent flow heat transfer in coils which resulted in the following:

The Nusselt number in a curved pipe, Nu_c, is written

$$Nu_c = \frac{2aQ_w}{k(T_w-T_m)} = \frac{2g_w}{g_m} \qquad (2.39)$$

where Q_w is the heat flux at the wall to the fluid and

$$q_w = \frac{Re.Pr}{4}, \qquad (2.39.1)$$

then eq. (2.39) is written

$$Nu_c = \frac{Re.Pr}{2g_m} \qquad (2.40)$$

g_m, the temperature difference, may be calculated by the order of the boundary layer thickness, δ, g_m is defined in Appendix (A.1).

Equation (2.40) becomes:

$$Nu_c = \frac{1}{2A} \cdot \frac{Pr}{Pr^{1-j-\Delta g_m}} \cdot Re^{m/(m+1)} \cdot \left(\frac{a}{R}\right)^{1/(2(m+1))} \left[1+\Delta Nu\{Re\left(\frac{a}{R}\right)^{\frac{m}{2}}\}^{\frac{-1}{m+1}}\right] \qquad (2.41)$$

where A, Δg_m and ΔNu are defined in Appendix (A.1).

Eventually eq. (2.41) becomes

$$Nu_c = \frac{Pr.Re^{0.8}}{26.2(P_r^{2/3}-0.074)} \cdot \left(\frac{a}{R}\right)^{0.1} \left[1 + 0.098 \left\{Re \left(\frac{a}{R}\right)^2\right\}^{-0.2}\right] \qquad (2.42)$$

for gases,

$$N_{uc} = \frac{Re^{5/6}}{41.0} \cdot Pr^{0.4} \cdot \left(\frac{a}{R}\right)^{1/12} \cdot \left[1 + 0.061 \left\{Re \left(\frac{a}{R}\right)^{2.5}\right\}^{\frac{-1}{6}}\right] \qquad (2.43)$$

for liquids which have generally high Prandtl numbers.

The other experimental correlations are listed below:

(1) Jaschke (35-1925)

$$Nu_c = (0.039 + 0.138 \left(\frac{a}{R}\right)) \cdot Re^{0.76}, \qquad (2.44)$$

for air.

(2) Merkel (36-1927)

$$Nu_c Pr^{-0.4} = 0.023 \left(1 + 3.54 \frac{a}{R}\right) \cdot R_e^{0.8} \qquad (2.45)$$

(3) Pratt (37-1947)

$$Nu_c Pr^{-0.4} = 0.0225 \left(1 + 3.4 \left(\frac{a}{R}\right)\right) \cdot Re_b^{0.8} \qquad (2.46)$$

(4) Seban and McLaughlin (22) have shown the experimental results of turbulent flow heat transfer coefficients in the large and small coils in Fig . (2.15). They also correlated the average turbulent heat transfer coefficient with the following equation:

$$Nu_c \cdot Pr^{-0.4} = 0.023 \left(\frac{a}{R}\right)^{0.1} Re^{0.85} \qquad (2.47)$$

(5) Rogers and Mayhew (38-1964)

$$Nu_c \, Pr_f^{-0.4} = 0.021 \left(\frac{a}{R}\right)^{0.1} Re_f^{0.85} \qquad (2.48)$$

$$Nu_c \, Pr_b^{-0.4} = 0.023 \left(\frac{a}{R}\right)^{0.1} Re_b^{0.85} \qquad (2.49)$$

The suffixes b and f denote evaluation of physical properties at bulk and film temperatures respectively.

(6) Dravid et al (19) disagree with eq. (2.43) of Mori and Nakayama because they integrated the energy integrals of the thermal boundary-layer analysis over the hydrodynamic boundary-layer rather than over the thermal boundary-layer for the case Pr > 1. They report the following equation,

$$Nu_c \, Pr^{-0.175} = 0.76 + 0.65 \left(Re \left(\frac{a}{R}\right)^{\frac{1}{2}}\right)^{\frac{1}{2}} \qquad (2.50)$$

The Fig. (2.16) shows the difference of equations (2.43), (2.47), (2.48) and (2.49).

Mori and Nakayama (24) also have concluded that for coils, entrance effects are negligible and that the heat transfer data for a constant heat flux are the same as those for a constant wall temperature.

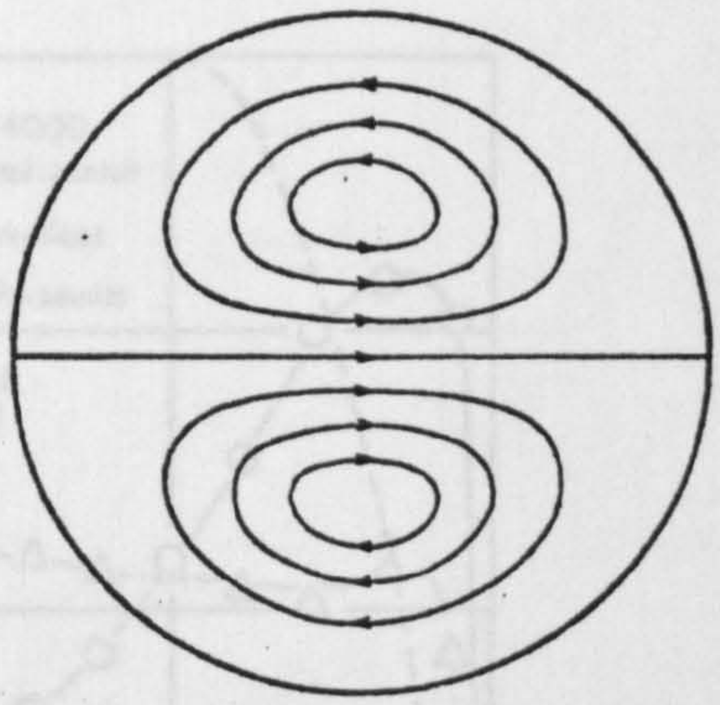


Fig. (2.1) : Flow pattern of the secondary flow for small K (< 17) from Dean (1).

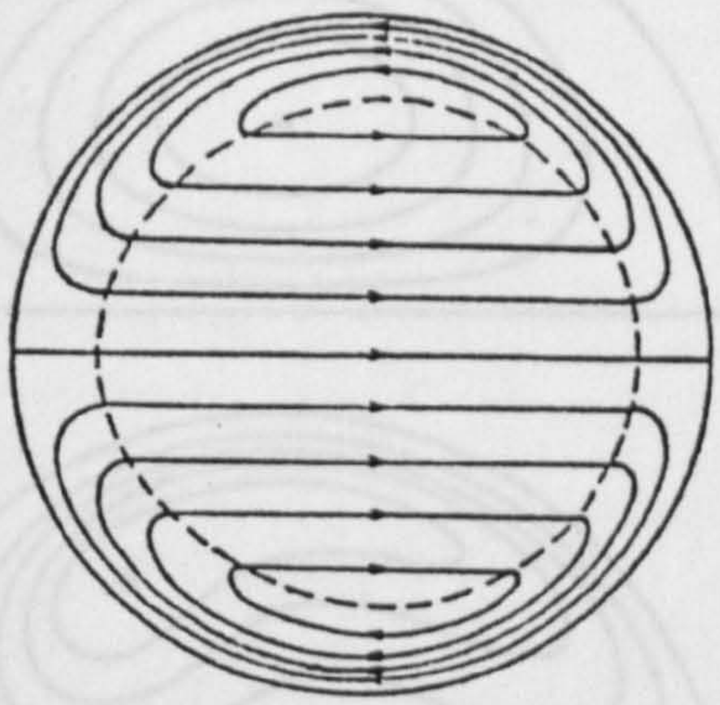


Fig. (2.2): Flow pattern of secondary flow for large K from Mori & Nakayama (5).

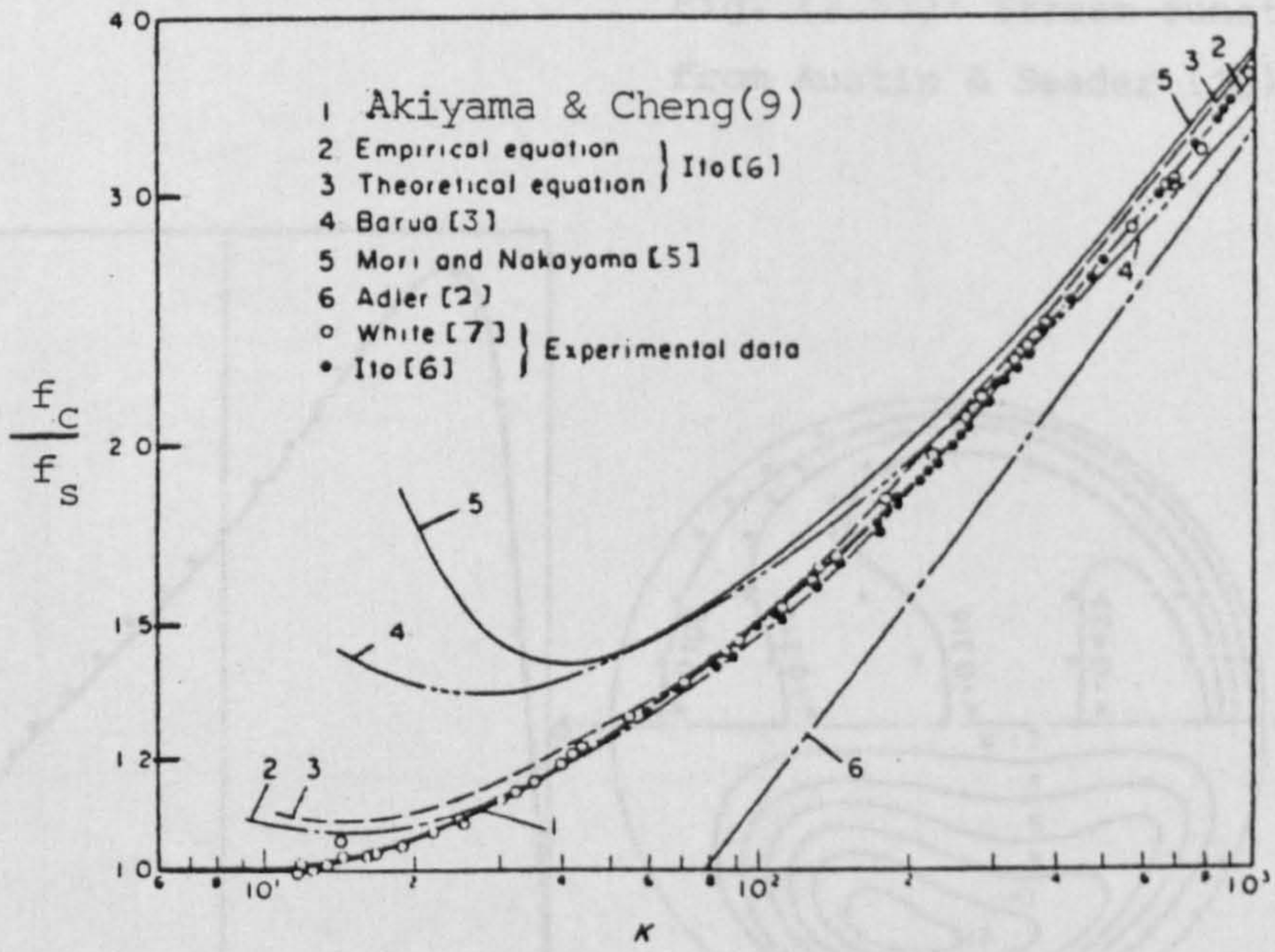
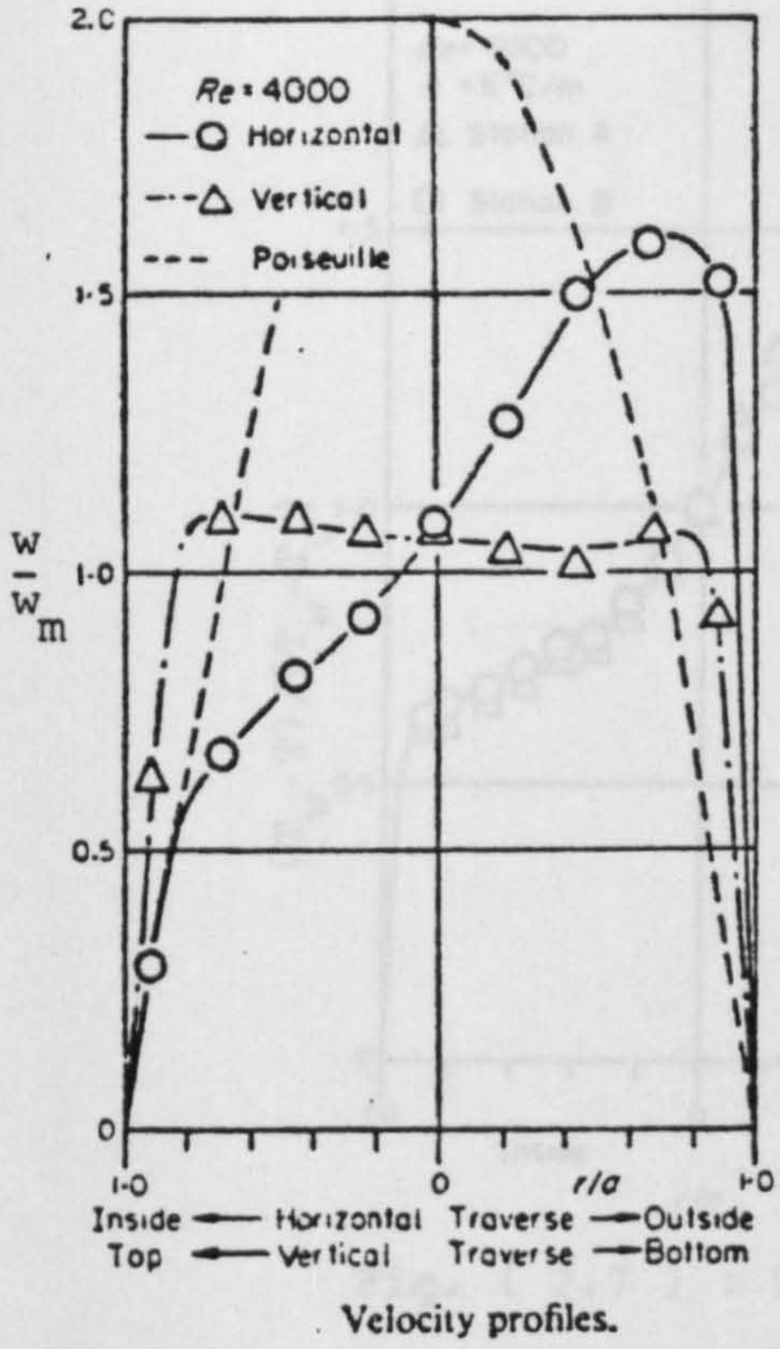
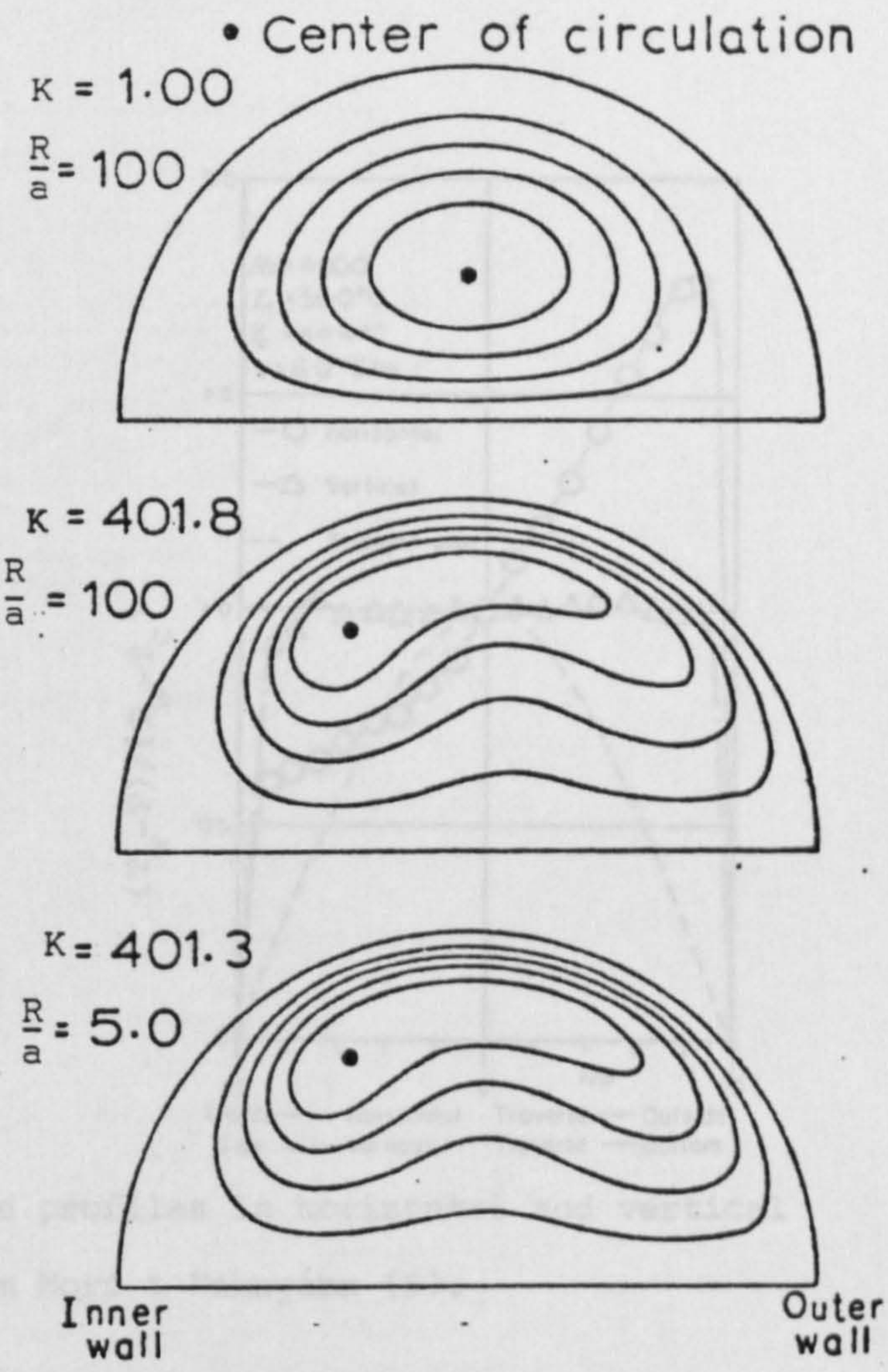


Fig. (2.3) : Comparison of laminar friction factor from Akiyama & Cheng (9).



Velocity profiles.

Fig. (2.4) : Velocity profiles in laminar flow from Mori & Nakayama (5).



Computed stream-function contours.

Fig. (2.5)): Stream-function contours from Austin & Seader (18).

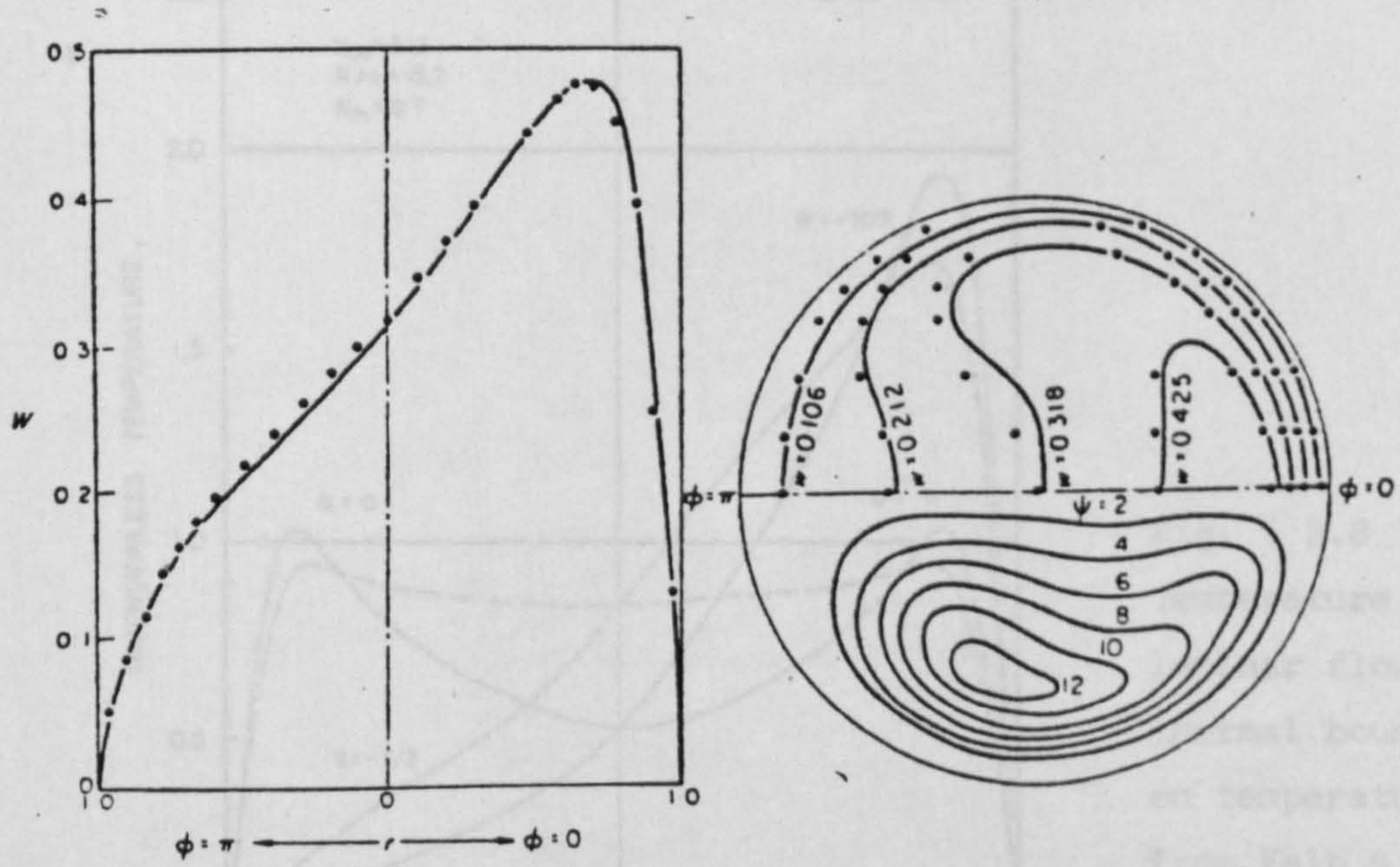


Fig.(2.6): Comparison of velocity profile along $\phi = 0$ and π and isolines for velocity at $K = 196$ from the work with Adler's experimental data at $K = 205$ and streamlines at $K = 196$ from the work.

from Akiyama & Cheng (9).

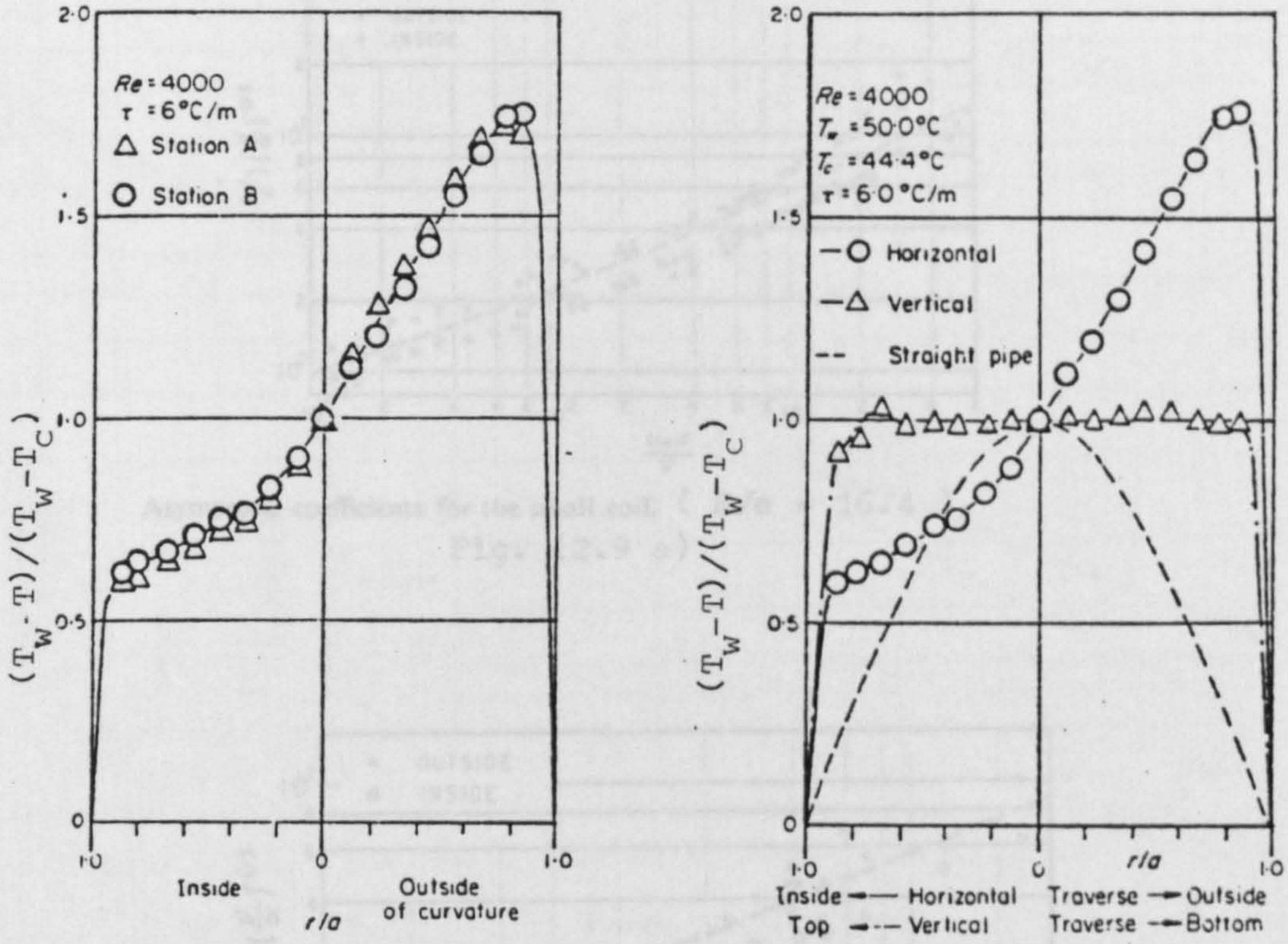


Fig. (2.7) : Temperature profiles in horizontal and vertical planes from Mori & Nakayama (5).

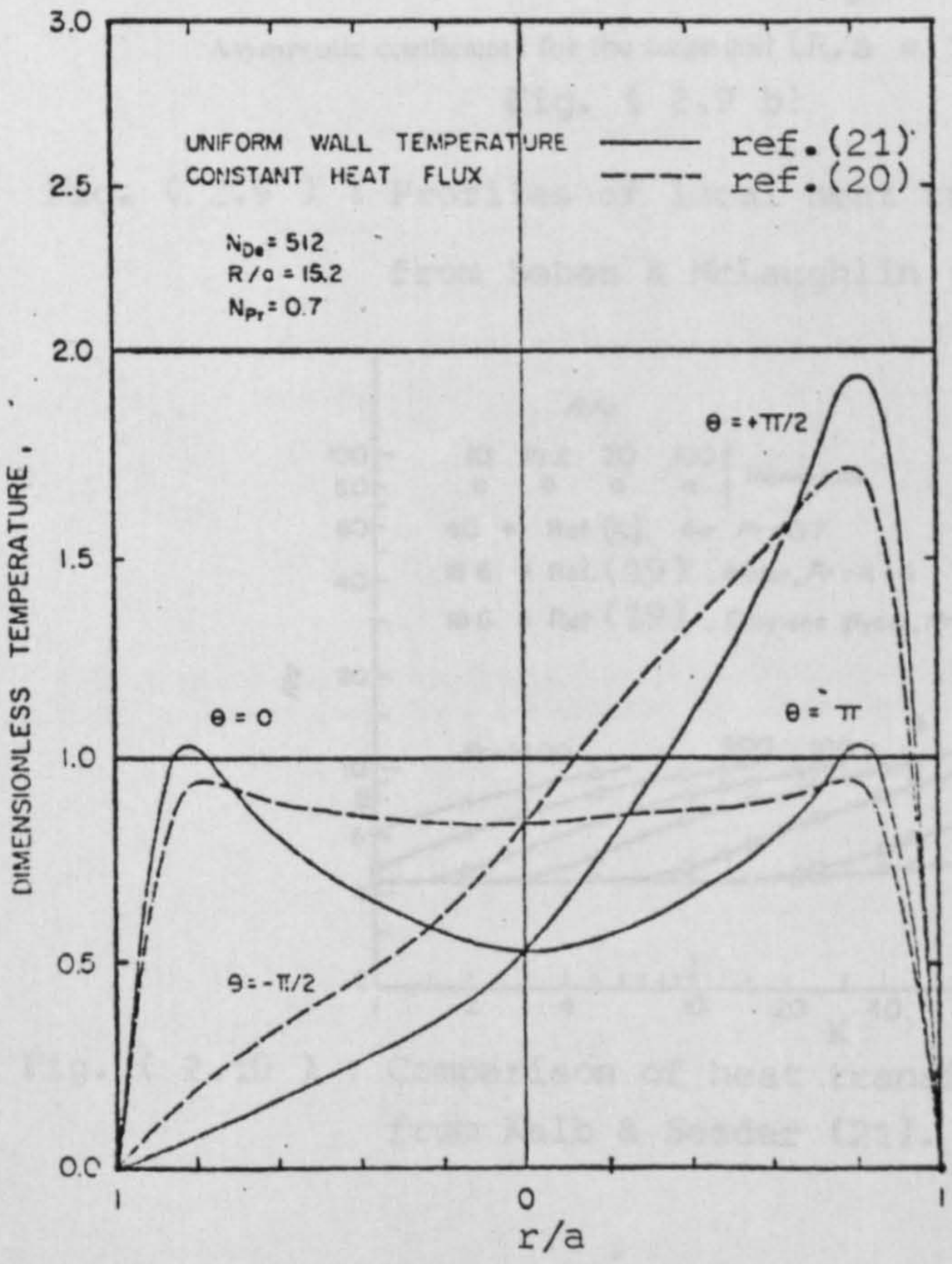
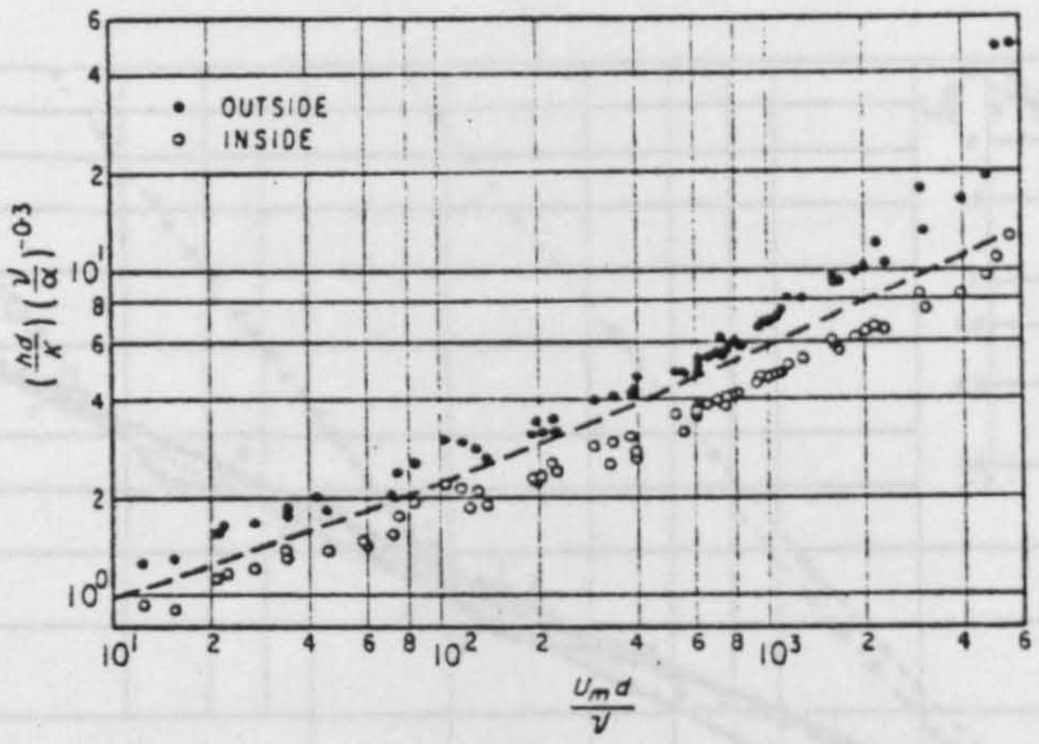
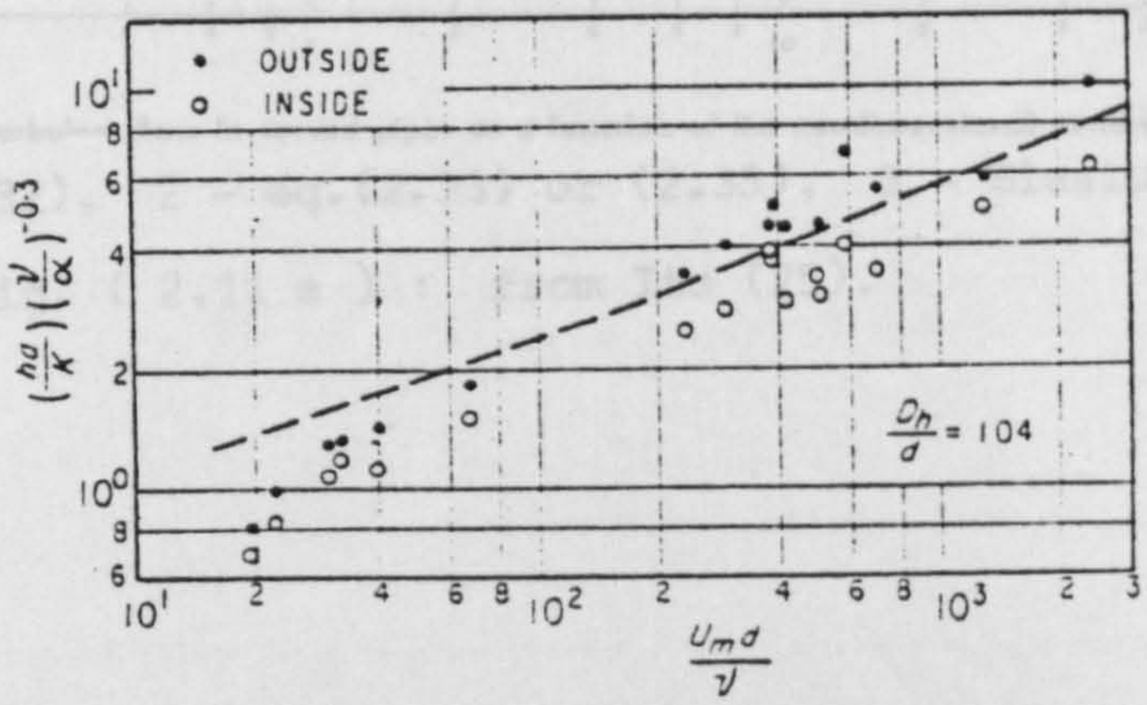


Fig. (2.8) : Temperature profile in laminar flow,(effect of thermal boundary conditions on temperature profiles) from Kalb & Seader (21).



Asymptotic coefficients for the small coil. (R/a = 16.4).

Fig. (2.9 a)



Asymptotic coefficients for the large coil (R/a = 104).

Fig. (2.9 b)

Fig. (2.9) : Profiles of local heat transfer coefficients from Seban & McLaughlin (22).

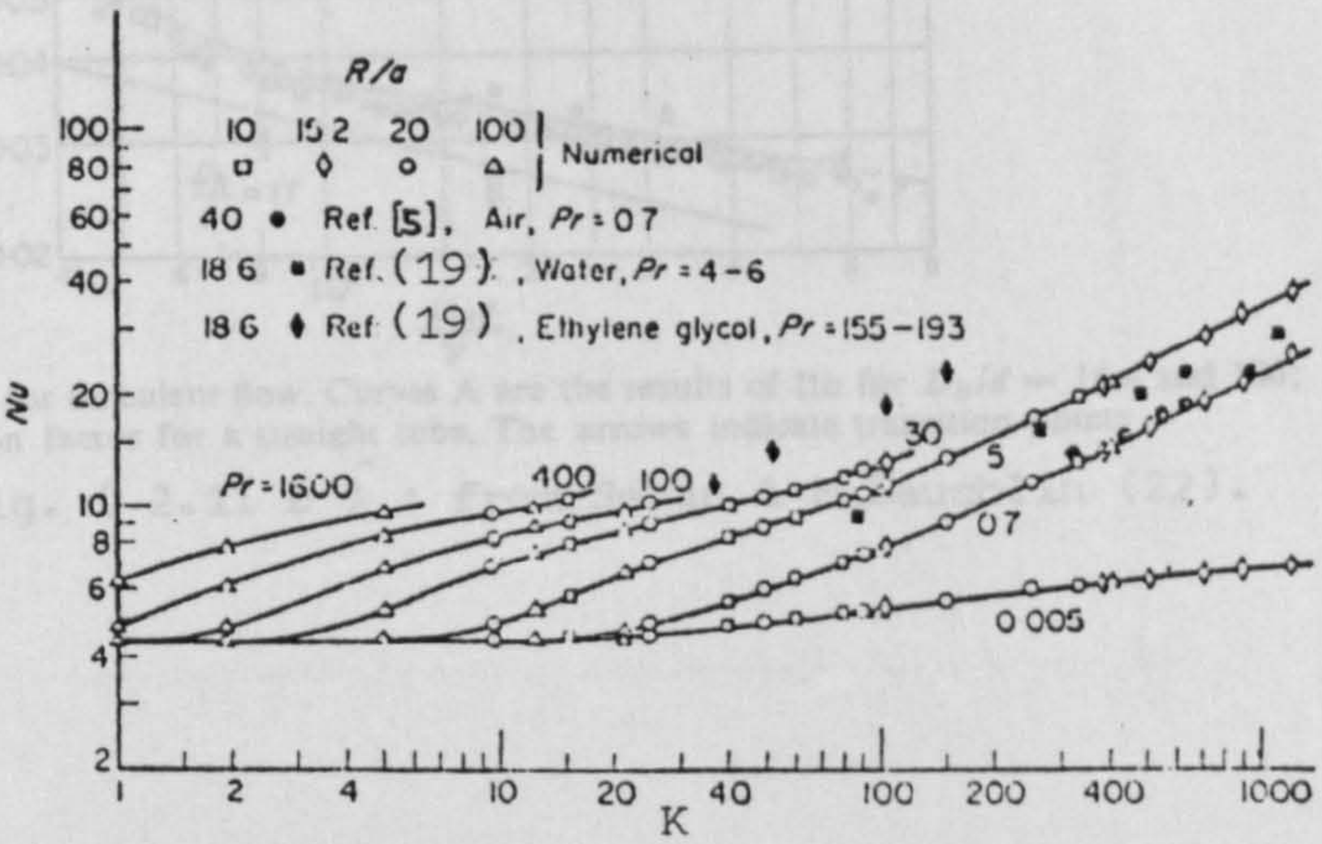
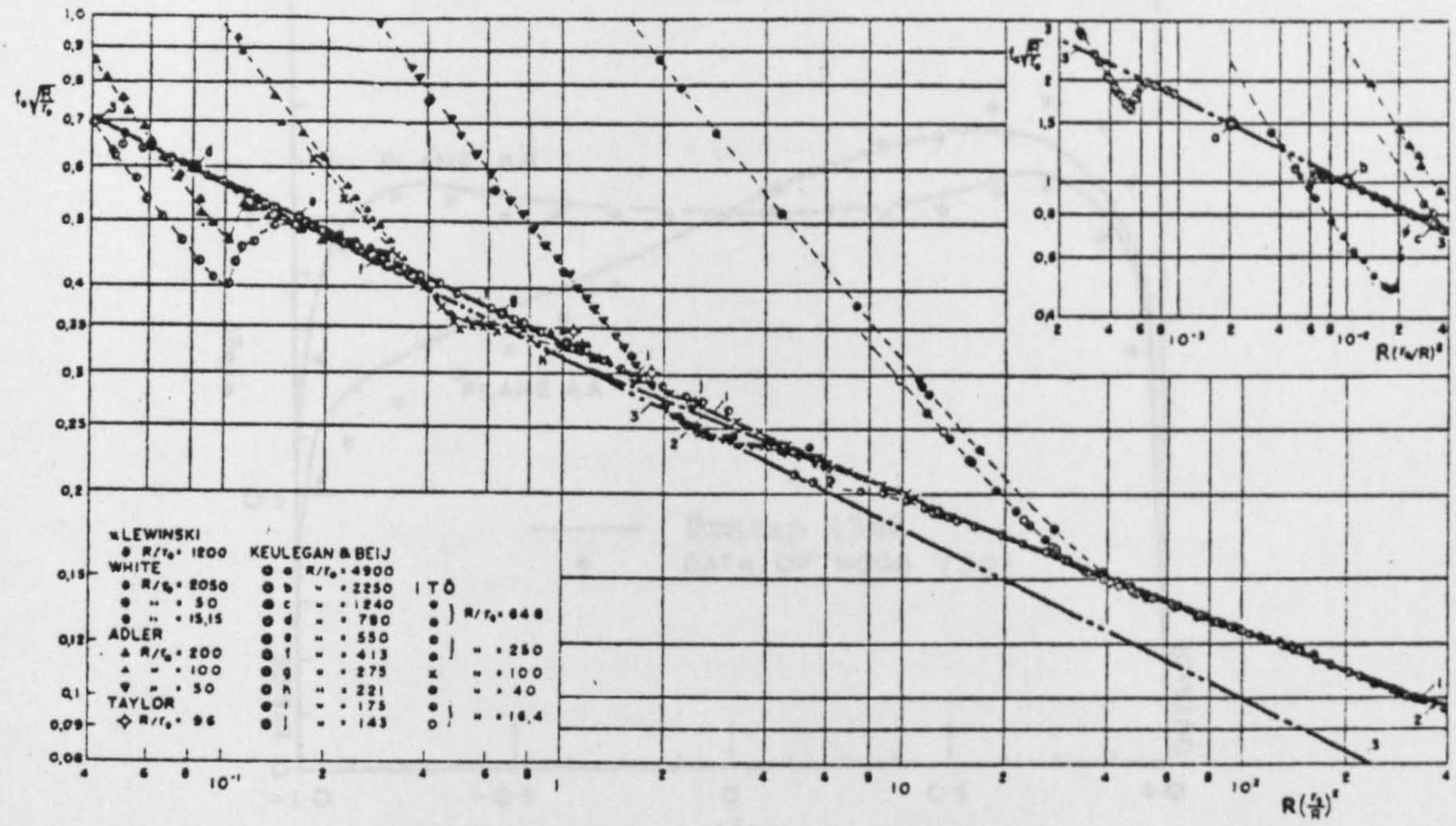


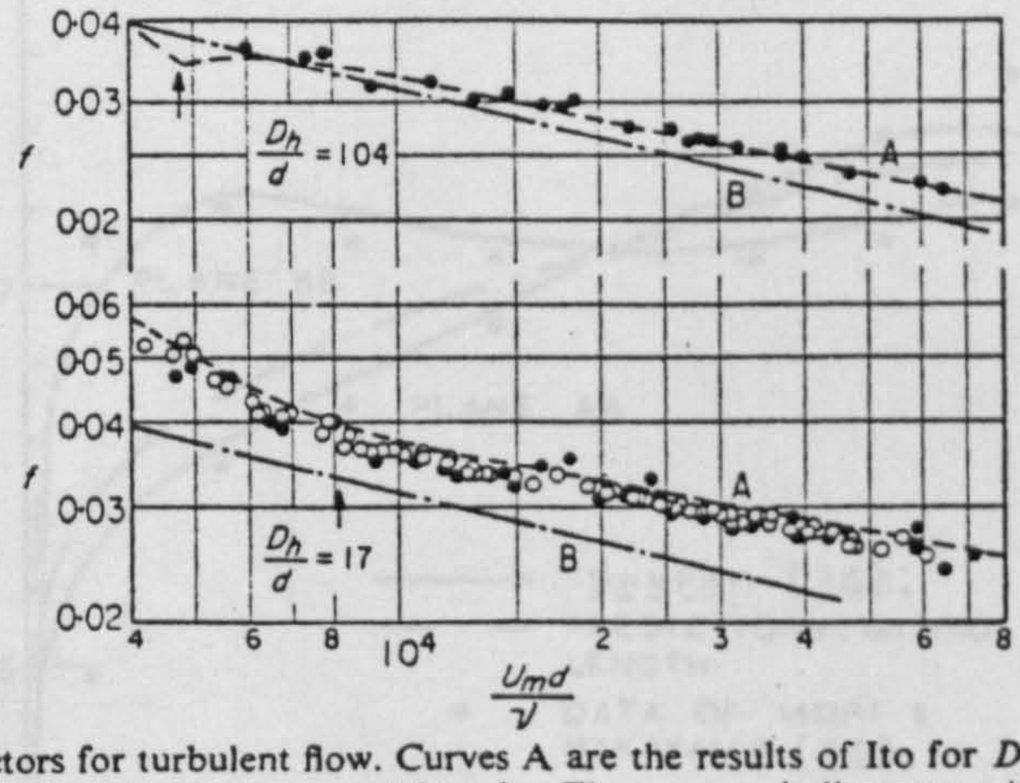
Fig. (2.10) : Comparison of heat transfer coefficients from Kalb & Seader (21).



Friction factor for turbulent flow in curved pipes as a function of the nondimensional number, $R(r_0/R)^2$:

1 - eq.(2.32), 2 - eq.(2.33) or (2.35), 3 - Blasius' formula.

Fig. (2.11 a) : from Ito (25).



Friction factors for turbulent flow. Curves A are the results of Ito for $D_H/d = 16{\cdot}4$ and 100; curves B are the friction factor for a straight tube. The arrows indicate transition points

Fig. (2.11 b) : from Seban & McLaughlin (22).

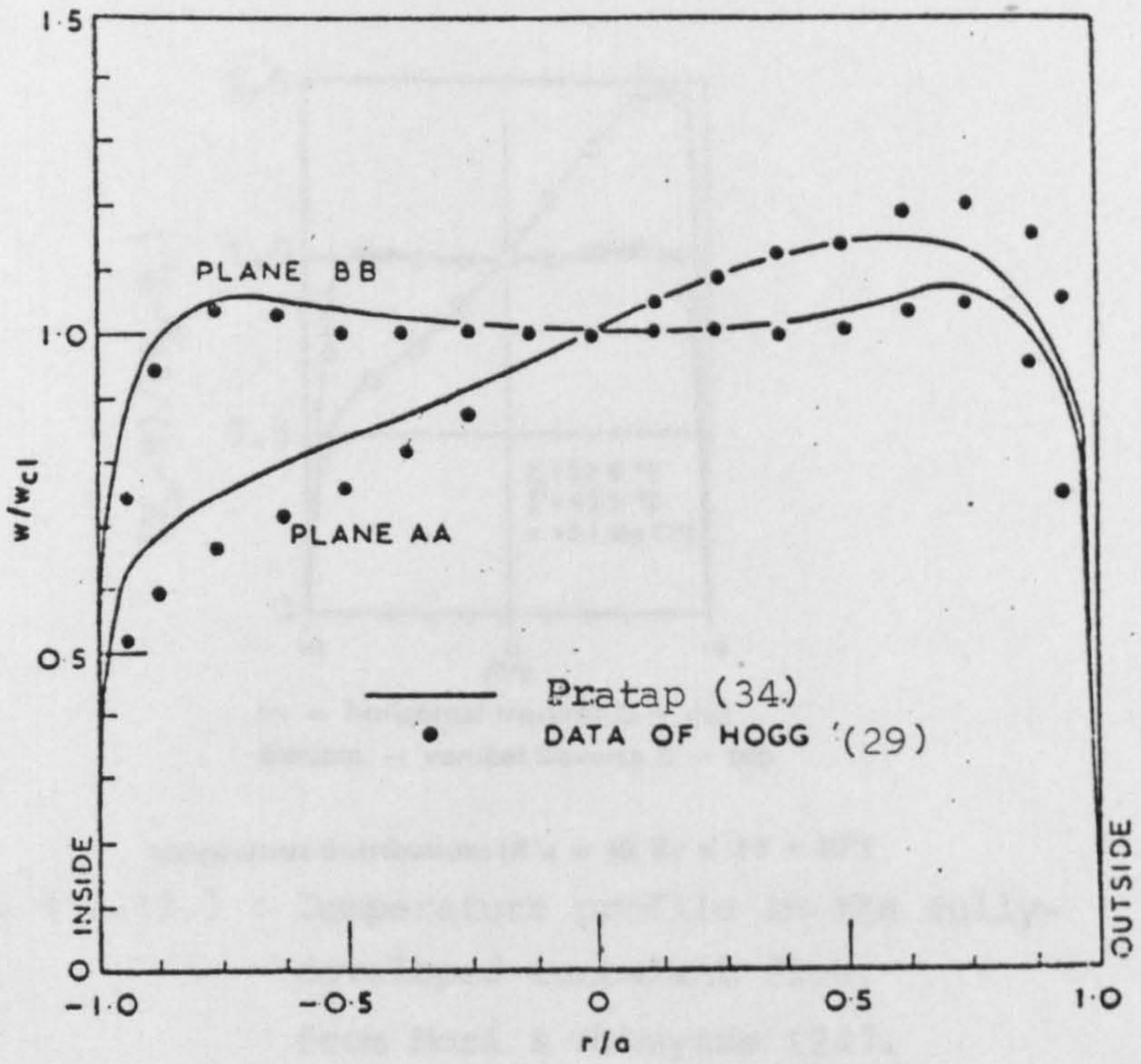


Fig. (2.12a): Comparison of fully-developed axial velocity profiles along plane AA and BB. Reynolds number = 6.8×10^4, R/a=25.9.

AA - horizontal plane,
BB - vertical plane.

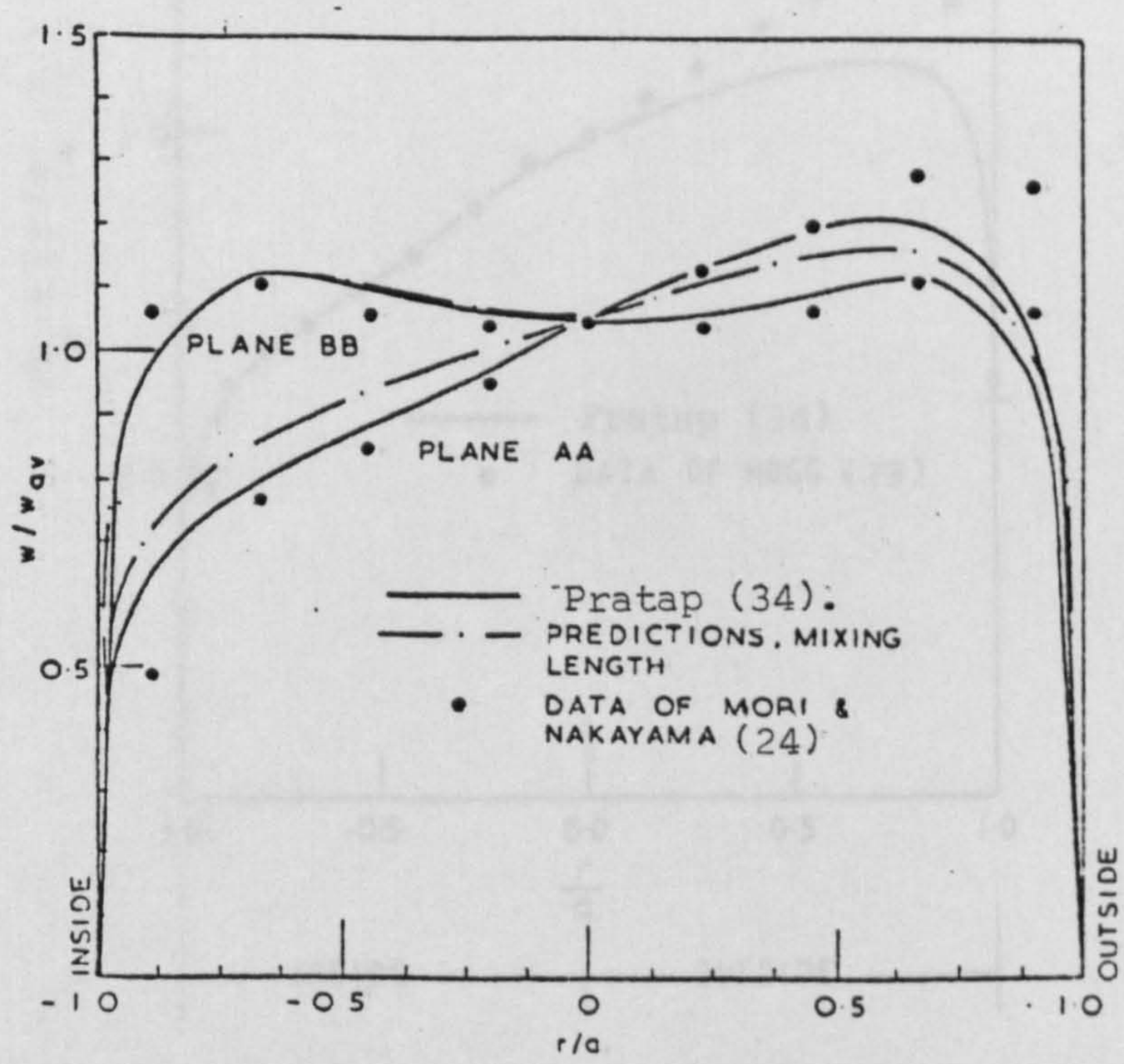
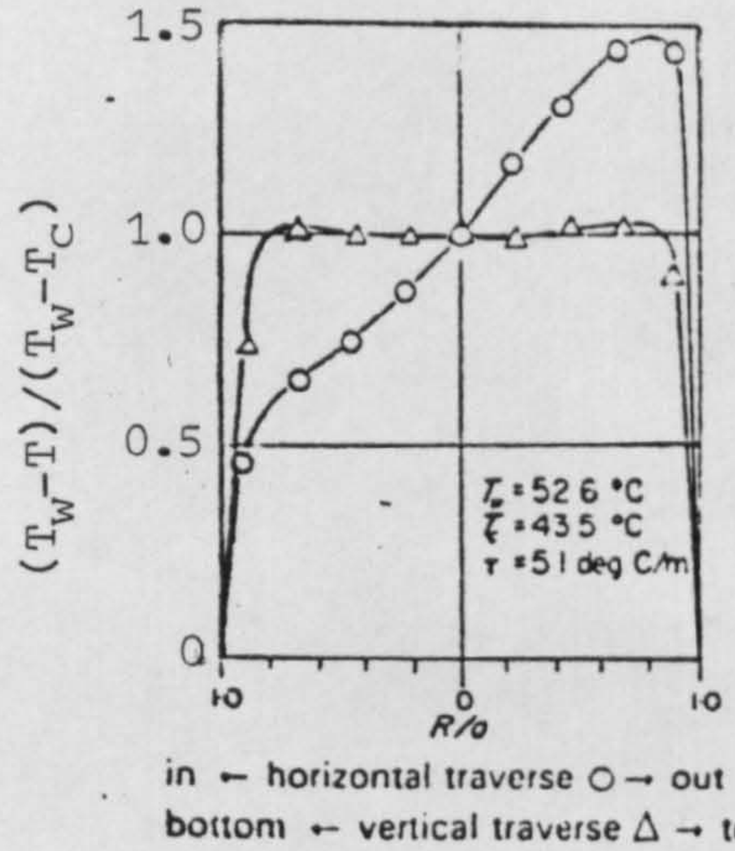


Fig. (2.12 b): Comparison of fully-developed axial velocity profiles along plane AA and BB. Reynolds number = 2.5×10^4 and R/a=40.

from Pratap (34).



temperature distributions ($R/a = 40$, $Re = 2.5 \times 10^4$).

Fig. (2.13) : Temperature profile in the fully-developed turbulent flow, from Mori & Nakayama (24).

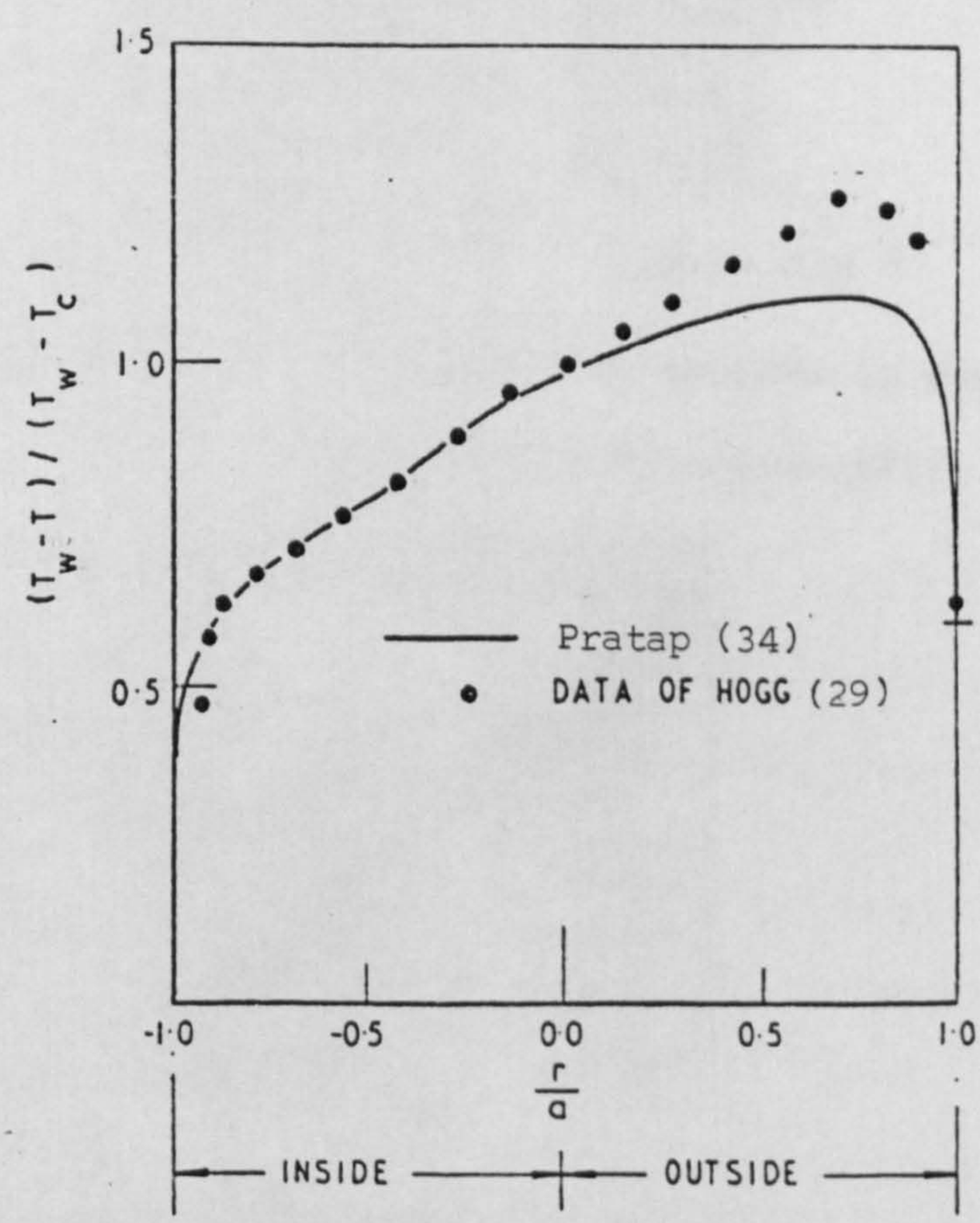
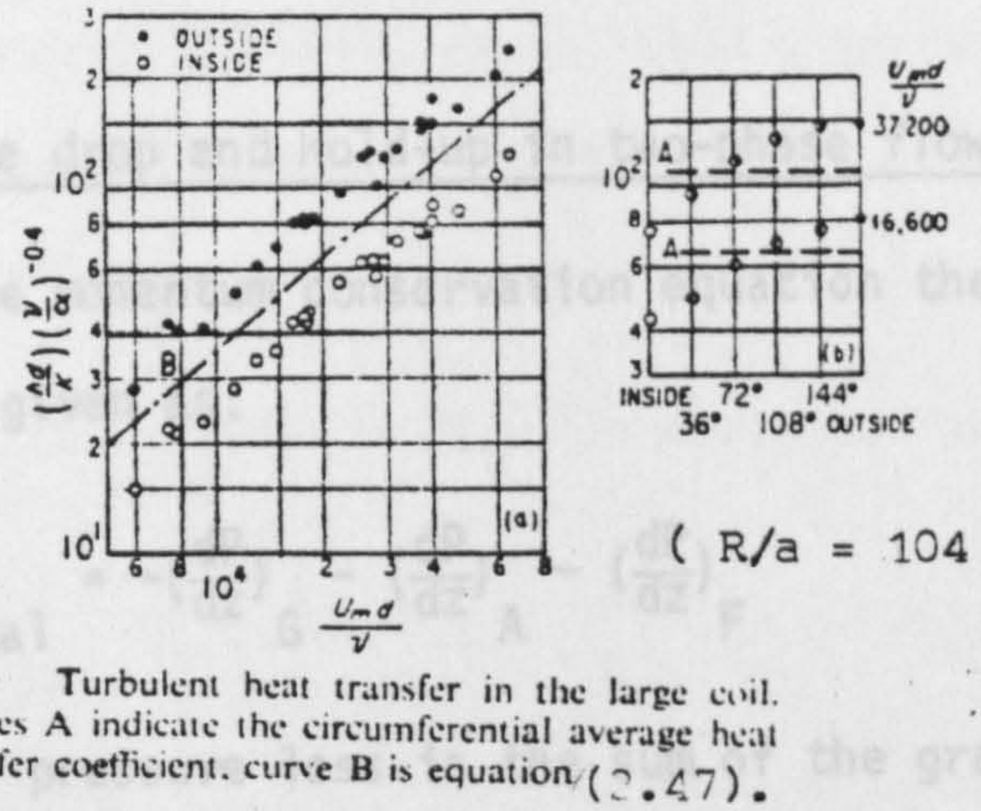


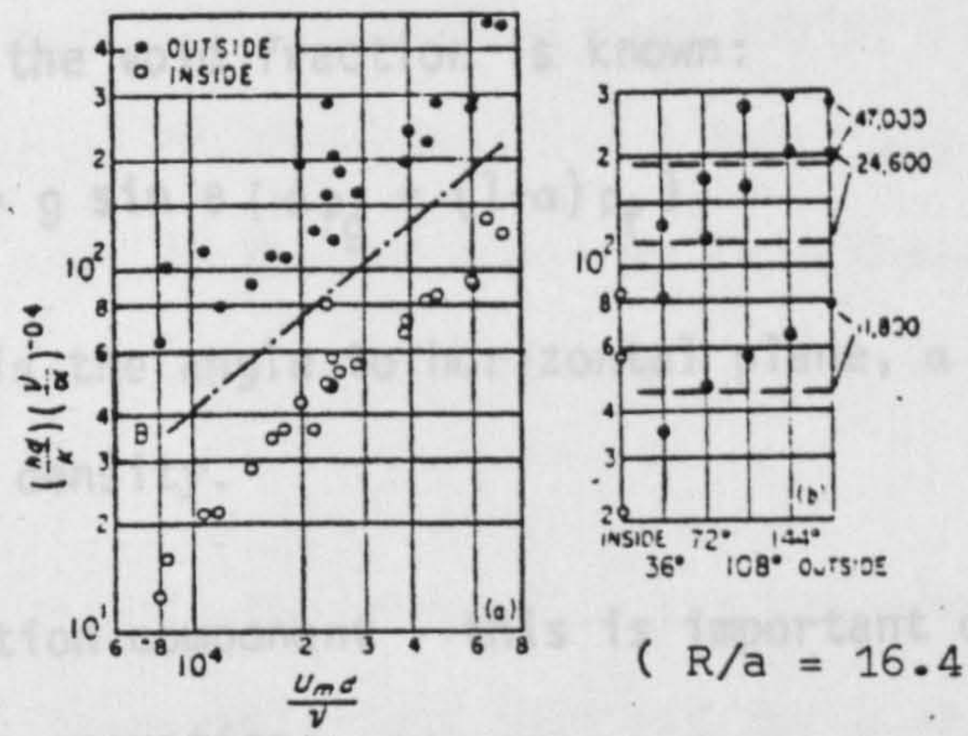
Fig. (2.14) : Comparison of predicted fully-developed temperature profiles with experimental data. Reynolds number = 6.8×10^4 R/a=25.9, Pr=0.71.



(R/a = 104)

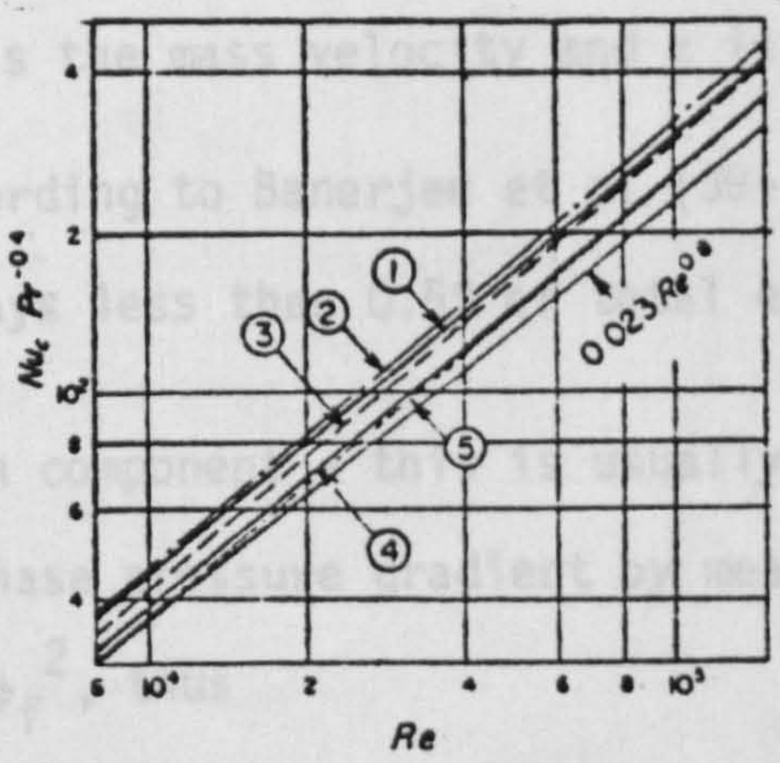
Turbulent heat transfer in the large coil. Curves A indicate the circumferential average heat transfer coefficient, curve B is equation (2.47).

Fig. (2.15 a): from Seban & McLaughlin (22).



(R/a = 16.4)

Fig. (2.15 b) : Turbulent heat transfer in small coil from Seban & McLaughlin (22).



① —— Theoretical curve Ref. (24)
② —·— Rogers & Mayhew [38] $Nu_c Pr^{-0.4}$
③ - - - - Rogers & Mayhew [38] $(Nu_c Pr^{-0.4})$
④ —— Theoretical curve [24]
⑤ —··— Seban & McLaughlin [22]

$\frac{R}{a}$ = 10.8 (①, ②, ③)
$\frac{R}{a}$ = 104 (④, ⑤)

Fig. (2.16). Comparison of the theoretical results with the empirical formulae (22 & 38) from Mori & Nakayama (24).

2.5 Two-phase flow

2.5.1 Pressure drop and Hold-up in two-phase flow

From the momentum conservation equation the total pressure loss in pipe flows is given as:

$$-\left(\frac{dP}{dz}\right)_{total} = -\left(\frac{dP}{dz}\right)_{G} - \left(\frac{dP}{dz}\right)_{A} - \left(\frac{dP}{dz}\right)_{F} \qquad (2.51)$$

The total pressure loss is the sum of the gravity, acceleration and friction components.

(i) Gravity component - this is usually very small but can be calculated if the void fraction is known:

$$-\left(\frac{dP}{dz}\right)_{G} = g \sin\theta \{ \alpha\rho_g + (1-\alpha)\rho_f \} \qquad (2.52)$$

where θ is the angle to horizontal plane, α is the void fraction and ρ is density.

(ii) Acceleration component - this is important component if the flow is with evaporation:

$$-\left(\frac{dP}{dz}\right)_{A} = G^2 \frac{d}{dz} \left\{ \frac{x^2}{\alpha\rho_g} + \frac{(1-x)^2}{(1-\alpha)\rho_f} \right\} \qquad (2.53)$$

where G is the mass velocity and x is mass vapour quality.

According to Banerjee et al (39-1969) the acceleration losses were always less than 0.5% of total energy loss.

(iii) Friction component - this is usually expressed in terms of the single-phase pressure gradient by means of appropriate multipliers ϕ_g^2 and ϕ_f^2, thus

$$\left(\frac{dP}{dz}\right)_{TPF} = \phi_g^2 \left(\frac{dP}{dz}\right)_{g} = \phi_f^2 \left(\frac{dP}{dz}\right)_{f} \qquad (2.54)$$

where $\left(\frac{dP}{dz}\right)_{g}$ and $\left(\frac{dP}{dz}\right)_{f}$ are the single phase pressure drops if the liquid or gas were flowing alone.

Lockhart-Martinelli (40-1949) established a correlation between the irreversible dissipation of energy and only the liquid and the gas flow rate, densities and viscosities.

ϕ_g or ϕ_f from equation (2.54) are plotted against X,

$$X^2 = \frac{(dP/dz)_f}{(dP/dz)_g} \tag{2.55}$$

Rippel et al (41-1966) carried out a limited experimental study of the concurrent down-flow of air and water and a number of gas-liquid systems through a coil constructed from tubing 1.02cm (0.402in) ID with a coil diameter of 20.32cm (8in) and a tube length 26.93m (88.3ft). Figs. (2.17a) and (2.17b) are obtained from these experiments and show that the coil data are in fair agreement with the Lockhart-Martinelli correlations.

Pressure drop in two-phase flow can be correlated by a two-phase drag coefficient. The correlations obtained for a spiralled tube in various flow patterns are:

For annular flow

$$\left(\frac{dP}{dz}\right)_{TP} = \left(\frac{dP}{dz}\right)_g + 4.44\,\lambda^{0.86}\,\frac{\rho_g v_o^2}{gD} \tag{2.56}$$

where v_o is the superficial linear velocity.

For bubble and slug flow

$$\left(\frac{dP}{dz}\right)_{TP} = \left(\frac{dP}{dz}\right)_g + 31.3\,\lambda^{1.25}\,\frac{\rho_g v_o^2}{gD} \tag{2.57}$$

For stratified flow

$$\left(\frac{dP}{dz}\right)_{TP} = \left(\frac{dP}{dz}\right)_g + 3.20\,\lambda^{0.875}\,\frac{\rho_g v_o^2}{gD} \tag{2.58}$$

where λ is the liquid fraction input flow

$$\lambda = \frac{Qf}{Q_f+Q_g} \qquad (2.58.1)$$

where Q is the volumetric input flow rate. Eqs. (2.56) - (2.58.1) are based on British units.

Liquid hold-ups in the spiralled tubes are less than the hold-ups obtained in horizontal pipes from Fig. (2.18).

Boyce et al (42-1968) measured the liquid hold-up and air-water two-phase pressure drop using four different diameters of coil - 10, 5, 2½ and 1 foot. The diameter of tube is 3.18 cm (1.25in). The experimental frictional pressure gradient was evaluated from the measurements.

$$\left(\frac{dP}{dz}\right)_{TPF} = \left\{\left(\frac{dP}{dz}\right)_{TP} (1 - D')\right\} - C' \qquad (2.59)$$

where

$$D' = W_g^2\left\{\left(\frac{dv_g}{dP}\right) / \frac{(\pi a^2)}{4}\right\}^2 . g_o.\alpha \qquad (2.60)$$

and $C' = \frac{g \sin\theta}{g_o} \{\alpha\rho_g + (1 - \alpha)\ \rho_f\}$ (2.61)

The dimensionless parameter Martinelli's parameter $\phi_f^2 = \frac{\left(\frac{dP}{dz}\right)_{TPF}}{\left(\frac{dP}{dz}\right)_f}$

is expressed as follows:

$$\phi_f = \frac{1}{(1-\alpha)} \quad \text{for } \frac{R}{a} = 96, 48 \text{ and } 24 \qquad (2.62)$$

and

$$\phi_f = \frac{0.75}{(1-\alpha)} \quad \text{for } \frac{R}{a} = 9.6 . \qquad (2.63)$$

Following Collier and Wallis's (43-1967) and Collier's (44-1972) notations, Banerjee et al (39) used the same approach as that of Lockhart-Martinelli for a helical coil,

$$\left(\frac{dP}{dz}\right)_{TPFH} = \left(\frac{dP}{dz}\right)_{gTPH} = \left(\frac{dP}{dz}\right)_{fTPH} \qquad (2.64)$$

where the subscript H refers to the helical coils. Banerjee et al derived the parameter X for helical coils as

$$X^2 = \frac{\left(\frac{dP}{dz}\right)_{fH}}{\left(\frac{dP}{dz}\right)_{gH}} \qquad (2.65)$$

Figs. (2.19a) and (2.19b) were obtained by them (39) who used nine coils of varying coil diameter and helical angles with liquids of three different viscosities and air at various pressures.

Agakawa et al (8) presented experimental data in the range of superficial water velocity W_{fo}; 0.35~1.16 $^{m}/s$, and superficial air velocity W_{go}: 0.5$^{m}/s$. Their coils were constructed of 9.92 mm I.D. copper tube and the ratios of tube diameter to coil diameter were 1/11 and 1/22.7 and the lengths were 4m and 5m respectively. A simple correlation of frictional pressure drop ratio $\frac{\left(\frac{dP}{dz}\right)_{TPS}}{\left(\frac{dP}{dz}\right)_{fs}}$ to void fraction in horizontal, inclined and vertical straight tubes was defined as follows:

$$\frac{\left(\frac{dP}{dz}\right)_{TPS}}{\left(\frac{dP}{dz}\right)_{fs}} = (1-f_g)^{-z} \qquad (2.66)$$

$$\text{where} \quad f_g = 0.833 \cdot \frac{W_{go}}{W_{go}+W_{fo}} \qquad (2.66.1)$$

For horizontal tube at atmospheric pressure z = 1.4,

" vertical tube at atmospheric pressure z = 1.51.

The value of z coincides with the empirical value of helical coiled tube;

helical coiled tube $\frac{a}{R} = \frac{1}{11}$ z = 1.2

helical coiled tube $\frac{a}{R} = \frac{1}{22.7}$ z = 1.28

Thus the values of z decrease with an increasing $\frac{a}{R}$, and this relationship is expressed by the following empirical equation:

$$\frac{(\frac{dP}{dz})_{TPC}}{(\frac{dP}{dz})_{fc}} = (1 - f_g)^{2.3\frac{a}{R} - 1.4} \qquad (2.67)$$

Eq. (2.67) becomes

$$\frac{(\frac{dP}{dz})_{TPC}}{(\frac{dP}{dz})_{fc}} = \left[1 - \{0.833 \frac{W_{go}}{(W_{fo}+W_{go})}\}\right]^{2.3\frac{a}{R} - 1.4} \qquad (2.68)$$

Martinelli and Nelson (45-1948) proposed a correlation for steam-water flow where ϕ_{fo}^2 was plotted against mass quality at various pressures.

$$\phi_{fo}^2 = \frac{(\frac{dP}{dz})_{TPF}}{(\frac{dP}{dz})_{fo}} \qquad (2.69)$$

where ϕ_{fo}^2 is the parameter based on pressure gradient for total flow assumed liquid.

Farmer (46-1972) put forward the relationship between the frictional pressure gradient and the wall shear stress and tube cross-section area,

$$(\frac{dP}{dz})_F = \frac{\tau S}{A} \qquad (2.70)$$

where A is the tube cross-section area, S is the tube perimeter and τ is the wall shear stress.

His conclusion that curvature does not affect two-phase flow pressure drop to the same extent that it affects single-phase flow is not in agreement with the work of other authors (e.g. Rippel et al (41), Boyce et al (42), Banerjee et al (44)) who used the single-phase friction factor measured in the coil when correlating two-phase data.

For the heated coils, Owhadi et al (47-1968) conducted experiments with an upward steam-water two-phase flow in a helical coiled tube of $\frac{a}{R} = 0.05$ in the range of Lochart-Martinelli parameter $X_c = 0.04 \sim 0.6$. Their experimental points dispersed in a range of 35% around the ϕ_{tt} curve of the Lockhart-Martinelli correlation, shown in Fig. (2.20a).

Kozeki (48-1973) conducted similar experiments to Owhadi et al with $\frac{a}{R} = 0.03$ in the pressure range of $10 \sim 30$ $^{kg}/_{cm^2}$ and in the flow rate range of $1.3 \times 10^6 \sim 1.95 \times 10^6$ $^{kg}/_{m^2h}$, shown in Fig. (2.20b).

Ruffel (49-1974) proposed a very complex pressure gradient formula, but this has only been verified for pressure above 70 bar.

From these reviews three characteristics of two-phase flow of curved or helical coiled tubes may be summarized:

a. For low pressure, two-component systems, the Lockhart-Martinelli method is generally effective.
b. For very viscous fluids, the calculated results are substantially too high.
c. Steam-water results have a rather wide spread (-40%~+30%), but the Lockhart-Martinelli and Martinelli-Nelson correlation can be used for the helical or curved tubes.

2.5.2 Flow patterns in the helically coiled tubes.

One flow pattern map, that of Baker (50-1958) has become generally accepted and widely used for horizontal channels. Baker plotted the observations of various workers in terms of the co-ordinates ($^{G_g}/_{\lambda}$) and ($^{G_f\lambda\Psi}/_{G_g}$). The factors λ and Ψ are given by the relationships:

$$\lambda = \left\{\left(\frac{\rho_g}{\rho_A}\right)\left(\frac{\rho_f}{\rho_W}\right)\right\}^{\frac{1}{2}} \tag{2.71}$$

and

$$\Psi = \left(\frac{\sigma_W}{\sigma}\right)\left\{\left(\frac{\mu_f}{\mu_W}\right)\left(\frac{\rho_W}{\rho_f}\right)^2\right\}^{\frac{1}{2}} \tag{2.72}$$

The subscript A and W refer to the values of the physical properties for air and water respectively at standard atmospheric pressure and temperature ($20^{o}C$). Scott (51-1963) has since modified Baker's map. Alves (52-1954) also plotted the flow patterns but instead used as co-ordinates the superficial mass velocities of the vapour and liquid phases.

Boyce et al (42) obtained the flow pattern data for a 3.18cm (1.25in) diameter tube with a 76.3cm (2.5ft) coil diameter using an air-water mixture, and these data are plotted on Baker's original map, Fig. (2.21a).

No bubbly flow pattern was observed presumably because of the method chosen to mix the phase. The water was introduced into the air stream through the porous wall of the mixer; had the air flow passed through the porous wall instead, bubbly flow would have been one of the flow patterns observed. In this figure it will be observed that although the flow patterns occur in the same relative locations as those noted on Baker's original map, the positions of the transition boundaries observed in their study do not agree with those suggested by Baker (50).

Banerjee et al (39) studied flow patterns with the help of high speed cine-camera taken at 10,000 frames/sec. They used nine coils of varying ratio of the tube diameter to the coil diameter (0.026∿0.104) and varying helical angle (2^{o}∿8^{o}) with liquids of three different viscosities and air at varying pressure (1∿3 atm). The data are plotted in Fig. (2.21b). No data were taken in bubble-plug or purely stratified flow regions.

Kozeki et al (53-1970) obtained the data of flow patterns in helical glass coils of varying tube diameter (14.3∿19.5mm) and coil diameters (300∿500mm) with air-water flow at atmospheric pressure. The data were plotted in the horizontal flow map of Alves (52) and were converted to a Baker's map, Fig. (2.21c). He reported that the position of the transition from wavy-stratified flow to annular flow in a curved pipe was less obvious than that of a straight pipe.

Farmer (54-1972) determined that the differences between upflow and downflow (angle against the horizontal is $\pm 5.88^{o}$) helices of the various diameter ratios ($\frac{a}{R}$ = 0.014∿0.052) are small as far as pressure drop and void fraction are considered, but that a region of stratified flow exists in downflow, Fig. (2.21d).

The most significant effects of coiling are seen in annular flow. Banerjee et al (55-1967) suggested that as the liquid density is usually considerably larger than that of the gas, it is reasonable to suppose that liquid would be forced to the outer wall of the coiled tube by centrifugal forces. However, it was observed that for certain ranges of liquid and gas flow rates the liquid travelled on the inner wall of the tube, shown in Fig. (2.22).

This phenomenon is called "Film inversion". The film inversion was found to occur at low liquid but high gas flow rates. At a constant water rate and low gas rates, the liquid film in upward helical concurrent flow was located mainly on the outer wall of the tube.

As gas velocity was increased the liquid film moved from this position, first into the neutral position shown in Figs. (2.22) and (2.23b) and then into the inverted position shown in the same Fig. (2.23c). As the gas velocity continued to increase, the film moved further and further up the inner wall of the tube, Fig. (2.23d).

When the liquid is in the neutral position it is assumed that the centrifugal forces acting on equal volumes of gas and liquid are equal, that is

$$\frac{\rho_f v_f}{r} = \frac{\rho_g v_g}{r} \qquad (2.73)$$

where v is the mean velocity in the neutral position in Fig. (2.22).

When the liquid film is in the inverted positions and if $\rho_f g >> \rho_g g$, they define the equation as follows:

$$\tan(\theta-\phi) = \frac{\left(\frac{\rho_g v_g^2}{r} - \frac{\rho_f v_f^2}{r}\right)}{\rho_f g} \qquad (2.74)$$

where ϕ is shown in Fig. (2.22).

The angle $(\theta-\phi)$ may assume any value, depending upon the relative magnitude of v_f^2 and v_g^2. For experimental purposes ϕ was fixed at $14^o \pm 1^o$ and θ was quite constant about 28^o.

Kooijman and Lacey (56-1968) have measured local film flow-rates, using similar high flow rates to Banerjee et al, (55) in vertical 90^{o}, 180^{o} and 360^{o} bends. The liquid became distributed around the inside of the tube with the main mass of the flow passing on the inner wall of the tube and a small mass travelling on the opposite outer wall (Fig. (2.23e)). These masses were separated by thin film sections. The peak flow on the inside bend of the tube was an order of magnitude greater than flow rates of either that of the thin film or that of the smaller peak.

Therefore, at higher velocities liquid was entrained from the film and thrown onto the outer part of the wall, Fig. (2.23e). Shires and Khanna (57-1971) also reported the same phenomenon as Fig. (2.23e).

Lacey (58-1970) performed a stability analysis of the pattern as Fig. (2.23d) and showed that a condition for stability was

$$\frac{U_g}{U_f} \cdot \sqrt{\frac{\rho_g}{\rho_f}} > 1 \qquad (2.75)$$

where U_g and U_f are the slopes of the velocity profiles at specific points in the flow.

More recent flow visualisation works using end-viewing cine-camera devices have indicated a far more complex situation than that shown in Fig. (2.23e) by Hewitt (59-1970), Fisher and Hopley (60-1971) and Maddock (61-1973).

2.5.3 Heat Transfer coefficient in two-phase flow

Boiling flow inside helically coiled tubes has concerned a number of researchers who have attempted to examine the flow phenomenon locally. Experimental results have revealed that the two-phase heat transfer coefficients of helically coiled tubes vary at different positions around the periphery of the tube, and it is higher than those of straight tubes under similar conditions. This has been interpreted as being due to the effect of secondary circulation of flow, gravity and centrifugal forces (as discussed in the section (2.5.2)).

In principle the correlations presented will apply to any flow regime in the absence of very high mass velocity. The two-phase forced convection region is usually associated with annular flow.

As suggested by Martinelli (40) many of the correlations which have been proposed for two-phase convective heat transfer coefficients, h_{TPK}, are of the form:

$$\frac{h_{TPK}}{h_{fo}} \text{ (or } \frac{h_{TPK}}{h_f} \text{)} = f_n \left(\frac{1}{X_{tt}}\right) \qquad (2.76)$$

where h_{fo} is the heat transfer coefficient if the total fluid were flowing with liquid properties in the tube. The parameter X_{tt} is the Lockhart-Martinelli parameter.

$$X_{tt} = \left(\frac{1-x}{x}\right)^{0.9} \left(\frac{\rho_g}{\rho_f}\right)^{0.5} \left(\frac{\mu_f}{\mu_g}\right)^{0.1} \qquad (2.77)$$

If there is some entrainments, the coefficient h_f should be calculated by assuming that the liquid in the film is flowing alone in the tube. Most empirical correlations based on this assumption are of the form:

$$\frac{h_{TP}}{h_f} = a \left(\frac{1}{X_{tt}}\right)^b \qquad (2.78)$$

In general h_f is calculated from Seban and McLaughlin's formula (22),

$$h_f = 0.023 \left(\frac{k_f}{D}\right) \cdot Re^{0.85} \cdot Pr^{0.4} \cdot \left(\frac{a}{R}\right)^{0.1} \qquad (2.79)$$

Values of the coefficients a and b produced by various workers are shown in Table (2.1).

TABLE (2.1) Coefficients in convective heat-transfer equations

Authors	a	b	Fluid	Two-phase systems	Vapour mass quality
Dengler & Addoms (1956)	3.5	0.5	water	straight vertical	x<0.7
Guerrier & Talty (1956)	3.4	0.45	various organics	"	x<0.12
Schrock & Grossman (1959)	2.5	0.75	water	"	x<0.59
Collier & Pulling (1962)	2.167	0.699	water	"	x<0.66
de La Harpe et al (66-1968)	1.8	0.75	helium	helically coiled $\frac{a}{R} = \frac{3}{110}$	0.2≤x≤0.8
Kozeki (48-1973)				helically coiled	
θ=0, 180°	2.5	0.75	water	14.3>a>19.5mm	0<x<100
θ = 90°	2.5	0.86		300<R<400mm	
θ = 270°	1.7	0.68			

FROM: BUTTERWORTH & HEWITT (62-1977)

Owhadi et al (47, 64-1967) calculated the local heat transfer coefficient from surface temperatures at different ranges of vapour mass quality shown Fig. (2.24). They took temperature measurements at four equally spaced points on the tube wall, with the top designated as 0°, the origin.

They concluded that near the coil inlet the heat transfer coefficient was the highest for the 90^{o} position and the lowest for the 270^{o} position. This is due to the varying extent of nucleate boiling around the circumference. The highest wall temperature (at 90^{o} position) gives rise to large nucleate boiling components at the point compared to the other three.

Further from the inlet, the heat transfer coefficient went through a minimum. This behaviour is thought to be a result of the suppressing effect of turbulence on nucleation.

Owhadi et al (47) and Bell and Owhadi (65-1969~70) also reported the local heat transfer coefficients at different coil diameter (9.86in and 20.57in). The correlations of $\frac{h_{TP}}{h_f}$ as a function X_{tt} for the two coils are plotted in Figs. (2.25a) and (2.25b).

For values of $1/X_{tt} <\sim 10$, the data is seen to scatter. This is due to the existence of a significant nucleate boiling component in these low-velocity experiments.

de la Harpe et al (66-1968) examined the local heat transfer coefficient with a helically coiled Monel tube, 3mm I.D., 11cm helix diameter and 488.5cm length using liquid helium. They indicated that local heat transfer in the nucleate boiling and forced convection regimes may be calculated from the equation:

$$h_{TP} = 0.023 \cdot \frac{h_f}{D} \cdot \left(\frac{aG}{\mu_m}\right)^{0.85} \cdot (Pr)^{0.4} \cdot \left(\frac{a}{R}\right)^{0.1} \qquad (2.80)$$

where μ_m is the mixture viscosity.

In the intermediate quality regime ($0.2 \lesssim x \lesssim 0.8$) the data are represented equally well by the equation which is shown in Table (2.1).

Kozeki et al (53) have reported the investigation of helically-coiled tube one-through boilers at pressures of 5∿21 bars. It was noticed that the local heat transfer coefficients were less likely to be affected by mass flow rate, vapour quality and pressure.

The average heat transfer coefficient, unlike the Owhadi correlation, did not alter with the increase of vapour quality. They attributed the discrepancy to the difference of test conditions. Later, Kozeki (48) correlated the heat transfer coefficient and applied the Lockhart-Martinelli parameter which we then compared to the Schrock and Grossman (98-1959) empirical equation shown in the Table (2.1). He defined the local heat transfer coefficients shown in the Table (2.1) and the average one as follows:

$$\left(\frac{h_{TPC}}{h_{fc}}\right)_{average} = 2.5 \left(\frac{1}{X_{tt}}\right)^{0.75} \qquad (2.81)$$

Comparing Bell and Owhadi's (65) results in the atmospheric pressure with those of Kozeki's results the differences are seen to be small.

The applicable limits from this comparison will be as follows:

Pressure : Atmospheric $\longleftrightarrow$ $30^{kg}/cm^2 g$

$\frac{a}{R}$: 0.023 - 0.05.

Duchatelle et al (67-1973) have employed the experimental results of Owhadi et al (64) for fitting the heat transfer coefficient in the nucleate boiling zone, and they can be well fitted by the equation:

$$\frac{h_{TPC}}{h_{fc}} = K \exp\left(4.436 - 29.722\, X_{tt} + 141.237\, X_{tt}^2 - 325.34\, X_{tt}^3 + 272.58\, X_{tt}^4\right) \qquad (2.82)$$

where $K = 1$ when $0.05 < X_{tt} < 0.2$

and $K = \left(\frac{R}{20a}\right)^{1/4}$ when $X_{tt} < 0.05$

This equation is valid for $X_{tt}<0.2$ and $0.014<\frac{a}{R}<0.04$.

2.5.4 Dryout* (or Burnout)

Since 1964, when Carver et al (68-1964) reported on their experiments with the diameter ratios $(\frac{R}{a})$ of 76 and 262, it has been well known that the departure from nucleate boiling (DNB) behaves differently between coiled and straight vertical tubes. In particular, the following differences are noted:

(a) in helical tubes the DNB steam quality is different for different positions around the tube periphery while being constant in a straight vertical tube, shown Fig. (2.26).

(b) a coiled tube has a higher average steam quality than a straight tube.

More experimental data on forced convection boiling of water at atmospheric pressure in two helically-coiled tubes was given by Owhadi et al (47). They have found a complete wetting of the tube wall up to high qualities (99%), and attribute this to the secondary flow in the vapour core which exerts a drag on the liquid phase and forces it to flow to the inner surface of the tube.

Miropolski and Pikus (69-1969) suggested the heat transfer for film boiling as follows:

$$(Nu)_{film} = C.Re^{0.8} \cdot Pr_f^{0.8} \cdot Z \qquad (2.83)$$

where

$$Re = \frac{Ga}{\mu_{g_{sat}}} \qquad (2.83.1)$$

$$z = y\left(x + \frac{\rho_{g_{sat}}}{\rho_{f_{sat}}}(1-x)\right)^{0.8} \qquad (2.83.2)$$

$$y = \frac{\rho_{fsat}}{\rho_{gsat}} \left(1 - \frac{\rho_{fsat} - \rho_{gsat}}{\rho_{fsat}} \cdot x^{0.2}\right) \qquad (2.83.3)$$

$$C = 0.017 \left(1 + 1.59 \frac{a}{R}\right) \qquad (2.83.4)$$

for $98 < p < 215$ bars and $10 < G < 200 g/cm^2 s$, and where the physical properties in the vapour Prandtl number are evaluated at the wall temperature.

Kozeki et al (48 & 53) described the dryout from the experiments. Fig. (2.27) shows the heat flux variations of four locations on the coiled tube section around the dryout steam quality for mass flow rates 1.75, 1.17 and 0.58×10^6 kg/m^2h.

As the mass flow rate increases, dryout appears at higher steam quality and heat flux drops more sharply. Dryout occurs first at upper and then lower, outer and inner sides of the tube cross section respectively. Increasing the steam quality up to 1, dryout at inner side begins.

It was also recognised that as the pressure increased the dryout steam quality became slightly higher, and as the heat flux increased it became lower.

Cumo et al (70-1972) investigated post dryout heat transfer comparatively in straight and coiled tubes using a Freon-12. They noted that in post-dryout heat transfer a wall temperature difference between the inner and outer sides of the coil appears. At first this difference increases, reaches a maximum then decreases monotonically with pressure.

Dutchatella et al (67) defined the following critical steam quality, x_{cr}, correlated from three coils:

$$x_{cr} = 1.69 \times 10^{-4} \; q^{0.719} \; G^{-0.212} \; \exp 0.0025.P \qquad (2.84)$$

for $0.014 < \frac{a}{R} < 0.040$.

They concluded that the tube diameter had very little effect on the average steam quality value at the DNB, the most important parameters being:

(i) critical heat flux,

(ii) water mass velocity

and (iii) saturation pressure.

Ruffell's (49) critical steam quality correlations were:

$$x_{cr\ \theta=0^o} = 1 - \frac{0.13\ (\frac{R}{100a})}{(G/10^3)^{1.5}} \quad (\frac{q}{100})^n \qquad (2.85)$$

where $n = 0.75\ (G/10^3)^{0.5}$ (2.85.1)

and q is the heat flux.

$$x_{cr\ \theta=270^o} = 1 - 0.0004q - 0.0109\ (\frac{G}{10^3})^2\ (\frac{R}{a})^{0.5} \qquad (2.86)$$

for $0.06 < \frac{q}{G} < 0.034$ KJ/kg

and $300 < G < 1800$ kg/m^2s.

The onset of dryout was found to be either at the inner (270^o) or upper (0^o) positions. Initiation at the upper position was confined to low mass velocity conditions in which gravity forces exceeded centrifugal forces. Rather more than half of the results were for dryout starting at the inner position.

2.5.5 Convective heat transfer to vapour phase

When the fluid has become nearly dry vapour, it behaves once more as a single-phase fluid and obeys similar laws to the liquid phase. The single-phase heat transfer coefficient of the following form is employed beyond the superheated boundary.

$$Nu_s = K \ Re^{m} . Pr^{n} \qquad (2.87)$$

A comprehensive review of the dry steam heat transfer coefficients in a vertical straight tube has been carried out by Bailey et al (71-1973).

At pressure ranges of 20-100 bars Heineman's correlation (72-1960) can be used where the constants of equation (2.87) are:

$$K = 0.0133 \quad m = 0.84 \quad n = {}^{1}/3 \qquad (2.88)$$

for $60 < (\frac{R}{a})$

and

$$Nu_s = 0.0157 \ (Re)^{0.84} . \ Pr^{1/3} . (\frac{R}{a})^{-0.04} \qquad (2.89)$$

for $6 < (\frac{R}{a}) < 60$

The correlation of Bishop et al (73-1965) can be used more accurately than that of Heineman at the higher pressures (150-210 bars) where

$$K = 0.0133 \quad m = 0.886 \quad n = 0.61 \qquad (2.90)$$

Ruffel (49) reported a correlation at the pressure range of 80∿180 bars in a helically-coiled tube as follows:

$$K = 0.0359 \quad m = 0.76 \quad n = 0.53 \qquad (2.91)$$

for $2 \times 10^5 < Re < 8 \times 10^5$.

and also recommended the Heineman's correlation for superheated steam.

---

*Throughout this Chapter, Dryout, Burnout and DNB are employed indifferently as synonyms. The precise definition is in section (4.3.5).

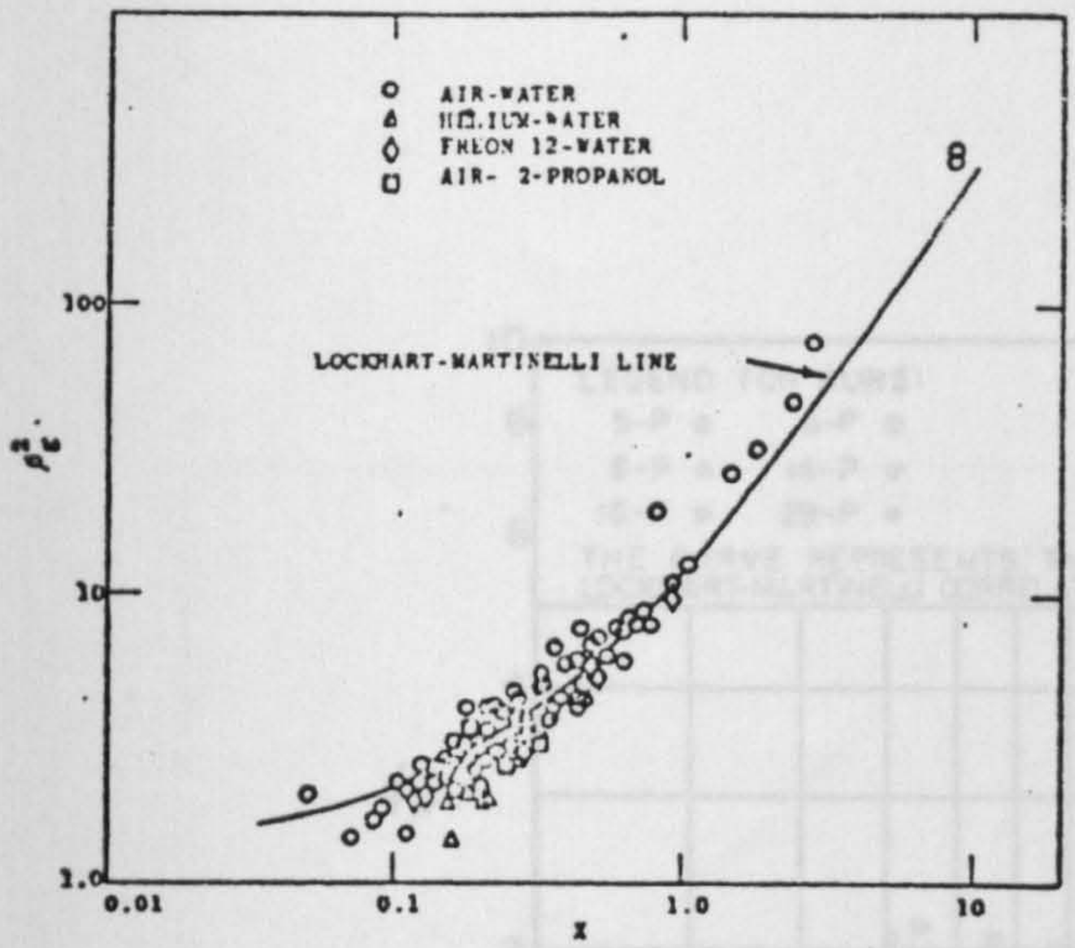


Fig.(2.17a). Pressure drop in two-phase flow from Rippel et al (41).

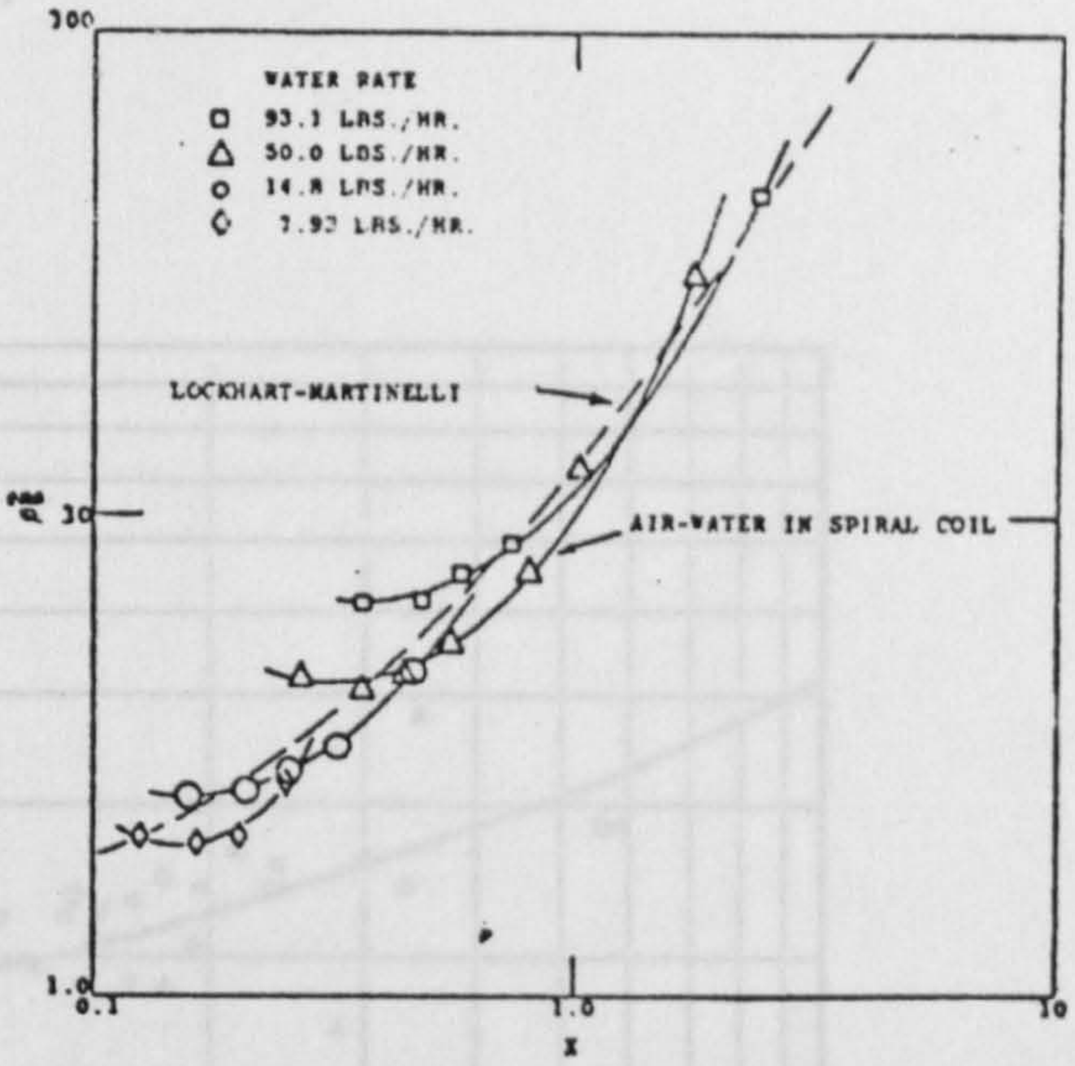


Fig.(2.17b): Liquid rate parameters in X vs. ϕ_o^2 type pressure drop correlation from Rippel et al (41).

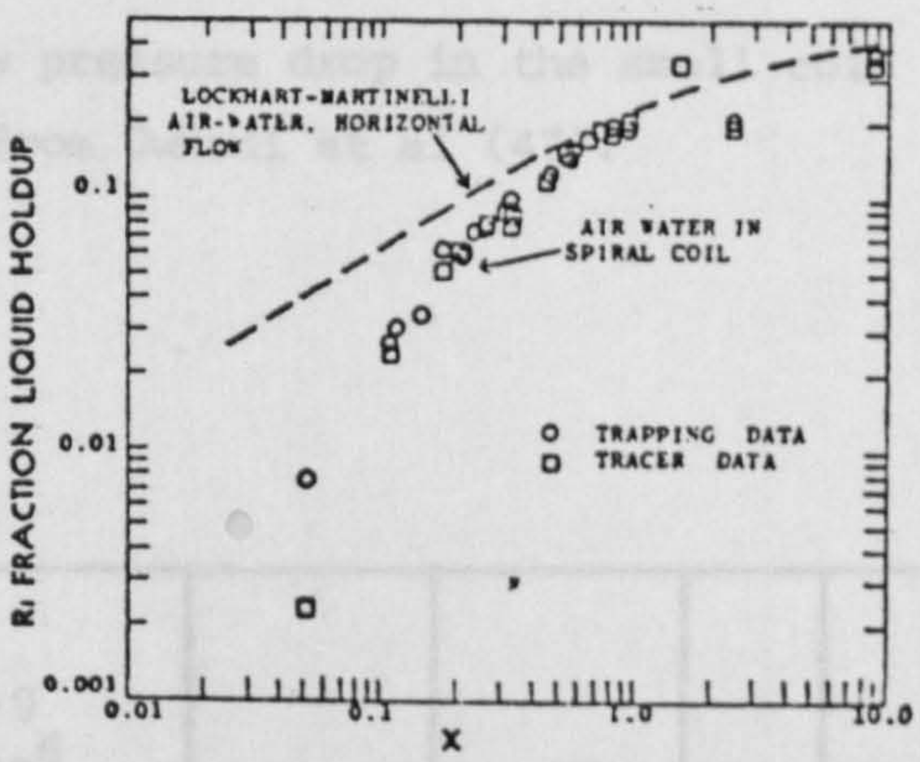


Fig.(2.18): Holdup in spiral coil compared with data from horizontal flow from Rippel (41).

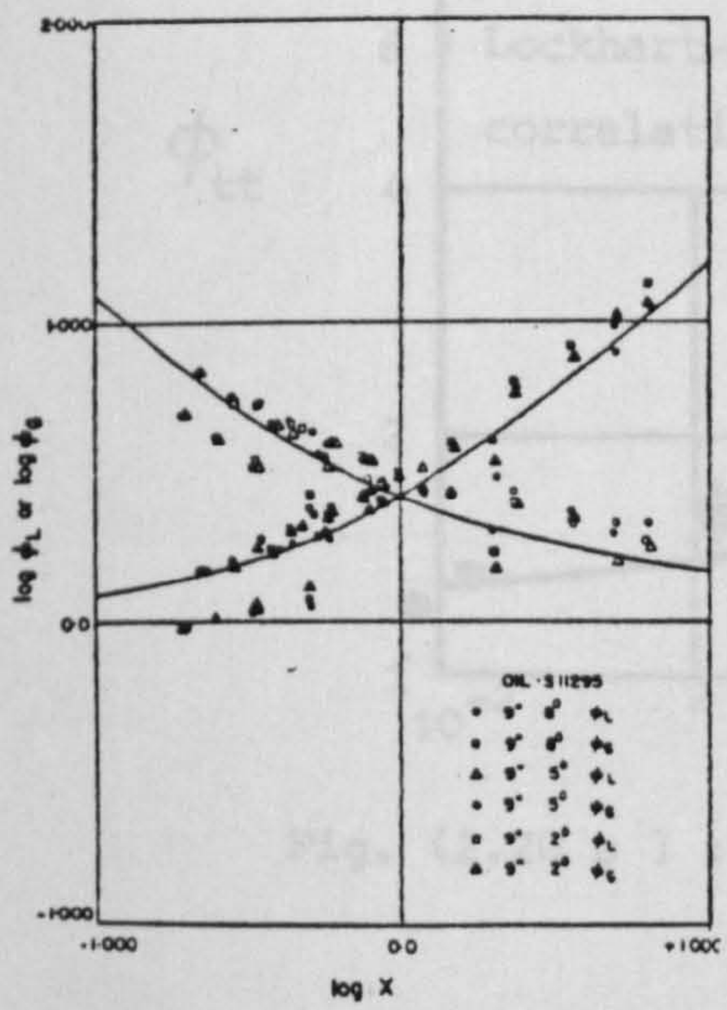
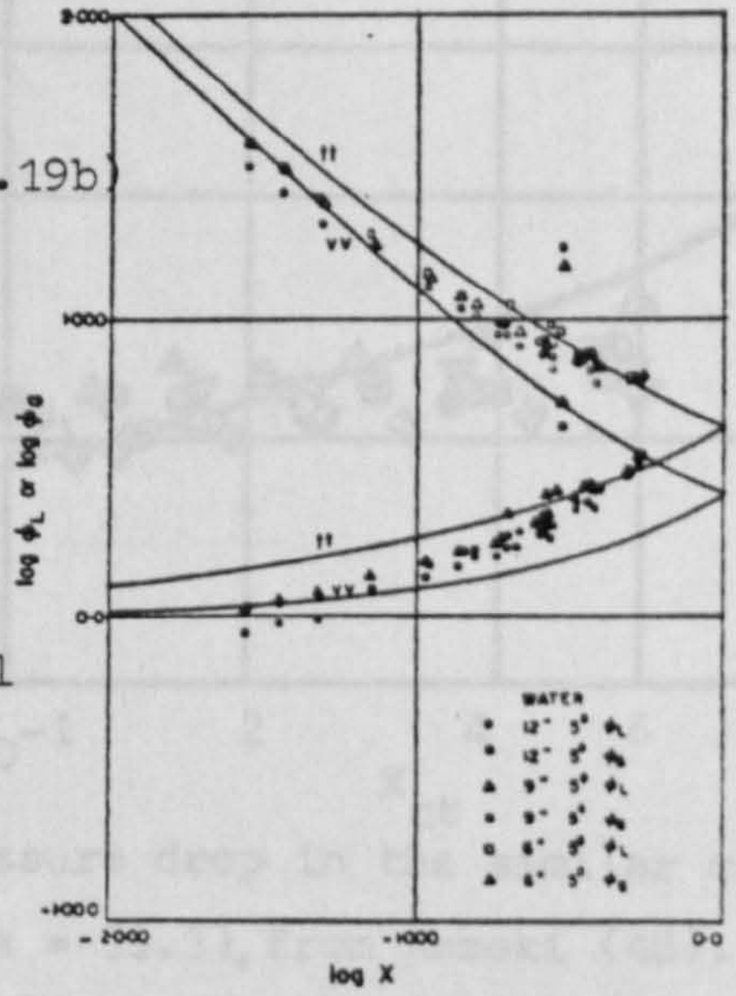


Fig. (2.19a)

Effect of coil angle on pressure drop in helically coiled tubes for Oil No. I — air system in 9-in. coils. Lines are the Lockhart-Martinelli viscous-viscous correlations for straight tubes.

from Banerjee et al (39).



Effect of coil radius on pressure drop in helically coiled tubes for water-air systems in 5° coils. Lines (vv), (tt) are the Lockhart-Martinelli viscous-viscous and turbulent-turbulent relationships; respectively, for flow in straight pipes.

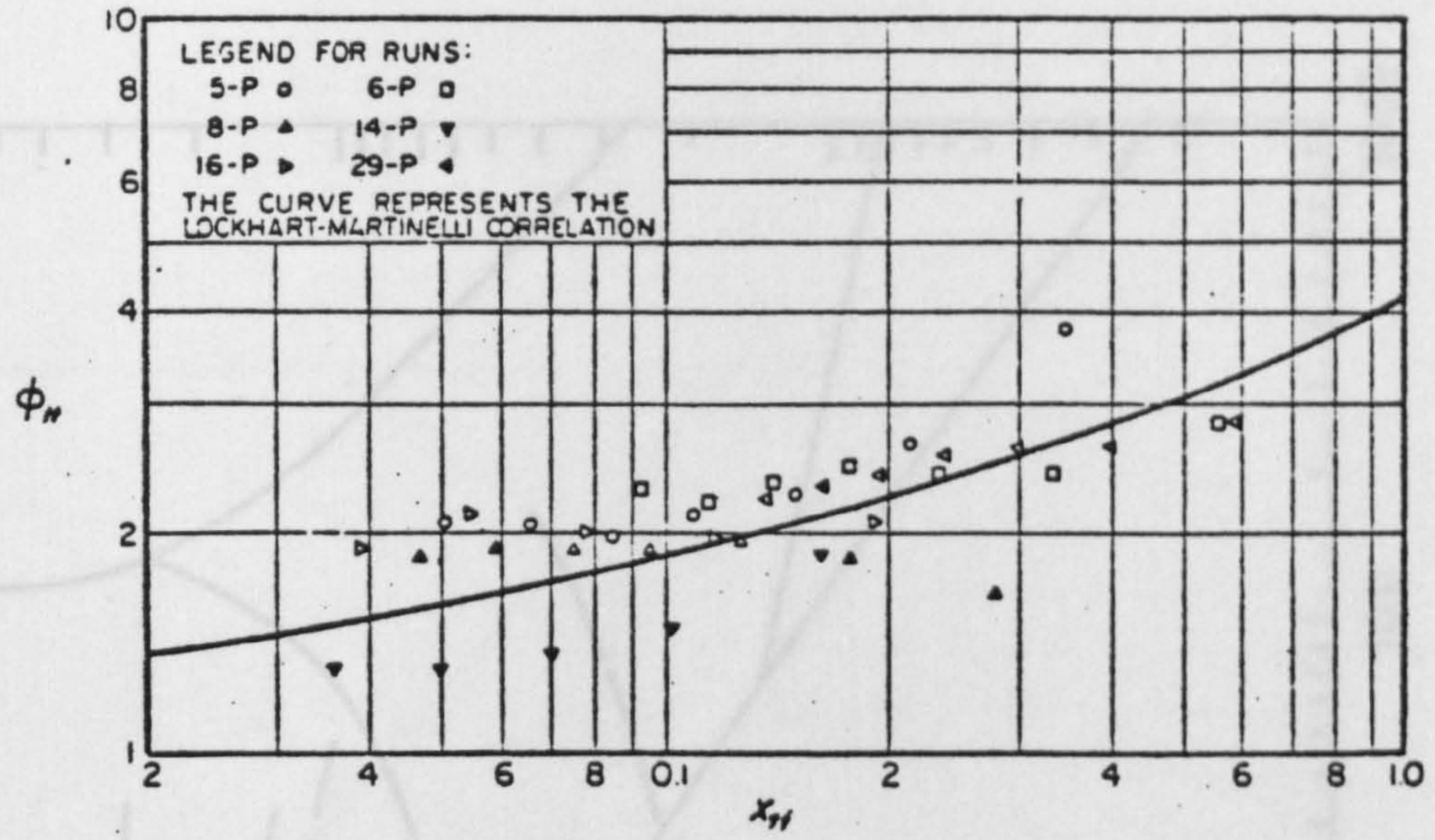


Fig. (2.20 a) : Two-phase flow pressure drop in the small coil (R/a = 20.0) from Owhadi et al (47).

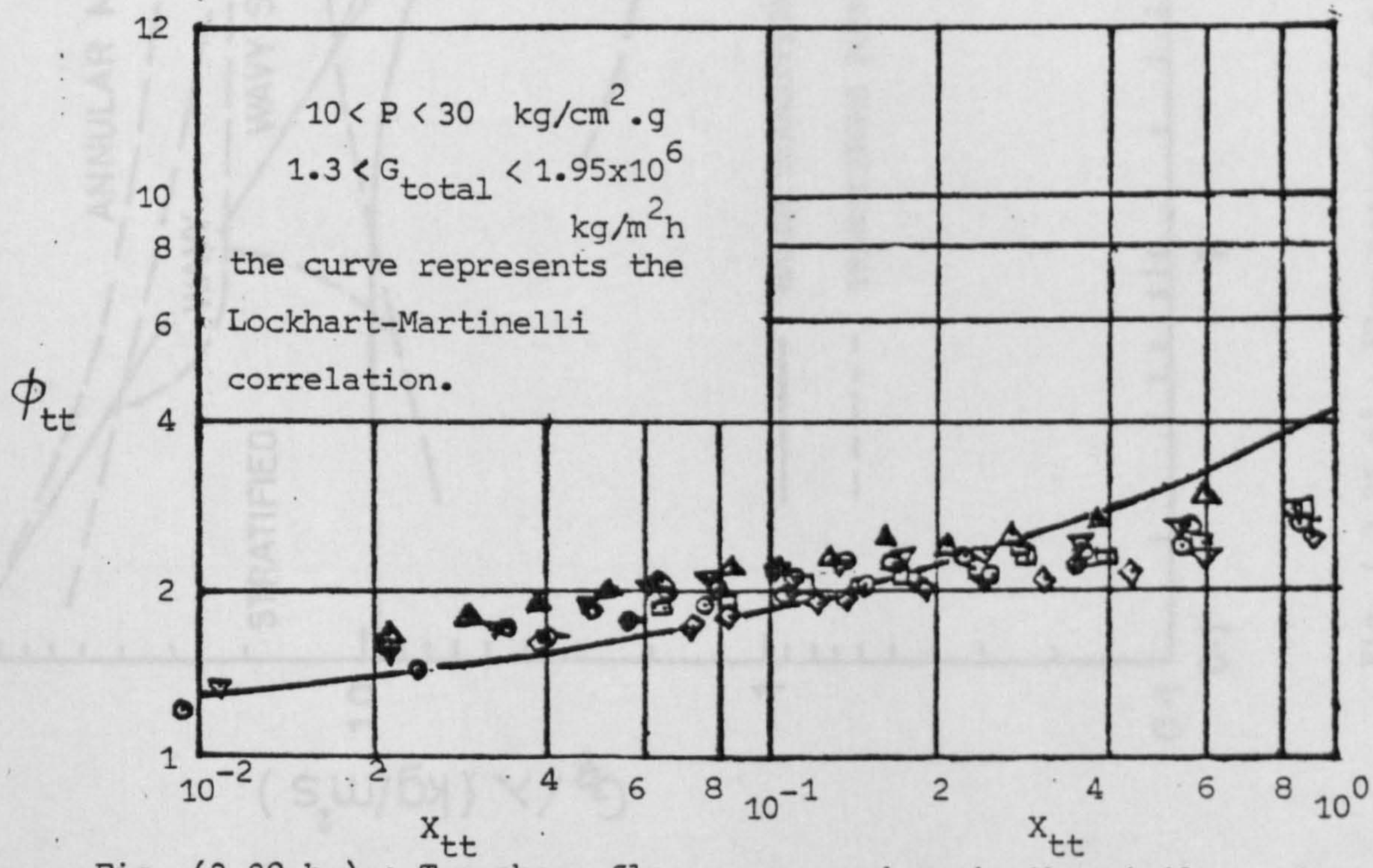


Fig. (2.20 b) : Two-phase flow pressure drop in the similar coil as Fig.(2.20a) (R/a = 33.3), from Kozeki (48).

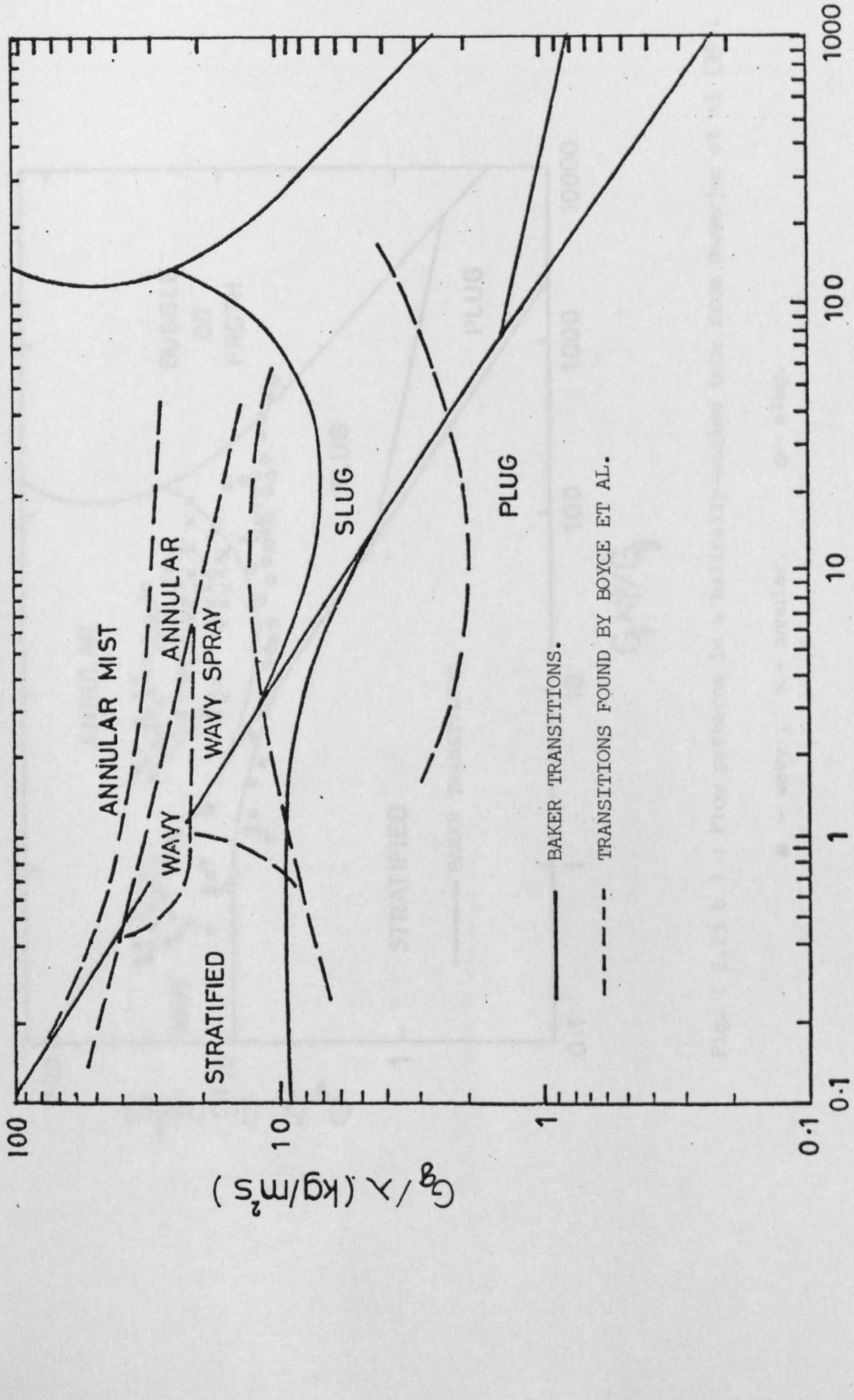


Fig. (2.21 a) : Flow patterns in a helically-coiled tube from Boyce et al (42).

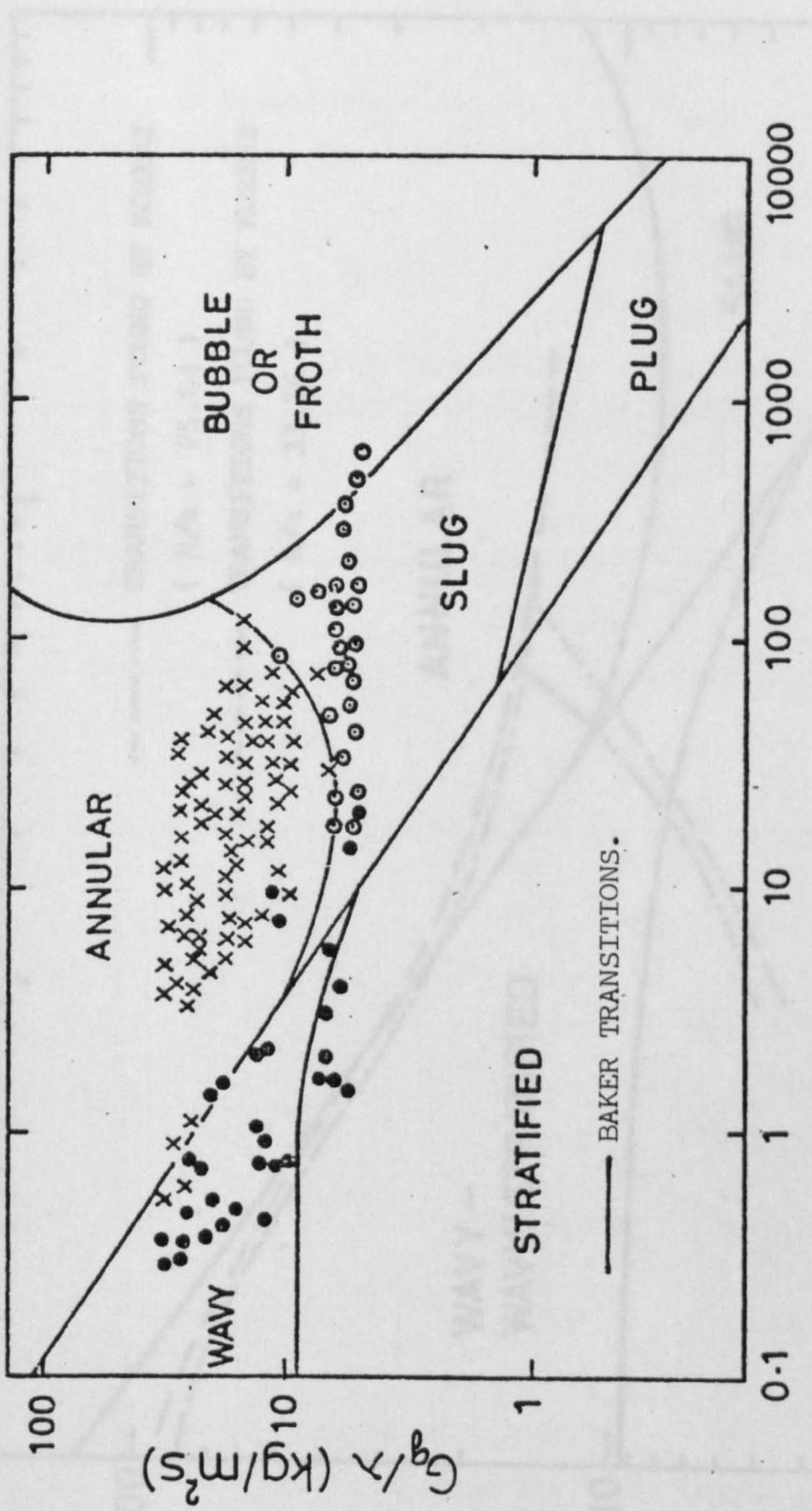


Fig. (2.21 b) : Flow patterns in a helically-coiled tube from Banerjee et al (39).

● - wavy , × - annular,

⊙- slug.

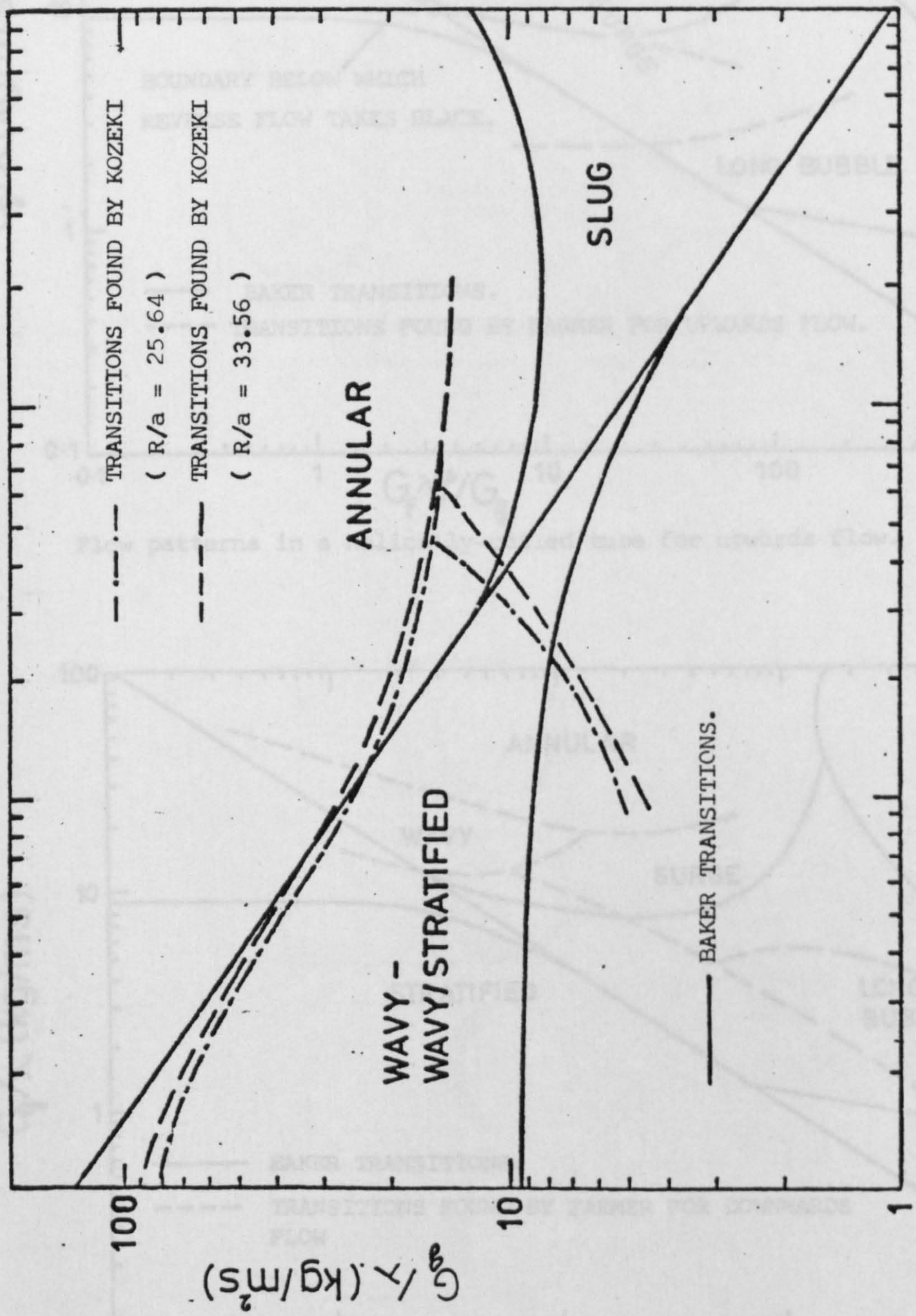
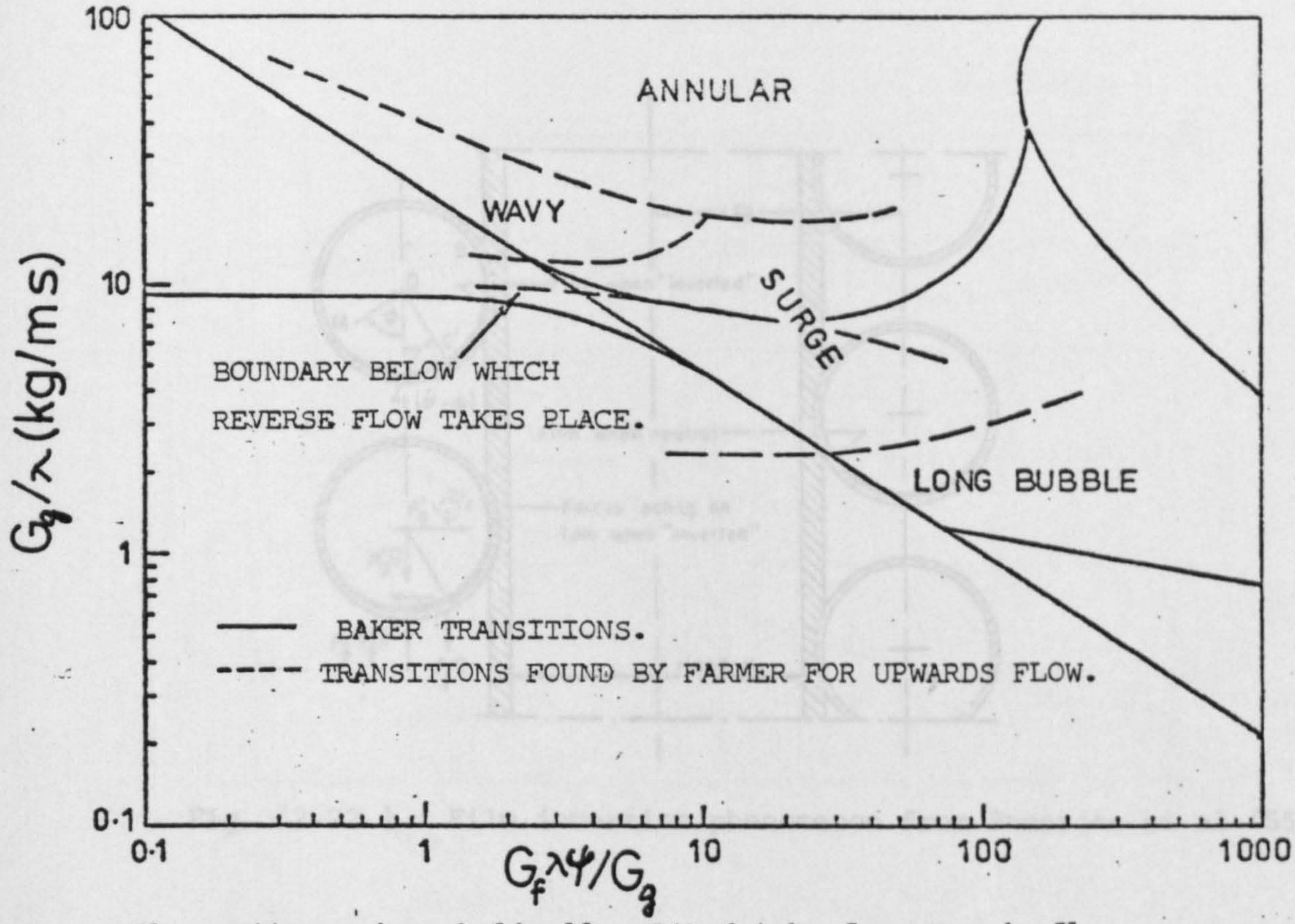


Fig. (2.21 c) : Flow patterns in a helically-coiled tube from Kozeki et al (53).



Flow patterns in a helically-coiled tube for upwards flow.

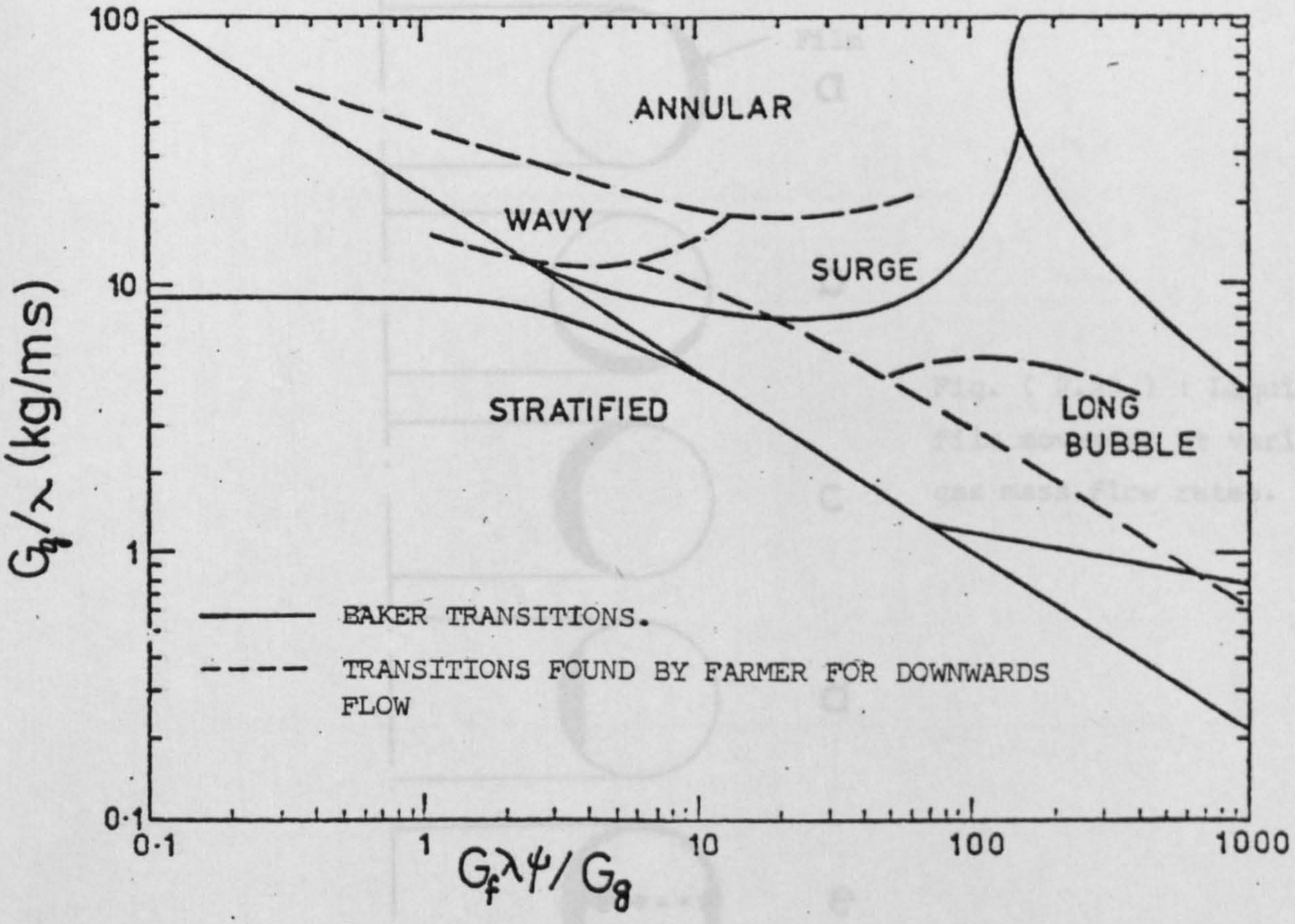


Fig. (2.21d) : Flow patterns for UPWARDS and DOWNWARDS flows from Farmer (54).

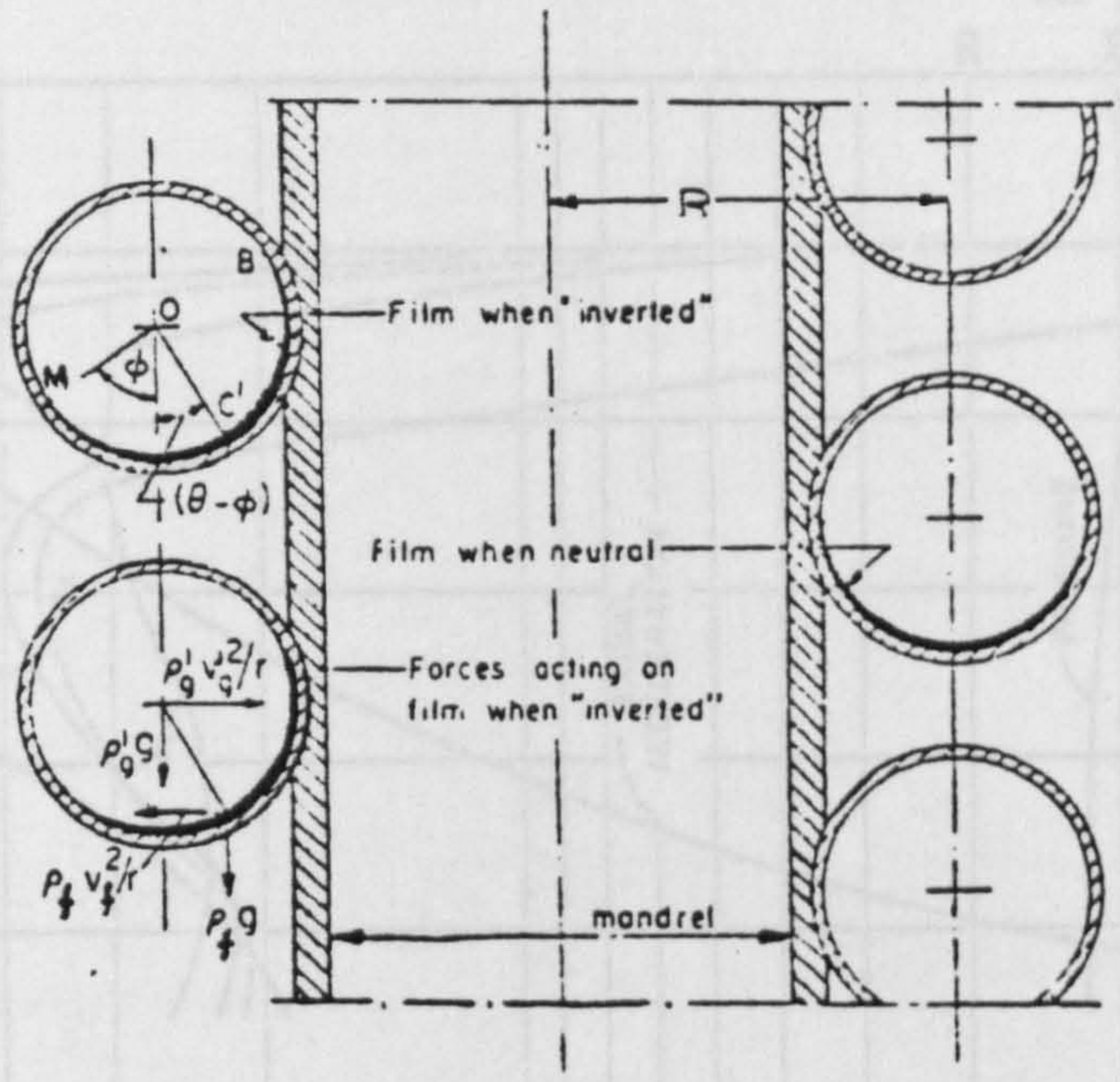


Fig. (2.22) : Film inversion phenomenon from Banerjee et al (55).

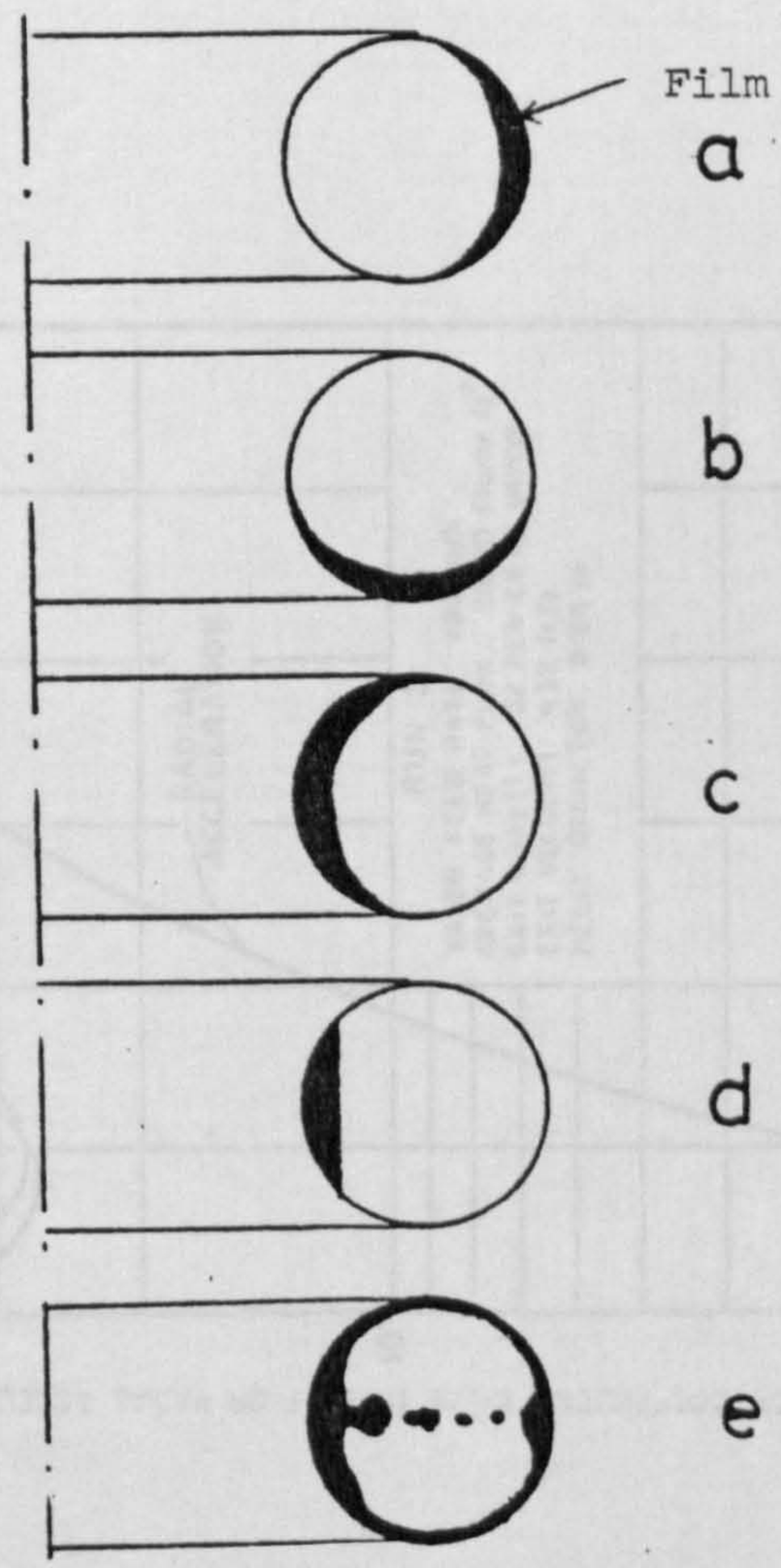
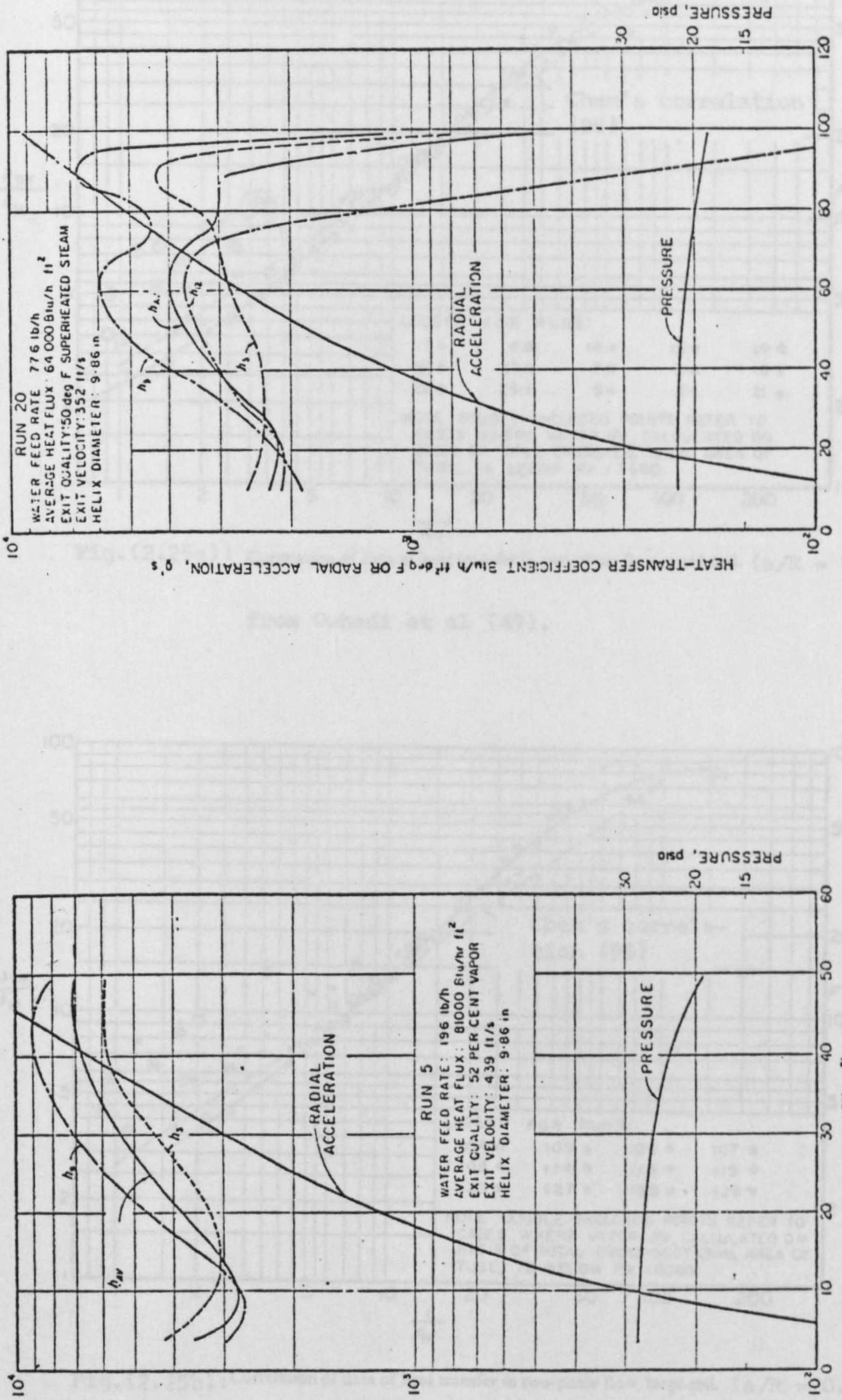


Fig. (2.23) : Liquid film movement at various gas mass flow rates.



Typical experimental results with superheated vapor at exit.

Typical experimental results with two-phase exit conditions.

Fig. (2.24) : Local heat transfer coefficients for two-phase flow , from Owhadi et al (47).

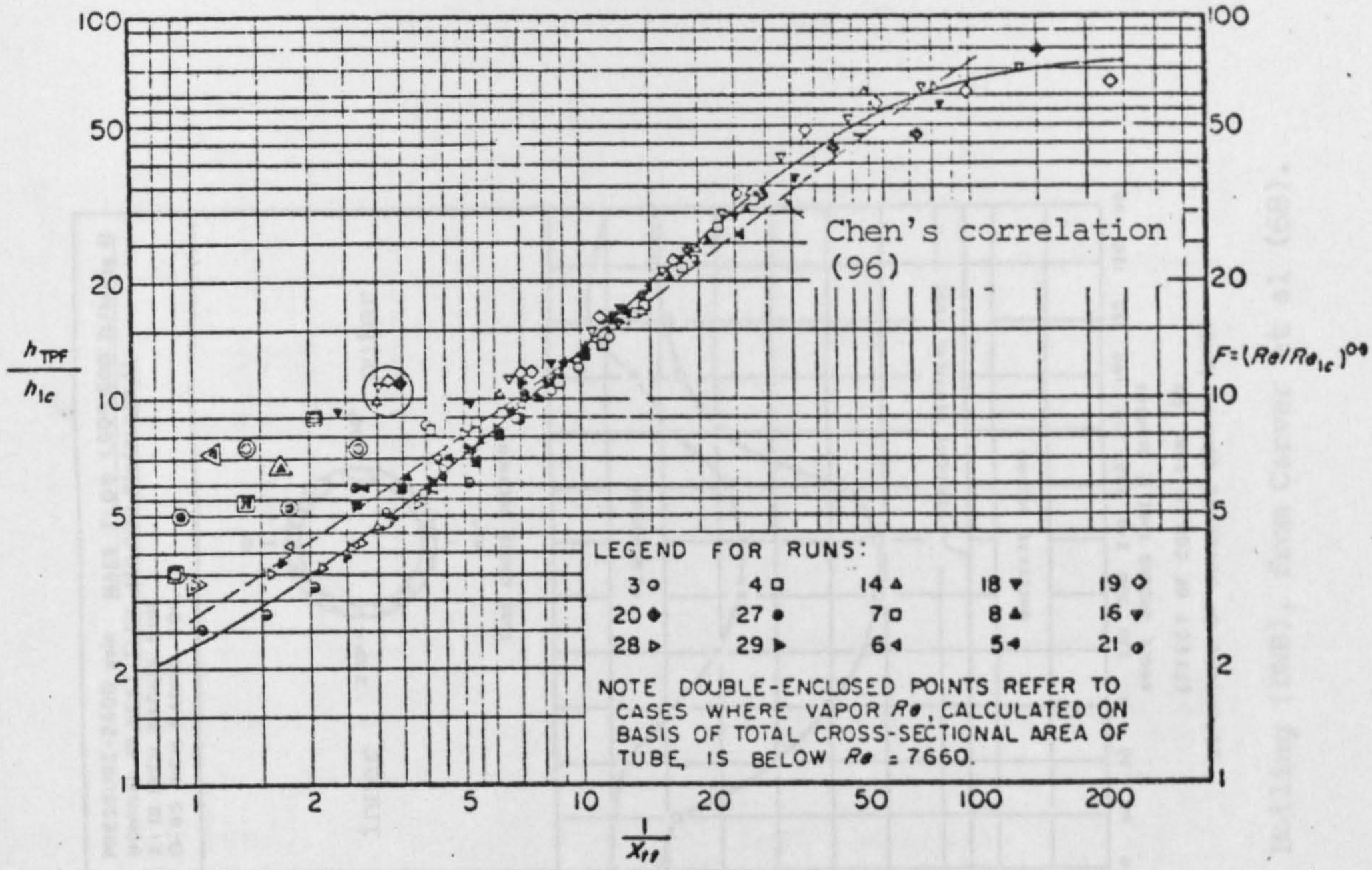


Fig.(2.25a): Correlation of data of heat transfer in two-phase flow, small coil. (a/R = 0.05)

from Owhadi et al (47).

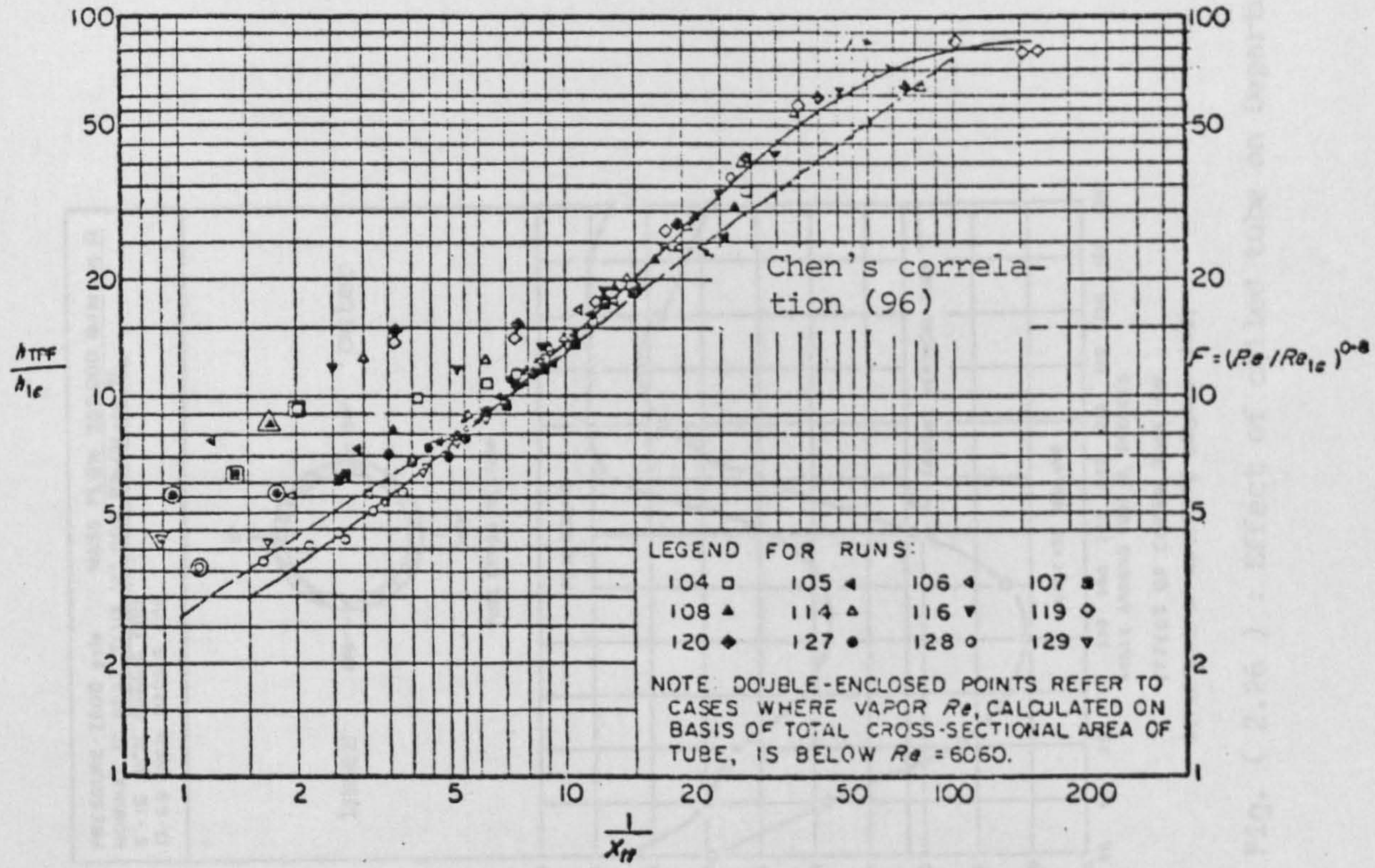


Fig.(2.25b): Correlation of data of heat transfer in two-phase flow, large coil. (a/R = 0.024)

from Owhadi et al (47).

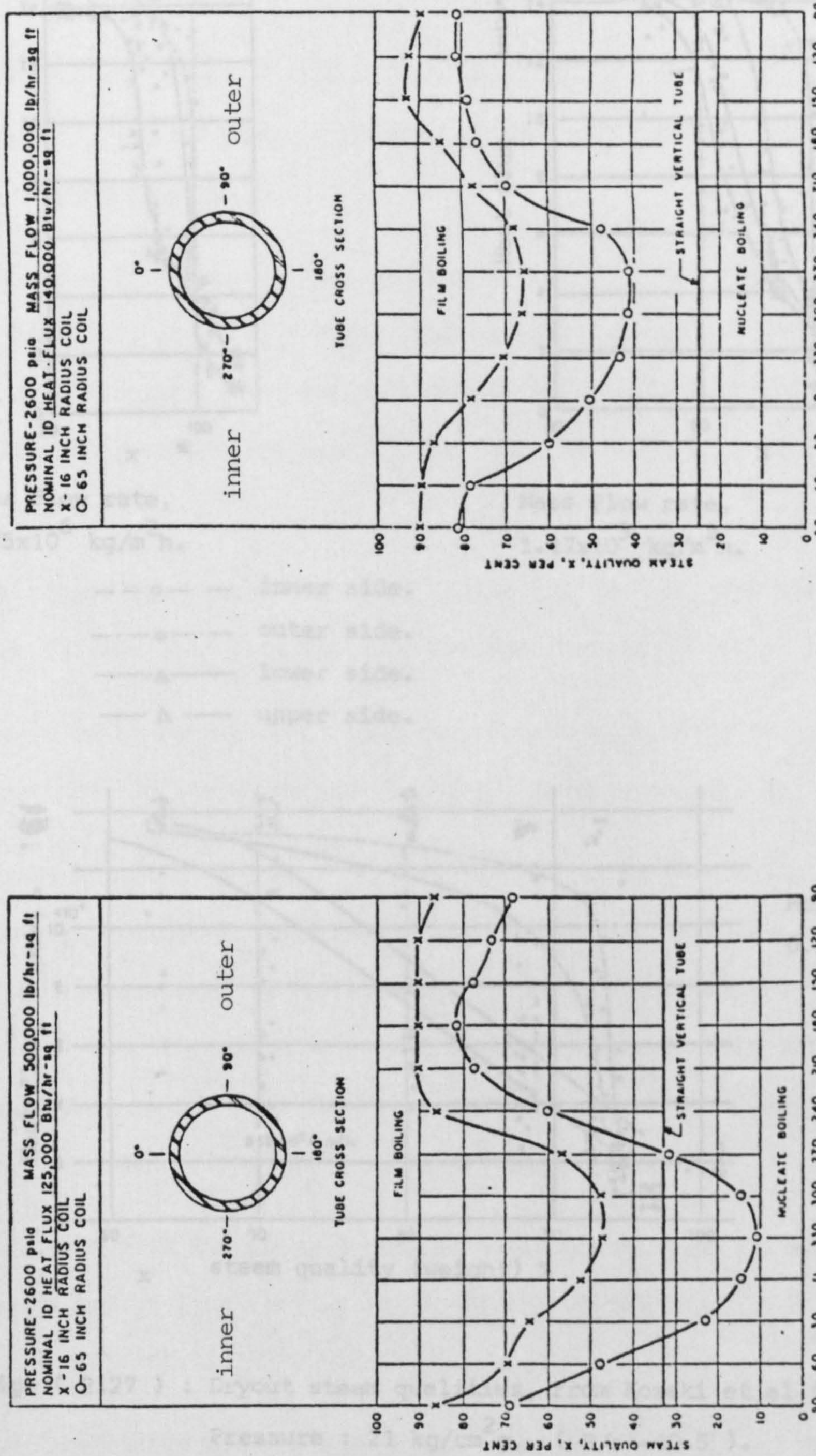
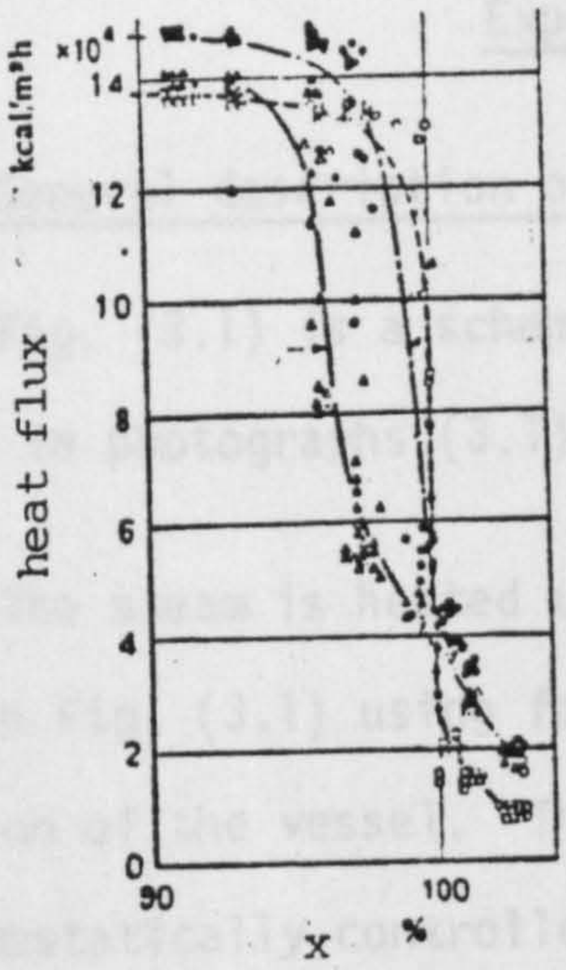
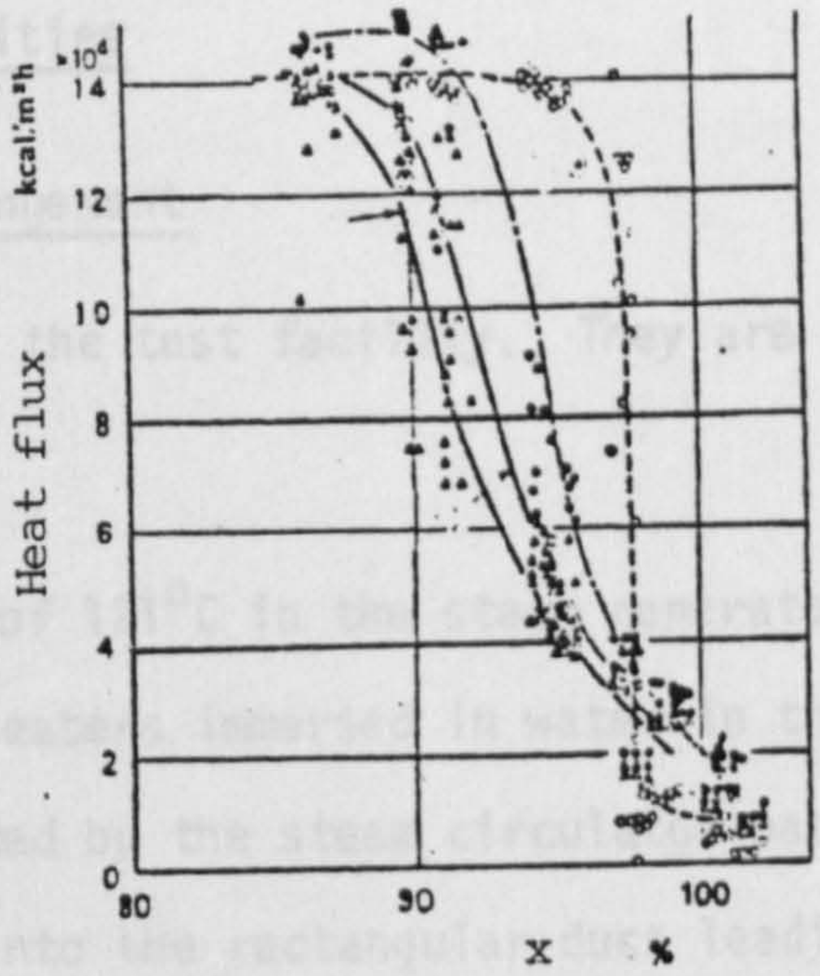


Fig. (2.26) : Effect of coiled tube on Departure of Nucleate Boiling (DNB), from Carver et al (68).



Mass flow rate,
1.75×10^6 kg/m^{2}h.



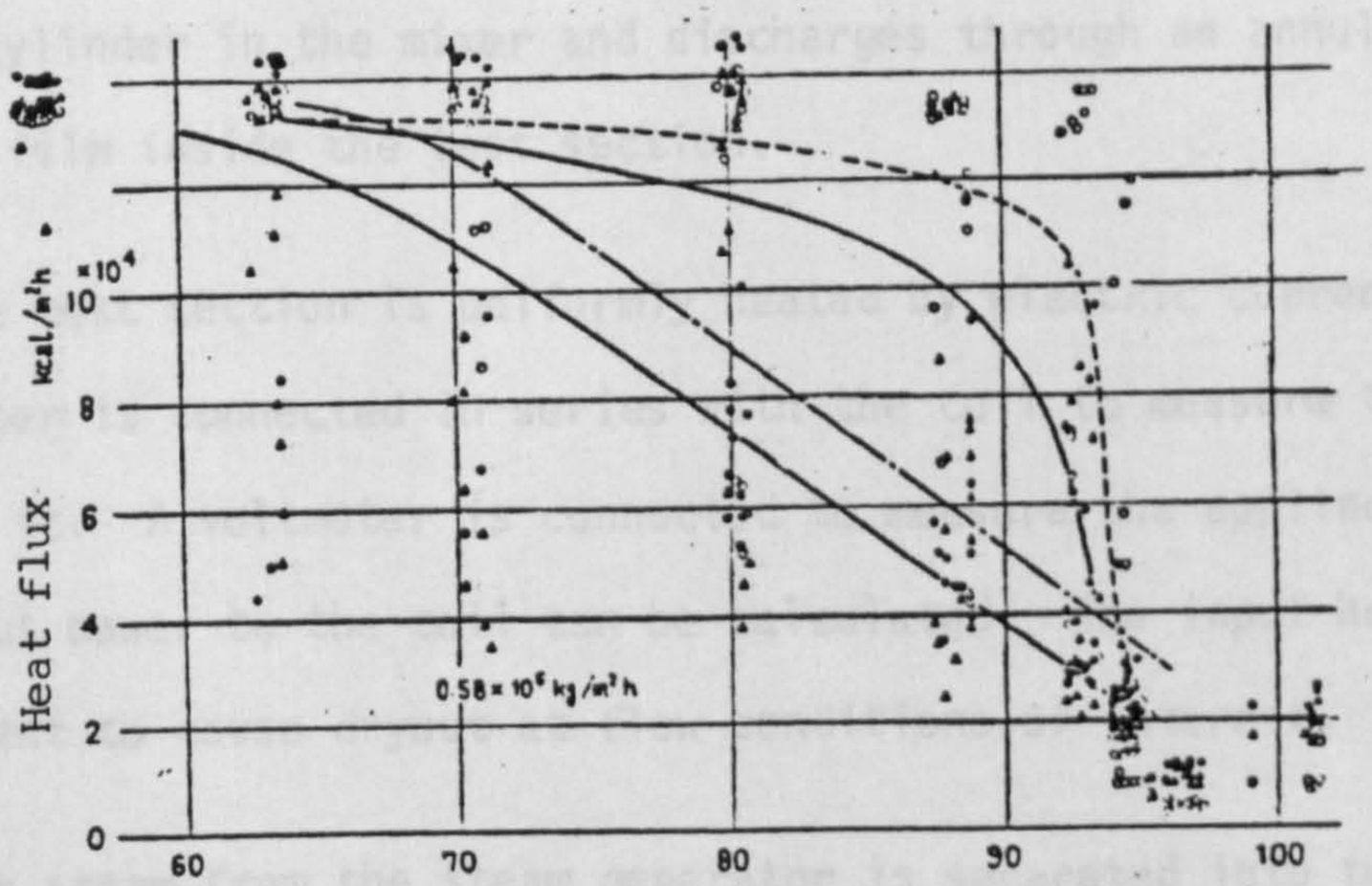
Mass flow rate,
1.17×10^5 kg/m^{2}h.

—— o —— inner side.

—·—●—·— outer side.

—— ▲ —— lower side.

—— Δ —— upper side.



Mass flow rate,
0.58×10^6 kg/m^{2}h.

Fig. (2.27) : Dryout steam qualities, from Kozeki et al (48,53).

Pressure : 21 kg/cm^{2}g, (R/a =40.5).

C H A P T E R 3

Experimental Facilities

3.1 General description of the test arrangement

Fig. (3.1) is a schematic diagram of the test facility. They are also shown in photographs (3.1).

The steam is heated up to a maximum of 121^{o}C in the steam generator vessel (1) in Fig. (3.1) using four electrical heaters immersed in water in the lower section of the vessel. The steam is forced by the steam circulator past a thermostatically controlled superheater into the rectangular duct leading out of the vessel.

The steam flow rate is measured by the orifice (2), the steam flows into the mixer (3) and then into the test section (helically-coiled tube).

Heated water (about 85^{o}c) from the vessel (1) is also forced through a porous cylinder in the mixer and discharges through an annulus to form an annular film inside the test section.

The test section is uniformly heated by electric current through the coil. An ammeter is connected in series with the coil to measure the current passing through it. A voltmeter is connected to measure the applied voltage, hence the input power to the coil can be calculated. The input heat to the coil is sufficient to cause dryout at flow conditions of interest.

The steam from the steam generator is separated into two ways, one flows through the bypass line (16) up to the water-separator, while the other flows through the orifice (2) into the mixer.

The steam-water mixture enters the water-separator (5). The separated water flows back into the reservoir (9) via the steam trap (8). It is pumped

by the return water pump (10) through the banks of rotameters (11) and returned to the vessel.

The separated steam flows through the venturimeter (6), the steam circulator (7) and back into the steam generator.

A condenser is located at the entrance to the steam generator to rid the steam of superheat developed in passing through the steam circulator. The resulting-water-laden steam is routed so that the water is dropped and the steam carries on to rise with newly generated steam. The mixture passes the superheater and enters the exit duct to repeat the circuit as before.

The steam and water circuits and major components are made of copper or its alloys. Wherever possible insulation is applied throughout the circuit to minimise heat loss into the atmosphere.

3.2 Steam circuit

3.2.1 Steam generator

The steam generator vessel was manufactured by Plant & Vessel Ltd. It is a 1982 litre copper cylinder with dished ends designed to a maximum pressure of $0.156^{MN/m^2}$ (8 psig). It is divided into two concentric annuli encircling an inner cylinder. The vessel is about one-quarter filled with water and holes in the annular walls permit free flow into the three concentric chambers. The water is supplied through a Permutit Mark 7 "Deminrolit" unit at a purity in compliance with the BP specification (1958) for "Purified Water" and at a PH of 6.5~7.0. Four 2 Kw immersion heaters keep the water at saturation temperature and each is controlled by a "Satchwell" pressure switch (The Rheostat Co. Ltd.), adjusted to maintain a pressure somewhat less than $0.136^{MN/m^2}$ (5 psig) in the vessel. A Levikator low level cut-out switch (Burndept Electronics) protects the heaters from overheating.

The steam enters the steam generator at the top centre, Fig. (3.1), where a condenser removes any superheat picked up in the steam circulator. The condenser coolant is once-through mains water whose flow is controlled by a Sacro Thermostat (Spirax-Sacro Ltd.). The wet steam is led down the outer annular passage where it meets the surface of the saturated water and turns sharply into the inner cylinder through holes in the annulus wall above the water's surface.

Most of the water droplets are deposited on the inner cylinder and drain into the water below, while the dried steam mixes with steam rising from the surface of the inner annulus and travels up inside the cylinder. The steam is again directed downwards giving any entrained water another chance to be deposited out.

A nichrome filament superheater controlled by a Sirect Temperature Controller (C.N.A. Instruments Ltd.) is located across the path of the descending steam near the entrance to the horizontal duct which leads to the test section.

3.2.2 The mixer of steam and water

A mixer block, Fig. (3.2) and photograph (3.2) is designed to supply the test section with an annular thin film of water and steam in the tube core to simulate the condition of the annular flow regime in boiling . This arrangement is chosen so as to reduce the length of tube if we have to start with single-phase (subcooled water or water at saturation condition).

The mixer is made of mild steel and is placed between the orifice and the test section.

The steam from the orifice (1) in Fig. (3.2) flows through a stainless steel tube (2) to the test section (4). The saturated water from the

steam generator is pumped via a bank of rotameters to a compartment in the mixer. It flows through the porous cylinder (3) and enters the test section tube (4) via a narrow annulus which is formed by the space between tubes (2) and (4) respectively. The width of the annular space is 0.5 mm. The mixer is connected to the test section by flanges separated by an electrically insulated gasket. The flanges are bolted together with bushes in their holes to ensure complete electrical isolation between the test section and the rest of the test facility. The water supply to the mixer is via a plastic fibre-glass reinforced tube. The glass-wool insulation is applied on the mixer to minimise heat losses to the atmosphere.

3.2.3 Water separator

This component is a "Helix Dryer" manufactured by The Superheater Company. It receives both the steam-water mixture from the test section and steam via the by-pass steam pipe, and induces a helical motion in the flow so that the water is spun outwards, collected and drained off to the steam traps. The separation efficiency is 95%.

3.2.4 Steam circulation

The main steam loop is driven by a five-stage centrifugal blower manufactured by Plannair Ltd. The impellers and stators are made of LM 8WP aluminium alloy and the shaft speed is 4500 r.p.m. on air cooled, sealed end bearings. The power is supplied through a belt drive and fluid clutch by a 25 h.p. squirrel cage motor manufactured by the English Electric Company.

The steam flow rate is controlled by inlet and outlet valves. When these are fully open the flow rate of saturated steam at $105^{o}c$ ($220^{o}F$), exceeds the design value of 679.68 m^3/hr.

3.3 Water Circuit

The saturated water is pumped from the bottom of the steam generator by a Stuart type 10 centrifugal pedestal pump (Stuart Turner Ltd.). It is passed through the bank of three glass-tube rotameters (Rotameter Manufacturing Co.) where it is metered over the range 0-454 $^{kg}/_{hr}$ with an accuracy of ±2%. The flow rate to the water injector (the mixer) is controlled by Vee-Reg valves.

When the water has passed through the test section and has been removed by the separator, it flows through the steam traps (Spirax Sarco Ltd.) and into a reservoir. The reservoir prevents flooding the separator and provides a constant heat of water to the return pump (identical to the injector pump). The water is pumped from the reservoir through manually controlled Vee-Reg valves, into the bank of rotameters and finally returned to the steam generator.

3.4 The Coils

The three different diameter helically coiled tubes are shown in Photographs (3.3a) and (3.3b). They are fabricated from INCONEL ALLOY 600 tubes of 13mm inside diameter and 14mm outside diameter. The electrical resistivity, Rt, and thermal conductivity, K_c, of the coils are as follows:

$$R_t = \{103 + 0.01081\ (T-20)\} \times 10^{-8} \quad \Omega\, m \qquad (20^oC < T < 250^oC)$$

$$K_c = 12.290 + 0.0134T \qquad {Kcal}/{mh^oc} \quad (93.3^oc < T < 204.4^oc).$$

The diameters, lengths, pitches and inclined angles are shown in Table (3.1) and in Figs.(3.3a-3.3c).

Each of the two ends of the coil are connected to an electric power supply hence the coil acts as an electric resistance. The test section is isolated electrically from the rest of the test facility by using fibre-glass reinforced plastic hose at the outlet and an insulator gasket and bushes at the inlet.

TABLE (3.1)

	COIL A	COIL B	COIL C
Tube outside diameter	14 mm	14 mm	14 mm
Tube inside diameter	13 mm	13 mm	13 mm
Wall thickness	0.5 mm	0.5 mm	0.5 mm
Average center diameter of coil	261 mm	383 mm	541 mm
Diameter ratio	0.0498	0.0339	0.0240
Whole pipe length	7.005 m	6.821 m	6.020 m
Heated " "	6.680 m	6.586 m	5.735 m
Length of inlet straight part	0.495 m	0.504 m	0.517 m
Pitch	0.042 m	0.042 m	0.042 m
Inclined angle	2.93^{o}	2.00^{o}	1.42^{o}
Coil turns	7	5	3
Wind direction	Anti-clockwise	Clockwise	Clockwise
Number of T/C^{*} on the tube	118	88	72

* T/C: Thermo-couple

Heat is generated uniformly in the coil by electric currents up to 100 amperes through the coil supplied by a heavy current transformer. The main 240 volts power supply is stepped down by Variac which is connected to the heavy current transformer. For temperature measurement 118 thermocouples on Coil A, 88 thermocouples on Coil B and 77 thermocouples on Coil C were soldered onto the tube wall using high temperature solders (EUTECROID 155, melting point $320^{o}C \sim 360^{o}C$, and BS219 GRADE 96s melting point $236^{o}C$).

Four thermocouples are located 90^{o} apart on the circumference of the helical tube at each section at which temperatures were measured. The first four thermocouples are located on the straight part of the test section. The rest of the thermocouples were placed at sections, each separated by 0.3m, from the starting point of helix to the end of the helix.

The arrangement of the thermocouples are described more fully in the section (3.7). The arrangement is such that an account of temperature variation along the whole tube surface can be detected.

The last three thermocouples (120^{o} apart) near the exit of the test section are mainly intended to indicate the highest temperature. They are connected to an anti-burn out alarming system, which detects when the wall temperature reaches $200^{o}C$ which is $40^{o}C$ lower than the melting point of the solder. Hence three thermocouples are monitored continuously to avoid any burn out.

3.5 Heating System

The test sections (helically-coiled tubes) are heated directly by A.C. electrical power supply. The main 240 V. power supply is controlled by a Variac which is connected to the transformer. A capacity of the transformer (Zenith Electric Co. Ltd.) is 4.8 kVA, 100A and 50 Hz on the secondary side. The resistances of the coils are already known therefore the input power to the coils can be calculated. The ranges of input power in this case are 0 to 11.41 $^{kw}/_{m2}$ (9813 $^{kcal}/_{m^2h}$).

3.6 Instrumentation

In this section, we deal with basic instrumentation, principally temperature and pressures which are indicated in Fig. (3.1) by the symbols T and P, respectively.

3.6.1 Instruments of steam circuit

Temperatures T_0 (vapour in the steam generator) and T_2 (return vapour in venturi) are measured by mercury-in-steel distant reading thermometers (British Petroleum Co.) (-18°c to 149°c (0°F to 300°F)) with an accuracy of $\pm$ 0.8°c (1.5°F).

Pressures P_0, P_1 and P_2 are measured with Bourdon gauges (0.1013 to 0.170 $^{MN}/_{m^2}$ (0 to 10 psig)) with an accuracy of $\pm$2.07 $^{KN}/_{m^2}$ ($\pm$0.3 psig). Differential pressures ΔP_{12} and ΔP_4, are measured with Bourdon gauges (0 to 127 cm H_2O (0 to 50 in H_2O)) with an accuracy of $\pm$0.254 cm H_2O ($\pm$0.1 in H_2O).

Pressure P_3 is measured with a Bourdon gauge (-76.2cm Hg to 0.205 $^{MN}/_{m^2}$ (-30 in Hg to 15 psig)) and P_4 is measured with a Bourdon gauge (-25.4cm Hg to 0.136 $^{MN}/_{m^2}$ (-10 in Hg to 5 psig)). All steam pressure measurements are made through condensation pots located adjacent to the appropriate pressure point.

Two orifices of 9.53mm and 12.7mm are used for measurement of steam flow rate. They were manufactured following the appropriate British Standard and their material is brass.

The steam flow rate through the orifice is calculated in accordance with the British Standard Code flow measurement, B.S. 1042, (74-1964) and shown in Fig. (B.1) in the Appendix.

The values of tolerances for Reynolds numbers above 10,000 are related to a basic coefficient, Reynolds number correlation factor, pipe size correlation factor and expansibility factor. These total values of tolerances are at a maximum of 3.82%.

3.6.2 Instruments of water circuit

All water temperatures, T_o, T_1, T_2, T_4, T_5 and T_6 are measured by mercury-in-steel thermometers with an accuracy of $\pm 0.8^oc$ ($\pm 1.5^oF$).

All pressures P_5, P_6 and P_7 are measured with Bourdon gauges (0 to $0.239^{MN/m^2}$ (0 to 20 psig) and 0 to $0.17^{MN/m^2}$ (0 to 10 psig)) with an accuracy of $\pm 2.07^{KN/m^2}$ (0.3 psig).

The readings of the rotameters, measuring the water flow, are corrected for the effect of temperature. They are calculated and shown in Figs. (B2.1) - (B2.2) in the Appendix.

3.7 Thermocouple distribution

The features of thermocouples are shown as follows:

TYPE	:	copper constantan	
DIAMETER	:	0.305 mm	
TOLERANCE	:	0^oC - 100^oC	$\pm 1^oC$
		100^oC - 400^oC	$\pm 1\%$

SENSITIVITY OVER TEMPERATURE RANGE

NEGATIVE	5.5 to 28	$\mu v/^oC$
POSITIVE	38 to 61	$\mu v/^oC$

These thermocouples were soldered on the walls of three helically-coiled tubes shown in Photograph (3.3a). There were 118 thermocouples soldered on the smallest coil (coil diameter 0.261 m). At 0.24 m from the mixer four thermocouples were soldered 90^o apart. From the end of the straight part, the coil is divided into 0.3m sections. In the first three sections four thermocouples are soldered 90^o apart at each section (shown in Fig. (3.4a)).

From the fourth section four thermocouples were soldered 90^{o} apart then two thermocouples were soldered 180^{o} apart at 0.15m from the four thermocouples in the same section. Their positions are at the outer side of the tube cross-section while the other is at the inner side with respect to the coil central axis. These same thermocouple distributions are repeated up to the last section, the 20th section, (shown in Fig. (3.4b)).

There were 88 thermocouples and 72 thermocouples soldered onto the middle coil (coil diameter 0.383m) and the largest coil (coil diameter 0.541m) respectively. At 0.243m from the mixer of the middle coil and at 0.207m from the mixer of the largest coil four thermocouples were soldered 90^{o} apart. From the end of the straight part two coils also were divided into 0.3m. At each 0.3m four thermocouples were soldered 90^{o} apart (shown in Fig. (3.4a)).

One thermocouple for measuring bulk temperature was installed at the beginning of the helix, 3.31m and 4.41m positions from the entrance of the test section as shown in Fig. (3.5).

3.8 Temperature measurement

The copper-constantan thermocouples for this experiment were supplied from a manufacturer (Saxonia). These thermocouples were used to test the reading difference between the digital thermometer and a standard thermo-bath in the range of $70^{o}C$ and $200^{o}C$. The readings of the digital thermometer using these thermocouples were 0.5∿2% lower than the standard at $80^{o}C$ and 2∿3.7% lower at $150^{o}C$. These readings are shown in Fig. (C.1) in the Appendix.

The negative and positive leads of thermocouples on the coils were connected to gold-plated sockets (RS 466-983). Each set of 12 thermocouples were placed in the chassis parts (RS 466-781), photograph (3.6). The negative and positive leads of copper-constantan leads from the selector switch (Crydon Precision Instrument Co. Ltd.) were connected to gold-plated pins (RS 466-977). Each

set of thermocouples were placed in the chassis parts for readings to be taken. The sockets and their corresponding pins all had gold-plated contacts to minimise contact resistance.The selector switch had 24 channels and two chassis parts from the coil were connected at a time to coincide with the selector switch. The connection of chassis is shown in Photograph (3.5).

A digital thermometer, (Schlumberger 1230-TC) with an accuracy of 0.5^{o}C in the range 0^{o} to 200^{o}C and 6.25 per second of read rate, and a digital line printer, (Electron systems, ES12), which print at a rate of two lines per second, and were also connected with the selector switch.

An arrangement of measuring devices is shown in Fig. (3.6). Measuring the temperatures using a manual selector switch did not affect the reproduction of the results. This is understandable because steady state conditions were achieved during every test.

3.9 Test Procedure

The steam generator generated saturated steam. The steam flow in the steam circuit became under steady conditions, about twenty minutes after the steam circulator was started. The venturi (6) in Fig. (3.1) showed a constant steam flow (=127^{kg}/hr). The steam flow rate and pressure were measured ΔP_{12} and P_1. The steam flow rate through the test section was adjusted by the valve (18) in Fig. (3.1). The pressure drop between the entrance and the exit of the test section was measured by P_2 and P_3. The steam temperature in the steam circuit was measured by T_o, T_2 and T_3.

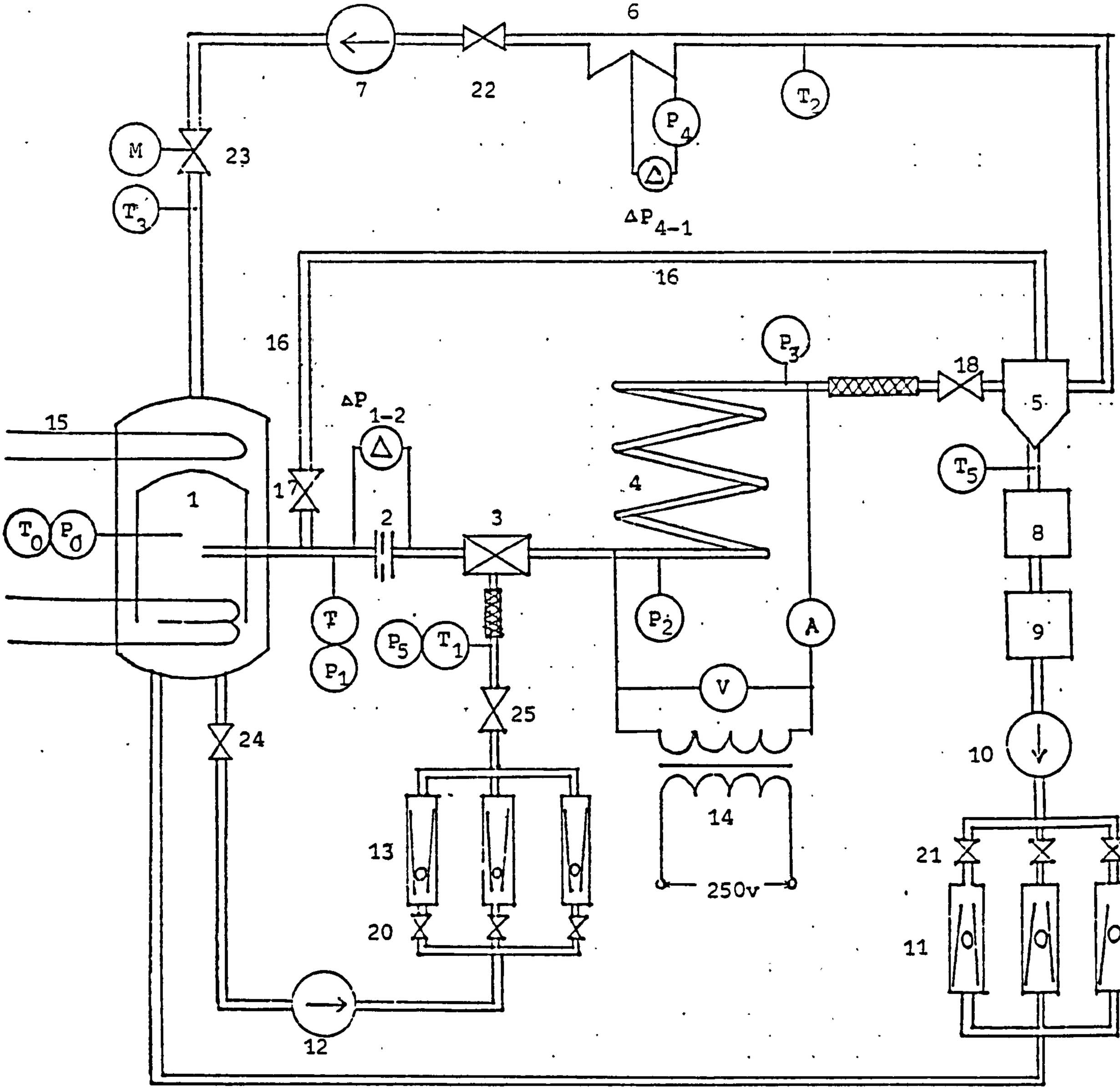
The steam generator supplied the test section with saturated water via a pump (12), a bank of rotameters (13) and the mixer (3). The bank of rotameters had a choice of different measuring capacities (0 to 453.6^{kg}/hr). This was to maintain an acceptable percentage error in the flow readings.

The water flow rate was adjusted by valves (20) and (25) for forming an annular region flow in the mixer. The temperatures and pressure were measured by T_1, T_4 and P_5 respectively. The steam and water were mixed and formed annular flow before the entrance of the test section (4).

The temperature profiles in the test section in the cases of steam flow, water flow and mixture flow were measured by thermocouples on the helical tube wall (the test section). The temperatures on the helical tube wall were selected by the manual selector switch. The temperatures which were measured by the thermocouples were shown by the digital thermometer and printed by the manual printer. The thermocouple distributions on the tube are described in the section (3.7).

The two-phase mixture was separated to steam and water at the water separator (5). The separated steam flowed back to the steam generator via the steam circulator and the separated steam flow rate and temperatures were measured by ΔP_{34} and T_2 and T_3. The separated water is pumped from the reservoir (9) to the steam generator via the bank of rotameters (11). The flow rate, temperature and pressures were measured by the rotameter, T_6 and P_6 and P_7, respectively.

The calibrations of flow-meters, thermometers and pressure gauges are shown in Figs. (C.3) - (C.6) in the Appendix.



T : Thermometre, P : Pressure gauge, M : Motor, ΔP : Differential pressure.

1. Steam generator vessel.
2. Orifice.
3. Mixer.
4. Test section.
5. Water separator.
6. Venturi.
7. Steam circulator.
8. Steam trap.
9. Resevoir.
10. Return water pump.
11. Return water rotameter bank.
12. Injection water pump.
13. Inlet water rotameter bank.
14. Transformer for input heat.
15. condenser.
16. Steam by-pass line.
17 - 25. Valves, (23). motor driving.

Fig. (3.1) : Diagram of the test facility.

Steam generator

Rotameters

Selector switch

Test section

Mixer

Thermometer

Amplifier

Switch board of-steam generator

Alarm

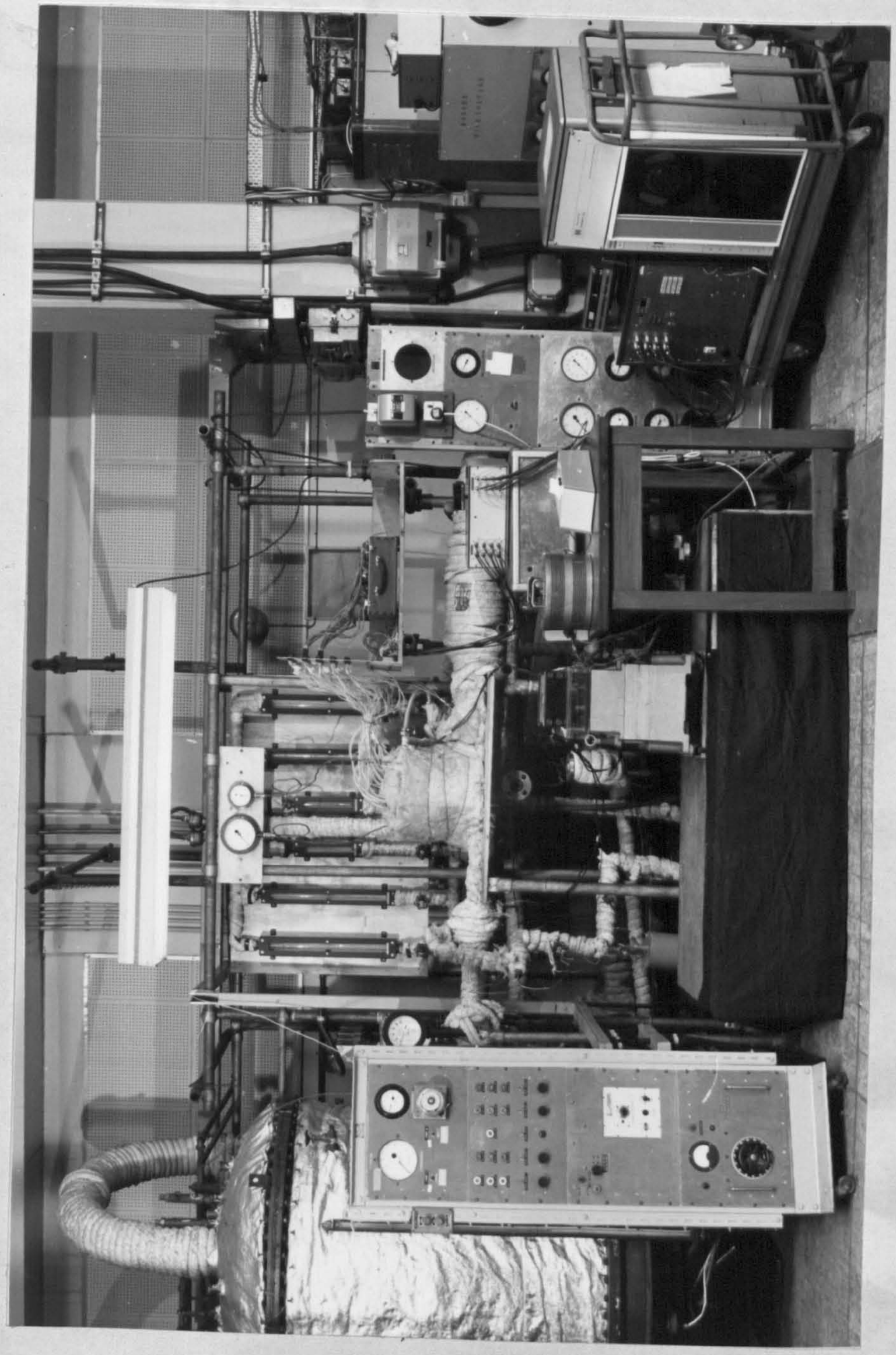
Variac

Printer

Transformer

Converter

Tape-recorder

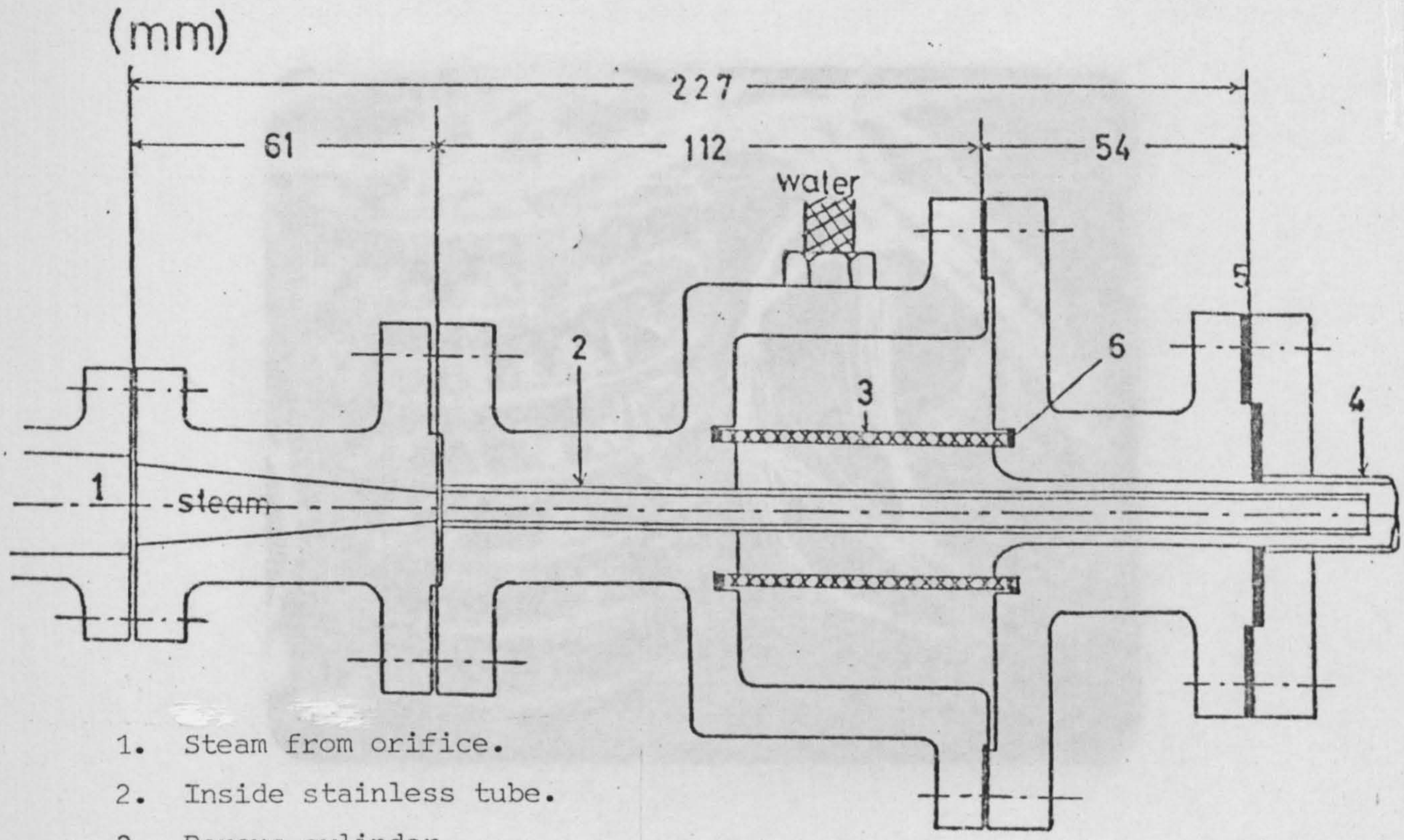


Photograph (3.1) : Test facility and auxiliary devices.



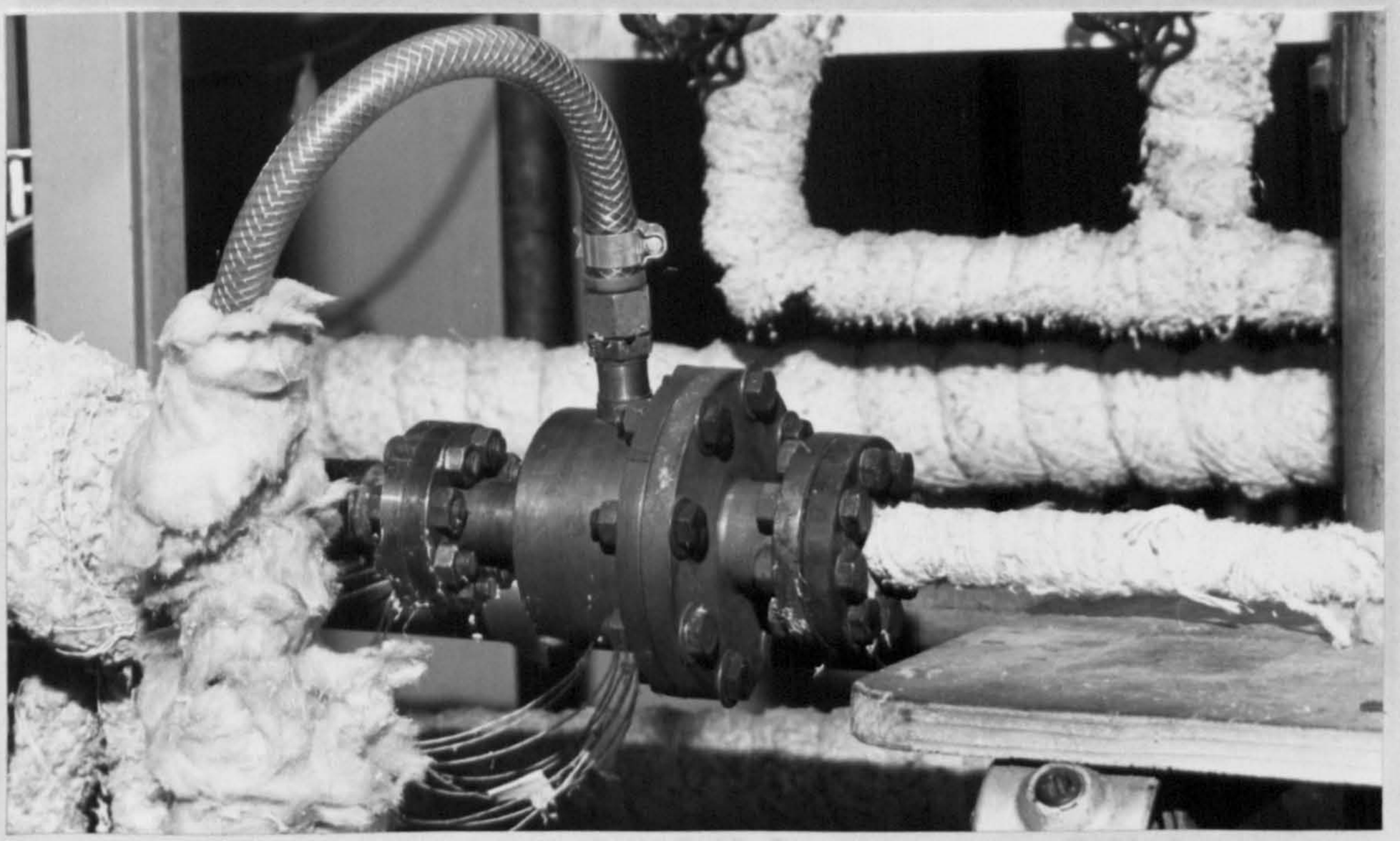
Photograph (3.1) : Test facility and auxiliary devices.

107 108

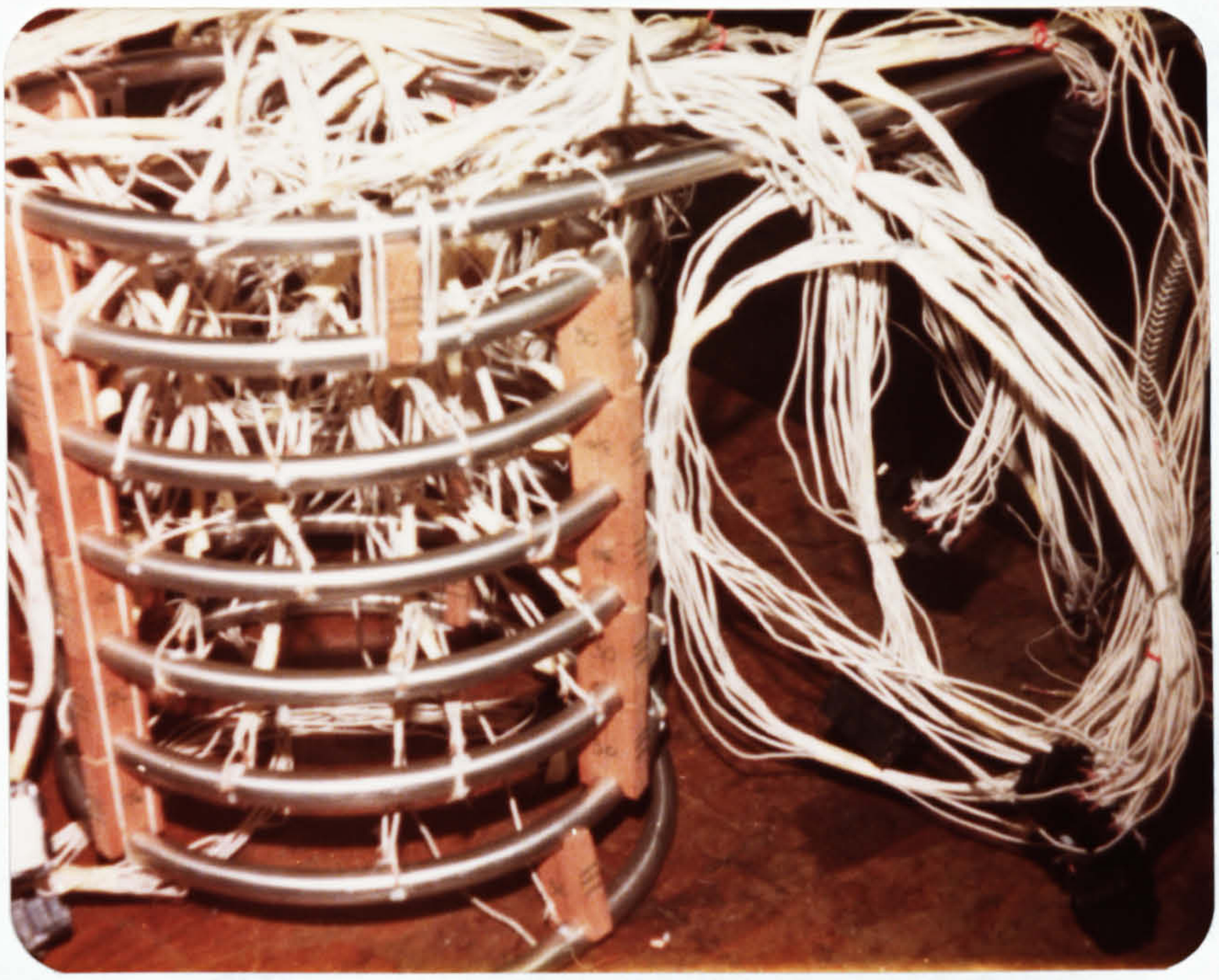


1. Steam from orifice.
2. Inside stainless tube.
3. Porous cylinder.
4. Test section tube.
5. Insulator.
6. O-ring.

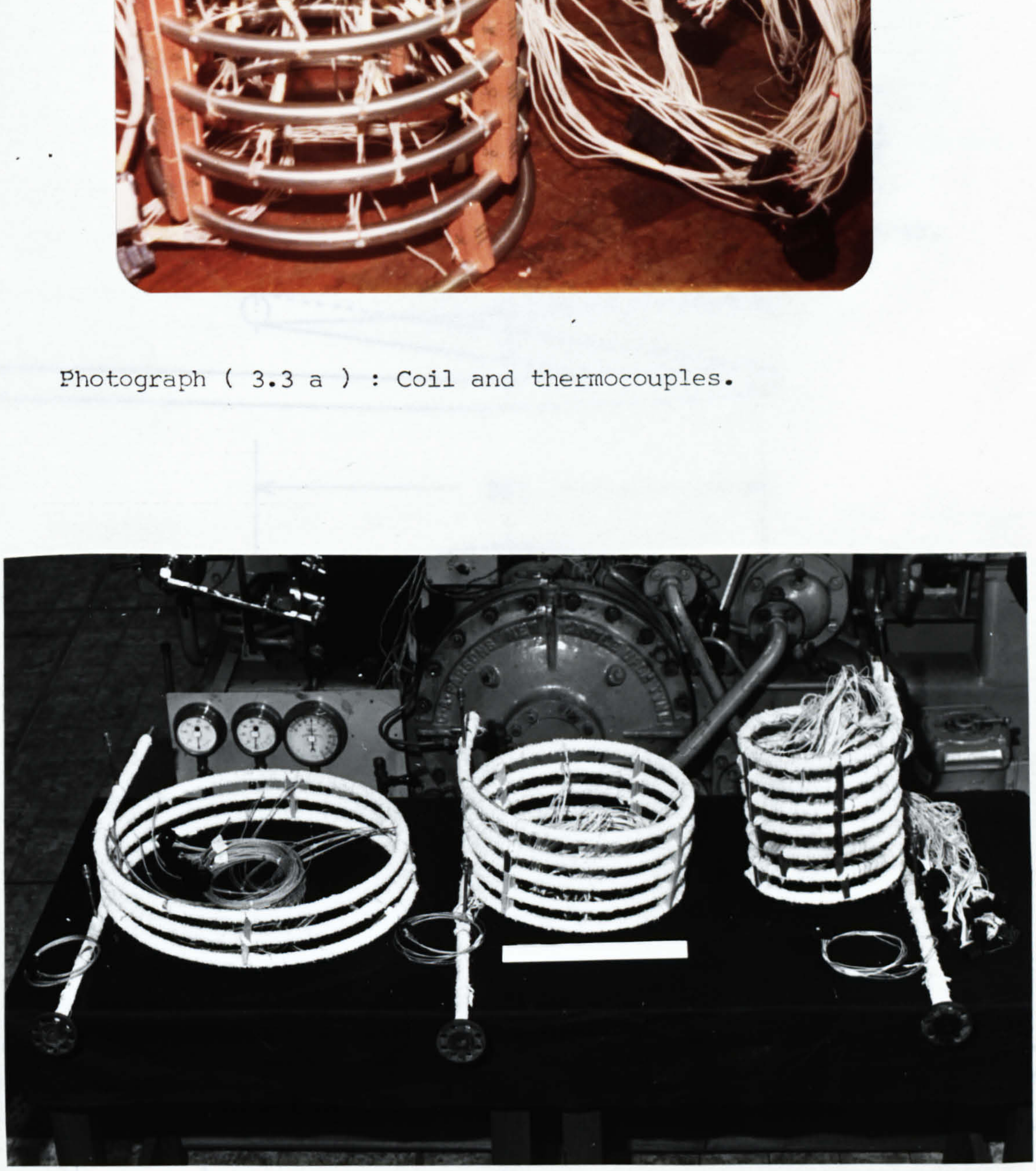
Fig. (3.2) : Diagram of the steam-water mixer.



Photograph (3.2) : MIXER.

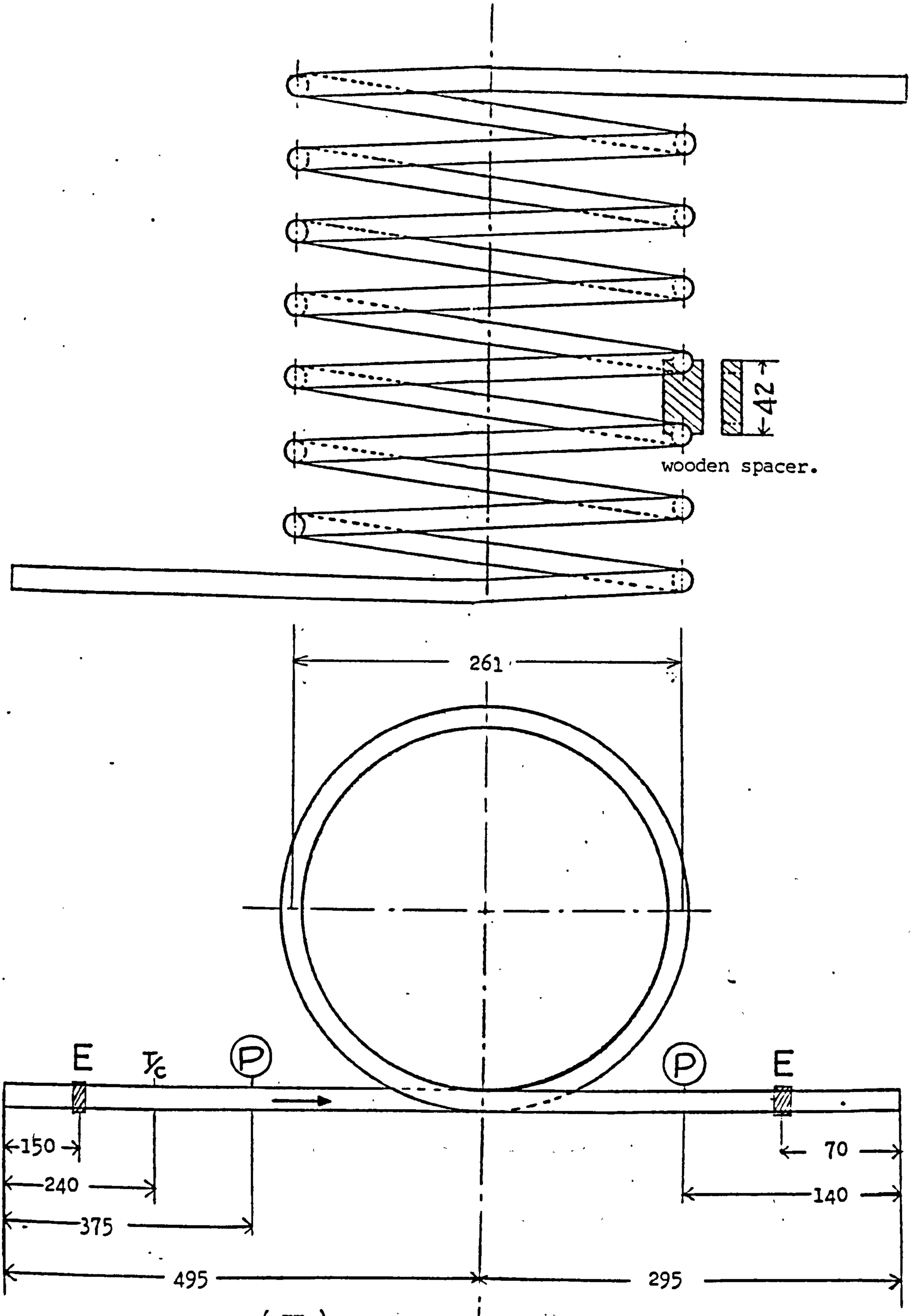


Photograph (3.3 a) : Coil and thermocouples.



Coil C Coil B Coil A

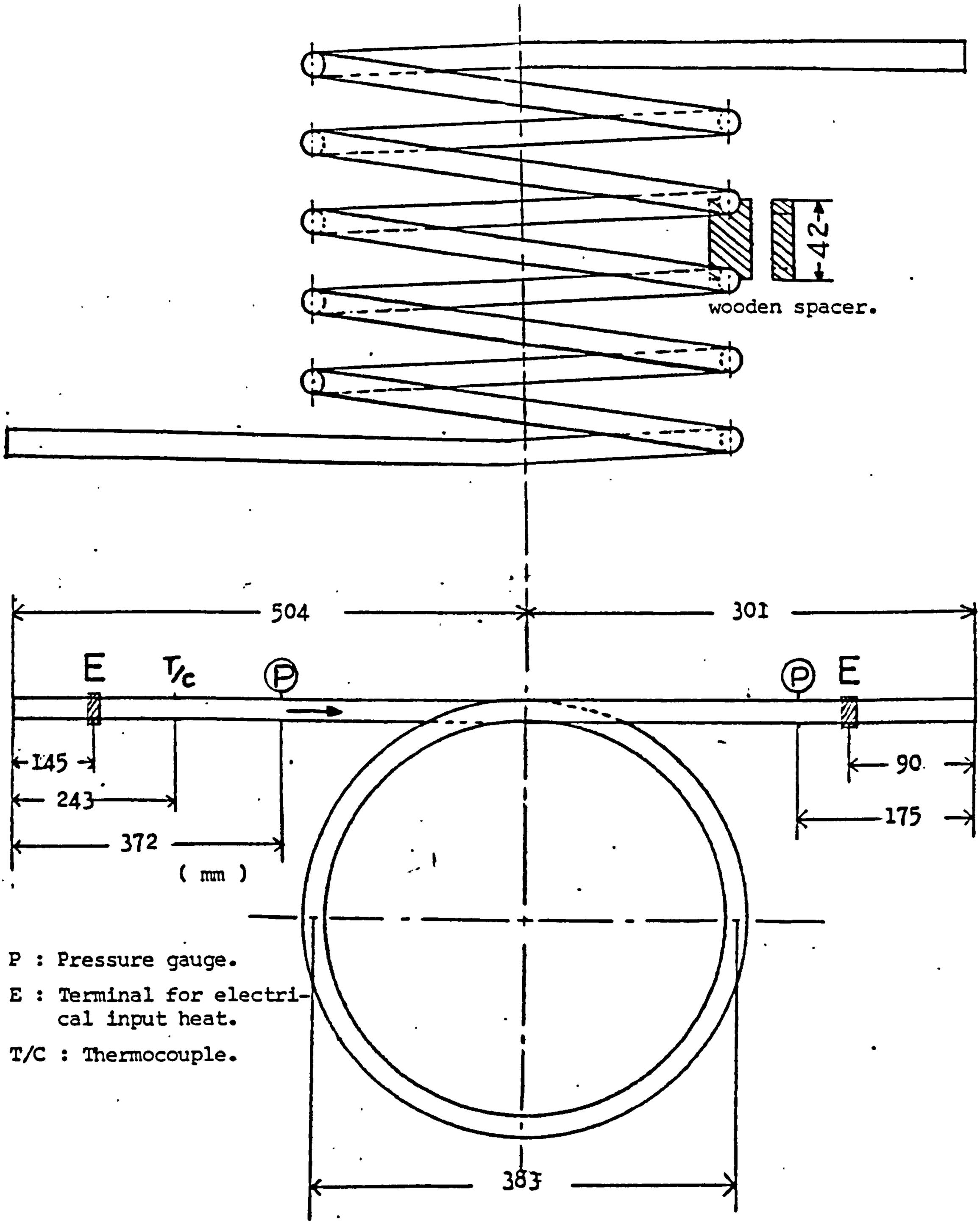
Photograph (3.3 b) : Coils.



P : Pressure gauge.

E : Terminal of electrical input heat.

Fig.(3·3a) : Coil A

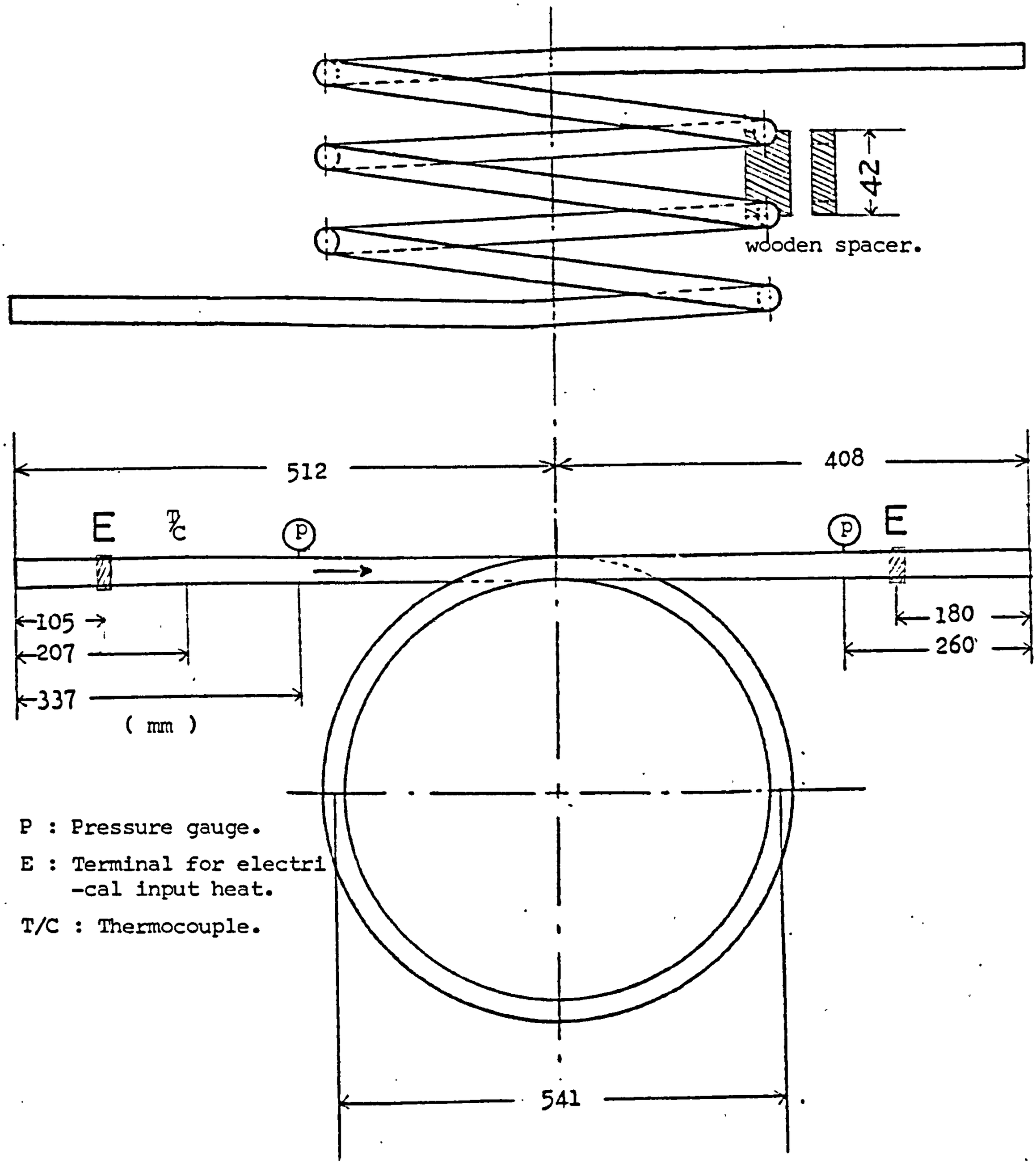


P : Pressure gauge.

E : Terminal for electrical input heat.

T/C : Thermocouple.

Fig (3.3b) : Coil B



Fig(3.3c) : Coil C

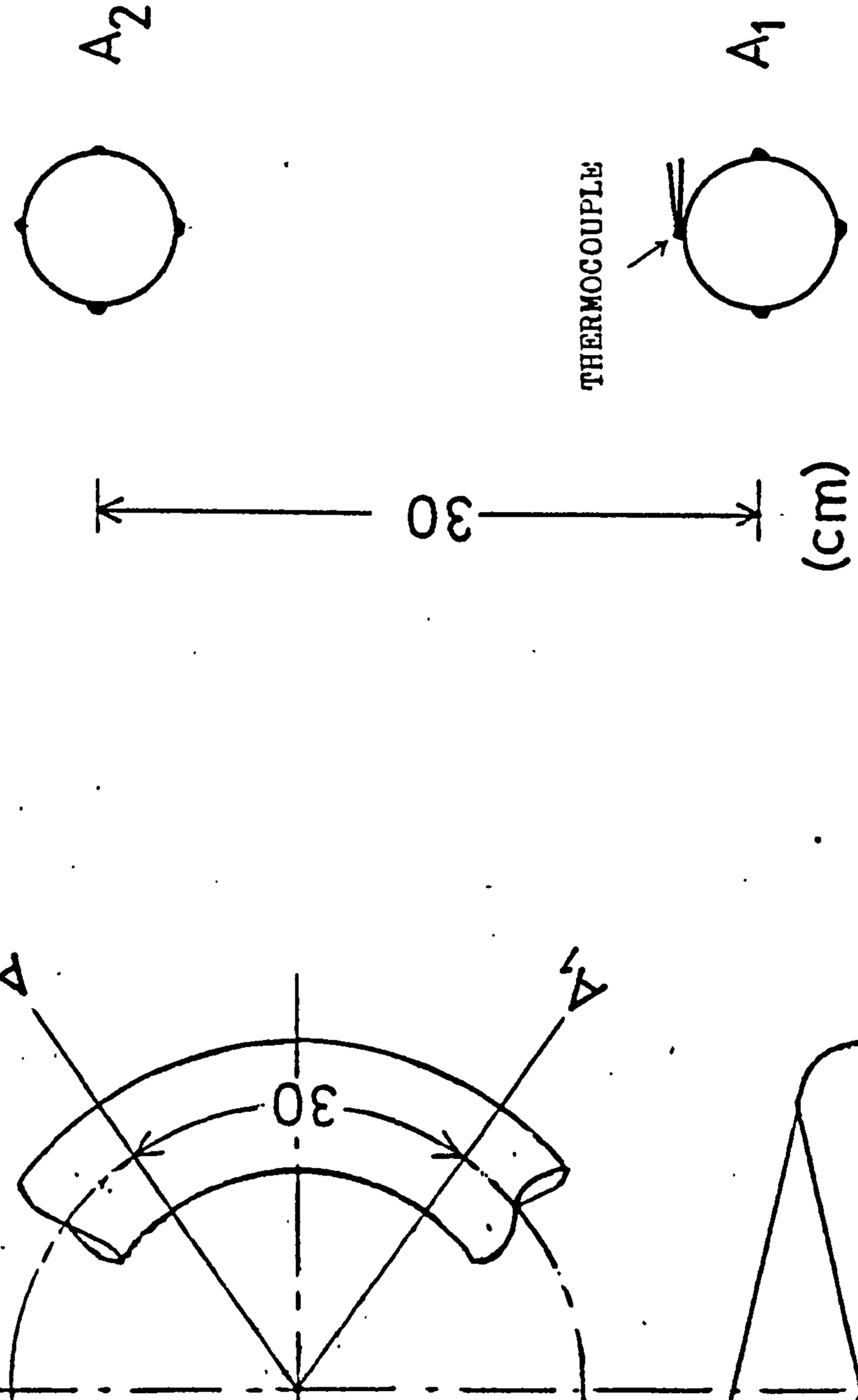


Fig. (3.4 a) : Thermocouple distributions
on the tube surfase,
for the first three sections
on Coil A and for Coils B and C.

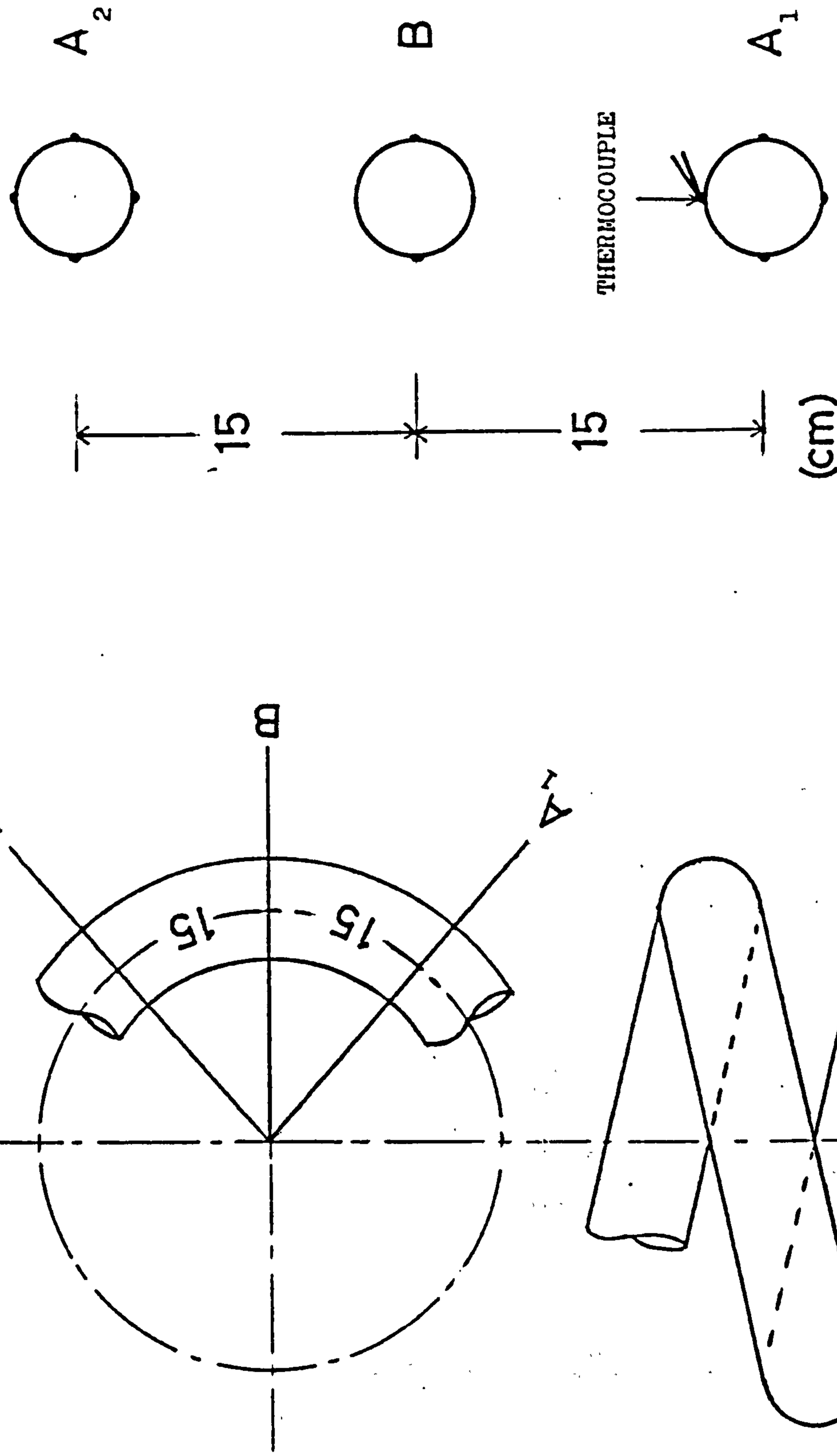
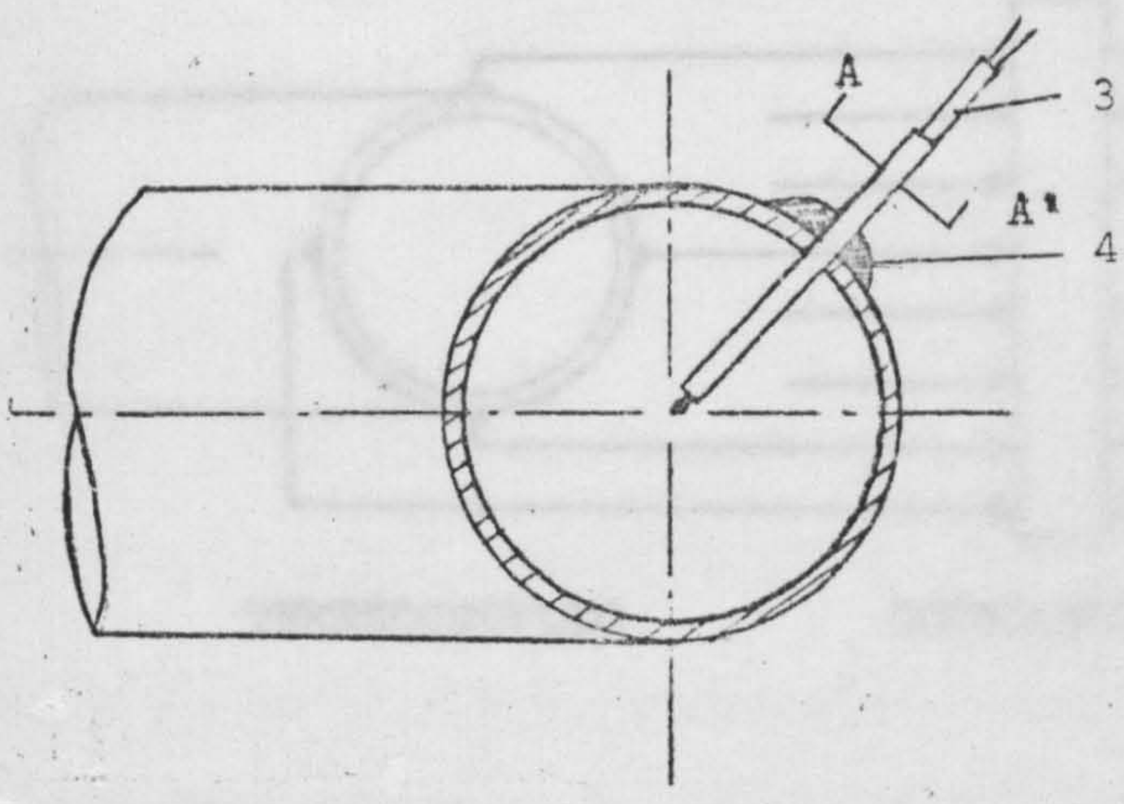
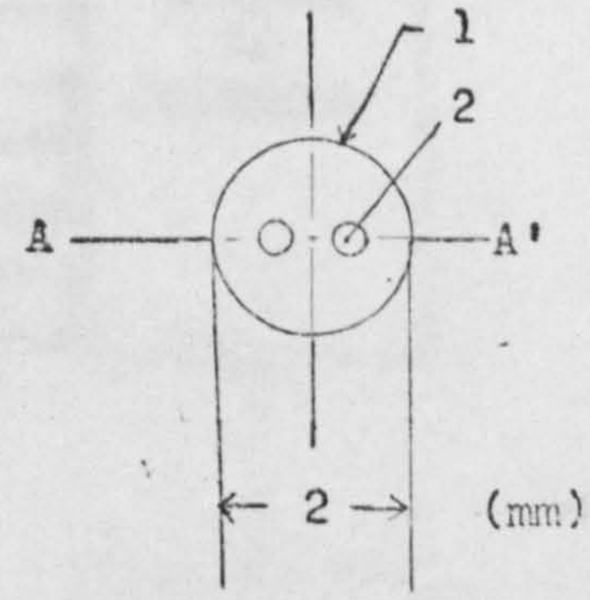


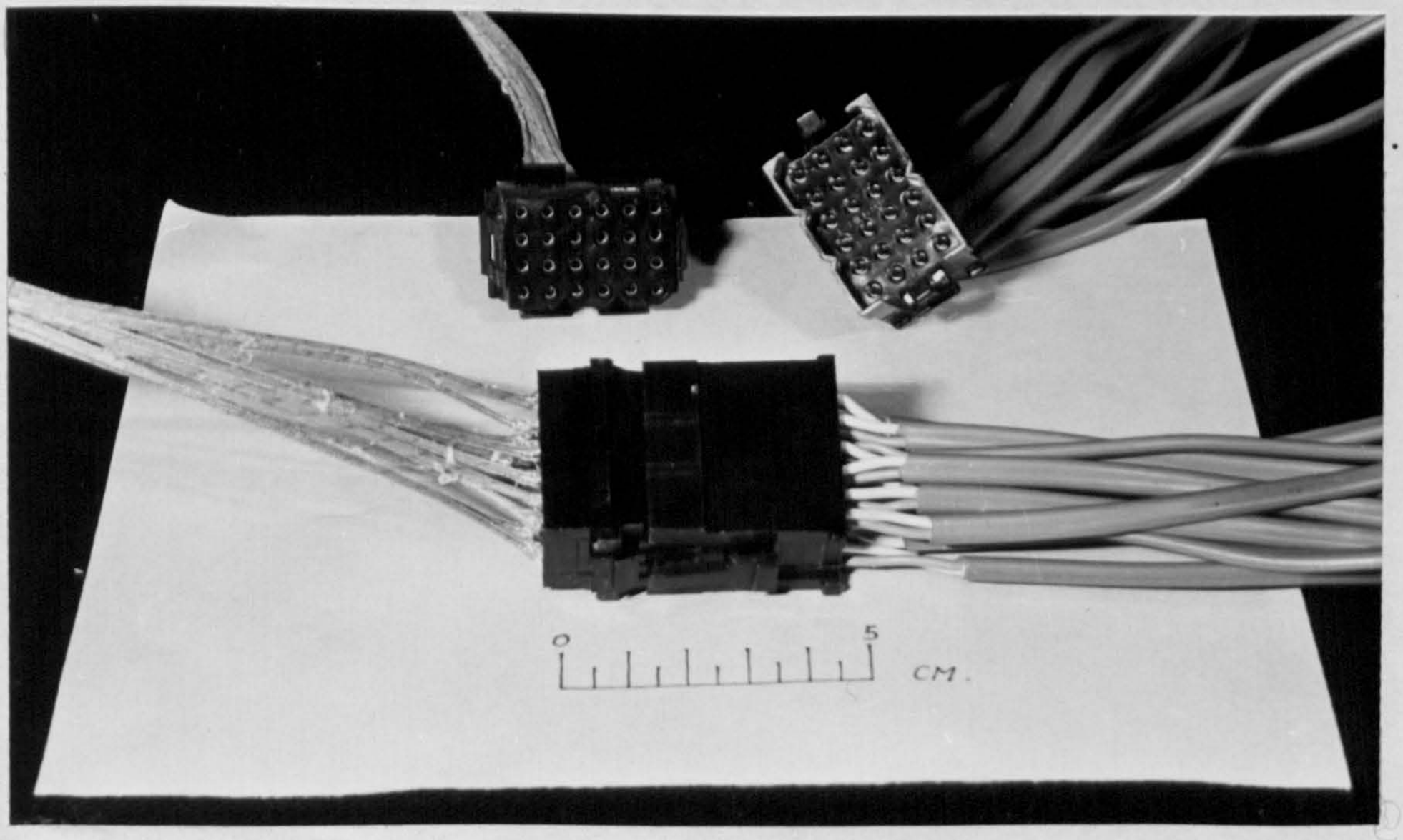
Fig. (3.4b) : thermocouple distributions on the tube surface, for the 3rd - 20th sections on COIL A.





1. small silicone tube
2. hole for thermocouple
3. thermocouple
4. adhesive material

Fig.(3.5) : Thermocouple for measuring bulk temperature.



Photograph (3.4) : Connection between thermocouples and selector - switch.

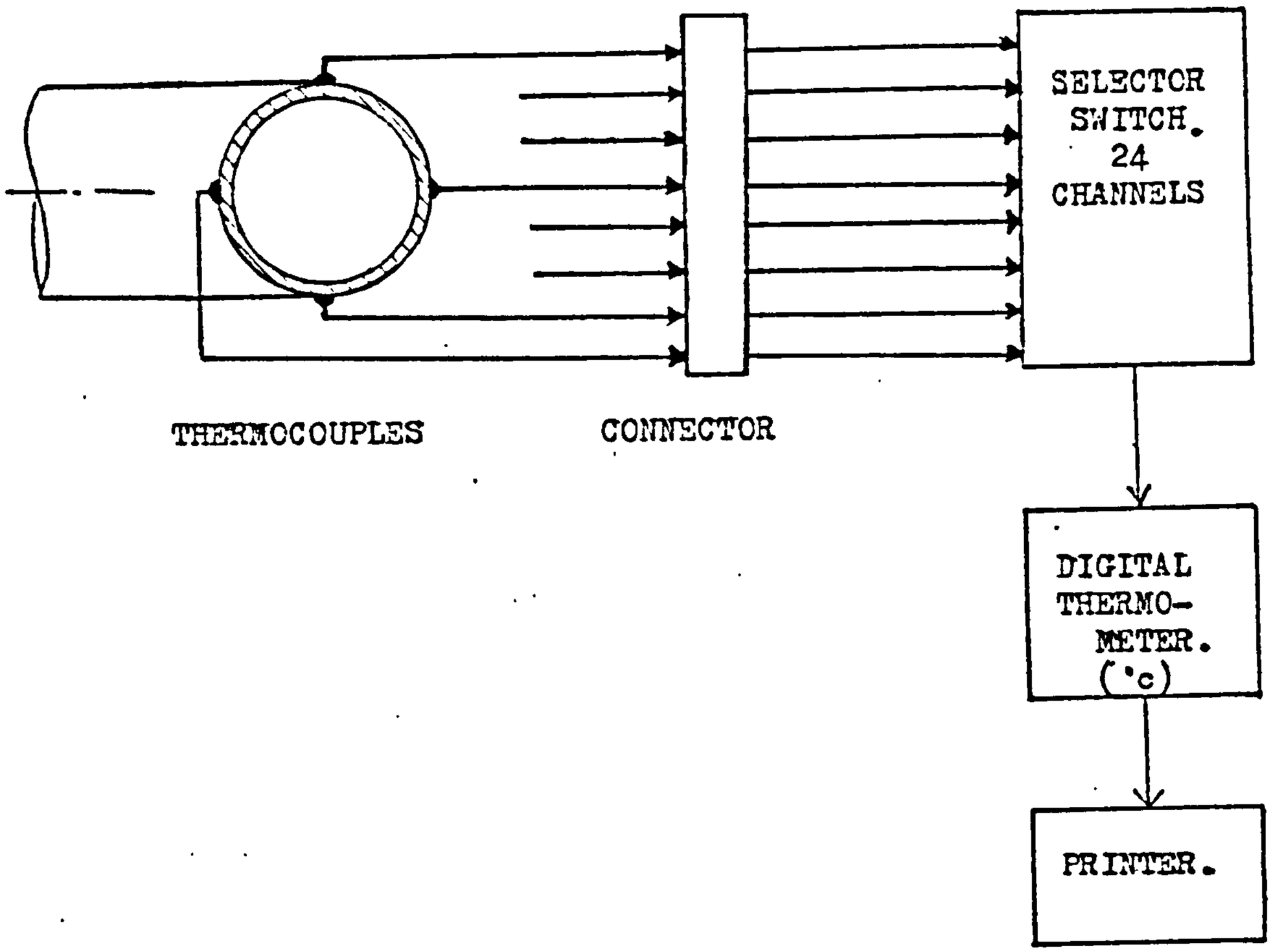


Fig. (3.6) : Arrangement of measuring devices.

C H A P T E R 4

Experimental Results and Analysis

4.1 Introduction

Chapter 3 describes the experimental facilities used in this project. In Chapter 4 the author investigated the following:

(a) Pressure drop of steam (single-phase flow);

(b) Wall temperature profiles along the coiled tubes of steam,

(c) Heat transfer coefficients of steam,

(d) Wall temperature profiles along the coiled tubes when water flows,

(e) Heat transfer coefficients of water,

(f) Pressure drops of steam-water mixture (two-phase flow),

(g) Wall temperature profiles along the coiled tubes of the steam-water mixture flow,

(h) Flow patterns of steam-water mixture,

(i) Dryout behaviour, and

(j) Heat transfer coefficients of steam-water mixture.

These results are compared in three different coil diameters, (0.261, 0.383 and 0.541 m).

The wall temperatures are thought to be always fluctuating with time but these results show stable values for a given set of test conditions for all regimes except wavy flow.

This experiment is considered to obtain data for annular, wavy and stratified flows.

The following assumptions are made to analyse the data:

(i) All temperatures and pressures are measured under steady conditions;

(ii) There are no heat losses from the test section;

(iii) Heat flux around the tubes' peripheries are the same;

(iv) Temperature differences between inside and outside surfaces of the pipe are neglected.

4.2 Results of single-phase flow

4.2.1 Water flow

4.2.1.1 Pressure drop of water flow

The water flows upwards in the coils which are defined in the section (3.4).

The operation conditions of pressure and temperature measurements are as follows:

Flow rate	1.71×10^5 and 3.42×10^5 Kg/m^2h
Heat flux	0.93×10^3, 2.10×10^3 and 3.74×10^3 $Kcal/m^2hr$
Inlet water temperature	82 - 90°C
Inlet pressure	0.108 - 0.112 MN/m^2
Reynolds number	0.185×10^4 - 0.384×10^4
Prandtl number of inlet water	1:96 - 2.17

No pressure loss measurements are obtained because of relatively low flow rates and the accuracies of gauges. A result of simple pressure loss calculation using Fanning equation for laminar flow (from Kay and Nedderma (75,1974)) is 3.38×10^{-4} Kg/cm^2 (3.42×10^{-5} MN/m^2), the pressures of the water head of three coils are between 1.26×10^{-3} and 2.94×10^{-3} MN/cm^2. Therefore the pressure gauges on the test section are not able to measure such low pressure losses.

4.2.1.2 Wall temperature profile (water flow)

Wall temperatures at various water flow rates (3.42×10^5 x 1.71×10^5 Kg/m^2h and input heat fluxes (934, 2102 and 3736 $Kcal/m^2h$) are plotted in Figs. (4.2.1a) to Fig. (4.2.1c).

Using a heat flux over 3736 $^{Kcal}/_{m^2h}$, the wall temperatures start to become highly unstable and intermittent small explosions or "bangs" begin in the test section. Figs (4.2.1a), (4.2.1b) and (4.2.1c) are temperature profiles at input heat of 3736 $^{Kcal}/_{m^2h}$ before the "bangs" start. Therefore heat fluxes are kept below the maximum of 3736 $^{Kcal}/_{m^2h}$.

Figs. (4.2.1a) to (4.2.2c) show three main features as follows:

(i) Wall temperature has its highest value on the inner side for all heat fluxes at 3.42×10^5 $^{Kg}/_{m^2h}$ flow rate and at 934 $^{Kcal}/_{m^2h}$ at 1.71×10^5 $^{Kg}/_{m^2h}$ water flow rate.

(ii) Wall temperature of the upper side shows higher or same temperature as inner side at large heat fluxes (2102 and 3736 $^{Kcal}/_{m^2h}$) of 1.71×10^{5} $^{Kg}/_{m^2h}$ flow rate, (shown in Figs. (4.2.2a), (4.2.2b) and (4.2.2c)).

(iii) In the case of small flow rate and heat flux of 3736 $^{Kcal}/_{m^2h}$ (shown A, B & C in Figs. (4.2.2a), (4.2.2b) and (4.2.2c)), at a certain point along the tube when the temperature of the upper side reaches around 103~107^{o}C, it is exceeded by that of the lower side and then both keep a constant value up to the exit of the pipe. This temperature inversion occurs earlier for smaller coils (Coil A) than for larger coils (Coils B, C).

The first feature is explained by a mechanism of secondary flow and growth of thermal boundary layer. In general, for very short distances from the tube inlet, the development of the temperature field in a coiled tube is similar to that in a straight tube except for the effect of the skewed axial velocity profile, which sets up a circumferential temperature gradient, and it is called the Leveque region. In this region, the thermal boundary layer is very thin and its penetration into the secondary flow field is insufficient for the effect of the latter to become significant. However radial

and axial velocities increase very rapidly with increasing distance from the tube wall. Therefore, as the thermal boundary layer grows with advancing axial distance, the secondary convection of heat becomes pronounced in a short distance downstream from the Leveque region, around 0.75m from the helix beginning point in Figs. (4.2.1a) and (4.2.2c). The growth of the thermal boundary layer becomes maximum at the inner side in Fig. (4.2.3), with secondary convection transferring most of the heat into the fluid core.

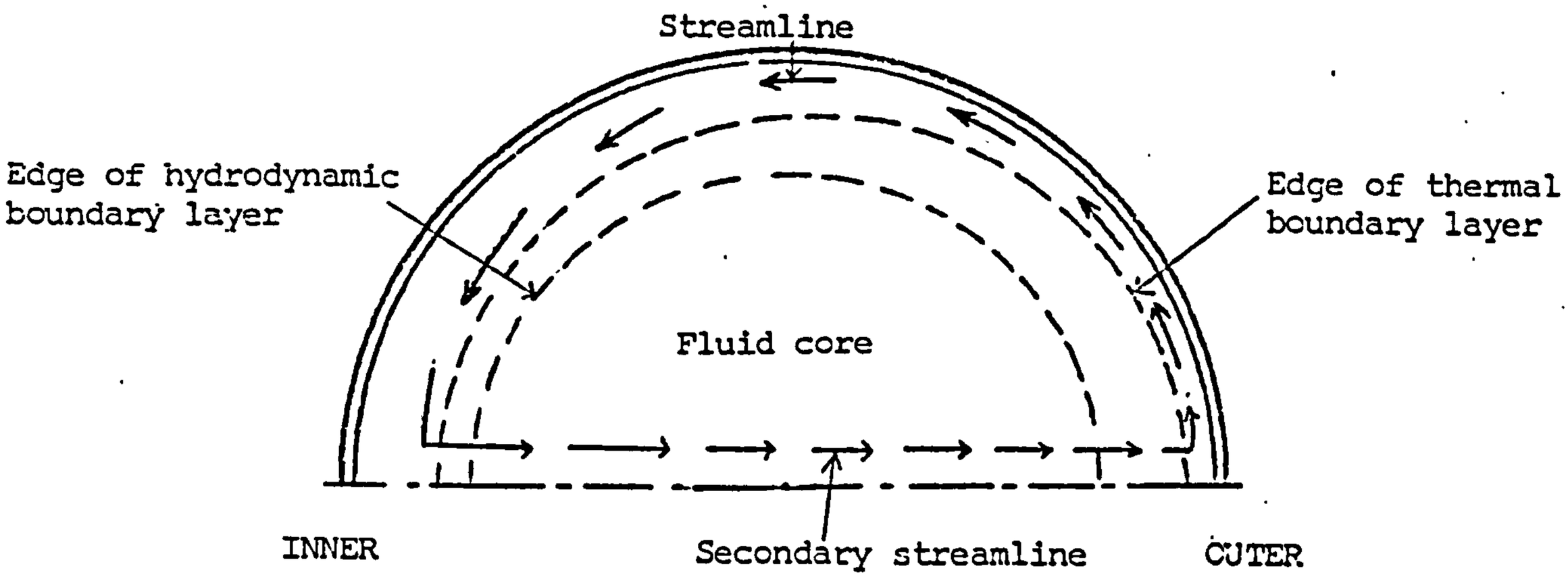


Fig. (4.2.3) : The interaction between secondary flow and propagating thermal boundary layer.

The magnitude of secondary flow can be considered as the temperature difference between inner and the other sides. The largest temperature diffe-

rence occurs in the flow of the smaller coil (Coil A) and obviously at larger heat fluxes.

Seban and McLaughlin (22) and Dravid et al (19) reported the oscillating temperature profiles in the coiled tube. Figure (4.2.4) is obtained in almost identical conditions as Fig. (4.2.1a) shows the temperature oscillations clearly at the inner and the upper sides. Seban and McLaughlin (22) also mentioned two other possible factors affecting oscillation. Firstly a high heat transfer coefficient made a temperature difference between wall and fluid temperatures, and secondly an inaccuracy of measurement produced significant scatter. Dravid et al (19) concluded that the cyclic temperature oscillation must be a result of the fluid mechanics of the system - clearly secondary flow is the cause of this phenomena.

From Fig. (4.2.4) the flow mechanics at the low heat flux agrees with Dravid et al (19) but at the high heat flux the flow is affected strongly by buoyancy. When the magnitude of secondary flow is greater than that of the buoyancy effect the temperature at the inner side continues to rise. (Described previously in feature (i)). When the magnitudes of buoyancy effect and secondary flow are in balance the temperature rises at the inner and the upper sides become gradual. The phenomenon when the magnitude of the buoyancy effect is predominant is explained previously in the third feature (iii).

The second (ii) and third (iii) features in the coiled tube flow have not been reported by the past investigations.

Kenning et al (76-1974) and Abdelmessih et al (77-1974) have reported the buoyancy affects the incipient boiling in upward turbulent flow in vertical tubes. But both of them did not explain the temperature deteriorations that occur after the temperatures reach the peak.

Katto (78-1976) and Mori and Hijikata (79-1978) have summarized the factors affecting the buoyancy force in a forced convection field of a channel

between two plates and in a round horizontal straight tube.

In the forced convection field, increasing heat flux and temperature difference between the fluid and tube wall, causes the flow to be affected by buoyancy forces. This force of buoyancy becomes predominant when the flow rate is low. The relation between Reynolds number and Rayleigh number is shown in Fig. (4.2.5).

Rayleigh number is defined as:

$$R_a = \frac{q\beta\Delta T D^3}{\nu^2} \cdot \frac{\nu}{k} = Gr \cdot Pr \qquad (4.2.1)$$

where g is the acceleration due to gravity, β is the coefficient of expansion, ΔT is the temperature difference between the inside wall and the fluid, D is the tube diameter, ν is the kinetic viscosity and k is the thermal conductivity of fluid.

Rayleigh numbers are calculated when the value of wall temperatures at the upper side become greater than or equal to the wall temperature at the inner side, (plotted in Fig. (4.2.5)). The figure shows that all results appear in the Laminar Forced-Natural convection region (in which either of the two modes of convection are possible). The results indicate that the buoyancy effect in coiled tubes occur earlier (i.e. at lower Rayleigh numbers) than that of straight horizontal tubes, (shown as a dotted line in the figure).

A, B and C in Fig. (4.2.5) are the changing points of the temperature profiles in Figs. (4.2.2a) - (4.2.2c).

When the temperature peaks at the inner and upper sides reach the point of onset of nucleate boiling, the bubbles in the bubble boundary layer grow rapidly on the surface of the inner half of the tube. These large vapour bubbles eventually separate from the tube surface and immediately break up into small bubbles. The part of the tube surface which is exposed is then cooled by the liquid phase. Therefore the temperature at the bubble boundary layer decreases to the bulk fluid temperature.

Intermittent clouds of tiny bubbles and intermittent plug-type bubbles were both observed through the plastic fibre-glass reinforced tube which was placed at the exit of the test section.

The effect of the buoyancy in the laminar and turbulent single-phase flows in the coiled tube can be seen in Fig. (4.2.5) which shows the relation between Reynolds number and Rayleigh number. The positions of temperature peak can be also predicted by the factors, f (K, Pr, Gr), (K is the Dean number and Gr is the Grashof number). The phenomena being studied are so complex, in nature, that it is not possible to investigate the relationship of each parameter to every other parameter.

4.2.1.3 Heat Transfer Coefficient of water flow

Local heat transfer coefficients are obtained under the same conditions as section (4.2.1.1).

The tubes are divided into 0.3m sections for evaluating the local heat transfer coefficients. The local heat transfer coefficients at upper (0^o), outer (90^o), lower (180^o) and inner (270^o) sides are calculated using the differences between bulk and wall temperatures. The mean local heat transfer coefficients from all sections at four positions of the tube periphery are plotted in Figs. (4.2.6a) - (4.2.7c) at different liquid flow rates (1.71×10^5 and 3.42×10^5 Kg/m^2h) and input heat fluxes (934, 2102, and 3730 $Kcal/m^2h$).

The values of heat transfer coefficients at four positions in Figs. (4.2.6a) - (4.2.7c) are plotted in Fig. (4.2.8). From this figure the heat transfer coefficients at the inner side always show the smallest with constant value around 900 $Kcal/m^2h^oc$. The other heat transfer coefficients at three positions (0^o, 90^o and 180^o) spread over a wider range, about $\pm$1500 $Kcal/m^2h^oc$, than that of steam single-phase flow shown in Fig. (4.2.1b) in the section (4.2.2.3).

The secondary flow effect on the heat transfer coefficient of Coil A ($\frac{a}{R}$ = 20) is larger than that of larger coils.

Seban and McLaughlin (22) have discussed the heat transfer coefficients of outer and inner sides with Reynolds number ranges of 10 to 6,000 as Fig. (2.9) and empirical heat transfer coefficients from the present work are evaluated using the following relation:

$$(\frac{hd}{k})\ (\frac{\nu}{\alpha})^{-0.3} = f\ (R_e) \qquad (4.2.2)$$

where h is the heat transfer coefficient, d is the tube diameter, k is the thermal conductivity, ν is the kinetic viscosity and α is the thermal diffusivity.

The results at Reynolds numbers between 1.9×10^3 and 3.8×10^4 are plotted in Fig. (4.2.9).

The figure shows clearly that the heat transfer coefficients at the outer side are higher than that at the inner side. The coefficients for the inner and the outer sides of the coil are in the ratio of about 1:1.5 from Seban and McLaughlin's result (22).

Up to the present, only Seban and McLaughlin (22) have mentioned a profile of local heat transfer coefficients in laminar flow as Fig. (2.9a) in the section (2.2.4.1). The ratio of heat transfer coefficients between the outer and inner sides from their results with a similar Reynolds number to the present work ($1.9 \times 10^3 < Re < 3.8 \times 10^4$) are calculated by the author as the following:

$$\left(\frac{h\ \text{outer}}{h\ \text{inner}}\right)_{\text{Laminar}} = 3.03\ \left(\frac{a}{R}\right)^{0.113} \qquad (4.2.3)$$

Fig. (4.2.10) shows the ratio of heat transfer coefficient of inner and outer sides from the present work and their results. A formula can be

defined for the present work as follows:

$$\left(\frac{h \text{ outer}}{h \text{ inner}} \right)_{\text{water}} = 15.45 \left(\frac{a}{R}\right)^{0.451} \qquad (4.2.4)$$

A discrepancy between eq. (4.2.3) and eq. (4.2.4) is due to the difference of Prandtl numbers, their laminar flows were obtained by the use of a medium heavy oil with Prandtl numbers from 100 to 657. The secondary flow effects at low Prandtl numbers occur more rapidly and are more significant than that at higher Prandtl numbers if the diameter ratio were the same.

The local heat transfer coefficients of the single-phase flow in helically-coiled tubes are affected strongly by the secondary flow. The secondary flow particularly affects the inner and outer sides of the tube producing large differences of temperature profiles and heat transfers. Therefore the diameter ratios can be thought as the main function determining the temperature differences and heat transfer differences between the outer and inner sides of the tube.

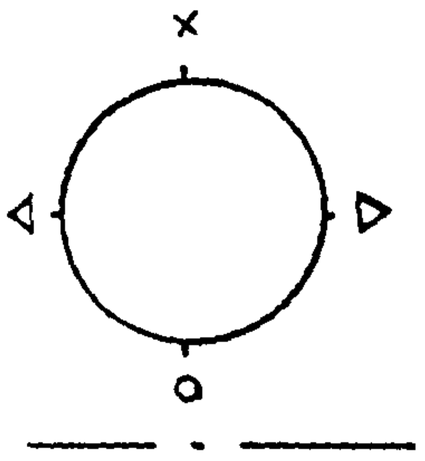
COIL A

G_f = 3.42×10^5 kg/m^{2}h

q ; Input heat flux.

---△--- upper
—x— outer
---▽--- lower
—o— inner

↕ Bulk temperature.



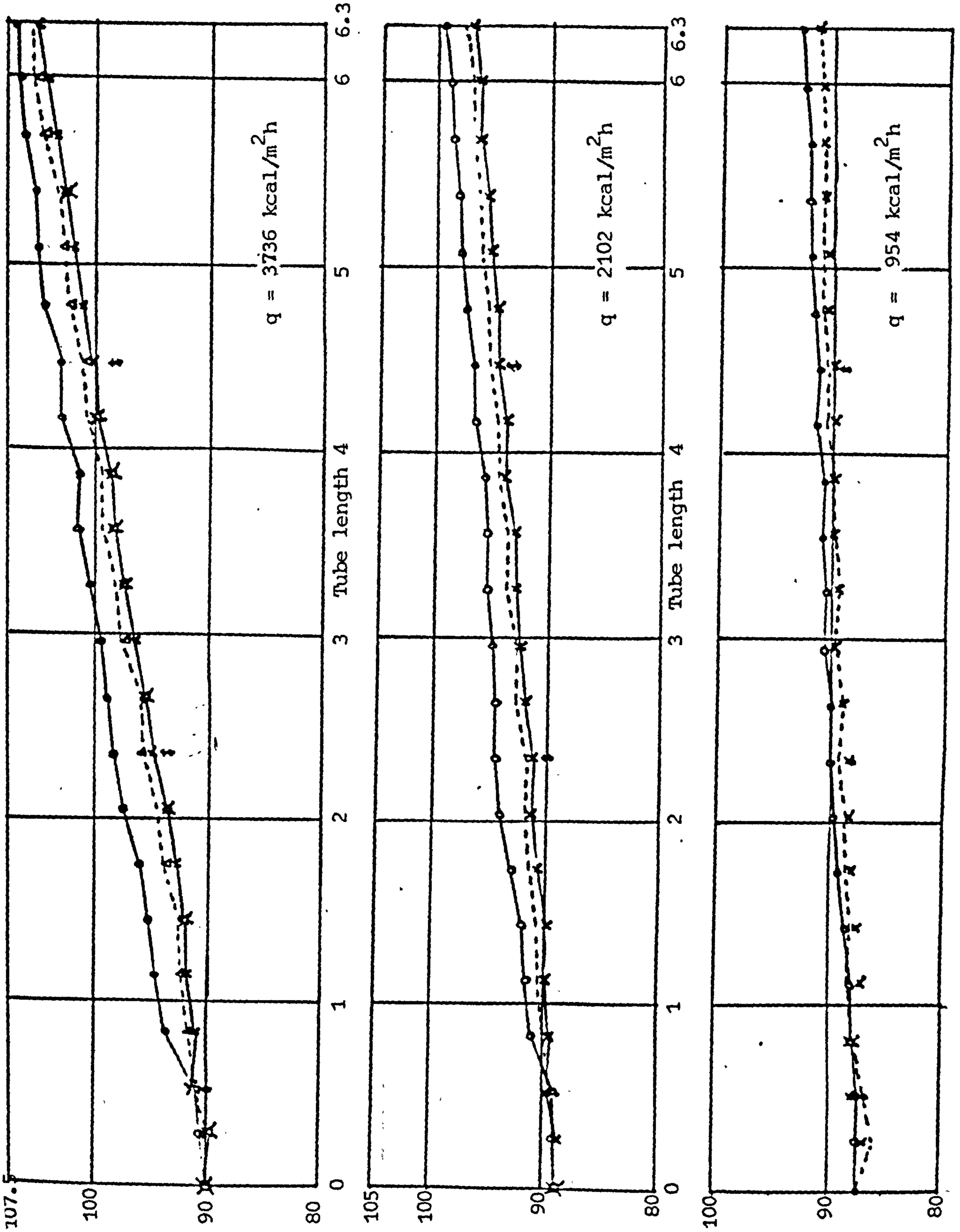
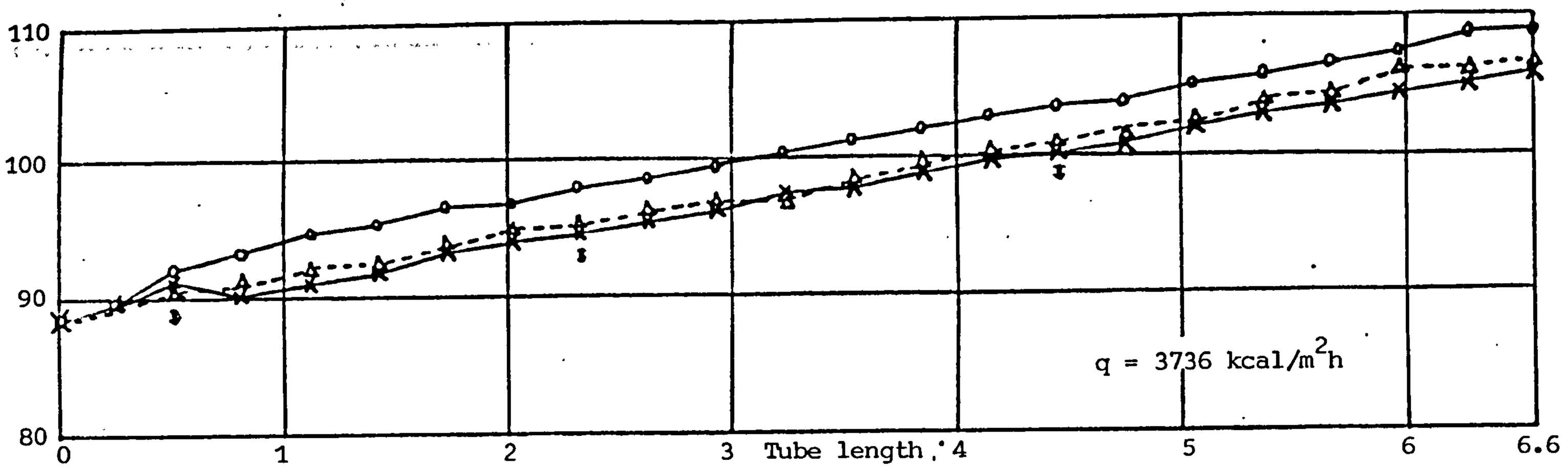


Fig. (4.2.1 a) : Wall temperature profiles for water single-phase flow (Coil A)



COIL B

$G_f = 3.42 \times 10^5$ kg/m²h

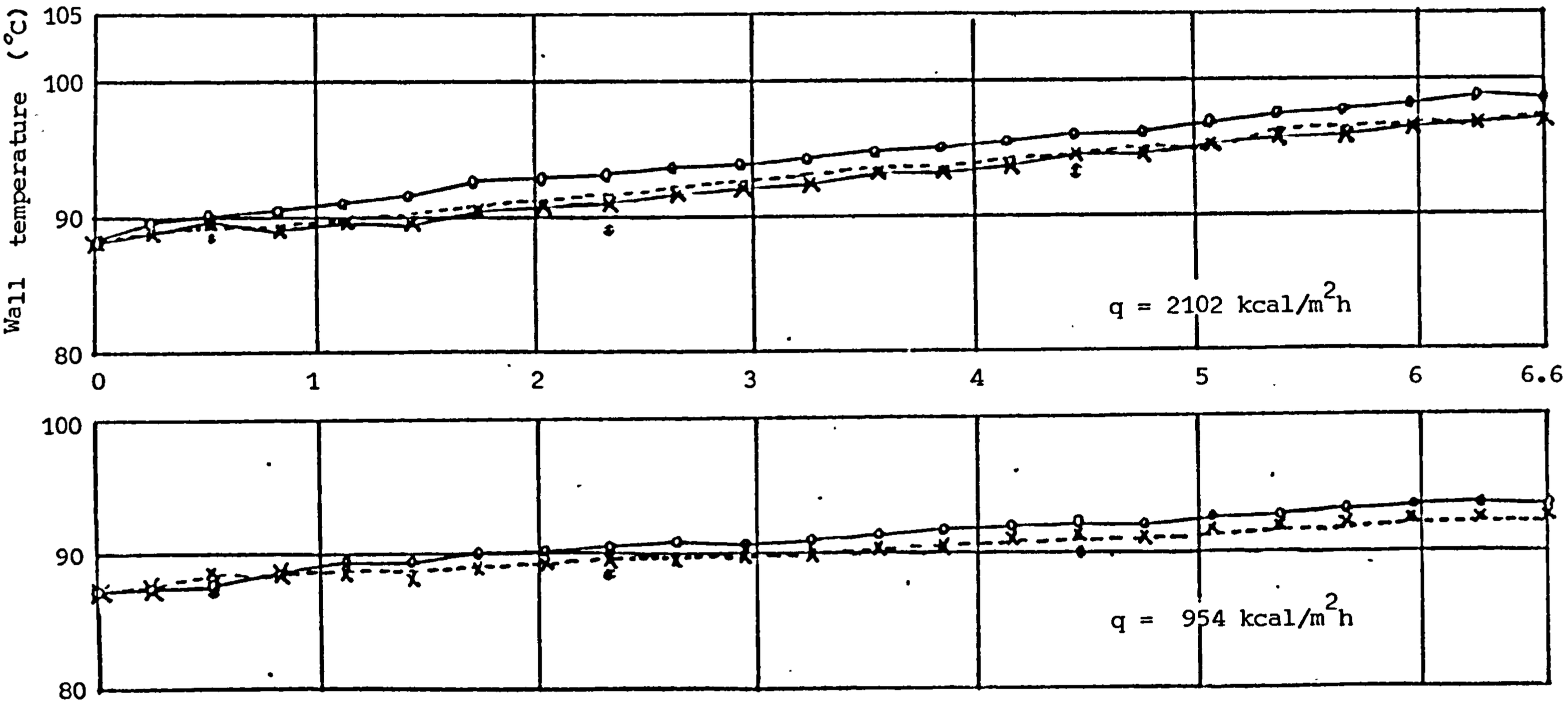


Fig. (4.2.1 b) : wall temperature profiles for water single-phase flow (Coil B)

COIL C

$G_f = 3.42x10^5$ kg/m^{2}h

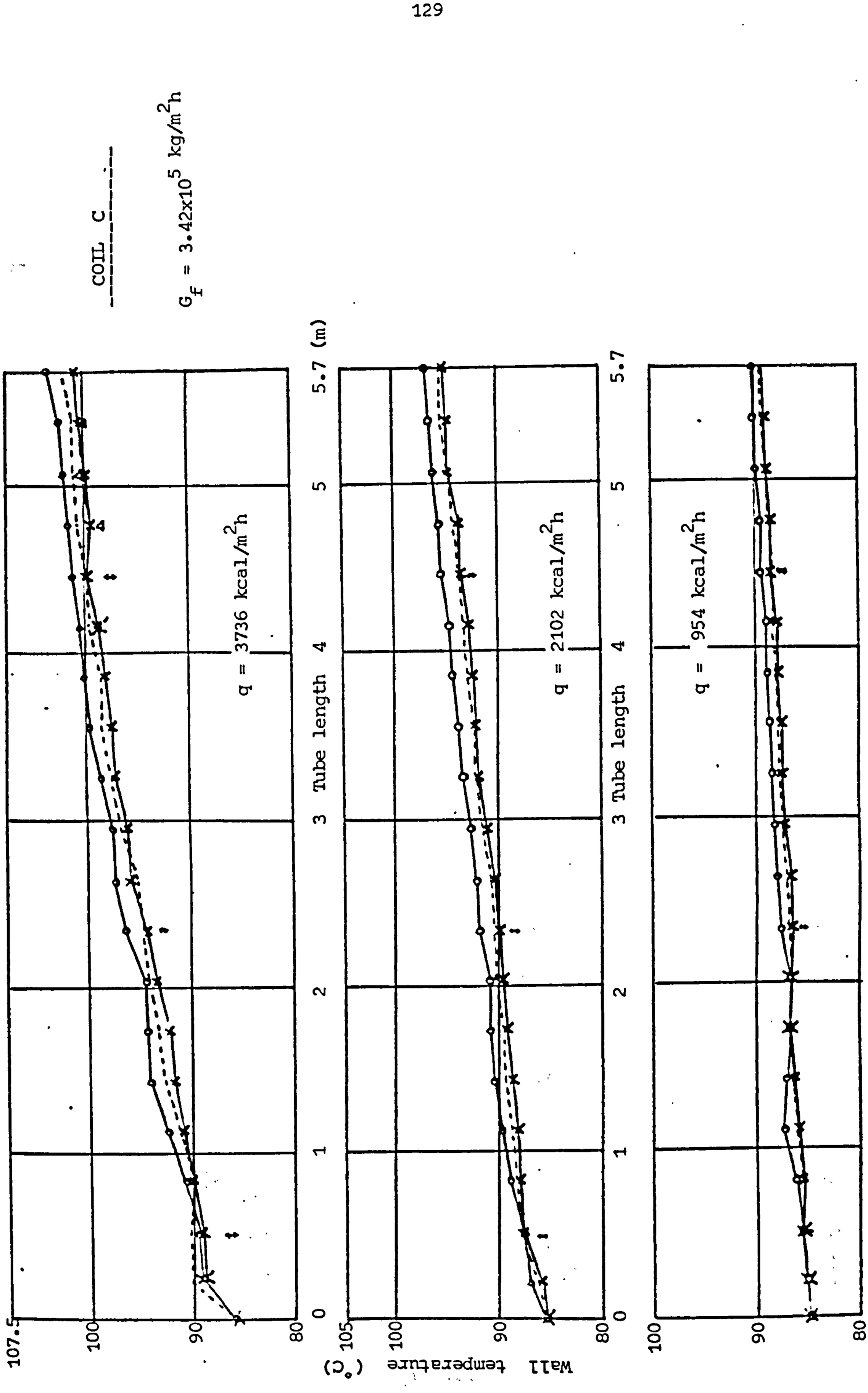
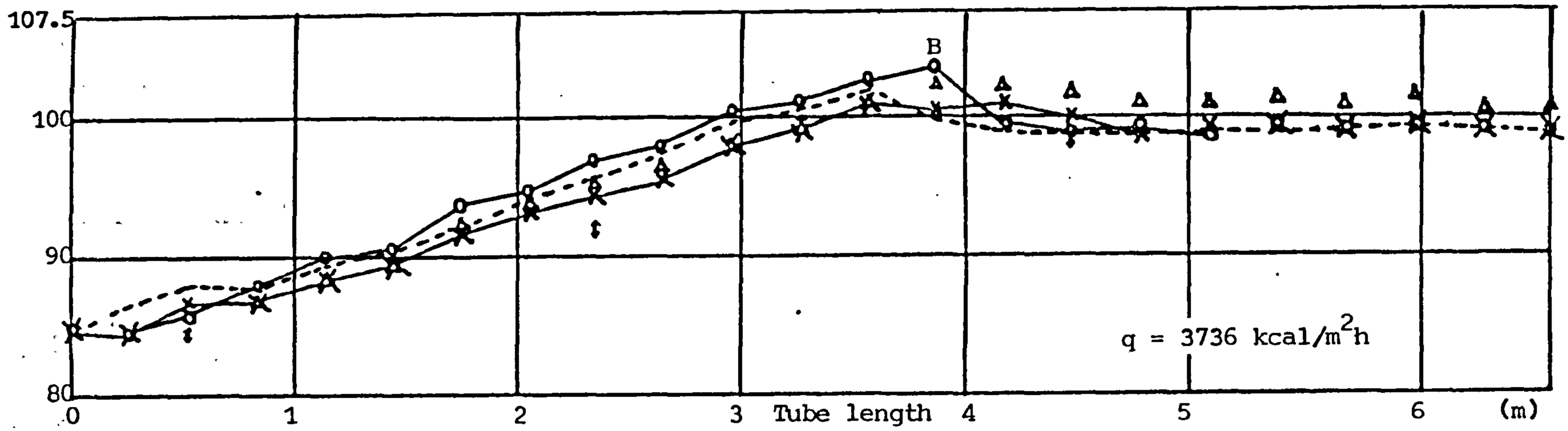


Fig. (4.2.1 c) : Wall temperature profiles for water single-phase flow (Coil C)

Fig.(4.2.2a) : Wall temperature profiles for water single-phase flow (Coil A)



COIL B

$G_f = 1.71 \times 10^5$ kg/m²h

q : Input heat flux.

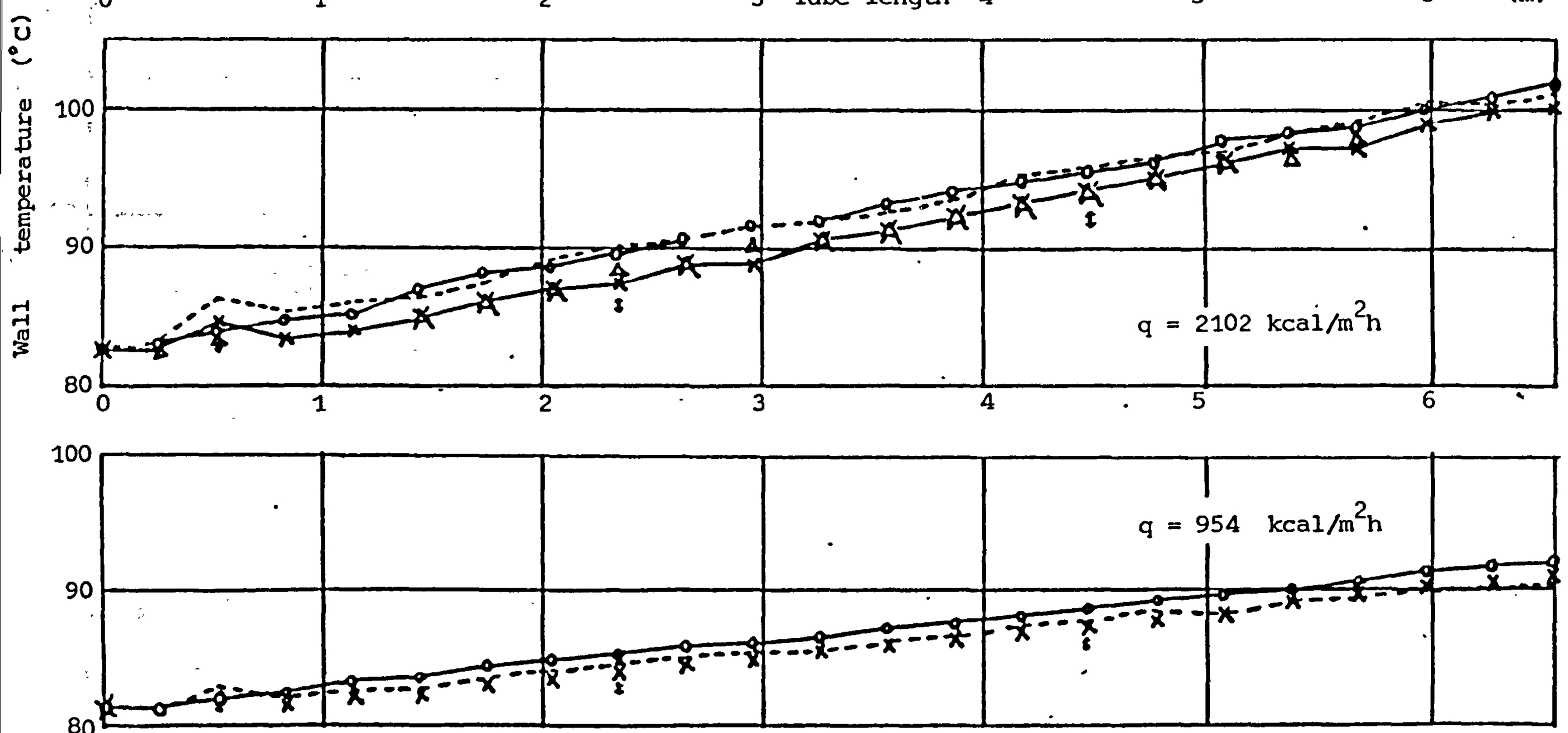
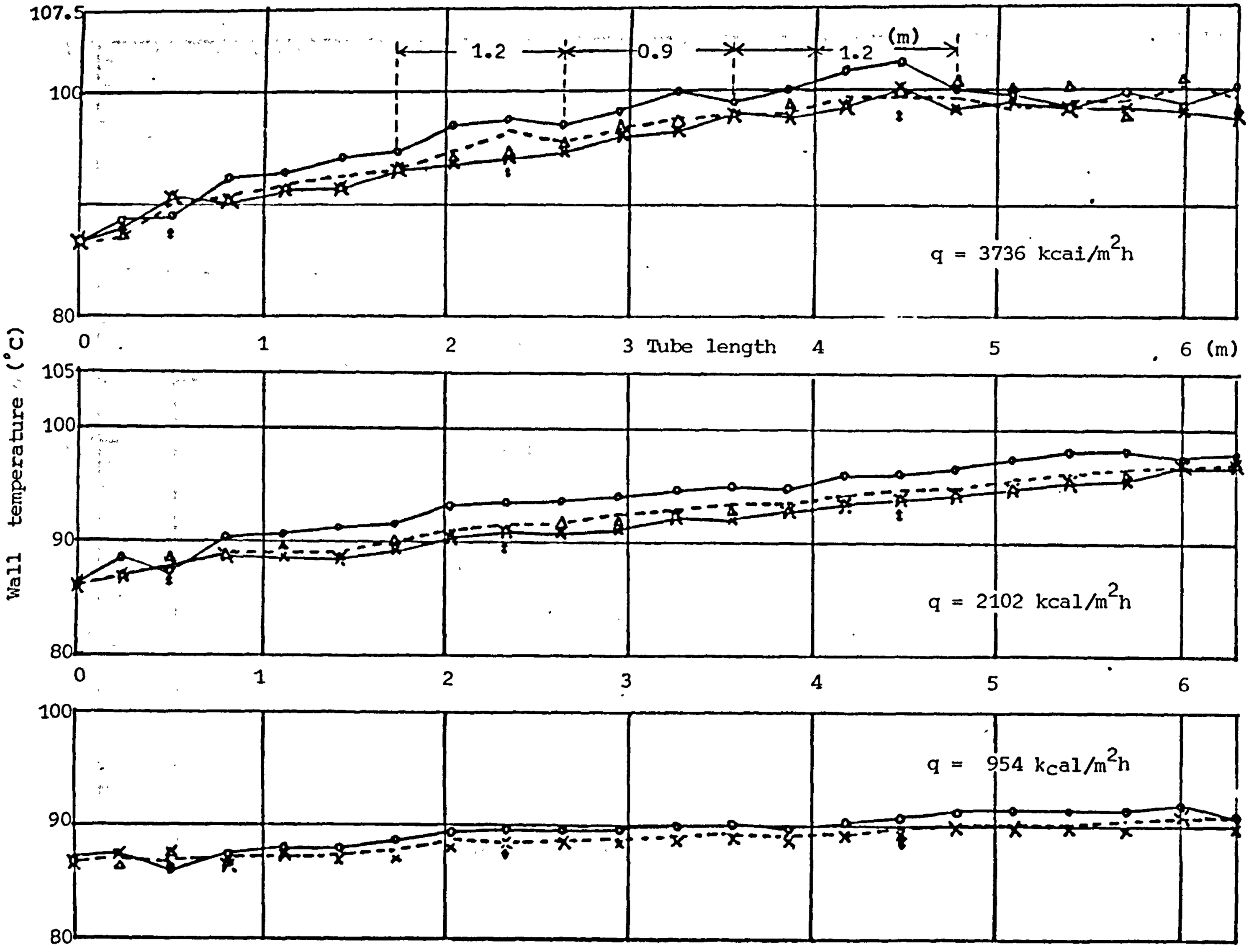


Fig. (4.2.2 b) : wall temperature profiles for water single-phase flow (Coil B).

COIL C

$G_f = 1.71 \times 10^5$ kg/m²h

Fig. (4.2.2 c) : Wall temperature profiles for water single-phase flow (Coil C)



COIL A

$G_f = 3.42 \times 10^5$ kg/m²h

(• Observed oscillation.)

Fig. (4.2.4) : Oscillating wall temperature profiles at similar condition to Fig. (4.2.1 a).

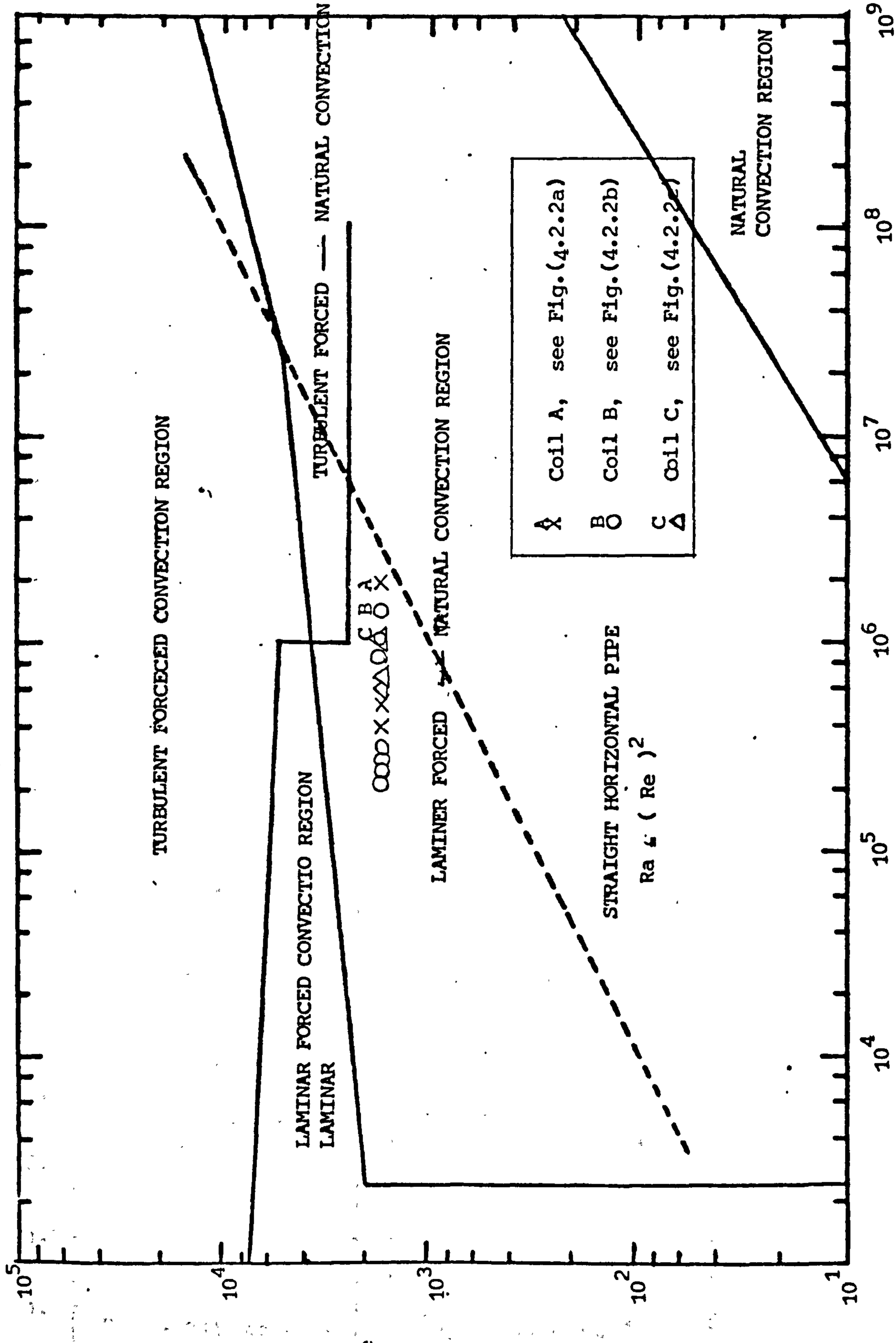


Fig. (4.2.5) : Effect of buoyancy force, Rayleigh number — Reynolds number.

Fig.(4.2.6a)

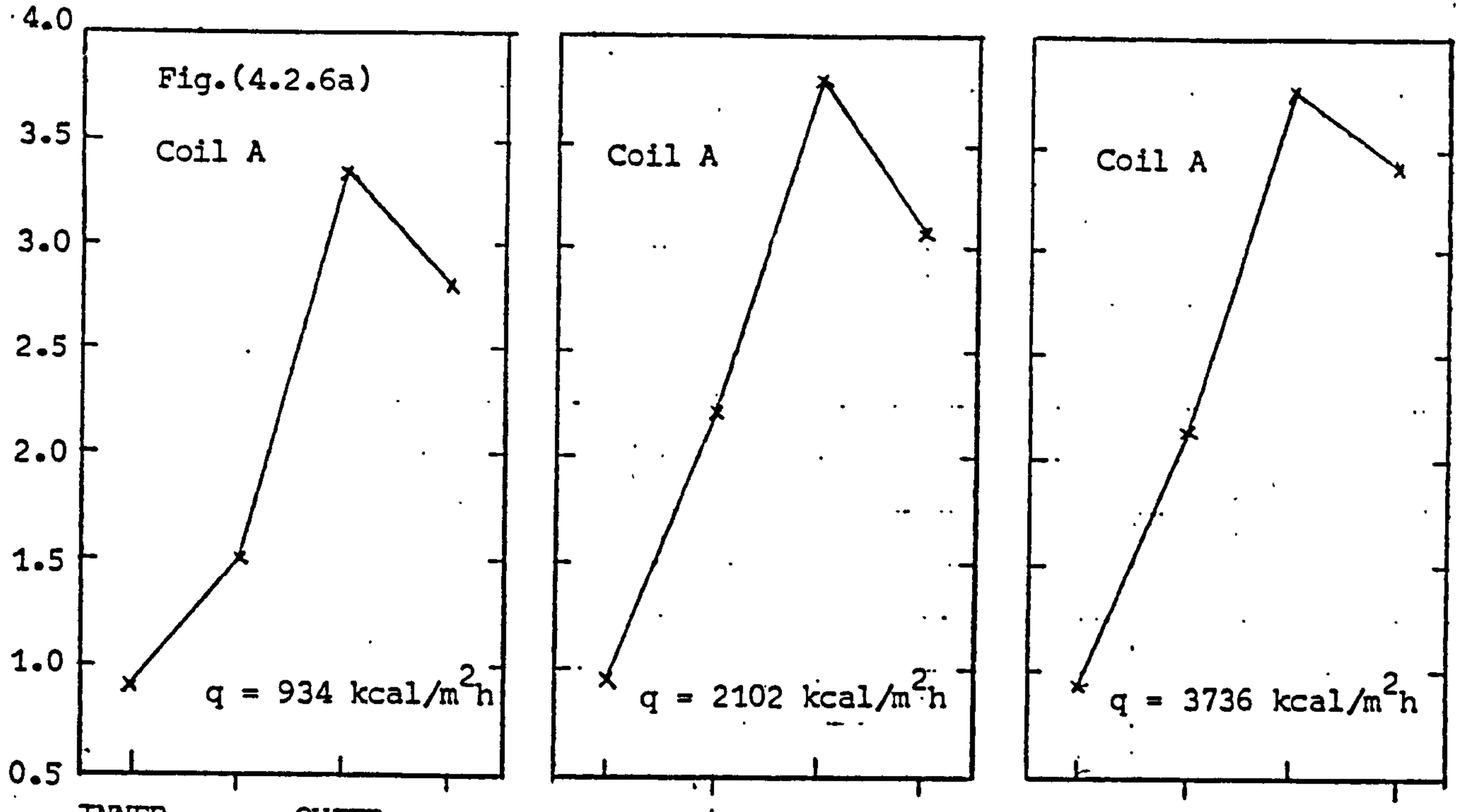
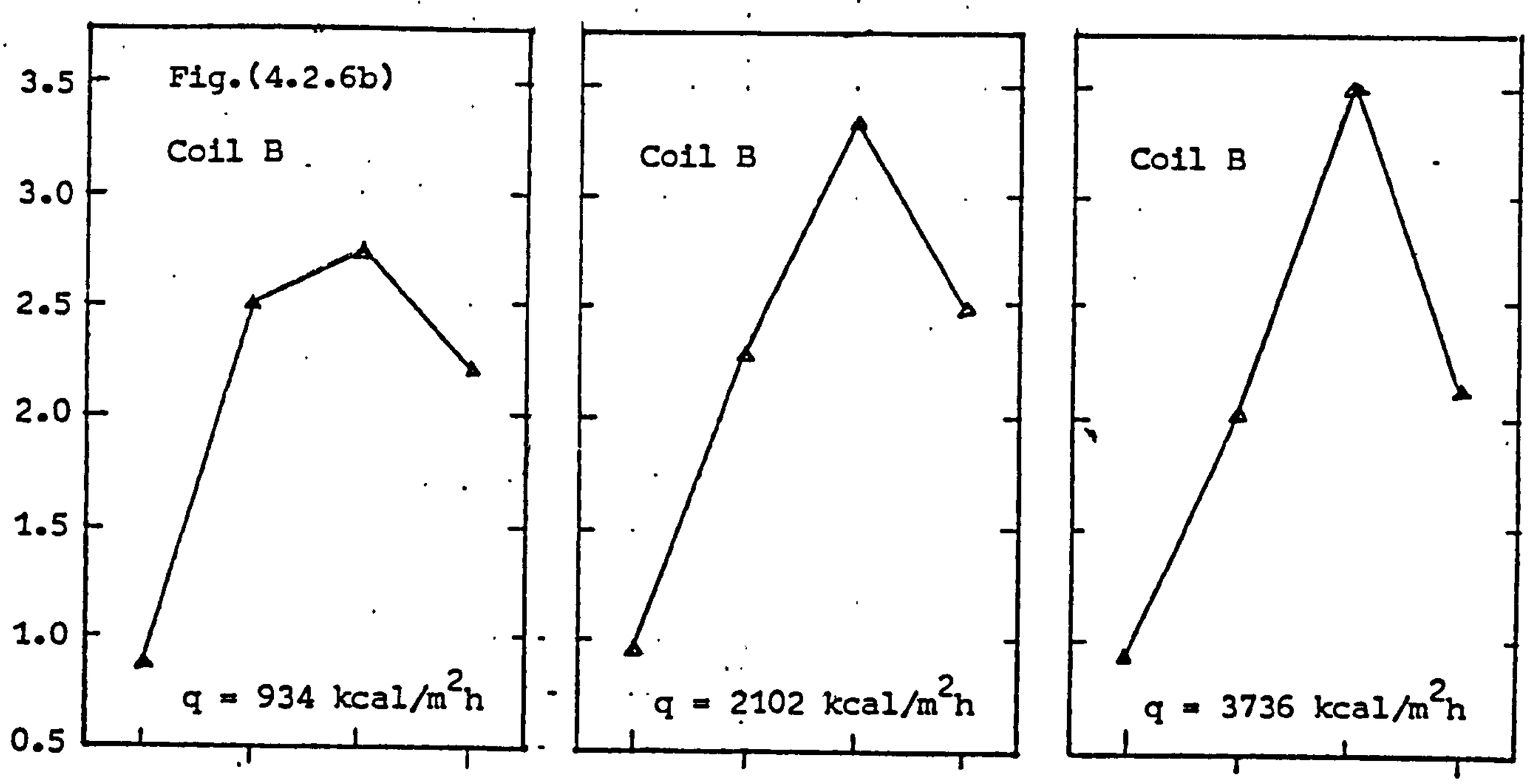
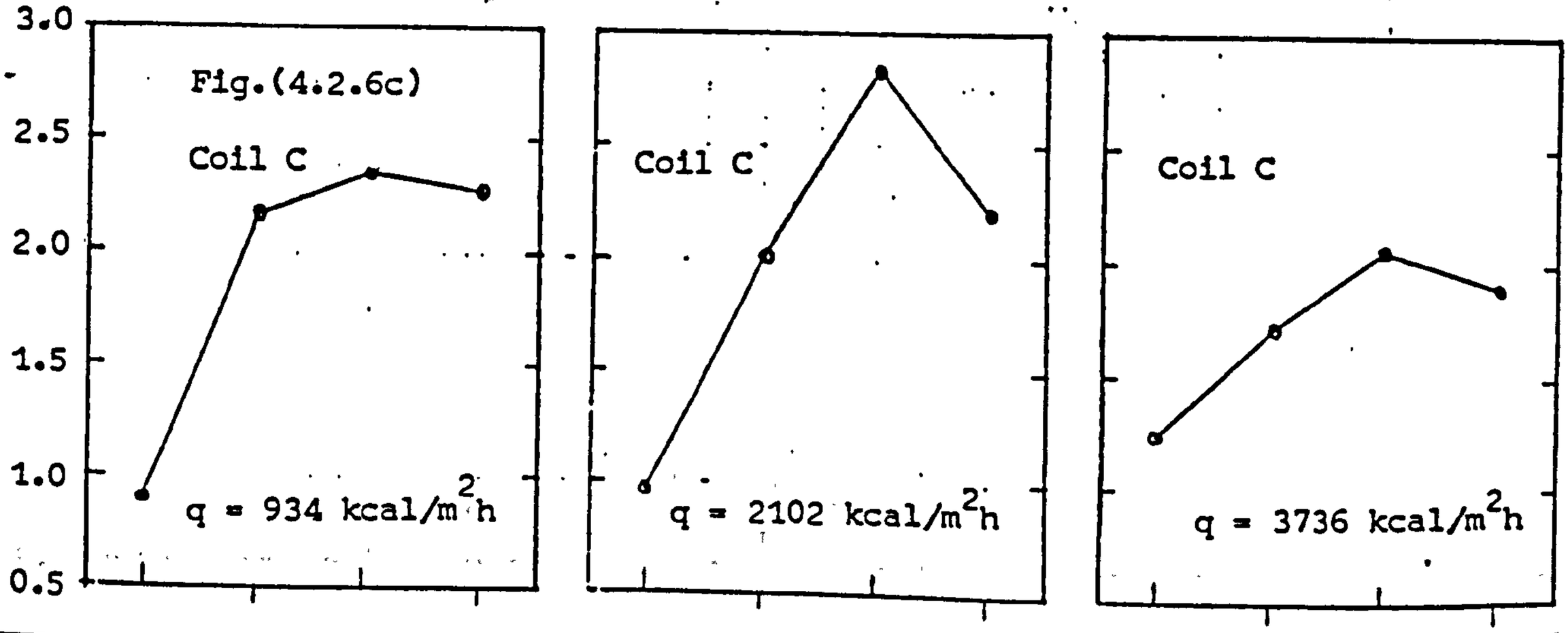


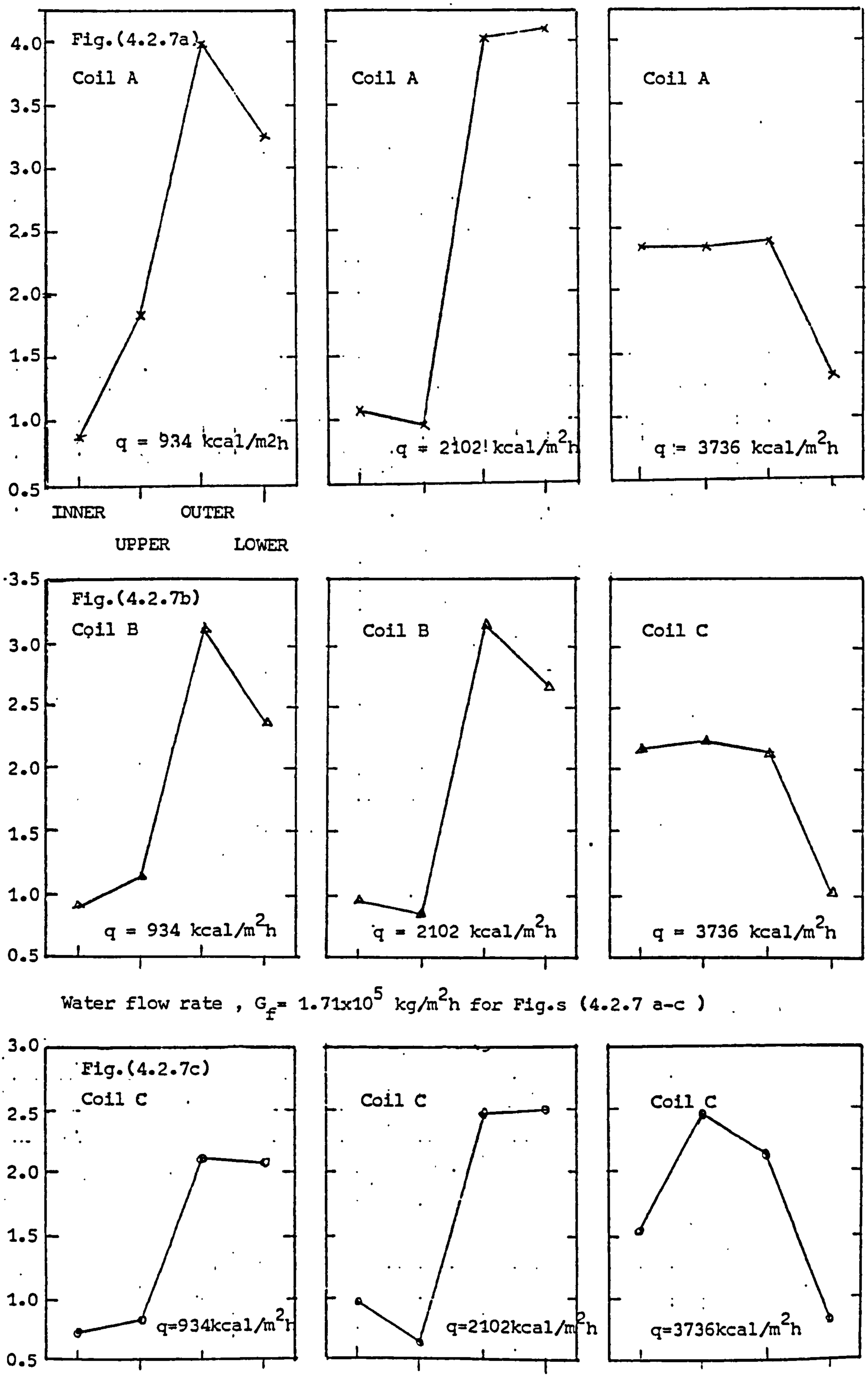
Fig.(4.2.6b)



Water flow rate, G_f=3.42x10^5 kg/m^{2}h for Fig.s (4.2.6 a-c)

Fig.(4.2.6c)




Fig.(4.2.7a)
Coil A
q = 934 kcal/m2h
Coil A
q = 2102 kcal/m2h
Coil A
q = 3736 kcal/m2h
INNER
OUTER
UPPER
LOWER
Heat transfer coefficient , (x10^3 kcal/m^2h°c)
Fig.(4.2.7b)
Coil B
q = 934 kcal/m2h
Coil B
q = 2102 kcal/m2h
Coil C
q = 3736 kcal/m2h
Water flow rate , Gf= 1.71x10^5 kg/m^2h for Fig.s (4.2.7 a-c)
Fig.(4.2.7c)
Coil C
q=934kcal/m2h
Coil C
q=2102kcal/m2h
Coil C
q=3736kcal/m2h

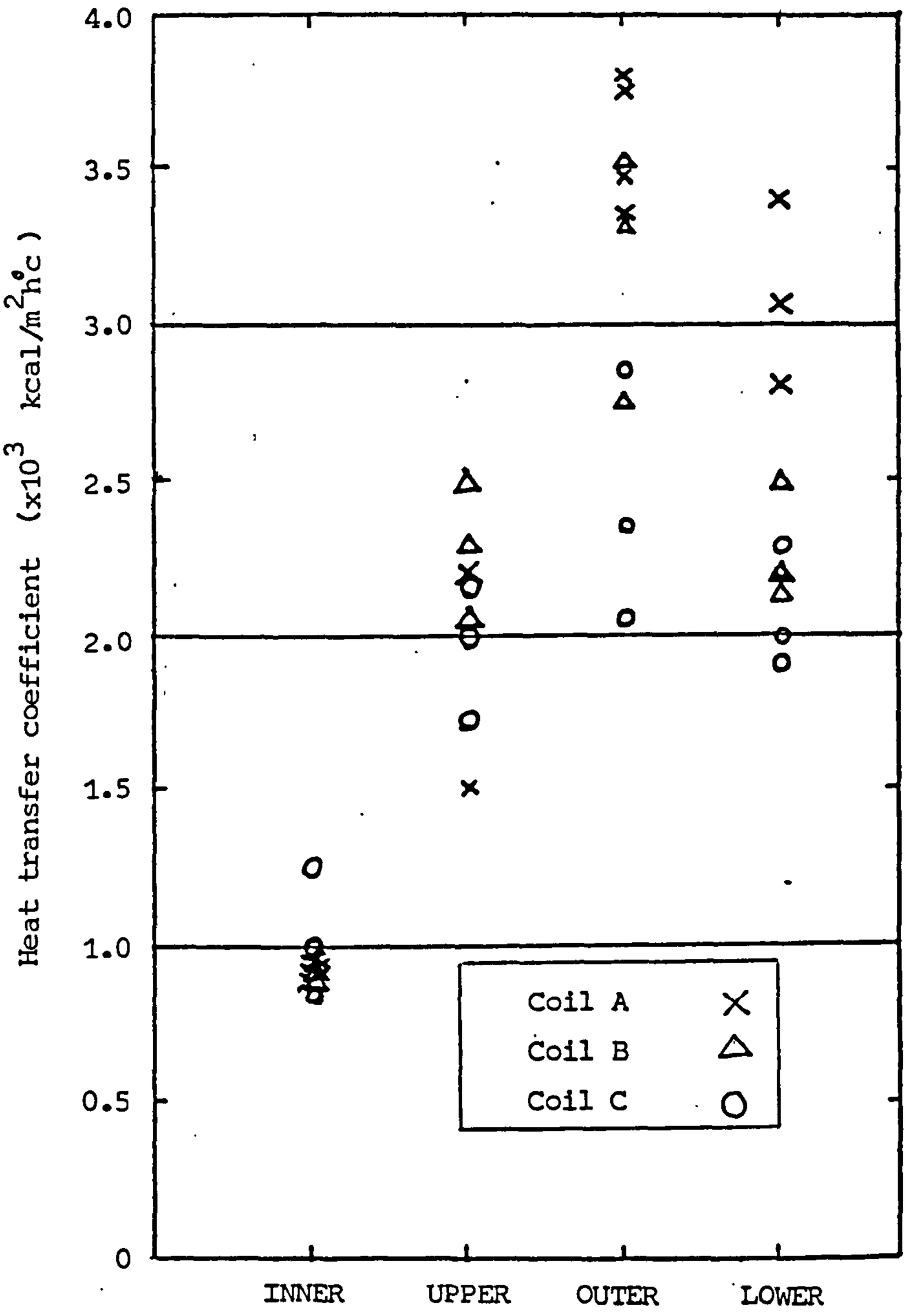


Fig. (4.2.8) : Local heat transfer coefficient distributions in the tube cross-section of water flow, values are obtained from Fig.s (4.2.6) and (4.2.7).

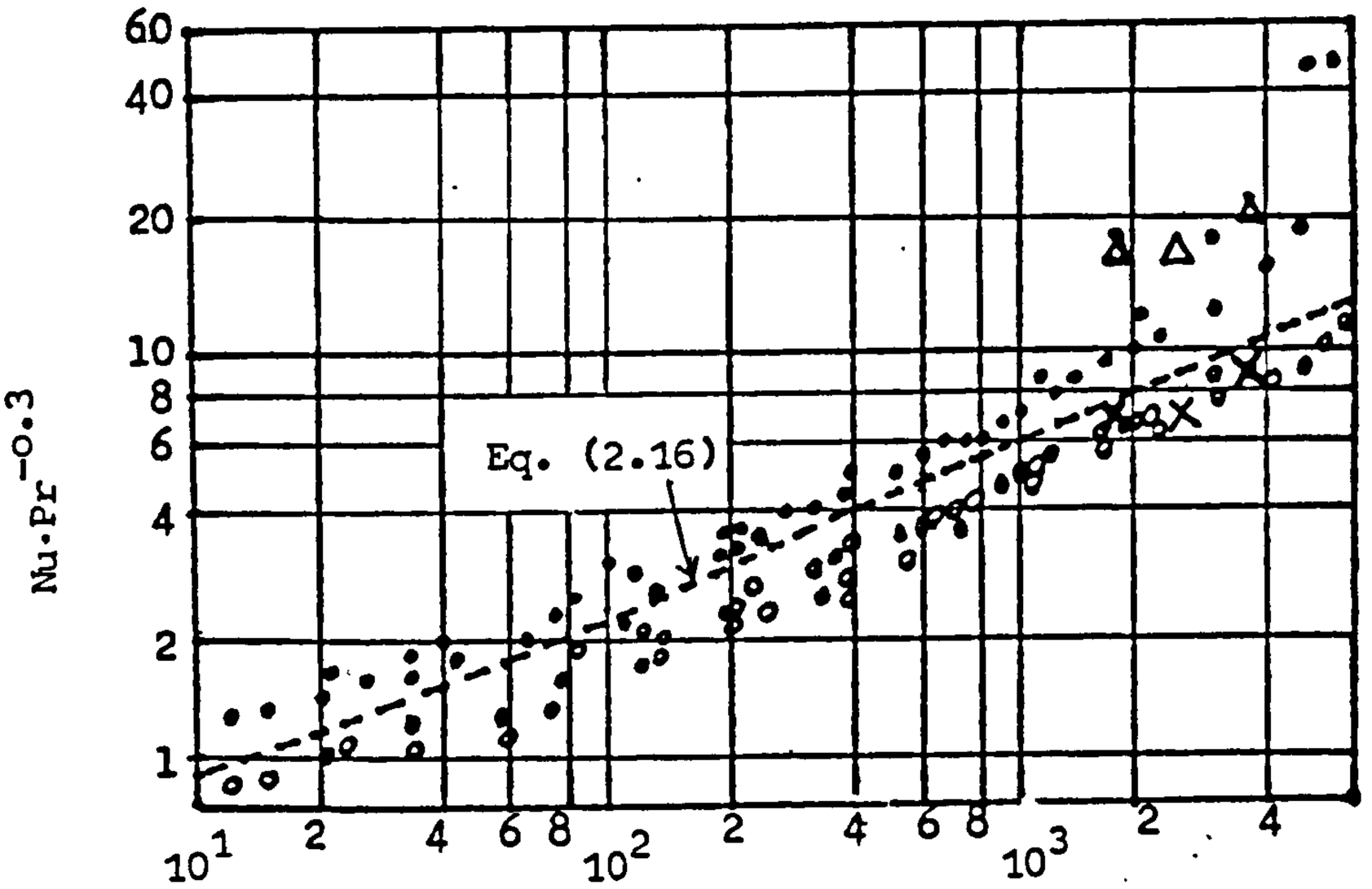


Fig. (4.2.9) : Comparison of heat transfer coefficients of the present work with the results of Seban & McLaughlin (22).

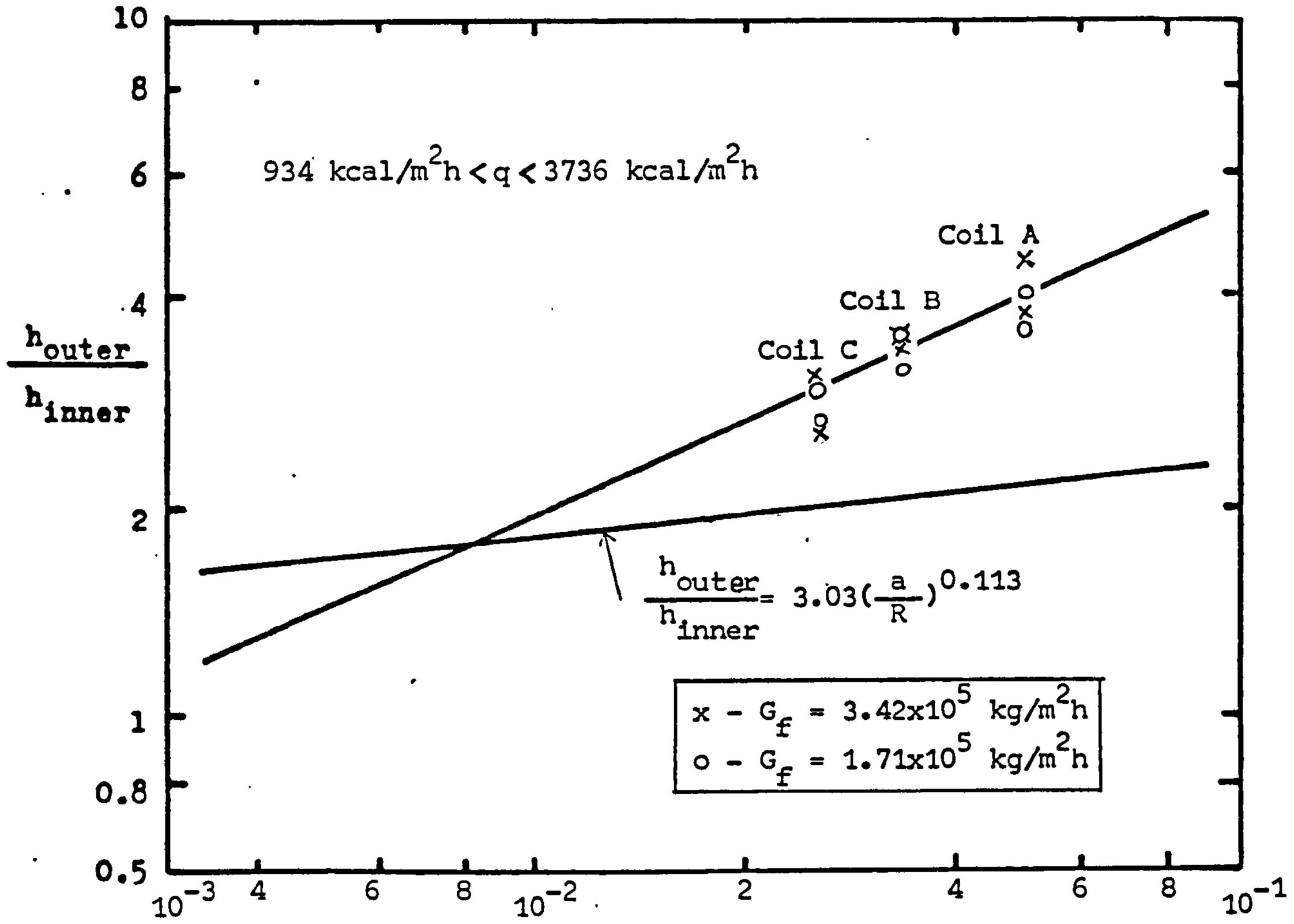


Fig. (4.2.10) : Ratio of heat transfer coefficients between the outer and inner sides, (water flow).

4.2.2 Steam flow

4.2.2.1 Pressure drop of steam flow

The steam flows upwards in the coils. The operational conditions of pressure measurements are as follows:

Flow direction	upwards
Flow rate	$8.55 \times 10^4 \sim 1.84 \times 10^5$ Kg/m^2h
Heat flux	415 $Kcal/m^2h$ - 1875 $Kcal/m^2h$
Fluid temperature	105^o - 175^oC
Inlet pressure	0.129 MN/m^2
Reynolds number	3.15×10^4 - 6.98×10^4
Prandtl number	1.09 - 1.185

The friction factor of a straight pipe, f_s is defined as:

$$f_s = \left(- \frac{\partial P}{\partial z} \right) \frac{2a}{\frac{1}{2}\rho Wm^2} \qquad (4.2.5)$$

where Wm is a mean velocity.

The empirical friction factors using eq. (4.2.5) are plotted in Fig. (4.2.11) and the results are compared with Ito's formula (25) eq. (2.32) and Blasius' formula, eq. (2.34) for a straight tube. The coiled tube friction factor is generally greater than that of an equivalent straight tube. However, Fig. (4.2.11) shows that six of nine empirical friction factors are lower than that of Blasius' value. The causes of the low friction factors are the negligence of diameter ratio between the tube and coil and poor accuracy of the pressure measurement.

Mori and Nakayama (24) reported that the friction factor of coiled pipe is 1.05∿1.29 times larger than that of straight tube at $\{Re \left(\frac{a}{R}\right)^2\}$ range of 1-200. The present results are taken in the $\{Re \left(\frac{a}{R}\right)^2\}$ range of 18-157. Employing Mori and Nakayama's multipliers 1.05∿1.25 for this work, six of nine results become greater than the Blasius's values.

Friction factors of the Coil A, (the smallest coil) show the largest friction factors at every heat flux. The higher heat fluxes (1875 $^{Kcal}/_{m^2h}$) show larger friction factor than that of lower input heat fluxes (934 and 415 $^{Kcal}/_{m^2h}$). The term of $\{Re\ (\frac{a}{R})^2\}^{-\frac{1}{4}}$ from Ito's formula is acceptable for all present results but it should be changed at each value of input heat flux.

4.2.2.2 The wall temperature profiles

The wall temperatures and bulk temperatures are measured under the same conditions as in section (4.2.2.1) and plotted in Figs. (4.2.12a) - (4.2.13c). The bulk temperatures are measured at the starting point of the helix,at 3.31m and at 4.41m positions from the entrance of the test section respectively.

From these figures, temperatures of inner side are highest, the outer side values are lowest and the upper and lower sides show intermediate values. The temperature profiles of steam turbulent single-phase flows from these results show the similar profiles as the other investigator's works.

No data regarding buoyancy effects are obtained from this work.

The effects of secondary flows in turbulent flow are considered to be the same mechanisms as described in the definition of liquid flow in section (4.2.1.2).

4.2.2.3 Heat transfer coefficient of steam flow

The operation conditions are the same as the section (4.2.2.1).

The tube is divided into 0.3m sections for evaluating the local heat transfer coefficients. The local heat transfer coefficients at upper (0^o), outer (90^o), lower (180^o) and inner (270^o) positions are evaluated from temperature differences between bulk and wall. The mean local heat transfer coefficients from all sections at four positions of the tube periphery are plotted in Figs. (4.2.14a) - (4.2.15c) at different steam flow rates ($8.55 \times 10^4 \sim 1.84 \times 10^5$ Kg/m^2h) and input heat fluxes (415, 937, and 1875 $Kcal/m^2h$).

Fig. (4.2.16) shows all local heat transfer coefficients at four positions from Figs. (4.2.14a) - (4.2.15c). The heat transfer coefficient at the outer side is about 2.3 times that at the inner side. The upper and lower sides show almost the same heat transfer coefficients (about 500 $Kcal/m^2h^oc$).

In general Nusselt number is related to

$$Nu = f\ (Re,\ Pr) \qquad (4.2.6)$$

most investigators reported a common formulae for turbulent single-phase flow as:

$$NuPr^{-0.4} = f\ (Re) \qquad (4.2.7)$$

Nusselt numbers from the present work are evaluated and compared with Seban and McLaughlin (22) in Fig. (4.2.17). The trend of the $Nu.Pr^{-0.4}$ term of the outer and inner sides agree with their results in the ranges of Reynolds numbers between 3.1×10^4 and 7.4×10^4.

Kozeki (80-1973) discussed the ratio of heat transfer coefficients of the outer and inner sides in turbulent flow. Using his own results together with those of Seban and McLaughlins' results (22), he formulated the following expression:

$$\left(\frac{h\ \text{outer}}{h\ \text{inner}}\right)_{\text{turb.}} = 10.5\ \left(\frac{a}{R}\right)^{0.365} \qquad (4.2.8)$$

The ratios from the present work also are plotted in Fig. (4.2.18) with eq. (4.2.8) and a formula is obtained as follows:

$$\left(\frac{h\ \text{outer}}{h\ \text{inner}}\right)_{\text{turb.}} = 7.70\ \left(\frac{a}{R}\right)^{0.345} \qquad (4.2.9)$$

It can be seen that this function is similar in character to eq. (4.2.8).

The mean heat transfer coefficient of the coiled tube can be the same as that of the upper or lower sides of the coiled tube having heat transfer coefficients with values approximately equal to the mean of the outer and inner side values.

The theoretical discussion of turbulent heat transfer coefficient appears in section (5.1.2).

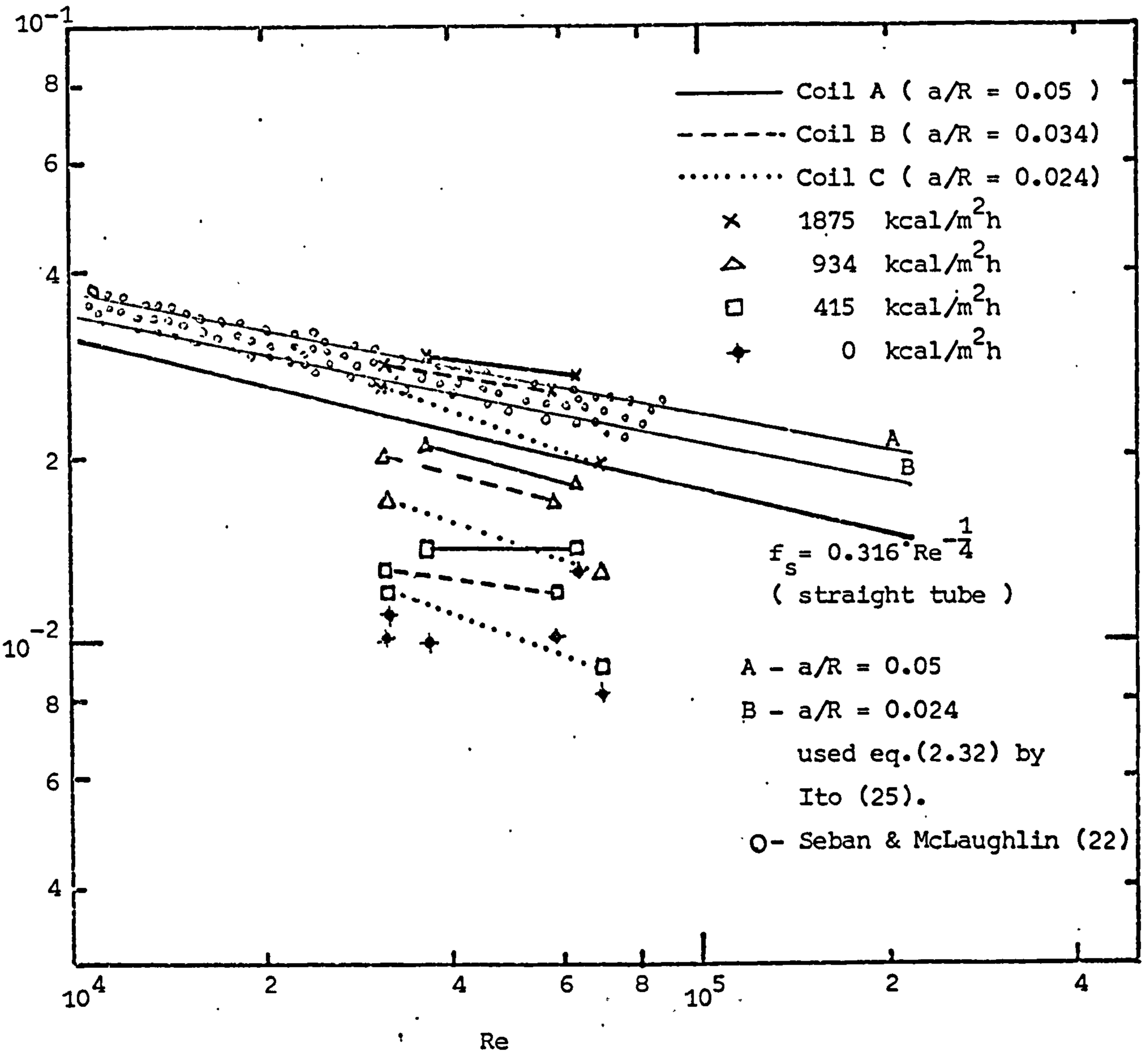


Fig. (4.2.11) : Pressure drops of steam flow of the present work,

$$8.55 \times 10^4 \lesssim G_g \lesssim 1.84 \times 10^5 \ kg/m^2h.$$

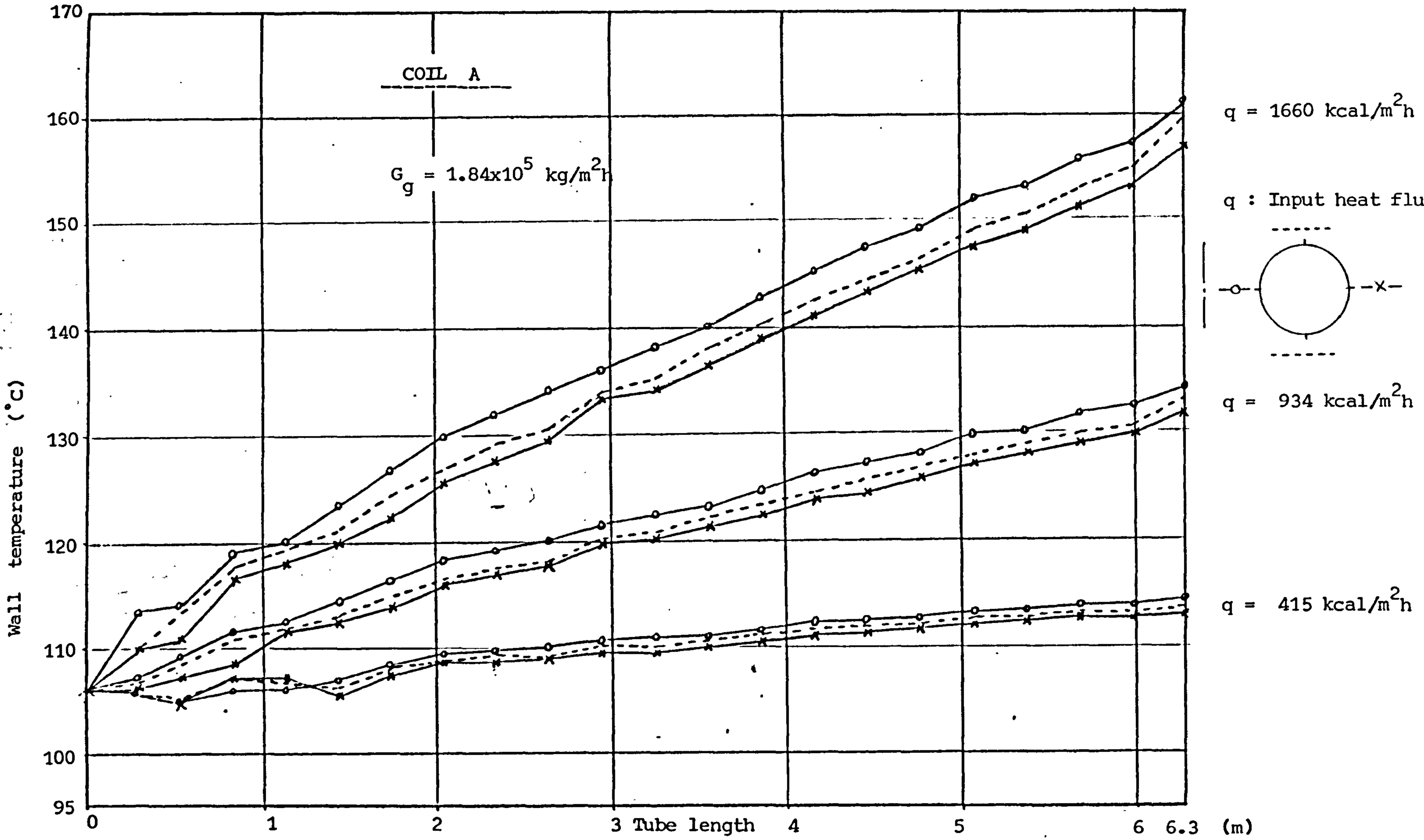


Fig. (4.2.12 a) : Wall temperature profiles for steam single-phase flow (Coil A)

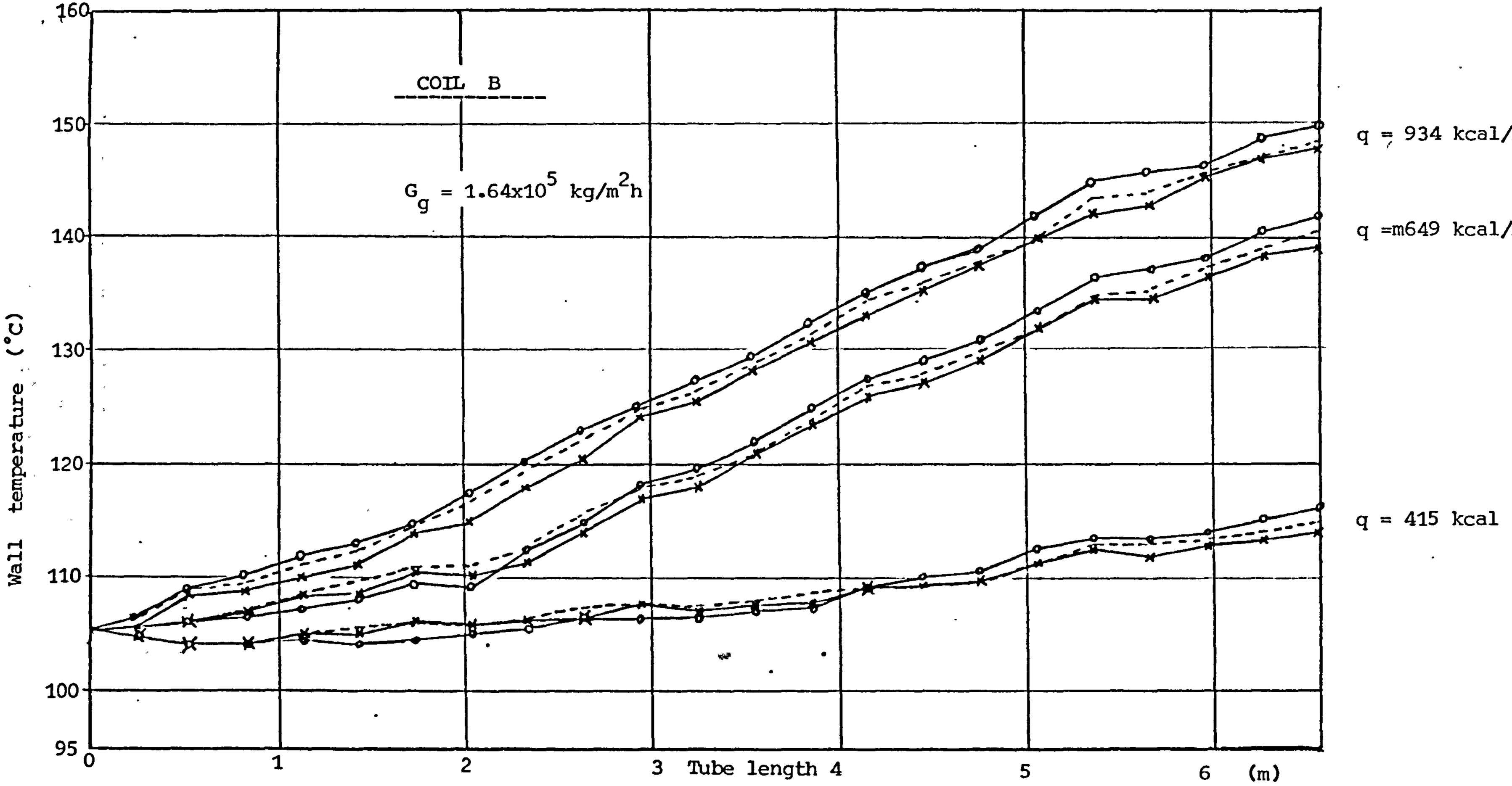


Fig. (4.2.12 b) : Wall temperature profiles for steam single-phase flow (Coil B).

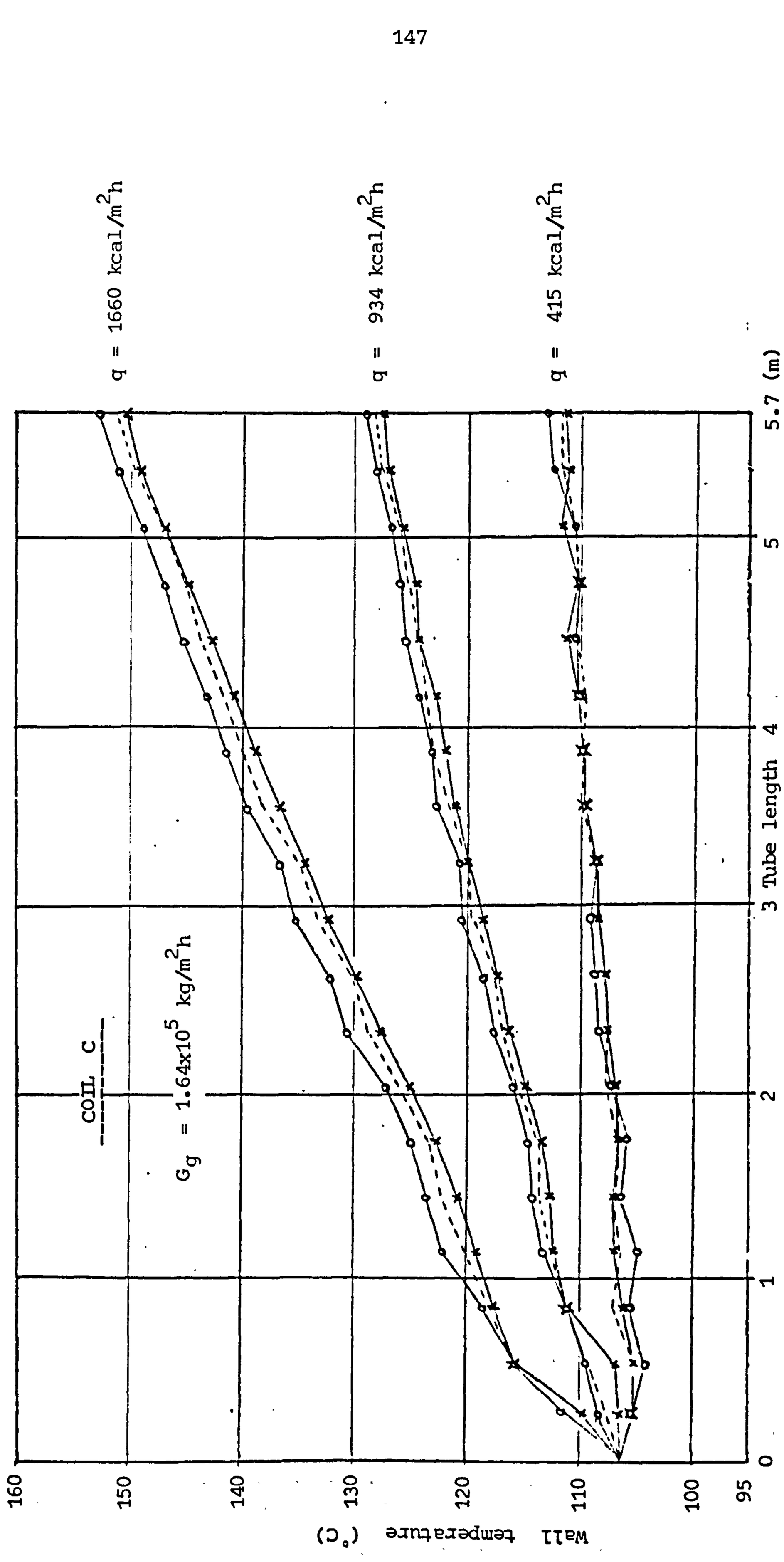
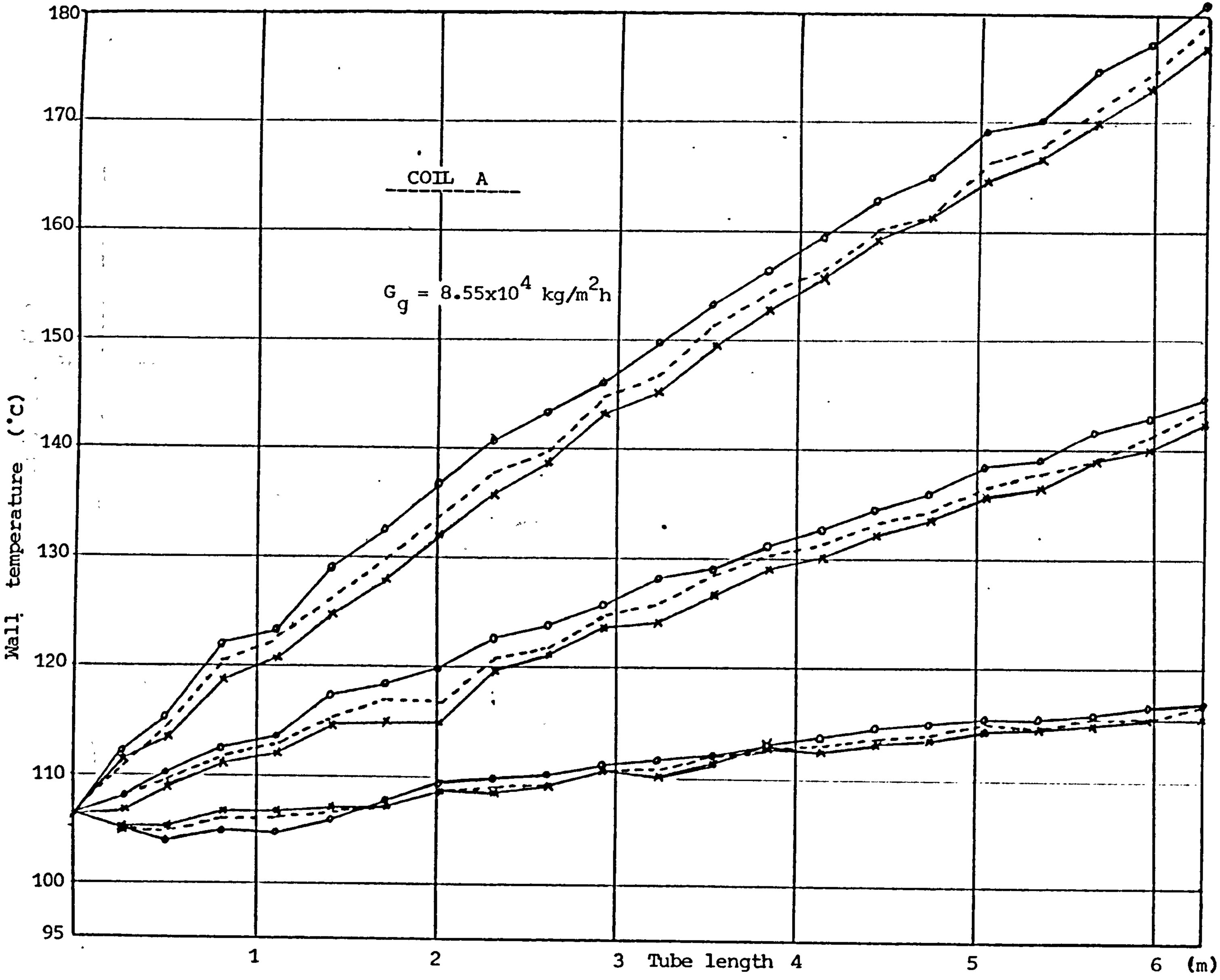
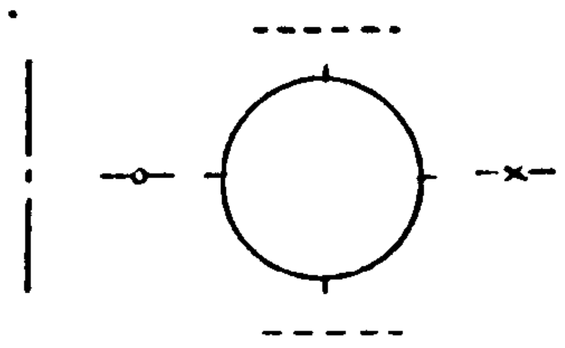


Fig. (4.2.12 c) : Wall temperature profiles for steam single-phase flow (Coil C)





q = 1660 kcal/m^{2}h

q = 934 kcal/m^{2}h

q = 415 kcal/m^{2}h

Fig. (4.2.13 a) : Wall temperature profiles along the tube length for steam single-phase flow (Coil A).

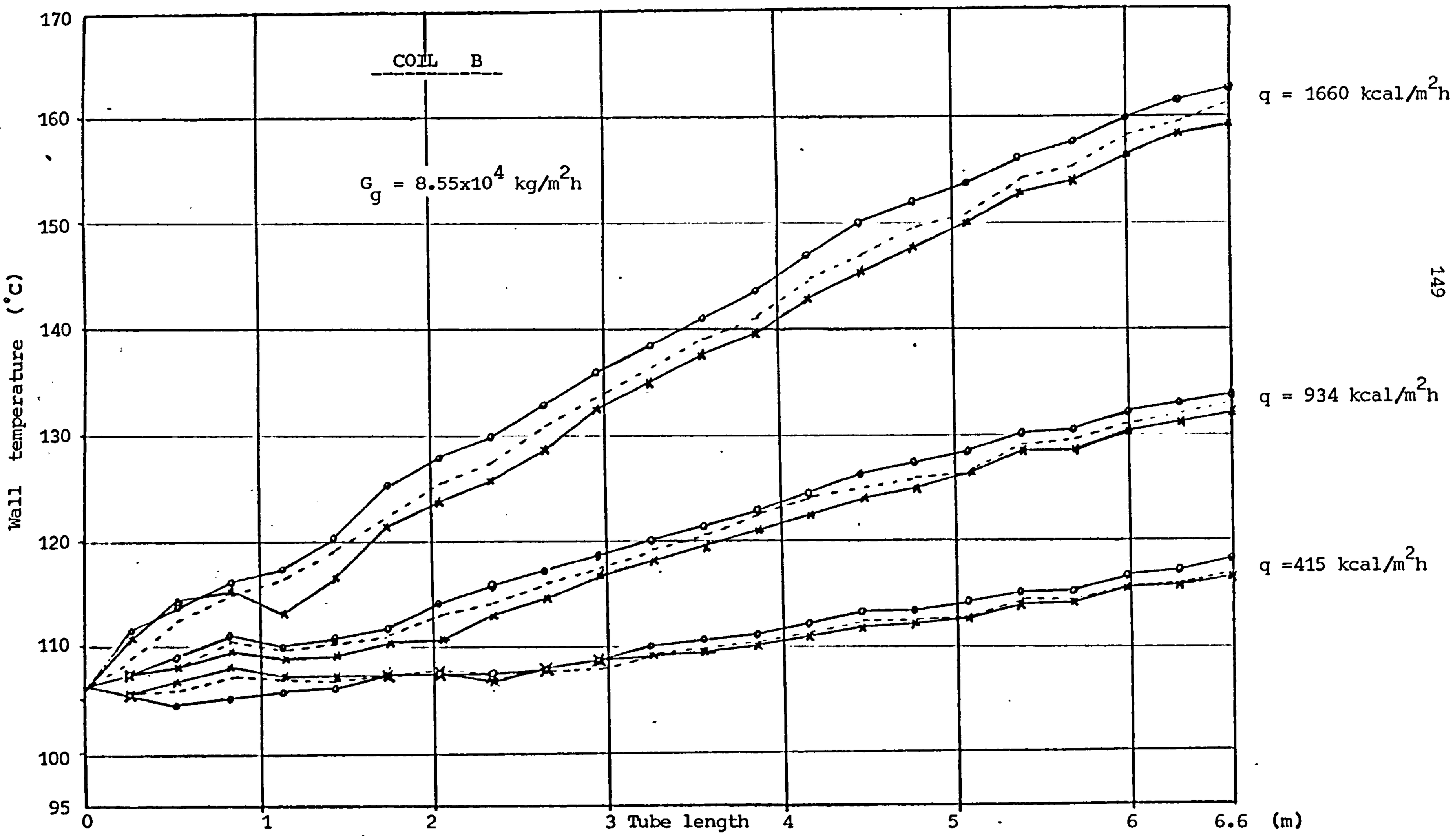


Fig. (4.2.13 b) : Wall temperature profiles for stea single-phase flow (Coil B).

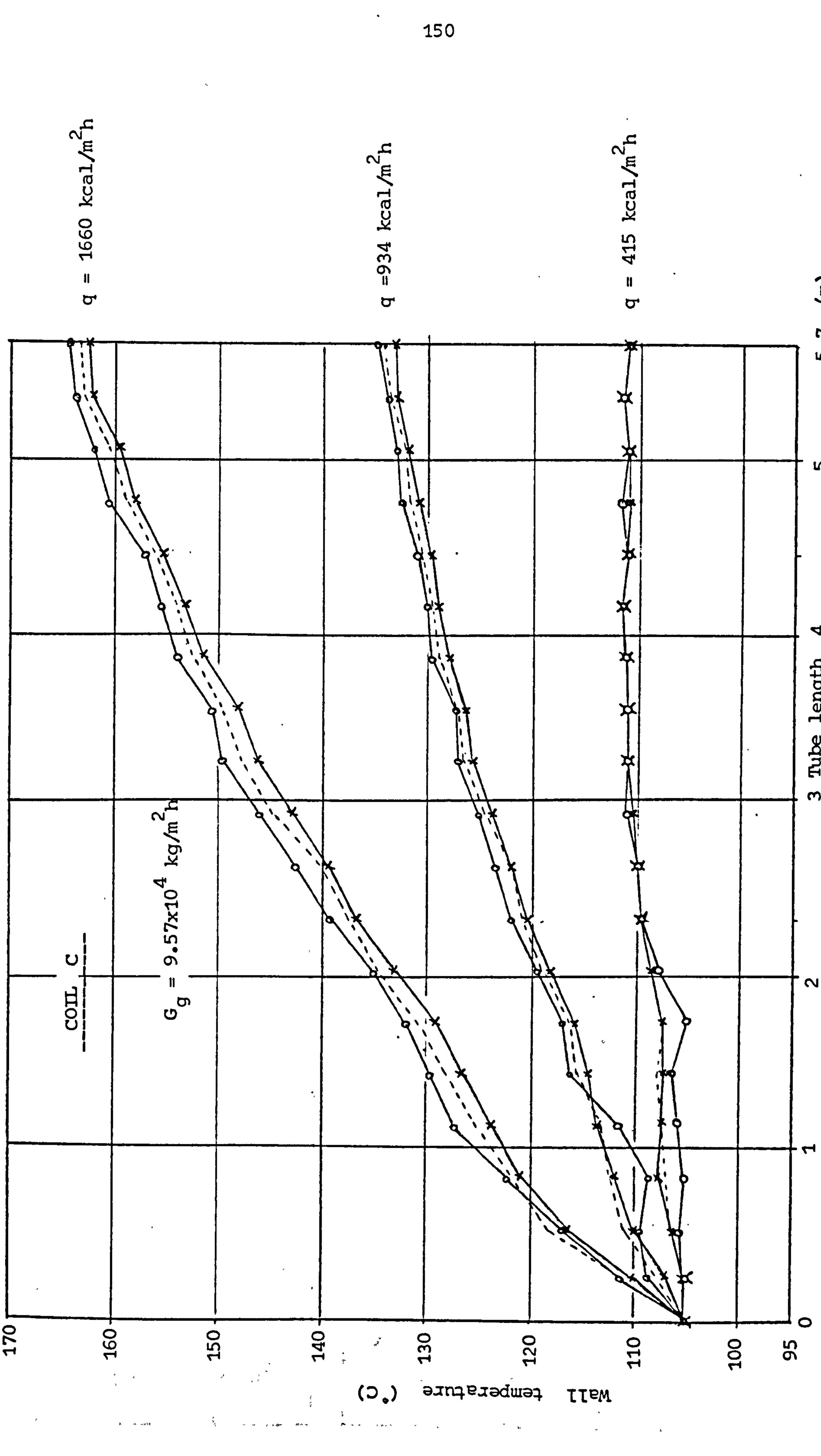
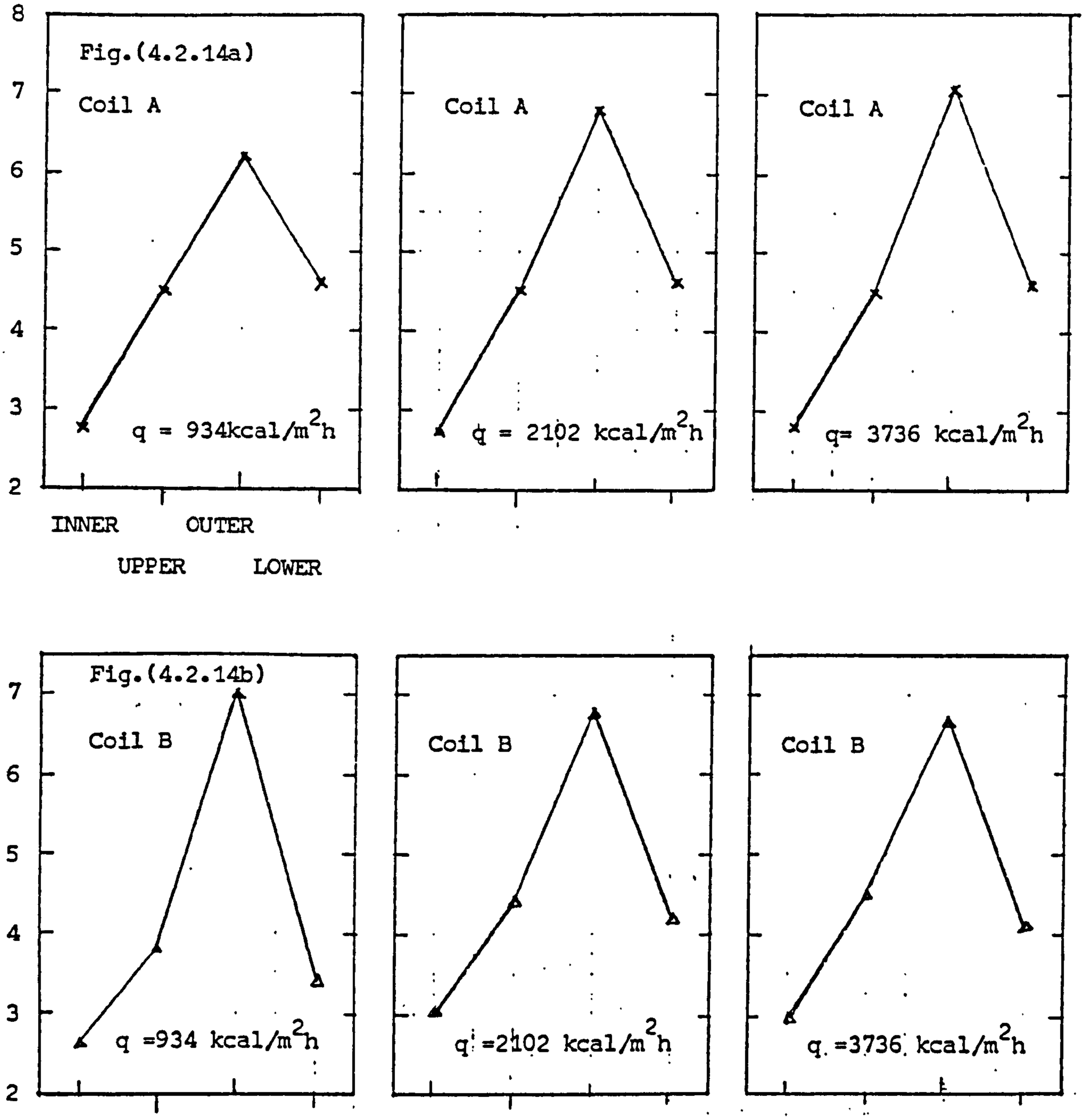
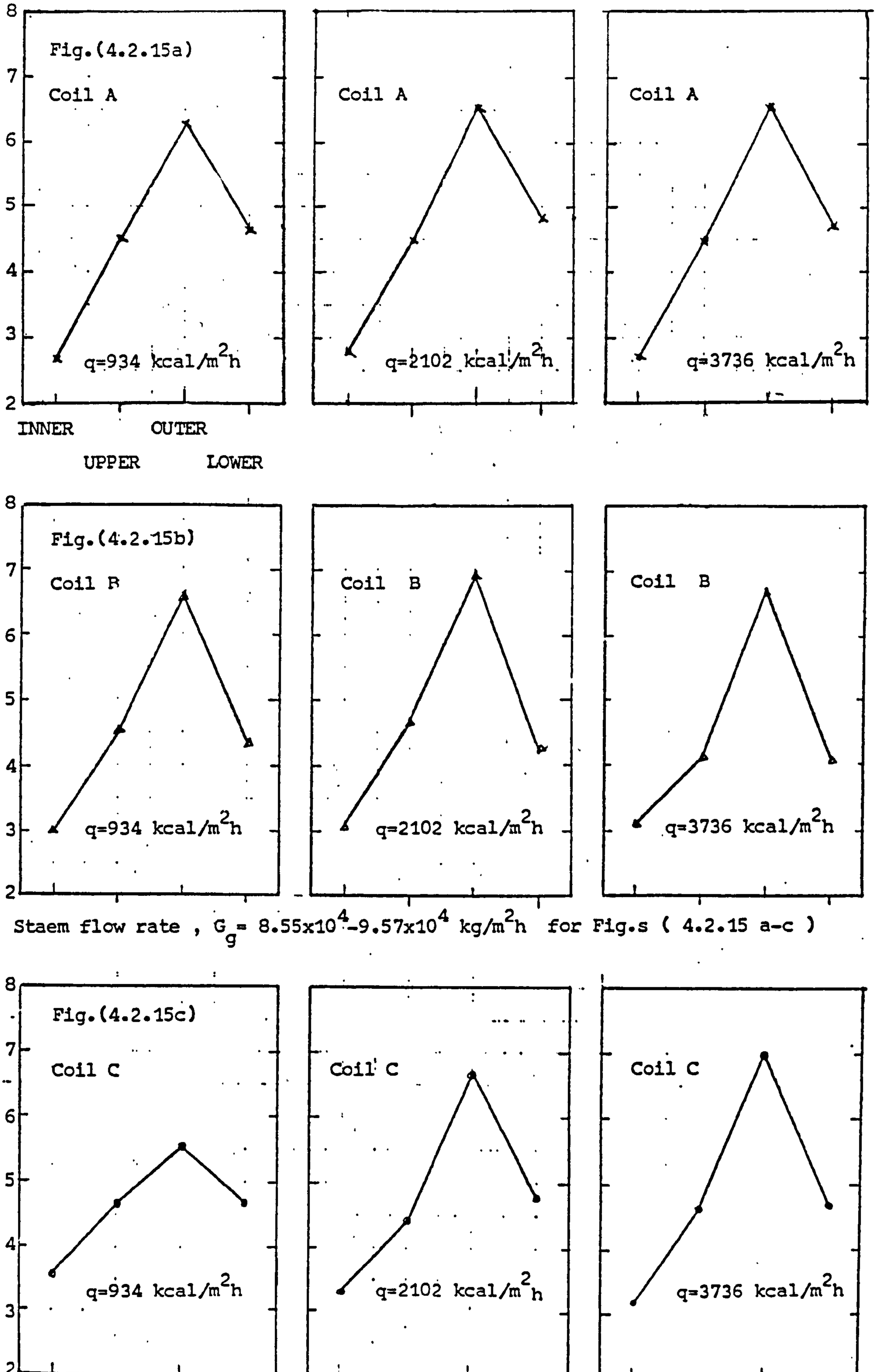


Fig. (4.2.13 c) : Wall temperature profiles for steam single-phase flow (Coil C).


Fig.(4.2.14a)
Coil A
q = 934kcal/m2h
Coil A
q = 2102 kcal/m2h
Coil A
q= 3736 kcal/m2h
INNER
OUTER
UPPER
LOWER
Fig.(4.2.14b)
Coil B
q =934 kcal/m2h
Coil B
q =2102 kcal/m2h
Coil B
q =3736 kcal/m2h
Heat transfer coefficient , (x10^2 kcal/m2hc)
Steam flow rate,Gg= 1.64x10^5- 1.84x10^5 kg/m2h for Fig.s (4.2.14 a-c)
Fig.(4.2.14c)
Coil C
q = 934 kcal/m2h
Coil C
q = 2102 kcal/m2h
Coil C
q = 3736 kcal/m2h



Staem flow rate , G_g= $8.55x10^4$-$9.57x10^4$ kg/m^2h for Fig.s (4.2.15 a-c)

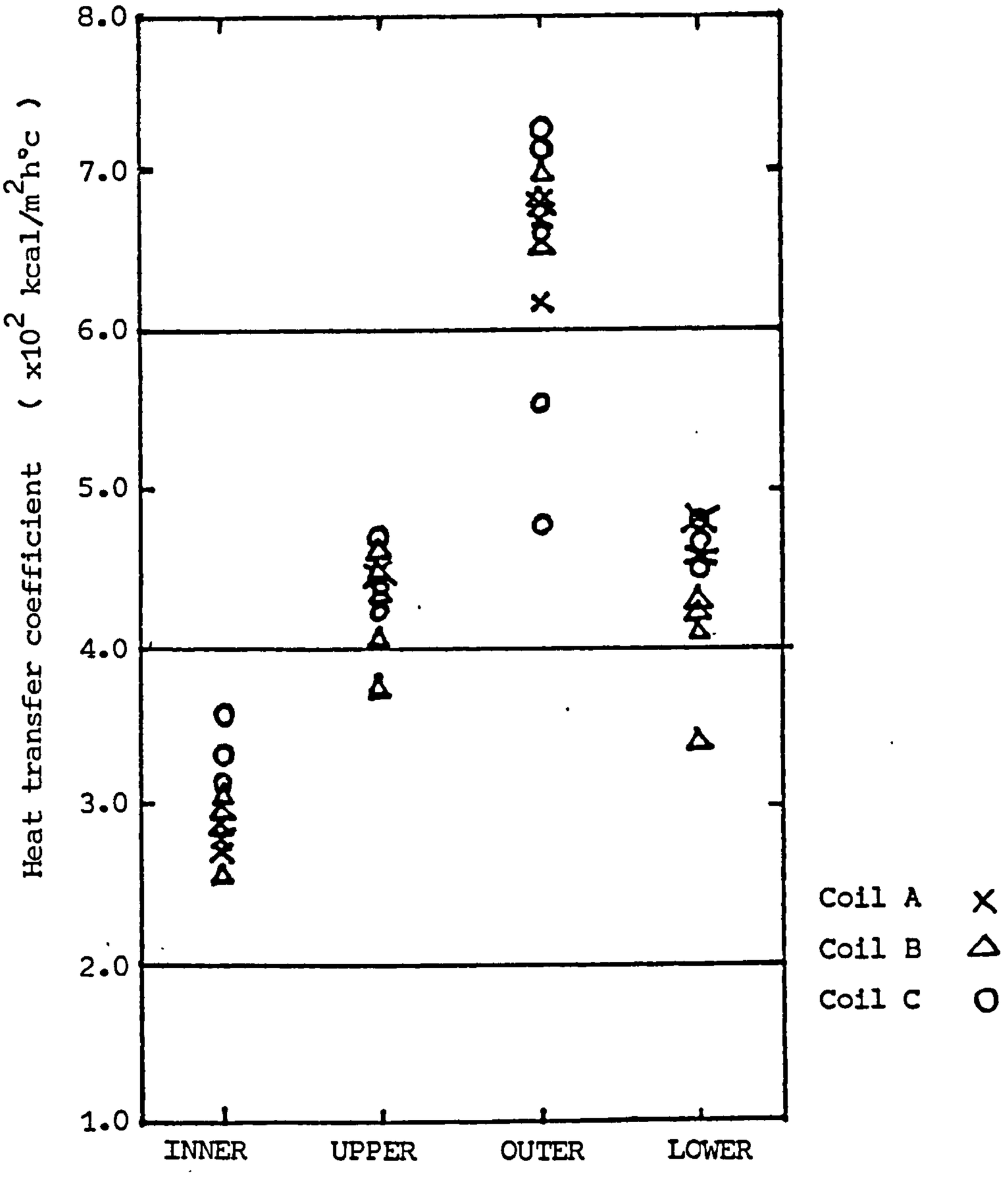


Fig. (4.2.16) : Local heat transfer coefficients in cross-section of steam single-phase flow, values are obtained from Fig.s (4.2.14) and (4.2.15).

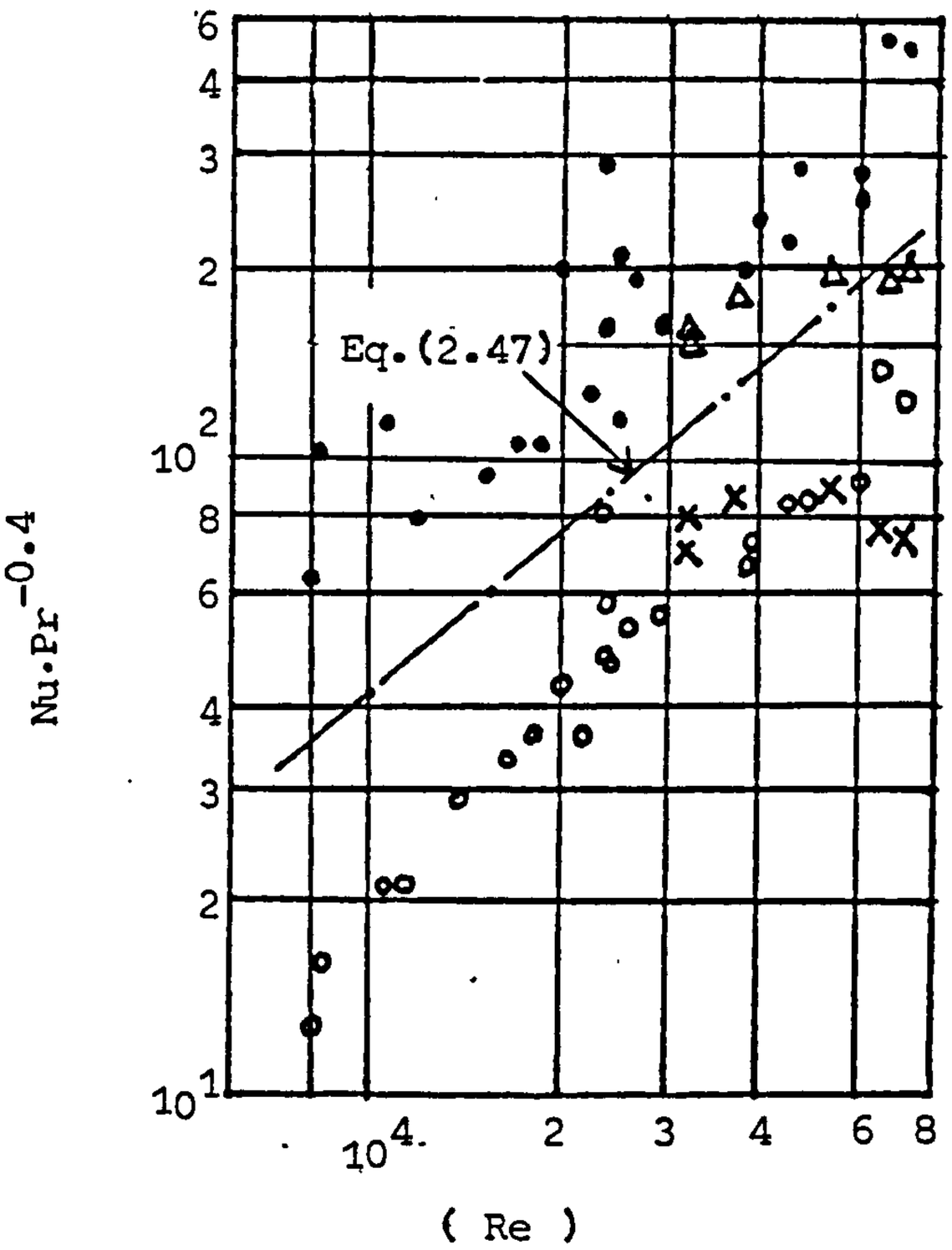
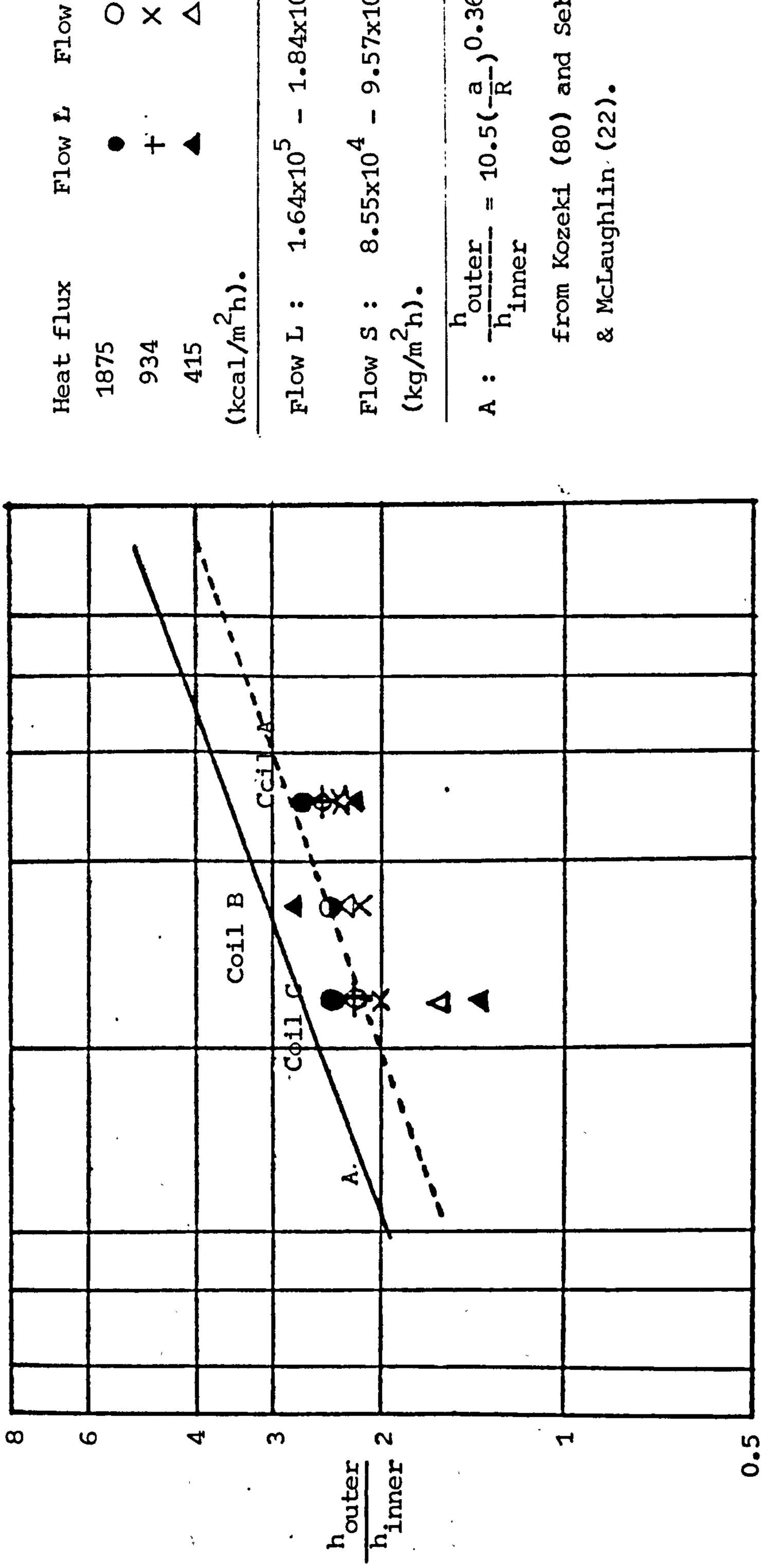


Fig. (4.2.17) : Comparison of heat transfer coefficients of the present work with the results of Seban & McLaughlin (22).



Flow L	Flow S
●	○
+	×
◀	△

Heat flux (kcal/m²h).	Flow L : 1.64x10⁵ − 1.84x10⁵	Flow S : 8.55x10⁴ − 9.57x10⁴ (kg/m²h).
1875		
934		
415		

$\frac{h_{outer}}{h_{inner}} = 10.5(\frac{a}{R})^{0.365}$

A : from Kozeki (80) and Seban & McLaughlin (22).

Fig. (4.2.18) : Ratios of heat transfer coefficient between the outer and inner sides, (for steam flow).

4.3 Results of Two-phase flow

4.3.1 Flow patterns

Flow-pattern information is usually obtained by visual observation of the flow. A review of visualization techniques is given by Hewitt and Hall Taylor (81-1970) and a review of special techniques is also given by Hewitt (82-1978).

Flow patterns in the coiled tubes of other investigators are summarised in section (2.5.2) although these were obtained without heat fluxes on the tube periphery.

Regions of annular, wavy and stratified flow in the coiled tubes are unstable and it was difficult to determine exact flow patterns along the pipe. The main reasons for this instability were entrainment and deposition of droplets, geometry of the coil and complex flow mechanism.

Up to the present the reported flow pattern maps, (e.g. Baker (50), Scott (51), Alves (52), Bennet et al (83-1965-6) and Hewitt and Roberts (84-1969)) were observed mainly without heat fluxes.

However, in the design of a practical heat exchanger coil it is vital to know the flow patterns during heating or cooling .

In the regions of annular, wavy and stratified flow wall temperature measurements can be a simple method of determining the flow patterns.

The object of this experiment is to observe the flow behaviours in these regions during heating on the tube periphery. The operation was done under the following conditions:

flow direction	upwards
water flow rate	$3.39 \times 10^4 \sim 2.57 \times 10^5$ Kg/m^2h
inlet water temperature	$64 \sim 84^oC$
steam flow rate	$6.86 \times 10^4 \sim 1.67 \times 10^5$ Kg/m^2h
inlet steam temperature	107^oC
pressure of steam-water mixture	$0.127 \sim 0.134$ MN/m^2
inlet vapour mass quality (weight)	32 ~ 83%

input heat flux

coil A 8.604 Kw/m^2 (7399 $Kcal/m^2h$)

coil B 9.245 Kw/m^2 (7951 $Kcal/m^2h$)

coil C 9.235 Kw/m^2 (7942 $Kcal/m^2h$)

The flow patterns in this experiment being with annular flow which was produced artificially at the coil entrance. At each set heat flux, steam and water rates were adjusted by two valves which are shown as 18 and 25 in Fig. (3.1) in section (3.1).

The flow patterns of annular, wavy and stratified are determined by the temperature oscillations of four measuring points (0^o, 90^o, 180^o and 270^o) and the wall temperature profiles of the tube. The data from the Coil B are analyzed as an example.

The temperature printer which was connected to the thermocouples on the tube via a digital thermometer can print at a rate of up to twice a second. Four measuring points at 4.40 m from the coil entrance were used, temperatures being taken at 10 second intervals by the printer at different steam and water flow rates (inlet steam pressure was the same). These measured temperatures are plotted in Figs. (4.3.1a) and (4.3.1b).

The temperatures at the upper side of the tube oscillate a maximum of $\pm 10^oC$ in the Fig. (4.3.1a) and $\pm 6^oC$ in the Fig. (4.3.1b) between 6.19×10^4 Kg/m^2h and 4.08×10^4 Kg/m^2h of water flow rates. The temperatures at the outer side (90^o) of the tube oscillate in a smaller range than at the upper side. At low water flow rate ($W_f < 4.83 \times 10^4$ Kg/m^2h) the temperature fluctuations at the outer side exceed those at the upper side, whereas the lower and inner sides do not oscillate appreciably and remain constant. The average values of the outer and upper sides are also significantly higher.

From these temprature oscillations, flow patterns in the tube are thought to fall into three regimes; annular, wavy and wavy stratified.

The points in Fig. (4.3.1a) show the characteristics of annular flow for water flow rates in the range above 6.87×10^4 Kg/m^2h. Between 6.87×10^4 Kg/m^2h and 4.08×10^4 Kg/m^2h the points show characteristics expected of wavy flow pattern.

At water flow rates less than 4.08×10^4 Kg/m^2h characteristics of wavy-stratified flow are exhibited. Fig. (4.3.1b) shows similar flow regimes for a substantially lower steam flow rate.

Temperatures along the whole length of the coil at the same steam conditions as Fig. (4.3.1a) are plotted in Fig. (4.3.2). All the temperatures of the tube periphery show almost the same values at the 6.87×10^4 Kg/m^2h of water flow rate.

At a distance of 2.60 m from the coil entrance, the four temperatures (0^o, 90^o, 180^o and 270^o) show similar behaviour with nearly constant values. This is found only for water flow rates of 5.52×10^4 Kg/m^2h and above. The results are indicative of an annular flow pattern existing. The flow pattern between 1.10 m and 2.60 m of the coil length is thought to be annular-wavy flow.

The temperature differences between the upper half and the lower half of the tube significantly increase at a smaller water flow rate than 4.87×10^4 Kg/m^2h. The results for these conditions are characteristics of a stratified flow pattern.

The flow pattern up to 2.60 m from the coil entrance with water flow rates between 4.87×10^4 and 5.23×10^4 Kg/m^2h are considered to be annular-wavy flows but after 2.0 m the flow patterns become totally annular flows.

The results from Fig. (4.3.2) are marked as ⊗ in Figs. (4.3.3b) and (4.3.4b).

The data of flow patterns for Coils A, B and C are plotted in Figs. (4.3.3a) to (4.3.3d) using the co-ordinates $(\frac{G_g}{\lambda})$ and $(\frac{G_{f\lambda\psi}}{G_g})$ recommended by Baker (50) for the characterisation of flow patterns in a straight horizontal pipe. (G_g is gas mass flow rate, G_f is liquid mass flow rates). The factors λ and Ψ are defined as eq's (2.71) and (2.72). All values used in the calculation of these parameters are mean values between inlet and outlet conditions of the coils.

In the present work, the attention was mainly focussed on the annular, wavy and stratified flow patterns with heat fluxes.

From Figs. (4.3.3a) - (4.3.3d), new phenemena, prominent features and results of comparison with the other investigators' results were obtained. These can be listed as the following:

(a) The annular flow regions for the three coils used occupy an area very similar to the annular flow region on the original Baker map. The annular flow pattern being at a smaller steam flow rate than that for a horizontal straight tube (Baker's original region) at high water mass flow rate. It is also at a smaller steam flow rate than that of the straight tube at low water flow rate in the small coil (Coil A).

The annular flow pattern forms at very similar steam and water flow rates to Baker's annular region in the middle coil (Coil B).

The causes of these differences between the present study and Baker's original divisions are due to the balance between the magnitudes of the secondary flow force and the gravity force of the water film in the tube. The smallest coil, Coil A, generates a large magnitude of secondary flow force than that of the straight horizontal tubes and the other two coils. As a result, a thick water film tends to build up on the inner side of the tube,from which water droplets are shed from the inner to the outer sides by an entrainment process.

(b) The wavy-stratified flow exists as a strip between an annular and stratified region. It had an almost identical breadth for all three coils. This flow pattern is determined by the wall temperature profiles. In the straight tube "Surge" flow (see Coney (86-1971) or "Slug" flow (see Wallis (87-1970)) are found to occur in this region; however the intermittent temperature oscillations typical of these two flows were not observed in the present work.

(c) Studying the wavy-stratified flow regions for each of the coils, shown in Figs. (4.3.3a)- (4.3.3c) it can be seen that they are all narrow strips inclined with an inverse gradient. On comparison Coil A has the steepest slope with respect to G_g/λ and Coils B and C have successively smallest gradients. The regions for all three coils originate in the same area of high $(\frac{G_g}{\lambda})$ and low $(\frac{G_f \lambda \psi}{G_g})$ but finish at different values of $(\frac{G_g}{\lambda})$, Coil A being lowest and C highest.

(d) At high mass flow rates where the wavy-stratified flow regions for the three coils overlap, indicating that the centrifugal force mainly affects the gas phase. Also at lower gas mass flow rate and higher water mass flow rate the magnitude of secondary flow force exceeded the gravity force in Coil A and however, did not exceed it in Coil C.

(e) In all coils, a stratified flow region was found to occupy the wavy flow region described by, originally, Baker and later by Banerjee et al (39). Results showing the same divisions of the Baker map as in the present study, have been reported by two investigators, Boyce et al (42) and Kozeki (80). According to the usual terminology of flow patterns the upper side of the straight horizontal tube in the stratified flow is dry. However, the wall temperatures at both the upper and outer sides in the present work remain constant throughout the tube at a temperature and distinctly higher than the bulk temperature (see Fig. (4.3.2)).

This means that a very thin water film or wet vapour layer may flow along the upper and outer sides. The flow mechanism in this region can be explained by "Film inversion" which was first mentioned by Banerjee et al (55). He explained the phenomenon in terms of centrifugal effects and the difference in mean velocities for the water and gas phases which may only be significant at the mass flow rates characteristic of stratified flow.

In Figs. (4.3.3a) to (4.3.3d) it is observed that although the flow regions occur in similar parts of the map relative to each other as those described by Baker, the positions of the transition-boundaries observed in the present study do not agree with Baker's.

Boyce et al (42) reported a wavy-stratified flow region covering the wavy region on Baker's map, Fig. (2-21a) using steam-water mixture at 18.62 $^{MN}/_{m^2}$ (2700 psia).

The flow pattern of Kozeki (80) using two coils ($\frac{R}{a}$ = 21.0, 33.6) with air-water mixture at atmosphere is very close to that of the present work.

Whalley and Williams (88) using a coil ($\frac{R}{a}$ = 49.5) with air-water mixture at 1.69 bars mentioned a very similar flow pattern, shown in Fig. (4.3.3d) to the present work. The common factors of Kozeki, Whalley and Williams and the present work are a similar diameter ratio ($20 < \frac{R}{a} < 49.5$), a similar pressure condition ($0.127 < P_{mixture} < 0.233^{MN}/_{m^2}$) and similar Prandtl numbers ($2.0 \simeq Pr_f = 4.0$, $0.7 < Pr_g < 1.06$).

The data of flow patterns for Coils A, B and C are plotted in Figs. (4.3.4a) to (4.3.4d) using the co-ordinates of total mass flow rate and steam quality. The axes are recommended by Goldmann et al (85) for the characterisation of steam-water mixtures flow patterns in a straight horizontal tube. The steam qualities of this study are taken at the inlet condition.

An annular region at 14.7 psia (0.10/$^{MN}/_{m^2}$) begins to grow narrower from 75% of steam quality, compared with 50% in the present work.

The annular region of a coiled tube with a heat flux in the range from 50% to 85% of steam quality is narrower than that of the straight horizontal tube.

The conclusions from this work are that the "film inversion" phenomenon is the main factor in wavy-stratified and stratified flow formation, and the secondary flow and centrifugal forces also contribute to produce an annular flow region wider than that of the straight horizontal tube. These factors are very important in understanding film profile and burnout phenomena discussed in section (4.3.5).

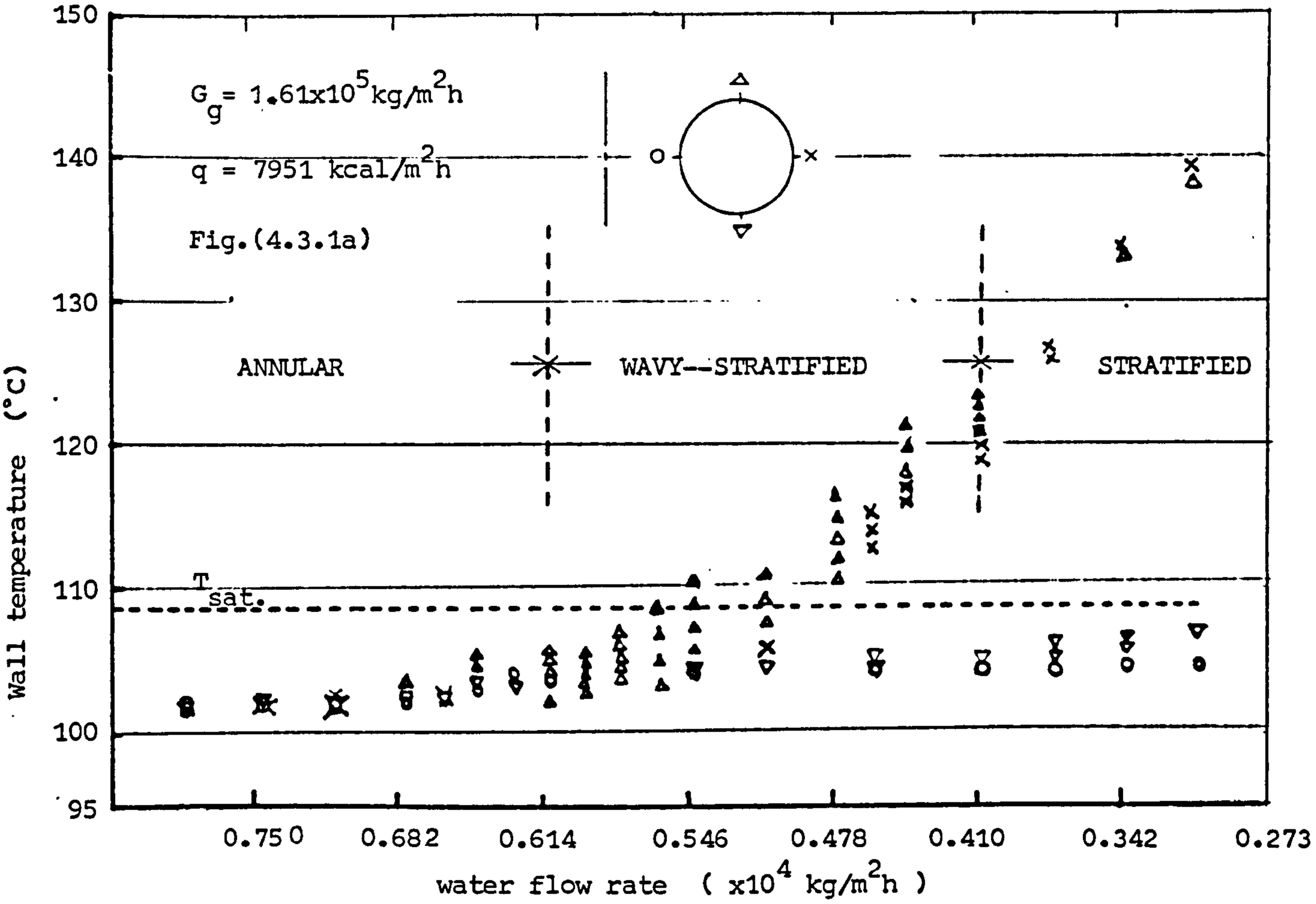
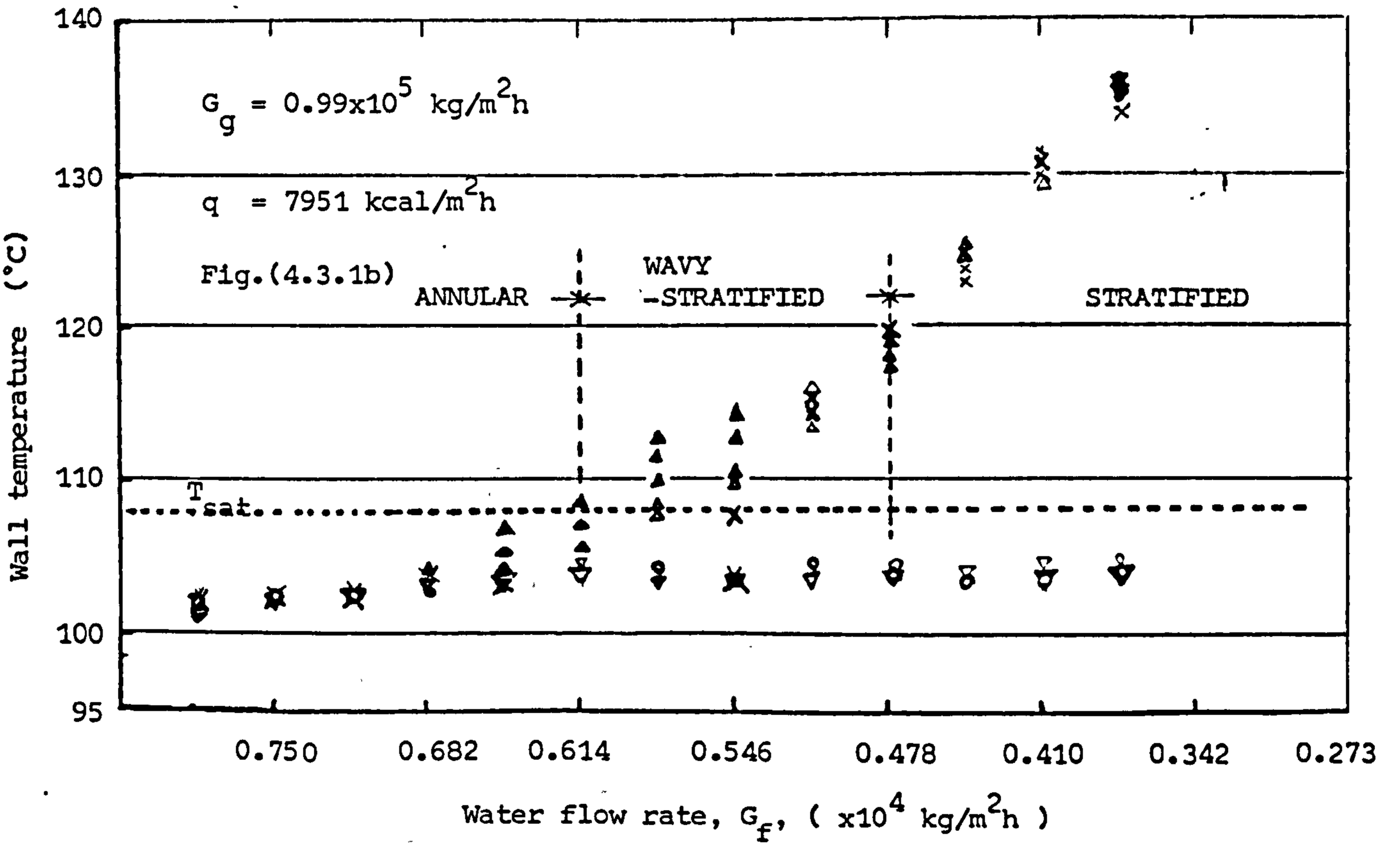


Fig.(4.3.1 a-b) : Wall temperature profiles at various water flow rates.



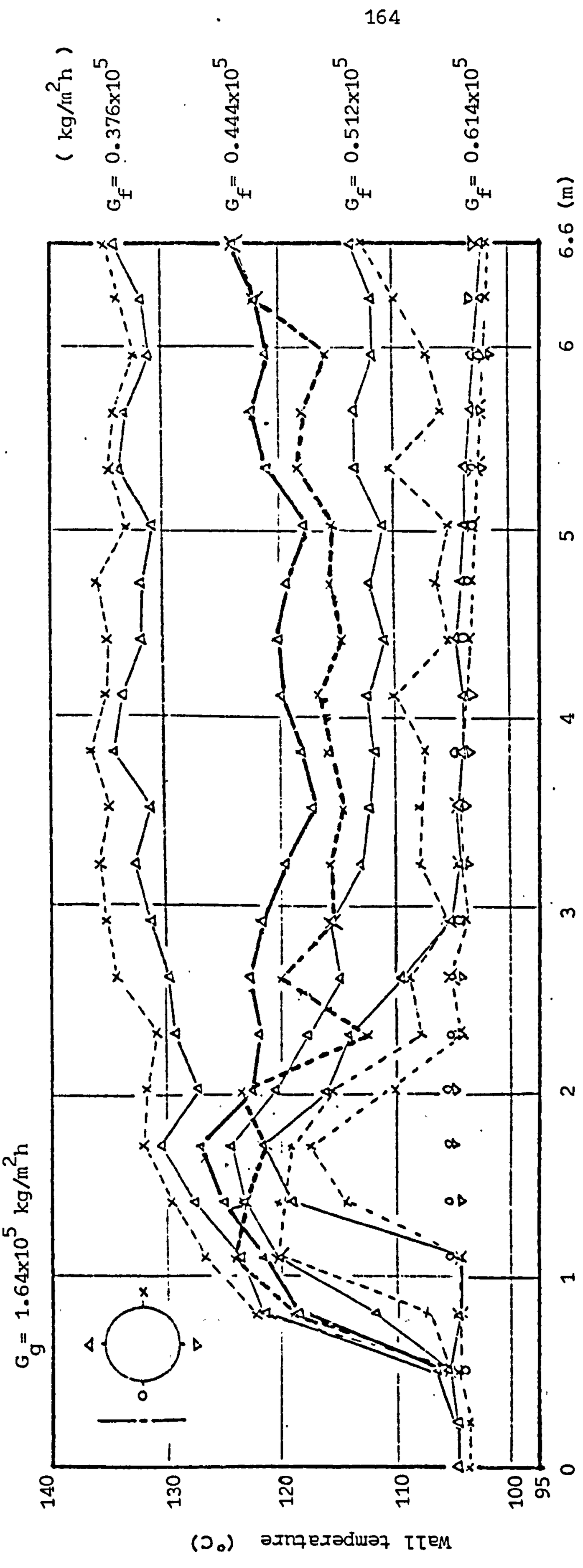


Fig. (4.3.2) : A model of wall temperature profiles to determine the flow pattern ,(for Coil B).

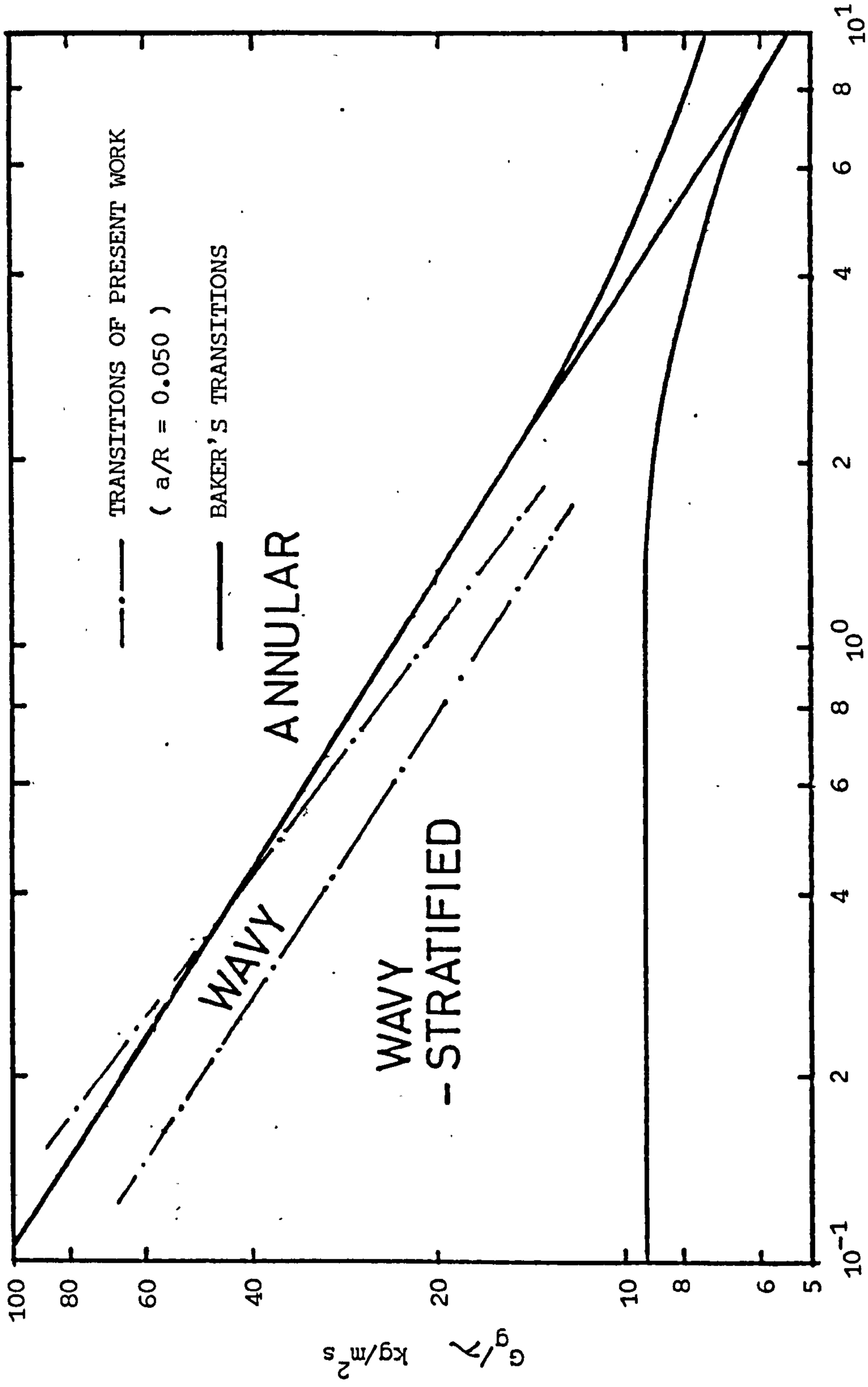


Fig. (4.3.3 a) : Flow patterns of the present experimental work in Coil A,
(steam-water mixture at 1.32 kg/cm^2.g).

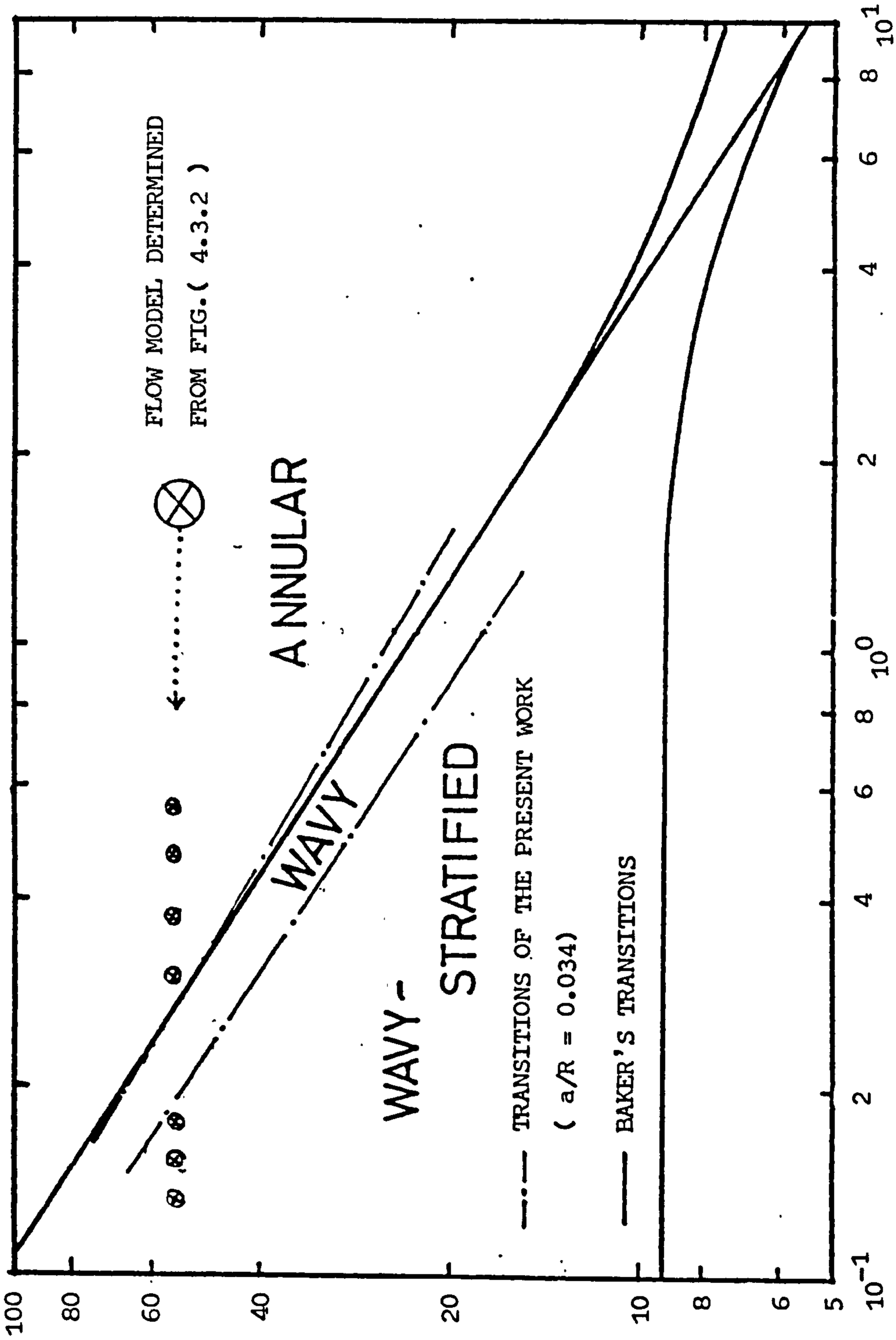


Fig. (4.3.3 b) : Flow patterns of the present experimental work in Coil B,
(steam-water mixtuer at 1.32 kg/cm^2.g).

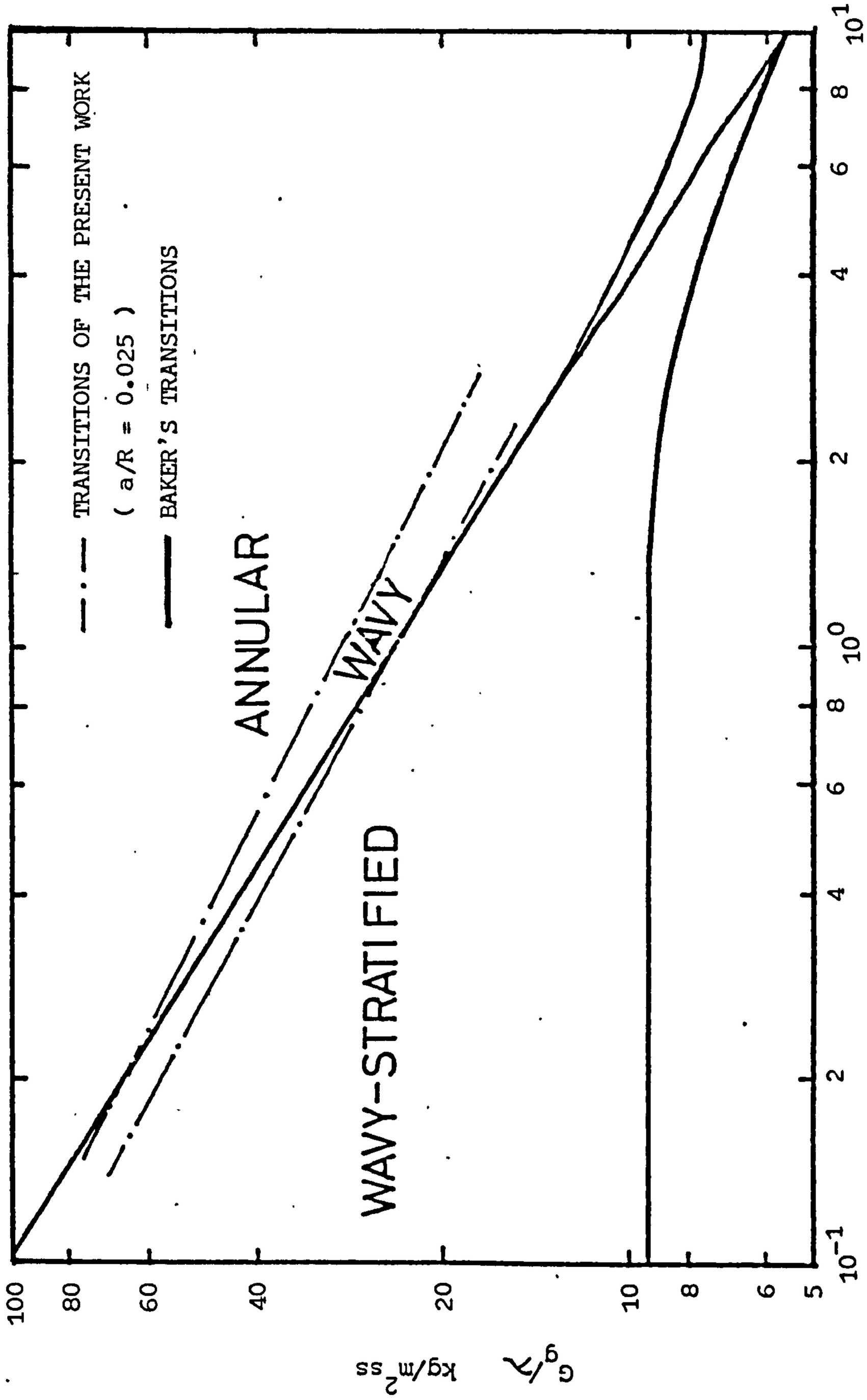


Fig. (4.3.3 c) : Flow patterns of the present experimental work in Coil C , (steam-water mixture at 1.32 kg/cm^2.g).

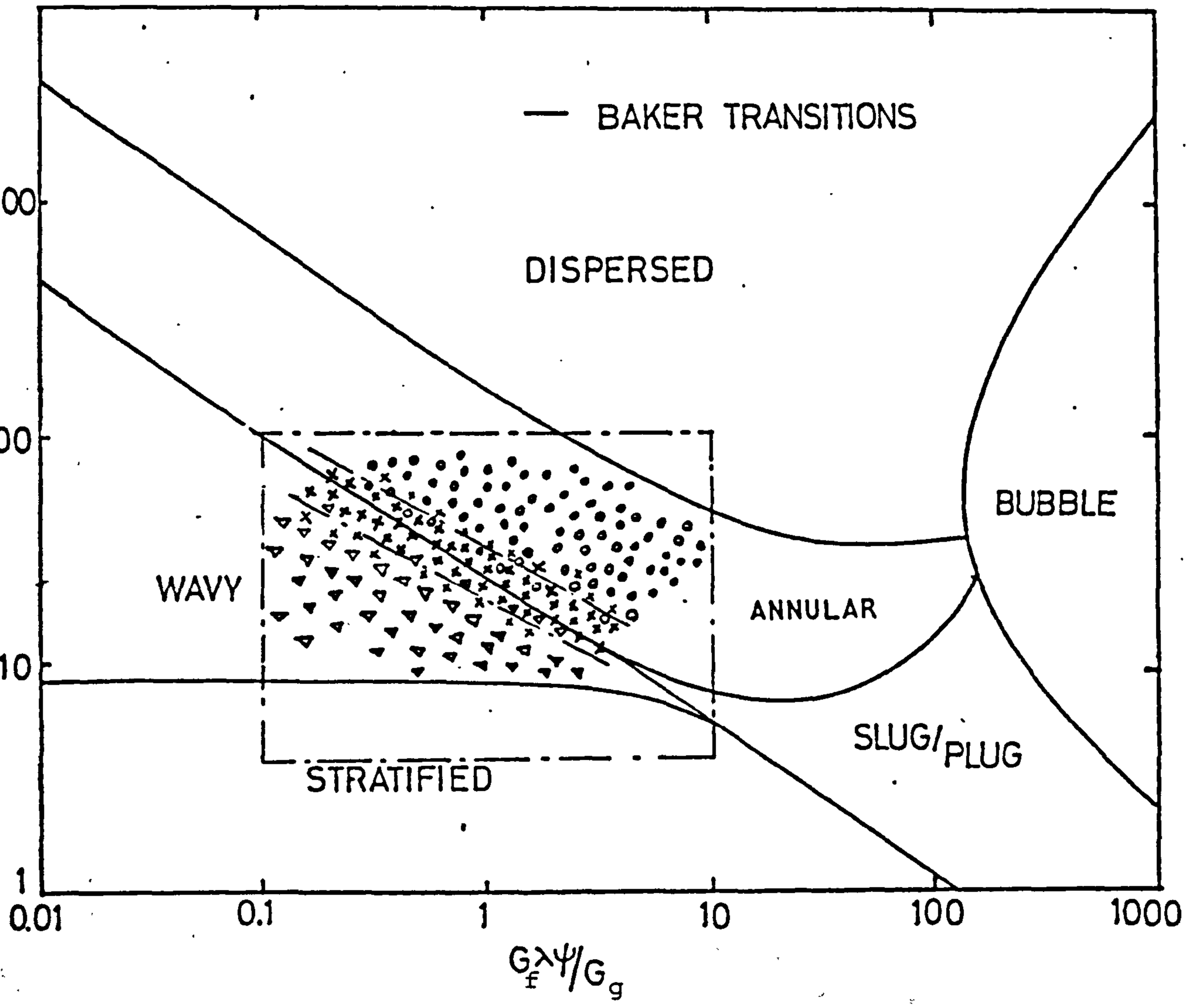


Fig. (4.3.3 d) : Flow patterns of the present experimental work in the three coils.

o - ANNULAR, x - WAVY, △- WAVY-STRATIFIED or STRATIFIED

—·—·— The range of the present experiment.

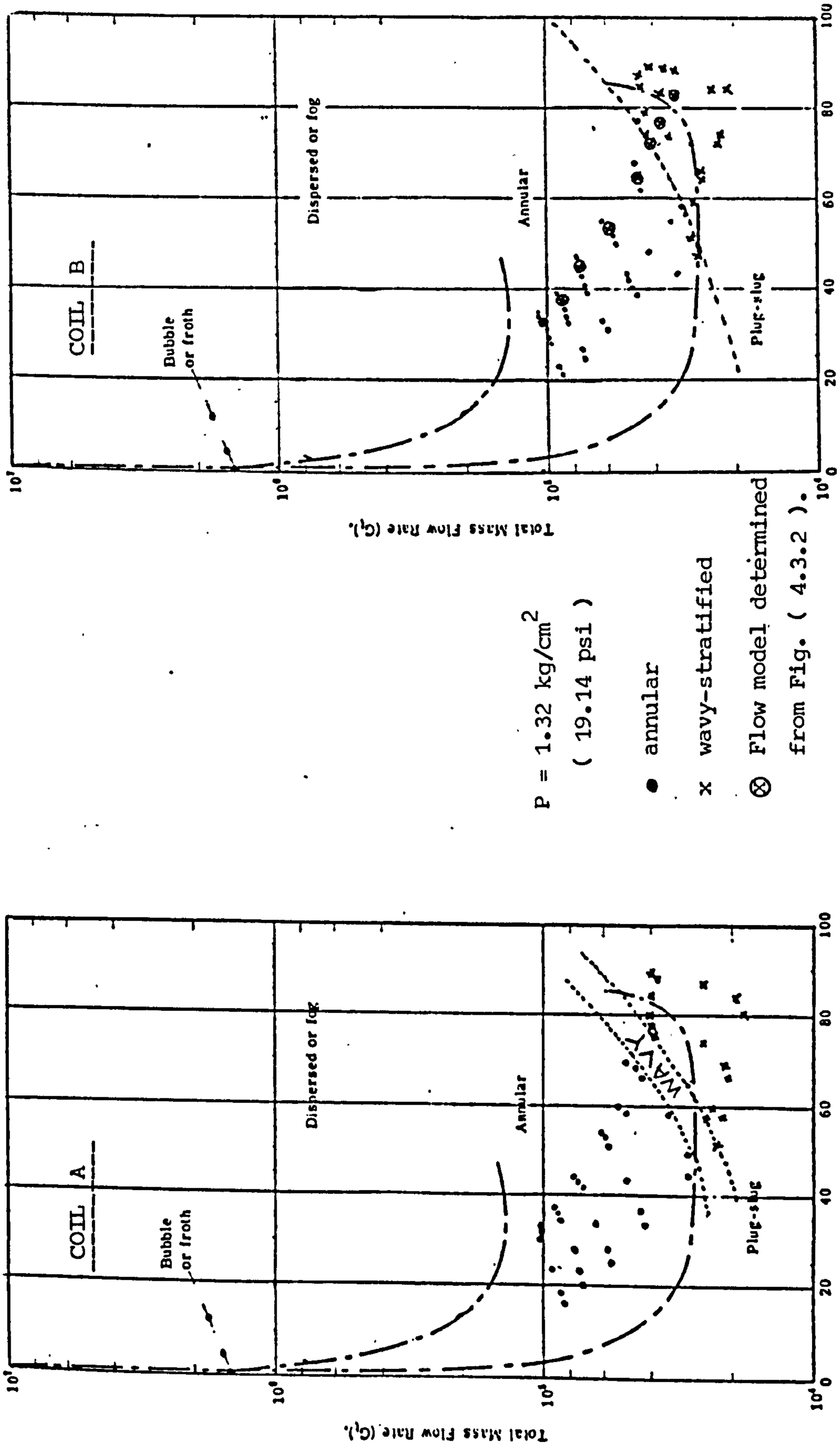


Fig. (4.3.4 b) : Flow patterns of the present work on Goldmann's map (85). The same experimental conditions as in Fig. (4.3.3 b).

Fig. (4.3.4 a) : Flow patterns of the present work on Goldmann's map (85). The same experimental condition as in Fig. (4.3.3 a).

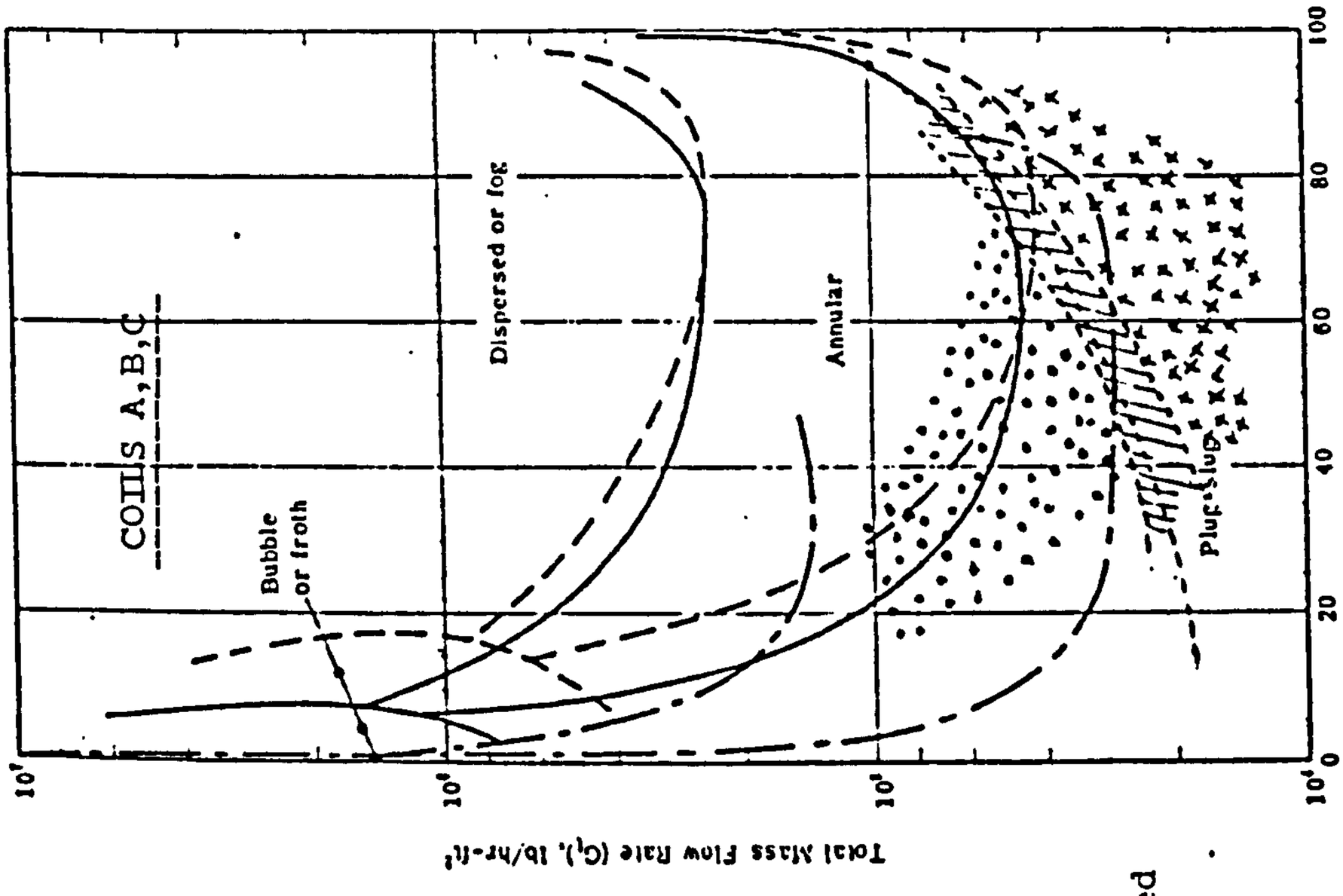


Fig. (4.3.4 d) : Flow patterns of the present experimental work in the three coils.

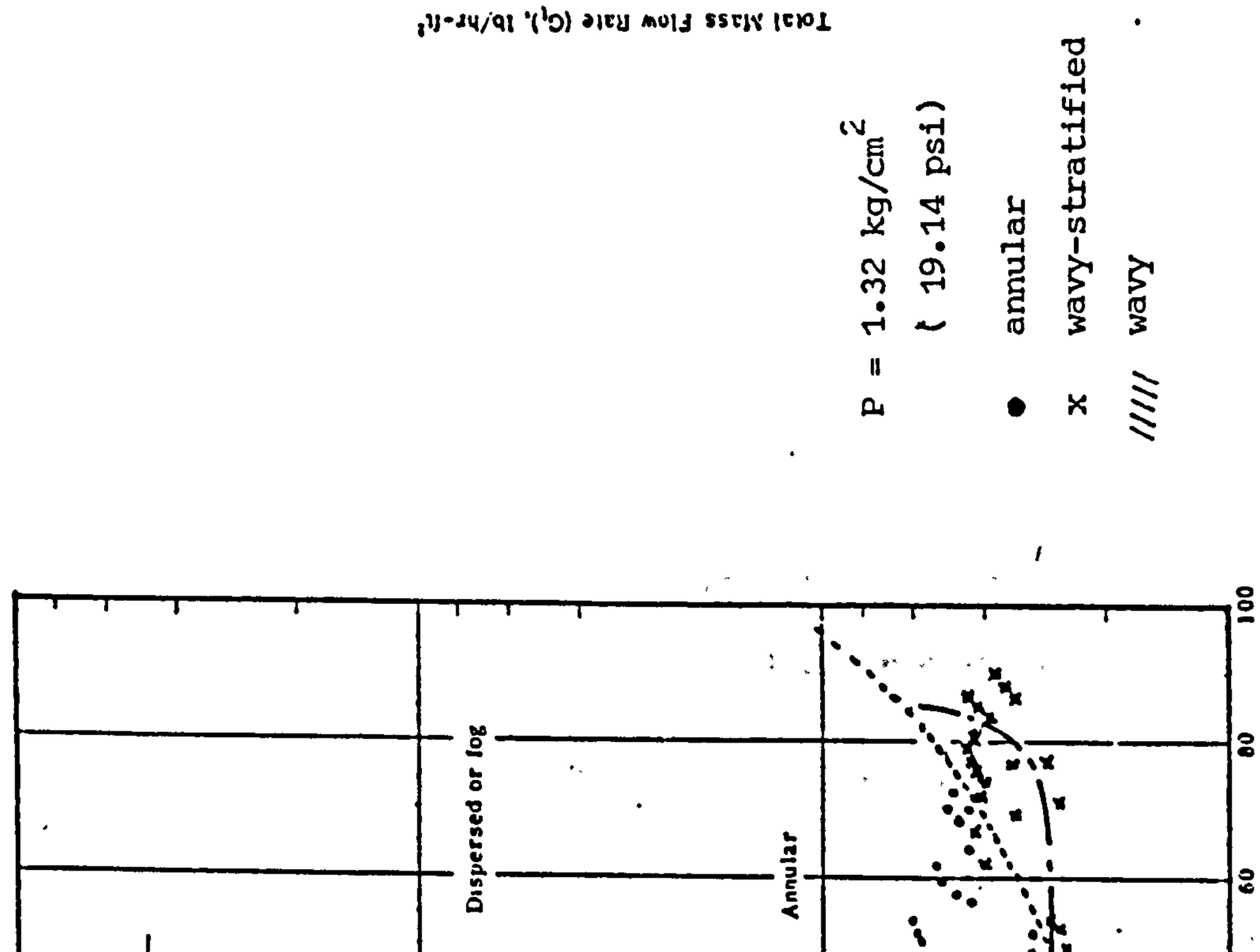


Fig. (4.3.4 c) : Flow patterns of the present experimental work on Goldmann's map (85). the same experimental conditions as in Fig.(4.3.3 c).

4.3.2 Pressure drop in Two-phase flow

The operating conditions at which the pressure drops were measured are the same as the section (4.3.1).

The static head pressure drop is ignored. For obtaining the frictional pressure drop, the acceleration pressure drop which is assumed as a homogenous flow is subtracted from measured total pressure drop.

According to Collier's derivations (45) the total static pressure drop, as evaluated from the homogeneous model, is defined as:

$$\left(\frac{dP}{dz}\right)_{total} = \frac{\frac{f_{TP}G^2v_f}{a}\{1+x(\frac{v_{fg}}{v_f})\}+G^2v_f(\frac{v_{fg}}{v_f})\frac{dx}{dz}+\frac{g\cdot\sin\theta}{v_f\{1+x(\frac{v_{fg}}{v_g})\}}}{1+G^2x\,(\frac{dv_g}{dP})} \qquad (4.3.1)$$

where f_{TP} is the friction factor for two-phase flow, v is the specific volume, G is the total mass flow and θ is the angle between pipe axis and the horizontal . In order to be of use in the evaluation of pressure drop, eq. (4.3.1) must be integrated with the axial length. This can be integrated analytically in some cases, provided a number of simplifying assumptions are made, for example, as follows:

(i) That $|G^2x\,(\frac{dv_{fg}}{dP})| << 1$, i.e., the compressibility of the gaseous phase may be neglected.

This approximation is valid in many cases:

(ii) That the term $(\frac{v_{fg}}{v_f})$ and the friction factor f_{TP} remain constant over the length considered. Eq. (4.3.2.1) becomes

$$-\left(\frac{dP}{dz}\right)_{total} = \frac{f_{TP}\,LG^2v_f}{a}\{1+\frac{x}{2}(\frac{v_{fg}}{v_f})\}+G^2v_f\,(\frac{v_{fg}}{v_f})x+\frac{g\cdot L\cdot Sin\theta}{v_{fg}\cdot x}\ln\{1+x(\frac{v_{fg}}{v_f})\} \qquad (4.3.2)$$

where x is mass quality.

The acceleration pressure drop is defined from eq. (4.3.2) as follows:

$$-\left(\frac{dP}{dz}A\right)_g = G^2 V_{fg} x \qquad (4.3.4)$$

The frictional pressure drop is obtained by:

$$-\left(\frac{dP}{dz}F\right)_{TPC} = -\left(\frac{dP}{dz}\right)_{measured} - \left(\frac{dP}{dz}A\right) \qquad (4.3.5)$$

All data are analysed using the Lockhart-Martinelli correlation parameter, X, and the two-phase frictional multiplier ϕ_g. The latter is the ratio of two-phase frictional pressure drop to that which would exist if the gas phase were to be flowing alone in the tube.

$$\phi_{gc}^2 = \frac{\left(\frac{dP}{dz}\,F\right)_{TPC}}{\left(\frac{dP}{dz}\,F\right)_{gc}} \qquad (4.3.6)$$

The subscripted (gc, TPC) are gas phase and two-phase in coiled tubes.

where $$\left(\frac{dP}{dz}\,F\right)_{gc} = \frac{f_{gc} G^2 v_m}{a} \qquad (4.3.7)$$

where $v_m = (v_f + x v_{fg})$

Eq. (2.30) by Mori and Nakayama (24) is used for f_{gc} as follows:

$$f_{gc}\left(\frac{a}{R}\right)^{-\frac{1}{2}} = 0.3\left\{Re\left(\frac{a}{R}\right)^2\right\}^{-1/5}\left[1 + 0.112\left\{Re\left(\frac{a}{R}\right)^2\right\}^{-1/5}\right] \qquad (2.30)$$

The Lockhart-Martinelli parameter, X, from eq. (2.55) is defined as:

$$X^2 = \frac{\phi_{gc}^2}{\phi_{fc}^2} \qquad (4.3.8)$$

If the liquid flow rate for the present work was using the superficial liquid velocity, it would indicate there was (460<Re<1420). However, since the flow pattern during the measurement is an annular-wavy, in this region, the liquid flow area becomes narrower than the superficial liquid flow area. Therefore the actual liquid Reynolds numbers in the annular-wavy region are thought to be large enough to be turbulent values (Kozeki (80) reported the liquid Reynolds numbers above 1,000 in the coiled tube were dealt with as being turbulent).

From a Blasius-type friction factor, f relationship, the Lockhart-Martinelli parameter, X, may be evaluated in terms of the mass quality x and physical properties.

$$f = C_1 . Re^{-\frac{1}{n}} \qquad (4.3.9)$$

where n is 0.2 for turbulent flow in a smooth tube, C_1 is constant.

Eq. (4.3.9) for the liquid flowing alone in the tube yields

$$f_f = C_1 . \left\{\frac{\mu_f}{(1-x)GD}\right\}^{0.2} \qquad (4.3.10)$$

where D is the tube diameter

The frictional pressure drop for the liquid flowing alone is therefore:

$$-\left(\frac{dP}{dz}F\right)_f = \frac{4f_f}{D} \cdot \frac{(1-x)^2 G^2}{2\rho_f} = \frac{2\mu_f^{0.2} (1-x)^{1.8} G^{1.8}}{D^{1.2} \rho_f} \qquad (4.3.11)$$

Similarly, for the gas-phase flowing alone:

$$-\left(\frac{dP}{dz}F\right)_g = \frac{2.\mu_g^{0.2} \cdot x^{1.8} \cdot G^{1.8}}{D^{1.2} . \rho_g} \qquad (4.3.12)$$

Dividing eq. (4.3.11) by eq. (4.3.12) gives the same eq. (2.77)

$$X_{tt} = \left(\frac{1-x}{x}\right)^{0.9} \left(\frac{\rho_g}{\rho_f}\right)^{0.5} \left(\frac{\mu_f}{\mu_g}\right)^{0.1} \qquad (2.77)$$

where ρ is density and μ is viscosity.

The subscript tt is for turbulent flow in both phases.

The results which come through these procedures are plotted in Fig. (4.3.5) in the range of X_{tt} between 1.3×10^{-2} and 4.0×10^{-2}.

Two main features are observed in this figure:

(i) The values of ϕ_{gtt} for the smaller coils (Coil A and B) are greater than that for a straight tube and Coil C shows smaller values of ϕ_{gtt} than that for the straight tube.

(ii) The values of ϕ_{gtt} for smaller coils (Coil A and B) are almost the same as each other and are larger than that of the larger Coil C.

The first feature is affected by heat flux ($3736^{Kcal/m^2h}$) and the characteristics of the coiled tube. For example the pressure drop per unit length in the once-through steam generator shows the largest value, around 70~80%, of steam mass quality instead of 57~81% in the present work. In these steam mass quality regions for a straight tube, the flow is considered as a homogeneous flow due to the entrainment from the water film. But in the case of the coiled tube a thick water film tends to build up on the inner side of the coil by the effect of secondary flow. At the same time, entrainment occurs from the water film at the inner side to the core flow, then water droplets are shed, due to centrifugal force, and are deposited on the outer side of the tube. The deposited water flows in a thin water film along the tube, and travels around the internal surface of the tube and meets the thick film of the inner side once again. This phenomenon is observed in both annular and

annular-wavy flow.

The loss of kinetic energy due to continuous repetition of this phenomenon (droplets entrainment at the inner side → droplets travel into the core → deposition at the outer side → droplet travelling in the water film from the outer to the inner sides) is considerably larger than that for the straight tube. This cyclic phenomenon is the main factor in increasing the frictional pressure drop.

According to Wallis' (87-1970) description, the frictional pressure drop for annular flow is related to the liquid film thickness and at large gas phase velocity it becomes larger in the coiled tube compared with an equivalent straight tube.

The values of ϕ_{gtt} of Coil C are plotted below the curve for the straight tube and are all close to unity.

From Fig. (4.3.3c) in section (4.3.1), an annular flow region at middle and low gas flow rates becomes narrower in Coil C compared with Coils A and B. This means that the kinetic energy loss in Coil C is smaller than that of Coils A and B due to its smaller internal surface area with its thicker water film.

In Fig. (4.3.5) the results between 0.2 and 0.6 of X_{tt} are plotted assuming turbulent gas phase-laminar liquid phase flow, i.e. ϕ_{gvt}. They all appear below the curve of ϕ_{gvt} therefore the liquid flow with Reynolds number above 1,000 has clearly very similar characteristics to turbulent flow from a comparison between the two results of ϕ_{gvt} and ϕ_{gvt}.

Fig. (4.3.6) is rearranged from the results of Banerjee et al (39), Owhadi et al (47) and Kozeki (80). The common feature of all three is that, for $X_{tt} < 0.2$, they agree well with Lockhart-Martinelli curve ϕ_{gtt}, but in $X_{tt} < 0.2$ they show comparatively high values compared to

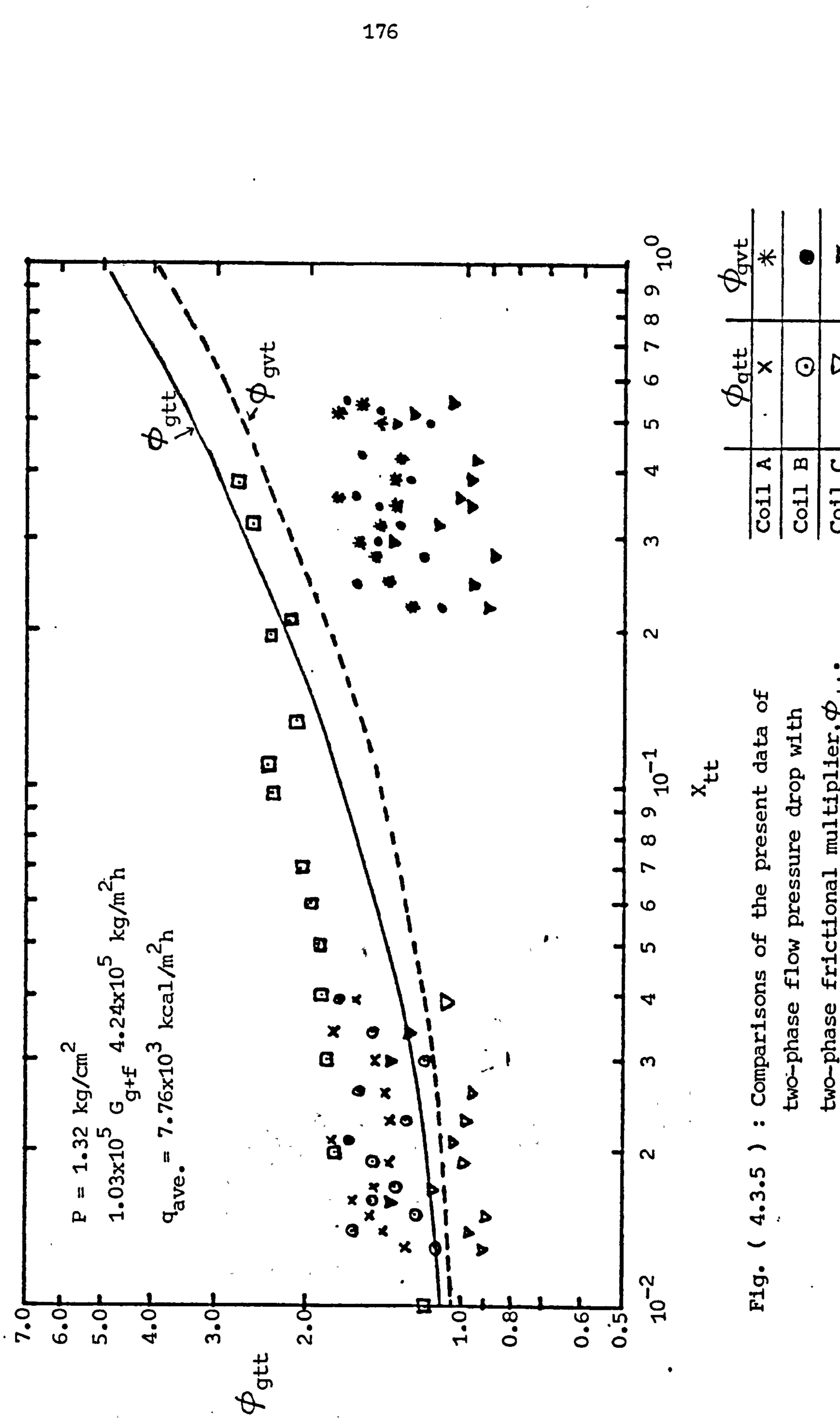


Fig. (4.3.5) : Comparisons of the present data of two-phase flow pressure drop with two-phase frictional multiplier, ϕ_{gtt}.

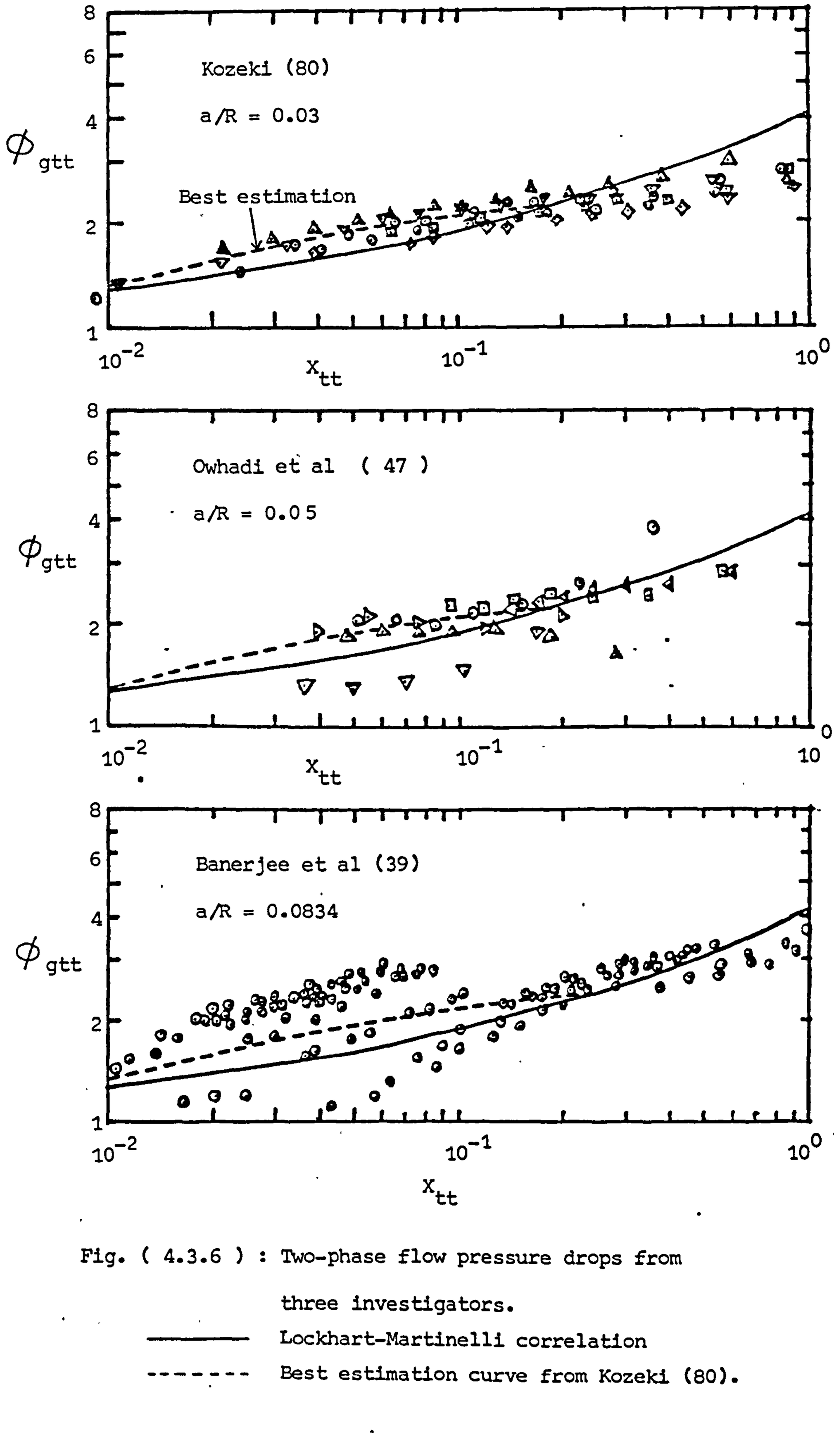


Fig. (4.3.6) : Two-phase flow pressure drops from three investigators.

———— Lockhart-Martinelli correlation

- - - - - - - Best estimation curve from Kozeki (80).

the curve for ϕ_{gtt}. Results from the present in the latter range showed good agreement with this trend.

Banerjee et al (39) and Owhadi et al (47) proposed that the Lockhart-Martinelli correlation can be employed for the whole range of X_{tt} for a coiled tube, but the results have distinctly high values when X_{tt} becomes smaller than 0.2. Kozeki (80) proposed "the best estimation" ϕ_{gtt} curve advisedly which is also shown in Fig. (4.3.6).

Some values reported by Banerjee et al (39) and Owhadi et al (47) appear below the curve of ϕ_{gtt}; these points would be explained by the presence of laminar flow in the liquid phase.

4.3.3 Wall temperature profile in Two-phase flow

The operating conditions under which the wall temperatures were measured are the same as in section (4.3.1).

Many investigations of two-phase flow characteristics of bends and horizontal and helical coiled tubes have been mentioned, but they only cover a few points in a part or small section of their tubes. Therefore these studies were insufficient for the understanding of the entire flow characteristics in those coiled tubes.

The wall temperatures in this section were measured at various steam flow and water flow rates at the constant heat fluxes (7.40×10^3 Kcal/m^2h for Coil A, 7.95×10^3 Kcal/m^2h for Coil B and 7.94×10^3 Kcal/m^2h for Coil C). The steam flow rates and water flow rates are categorized as High, Middle and Low in Table (4.3.1).

The water and steam flow rates were set and all the temperatures were measured once all conditions had become stable.

The temperature measurements were started from the most down-stream section nearest the tube exit and were taken at successive

TABLE (4.3.1) (UNIT: $^{Kg}/_{m^2 s}$)

	STEAM MASS VELOCITY	WATER MASS VELOCITY
HIGH	$37 < G_g$	$24 < G_f$
MIDDLE	$24 < G_g < 37$	$17 < G_f < 24$
LOW	$G_g < 24$	$G_f < 17$

cross-sections along the tube length towards the entrance of the test section. Then the same first four thermo-couples (0^o, 90^o, 180^o and 270^o) at the downstream section were measured again. (The thermo-couple distributions on the coils are shown in Figs. (3.4) and (3.5) in Chapter 3.)

If the temperature differences of the first four positions between the first and the second measurements were greater than $\pm 5^oC$ the results of the experiments were discarded. Most experiments showed values with smaller differences than $\pm 5^oC$ and so were accepted.

The measured results are plotted along the pipe length in Figs. (4.3.7a)-(4.3.7e) for Coil A, Figs. (4.3.8a)-(4.3.8f) for Coil B and Figs. (4.3.9a)-(4.3.9g) for Coil C. The figures are divided into two parts, in which the upper halves show the temperature profiles of the upper side (0^o) of the tube and the lower halves show the temperature profiles of the outer (90^o) lower (180^o) and inner (270^o) sides of the tube. The features of temperature profiles at the upper side are considered to be due to dryout phenomena, however in this section the evaporation phenomenon can be considered due to a form of the entrainment. (The evaporation and burnout are discussed in the section (4.5.3).

From the figures, the typical features are as follows:

(a) Wall temperatures at the upper side show always greater values than that of the other three positions at all water and steam flow rates. (In the case of single-phase flow, the inner side showed the highest value.) The wall temperatures at the outer side of the tube show similar temperature profiles to the upper side at Middle and High steam flow rate in all three coils.

(b) Temperature profiles along the length of tube for the upper and outer sides.

(b-i) In Coil A, the incipient point of temperature rise at the upper side becomes sharply high downstream towards the exit of the test section at High steam flow (shown in Fig. (4.3.7a). This incipient point moves to the middle area of the test section at Middle steam flow rates shown in Figs. (4.3.7b) and (4.3.7c) and then the incipient point occurs near the starting point of the coil (Figs. (4.3.7d) and (4.3.7e)).

The incipient point of the temperature rise at the outer side moves as that of the upper side moves at Middle and High steam flow rates (Figs. (4.3.7a)-(4.3.7c)).

(b-ii) In Coil B, the incipient points of temperature rise at the upper and outer sides show very similar features to (b-i) at High steam flow rate. In one case the incipient point occurs at 1.20m from the starting point of the coil (Fig. (4.3.8a)).

(b-iii) In Coil A, the incipient point of the upper side only occurs at the start of the main helical section at Middle and Low

steam flow and water flow rates (Figs. (4.3.9a)-(4.3.9g)).

(c) In coil A, the incipient point of temperature rise at the upper side occurs on a small scale at the starting point of the helix at a Low steam flow rate while the incipient point in the downstream section of the coil. There is also a sharp temperature rise in the downstream section of the coil, whose progressively lower water flow rates shift back towards the tube entrance, (See Figs. (4.3.7d) and (4.3.7e)).

The same type of incipient point as those described for Coil A, occur at Coils B and C at High steam flow rates. (Figs. (4.3.8b)-(4.3.8d), (4.3.9b) and (4.3.9c)).

(d) After temperatures at the upper side reach around 130^{o}C the temperatures drop sharply to the same temperatures (about 110^{o}C) as the lower and inner sides at Low steam flow and Middle water flow rates in Coil A. (Figs. (4.3.7d) and (4.3.7e). This also occurs at High steam flow and Middle water flow rates in Coil B (Figs.(4.3.8d)-(4.3.8f)), and at all steam flow and at Middle and High water flow rates in Coil C (Figs. (4.3.9c)-(4.3.9g)).

(e) The temperature profiles of the lower and inner sides of the tube are always constant and are steady at around 110^{o}C in all three coils.

The factors affecting the temperature differences in the above features are mainly due to the film thickness profiles, magnitude of interfacial shear stress, entrainment and deposition rates and amount of heat addition. In a helically-coiled tube as in a horizontal tube but unlike a vertical tube, the liquid film flow rate can vary substantially with circumferential position, therefore it was necessary to prepare two figures. Firstly Fig. (4.3.10) showing the temperature

values of four circumferential positions (0^o, 90^o, 180^o and 270^o) at 1, 2, 3, 4 and 5m from the entrance of the test section at different steam and water flow rates. Secondary Fig. (4.3.11) showing the film profiles taken by Whalley and Williams which were measured under identical conditions to the present work (i.e. the same water and gas flow rates, operation pressure and diameter ratio between the tube and coil).

Banerjee et al (55) and Lacey (58) have considered the situation shown in Fig. (2.22), Banerjee et al have referred to the situation where a stratified film flows on the inside of the tube as "film inversion", and have argued that the angle ϕ of eq. (2.74), which is equal to $(180^o-\theta)$, can be found from:

$$\tan \phi = \frac{(\rho_g U_g^2 - \rho_f U_f^2)}{g \cdot R \cdot \rho_f} \qquad (4.3.13)$$

where U_g and U_f are the actual velocities of the gas and liquid. Lacey (58) interpreted this as meaning that there is a reasonable average gas velocity near the film in this phenomenon. The following eq. (2.75) gives the conditions for film inversion to occur:

$$\frac{U_g}{U_f} \left(\frac{\rho_g}{\rho_f}\right)^{\frac{1}{2}} > 1 \qquad (2.75a)$$

or

$$\rho_g U_g > \rho_f U_f \qquad (2.75b)$$

These values of the angle ϕ and $\left\{\frac{U_g}{U_f}\left(\frac{\rho_g}{\rho_f}\right)^{\frac{1}{2}}\right\}$ for the present work were calculated and are as follows:

$$26.2^o < \phi < 68.4^o \quad \text{for Coil A,}$$

$$29.3^{o} \lesssim \phi \lesssim 62.4^{o} \quad \text{for Coil B}$$

$$15.9^{o} \lesssim \phi \lesssim 57.9^{o} \quad \text{for Coil C}$$

and

$$39.6 \lesssim \frac{U_g}{U_f} \left(\frac{\rho_g}{\rho_f}\right)^{\frac{1}{2}} \lesssim 62.0$$

From these values and Fig. (4.3.10), it is obvious that the water film tends to travel along the inner side of the tube. This phenomenon explains the behaviour described in features (a) and (e).

These features are most distinct when the steam flow rate is High and the liquid flow rate is Low, (shown (B) in Fig. (4.3.10), (A) and (B) in Fig. (4.3.11)). However when the steam flow rate is Low and the liquid flow rate is Middle or High, the liquid tends to travel around the lower half of the tube (the temperature at the only upper side has a sharply higher value than the other cases shown in (D) in Fig. (4.3.10) and (D), (E),(F) in Fig. (4.3.11)).

The position of minimum film flow rate is thought to be between 0^{o} and 30^{o}.

The mechanisms of entrainment and deposition during heat transfer are the main elements in understanding features (b), (c) and (d).... (temperature shifts and the incipient point of temperature rise). At a constant liquid flow rate, an increase in the steam flow rate results in a reduction in the film thickness. This would be expected from mass balance principles, because the greater interfacial shear stress increases the film velocity. In addition to this, the film flow rate is reduced because more of the liquid tends to travel as droplets in the gas core. The increased interfacial shear stress also gives rise to higher liquid entrainment and mass fluxes, mainly at the inner side.

The droplets are formed by entrainment from waves on the film surface and more liquid is entrained from the film if the tube is being heated. The mechanisms of wave formation are described by Ishii and Grolmes (89-1975) and Tatterson et al (90-1977).

The entrained droplets are rapidly redeposited on the outer side under the effect of the radial velocity components of the turbulent gas core. The rate at which a particular droplet is redeposited depends on its size and on the radial velocity component for its position in the flow. If the liquid flow rate is increased at constant gas flow rate, the gas velocity profile, which is similar to that for turbulent flow in a rough pipe, becomes more peaked. This is assumed to be a result of an increase in interfacial roughness which causes the film flow rate and thickness to be reduced because a larger proportion of the liquid is entrained.

According to Whalley and Williams no more than 30% of the liquid flows as entrained drops. There are difficulties of measuring the amount of entrainment and deposition especially in the helical coiled tube. A number of empirical reports of entrainment and deposition have been presented by various investigators. Up to the present a satisfactory relationship for entrainment has proved to be elusive; meanwhile an approximation such as the one obtained by Hutchinson and Whalley (91-1973) must be used. They suggest that the entrainment rate (E) is a function as follows:

$$E = fn\left(\frac{m.\tau_i}{\sigma}, C_e\right) \qquad (4.3.14)$$

where τ_i is the interfacial shear stress, m is the film thickness, σ is the surface tension and C_e is the droplet concentration. In order to obtain values for entrainment at rate E, data was used for

annular flow at hydrodynamic equilibrium (i.e. entrainment rate, E equal to deposition rate D). Fig. (4.3.12) obtained by Hutchinson and Whalley(91) shows a plot of Ce against the group $(\frac{m.\tau_i}{\sigma})$ and correlates all the data for entrainment.

Similarly, an empirical law for deposition was proposed, in this case by Paleev and Filippovich (92-1966). Their empirical relationship was as follows:

$$G_{deposition} = \frac{0.022\ \rho_g}{Re_g^{0.25}} \cdot Ug \cdot C_d^{0.74} \qquad (4.3.15)$$

$$3 \times 10^4 < Re_g < 8.5 \times 10^4$$

where Ug is the mean gas velocity, C_d is the mass liquid constant in 1Kg gas in a flow core and $G_{deposition}$ is the mean integral flow of deposited liquid.

A simple equation for evaluating deposition rate, D, was formed as:

$$D = K_d C \qquad (4.3.16)$$

where K_d is the mass transfer coefficient for deposition and C is the droplet concentration in the gas core. Whalley et al (93-1974) proposed tentatively that K_d can be correlated with surface tension as shown in Fig. (4.3.13). According to this figure, the surface tension and K_d for a pressure of 1.5 bar show higher values than that of high pressure flows. (The pressure of the present work is around 1.3 bar). Hence the entrainment rate of the present work was thought to be held back more than the deposition rate.

A temperature rise commences firstly close to the starting point of the helix and secondly towards the end of the test section, at Middle

and Low water flow and steam flow rates as in features (c) and (d).... (Phenomena of temperature rises and drops at different positions along the pipe). The occurrence of these temperature rises and drops is due to an imbalance between gravity of the film and dragging forces. It is supposed that the circumferential variation in roughness experienced by the gas phase induces secondary flow in that phase. (See Fig. (4.3.14)). The upward gas flow near the film surface drags the liquid upwards while the liquid near the tube wall flows downwards. When both the steam flow rate and water flow rate are at Middle and Low values, the downwards gravitational force becomes predominant so that film thickness at the upper side becomes thinner. The wall temperatures at the upper side jump up rapidly and maintain a high value for a 1.2∿1.5m length from the entrance of the test section shown in Figs. (4.3.7e) of Coil A, (4.3.8e-f) of Coil B and (4.3.9e-f) of Coil C.

At the same time, the amount of entrainment increases at the upper side (due to evaporation to wet steam) and at the inner side (due to the secondary flow force). This means that values of Ce and C in eqs. (4.3.14) and (4.3.16) increase. The entrained droplets are deposited on the outer side and coalesce with the water film already there. The thicker water film that results has a greater interfacial roughness when ruffled by the passing gas flow. This dragging phenomenon results in the wall temperature at the upper side drop to the same level of the inner and lower sides for 0.6∿0.9m section after first temperature rise. (see Fig. (4.3.7e) of Coil A, Figs. (4.3.8d) - (4.3.8f) of Coil B).

The high wall temperature at the upper side in Coil C tends to continue up to the exit of the test section at Middle and Low water flow rates as shown in Figs. (4.3.9d) - (4.3.9g) of Coil C.

The sizes of the coil diameters affects considerably the magnitudes of the secondary flow and centrifugal forces especially at Low steam flow and water flow rates, but at High steam flow and Middle and High water flow rates the effect of coil diameter is less important.

Ishida (63-1977) observed the comb-type temperature fluctuation along the pipe and described it using a twin-helix flow. The phenomenon of twin-helix flow was idealized by Lacey (58) as shown in Fig. (4.3.15), but it was not observed in the present work.

The "Surge" flow observed by Coney (86) and "Disturbance waves" observed by Hall-Taylor and Nedderman (94-1968) and Hewitt (59) are thought to be the main causes of the intermittent temperature oscillation, neither of them were observed in this work.

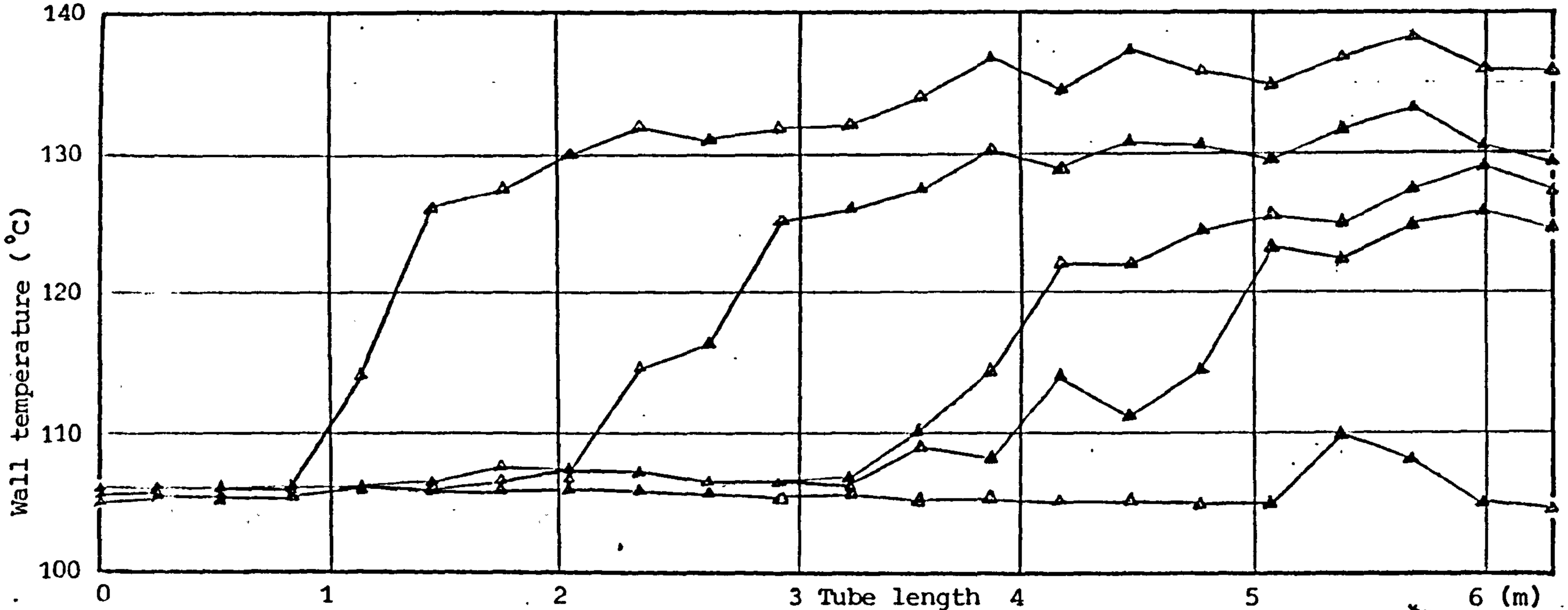
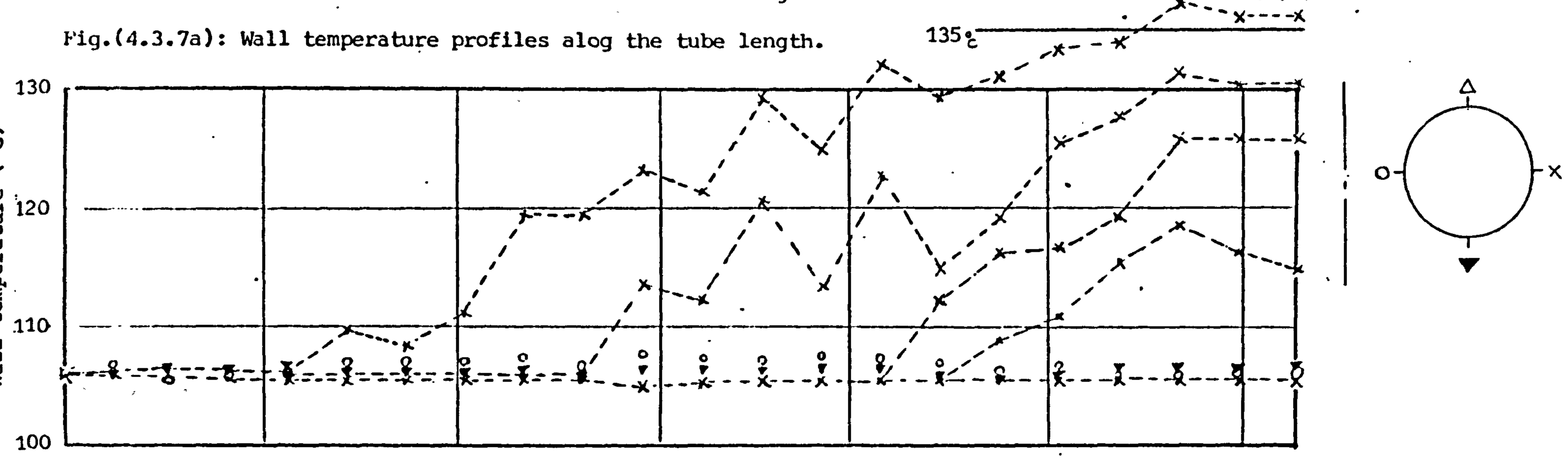


Fig.(4.3.7a): Wall temperature profiles alog the tube length.



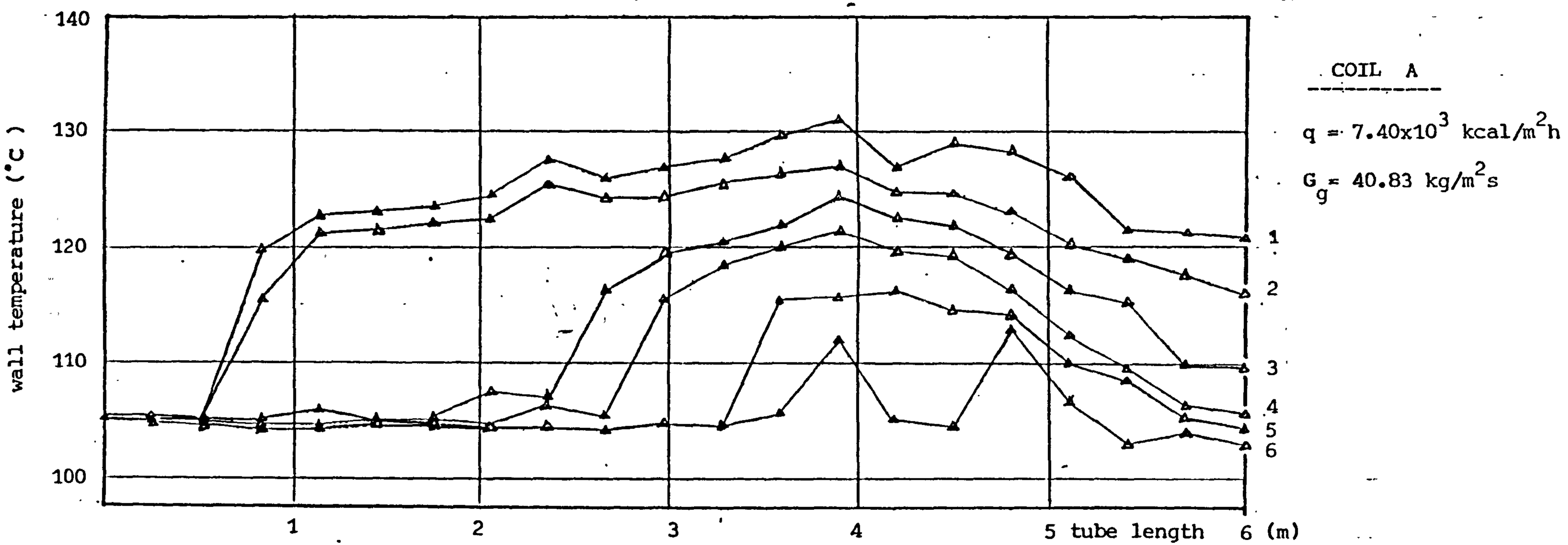
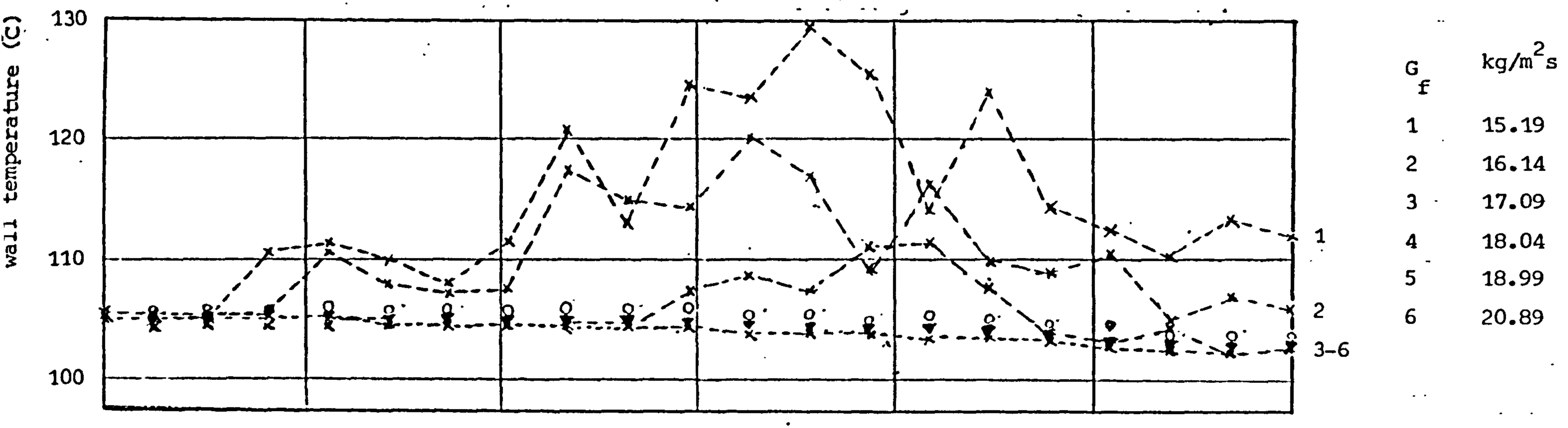


Fig.(4.3.7b): wall temperatuer profiles along the tube length.



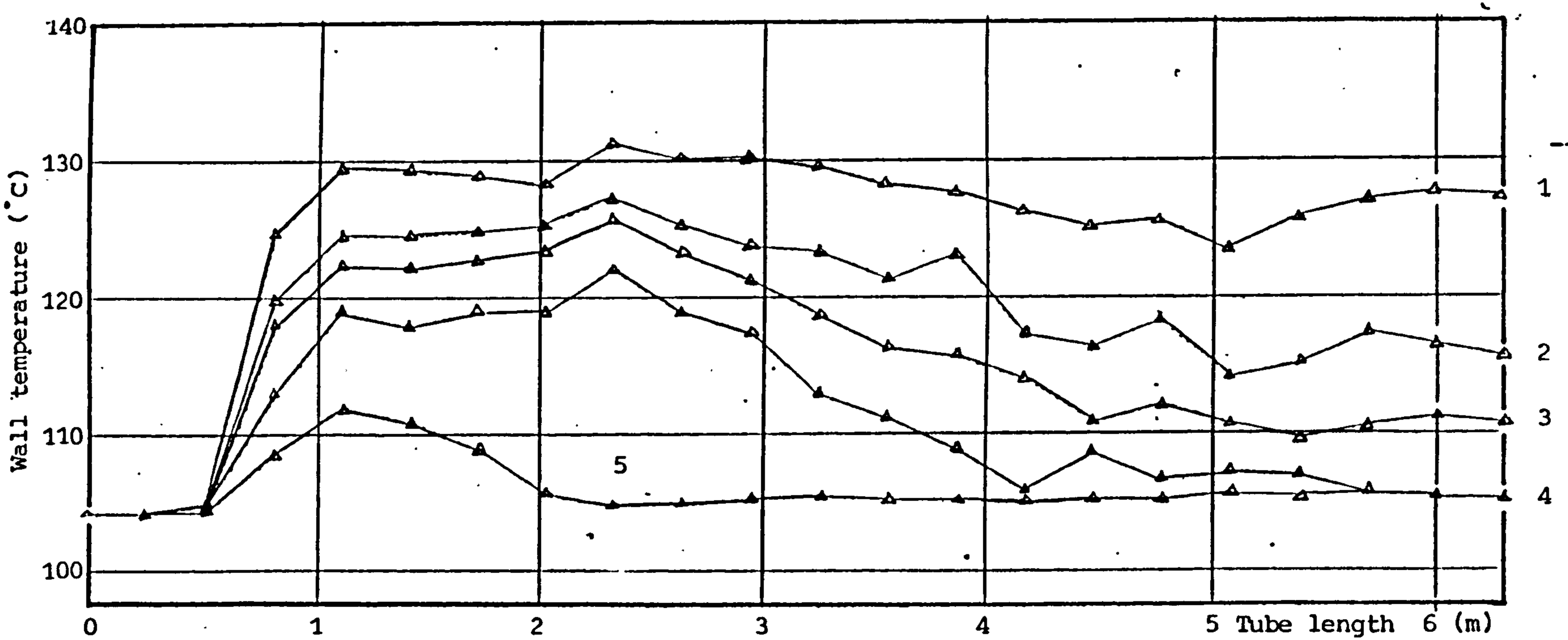
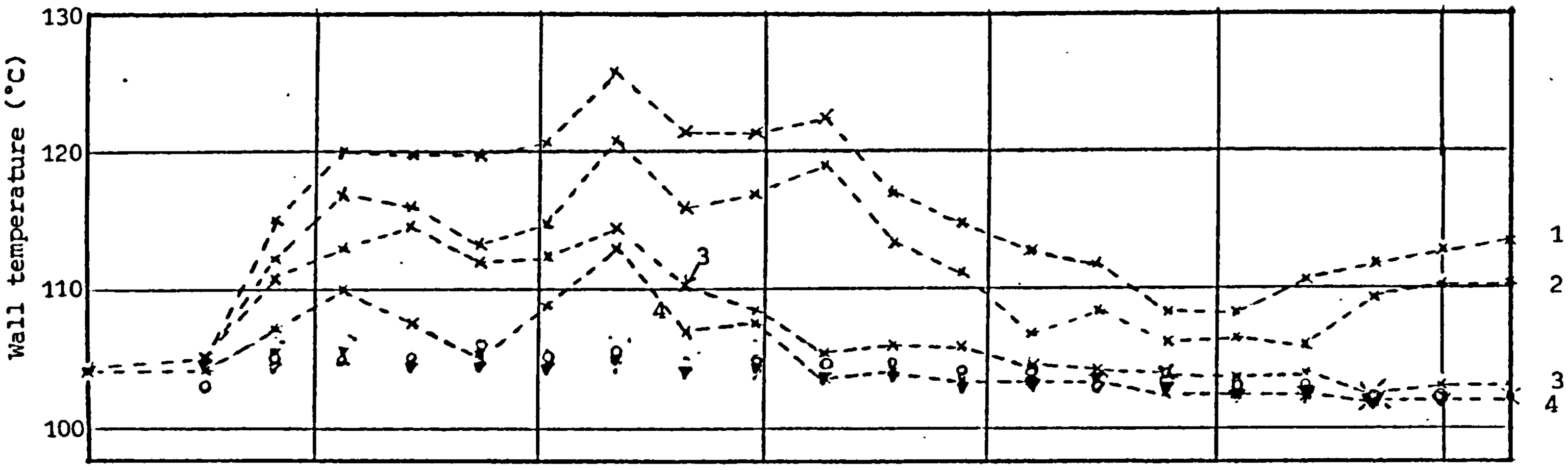


Fig.(4.3.7c) : wall temperature profiles along the tube length.



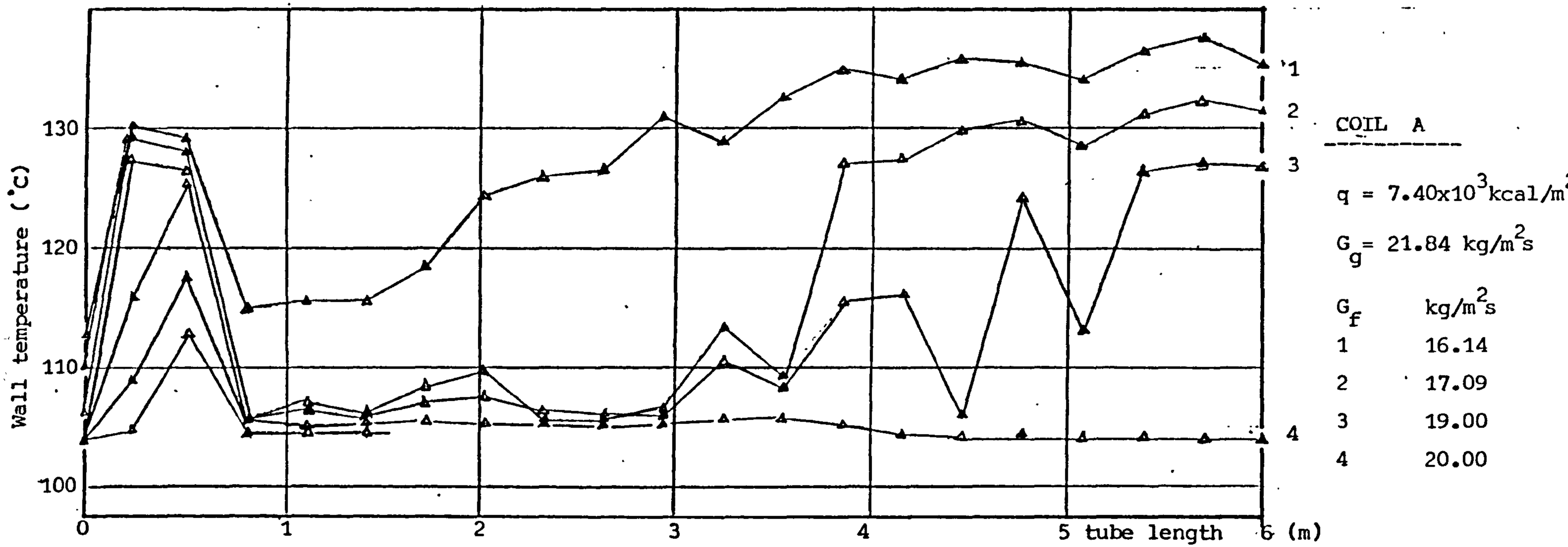
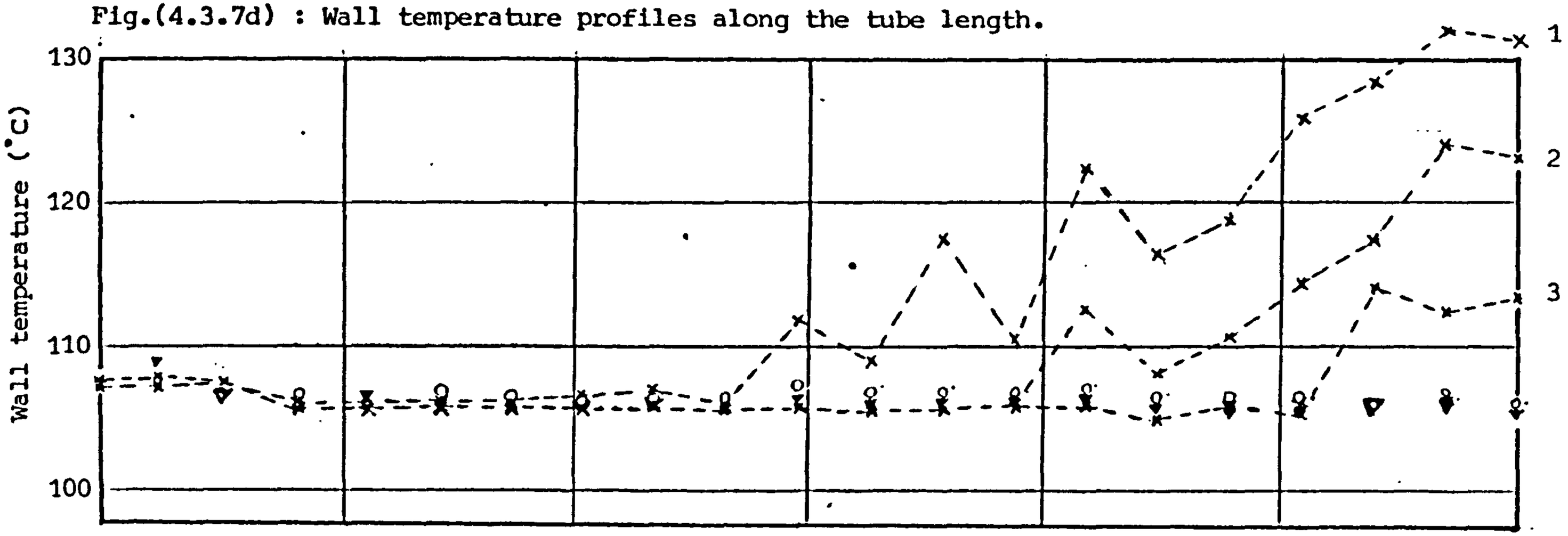


Fig.(4.3.7d) : Wall temperature profiles along the tube length.



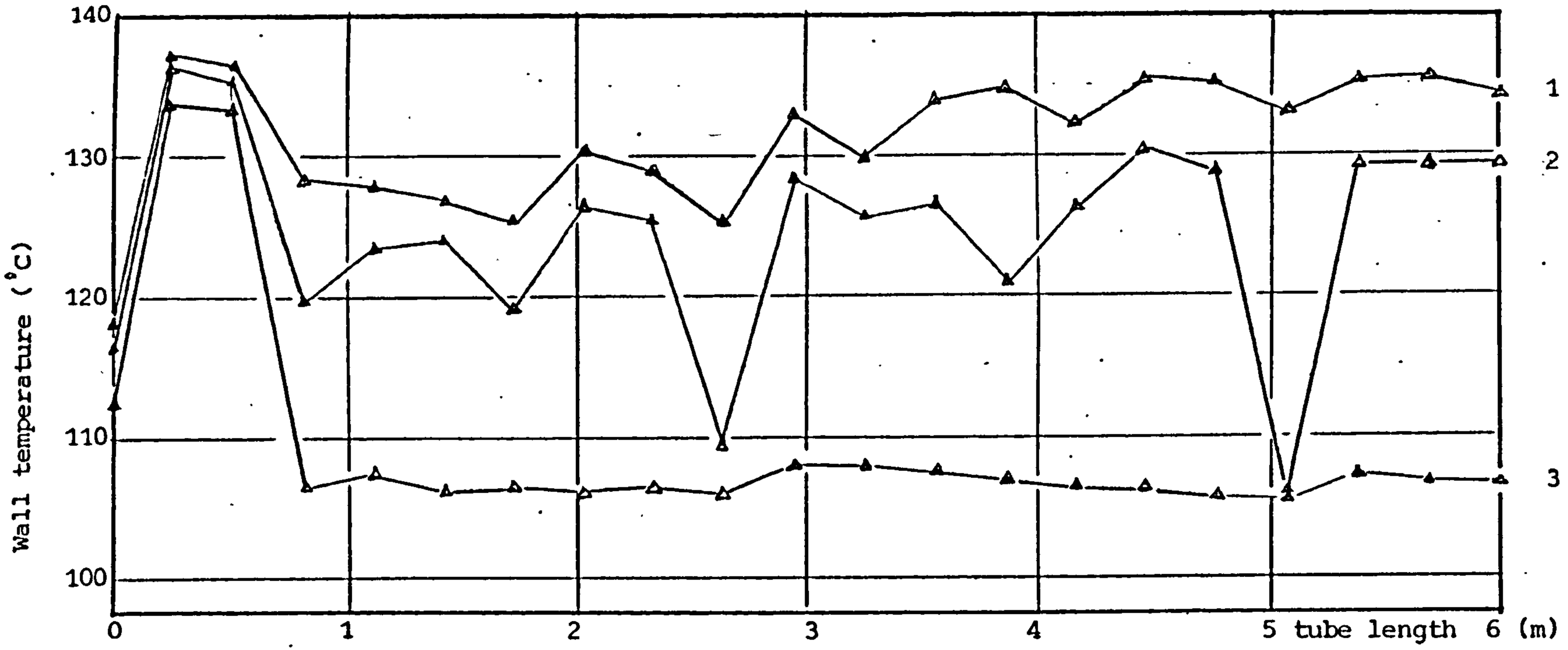
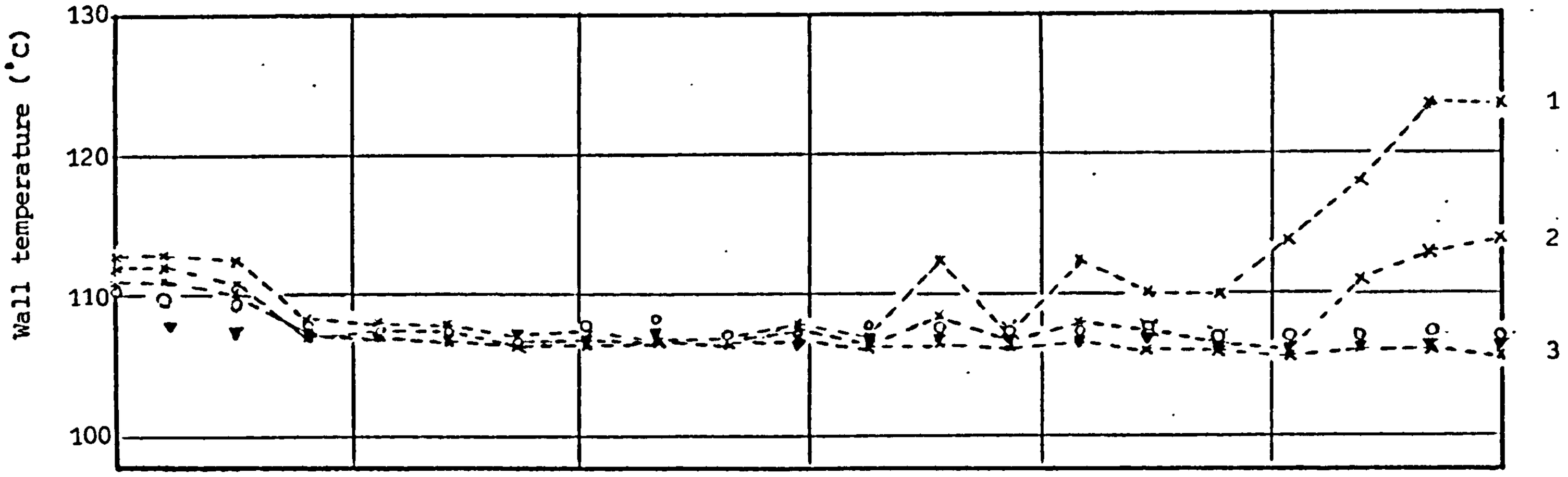


Fig. (4.3.7 e) : Wall temperature profiles along the tube length.



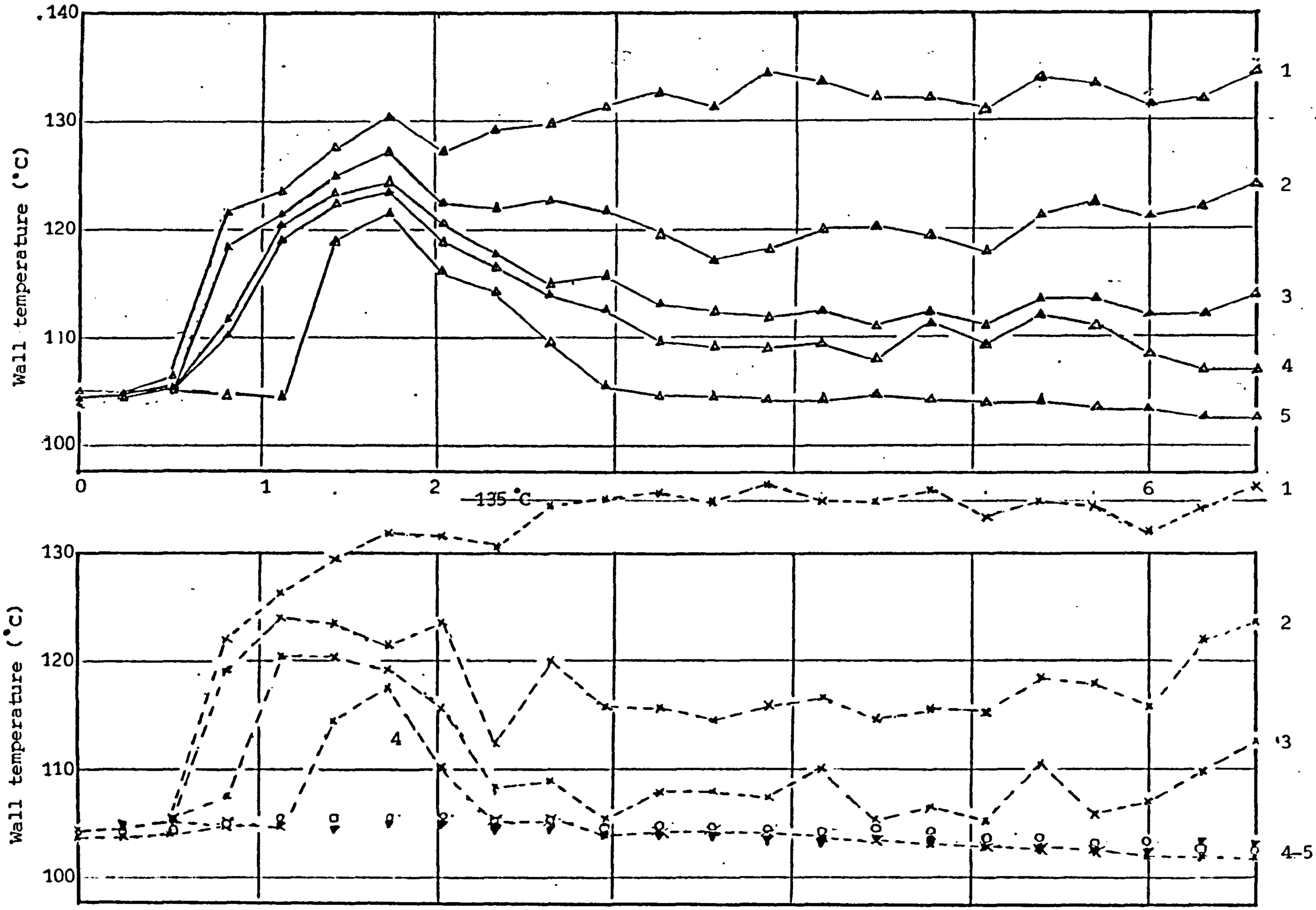


Fig. (4.3.8 a) : Wall temperature profiles alog the tube length.

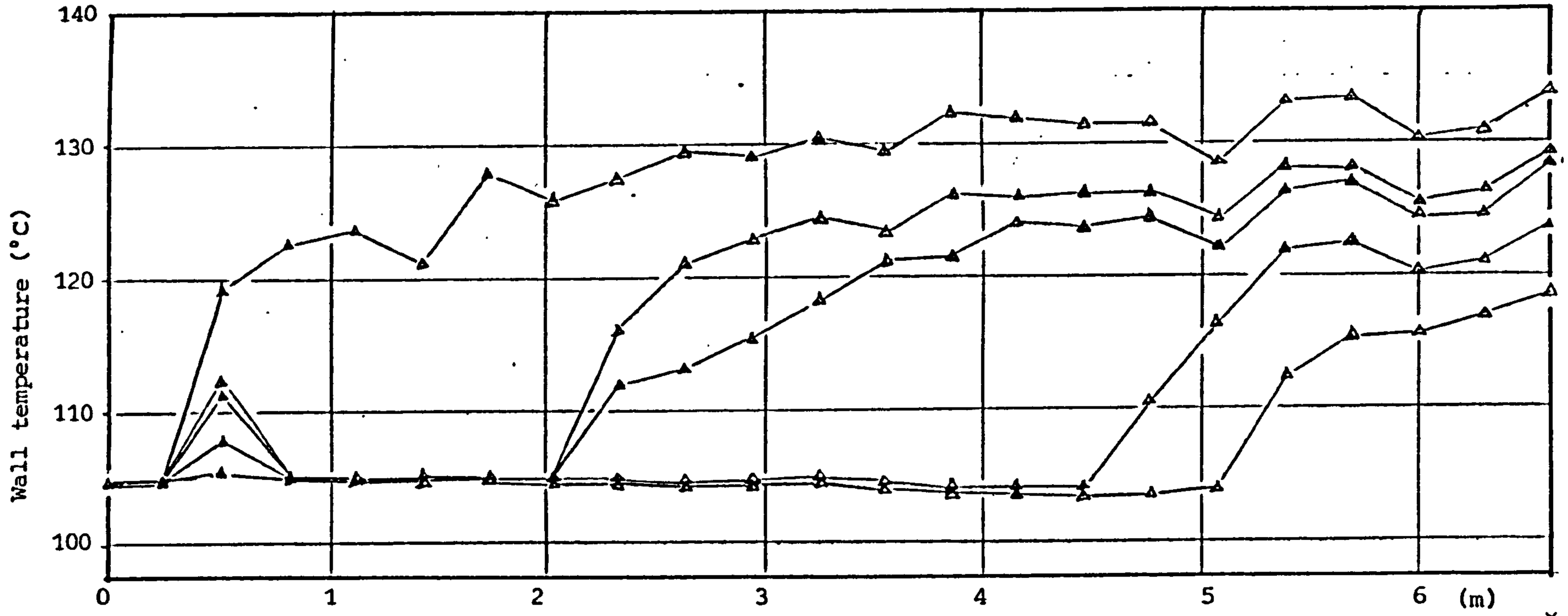
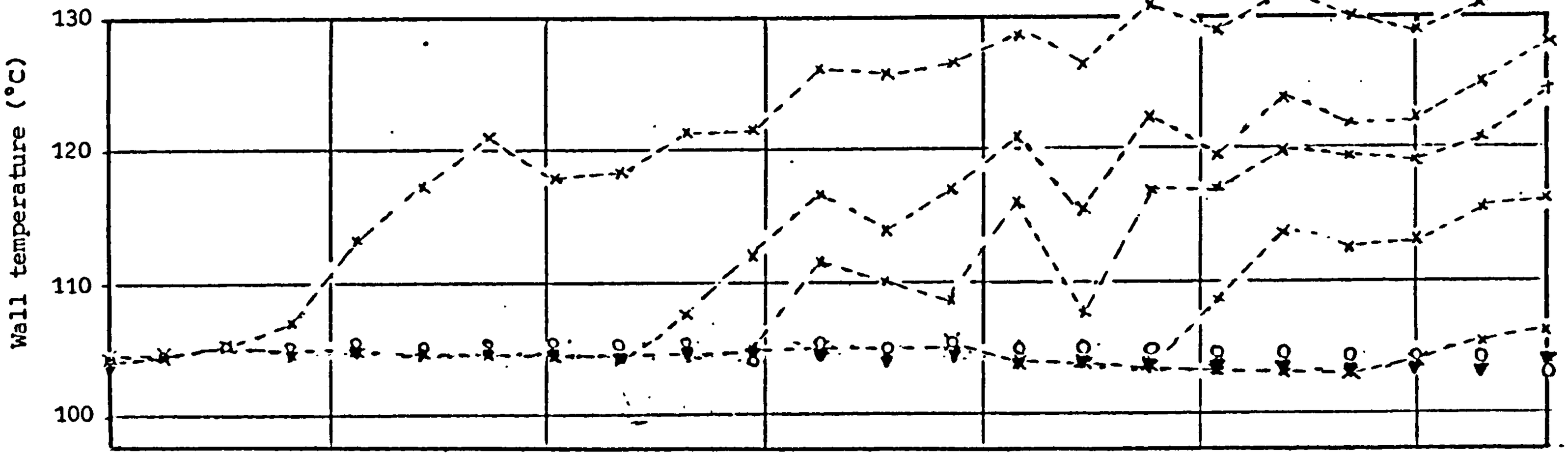
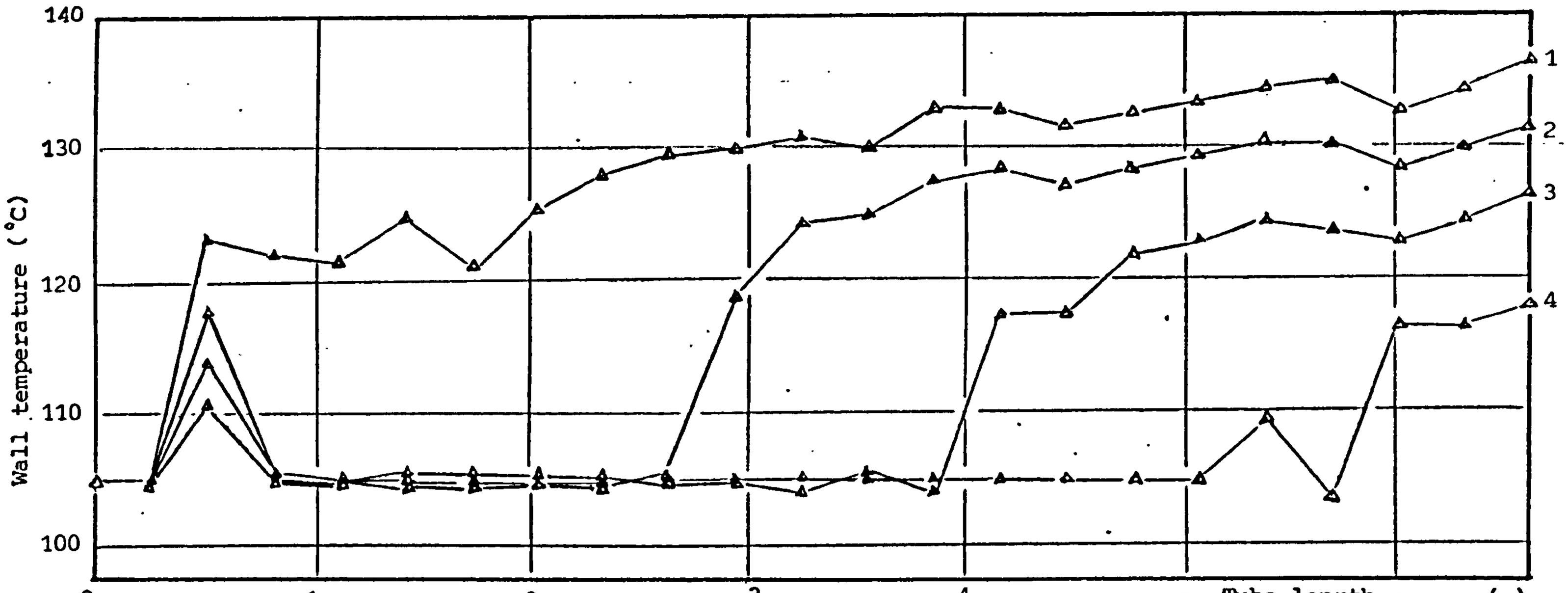


Fig. (4.3.8 b) : Wall temperature profiles along the tube length.





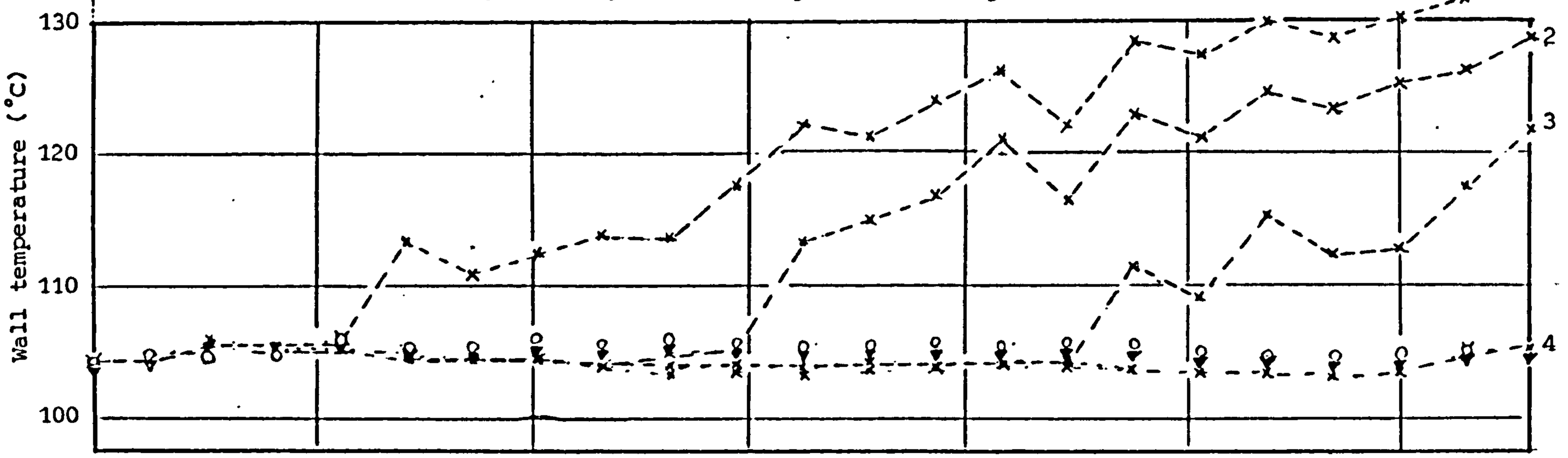
COIL B

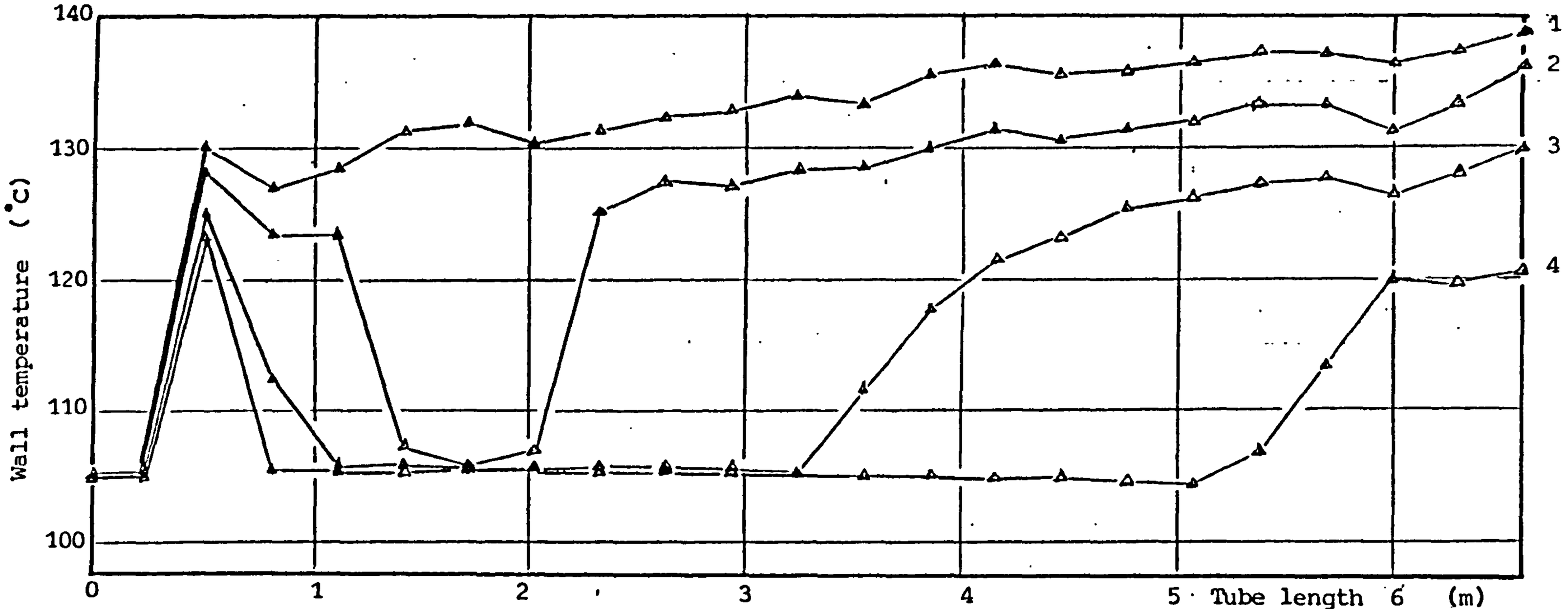
$q = 7.95 \times 10^3$ kcal/m^{2}h

$G_g = 38.93$ kg/m^{2}s

G_f	kg/m^{2}s
1	15.19
2	17.09
3	18.99
4	21.36

Fig. (4.3.8 c) : Wall temperature profiles along the tube length.





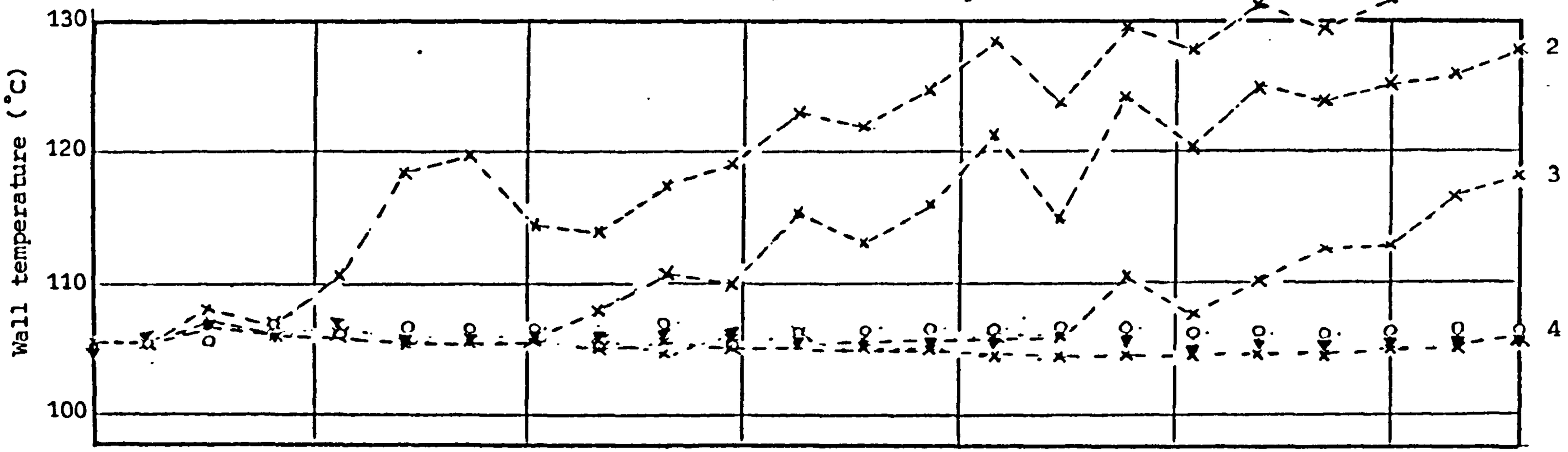
COIL B

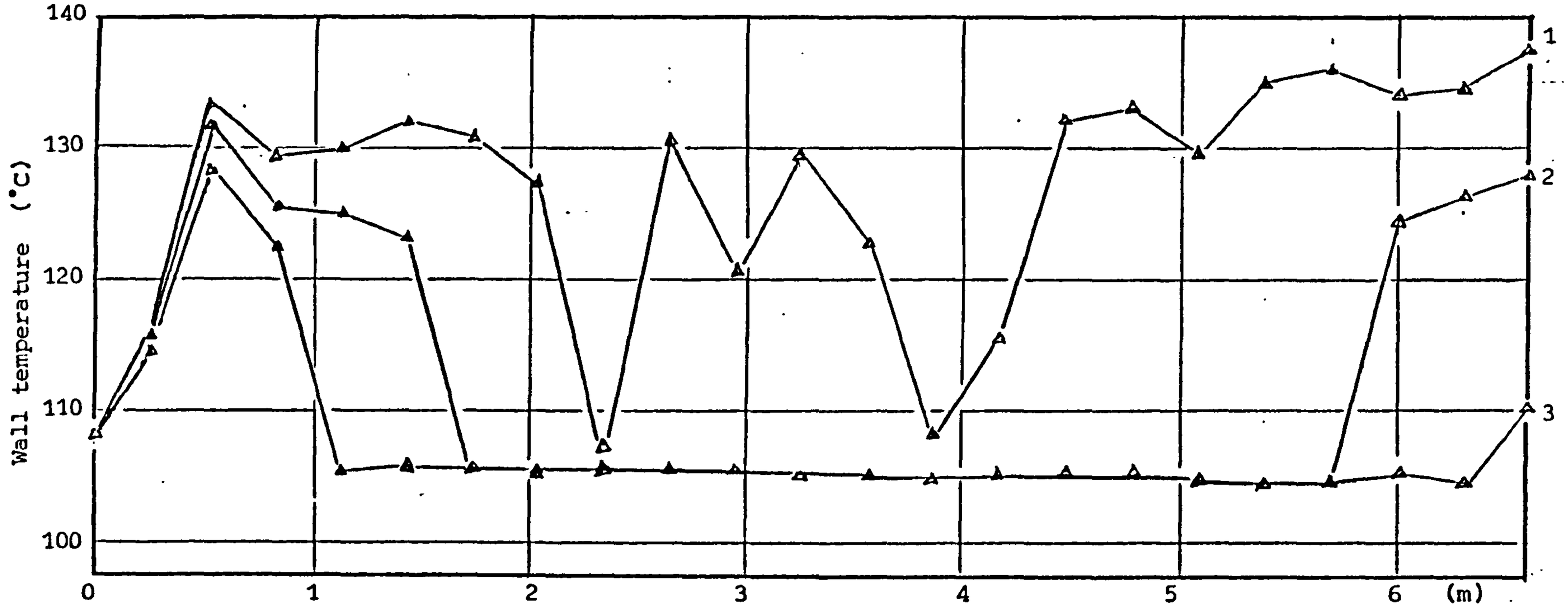
$q = 7.95 \times 10^3$ kcal/m^2h

G_g=37.03 kg/m^2s

G_f	kg/m^2s
1	15.19
2	16.61
3	18.99
4	20.89

Fig. (4.3.8 d) : Wall temperature profiles along the tube length.





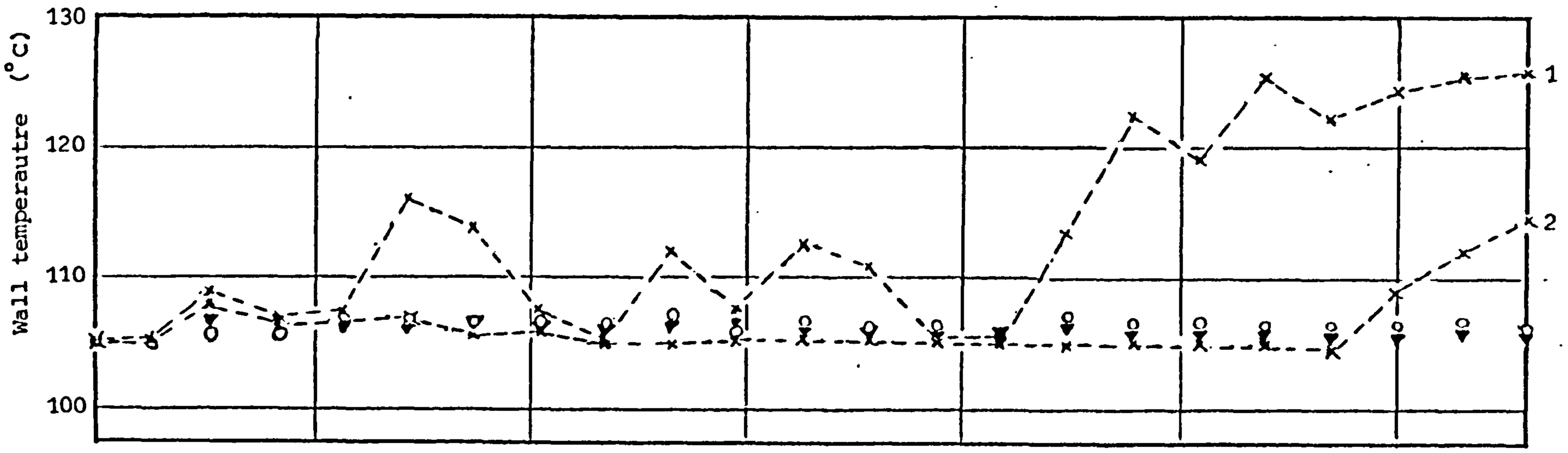
COIL B

q = 7.95×10^3 kcal/m^2h

G_g = 35.13 kg/m^2.s

G_f	kg/m^2s
1	16.90
2	18.52
3	20.41

Fig. (4.3.8e) : Wall temperature profiles along the tube length.



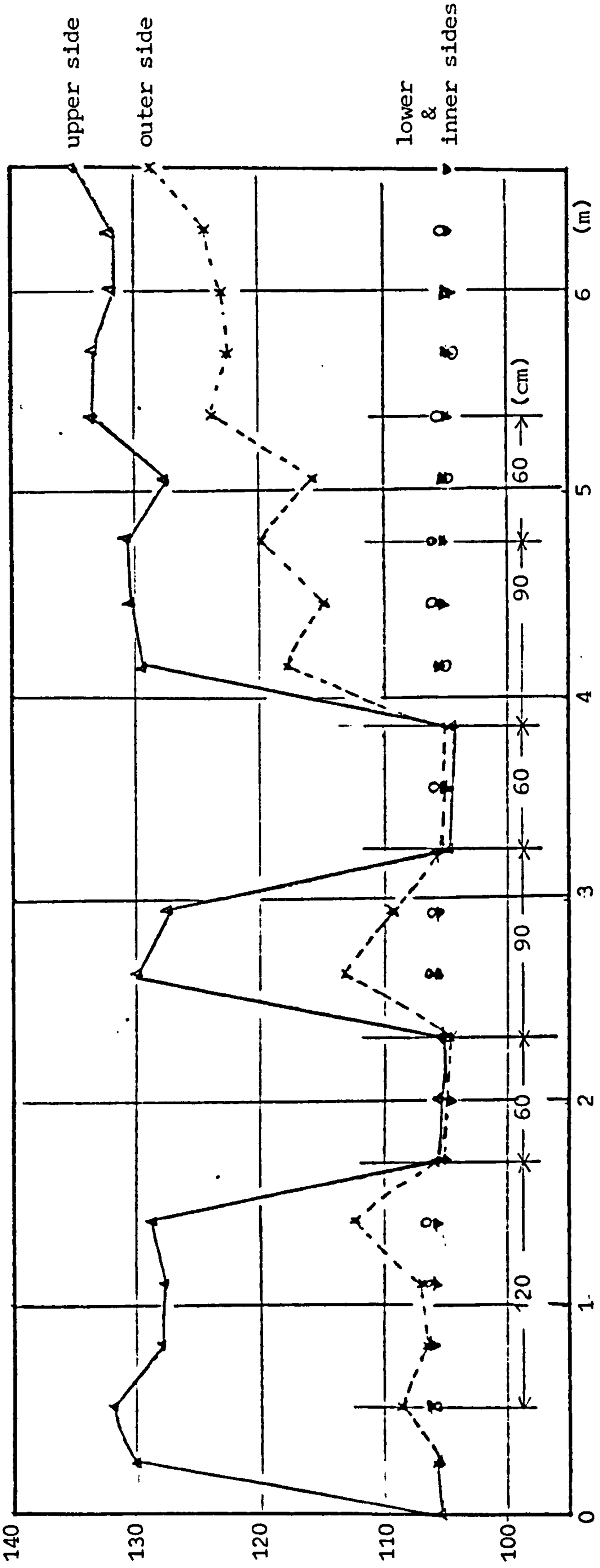
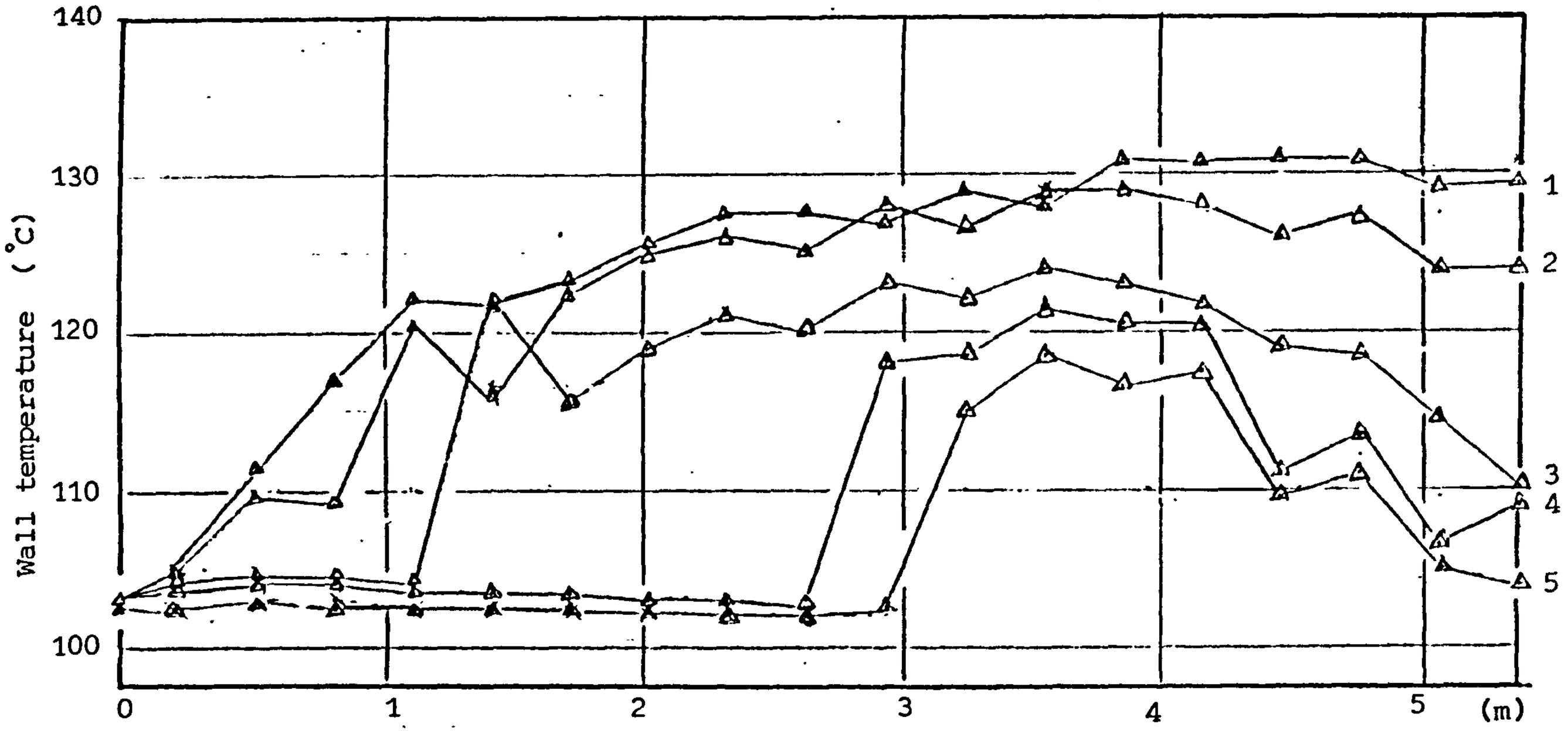


Fig. (4.3.8 f) : Wall temperature profiles along the tube length. (typical comb.-shape profile).
q =7.95x10^3 kcal/m^{2}h, G_g= 24.69 kg/m^{2}s , G_f= 17.09 kg/m^{2}s .



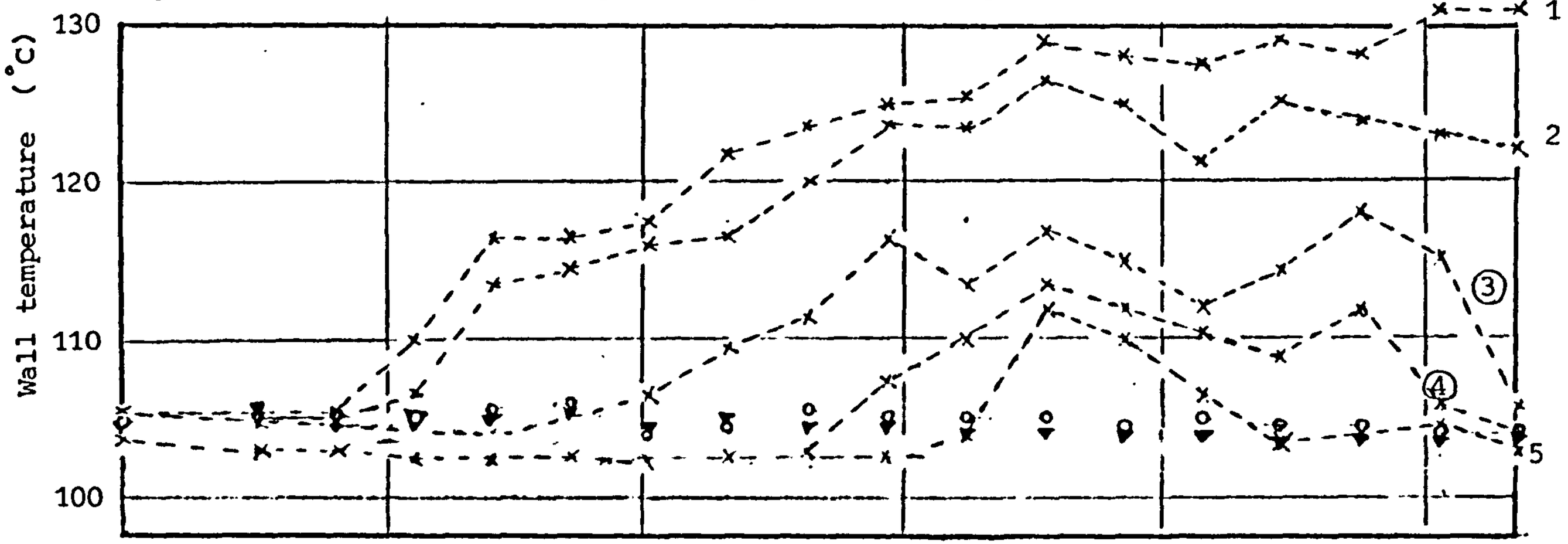
COIL C

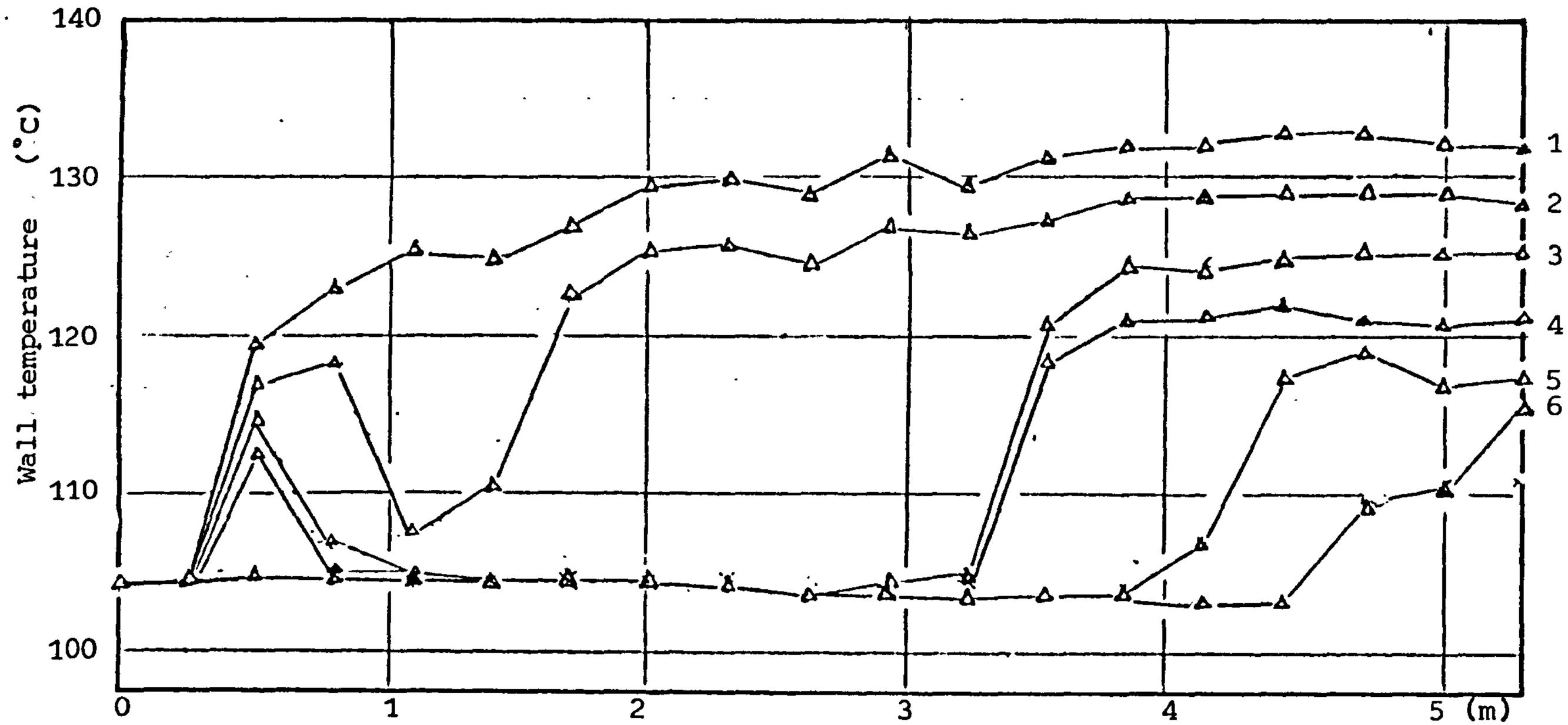
$q = 7.94 \times 10^3$ kcal/m^2h

G_g = 44.63 kg/m^2s

G_f	kg/ m^2s
1	14.24
2	15.19
3	17.09
4	18.04
5	18.99

Fig . (4.3.9 a) : Wall temperature profiles along the tube length.





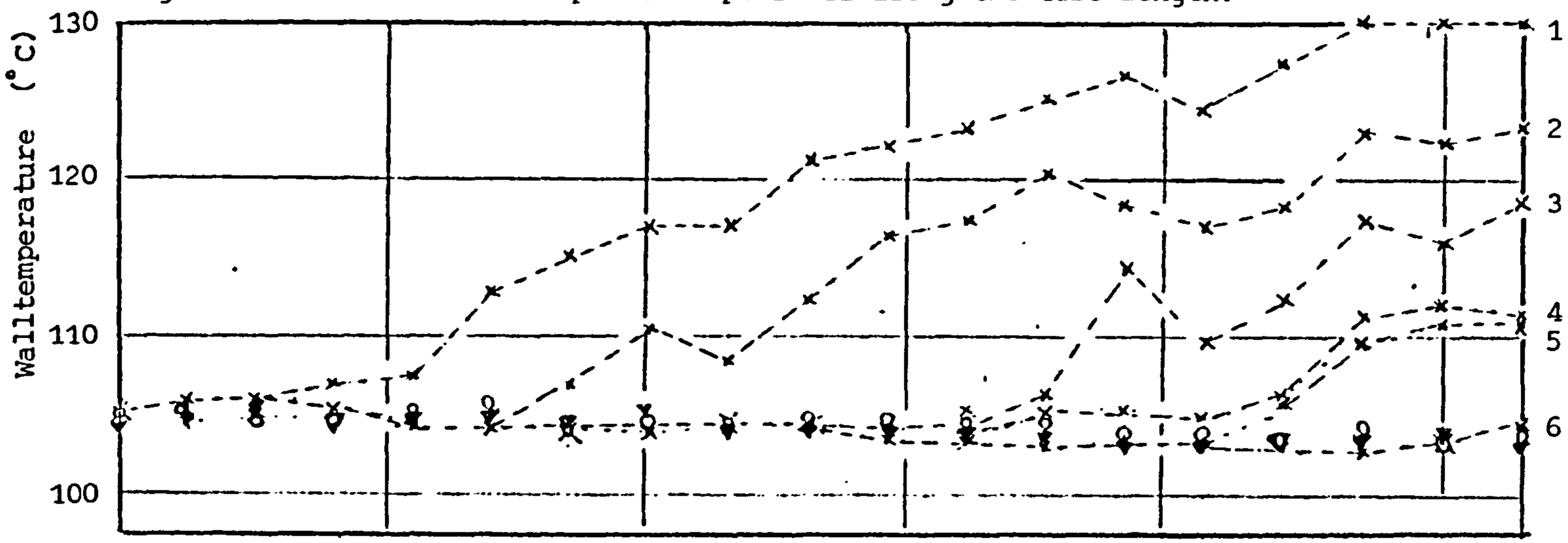
COIL C

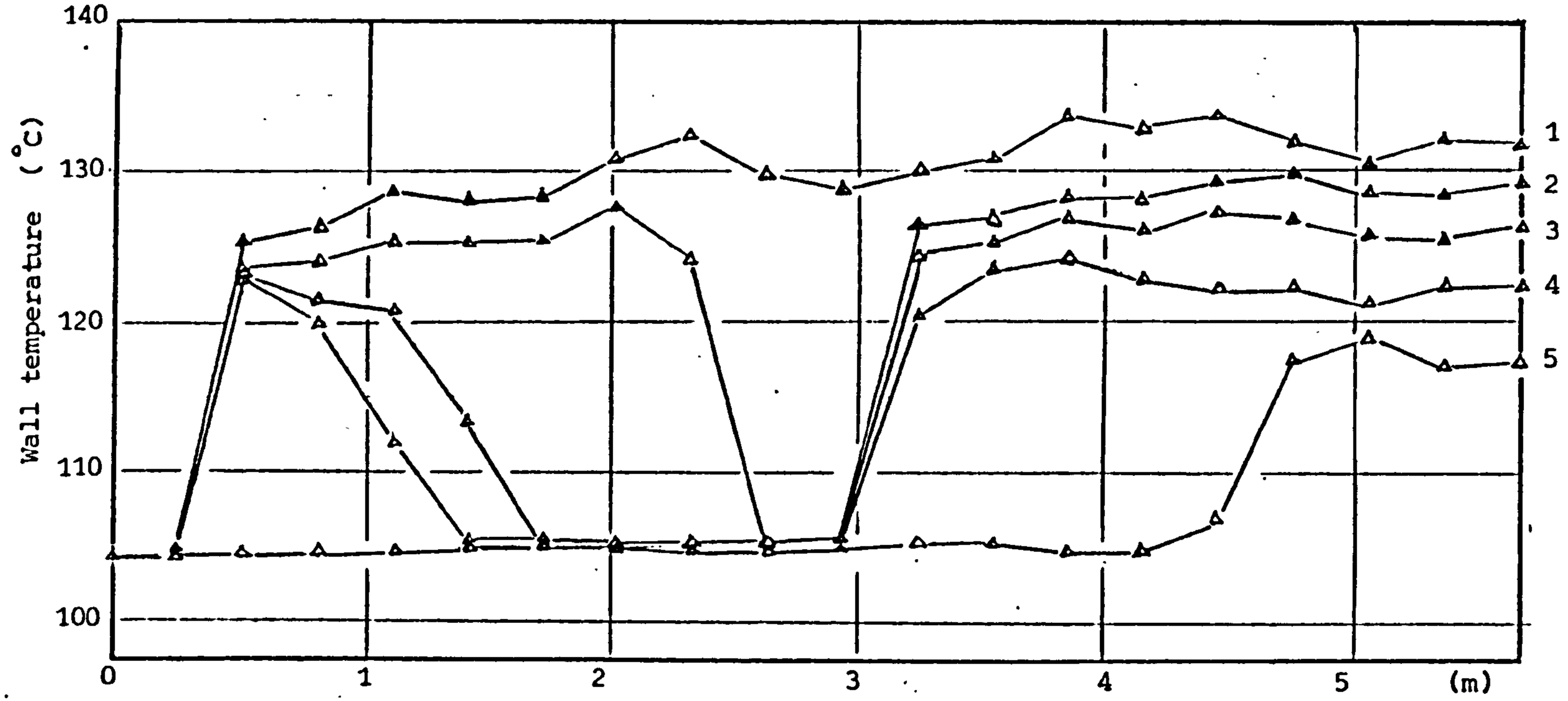
$q = 7.94 \times 10^3$ kcal/m^2h

G_g = 41.78 kg/m^2 s

G_f	kg/m^2 s,
1	14.24
2	15.90
3	17.09
4	18.99
5	19.94
6	20.89

Fig.(4.3.9 b) : Wall temperature profiles along the tube length.





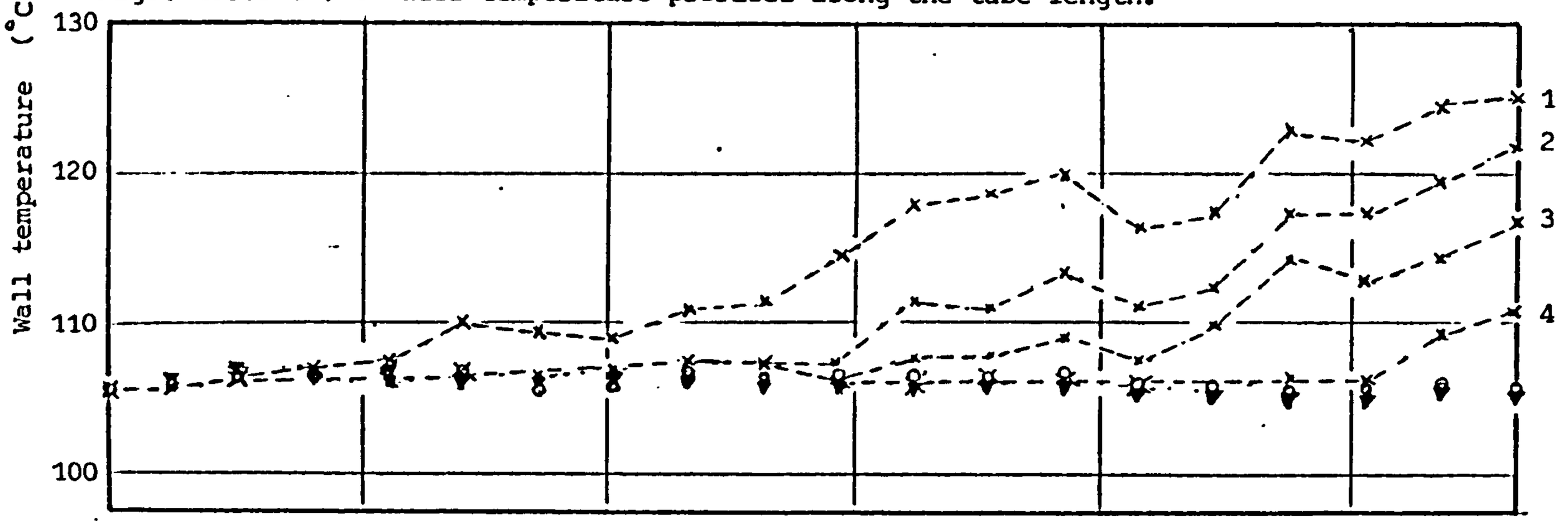
COIL C

$q = 7.94 \times 10^3$ kcal/m^{2}h

$G_g = 38.93$ kg/m^{2}s

G_f	kg/m^{2}s
1	16.14
2	17.09
3	18.04
4	18.99
5	19.94

Fig.(4.3.9 c) : Wall temperature profiles along the tube length.



COIL C

$q = 7.94 \times 10^3$ kcal/m^{2}h

$G_g = 36.08$ kg/m^2 s

	G_f kg/m^2 s
1	17.09
2	18.04
3	18.99
4	19.94
5	20.89
6	21.84
7	23.74

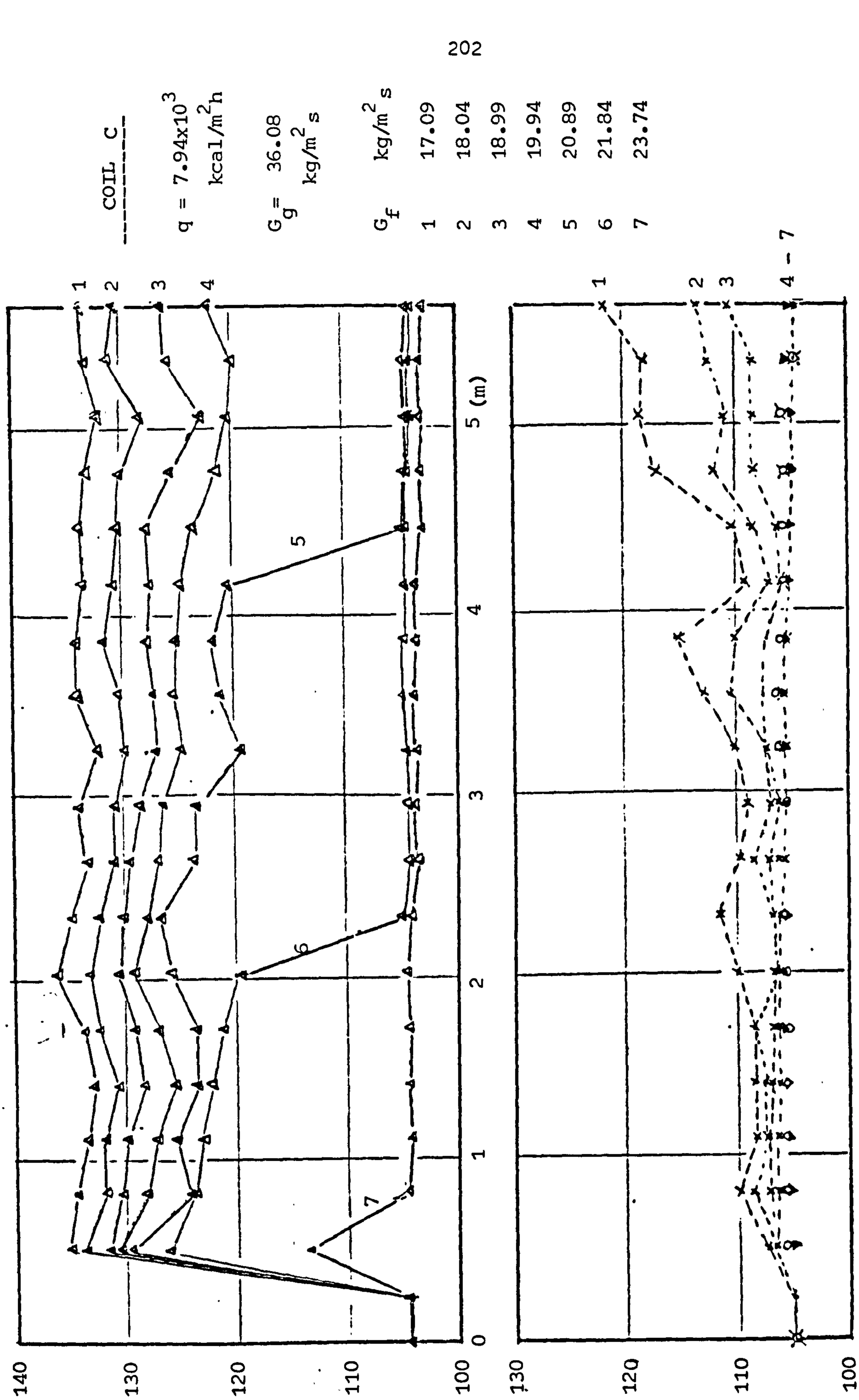


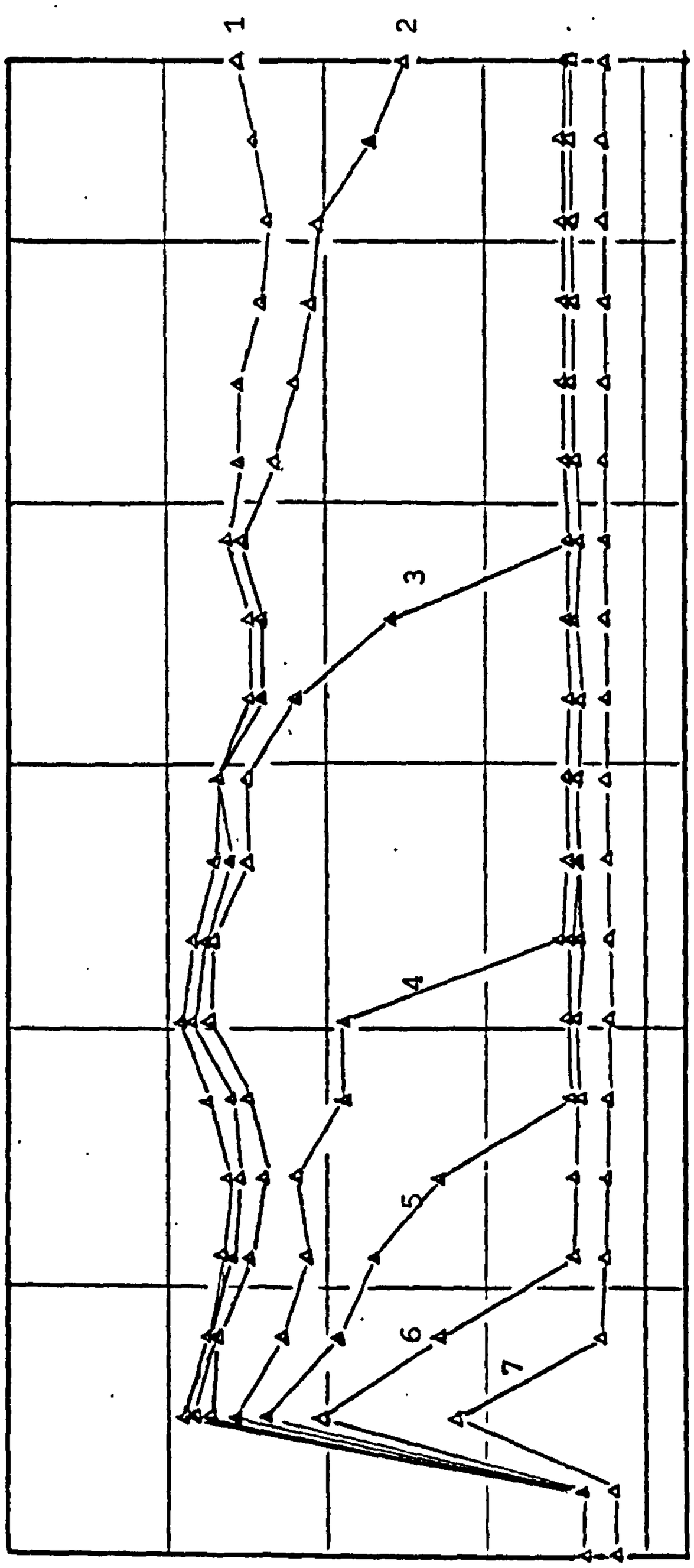
Fig. (4.3.9 d) : Wall temperature profiles along the tube length.

COIL C

$q = 7.94x10^3$ kcal/m^2h

$G_g = 22.79$ kg/m^2s

G_f	kg/m^2s
1	18.99
2	19.46
3	19.94
4	21.84
5	23.74
6	25.64
7	29.43



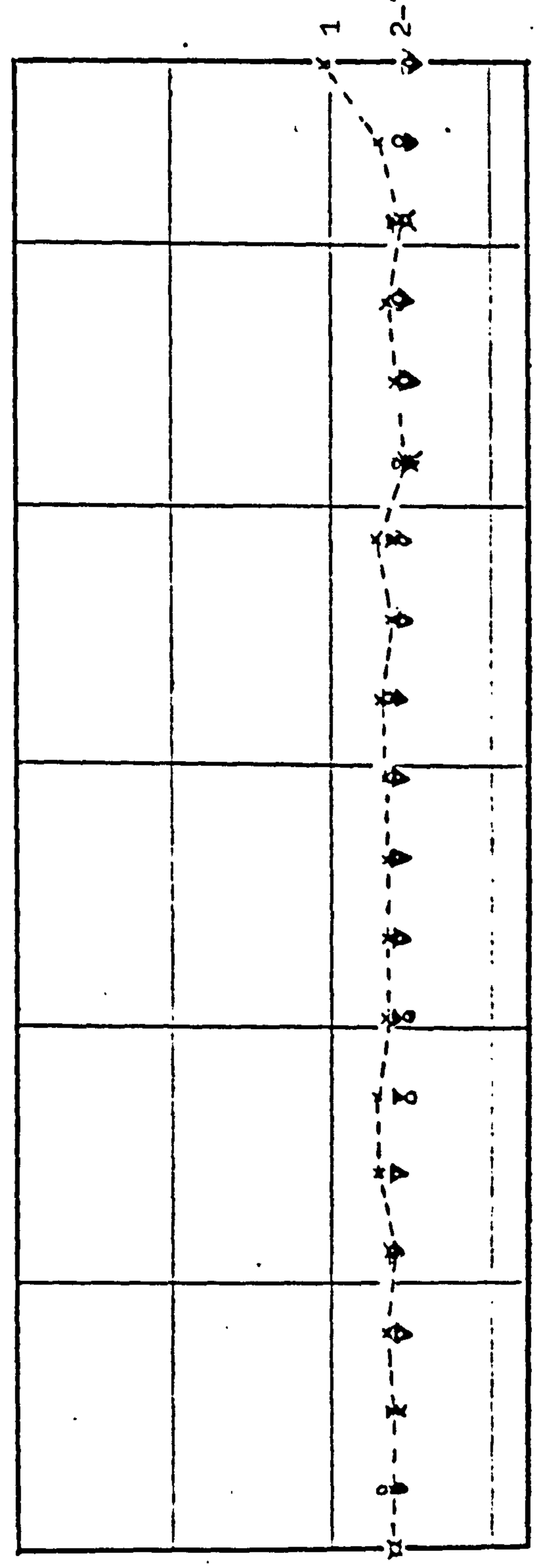
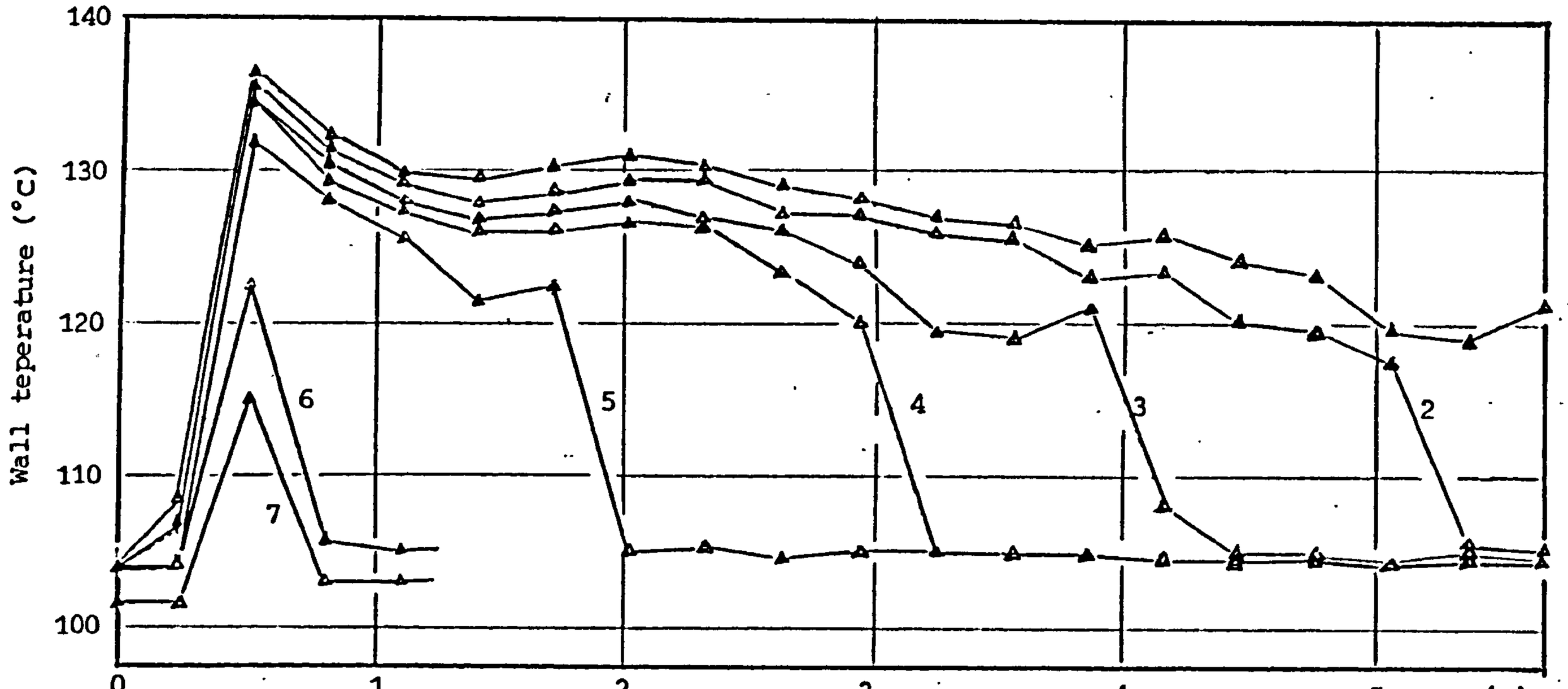


Fig. (4.3.9e) : Wall temperature profiles along the tube length.



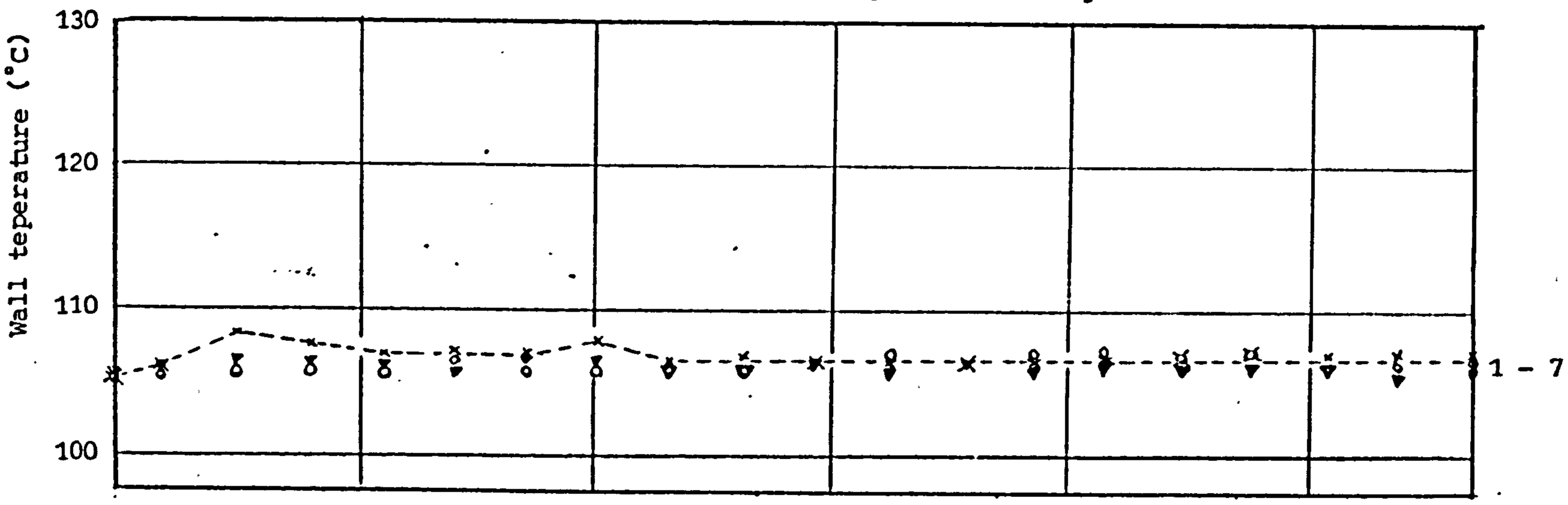
COIL .. C

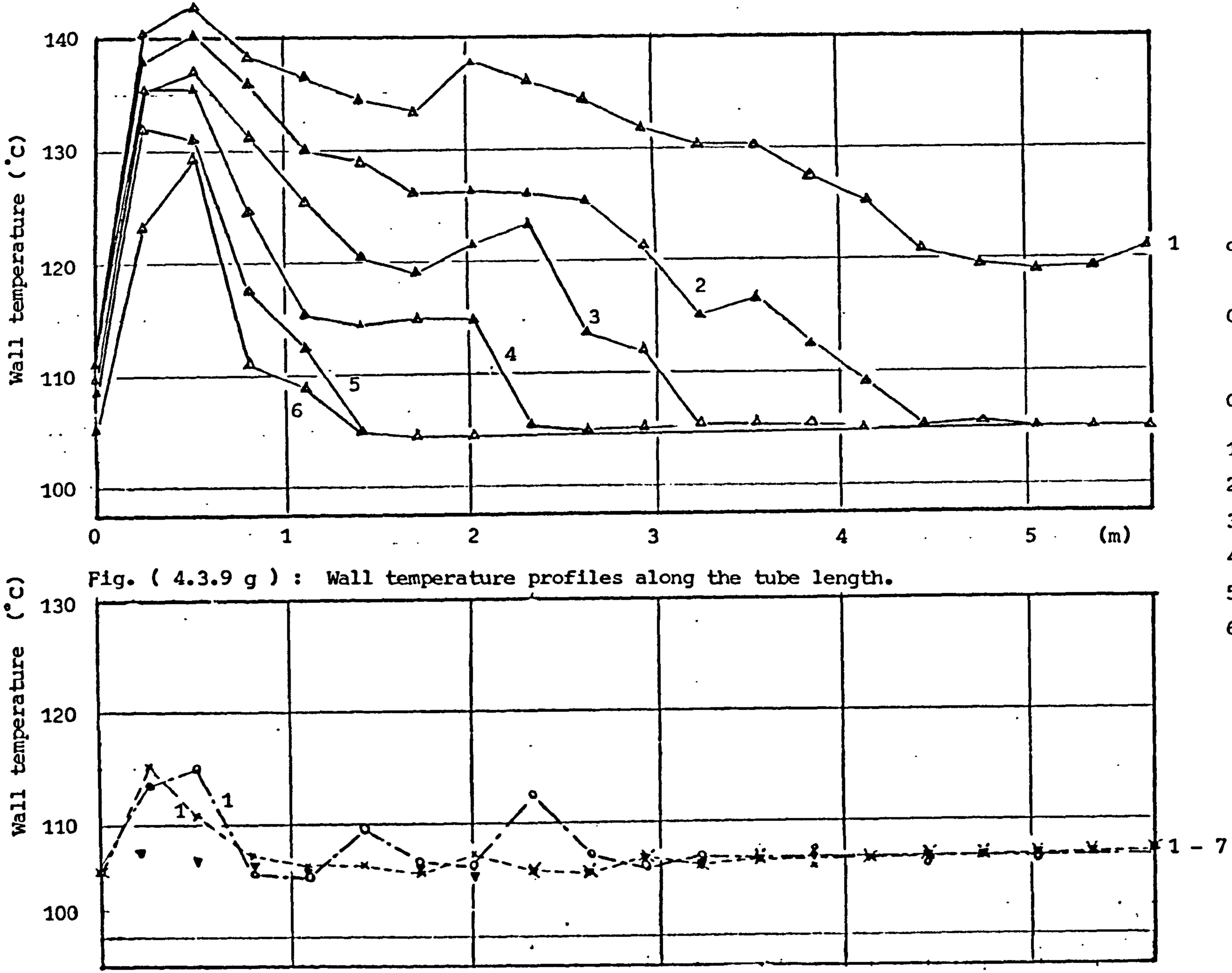
$q = 7.94 \times 10^3$ kcal/m^2h

$G_g = 20.89$ kg/m^2s

G_f	kg/m^2s
1	20.89
2	21.84
3	22.79
4	23.74
5	24.69
6	26.59
7	29.43

Fig. (4.3.9 f) : Wall temperature profiles along the tube length.





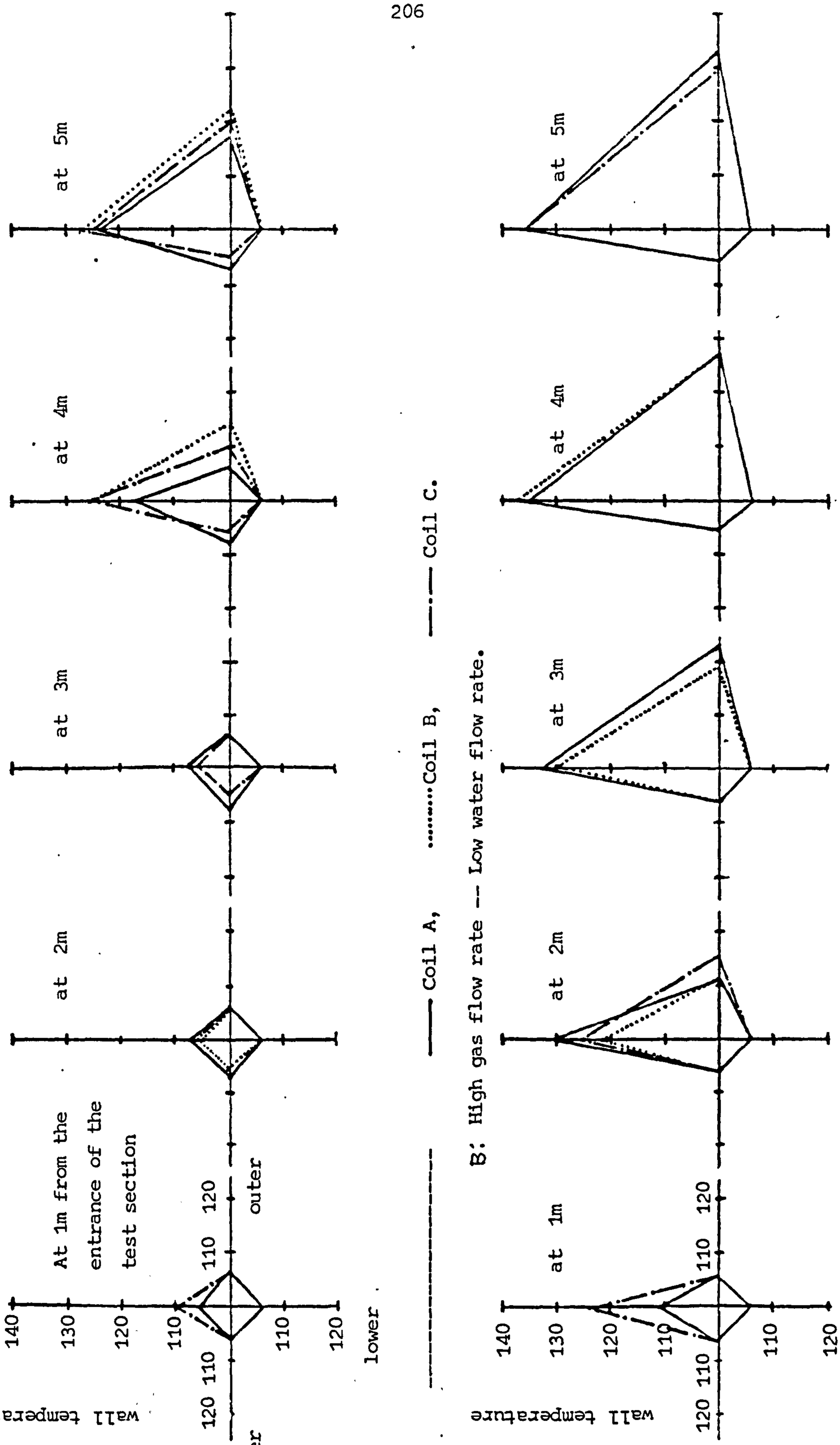
Coil C

$q = 7.94 \times 10^3$ kcal/m^{2}h

$G_g = 18.99$ kg/m^{2}s

G_f	kg/m^{2}s
1	24.69
2	32,76
3	36.08
4	40.83
5	44.63
6	46.58

Fig. (4.3.9 g) : Wall temperature profiles along the tube length.



Fig,(4.3.10) : Wall temperature profiles of four positions at 1, 2, 3, 4 and 5 m from the entrance of the test section.

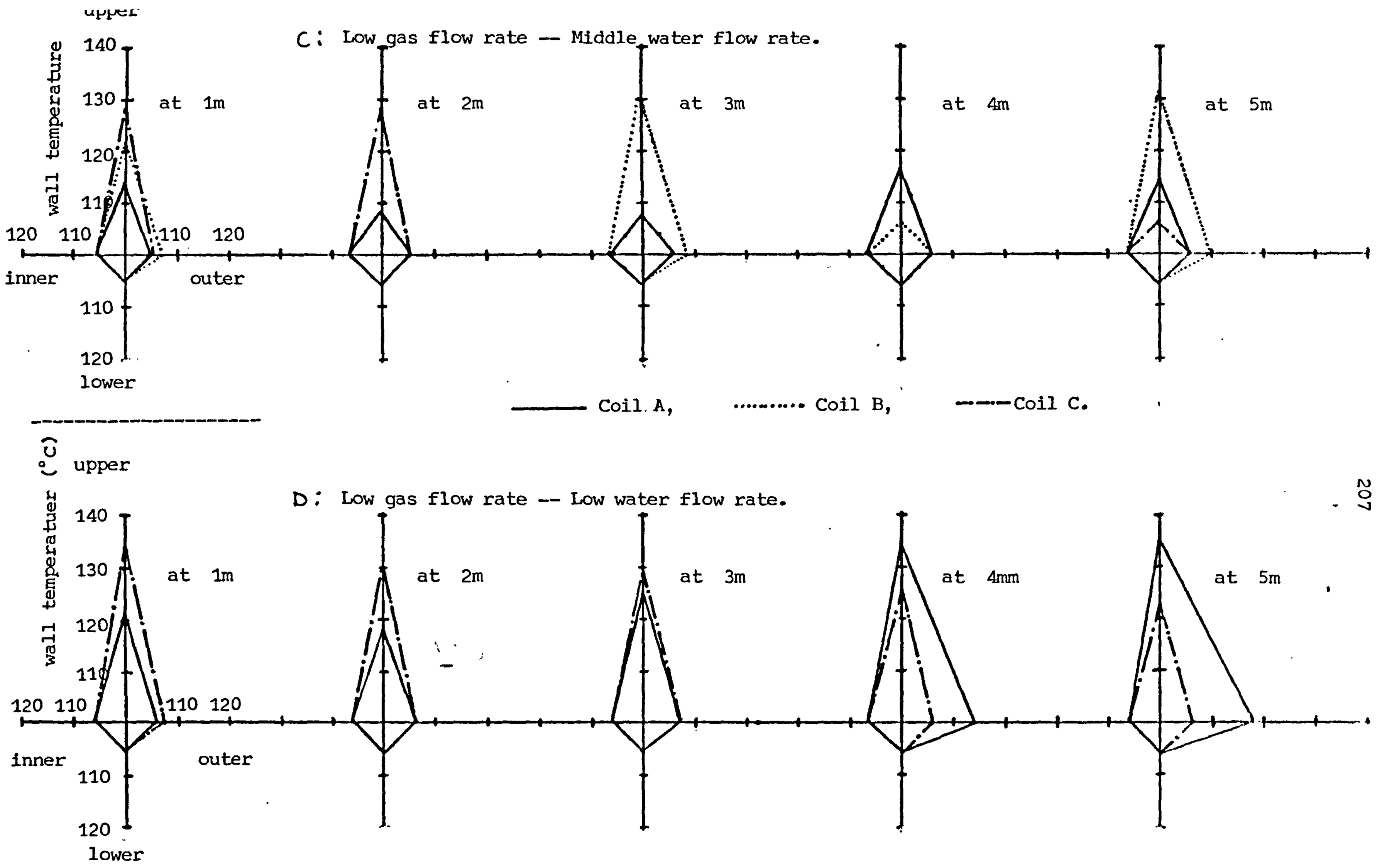
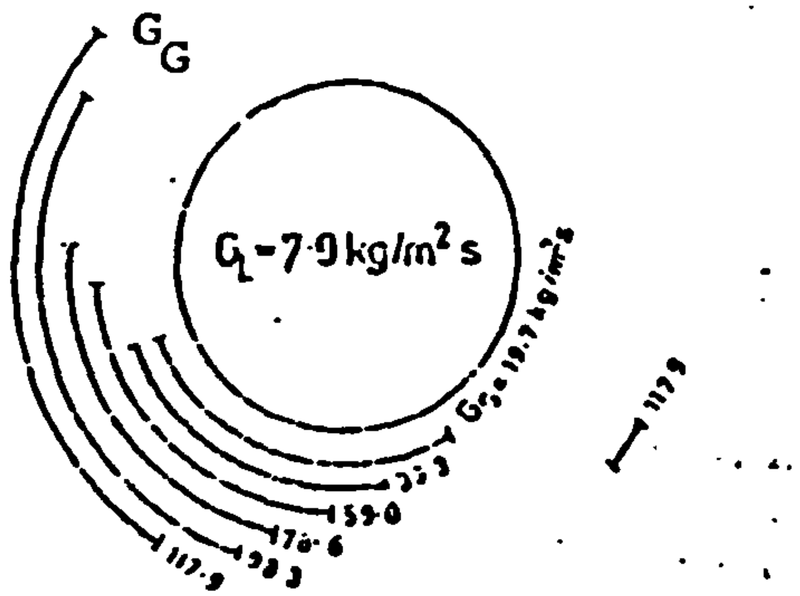
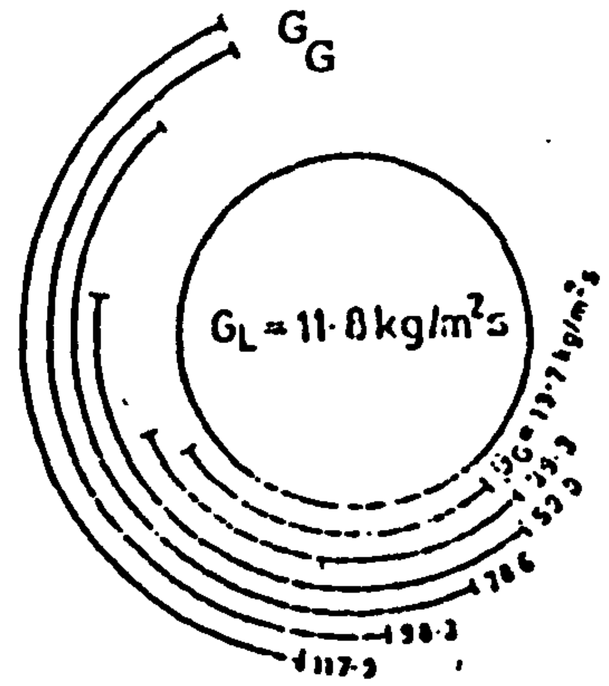


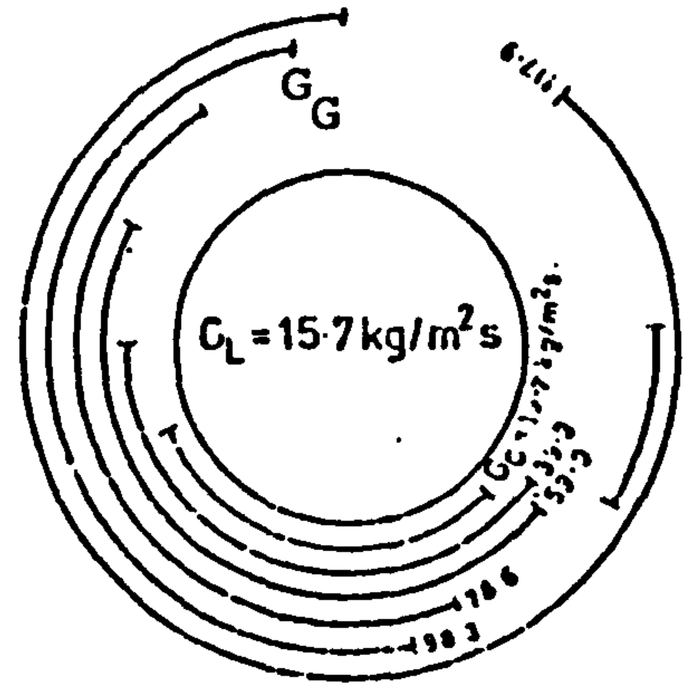
Fig.(4.3.10) : Wall temperature profiles of four positions at 1, 2, 3, 4 and 5 m from the entrance of the test section, (High,Middle and Low are categorized in Table (4.3.1))



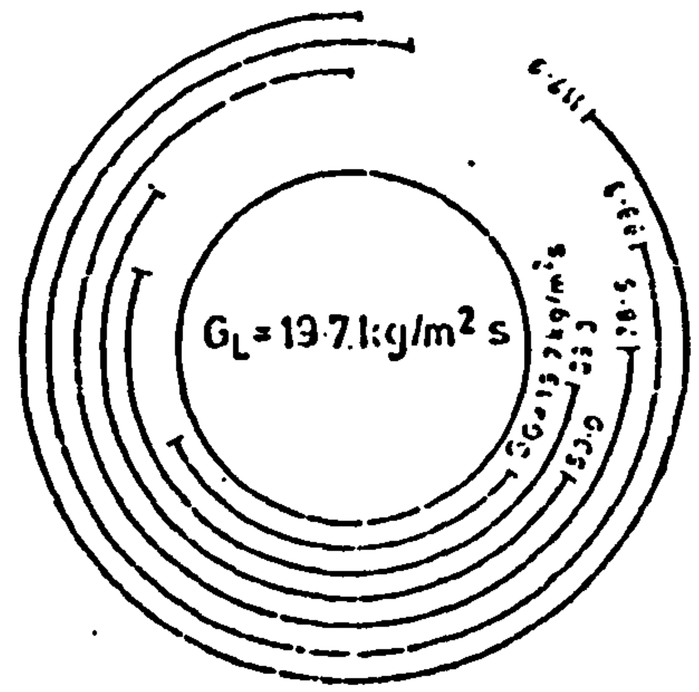
A - LOW



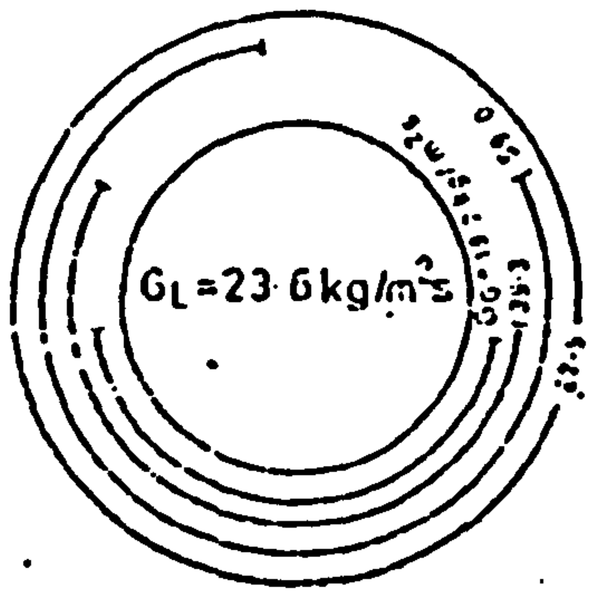
B - LOW



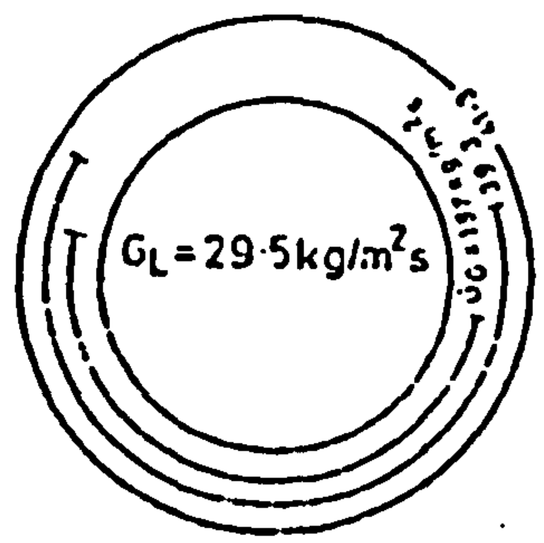
Ç -LOW



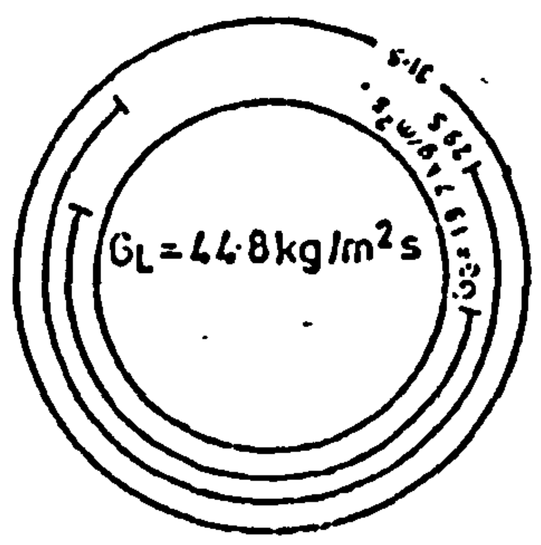
D - MIDDLE



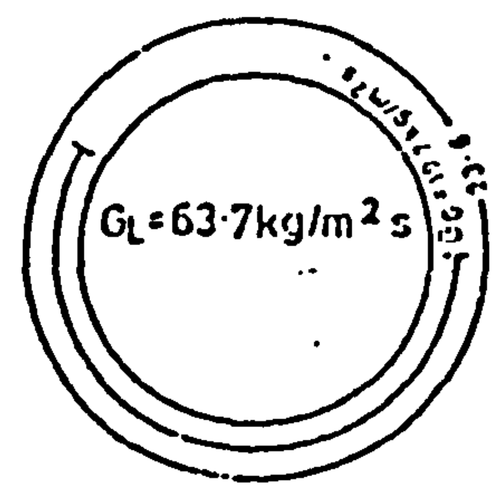
E - MIDDLE



F - HIGH



G - HIGH



H - HIGH

G_G : mass flux of gas.

G_L : mass flux of liquid.

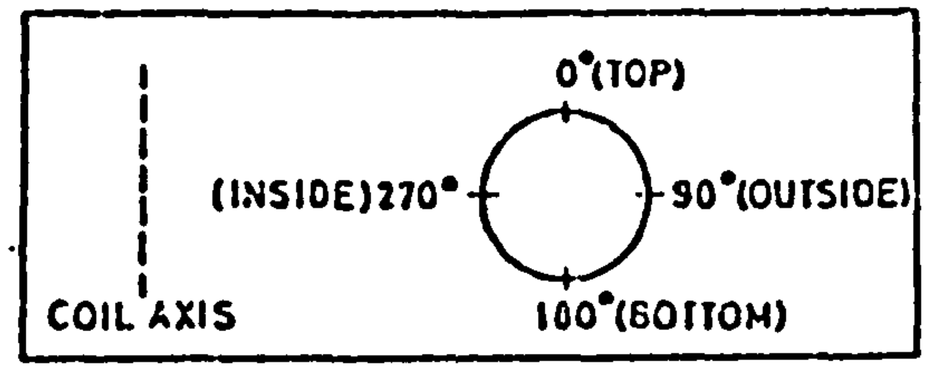


Fig. (4.3.11) : Position of film flow in stratified flows, from Whalley and Wiliams (88).

LOW, MIDDLE and HIGH are categories of the flow rates in Table (4.3.1)

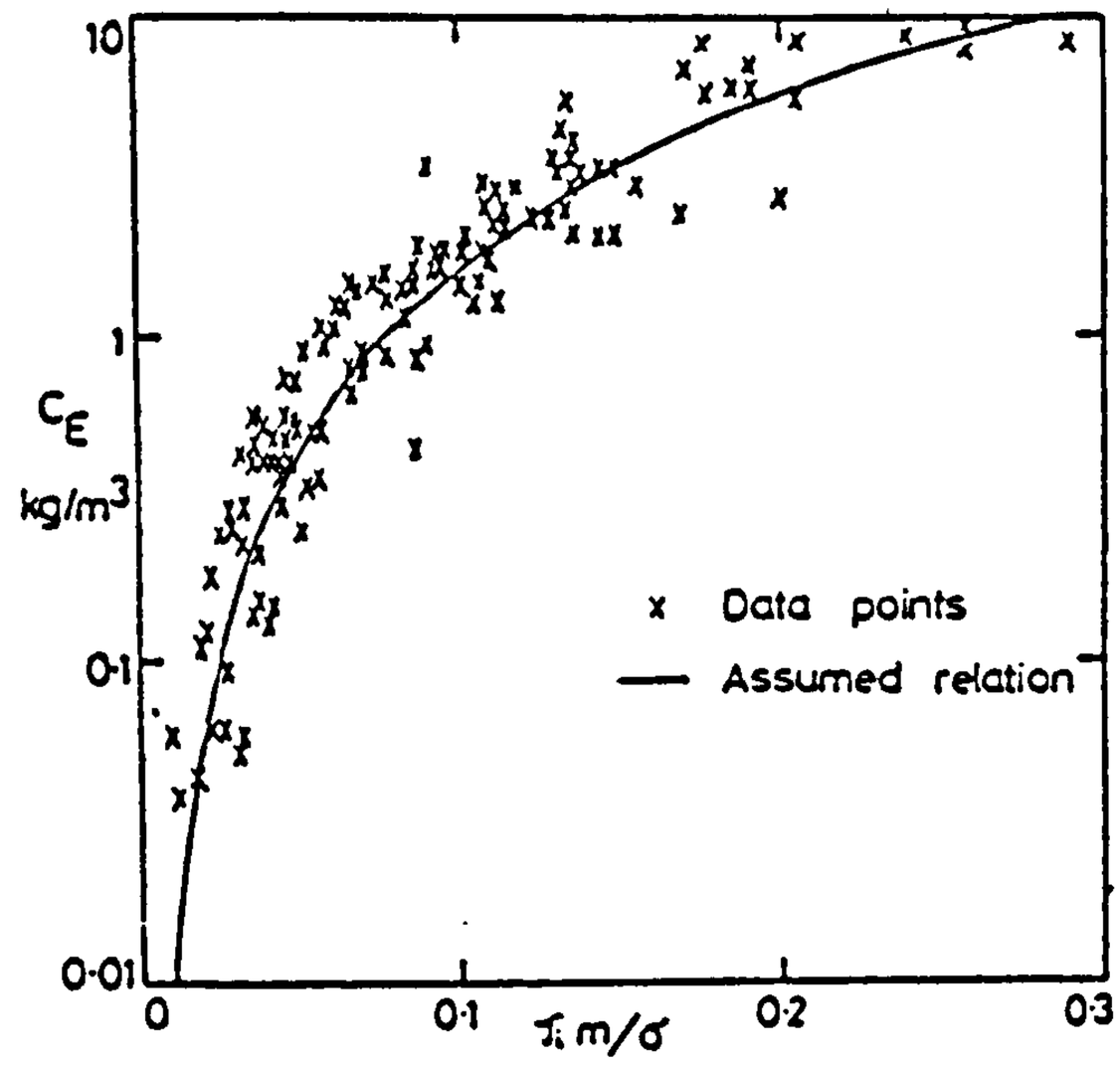


Fig. (4.3.12) : Entrainment correlation ,
from Whalley et al (93).

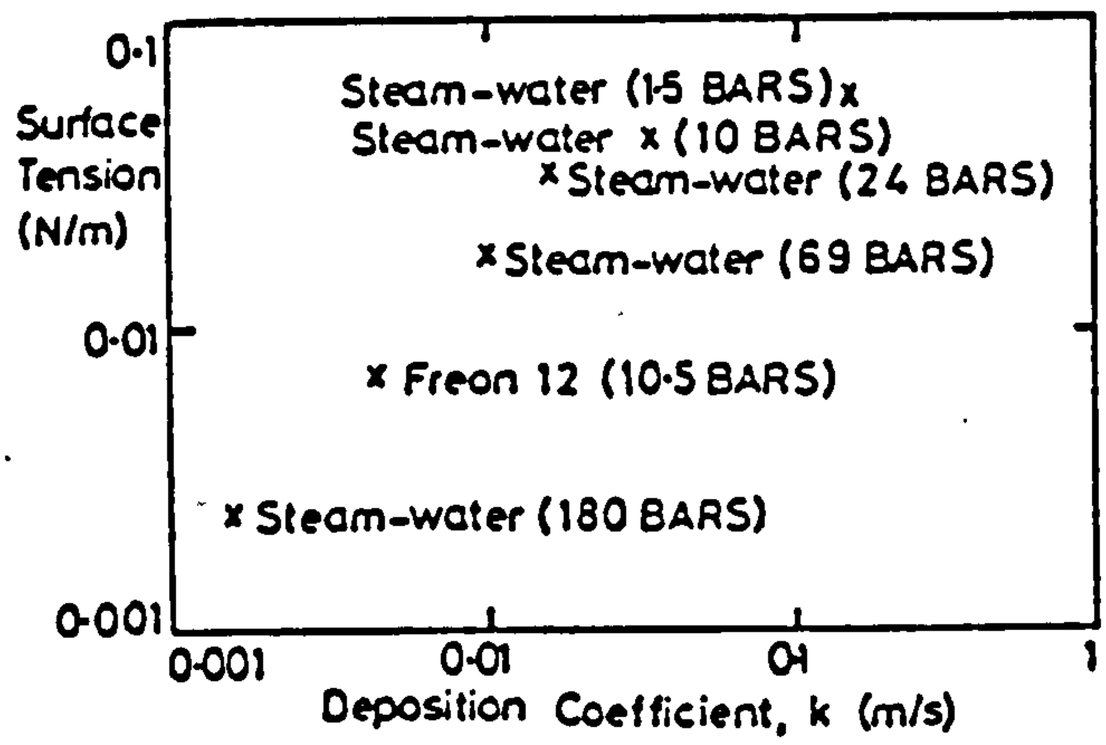


Fig. (4.3.13) : Variation of deposition coefficient
with surface tension, from Whalley et al (93).

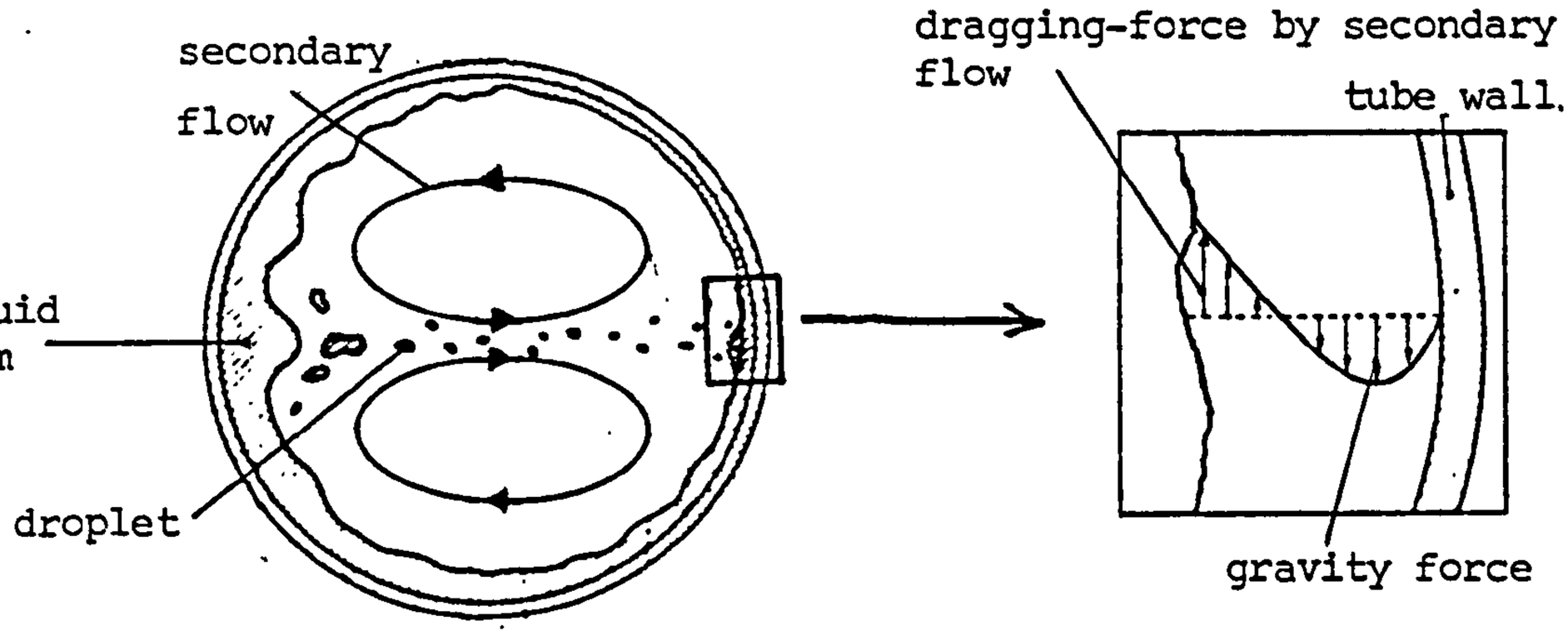


Fig. (4.3.14) : Effects of secondary flow force on the liquid surface.

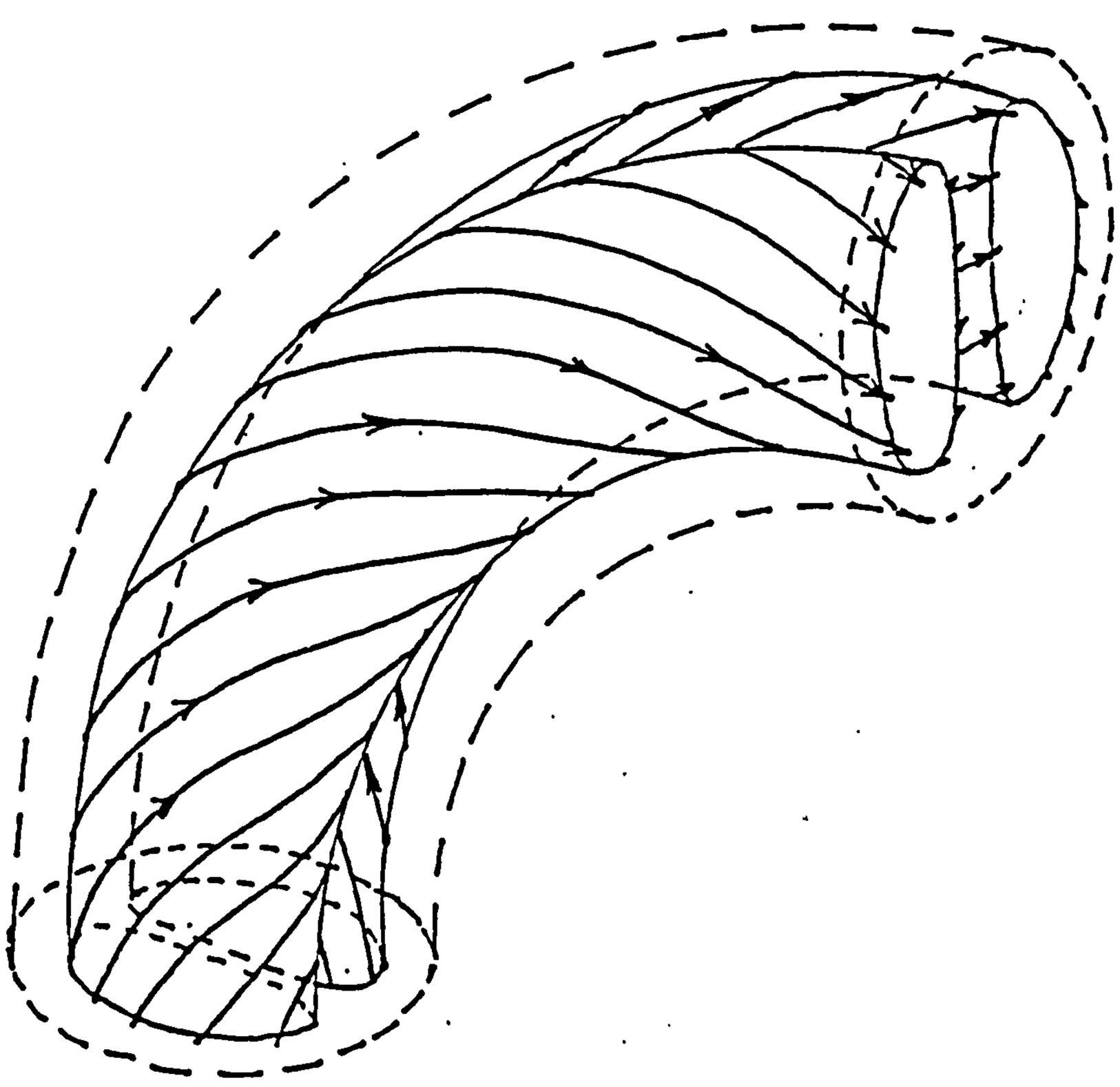


Fig. (4.3.15) :

DOUBLE HELICAL SECONDARY GAS FLOW

from Lacey (58).

4.3.4 Heat Transfer coefficient of flow boiling in Two-phase flow

A theoretical analysis of heat transfer in Two-phase flow is difficult due to the complex flow patterns, slip between vapour and liquid, the unknown conditions at the vapour-liquid interface and the phenomena associated with the formation and motion of bubbles. Hence, a satisfactory theoretical treatment of subject has not yet been offered for any geometry.

Up to the present several empirical correlations have been proposed for the straight tube and four reports (Bell and Owhadi (65), de La Harpe et al (66), Kozeki (48) and Duchatelle et al (67)) have proposed the empirical correlations for helically-coiled tubes which are summarized in section (2.5.3).

Rohsenow (95-1952) and others have suggested that forced convective heat transfer in subcooled or saturated boiling is composed of a nucleate boiling and a convective component, each of which is correlated separately.

Although this concept has been successfully applied to some problems, in general it is not clear how these two components should be combined, since the two-mechanisms affect each other. For example, agitation suppresses bubble nucleation and growth, while at high nucleate boiling fluxes the effect of forced convection is substantially diminished.

Heat transfer to a two-phase flow in straight tubes has been correlated as a function of the Lockhart-Martinelli parameter (X_{tt}) by most of the authors in this field. A number of relationships of the form of eqs. (2.77) and (2.78) in the section (2.5.3) have been proposed.

$$X_{tt} = \left(\frac{1-x}{x}\right)^{0.9} \left(\frac{\rho_g}{\rho_f}\right)^{0.5} \left(\frac{\mu_f}{\mu_g}\right)^{0.1} \qquad (2.77)$$

$$\frac{h_{TP}}{h_f} = a \left(\frac{1}{X_{tt}}\right)^b \tag{2.78}$$

where h_{TP} is the heat transfer coefficient and h_f is the heat transfer coefficient for liquid flow alone.

Table (2.1) in section (2.5.3)shows the correlations of a and b of eq. (2.78).

Chen (96-1963) proposed a new correlation, which proved very successful in correlating all the forced convective boiling heat transfer data for water and organic systems. The proposed correlation covers both the "Saturated nucleate boiling region" and the "Two-phase forced convective region". It was assumed that both mechanisms occur to some degree over the entire range of the convection and that the contributions made by the two mechanisms are additive. This assumption is similar to that used by Rohsenow (95) in the "Partial boiling" region for subcooled conditions;

$$h_{TP} = h_{mic} + h_{mac} \tag{4.3.17}$$

where h_{TP} is the local heat transfer coefficient, h_{mic}, is the contribution from nucleate boiling, or microconvective heat transfer and h_{mac} is the contribution from single-phase convective, or macroconvective, heat transfer.

Based on the Dittus-Boelter relationship(97-1930) for a liquid flowing alone in a heated channel Chen (96) proposed for a two-phase fluid that:

$$h_{mac} = 0.023\ Re_{TP}^{0.8}\ Pr_{TP}^{0.4}\ \frac{k_{TP}}{D} \tag{4.3.18}$$

where k_{TP} is the thermal conductivity of two-phase flow.

For most fluids the Prandtl numbers of vapour and liquid are approximately the same except in the case of liquid metals. Furthermore,

the main resistance to heat transfer lies in the liquid layer near the wall. Chen suggested that Pr_{TP} and k_{TP} in eq. (4.3.18) should be determined from the liquid values.

The two-phase Reynolds number, Re_{TP}, is related to that for the liquid were it to be flowing alone, Re_f, by

$$F = \left(\frac{Re_{TP}}{Re_f}\right)^{0.8} \tag{4.3.19}$$

and Re_f is given by

$$Re_f = \frac{G(1-x)D}{\mu_f} \tag{4.3.19.1}$$

thus eq's. (4.3.17) - (4.3.19.1)

$$h_{mac} = 0.023 \left(\frac{G(1-x)D}{\mu_f}\right)^{0.8} \cdot Pr_f^{0.4} \cdot \frac{k_f}{D} \cdot F \tag{4.3.20}$$

Therefore h_{mac} can be found if F is known. Chen presumed F to be a purely hydrodynamic function and to depend on the Lockhart-Martinelli parameter, X_{tt}, defined by eq. (2.77).

As illustrated in Fig. (4.3.16) for the case of boiling from a superheated wall, in both pool boiling and forced convective boiling the degree of superheat is not in fact constant across the boundary layer but falls. Thus, the mean superheat temperature of the fluid in the bubble growth zone is lower than the wall superheat temperature (ΔT_{sat}). The difference between this lower mean superheat (ΔTe) and the wall superheat is small for the case of pool boiling, and was neglected by Foster and Zuber (98-1955). However, it is significant in the forced convection case and cannot be neglected since the boundary layer is much thinner and the temperature gradient much steeper.

In using Foster and Zuber's (98) formulation to represent microconvective (nucleate boiling) heat transfer, h_{mic}, in convective boiling

with effective values of the superheat and vapour pressure difference, Chen obtained the following correlation:

$$h_{mic} = 0.00122\{\frac{k_f^{0.79}\ C_{pf}^{0.45}\ \rho_f^{0.49}}{\sigma^{0.5}\ \mu_f^{0.29}\ i_{fg}^{0.24}\ \rho_g^{0.24}}\}\ .\Delta T_e^{0.24}\ .\ \Delta P_e^{0.75} \qquad (4.3.21)$$

where ΔP_e is the change in vapour pressure corresponding to temperature change ΔTe and ΔTe is the effective superheat into which bubble grows.

Chen defined a suppression factor, S, the ratio of the mean superheat (ΔTe) to the wall superheat ($\Delta Tsat$)

$$S = (\frac{\Delta Te}{\Delta Tsat})^{0.99} \qquad (4.3.22)$$

The exponent 0.99 allows S to appear to the first power in the final equation. Using the Clasius-Clapeyron equation, eq. (4.3.22) can be written

$$S = (\frac{\Delta Te}{\Delta Tsat})^{0.24}\ (\frac{\Delta Pe}{\Delta Psat})^{0.75} \qquad (4.3.23)$$

Combining with eq. (4.3.21) which remains valid for the effective superheat and becomes

$$h_{mic} = 0.00122\ \{\frac{k_f^{0.79}\ C_{p.f}^{0.45}\ \rho_f^{0.49}}{\sigma^{0.5}\ \mu_f^{0.29}\ l_{fg}^{0.24}\ \rho_g^{0.24}}\}\ .\Delta Tsat^{0.24}\ .\Delta Psat^{0.75}\ (S) \qquad (4.3.24)$$

The suppression factor, S, is a function of the two-phase Reynolds number and would approach unity at zero flow rate and zero at infinite flow rate.

The operations were carried out under the following conditions:

flow direction	upwards
water flow rate	3.39×10^4 2.57×10^5 kg/m^2h
inlet water temperature	64-84°C
steam flow rate	6.86×10^4 1.67×10^5 kg/m^2h
inlet steam temperature	107°C
pressure of steam-water mixture	0.127 0.134 MN/m^2
inlet vapour mass quality (weight)	32~83%
input heat flux	
Coil A	$8.604 Kw/m^2$ ($7399 Kcal/m^2h$)
Coil B	$9.245 Kw/m^2$ ($7951 Kcal/m^2h$)
Coil C	$9.235 Kw/m^2$ ($7942 Kcal/m^2h$)

Measured wall temperatures are plotted along the pipe length in Figs. (4.3.7a) - (4.3.9g) in the section (4.3.3) and the wall temperature of each position at the fixed flow condition is averaged. The local two-phase heat transfer coefficients, h_{TPC}, at four positions (0^o, 90^o, 180^o and 270^o) on the periphery are evaluated through the process, described previously in eq's. (4.3.17) - (4.3.24) and plotted against the inlet vapour mass quality (x) in Figs. (4.3.17a) - (4.3.17c) for three different coil diameters.

The nucleate boiling heat transfer coefficient defined by Jens-Lottes (99-1951):

$$\Delta T_{sat} = 0.82\, q^{1/4} \exp\frac{-P}{63.3} \qquad (4.3.25)$$

is marked at x=0 for comparing with h_{TPC} in these figures.

Several interesting features, including differences in profiles from the heat transfer coefficient of a straight tube were observed from these figures.

(1) The local heat transfer coefficients at the upper side are significantly higher than those of the other three sides. Also their values increase steeply if the steam quality was greater than 65% in all coils.

This result is at variance with the reports of Bell and Owhadi (65) and Kozeki (48). The discrepancy is due to a different total mass flow rate, which in the present work was considerably smaller. Due to the effect of gravity, the liquid film becomes thicker at the lower and inner sides leaving a thin film on the upper side. Hence the highest value of heat transfer coefficient occurs at the upper side.

This flow mechanism is already discussed in section (4.3.3.).

(2) At the higher steam quality region (x>50%) the local heat transfer coefficients at the outer side lie between those for the upper sides and the inner and lower sides. This phenomena and section (1) can be explained as follows; the droplets were entrained from the inner or lower sides by shearing stresses, and were carried in the gas core and then deposited on the liquid film at the outer side. These momenta of entrainment and deposition of the droplets disturb the stable temperature profile in the liquid film at the upper and outer sides and these mechanisms improve the heat transfer coefficients at the upper and outer sides.

At the lower steam quality region (x<50%) the heat transfer coefficients at the outer side have values at or slightly less than those of the inner side.

(3) When the steam quality is smaller than 50% the heat transfer coefficients at the inner, lower and outer sides have similar values to the nucleate boiling heat transfer coefficient obtained by Jens-Lottes (99).

The values of two-phase heat transfer coefficient at all four positions increase at the point where the steam quality is greater than 50%.

This means that the convective boiling heat transfer is the dominant mechanism in low steam quality region. Whereas in the high steam quality region the most important feature is the onset of nucleate boiling which improves the two-phase heat transfer.

(4) In Coil C, the profile of heat transfer coefficient at the upper side is clearly separated from those of the other three sides at all steam qualities. On the other hand, in Coils A and B all profiles closely resemble each other. This feature is due to the effect of the gravity force on the water film which is most significant for the largest diameter coil (Coil C).

However, in view of the fact that the results for the three coils give essentially identical profiles (see Figs. (4.3.17 a-c)), it may be assumed that, in the range of coil diameter investigated, the effect of the ratio of tube to coil diameter is not important.

The ratios between two-phase heat transfer coefficient (h_{TP}) and heat transfer coefficient for liquid alone flow, (h_f), are evaluated through the process described previously and are correlated against the reciprocal of the Lockhart-Martinelli parameter, $(\frac{1}{X_{tt}})$. These values were plotted in Figs. (4.3.18a-c) together with the Schrock-Grossman correlation (100-1959).

The empirical correlations which have been proposed for the two-phase convective heat transfer coefficient are generally formed as in eq. (2.78).

The heat transfer coefficient for liquid flow alone, h_f, of eq. (2.78) is evaluated from eq. (2.43).

$$h_{fc} = \frac{Re_f^{5/6}}{41.0} \cdot Pr_f^{0.4} \cdot \left(\frac{a}{R}\right)^{1/12} \left[1 + 0.061 \left\{Re \left(\frac{a}{R}\right)^{2.5}\right\}^{-1/6}\right] \frac{k_f}{D} \qquad (2.43)$$

From Figs. (4.3.18a) - (4.3.18c), a and b of eq. (2.78) are correlated in Table (4.3.2) which also includes the data of Bell and Owhadi (65), who used Tong's (101-1965) correlation, and Kozeki (48).

The empirical formulae for the ratio $(\frac{h_{TPC}}{h_{fc}})$ at four positions (0^o, 90^o, 180^o and 270^o) in three coils, yielded from the present work, are as follows:

The upper side (0^o)

$$\frac{h_{TPC}}{h_{fc}} = 4.21 \left(\frac{1}{X_{tt}}\right)^{0.73} \qquad (4.3.26)$$

The outer side (90^o)

$$\frac{h_{TPC}}{h_{fc}} = 2.81 \left(\frac{1}{X_{tt}}\right)^{0.72} \qquad (4.3.27)$$

The lower and inner sides (180^o and 270^o)

$$\frac{h_{TPC}}{h_{fc}} = 2.50 \left(\frac{1}{X_{tt}}\right)^{0.74} \qquad (4.3.28)$$

Schrock-Grossman's correlation (100) and eq. (4.3.28) are almost identical and their correlation on average gives rather greater values than the data for the inner and lower sides.

Fig. (4.3.19) shows the maximum and minimum ratios of $(\frac{h_{TPC}}{h_{fc}})$. The experimental conditions of the three studies in Fig. (4.3.19) are different (e.g. pressure, heat flux, diameter ratio $(\frac{a}{R})$). However, all ratios between the convective two-phase heat transfer coefficient and heat transfer coefficient for liquid flow alone, $(\frac{h_{TPC}}{h_{fc}})$, can exist in the following region:

Positions	0^o		90^o		180^o		270^o		average	
	a	b	a	b	a	b	a	b	a	b
Present work										
Coil A	5.22	0.68	3.27	0.71	2.22	0.75	2.22	0.75	3.23	0.72
Coil B	3.20	0.81	2.37	0.75	2.37	0.75	2.37	0.75	2.58	0.78
Coil C	4.20	0.71	2.80	0.71	2.80	0.71	2.80	0.71	3.15	0.71
Average	4.21	0.73	2.81	0.72	2.5	0.74	2.5	0.74	2.97	0.74
Bell & Owhadi (65) Small coil	1.47	0.87	1.7	1.01	1.47	0.87	1.35	0.79	1.50	0.89
Large coil	1.6	0.86	1.91	0.98	1.67	0.86	1.54	0.78	1.70	0.87
Average	1.57	0.865	1.81	0.995	1.57	0.865	1.45	0.785	1.60	0.88
Kozeki (48)	2.51	0.75	2.5	0.83	2.5	0.75	1.7	0.68	2.5	0.75

Table (4.3.2) Coefficients in convective heat-transfer equation from eq. (2.78)

$$1.7\left(\frac{1}{X_{tt}}\right)^{0.68} \leq \frac{h_{TPC}}{h_{fc}} \leq 5.22\left(\frac{1}{X_{tt}}\right)^{0.68} \qquad (4.3.29)$$

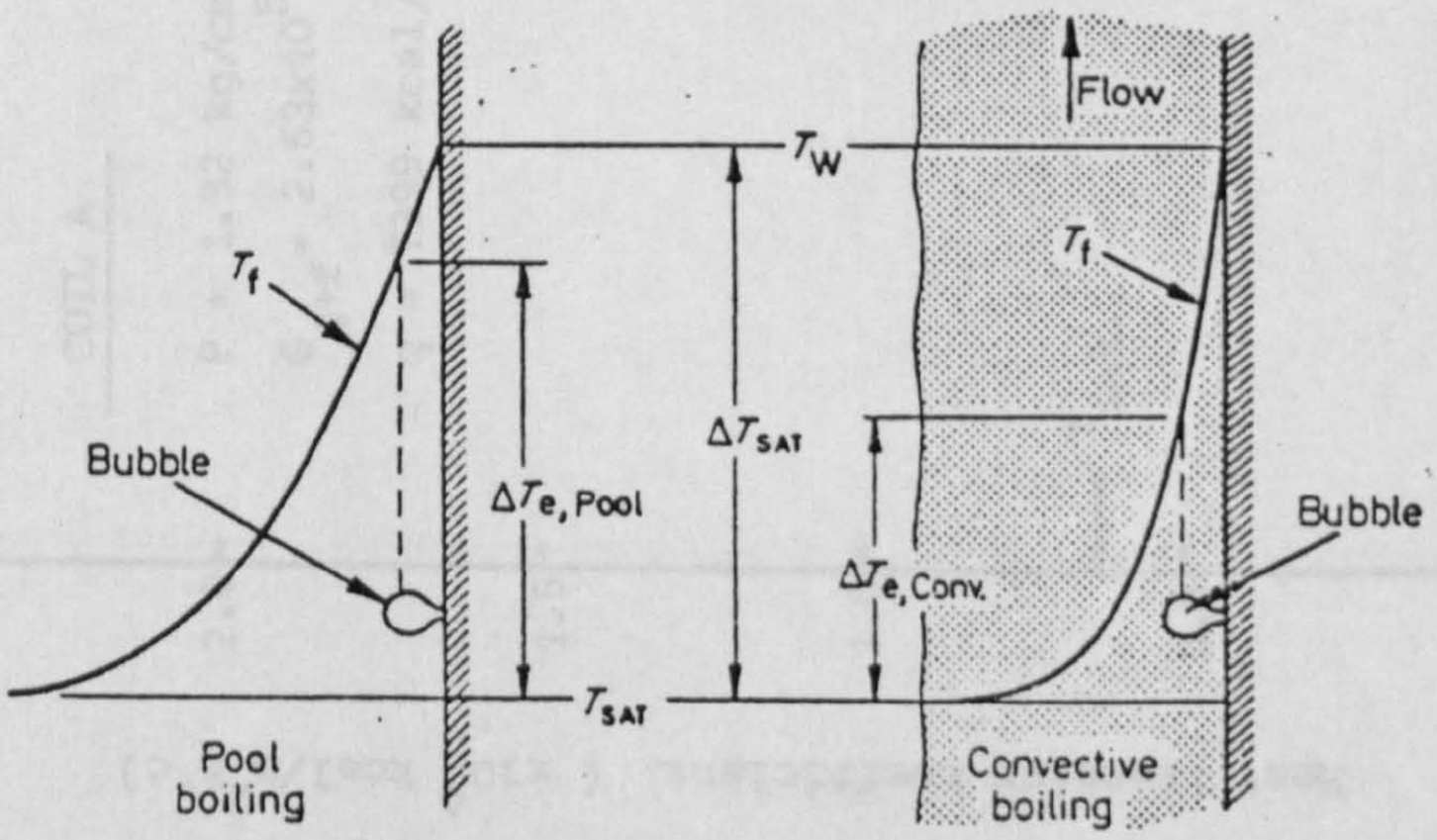
for atmosphere $< P < 30^{Kg/cm^2}g$,

$$20 < \frac{R}{a} < 50 ,$$

and $$5 < \frac{1}{X_{tt}} < 80$$

Schrock-Grossman's convective boiling correlation approximates very closely to the average of the maximum and minimum values defined in eq. (4.3.29). This equation is valid between 5 and 100 of $(\frac{1}{X_{tt}})$, in the low quality range $(\frac{1}{X_{tt}} < 5)$, but Bell and Owhadi (65) have observed that the data had a scatter with higher points having values sometimes several times that of the lowest. This is due to the existence of a significant nucleate boiling component.

The scatter in the data increases in the high quality range $(80 < \frac{1}{X_{tt}}$, corresponding to $x>0.8)$, and this is attributed to disruption of the liquid film. This occurs when the liquid supply is insufficient to maintain a continuous film and due to the difficulties of obtaining highly accurate data in the very high quality range.



Temperature Profiles for Pool Boiling and for Convective Boiling with Same Superheat , from Chen (96).

Fig. (4.3.16)

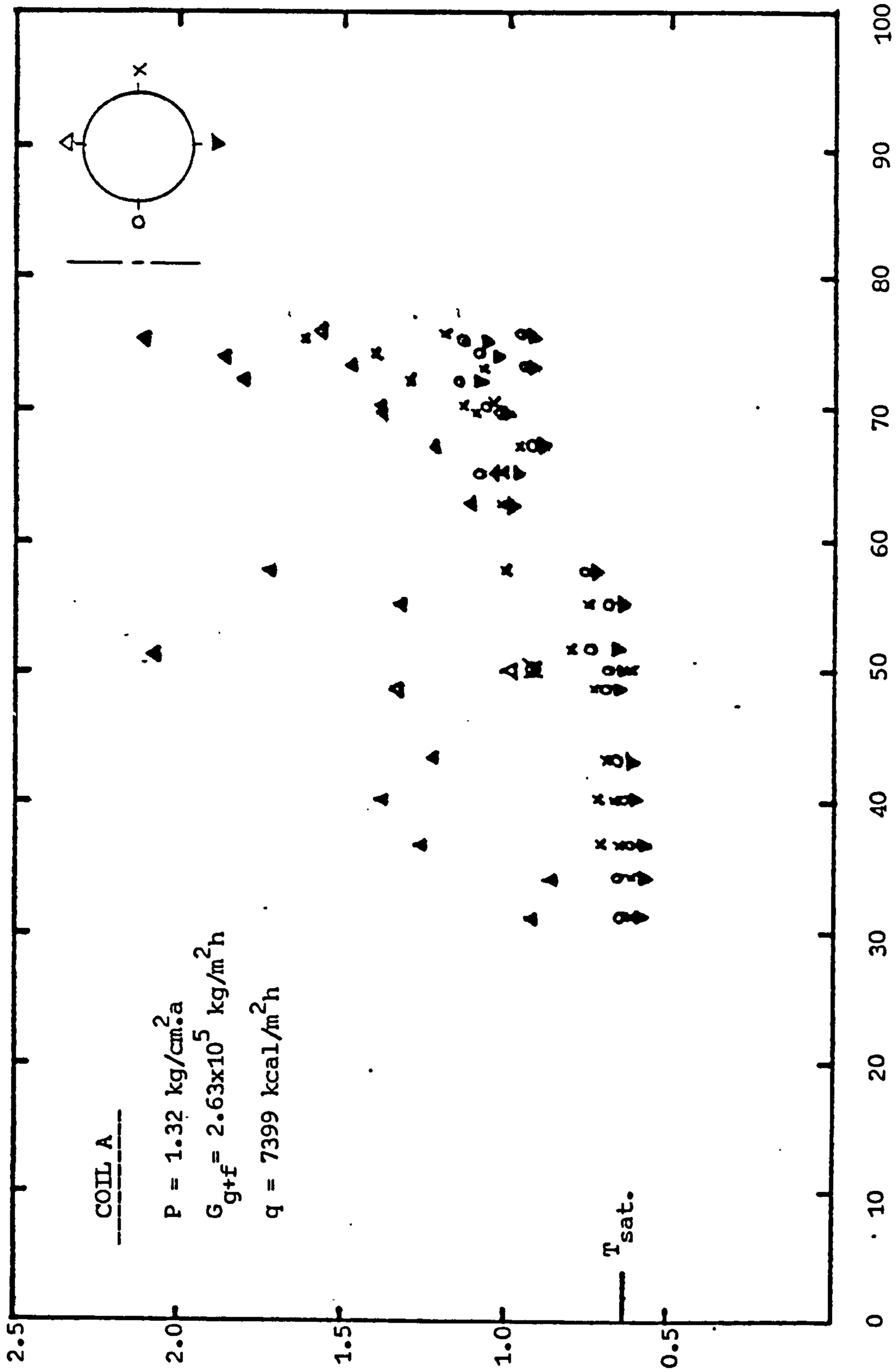


Fig.(4.3.17 a) : Local heat transfer coefficient profiles of two-phase flow.

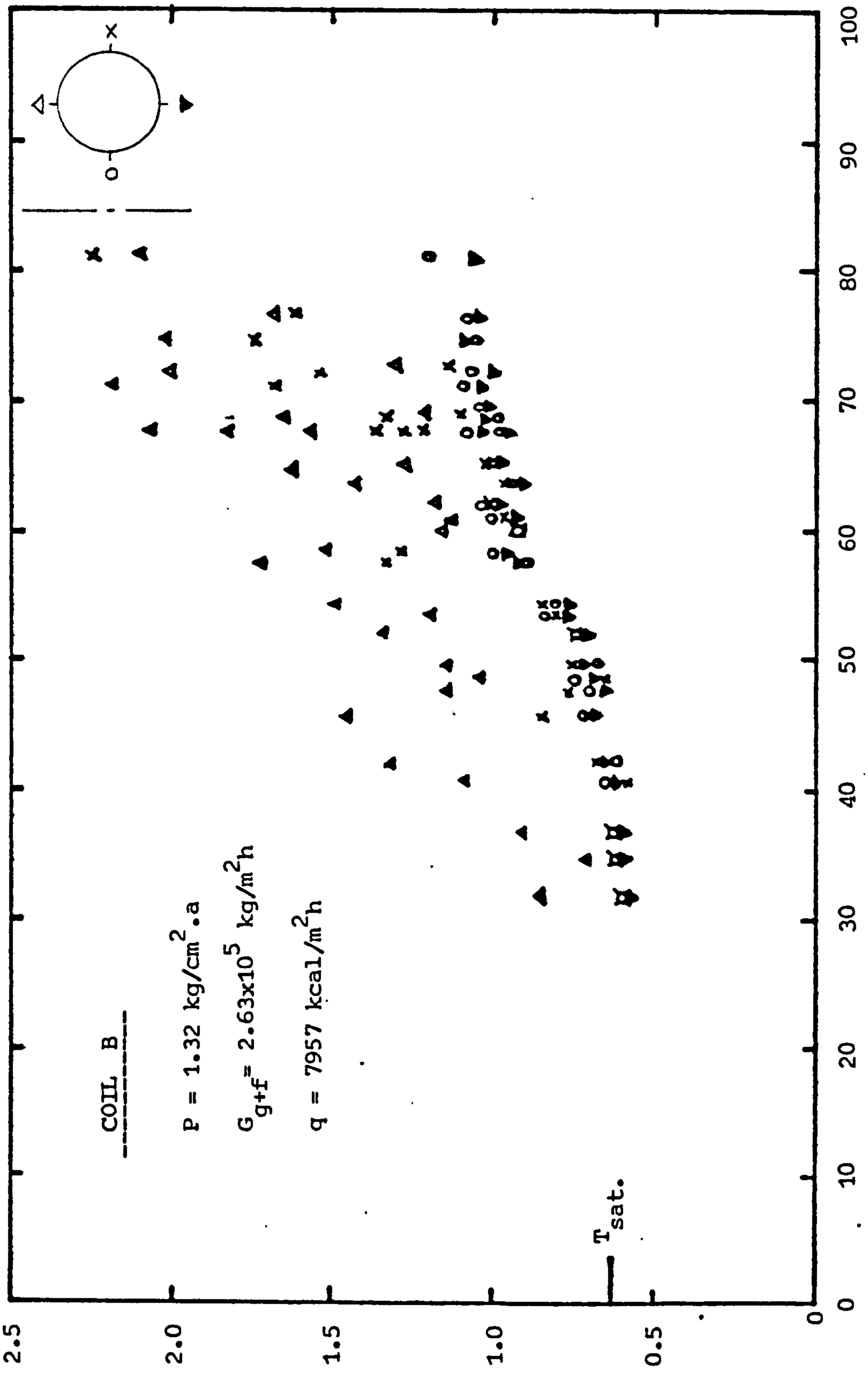


Fig. (4.3.17 b) : Local heat transfer coefficient profiles of two-phase flow;

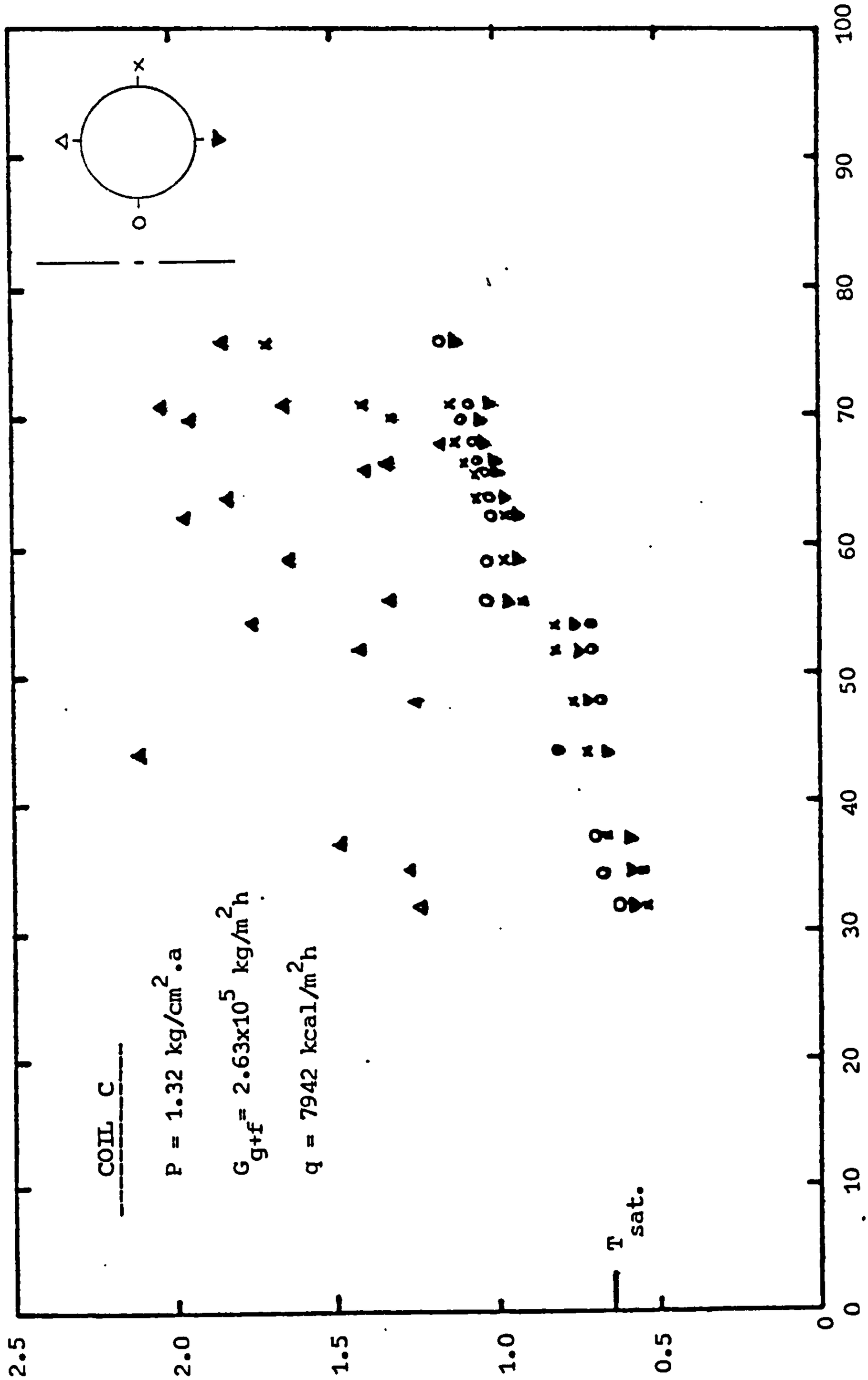


Fig. (4.3.17 c) : Local heat transfer coefficient profiles of two-phase flow.

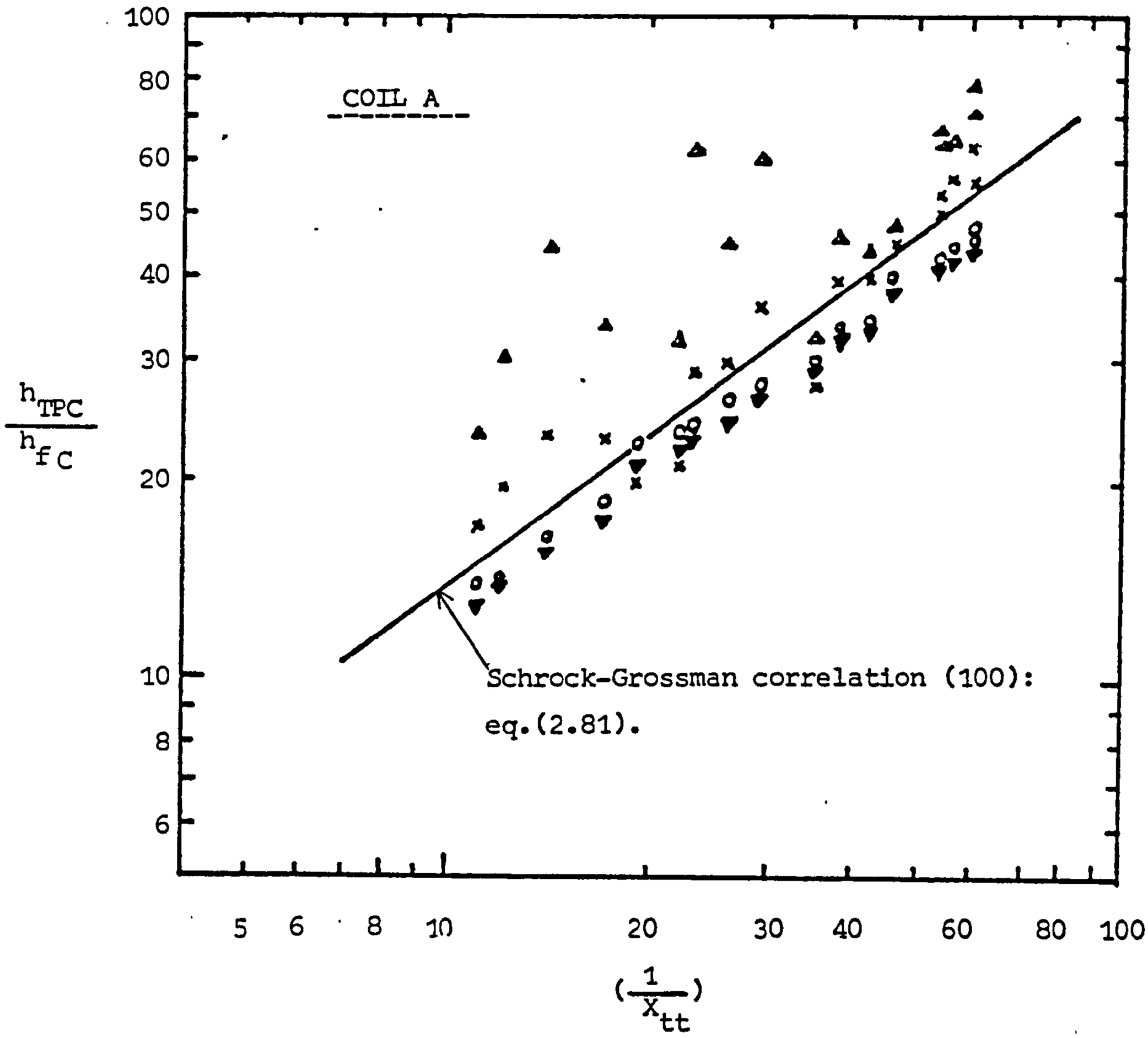


Fig. (4.3.18 a) : Ratios of heat transfer coefficients between two-phase flow and water single-phase flow, in Coil A, values are obtained from Fig. (4.3.17 a).

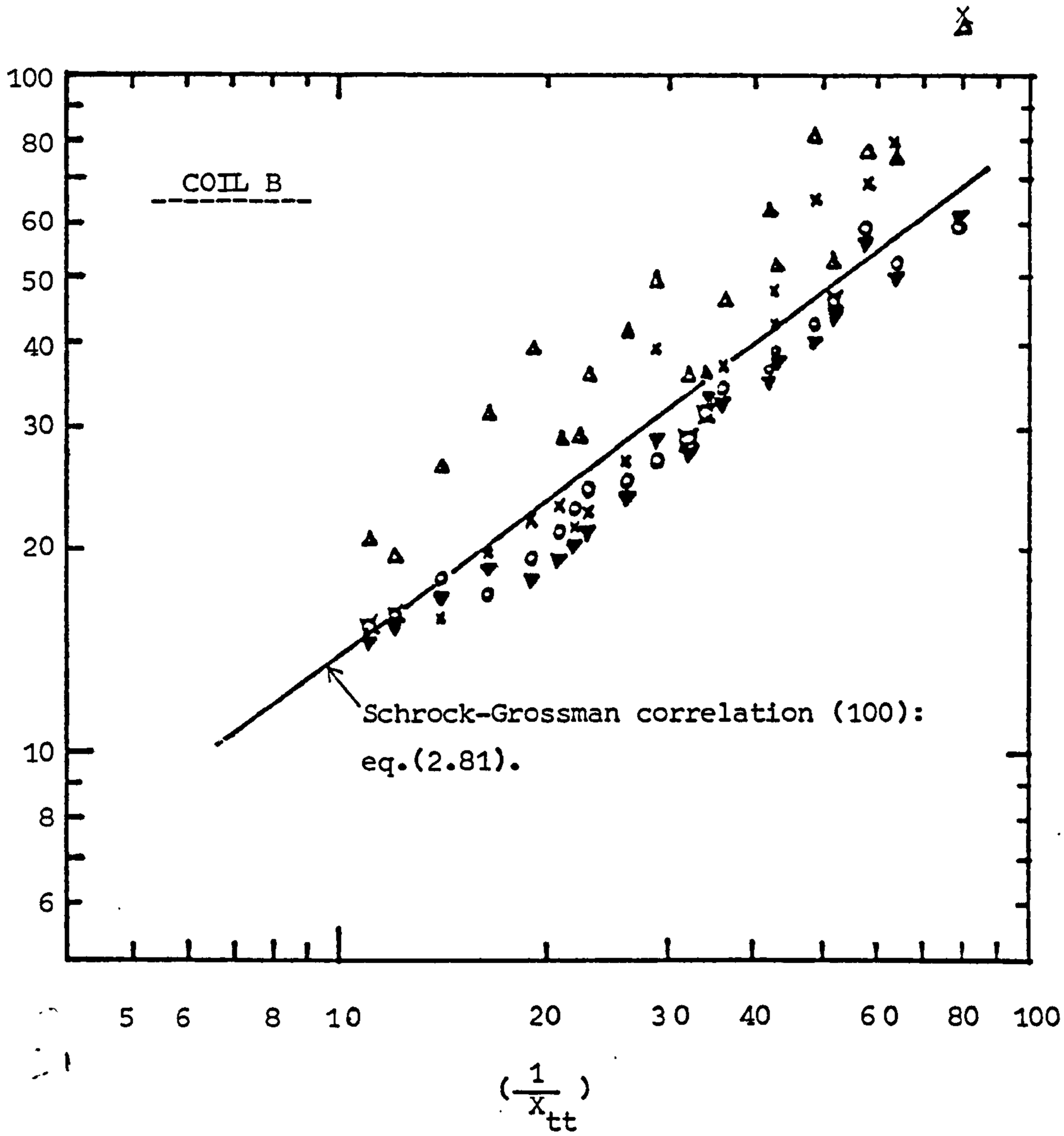


Fig. (4.3.18 b) : Ratios of heat transfer coefficients betwween two-phase flow and water single-phase flow in Coil B, values are obtained from Fig. (4.3.17 b).

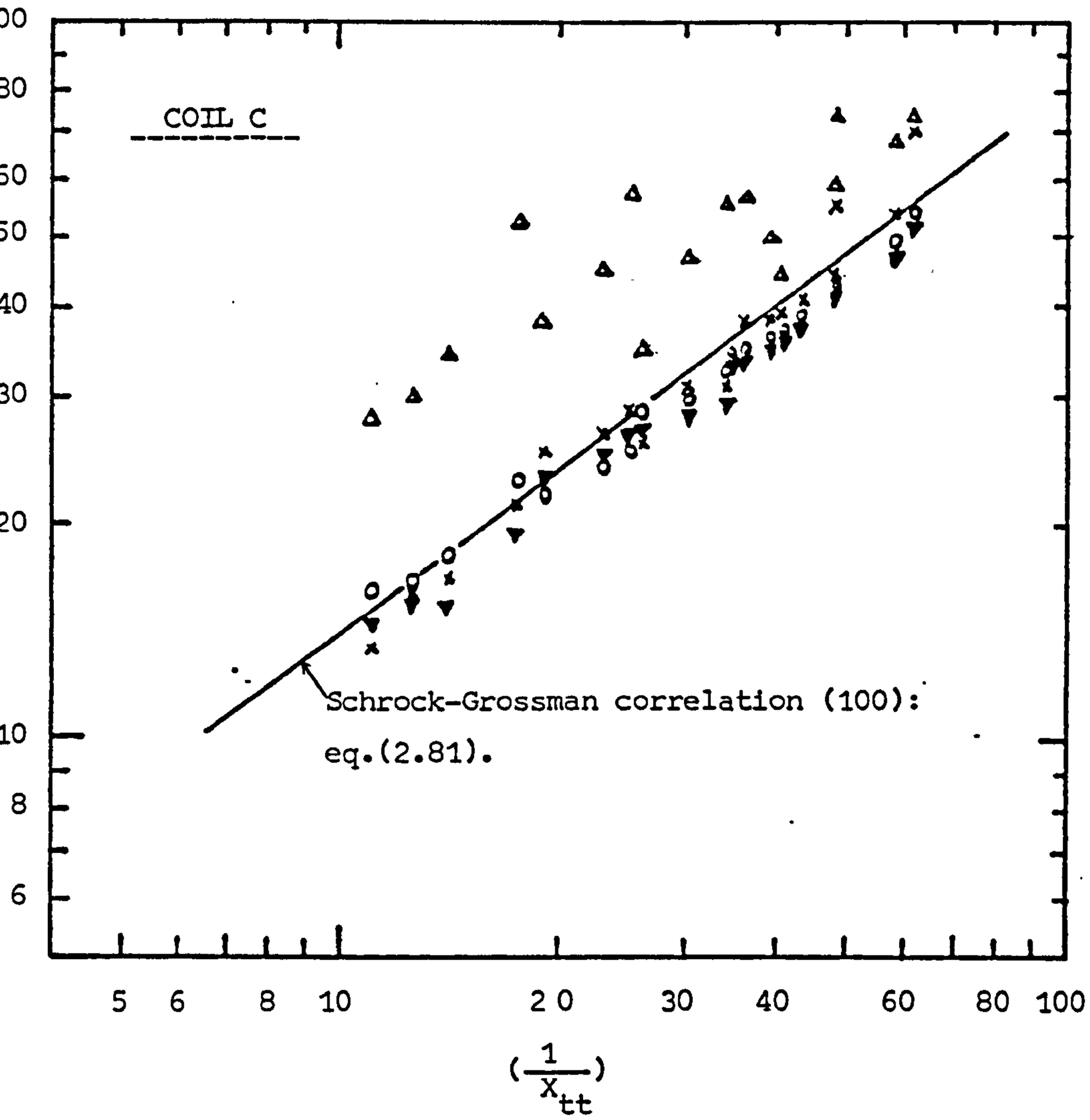


Fig. (4.3.18 c) : Ratios of heat transfer coefficients between two-phase flow and water single-phase flow in Coil C, values are obtained from Fig. (4.3.17 c).

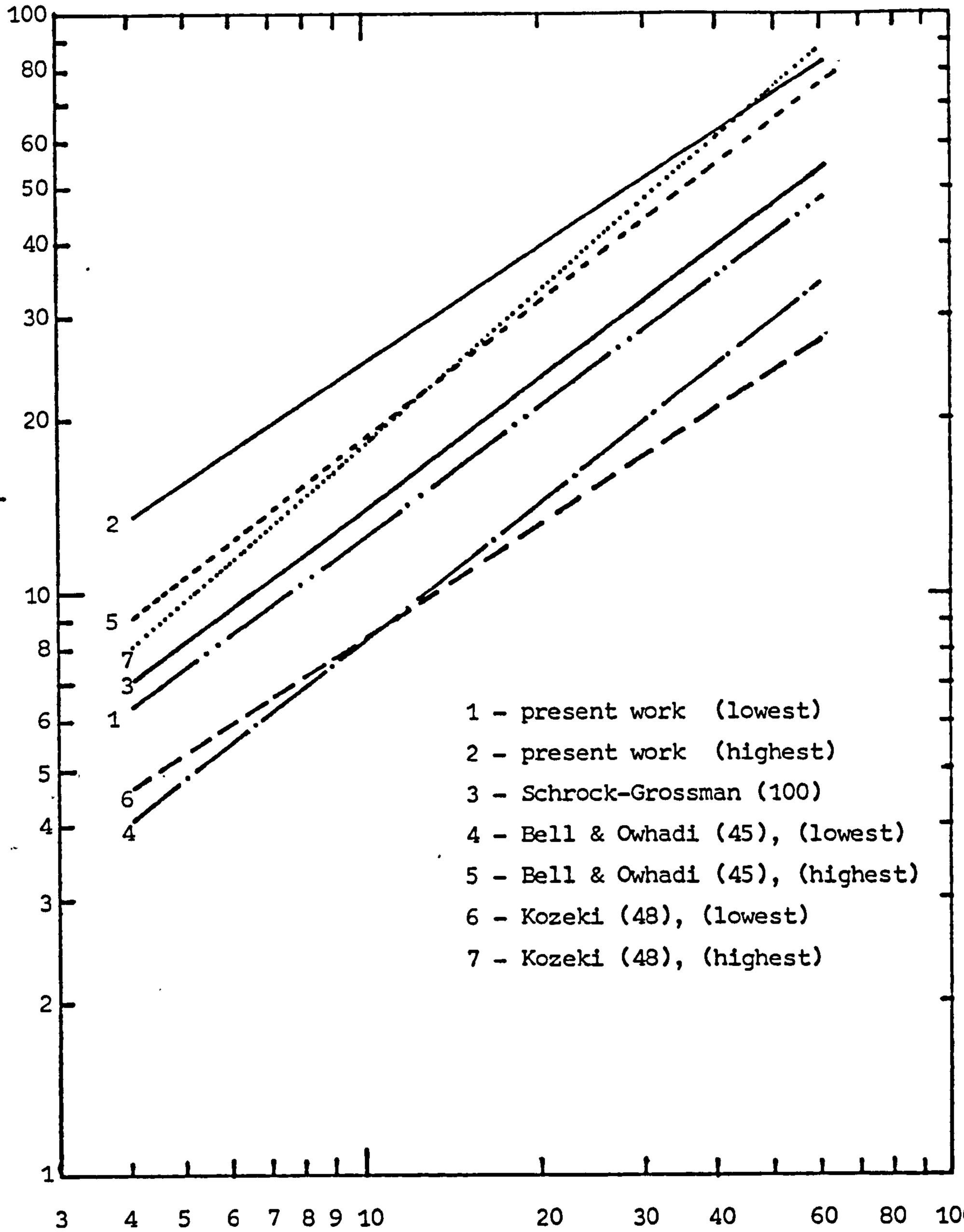


Fig. (4.3.19) : Comparison of the heat transfer coefficient ratios of the present work with other investigators'.

4.3.5 Burnout Phenomena

Terms of 'Burnout', 'Dryout', and 'Departure from nucleate boiling'(DNB) are employed almost synonymously in the field of heat transfer. The name "Burnout" has gained wide acceptance, but according to Hewitt (62) it must be used advisedly.

Burnout is defined here as follows: In a situation where the surface heat flux is controlled (e.g. electrically) burnout is said to occur when a small increase in surface heat flux gives rise to an inordinate rise in the wall temperature.

Describing the phenomenon as DNB is actually incorrect because nucleate boiling is, in fact, suppressed well before the burnout point. The term 'Dryout' implies a slightly different mechanism.

The mechanisms of the temperature rise that are considered in the present work are as follows:

(i) Film dryout: Here burnout simply corresponds to the point at which the liquid film dries out completely as a result of evaporation and liquid entrainment along the channel.

(ii) Sudden disruption on liquid film: The liquid film will be disrupted into large interfacial waves, and it is sometimes suggested that burnout corresponds to the point at which disruption occurs (e.g. by Lis and Strickland (102-1970), Robertson (103-1972) and Butterworth and Pulling (104-1972)).

The experimental operations were done under the following conditions:

flow direction	upwards
total mass flow rates	$1.91 \times 10^5 \sim 2.26 \times 10^5$ kg/m^2h
input heat fluxes	$3.30 \times 10^3 \sim 7.95 \times 10^3$ $Kcal/m^2h$
pressure	0.13 MN/m^2

The temperature measurements at four different input heat fluxes were taken by the same procedure as in section (4.3.3). The wall temperature rise moves from a point towards the tube exit to one near the tube entrance at medium and high steam qualities. These temperature differences at the upper side between the downstream and upstream are $7^{o}C \sim 10^{o}C$. However, the wall temperature rises along the pipe length and showed an identical tendency in all the experiments. Therefore, the measured wall temperatures at the four positions on the periphery (0^{o}, 90^{o}, 180^{o} and 270^{o}) were averaged and plotted against the inlet steam qualities. See Figs. (4.3.20a) - (4.3.22d). The saturation temperature is marked at x=0 in these figures.

From these figures, obviously the point of inception of burnout moves from the upper side to the outer and lower sides. The burnout at the upper side occurs at lower steam qualities than that for the outer side but the difference between these two burnout qualities is very small. The temperature gradient of the outer side is steeper than that of the upper side thus the wall temperatures at the outer side exceed the upper side at the higher steam qualities.

This result is similar to the burnout at the lowest mass flow rate of Fig. (2.27) reported by Kozeki et al, (53,80) in section (2.5.4).

Burnout at the inner side was not detected in the present work due to a lower value of the input heat flux being used. From Figs. (4.2.12a)-(4.2.13c) in section (4.2.2.2) the wall temperature at the inner side in the steam flow remains at a slightly higher value than the saturation temperature for about 1.5m from the test section entrance. This means that tiny droplets, which may be formed either by stagnation phenomena at the inner side or by the wet saturation

steam from the steam generator, tend to gather on the inner side. Owhadi et al (47) observed a complete wetting of the tube wall for all steam qualities up to a very high value (99%).

It may be deduced from the wall temperature profiles at the upper side shown in Figs. (4.3.7a) to (4.3.9f) that a very thin film still exists at the upper side after the wall temperature reaches the burn-out temperature. This 'film-presence' phenomenon is a typical feature of helically-coiled tube.

Hence, the temperatures at the point of film dryout (mechanism (i)) are about $10^{o}C$ higher than the saturation temperature and are plotted in Fig. (4.3.23). This shows the heat flux variations of three positions (the upper, outer and lower) on the tube periphery at around the burnout steam qualities in three different Coils. Fig. (4.3.24) shows the burnout points of the three different Coils at three different positions on the same axes as Fig. (4.3.23).

From these two figures the burnout point at the upper and outer sides of the larger coil (A) occurs earlier and at lower burnout steam qualities than that of smaller coils. The burnout point at the outer side occurs at almost the same burnout quality (x=85%) in all three Coils. Fig. (4.3.25) reported by Carver et al (68) is similar to the present result.

The points of inception of burnout are also plotted in Figs. (4.3.26a) - (4.3.26c) by Baker's Map (50). All points are plotted in the Wavy-Stratified flow regions shown in Fig. (4.3.3a) - (4.3.3c) in the section (4.3.1). It may be concluded from these distributions of burnout points that the inception of burnout in helically-coiled tubes at low pressures (up to about 20 atm) and low mass flow rates is determined by the process of transition to completely stratified flow and film inversion phenomena.

The various mechanisms of burnout in the helically coiled tube are analysed in the present work and the investigations of several workers (e.g. Carver et al (68), Awhadi et al (47), Miropolski and Pikus (69), Cumo* et al (70) and Kozeki (53 . 80)).

At high pressures (more than 160 atm) the position of burnout is very strongly influenced by the mass velocity. At high mass velocities centrifugal forces become predominant and the water film is centrifuged to the outer side so that burnout occurs on the inner surface of the coil. This results in the burnout pattern shown in (a) in Fig. (4.3.27) ... (Carver, Miropolski and Pikus, and Cumo et al).

At low mass velocities gravity effects dominate, so that most of the water film is flowing along the bottom surface of the tube and burnout occurs near the upper-inner (330^{o}) surface shown in the pattern (b) in Fig. (4.3.27).

At low pressures (atmosphere to about 20 atm) and high mass velocities in air-water or steam-water simulations a reversal of this process has been observed. In this case, the secondary flow patterns induced by the coil are powerful enough to carry the water from the outer side to the inner surface of the coil, which results in an initiation or burnout on the outside of the coil shown as the pattern (c) in Fig. (4.3.27) ... (Kozeki (80)).

At low mass flow rate a similar phenomenon to the pattern (b) occurs except that the water film tends to flow near the inner-lower surface of the tube due to the balance between gravitational force and the secondary flow force, i.e. a similar mechanism to film inver-

---

*They used Freon-12 as fluid material.

sion. Thus, burnout occurs on the upper or upper-outer sides as shown in pattern (d) in Fig. (4.3.27) ... (The present work and Kozeki (53)).

At atmospheric pressure and high mass flow rates it is thought that the secondary flow in the vapour core exerts a drag on the liquid phase forcing it to flow to the inner side. Owhadi et al (47) agreed with this explanation of the mechanism and reported burnout occurring at the inner side. The mechanism described results in pattern (e) shown in Fig. (4.3.27). The present work and Kozeki (53) shows that burnout occurred on the outer side where the water film is at its thinnest.

Sufficient experimental results covering the whole range of pressures are not available to predict precisely the change-over point of the patterns.

The overall effect of the centrifugal force introduced by the helically-coiled tube is to postpone the burnout point to a higher burnout quality than would occur for the same mass velocity in a vertical straight tube.

For a once-through system this means that the steam velocity at the burnout point is high. However, in practice this is completed by the peripheral variation of heat transfer around the tube circumference. In the case of a recirculation boiler, there is a clear advantage in being able to operate safely up to a high burnout quality, and in this respect helically-coiled tubes have certain advantages over straight tubes.

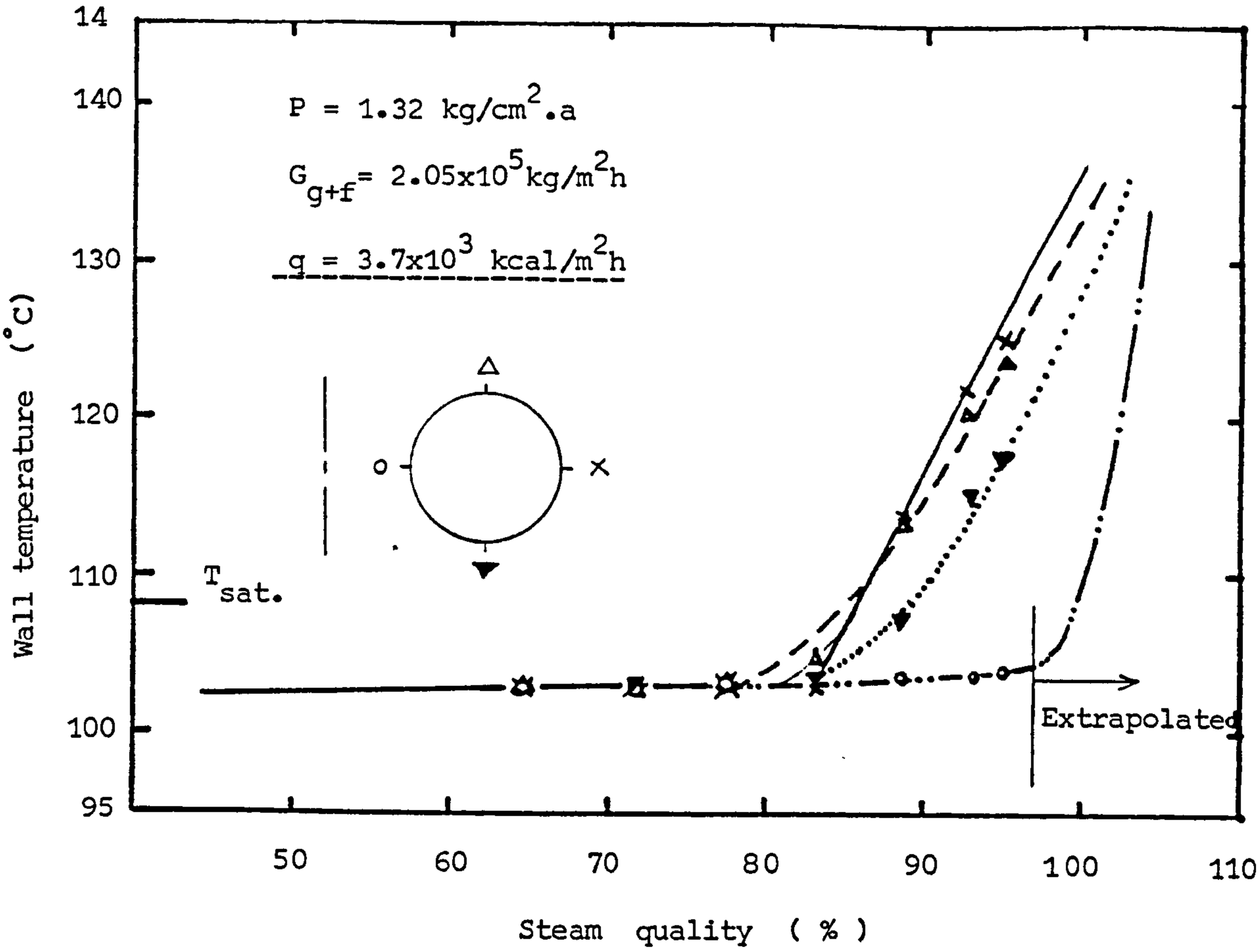


Fig.(4.3.20a) : Onset of burnout in Coil A.

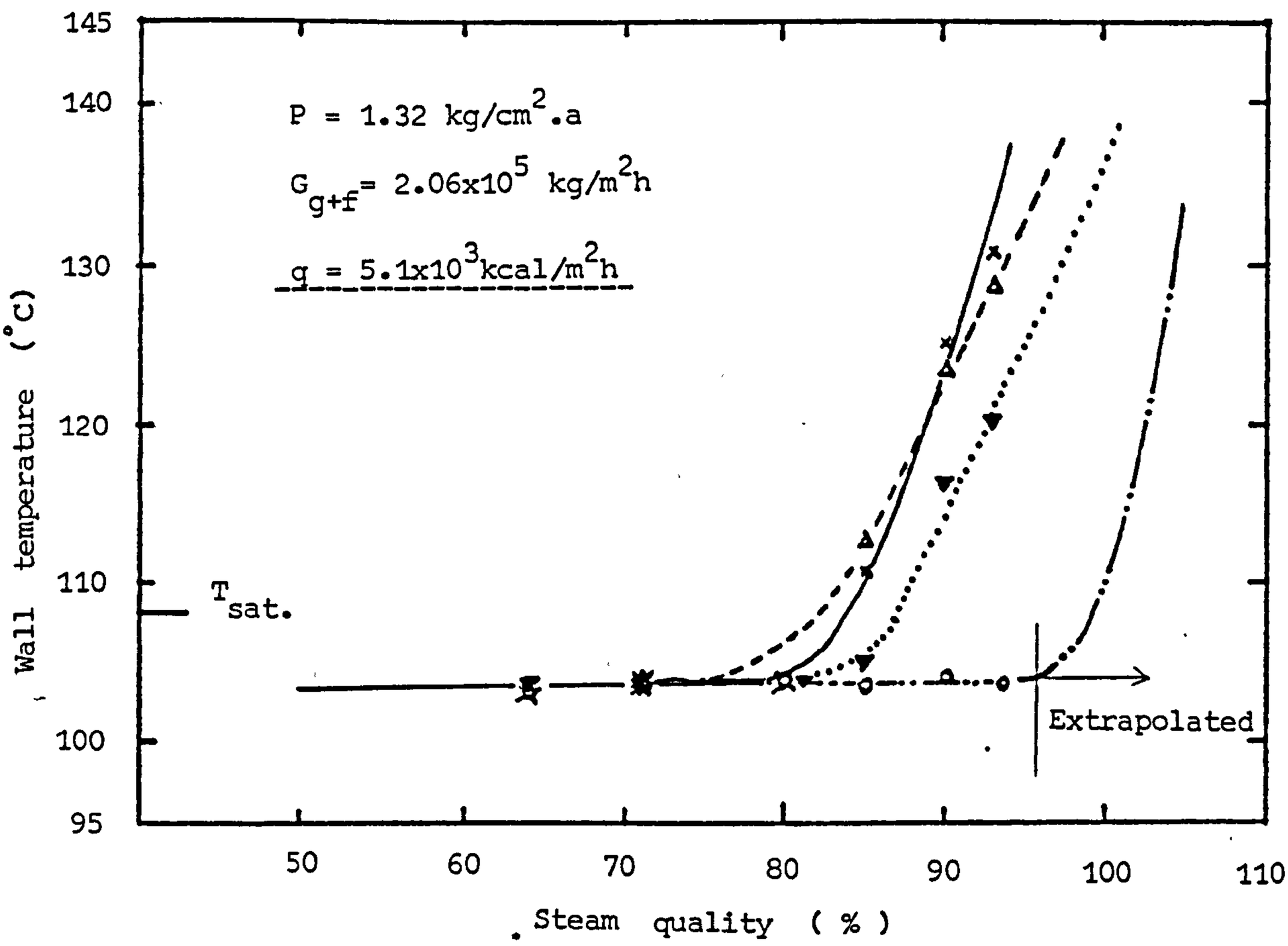


Fig.(4.3.20b) : Onset of burnout in Coil A.

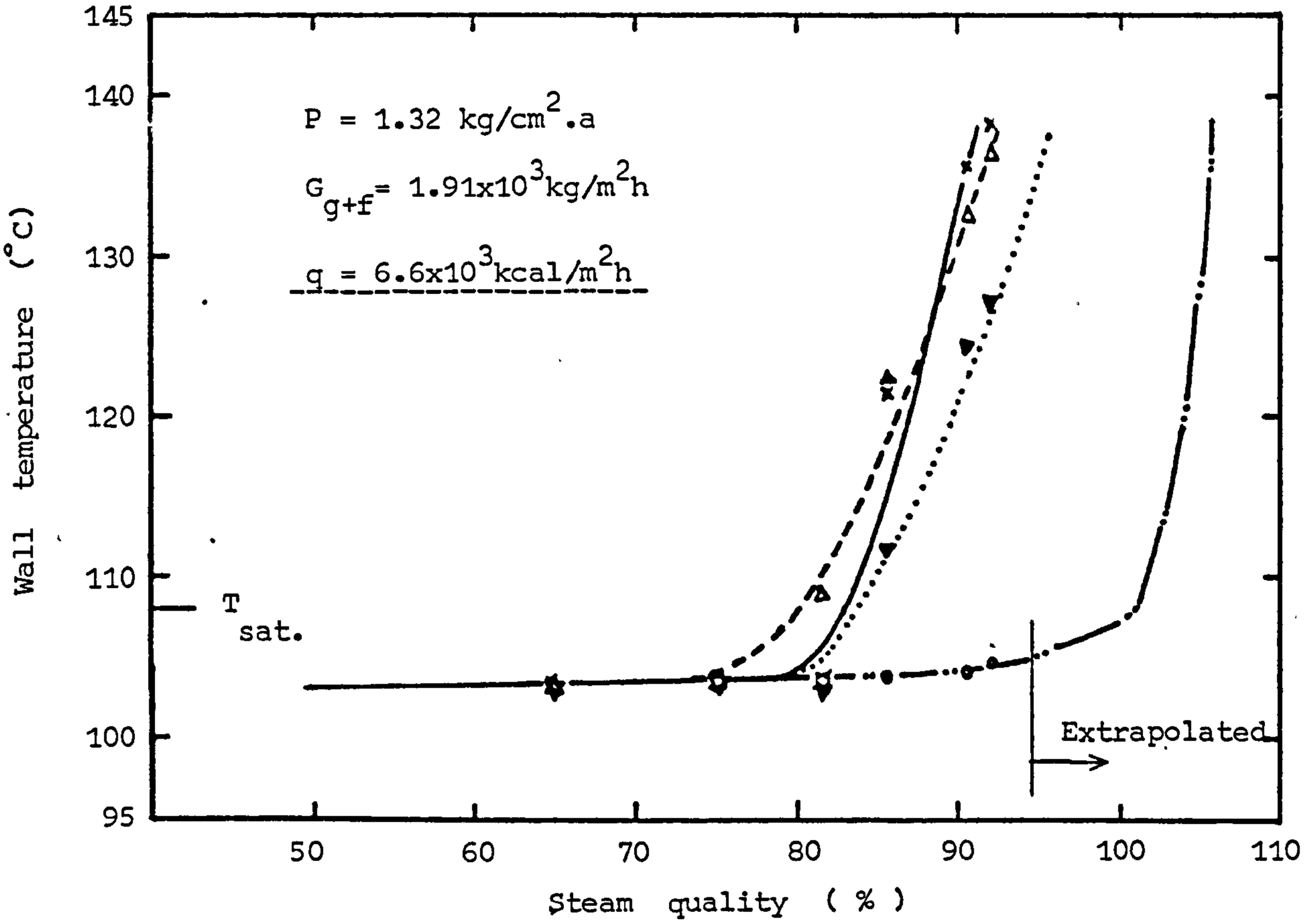


Fig. (4.3.20 c) : Onset of burnout in Coil A.

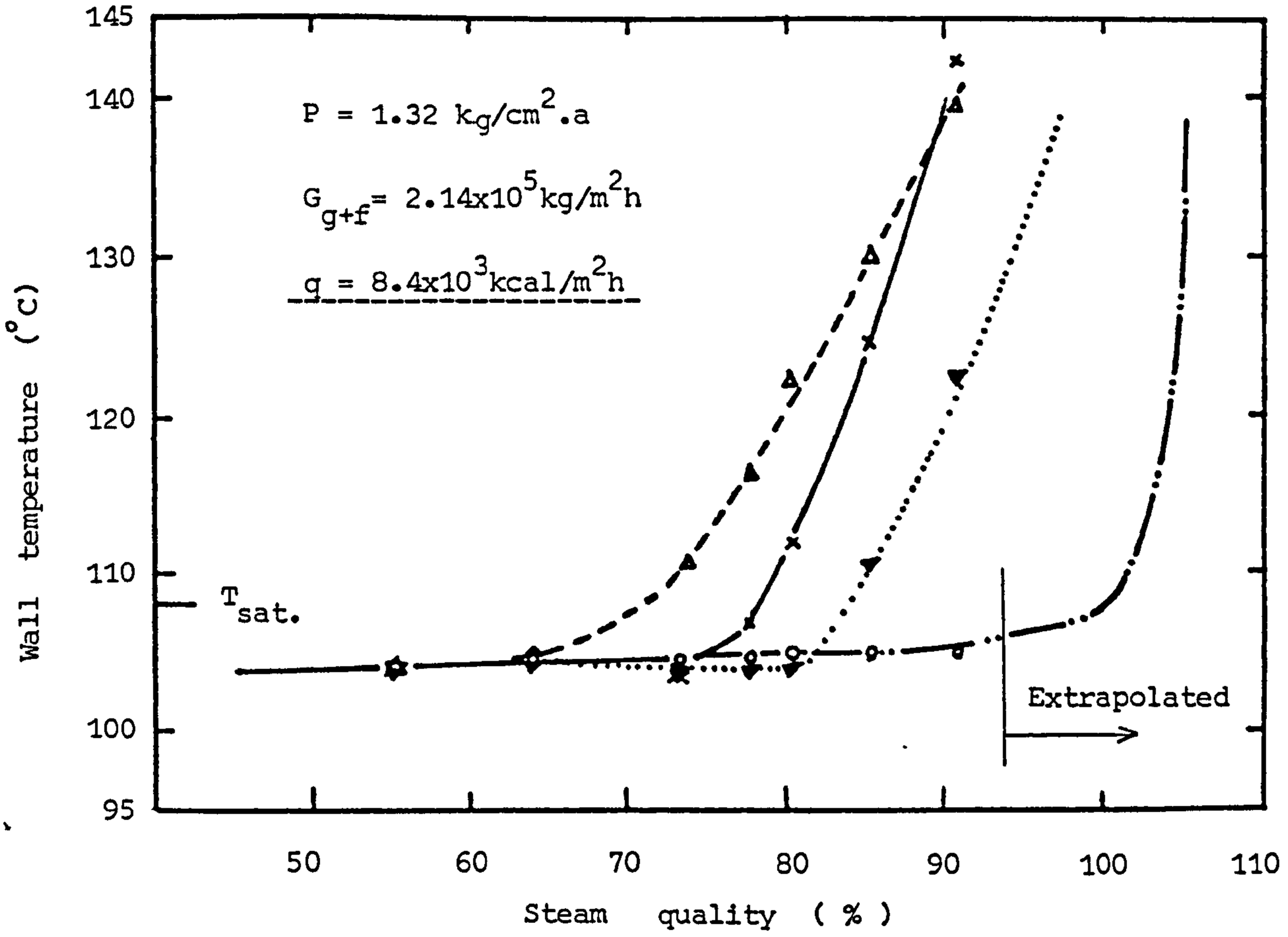


Fig. (4.3.20 d) : Onset of burnout in Coil A.

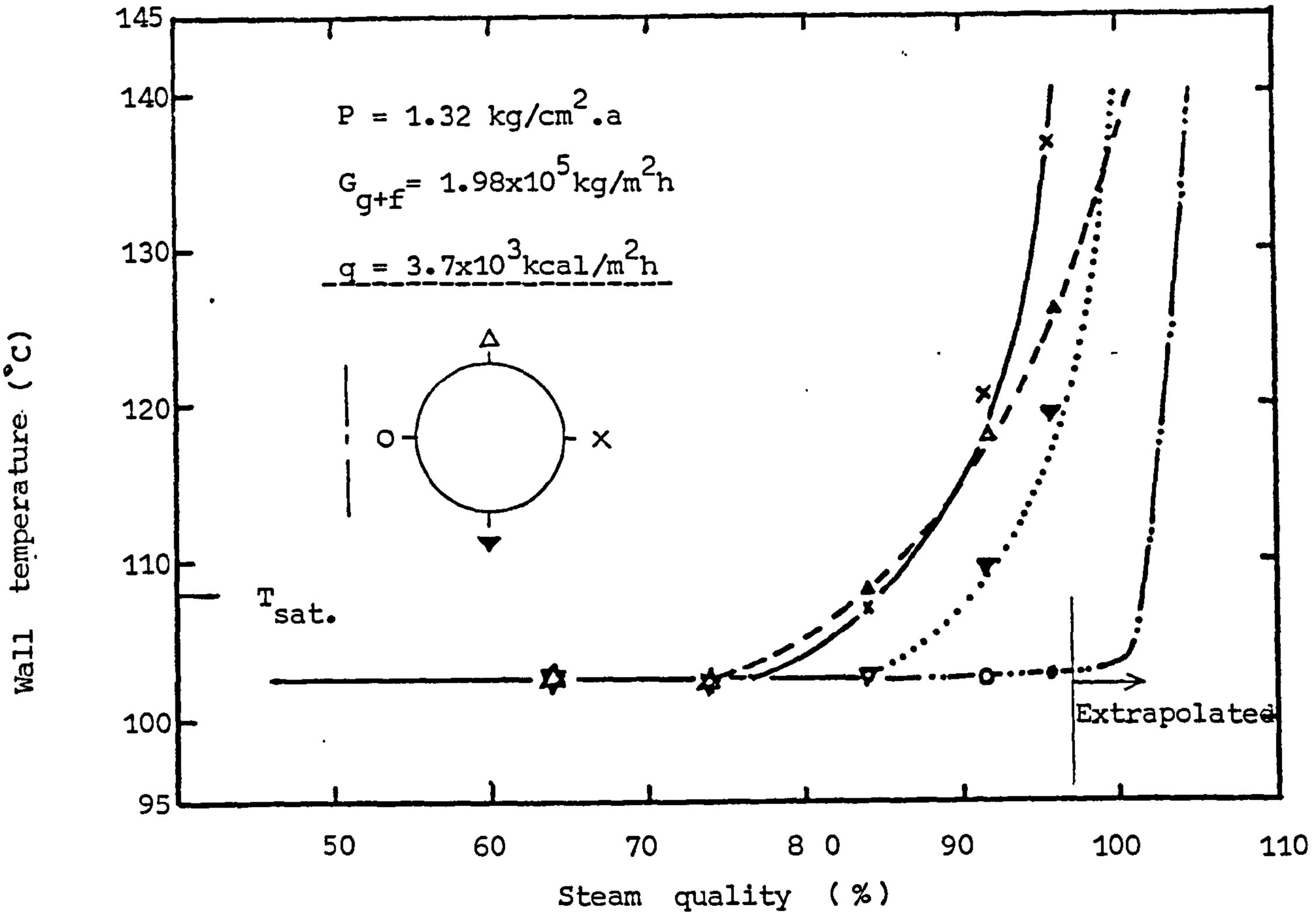


Fig.(4.3.21 a) : Onset of burnout in Coil B.

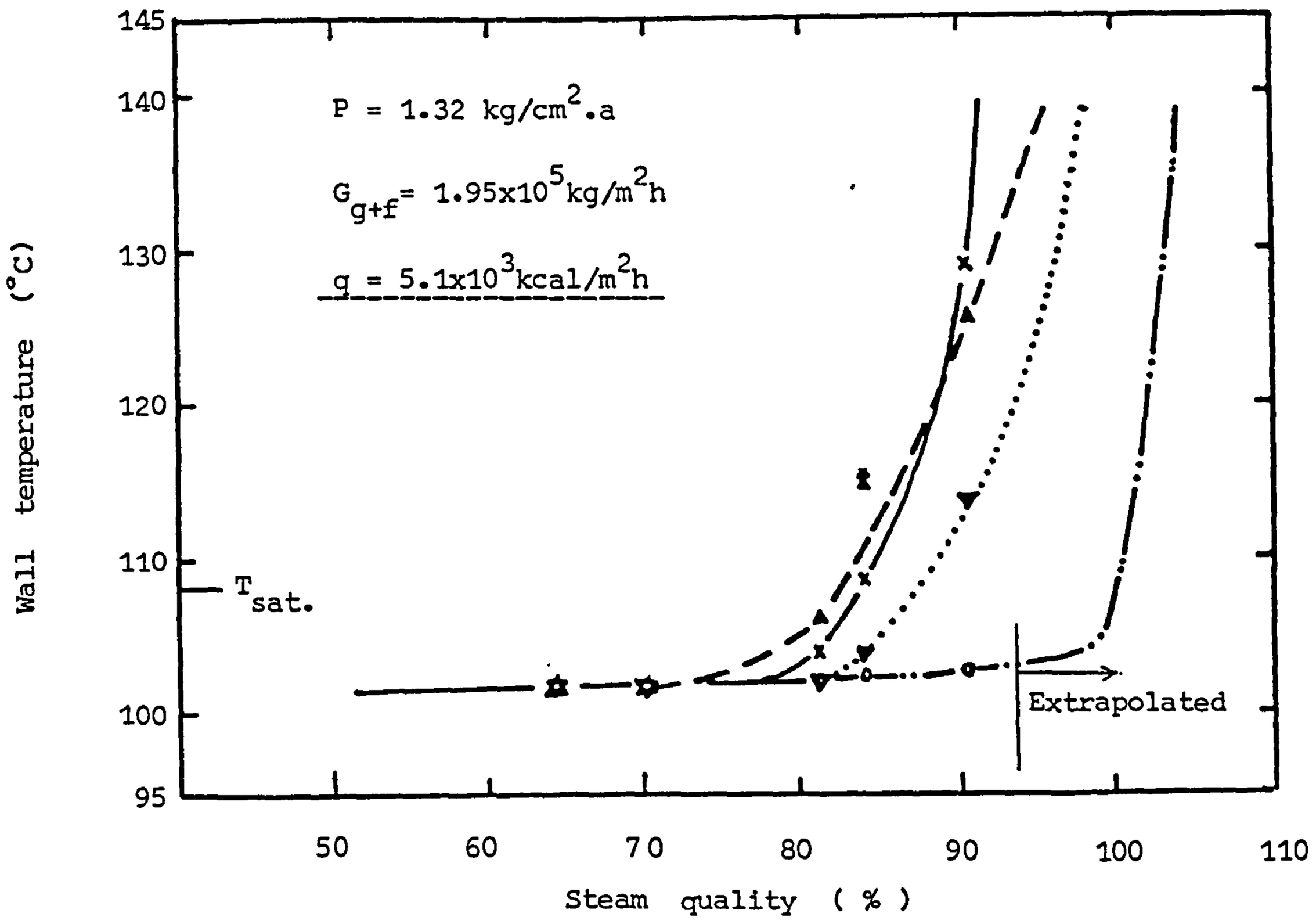


Fig. (4.3.21 b) : Onset of burnout in Coil B .

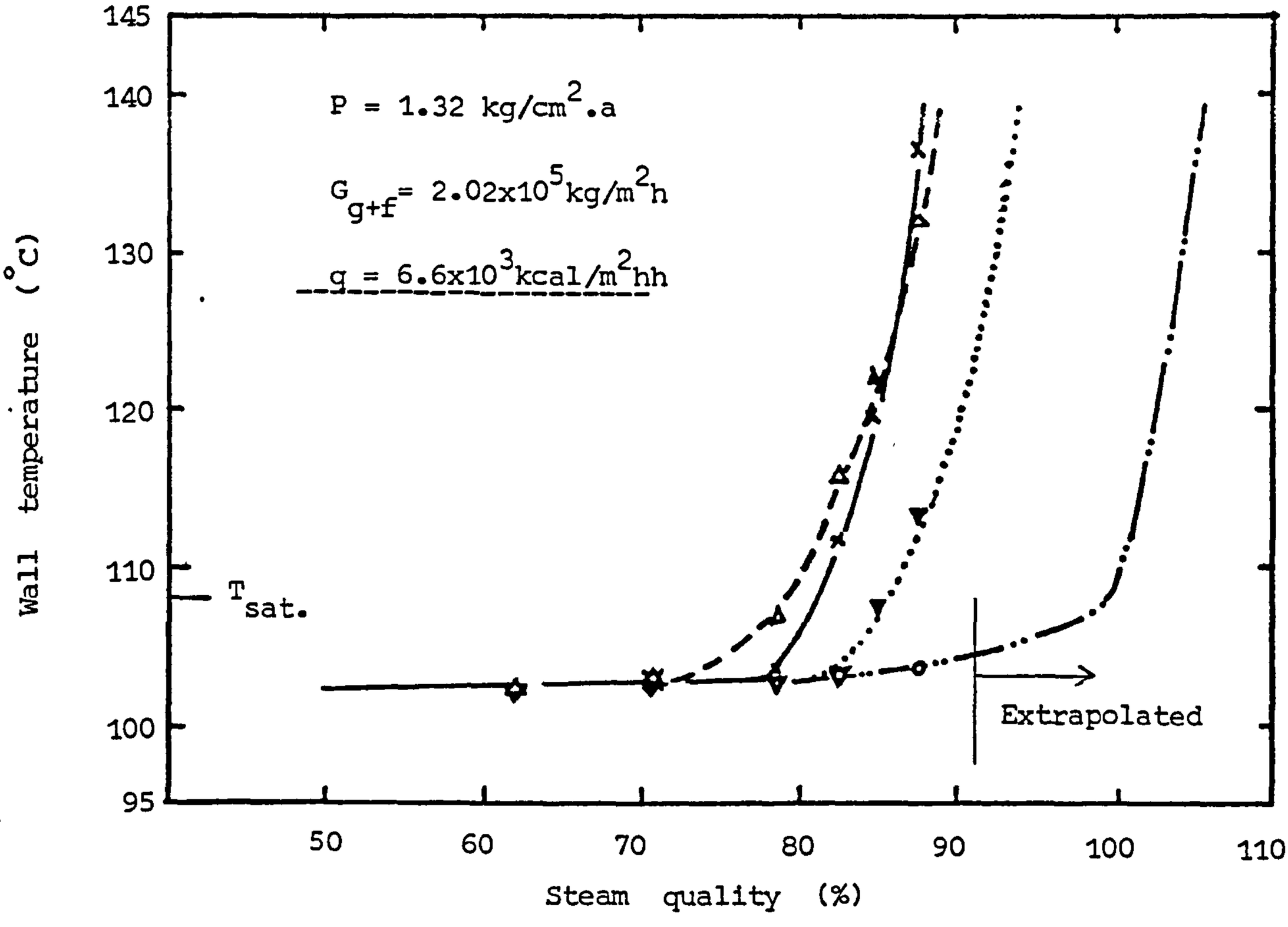


Fig. (4.3.21 c) : Onset of burnout in Coil B.

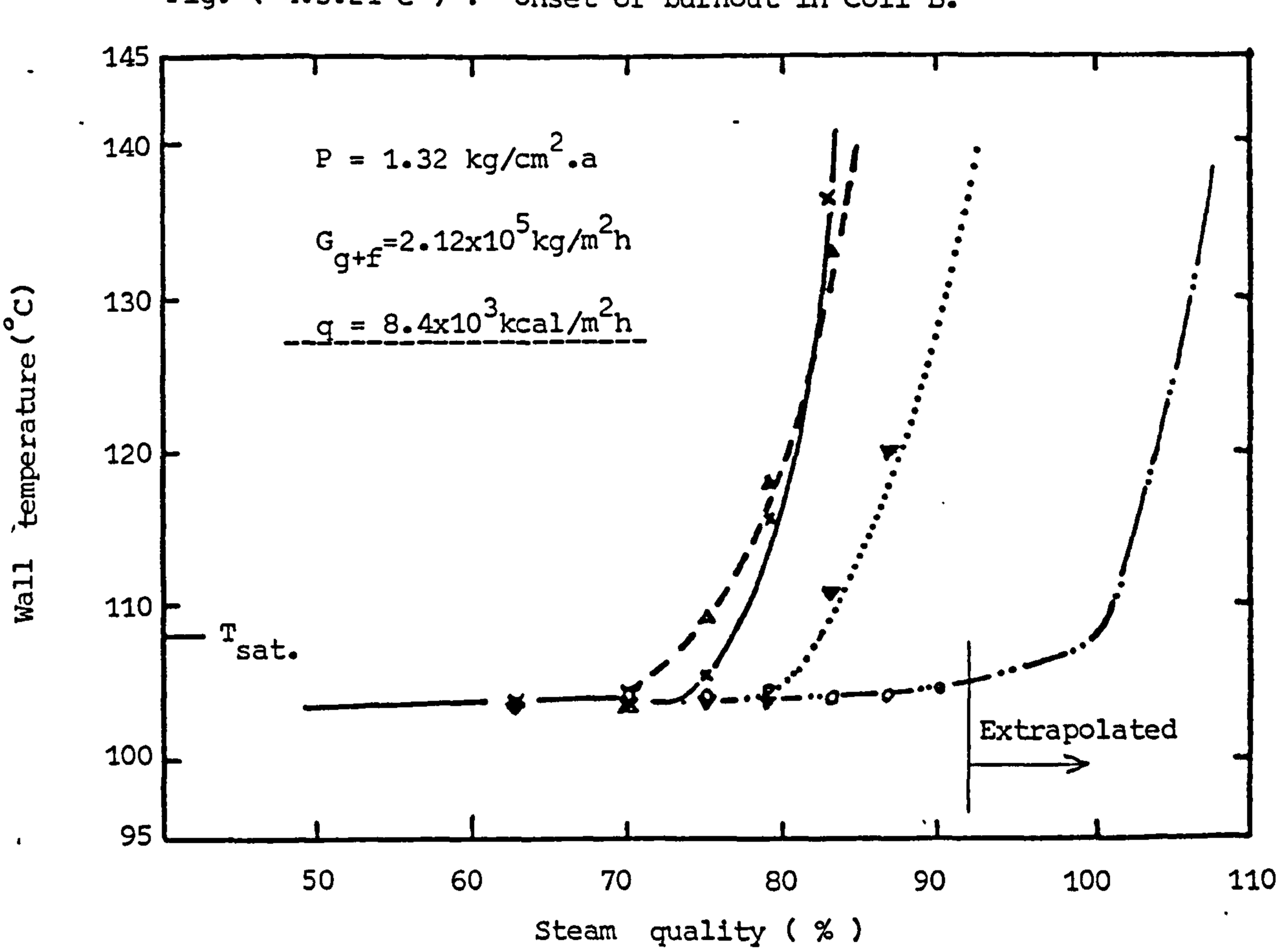


Fig. (4.3.21 d) : Onset of burnout in Coil B.

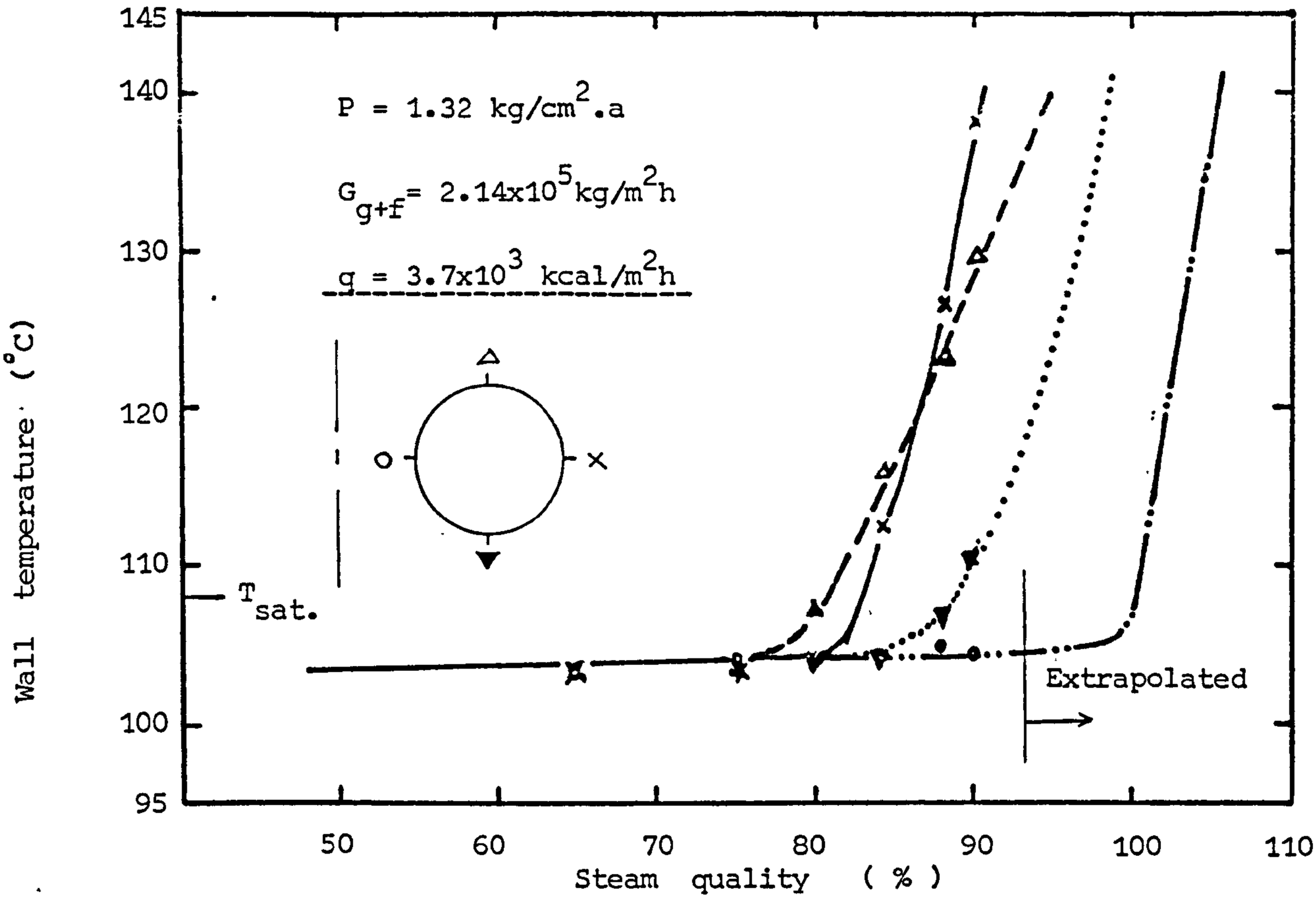


Fig. (4.3.22 a) : Onset of burnout in Coil C.

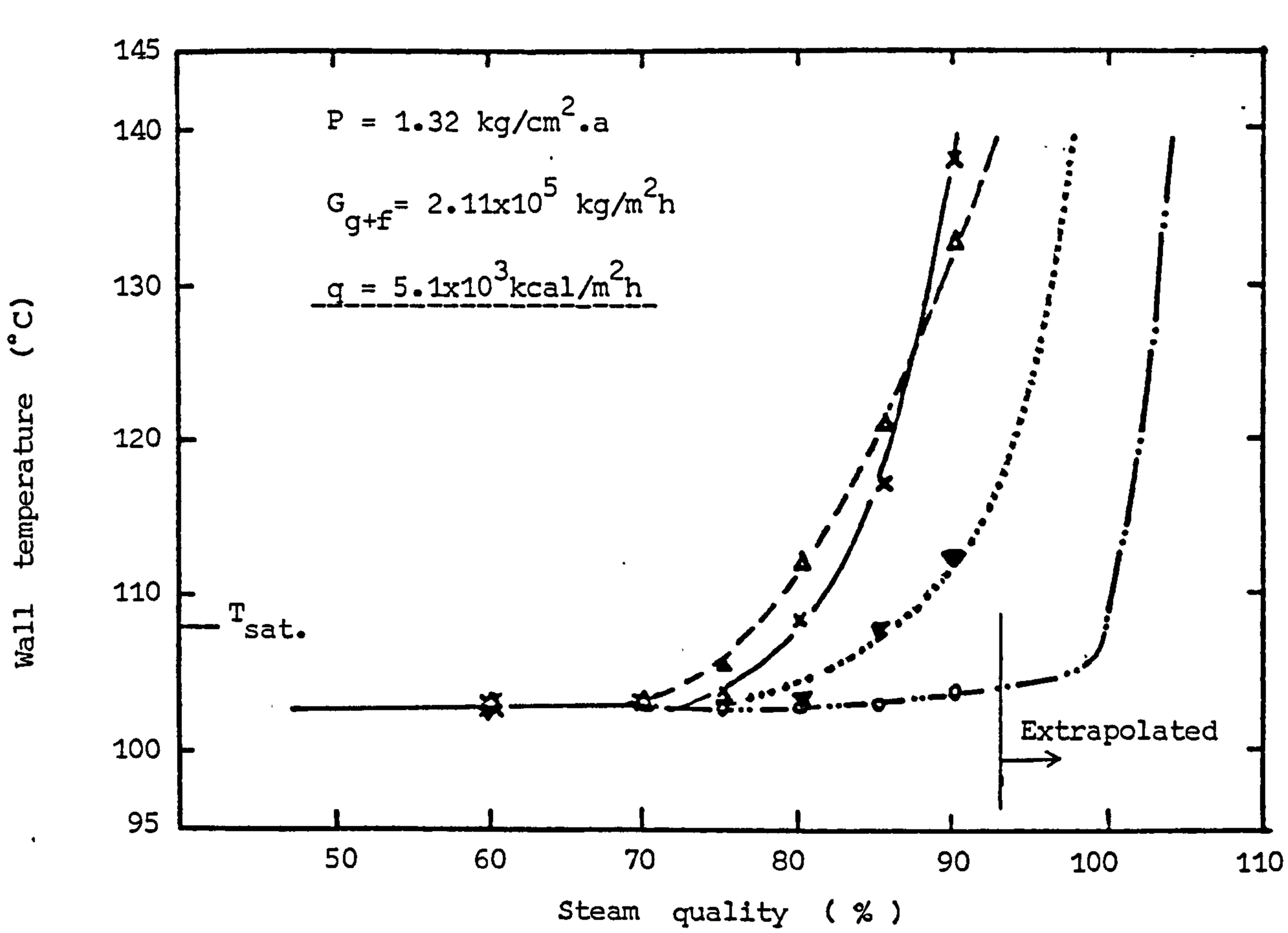


Fig. (4.3.22b) : Onset of burnout in Coil C.

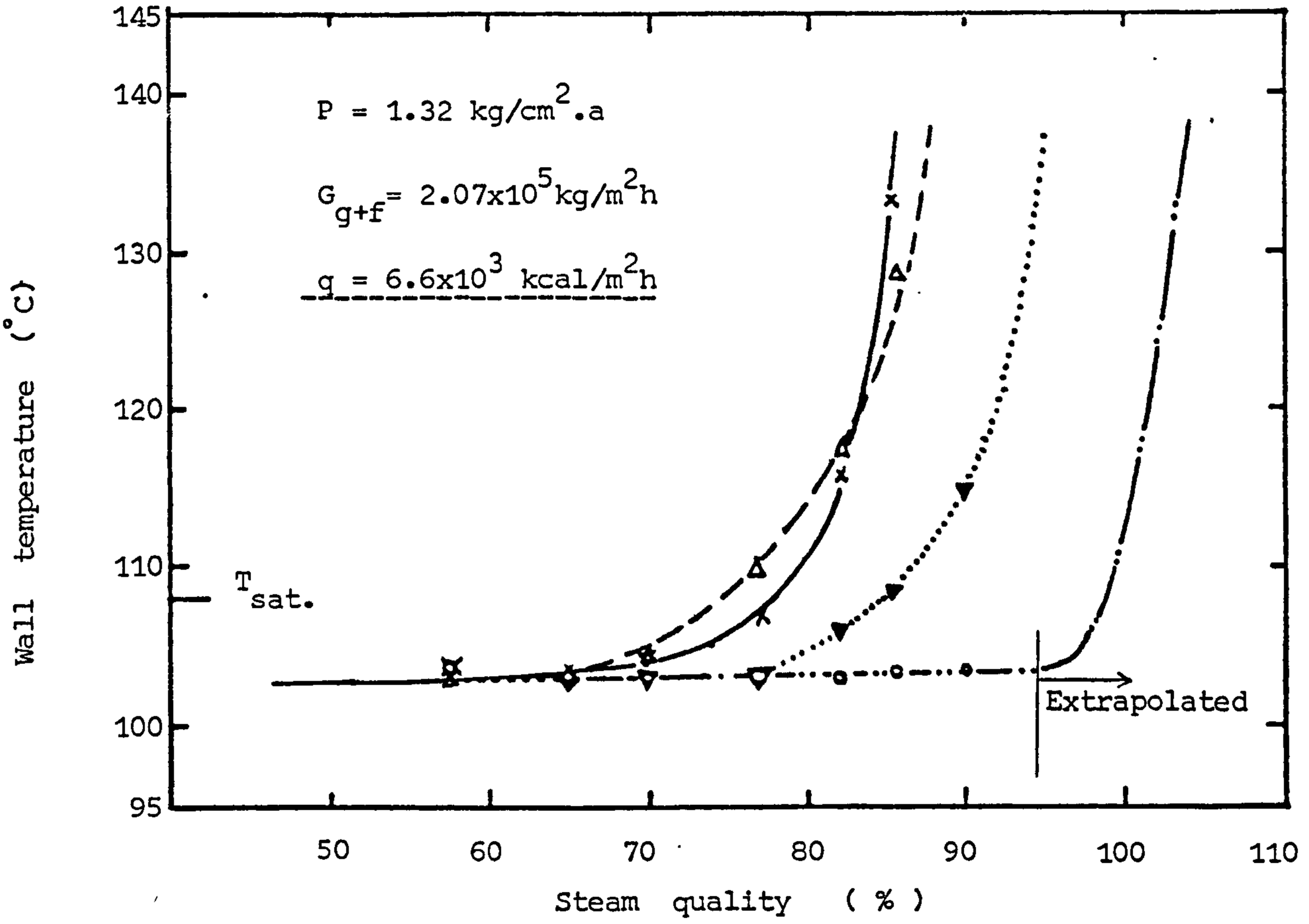


Fig. (4.3.22 c) : Onset of burnout in Coil C.

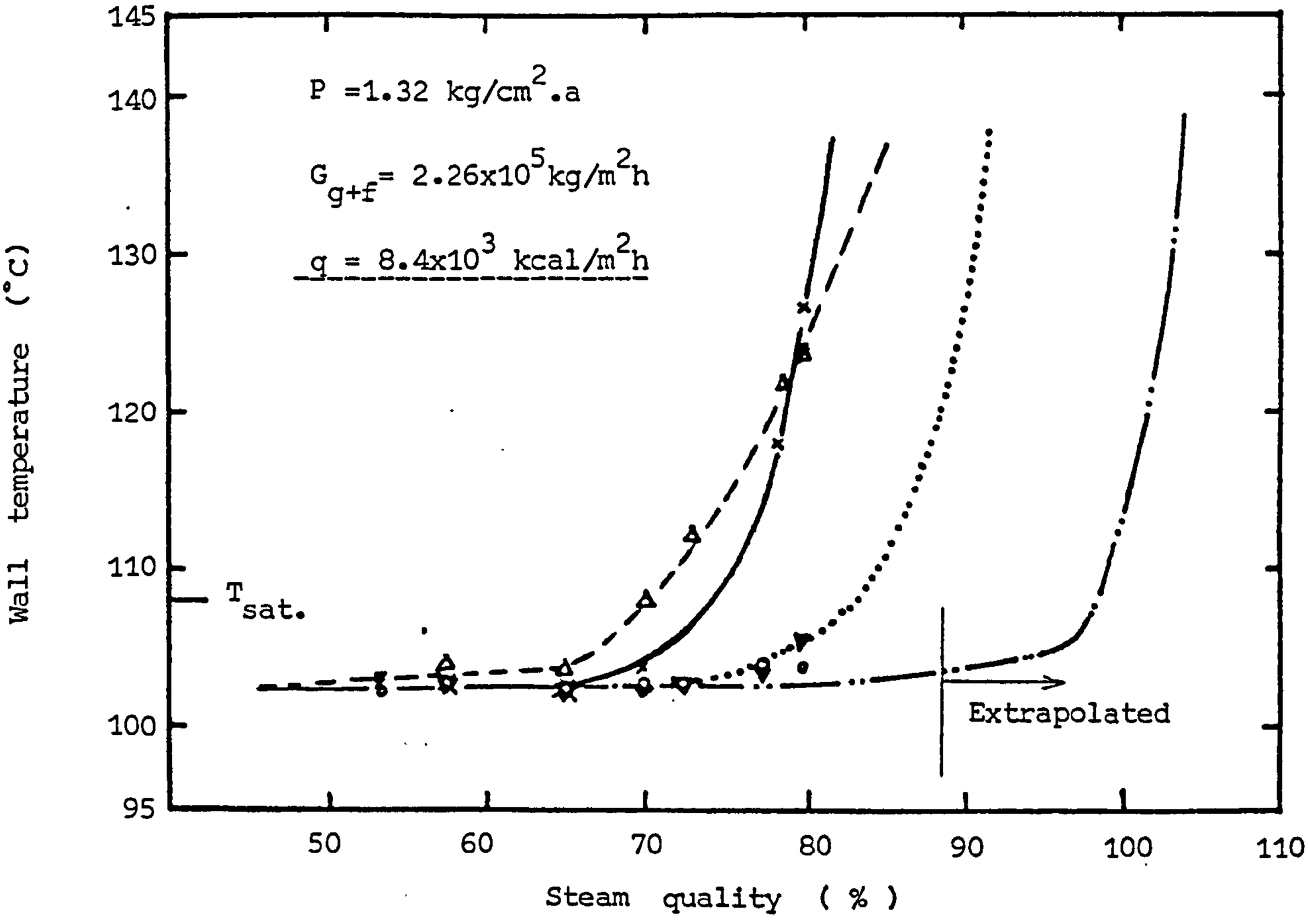


Fig. (4.3.22 d) : Onset of burnout in Coil C.

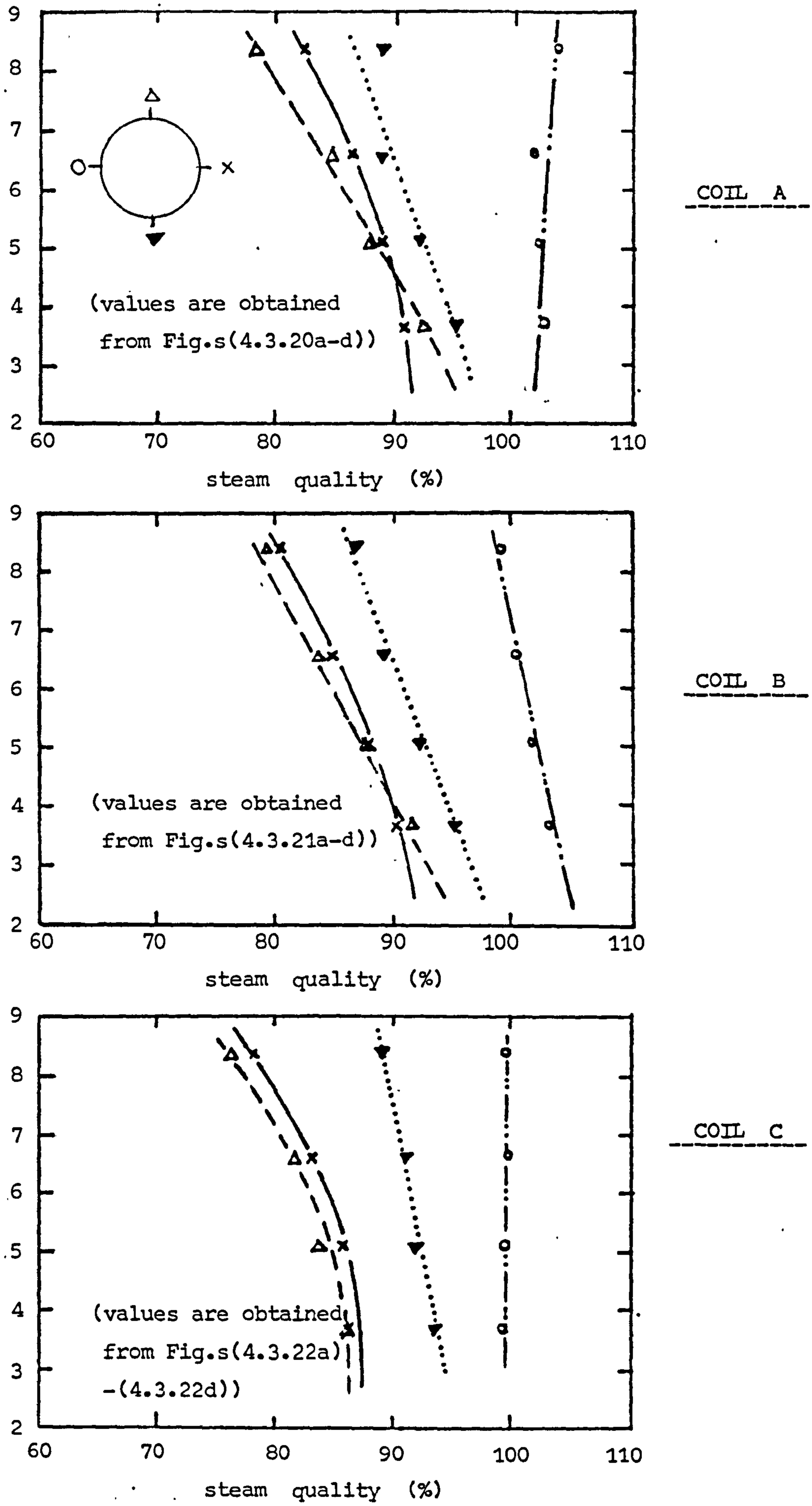


Fig.(4.3.23) : Burnout heat flux of four positions on the tube.

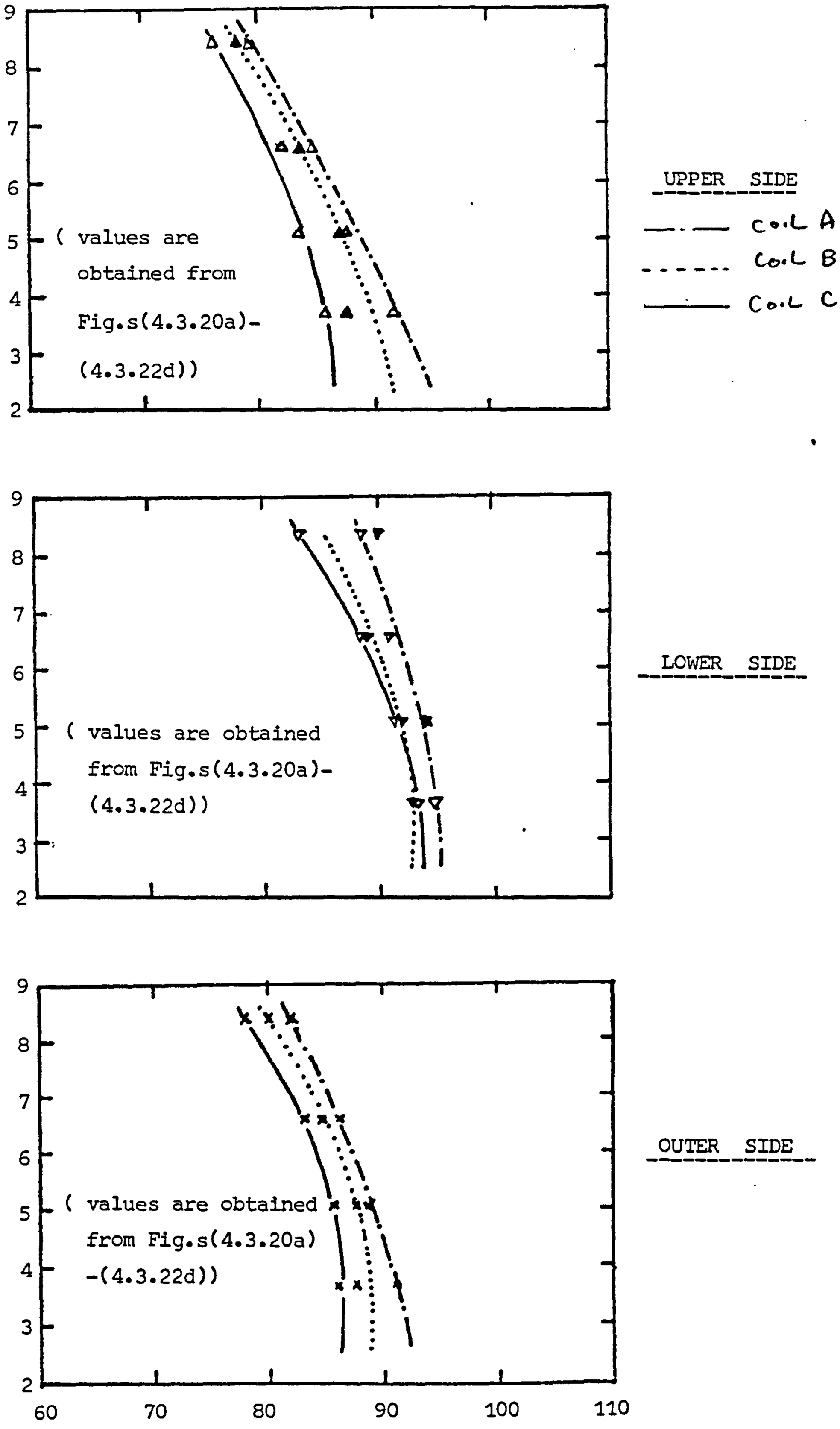


Fig.(4.3.24) : Input heat flux profiles at(T_{sat} +10 C) C in three coils.

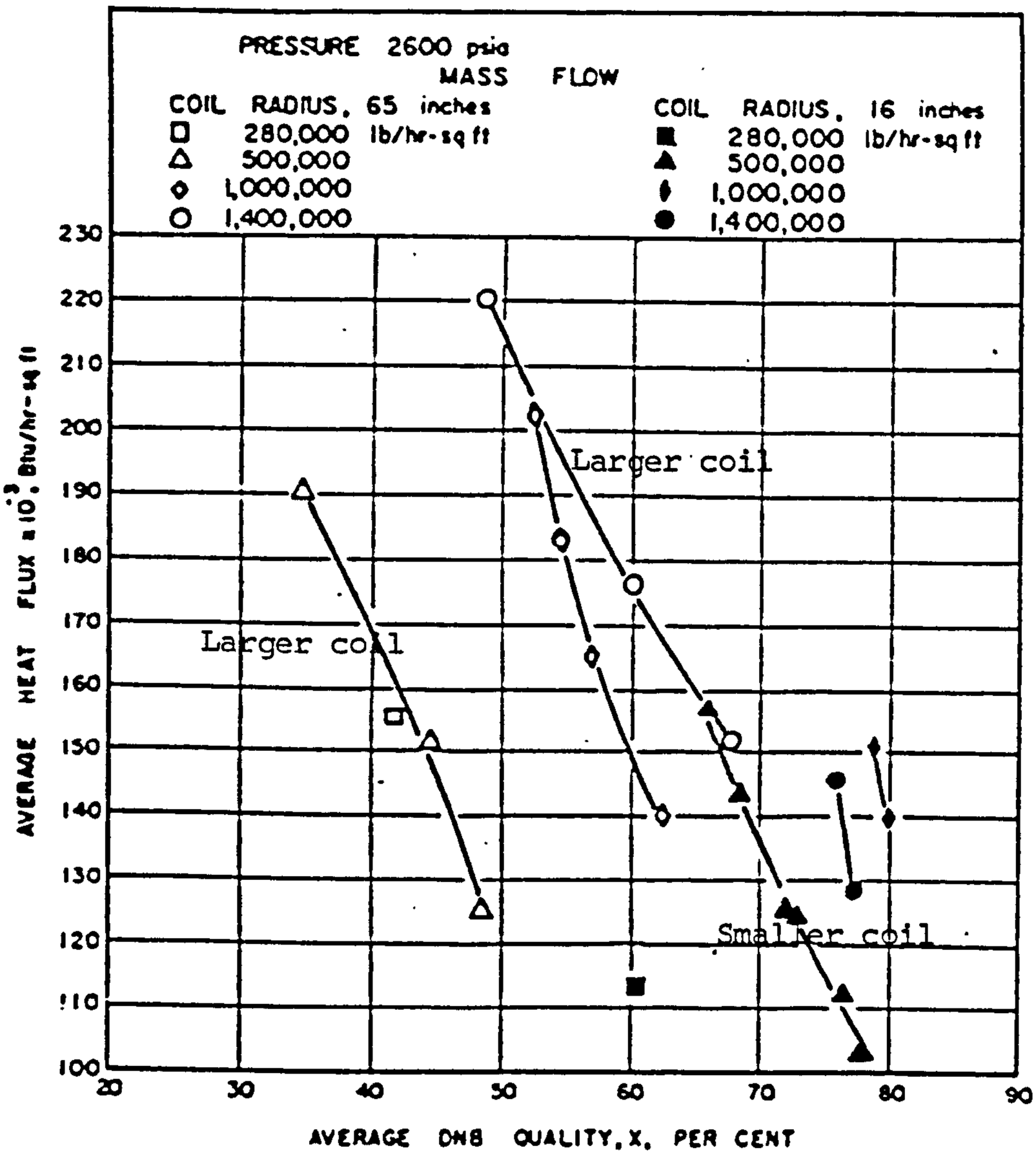
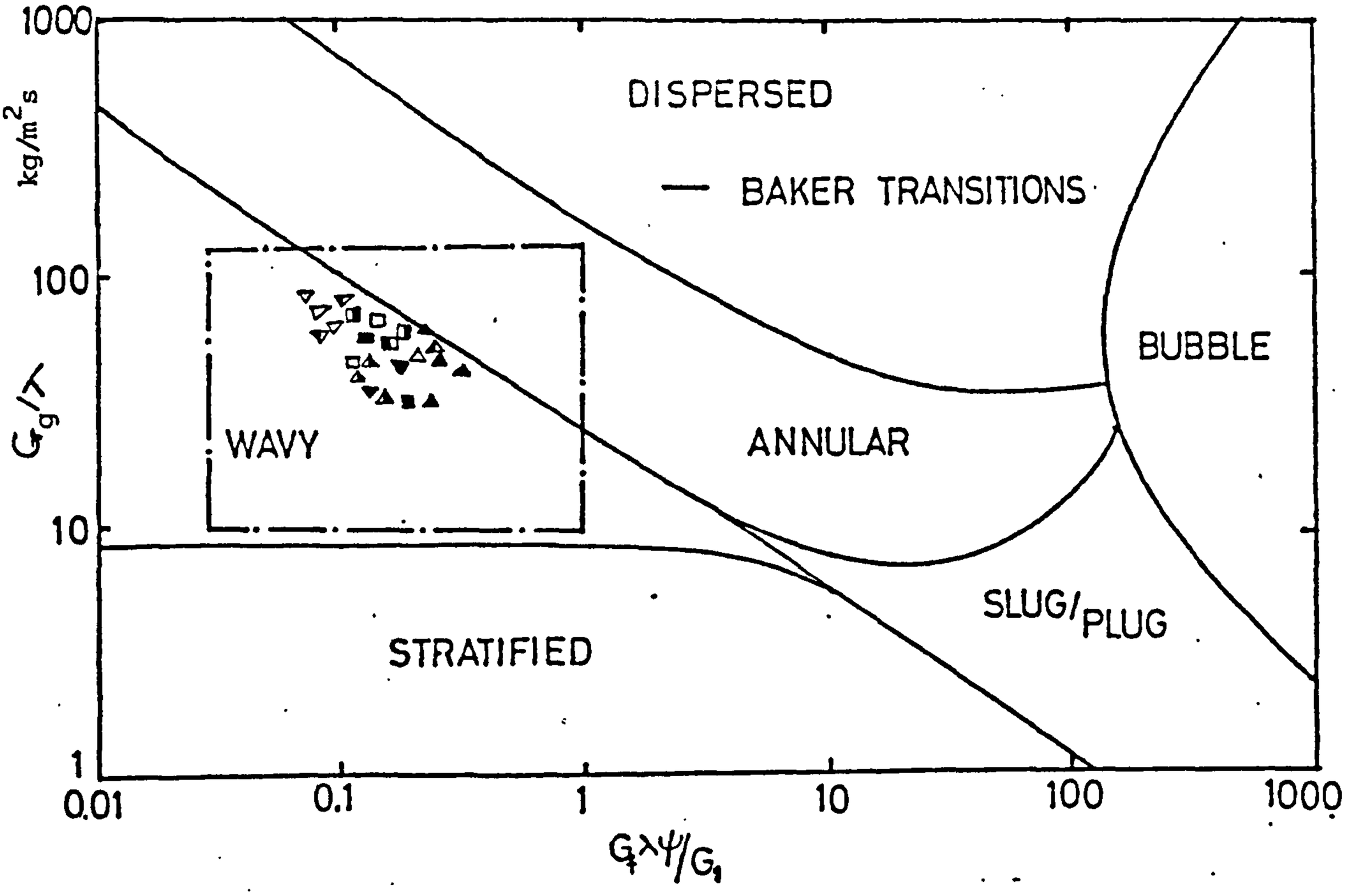


Fig. (4.3.25) : Comparison of average DNB quality, from Carver et al (68).



—•—•— The experimental range in Coils A,B and C.

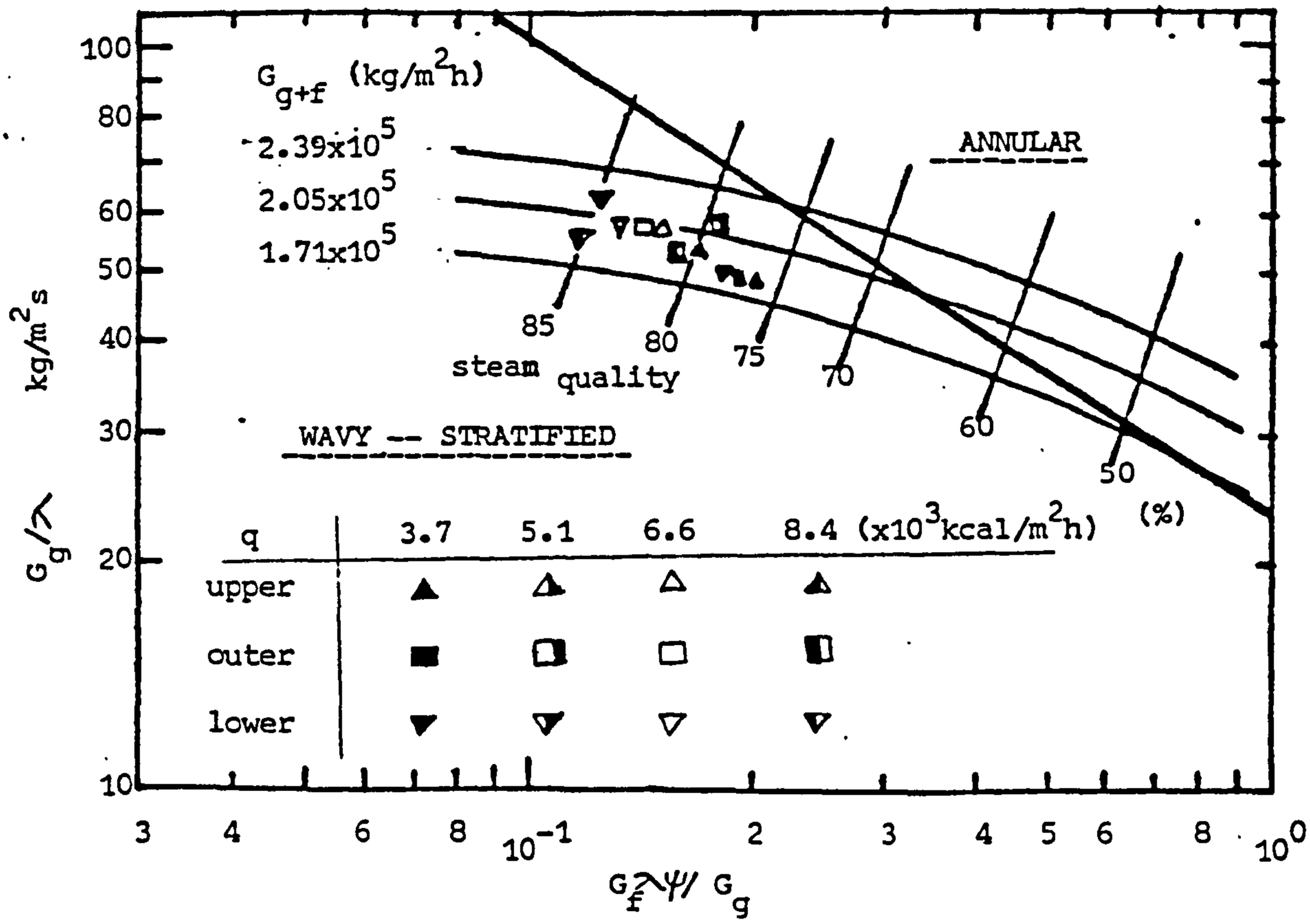
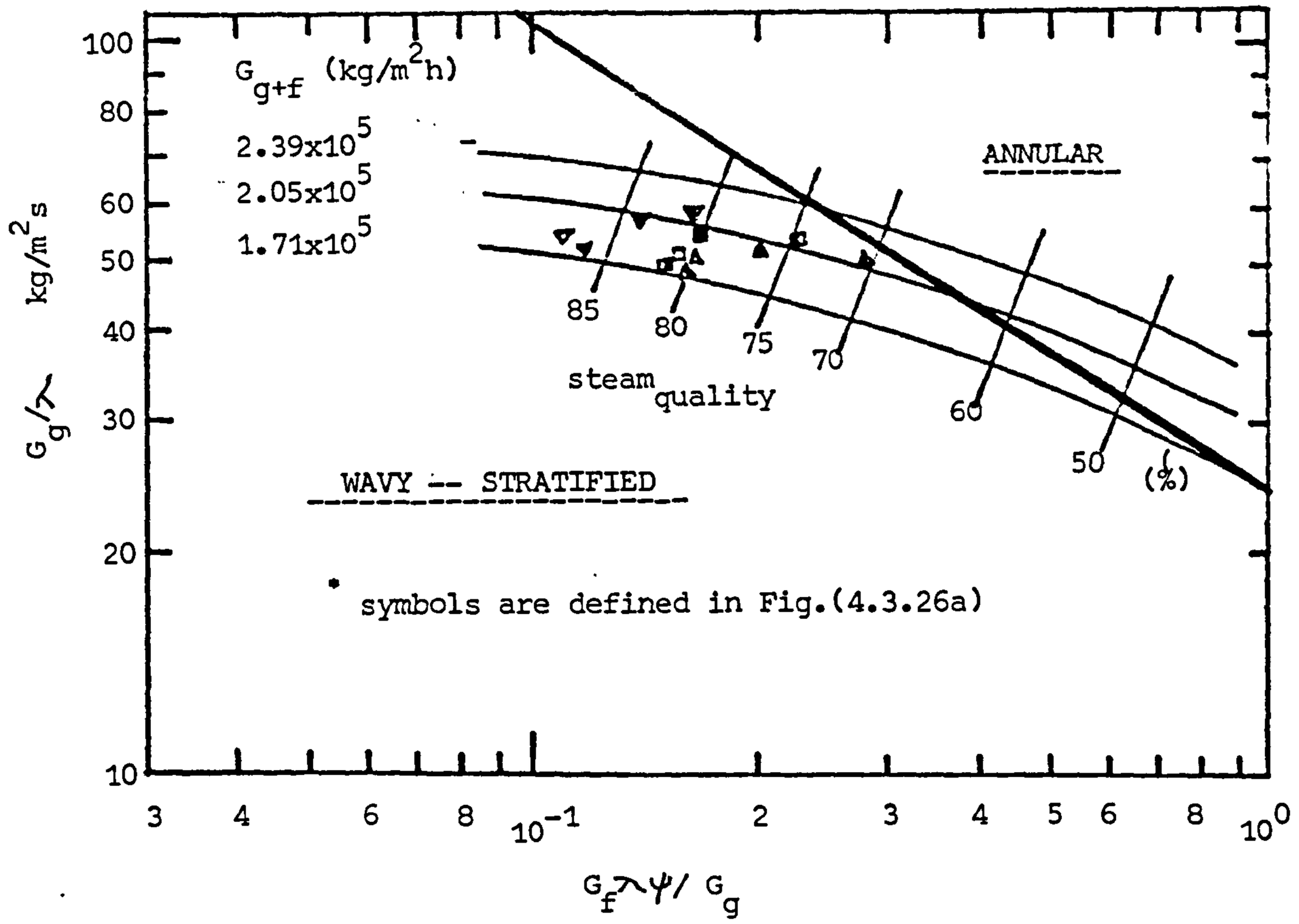
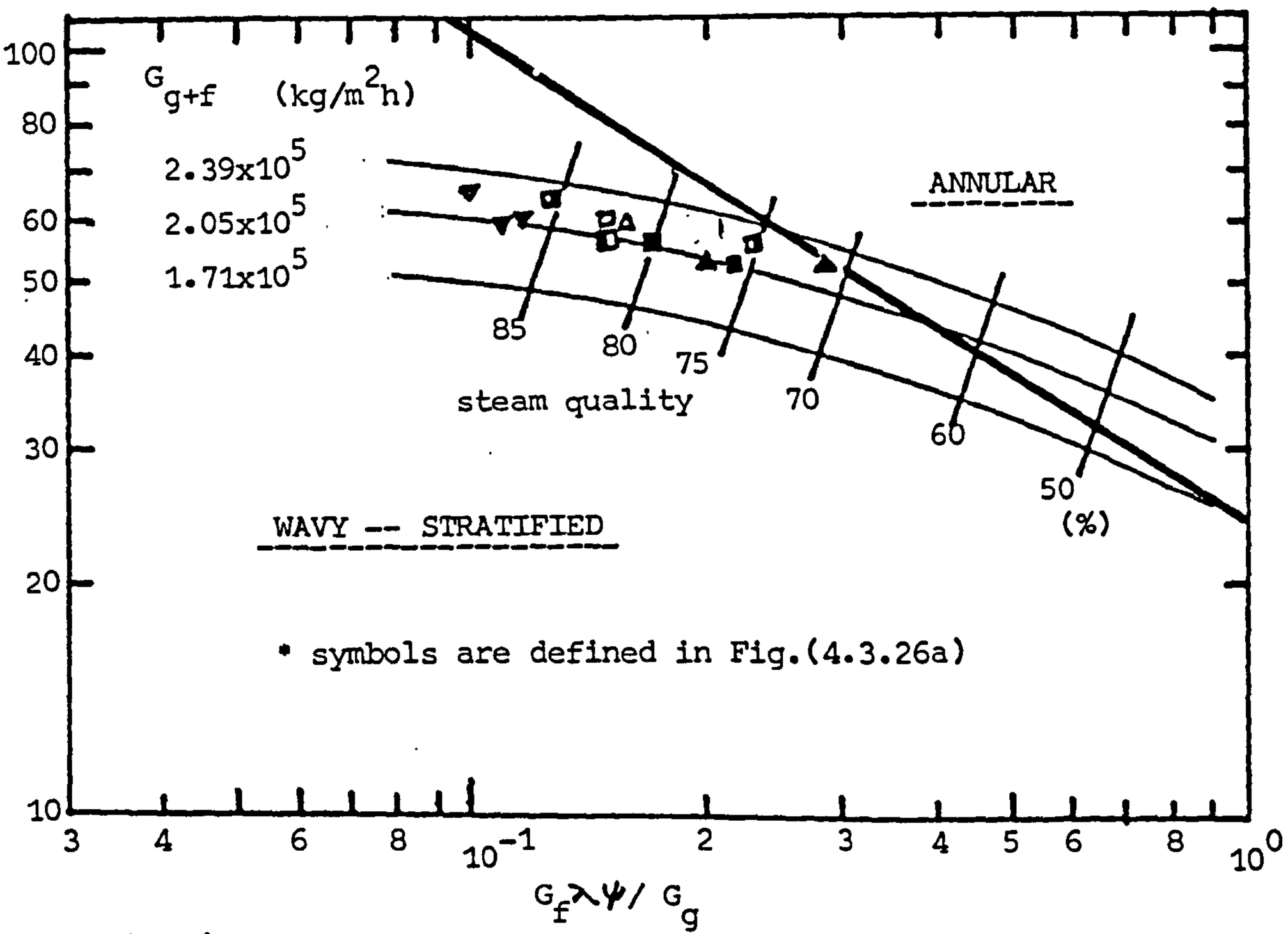


Fig. (4.3.26a) : Positions of burnout onset in Coil A.



* symbols are defined in Fig.(4.3.26a)

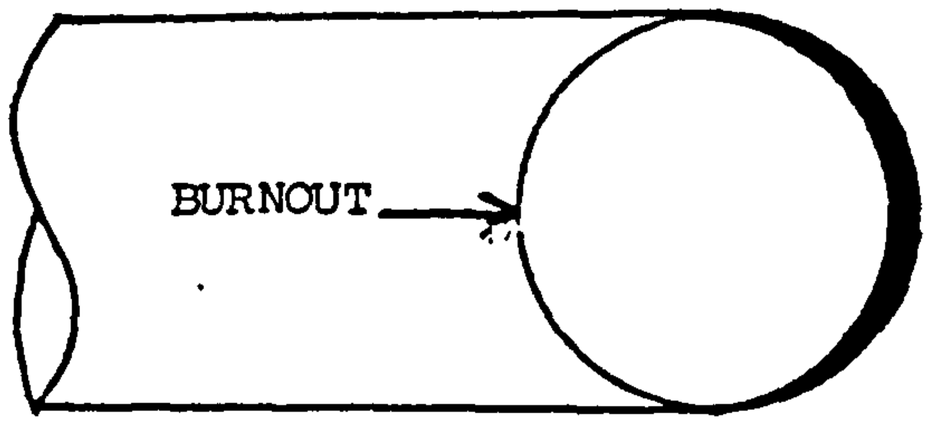
Fig. (4.3.26 b) : Positions of burnout onset in Coil B.



* symbols are defined in Fig.(4.3.26a)

Fig. (4.3.26 c) : Positions of burnout onset in Coil C.

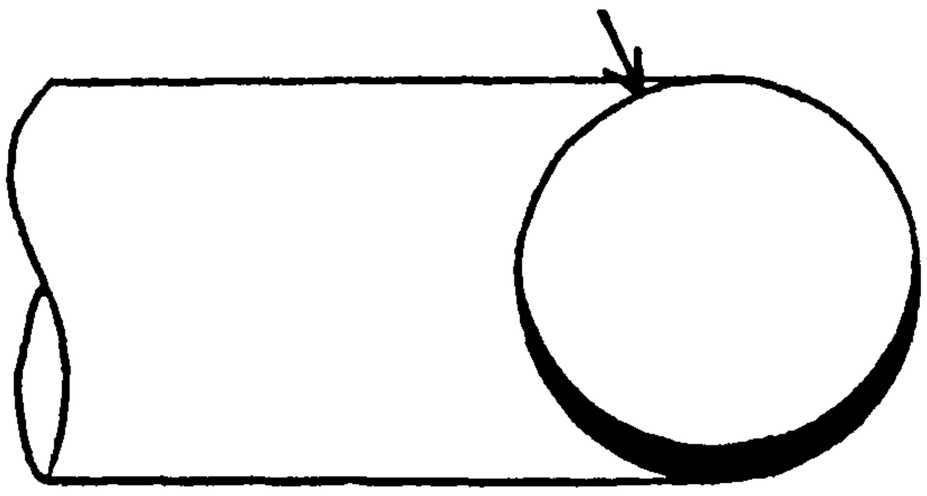
A



HIGH pressure,
ρ_f / ρ_g large,
and HIGH mass velocity.

(centrifugal force predominating)

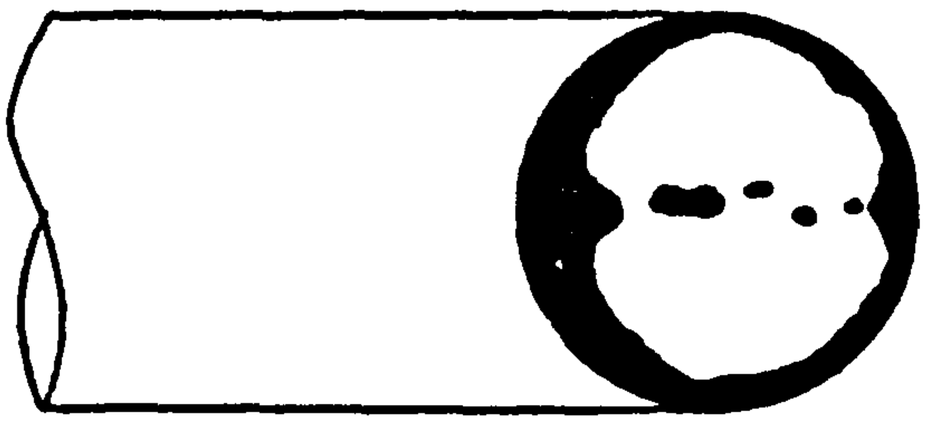
B



HIGH pressure,
ρ_f / ρ_g small,
and LOW mass velocity.

(gravity predominating)

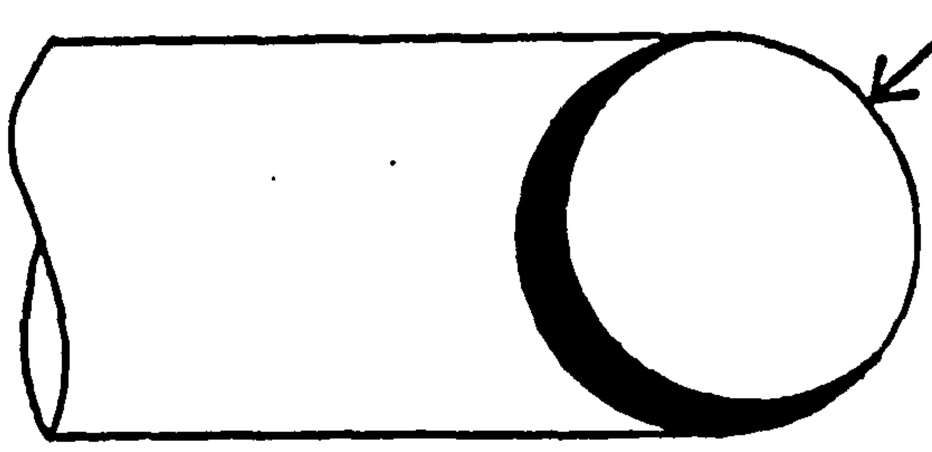
C



LOW pressure,
ρ_f / ρ_g large,
and HIGH mass velocity.

(secondary-flow effects predominating)

D



LOW pressure,
ρ_f / ρ_g large,
and LOW mass velocity.

(gravity predominating and film inversion)

⟵ BURNOUT POSITION.

Fig.(4.3.27) : Positions of burnout occurrence at various pressures and mass velocities. (patterns A,B,C : from Butterworth & Hewitt (62).)

4.4 SUMMARY OF THE CHAPTER

All data were taken from three different diameter coils ($\frac{R}{a} \doteqdot 20$, 30, 40) with steam, water, or steam-water flows. The ranges of input heat flux to the coils by direct electrical heat were $0.42 \times 10^3 \sim 3.74 \times 10^3$ $Kcal/m^2h$ for the single-phase flows and $3.30 \times 10^3 \sim 7.95 \times 10^3$ $Kcal/m^2h$ for the steam-water mixtures.

The results, discussions and conclusions in this chapter contribute to understanding of the flow mechanisms and heat transfer effect in the helically-coiled tubes.

4.4.1 Summaries of Single-phase flow

a. The wall temperature at the inner side showed the highest value on the tube periphery in all coils in both the case of water and steam single-phase flows. The upper side showed second highest value and the lower and outer sides the lowest temperatures. These temperature differences are due to the effect of the secondary flow in the tube. This part is explained fully in section (4.2.1.2).

b. When the wall temperature approaches the saturation point in the laminar water flow, the buoyancy force starts to influence the secondary flow and main core flow. The relationship between water flow Reynolds numbers and Rayleigh number is shown in Fig. (4.2.5). If this relationship in the helically-coiled tube was observed sufficiently, the changing point of heat transfer coefficient at certain Reynolds numbers could be determined easily. This part is explained fully in section (4.2.1.2).

c. The heat transfer coefficient at the outer side had the highest value in both single-phase flows, on the other hand the

inner side showed the lowest value.

The ratio of local heat transfer coefficients between the outer and inner sides for water and steam flows are:

(i) For water flow

$$\frac{h_{outer}}{h_{inner}} = 15.45 \left(\frac{a}{R}\right)^{0.451} \qquad (4.2.4)$$

$$0.185 \times 10^4 < Re_f < 0.384 \times 10^4$$

$$Pr \approx 2.0$$

(ii) For steam flow

$$\frac{h_{outer}}{h_{inner}} = 7.70 \left(\frac{a}{R}\right)^{0.345} \qquad (4.2.9)$$

$$3.14 \times 10^4 < Re_g < 6.98 \times 10^4$$

$$Pr \approx 1.0$$

Up to the present, only Kozeki (80), who proposed eq. (4.2.8) and Seban and McLaughlin (22) have investigated local heat transfer profiles in laminar and turbulent flows. This part is explained fully in section (4.2.2.3).

d. Friction factors from the present work were compared with Ito (25), Seban and MacLaughlin (22) and straight tube data in Fig. (4.2.11). Six of the nine results showed lower values than those for the straight tube because of the effect of coil diameter ratio was ignored and the limitations of the measurement facilities.

The term of $\{Re(\frac{a}{R})^2\}^{-\frac{1}{4}}$ from Ito's formula, eq. (2.32) is acceptable for all the present results but it should be changed at each value of input heat flux. This part is explained in section (4.2.2.1).

4.4.2 Summaries of two-phase flow

a. The studies of flow patterns were concentrated on the annular, wavy and stratified regions on the maps of Goldmann et al (85) and Baker (50). The ranges of water and steam flow rates on the Baker's map are:

$$5 \lesssim \frac{Gg}{\lambda} \lesssim 100$$

and

$$0.1 \lesssim \frac{G_f . \lambda . \psi}{G_g} \lesssim 10$$

From Figs. (4.3.3a) - (4.3.3c), the annular flow patterns were observed at almost the same region as Baker (50) for the two smaller coils (Coils A and B). The area of annular flow for the largest coil occupies a similar position to that in the Baker map but its area is decreased.

The wavy flow pattern was observed in a narrow strip between the annular and wavy-stratified flow regions.

A mixed flow pattern between wavy and stratified was observed instead of the wavy region put forward by Baker (50).

In the helically-coiled tube, the 'film inversion' phenomenon is a main factor of wavy-stratified and stratified flow formations. The effect of secondary flow and centrifugal forces in the helically-coiled tube contribute to the spreading of the annular flow region wider than that for the straight tube. This part is explained in section (4.3.1).

b. The two-phase frictional multiplier, ϕ_{gtt}, was evaluated from the pressure drop data and was plotted against the Lockhart-Martinelli parameter, X_{tt}, in Fig. (4.3.5). If the parameter,

X_{tt} were greater than 0.1, the frictional multiplier, as for the straight tube, ϕ_{gtt}, can be used for the helically-coiled tube, but at $X_{tt} <$ 0.1, the frictional multipliers show values that are about 45% higher.

In general the transition Reynolds number, Re_{TR}, in the straight round tube is about 2,000. However from Banerjee et al (39), Kozeki (53, 80) and the present work, the Reynolds numbers of liquid phase of around 800 ~1 000 in the helically-coiled tube showed transition characteristics. This part is explained fully in section (4.3.2).

c. Wall temperature rise normally shifts from a point towards the tube exit to one near the tube entrance. The wall temperature rise occurred at the upper side first, the outer side second. The temperatures at the inner and lower sides were almost constant at the inlet values, shown in Figs. (4.3.7a) - (4.3.9g). This shows that the phenomena of droplet entrainment and deposition or burnout and rewet occur at the same time at the different positions. The series of figures (4.3.7a) - (4.3.9g) also show that the phenomenon is dependent on the total mass flow rate and input heat flux.

Sufficient experimental results covering whole ranges of steam and water flow rates are not available from the present or that of other investigators. Therefore it is not possible to predict precisely the point of inception of the sharp temperature rise.

'Surge flow' and 'Disturbance waves', which are known as factors causing intermittent temperature oscillation, were not

observed in this work. This part is explained fully in section (4.3.3).

d. The data for local heat transfer coefficients were processed in Chen 's correlation (96) and plotted in Figs. (4.33a) - (4.33c). Also the ratios between two-phase heat transfer coefficient and heat transfer coefficient for water alone flow ($\frac{h_{TPC}}{h_{fc}}$) are plotted in Figs. (4.3.18a) - (4.3.18c).

When steam qualities, x, are greater than 50%, the upper side showed the highest heat transfer coefficient, the outer side second largest and the lower and inner sides showed the smallest. In this range (50% < x), the ~~nucleate~~ convective boiling heat transfer is thought to predominate, especially at the upper and outer sides. In the x < 50% range the upper side showed the highest heat transfer coefficient but the outer side decreased to the same values as the lower and inner sides. In this range the ~~convective~~ Nucleate boiling heat transfer is thought to predominate.

The most obvious contrasting features of the heat transfer mechanism in the helically-coiled tube and the straight tube are the film profiles. These are caused by secondary flow forces and centrifugal forces, of which the former is more important. this part is explained fully in section (4.3.4).

e. Formulae of the ratio, $(\frac{h_{TPC}}{h_{fc}})$, at four positions (0^o, 90^o, 180^o and 270^o) of the tube cross section in three coils were obtained and are as follows:

(i) the upper side (0^o)

$$\frac{h_{TPC}}{h_{fc}} = 4.21 \left(\frac{1}{X_{tt}}\right)^{0.73} \qquad (4.3.26)$$

(ii) the outer side (90^o)

$$\frac{h_{TPC}}{h_{fc}} = 2.81 \left(\frac{1}{X_{tt}}\right)^{0.72} \qquad (4.3.27)$$

(iii) the lower and inner sides (180^o, 270^o)

$$\frac{h_{TPC}}{h_{fc}} = 2.50 \left(\frac{1}{X_{tt}}\right)^{0.74} \qquad (4.3.28)$$

From Bell and Owhadi (65), Kozeki (48) and the present work, all heat transfer coefficient ratios in the helically-coiled tubes can exist in the following range:

$$1.7\left(\frac{1}{X_{tt}}\right)^{0.68} \leq \left(\frac{h_{TPC}}{h_{fc}}\right) \leq 5.22 \left(\frac{1}{X_{tt}}\right)^{0.68} \qquad (4.3.29)$$

for atmosphere $\leq P \leq 30$ Kg/cm^2g

$$20 \leq \frac{R}{a} \leq 50$$

$$5 \leq \frac{1}{X_{tt}} \leq 80$$

Schrock-Grossman's formula (100) is thought to be the average correlation of heat transfer coefficient for the helically-coiled tubes. This part is explained fully in section (4.3.4).

f. For a given set of test conditions, burnout occurred successively at the upper, outer and lower and inner sides. On decrease water flow, keeping steam flow and heat flux constant, burnout occurred initially at a point towards tube exit and then shifted progressively nearer to the tube entrance. While burnout occurred at three sides, burnout at the inner side was not observed at all in the present work, even at near 90% steam quality.

The first appearance of burnout occurred at different positions in all three coils and varied with different mass flow rates and pressures; these differences were summarized with Fig. (4.3.27).

In the present work, the inception of burnout is determined by the progress of transition to completely stratified flow and start of 'film inversion' phenomena. This part is explained fully in section (4.3.5).

C H A P T E R 5

THEORETICAL ANALYSIS OF THE FLOW IN COILED TUBE

5.1 Theoretical analysis of single-phase flow

Up to the present, many numerical analyses of single-phase flow mechanisms in the coiled tubes have been proposed. They are summarized in Chapter Two. Most of these results were compared with the empirical results such as those of Mori and Nakayama (5), Seban and McLaughlin (22), Ito (25), Hogg (29) and Kozeki (48, 80).

The present work is also based on experiment. The purpose of this section is to explain the turbulent flow mechanisms in the coiled tube which are main structures of two-phase flow in the present work. The analyses refer to the above works.

5.1.1 Analysis of friction factor

Consideration is given to a fully developed turbulent flow of incompressible fluid in a coiled tube under the thermal boundary conditions of axially uniform wall heat flux and peripherally uniform wall temperature at any axial position. In order to facilitate the analysis, the following assumptions are made:

(i) The radius of curvature of the tube axis is large in comparison to the radius of the tube and the pitch of the coil is so small that the tube is a horizontal curved tube.

(ii) The possible effect of curvature is allowed for in the body force (i.e. centrifugal force).

(iii) Physical properties are constant and buoyancy and gravitational effects are neglected.

Taking the origin of the cylindrical co-ordinates (r, ψ, θ) at the centre of the circular pipe cross-section as shown Fig. (5.1.1).

Continuity equation becomes

$$\frac{\partial}{\partial r}(rU) + \frac{\partial V}{\partial \psi} = 0 \qquad (5.1.1)$$

Momentum equations in r, ψ and θ directions on imaginary cubic elements (shown in Fig. (5.1.1) are in the following forms:

$$\rho U \frac{\partial U}{\partial r} + \rho V \frac{\partial U}{r\partial \psi} + \rho W \frac{\partial U}{R\partial \theta} - \rho \frac{V^2}{r} = \rho F_r - \frac{\partial P^*}{\partial r} + \frac{\partial \overset{*}{\tau}_{r.\theta}}{R\partial \theta} + \frac{\partial \overset{*}{\tau}_{r.\psi}}{r\partial \psi}$$

$$\rho U \frac{\partial V}{\partial r} + \rho V \frac{\partial V}{r\partial \psi} + \rho W \frac{\partial V}{R\partial \theta} + \rho \frac{UV}{r} = \rho F_\psi - \frac{\partial P^*}{r\partial \psi} + \frac{\partial r \overset{*}{\tau}_{\psi.r}}{r\partial r} + \frac{\partial \overset{*}{\tau}_{\psi.\theta}}{R\partial \theta}$$

$$\rho U \frac{\partial W}{\partial r} + \rho V \frac{\partial W}{r\partial \psi} + \rho W \frac{W}{R\partial \theta} = - \frac{\partial P^*}{R\partial \psi} + \frac{\partial r \overset{*}{\tau}_{\theta.r}}{r\partial r} + \frac{\partial \overset{*}{\tau}_{\theta.\psi}}{r\partial \psi} \qquad (5.1.2)$$

where two acceleration velocities are

$$F_r = \frac{W^2}{R} \cos \psi$$

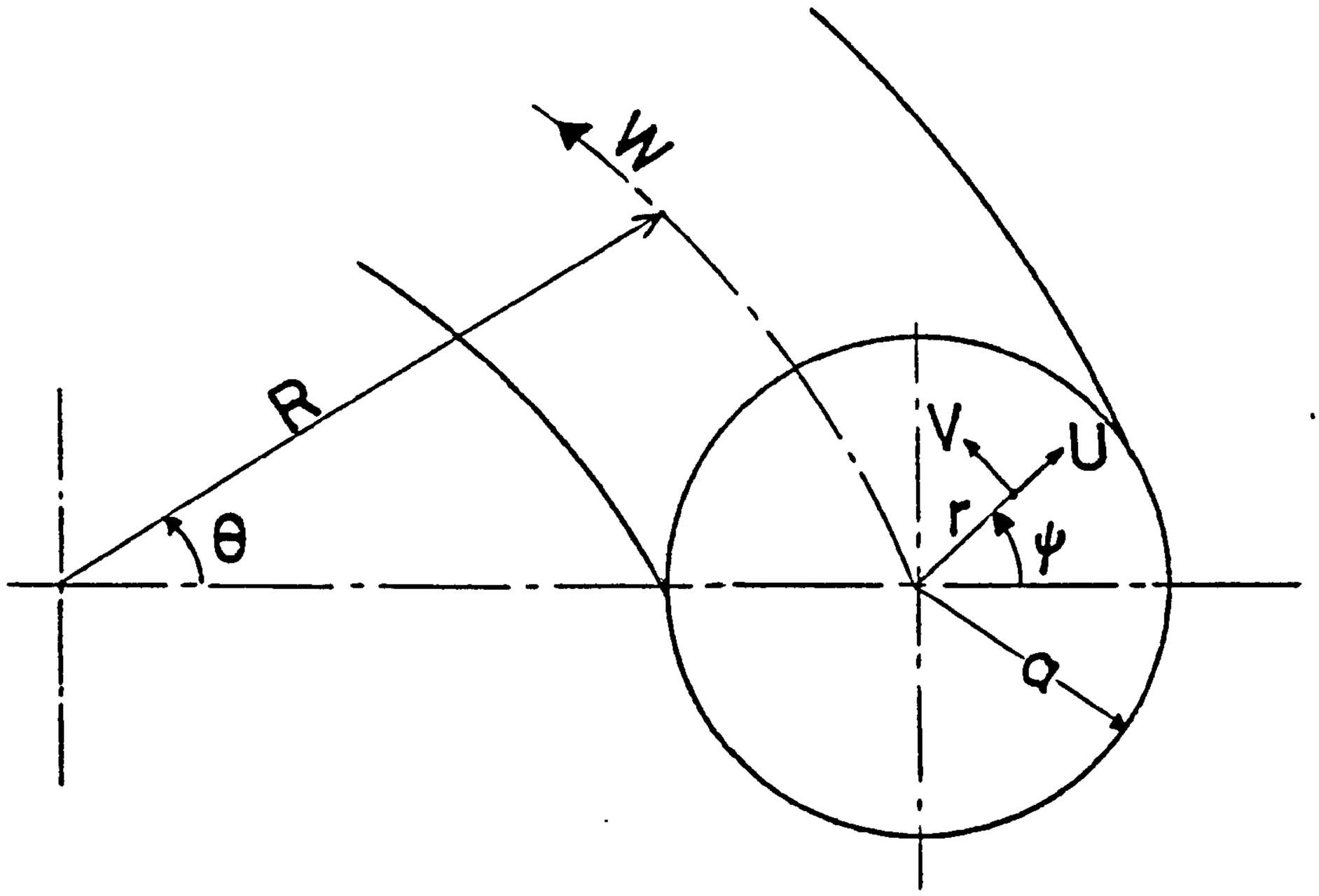
$$F_\psi = - \frac{W^2}{R} \sin \psi \qquad (5.1.3)$$

Assuming that the variation of the axial direction is negligible, $(\frac{\partial}{R\partial \theta} = 0)$, all quantities are expressed in non-dimensional forms as follows:

$$u = \frac{U}{w_m} \qquad v = \frac{V}{w_m} \qquad w = \frac{W}{w_m}$$

$$\xi = \frac{r}{a} \ , \qquad p = \frac{p^*}{\rho w_m^2} \ , \qquad \tau = \frac{\tau^*}{\rho w_m^2} \ ,$$

$$H = \frac{R}{a} \qquad (5.1.4)$$



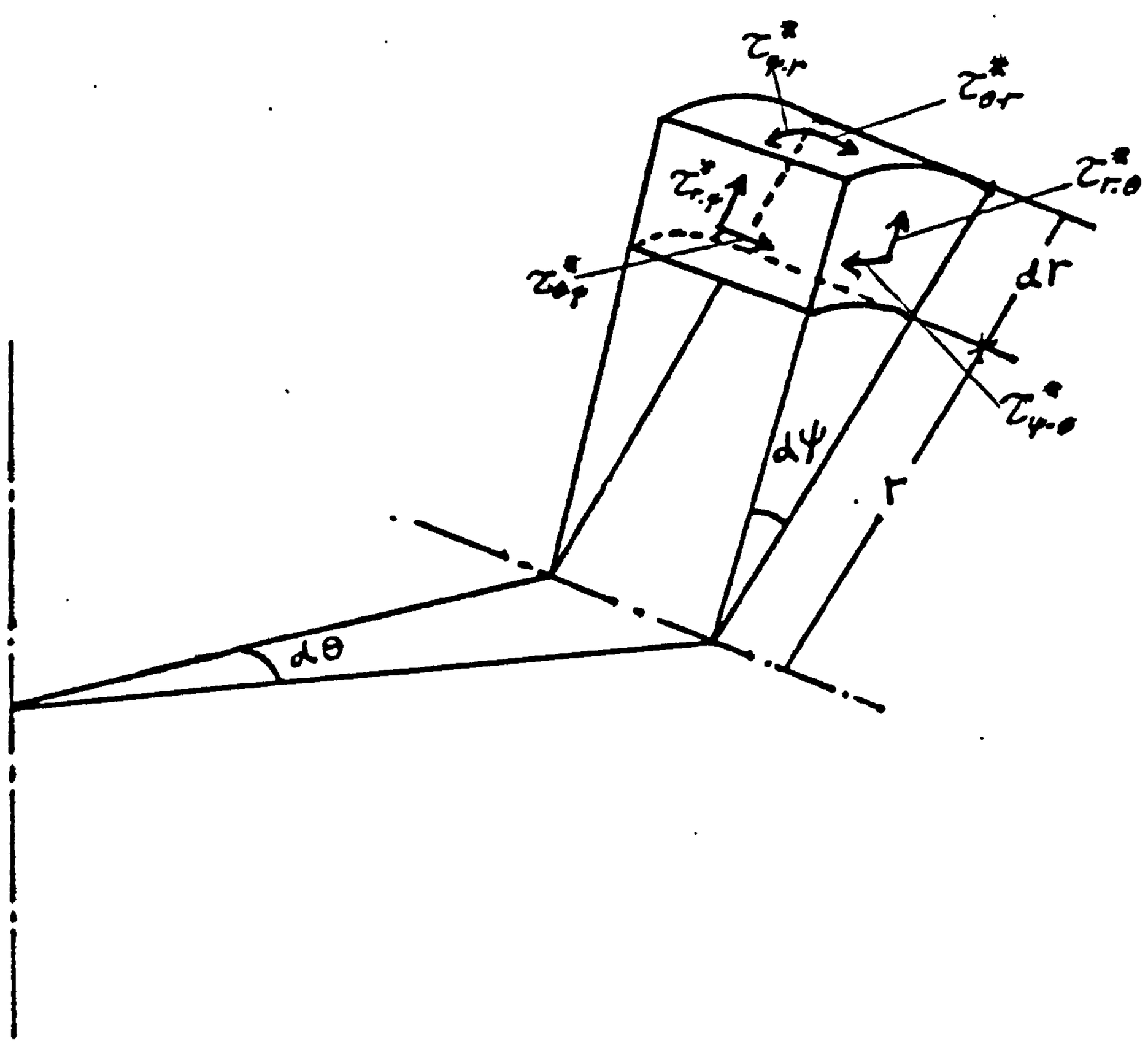


Fig.(5.1.1) Coordinate system for Helically-coiled circular tube.

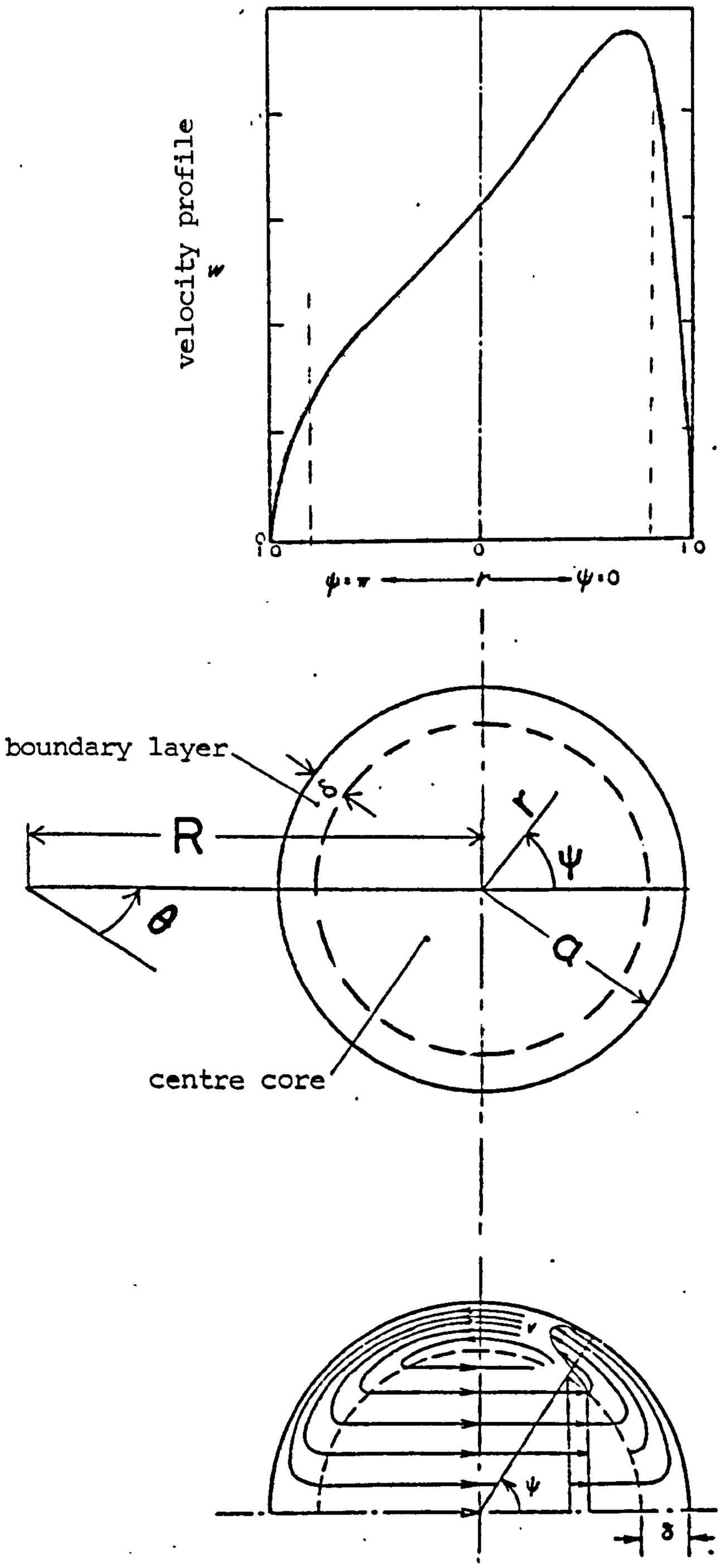


Fig.(5.1.2.) Single-phase flow model

where W_m is the mean axial component of the velocity. The non-dimensional continuity equation becomes

$$\frac{\partial \xi u}{\partial \xi} + \frac{\partial v}{\partial \psi} = 0 \qquad (5.1.5)$$

Equation (5.1.2) becomes as follows:

$$u\frac{\partial u}{\partial \xi} + v\frac{\partial u}{\xi \partial \psi} - \frac{v^2}{\xi} = \frac{w^2}{H}\cos\psi - \frac{\partial p}{\partial \xi} + \frac{\partial\, {}^{\tau}r.\psi}{\xi \partial \psi}$$

$$u\frac{\partial v}{\partial \xi} + v\frac{\partial v}{\xi \partial \psi} + \frac{uv}{\xi} = -\frac{w^2}{H}\sin\psi - \frac{\partial p}{\xi \partial \psi} + \frac{\partial \xi {}^{\tau}\psi.r}{\xi \partial \xi}$$

$$u\frac{\partial w}{\partial \xi} + v\frac{\partial w}{\xi \partial \psi} = -\frac{1}{H}\frac{\partial p}{\partial \psi} + \frac{\partial \xi {}^{\tau}\theta.r}{\xi \partial \xi} + \frac{\partial\, {}^{\tau}\theta.\psi}{\xi\ \partial\ \psi} \qquad (5.1.6)$$

When the flow is turbulent, mean velocity is always large enough to produce a secondary flow. The magnitude of this secondary flow is a main factor in determining the whole velocity distribution. Shear stresses act over a cross-section of the tube except a thin layer along the wall. The region where the stresses caused by the secondary flow are predominant is called the core region and Euler's equation can be applied. The thin layer next to the wall where all kinds of stresses cannot be ignored is called a boundary layer. The region of the boundary layer is denoted by δ. These regions are shown in Fig.(5.1.2).

5.1.1.1 The velocity distributions in the core region

When the flow is steady and fully developed, the pressure gradient along the pipe axis is constant. The constant in a dimensionless form is written as:

$$\frac{1}{H}\frac{\partial p}{\partial \theta} = C \qquad (5.1.7)$$

Also the velocity in the axial direction, w, is considerably larger than the velocity components u, v of the secondary flow which is produced by the centrifugal force. Therefore the small terms of the com-

ponents u and v may be omitted, then eq. (5.1.6) becomes:

$$u.\frac{\partial w}{\partial \xi} + v.\frac{\partial w}{\xi \partial \psi} = -c$$

$$\frac{\partial p}{\partial \xi} = \frac{w^2}{H} \cos \psi$$

$$\frac{\partial p}{\xi \partial \psi} = -\frac{w^2}{H} \sin \psi \qquad (5.1.8)$$

Elimination of the pressure terms from these equations yields the following relation for w:

$$\cos \psi . \frac{\partial w}{\xi \partial \psi} + \sin \psi \frac{\partial w}{\partial \xi} = 0 \qquad (5.1.9)$$

The velocity components u, v, w satisfying equations (5.1.5), (5.1.8) and (5.1.9) are put in the most simple forms as follows:

$$u = D \cdot \cos \psi$$

$$v = -D \cdot \sin \psi$$

$$w = A - \frac{C}{D} \xi . \cos \psi \qquad (5.1.10)$$

where A and D are constant. The secondary flow in the core region is a uniform horizontal flow towards the outer wall (see Fig. 5.1.2).

5.1.1.2 <u>The velocity distributions and the wall shear stresses in the boundary layer</u>

The thickness of the boundary layer, δ, is assumed to be $\delta = \frac{\delta}{a}^* \ll 1$. The values of velocity components u, v, w are approximately $u \sim \delta$, $v \sim 1$, $w \sim 1$ and the small terms of δ are omitted. Eq. (5.1.6) becomes at $\xi = 1 - \eta \doteqdot 1$ as follows:

$$-v^2 = \frac{w^2}{H} \cdot \cos \psi + \frac{\partial p}{\partial \eta}$$

$$-u \cdot \frac{\partial v}{\partial \eta} + v \cdot \frac{\partial v}{\partial \psi} = -\frac{w^2}{H} \cdot \sin \psi - \frac{\partial p}{\partial \psi} - \frac{\partial}{\partial \eta} . \tau_{\psi . r}$$

$$-u\cdot\frac{\partial w}{\partial \eta} + v\cdot\frac{\partial w}{\partial \psi} = -c - \frac{\partial}{\partial \eta}\cdot \tau_{\theta\cdot r} \qquad (5.1.11)$$

Integrating eq. (5.1.11) by η from 0 to δ

$$p_\delta - p_o = \int_0^\delta (v^2 + \frac{w^2}{H}\cdot\cos\psi)\, d\eta$$

$$(\tau_{\psi\cdot r})_{\eta=0} = \int_0^\delta \frac{\partial p}{\partial \psi}\, d\eta + \frac{1}{H}\sin\psi\int_0^\delta w^2 d\eta + \frac{\partial}{\partial \psi}\int_0^\delta v^2 d\eta - v_\delta\cdot\frac{\partial}{\partial \psi}\int_0^\delta v d\eta$$

$$(\tau_{\theta\cdot r})_{\eta=0} = c\,\delta + \frac{\partial}{\partial \psi}\int_0^\delta v\cdot w d\eta - w_\delta\frac{\partial}{\partial p}\int_0^\delta v d\eta \qquad (5.1.12)$$

The velocity component w in the boundary layer is put in the following forms:

at $\eta = 0$, $w = 0$

and follows the $^1/(2m-1)$ power law (see Goldstein (105-1957)) at $\eta = \delta$,

$$w = w_\delta\cdot(\frac{\eta}{\delta})^{\frac{1}{2m-1}} \qquad (5.1.13)$$

The boundary conditions for v are

at $\eta = 0$, $v = 0$

and at $\eta = \delta$, $v = v_\delta$

The condition of continuity is

$$\int_o^\delta v d\eta = -(1-\delta)\cdot D\cdot\sin\psi \qquad (5.1.14)$$

So as to satisfy these conditions and follow the $^1/(2m-1)$ power law near the wall, v is written as:

$$v = -D\cdot\sin\psi\{-\frac{m}{m-1}(\frac{2}{\delta}-1)(\frac{\eta}{\delta})^{\frac{1}{2m-1}} + \frac{1}{m-1}(\frac{2m}{\delta}-1)(\frac{\eta}{\delta})\} \qquad (5.1.15)$$

Supposing that $\delta << 2$ and $2m$, eq. (5.1.15) is simplified to the following:

$$v \doteq \frac{2m}{(m-1)\delta}\cdot\{(\frac{\eta}{\delta})^{\frac{1}{2m-1}} - (\frac{\eta}{\delta})\}\cdot D\cdot\sin\psi \qquad (5.1.16)$$

The shear stress in the direction of the pipe axis at the wall, $(\tau_{\theta.r})_{\eta=0}$ in eq. (5.1.12) becomes as follows, by integration of eqs. (5.1.15) and (5.1.16):

$$(\tau_{\theta.r})_{\eta=0} = C.\delta + \frac{4m(2m-1)}{(4m-1)(2m+1)} \{C(1-2\cos^2\psi) + AD\cos\psi\}$$

$$- (AD - C\cos\psi)\cos\psi \qquad (5.1.17)$$

The pressure term in eq. (5.1.12) is modified as follows:

$$p_\eta = p_\delta - \int_\eta^\delta (v^2 + \frac{w^2}{H} \cdot \cos\psi)\, d\eta \qquad (5.1.18)$$

The shear stress in the circumferential direction at the wall becomes as follows, using eq. (5.1.18) and neglecting small terms of δ:

$$(\tau_{\psi.r})_{\eta=0} = -\frac{2}{2m+1} \cdot \frac{w_\delta^2}{H} \cdot \sin\psi.\delta + \frac{32m^2D^2}{3(2m+1)(4m-1)} \cdot \frac{\sin\psi}{\delta} \cdot (2\cos\psi$$

$$- \frac{\sin\psi}{\delta} \cdot \frac{d\delta}{d\psi}) \qquad (5.1.19)$$

The distance from the wall where the circumferential component of the velocity, v, becomes the maximum value is denoted by η_s. Assuming that $(\tau_{\psi.r})_{\eta=0} / (\tau_{\theta.r})_{\eta=0}$ is equal to v/w at $\eta = \eta_s$, it becomes:

$$\left(\frac{v}{w}\right)_{\eta=\eta_s} = -\frac{4mv_\delta}{(2m-1)\delta w_\delta} \qquad (5.1.20)$$

and

$$(\tau_{\psi.r})_{\eta=0} = \frac{4mD\sin\psi}{(2m-1)\delta(A - \frac{C}{D}\cdot\cos\psi)} \cdot (\tau_{\theta.r})_{\eta=0} \qquad (5.1.21)$$

The circumferential and axial components of the velocity, v and w, are denoted by v_s and w_s at $n=n_s$ where v reaches maximum in the boundary layer. Supposing $v_s<<w_s$, then the resultant velocity is

$$S_r = (v_s^2 + w_s^2)^{\frac{1}{2}} \doteq w_s \qquad (5.1.22)$$

The $1/(2m-1)$ power law for a straight tube can be employed for S, thus

$$S = S_r \cdot (\frac{n}{n_s})^{\frac{1}{2m-1}} \qquad (5.1.23)$$

Supposing a short section of the coil is taken, whose length is small in comparison to the coil diameter. This imaginary tube element may be assumed straight. In this element, the velocity in the axial direction becomes S_r at $n=n_s$, and the mean velocity, S_m, is expressed as follows:

$$S_m = \int_0^1 2\xi \cdot S \cdot d\xi = \frac{(2m-1)^2}{m(4m-1)} \cdot n_s^{\frac{1}{2m-1}} \cdot S_r \qquad (5.1.24)$$

and using the following velocity relation:

$$w_s = w_\delta (2m-1)^{\frac{1}{2(m-1)}} \doteq S_r \qquad (5.1.24a)$$

Therefore the mean velocity in the supposed straight pipe is

$$S_m^* = \frac{(2m-1)^2}{m(4m-1)} \cdot W_m \cdot W_\delta \cdot \delta^{\doteq \frac{1}{2m-1}} \qquad (5.1.24b)$$

For simplifying the process of the analysis, B_m is employed, as follows:

$$\frac{(2m-1)^2}{m(4m-1)} = B_m \qquad (5.1.24c)$$

The formula of the straight tube friction factor is expressed in general form as eq. (2.29)

$$f_s = \alpha . Re_s^{-\frac{1}{m}} \qquad (2.29)$$

where

$$Re_s = \frac{2aS_m}{\nu} \qquad (5.1.25)$$

The shear stresses at the wall in the axial and circumferential components of the velocity in the coiled tube yield the following:

$$(\tau_{\theta . r})_{\eta=0} = -\frac{\alpha}{g} \cdot B_m \left\{\frac{2aw_m}{\nu}\right\}^{2-\frac{1}{m}} \cdot w_\delta^{-\frac{1}{m}} \cdot \delta^{2-\frac{1}{m}}$$

$$(\tau_{\phi r})_{\eta=0} = (\tau_{\theta . r})_{\eta=0} \cdot \frac{v_s}{w_s} = (\tau_{\theta . r})_{\eta=0} \cdot \frac{4m \cdot D \cdot \sin\psi}{(2m-1)\delta w_\delta} \qquad (5.1.26)$$

Hereafter in order to simplify the calculation

$$\Lambda_{\delta=\delta} = (\tau_{\theta . r})_{\eta=0} = -\frac{\alpha}{g} \cdot B_m \cdot \left\{\frac{2aW_m}{\nu}\right\}^{2-\frac{1}{m}} \cdot w_\delta^{-\frac{1}{m}} \cdot \delta^{2-\frac{1}{m}} \qquad (5.1.26a)$$

Eliminating $(\tau_{\theta . r})_{\eta=0}$ from eqs. (5.1.17) and (5.1.26)

$$C.\delta + \frac{4m(2m-1)}{(4m-1)(2m+1)} \{C(1-2\cos^2\psi) + AD.\cos\psi\} - (AD - C.\cos\psi)\cos\psi$$

$$= -\Lambda_{\delta=\delta o} \qquad (5.1.27)$$

Neglecting effects such as gravity, the secondary flow stream-lines in the upper and lower halves in a coiled tube are thought to be symmetrical. Assuming that δ is expressed as:

$$\delta = \delta_o \ (1 + K_1 \cos\psi + \text{---}), \qquad (5.1.28)$$

and also

$$w_\delta^{2-\frac{1}{m}} = A^{2-\frac{1}{m}} \left(1 - \frac{2m-1}{m} \cdot \frac{C}{AD} \cdot \cos\psi + \text{----}\right)$$

$$\delta^{-\frac{1}{m}} = \delta_o^{-\frac{1}{m}} \left(1 - \frac{K_1}{m} \cos\psi + \text{----}\right) \qquad (5.1.29)$$

The small terms of $\cos\psi$ (i.e. $\cos^2\psi$, $\cos^3\psi$--) are omitted, then substituting eqs. (5.1.28) and (5.1.29) into eq. (5.1.27), the following is obtained:

$$C\{\delta_o + \frac{4m(2m-1)}{(4m-1)(2m+1)} \cdot \frac{8m^2-10m+1}{(4m-1)(2m+1)} \cdot \cos^2\psi\}$$

$$+ \{CK_1\delta_o - \frac{6m-1}{(4m-1)(2m+1)} \cdot AD\} \cdot \cos\psi$$

$$= -\Lambda_{\delta=\delta_o} + \{\frac{2m-1}{m} \cdot \frac{C}{AD} + \frac{K_1}{m}\} \cdot \Lambda_{\delta=\delta_o} \cdot \cos\psi \qquad (5.1.30)$$

C must be independent on ψ in the first term of the left hand side in eq. (5.1.30) so the first term of the left hand side is obtained by substituting mean value of $\cos^2\psi$. The terms of constant, C and $\cos\psi$ in both sides are equated as follows:

$$C(\boxed{\delta_o} + \frac{1}{2}) = -\Lambda_{\delta=\delta o}$$

and

$$\{\boxed{CK_1\delta_o} - \frac{6m-1}{(4m-1)(2m+1)} \cdot AD\} = \{\frac{2m-1}{m} \cdot \frac{C}{AD} + \frac{K_1}{m}\} \cdot \Lambda_{\delta=\delta_o}$$

(5.1.31)

where

$$\Lambda_{\delta=\delta_o} = -\frac{\alpha}{8} B_m \cdot \{\frac{2aW_m}{n}\}^{2-\frac{1}{m}} \cdot W_\delta^{-\frac{1}{m}} \cdot \delta^{2-\frac{1}{m}} \cdot \delta^{-\frac{1}{m}}$$

Taking eqs. (5.1.21) and (5.1.28) and using the same method as for eqs. (5.1.30) and (5.1.31), yields the following:

$$\left(\frac{a}{R}\right)\left(\frac{A}{D}\right)^2 \cdot \delta_o^{\,2} + \boxed{\frac{2m(2m+1)}{2m-1} \cdot \frac{C}{AD} \cdot \delta_o} = \frac{16m^2}{3(4m-1)} K_1 + \frac{8m^2}{4m-1} \cdot \frac{C}{AD} = 0$$

and

$$\left(\frac{a}{R}\right)\left(\frac{A}{D}\right)^2 \cdot \delta_o^{\,2} \cdot \left(2K_1 - \frac{3C}{AD}\right) + \boxed{\frac{2m(2m+1)}{2m+1} \cdot \frac{C}{AD} \cdot \delta_o \cdot K_1} + \frac{16m^2}{3(4m-1)} \cdot K_1 \cdot \left(K_1 + \frac{C}{AD}\right)$$

$$- \frac{2m(32m^2 + 2m - 3)}{3(4m-1)(2m-1)} = 0 \qquad (5.1.32)$$

Assuming that $\delta_o \ll 1$, the enclosed terms of δ_o are omitted in eqs. (5.1.31) and (5.1.32) and then K_1, C and D are obtained from these two equations. Their values are $K_1 \sim 1$, $C/AD \sim 1$, $C \sim \delta_o$ and $D \sim \delta_o$.

Also A is obtained from the formula for total mass flow rate.

$$\pi a^2 W_m = \int_0^{2\pi} \int_0^{a} w.r.dr.d\psi \qquad (5.1.33)$$

where W_m is the mean velocity in axial direction. Since both of the velocity distributions in the boundary layer and that in the core region are established, the dimensionless formula becomes:

$$\pi = \int_0^{2\pi} \int_0^{1-\delta} \left(A - \frac{C}{D}\xi\cos\psi\right)\xi.d\xi.d\psi + \int_0^{2\pi} \int_0^{\delta} \left(A - \frac{C}{D}\cos\psi\right)\left(\frac{\eta}{\delta}\right)^{\frac{1}{2m-1}} \cdot (1-\eta)d\eta.d\psi \qquad (5.1.34)$$

In order to simplify, δ is replaced by its mean value δ_o and the relation A and δ_o is obtained.

$$A = \frac{1}{1 - \frac{1}{m} \cdot \delta_o + \frac{1}{4m-1} \cdot \delta_o^{\,2}} \doteq 1 + \frac{1}{m} \cdot \delta_o \qquad (5.1.35)$$

For the appropriate range of Reynolds numbers, α and m are determined in order to find an approximation for the actual relation between f_s and Re_s. The commonly used value of $\underline{m}$ is 4. When $\underline{m}$ is

taken as 4, the value of $\underline{\alpha}$ is 0.316 after Blasius's resistance formula which is valid for Reynolds numbers less than 10^5.

Eq's (5.1.31) and (5.1.32) are solved at $m = 4$ and $\alpha = 0.316$,

$$\frac{C}{AD} = - 0.469$$

$$K_1 = 0.378$$

$$\left(\frac{a}{R}\right)\left(\frac{A}{D}\right)^2 \cdot \delta_o^{\,2} = 6.147$$

$$C = - 0.0617\ Re^{\frac{.1}{5}} \cdot A^{\frac{9}{5}} \cdot \left(\frac{a}{R}\right)^{\frac{1}{10}} \qquad (5.1.36)$$

5.1.1.3 The friction factor

The definition of the friction coefficient for a curved tube is given by the following:

$$f_c = - \frac{\partial P}{R \partial \theta} \cdot \frac{2a}{\frac{1}{2} \cdot \rho \cdot W_m^2} = - 4\ C \qquad (5.1.37)$$

The formula of friction coefficient in a coiled tube is obtained from eq's (5.1.35) to (5.1.37) and the small terms are neglected,

$$f_c \left(\frac{a}{R}\right)^{\frac{1}{2}} = 0.247 \left\{Re \left(\frac{a}{R}\right)^2\right\}^{-\frac{1}{5}} \left[1 + 0.169 \left\{Re \left(\frac{a}{R}\right)^2\right\}^{\frac{1}{5}} \right] \qquad (5.1.38)$$

In order to simplify the later calculations,

$$F = \left\{Re \left(\frac{a}{R}\right)^2\right\}^{\frac{1}{5}} \qquad (5.1.38a)$$

Eq (5.1.38) agrees well with Ito's (25) empirical result, eq. (2.32)

$$f_c \left(\frac{a}{R}\right)^{\frac{1}{2}} = 0.029 + 0.304 \left\{Re \left(\frac{a}{R}\right)^2\right\}^{\frac{1}{4}} \qquad (2.32)$$

for $0.034 < R_e \left(\frac{a}{R}\right)^2 < 300$

Mori and Nakayama (24) also made a similar formula to eq. (2.30)

$$f_c\left(\frac{a}{R}\right)^{-\frac{1}{2}} = 0.300\{Re\left(\frac{a}{R}\right)\}^{\frac{-1}{5}}\left[1 + 0.112\{Re\left(\frac{a}{R}\right)\}^{\frac{-1}{5}}\right] \qquad (2.30)$$

These three formulae and the results for the present work in section (4.2.2.1) are shown in Fig. (5.1.3).

The thickness of the boundary layer is also obtained by eq's (5.1.35) and (5.1.36) as the following:

$$\delta_o = 0.327\{Re\left(\frac{a}{R}\right)\}^{\frac{-1}{5}}\left[1 - 0.0188\{Re\left(\frac{a}{R}\right)\}^{\frac{-1}{5}}\right] \qquad (5.1.39)$$

From eq. (5.1.28), δ becomes

$$\delta = \delta_o\ (1 + 0.378\ \cos\psi\ ) \qquad (5.1.40)$$

The values of δ_o for the three coils are shown in Fig. (5.1.4). Also shown are the values at the critical Reynolds number in coiled tube obtained by the following equation which was proposed by Ito (25):

$$Re_{cr} = 2 \times 10^4 \cdot \left(\frac{a}{R}\right)^{0.32} \qquad (2.24)$$

The velocity components in the axial direction for the coiled tube are formulated as the following:

For the core region obtained from eq. (5.1.10)

$$W = \left[1 + 0.0938\ \{Re\left(\frac{a}{R}\right)^2\}^{\frac{-1}{5}}\right](1 + 0.469\xi\ \cos\psi) \qquad (5.1.41)$$

For the boundary layer obtained from eq. (5.1.13)

$$W = (W)_{\xi=1}\ \left(\frac{n}{\delta}\right)^{\frac{1}{7}} \qquad (5.1.42)$$

The velocity profile of the axial component in the core region, eq. (5.1.41), is shown in Fig. (5.1.5) together with the empirical result of Mori and Nakayama (24).

The shear stress of the axial direction at the tube wall in the

coiled tube is expressed by eq's (5.1.26) and (5.1.29) as the following:

$$\tau_w = -(\tau_{\theta.r})_{\eta=0} = 0.366.\left(\frac{a}{R}\right)^{\frac{1}{2}}\left(1 + \frac{0.109}{F}\right).\frac{(1 + 0.727\cos\psi)}{F} \qquad (5.1.43)$$

where $F = \{Re(\frac{a}{R})^2\}^{\frac{1}{5}}$

5.1.1.4 Comparison of theoretical analyses and the empirical results

Comparison of the friction factors obtained by the present theoretical analysis with the empirical results of Ito (25), Mori and Nakayama (24), Seban and McLaughlin (22) and the present work. The formula is shown in Fig. (5.1.3), from the present work (shown as C) and appears slightly below the empirical formulae of Ito and Seban and McLaughlin (shown as A and B) and the theoretical formula of Mori and Nakayama (shown as B), however the present formula is in good agreement with others. The empirical results of the present work with heat transfer to the coiled tube are also compared with them, and the results at 1,875 and 934 $^{Kcal}/_{m^2h}$ heat inputs are also in good agreement.

Fig. (5.1.4) shows the mean thickness of the boundary layer against $\{Re(\frac{a}{R})^2\}$. The transition points to turbulent flow of three Coils are also shown. These three points show thick boundary layers therefore the assumption that $\delta_0 << 1$ is applicable in very high ranges of Reynolds numbers.

Fig. (5.1.5) shows the axial velocity profile in the core region of eq. (5.1.41) and the empirical velocity profiles taken by Mori and Nakayama (24). The present results at $\psi = 0^o$ show a greater incline than that of Mori and Nakayama but are well applicable. This gradient is determined by the value of $\frac{C}{AD}$ (see eq. (5.1.10)), the values of

$\frac{C}{AD}$ converged at -0.469 for the present work, - 0.441 for Mori and Nakayama and -0.38 for Ito at $\delta_o << 1$. The mean thickness of the boundary layer, δ_o, becomes constant at the higher range of $\{Re(\frac{a}{R})^2\}$, i.e. $\{Re(\frac{a}{R})^2\}$ 300 (see Fig. (5.1.4). Hence these values of the $(\frac{C}{AD})$ are constant in the higher range of Reynolds number.

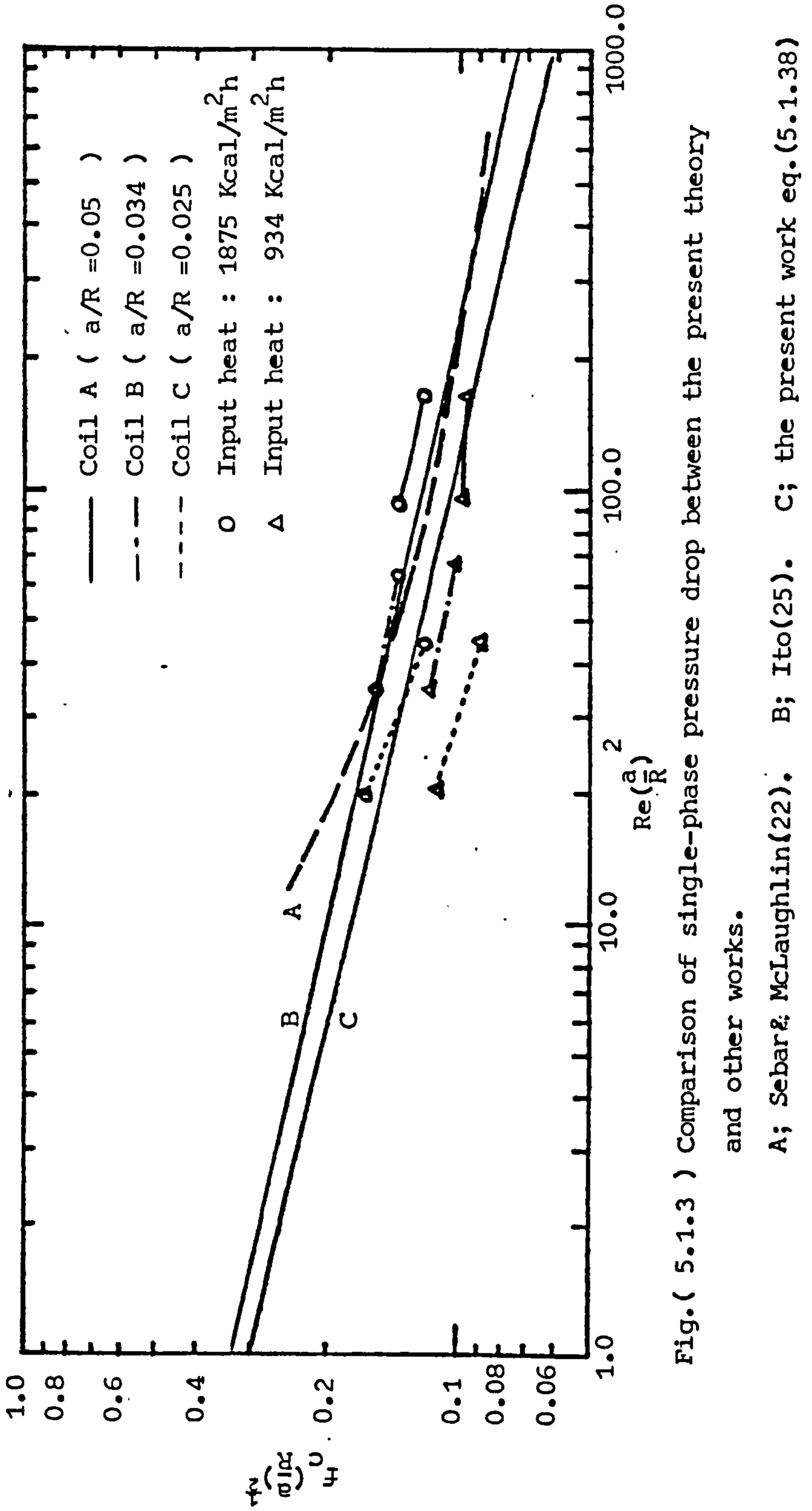


Fig.(5.1.3) Comparison of single-phase pressure drop between the present theory and other works.

A; Sebar& McLaughlin(22). B; Ito(25). C; the present work eq.(5.1.38)

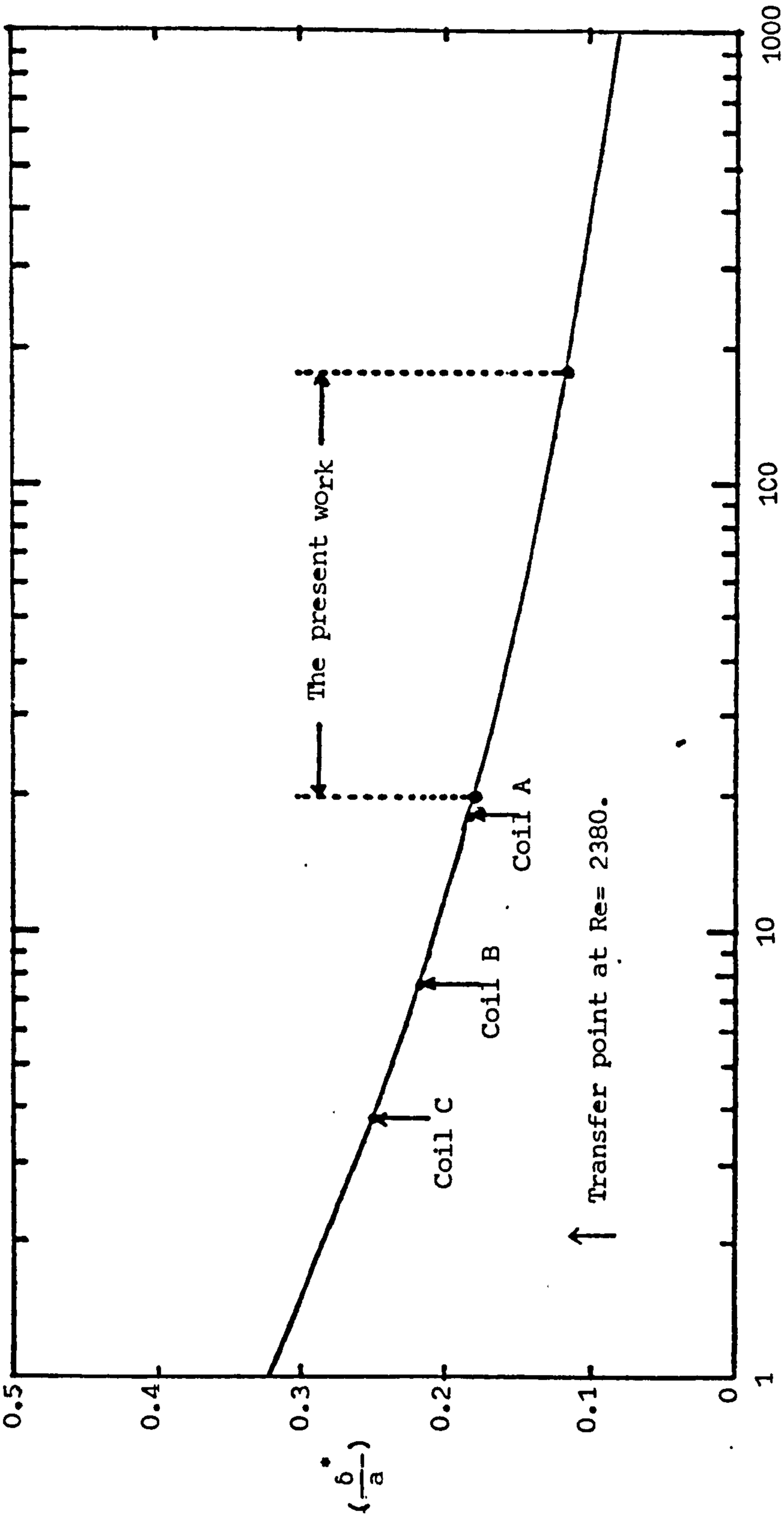


Fig. (5.1.4) Mean thickness of boundary layer.
δ^* is defined by eq.(5.1.39)

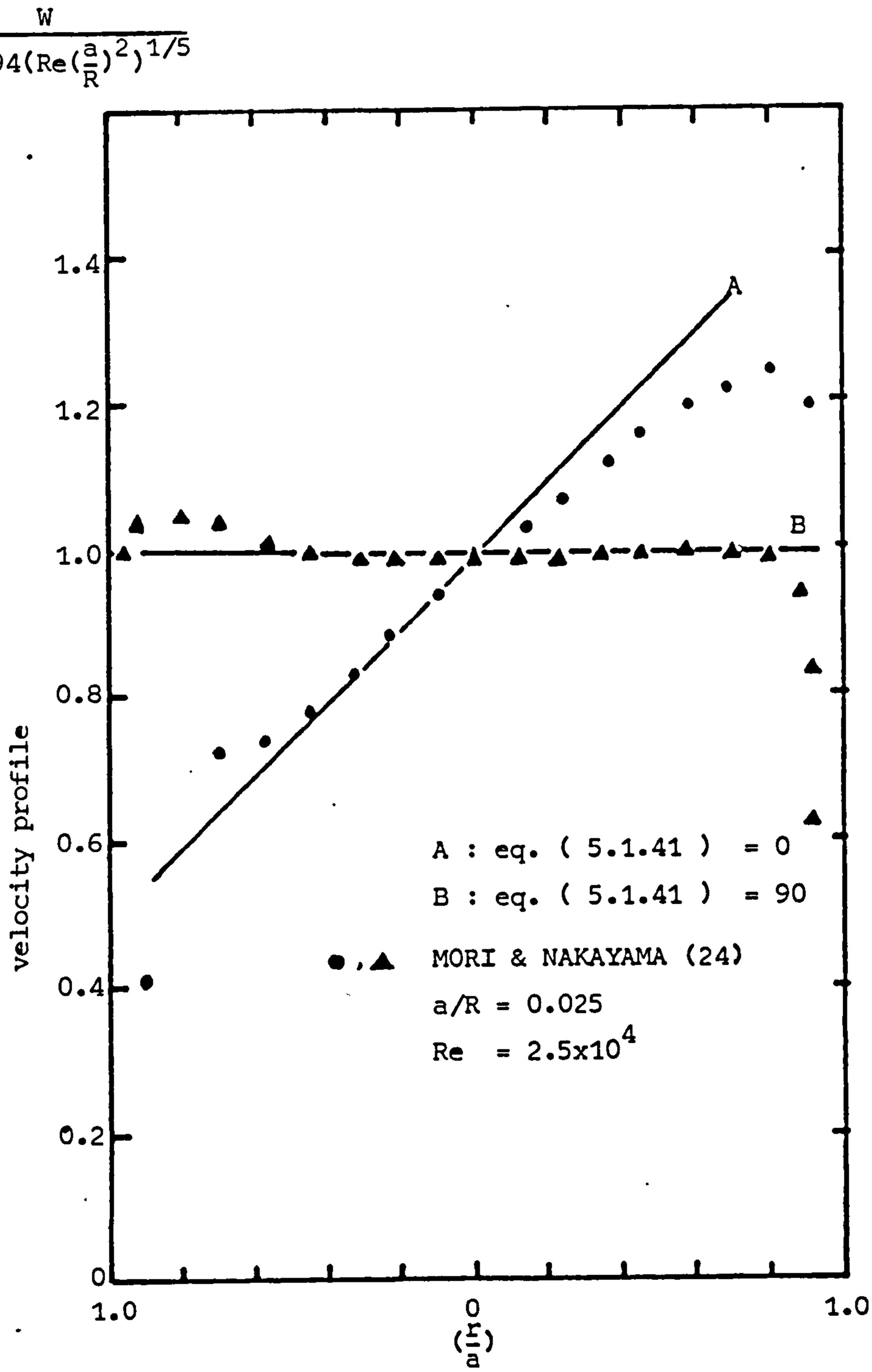


Fig. (5.1.5) Velocity profiles in horizontal and vertical planes of eq. (5.1.41)

5.1.2 Analysis of heat transfer coefficient in single-phase flow

In the present analysis, the heat transfer coefficient profile on the tube periphery is defined when the rate of total heat flux through a cross-section is constant along the tube axis. The Prandtl numbers of the steam for the present work were 1.09~1.19 (i.e. $\doteqdot$ 1.0) therefore the Taylor-Prandtl analogy may be employed to analyse the heat transfer coefficient.

It was assumed in this analysis that the following effects could be neglected:

a. Heat flux in the axial direction

b. Heat gain due to the friction loss

c. Heat transfer due to the work of compression and radiation,

d. The effects of the curvature to the energy equation

Consider a segment of the flow cross-section with a small radial length, dr, and a small circumferential angle, $d\psi$, shown as Fig. (5.1.6).

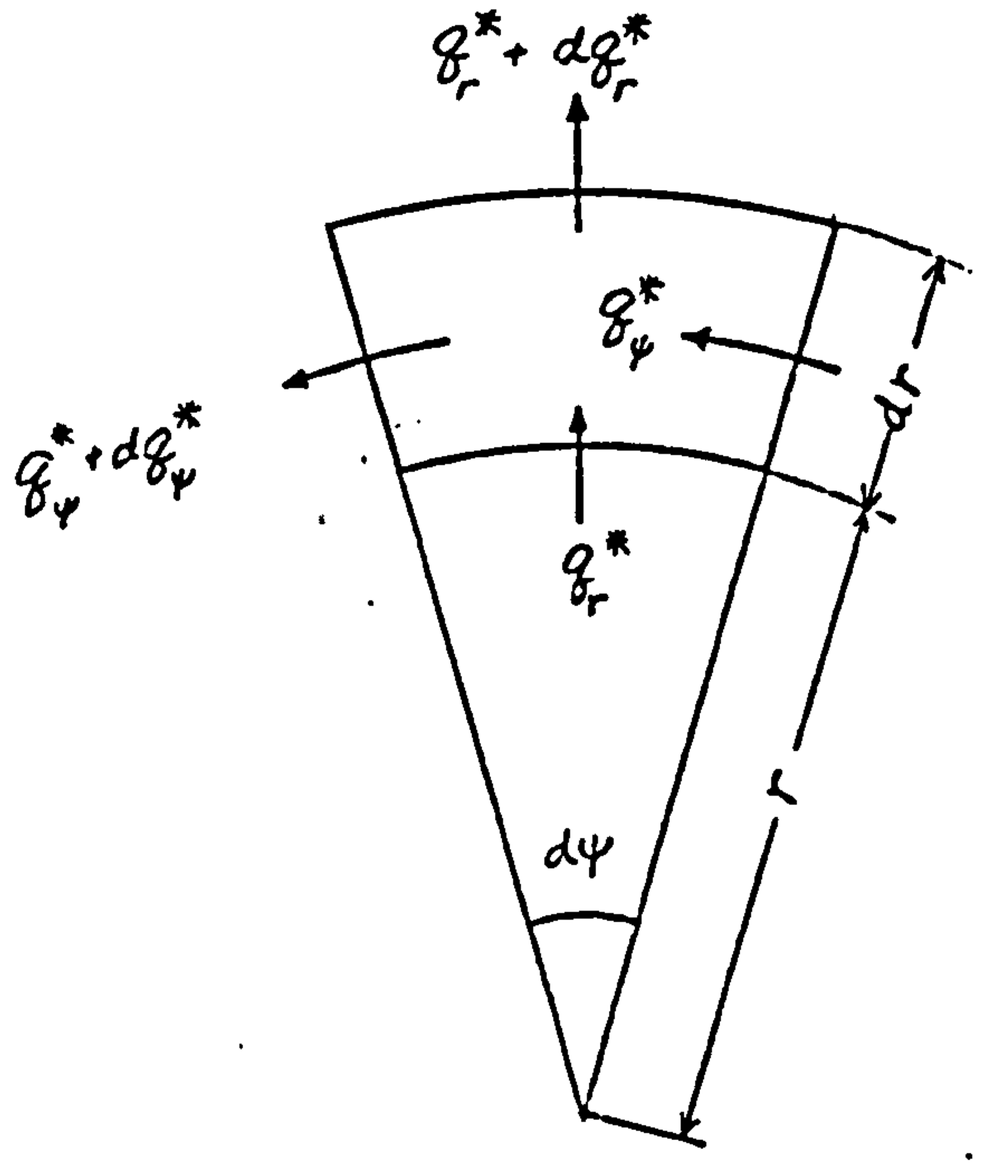


Fig. (5.1.6) Energy balance in r, ψ directions of the fluid.

The energy equation at the steady state in the supposed minute cube (see Fig. (5.1.1)) is defined as follows:

$$C_p \rho g \left(U\frac{\partial T}{\partial r} + V\frac{\partial T}{r\partial \psi} + W\frac{\partial T}{R\partial \theta}\right) = -\left(\frac{\partial r q_r^*}{r\partial r} + \frac{\partial q_\psi^*}{r\partial \psi} + \frac{\partial q_\theta^*}{R\partial \theta}\right) \qquad (5.1.44)$$

where C_p is the specific heat, ρ is density and q^* is heat flux.

The temperature gradient in the axial direction is constant, and is defined as follows:

$$\frac{\partial T}{R\partial \theta} = C_\theta,$$

and from the assumptions,

$$\frac{\partial q_\theta^*}{R\partial \theta} = 0 \qquad (5.1.45)$$

The equation (5.1.4) and the quantities T and q are expressed as follows:

$$T = \frac{T^*}{a.C_\theta}$$

$$q = \frac{q^*}{Cp.\rho.g.W_m.a.C_\theta} \qquad (5.1.46)$$

where a is the tube radius and W_m is the axial velocity component.

The energy equation, eq. (5.1.44) is rewritten in a dimensionless form, using eq's (5.1.4) and (5.1.46), as follows:

$$u.\frac{\partial T}{\partial \xi} + v.\frac{\partial T}{\xi\partial \psi} + w = -\left(\frac{\partial \xi q_r}{\xi\partial \xi} + \frac{\partial q_\psi}{\xi\partial \psi}\right) \qquad (5.1.47)$$

where $\xi = r/a$.

5.1.2.1 Temperature profile in the core region

In general, heat conduction is the predominant factor in a laminar flow and low Dean number region. The secondary flow introduces additional convective heat transfer. In a large Dean number region, when the secondary motion is strong, it is thought that the contribution of the secondary flow to heat transfer is predominant in the core region of the cross section except for a thin layer near to the tube wall. The secondary flow tends to make the temperature distribution uniform in the core region, while in the region adjacent to the wall a steep temperature gradient can be found.

Assuming that convective heat transfer only affects the core region of a turbulent flow, the right hand terms of eq. (5.1.47) disappear thus:

$$u\frac{\partial T}{\partial \xi} + v.\frac{\partial T}{\xi \partial \psi} = - w \qquad (5.1.48)$$

The dimensionless temperature T is written in the following form so as to satisfy eq. (5.1.48). Also terms for u, v, and w from eq. (5.1.10) have been substituted.

$$T - Tc = \frac{1}{2}\left(\frac{A}{D}\right).\xi.\left(\frac{C}{AD}\xi - 2.\cos\psi\right) \qquad (5.1.49)$$

where Tc is an integrating constant.

The constant Tc is determined by considering total heat balance about a cylindrical slice of the fluid at a cross section of the pipe.

A correction factor, S_c, is substituted into eq. (5.1.49). This has an empirical value which ensures the function in eq. (5.1.49) and describes closely the experimental data.

$$T - T_c = \frac{1}{2} \cdot S_c \cdot \left(\frac{A}{D}\right).\xi.\left(\frac{C}{AD}\,\xi - 2\cos\psi\right) \qquad (5.1.50)$$

5.1.2.2 Heat transfer in thermal boundary layer

The Prandtl numbers of the steam flow of the present work were 1.09∿1.19 (≒ 1.0). Therefore the flow may be divided into two zones (i.e. the laminar sub-layer and the turbulent zone) for the application of the Taylor-Prandtl analogy.

i.e. $$\tau = \frac{1}{a.w_m}\,(\nu + \varepsilon_m)\,\frac{dw}{d\eta}$$

$$q = \frac{1}{a.w_m}\left(\frac{\nu}{Pr} + \varepsilon_H\right)\frac{dT}{d\eta} \qquad (5.1.51)$$

where ε_M is the eddy diffusivity of momentum,

ε_H is the eddy diffusivity of thermal energy conductivity,

and ν is kinetic viscosity.

In the laminar sub-layer,

$\varepsilon_M = \varepsilon_H = 0$

$\tau = \tau_w$, and $q = q_w$

Referring to Katto (78) the transition point between laminar sub-layer and turbulent zone in a straight tube is defined as follows:

$$\frac{(\tau w^*/\rho)^{\frac{1}{2}} \cdot \delta_b^*}{\nu} \quad \text{or} \quad \frac{a.w_m(\tau_m)^{\frac{1}{2}}}{\nu} \cdot \delta_b = 12.26 \qquad (5.1.52)$$

where δ_b^* is the thickness of boundary sub-layer.

In the turbulent core region, where the effect of turbulent fluctuations is predominant, ν and ν/Pr of eq. (5.1.51) can be ignored.

The $^{1}/(2m-1)$ power law is used for velocity distribution and the eddy diffusivities and $^{\tau}/q$ ratios in this core region becomes as follows:

$$\varepsilon_M = \varepsilon_H \,, \qquad \frac{\tau}{q} = \frac{\tau_w}{q_w}$$

Using the same method of derivation as used for the resultant velocity (S_r) at $\eta = \eta_s$ (see eq. (5.1.22)) the following equation is obtained for the velocity profile (S):

$$S = S_r \cdot \left(\frac{\eta}{\eta_s}\right)^{\frac{1}{2m-1}} \qquad (5.1.53)$$

where $\eta = 1 - \xi$.

The mean resultant velocity (S_m) can be defined as in eq. (5.1.24a), thus τ_w and Re_s become

$$\tau_w = \frac{\alpha}{8} \cdot \left(\frac{S_m^*}{w_m}\right)^2 \cdot Re_s^{-\frac{1}{m}}$$

where $Re_s = \dfrac{2.a.S_m^*}{\eta}$

Substituting eq. (5.1.54) into eq. (5.1.52),

$$\delta_b = \frac{\delta_b^*}{a} = \left(\frac{4809.8}{\alpha}\right)^{\frac{1}{2}} \cdot Re_s^{\frac{2m-1}{2m}} \qquad (5.1.55)$$

(i) <u>For laminar sub-layer</u>, from eq. (5.1.51)

$$dT = Pr. \frac{q_w}{\tau_w} \cdot ds \qquad (5.1.56)$$

The conditions of the sub-layer region are at

$\eta = 0 \qquad T = Tw, \quad S = 0$

and

$$\text{at } \eta = \delta_b \qquad T = T_b, \qquad S = S_m \cdot \left(\frac{\delta_b}{\eta_s}\right)^{\frac{1}{2m-1}}$$

Integrating eq. (5.1.56) between the above limits:

$$T_b - T_w = Pr. \frac{q_w}{\tau_w} \cdot S_m \cdot \left(\frac{\delta_b}{\eta_s}\right)^{\frac{1}{2m-1}} \tag{5.1.57}$$

where Tw is wall temperature.

(ii) For turbulent core region, from eq. (5.1.51)

$$dT = \frac{q_w}{\tau_w} \, ds \tag{5.1.58}$$

The conditions of the turbulent core region are

$$\text{at } \eta = \delta_b \qquad T = T_b, \quad S = S_m \left(\frac{\delta_b}{\eta_s}\right)^{\frac{1}{2m-1}}$$

and

$$\text{at } \eta = \delta_\theta \qquad T = T_\delta, \quad S = S_m \left(\frac{\delta_\theta}{\eta_s}\right)^{\frac{1}{2m-1}}$$

then also integrating eq. (5.1.58) between the above limits:

$$T_\delta - T_b = \frac{q_w}{\tau_w} \cdot S_m \cdot \left\{ \left(\frac{\delta_\theta}{\eta_s}\right)^{\frac{1}{2m-1}} - \left(\frac{\delta_b}{\eta_s}\right)^{\frac{1}{2m-1}} \right\} \tag{5.1.59}$$

$(Tw - T_\delta)$ is derived from eq's (5.1.57) and (5.1.59) as follows:

$$T_w - T_\delta = - S_m \frac{q_w}{\tau_w} \cdot \left\{ \left(\frac{\delta_\theta}{\eta_s}\right)^{\frac{1}{2m-1}} + (Pr - 1) \left(\frac{\delta_b}{\eta_s}\right)^{\frac{1}{2m-1}} \right\} \tag{5.1.60}$$

where δ_θ is the thickness of thermal boundary layer.

5.1.2.3 Heat transfer coefficient of boundary layer

A heat transfer coefficient (h_δ) which is determined by

the temperature difference between the inside tube wall and the surface of boundary layer as follows:

$$h_\delta = -\frac{q_w^*}{T_w^*-T_\delta^*} = \frac{C_p.g.\tau_w^*}{S_m^*}\left\{\left(\frac{\delta_\theta}{n_s}\right)^{\frac{1}{2m-1}} + (P_r-1)\left(\frac{\delta_b}{n_s}\right)^{\frac{1}{2m-1}}\right\}^{-1} \qquad (5.1.61)$$

Eq. (5.1.51) is expressed in non-dimensional form, as follows:

$$Nu_\delta = \frac{Pr\cdot Re\cdot\tau_w}{S_m}\left\{\left(\frac{\delta_\theta}{n_s}\right)^{\frac{1}{2m-1}} + (Pr-1)\left(\frac{\delta_b}{n_s}\right)^{\frac{1}{2m-1}}\right\}^{-1} \qquad (5.1.62)$$

In the case of coiled tube, the velocity boundary layer thickness (δ) has different characteristics from the straight pipe because of the existence of the secondary flow. However this analysis considers the condition near Pr = 1, therefore the thermal boundary layer thickness can be assumed to be equal to the velocity boundary layer thickness.

From Eqs. (5.1.24a), (5.1.25) and (5.1.26);

$$S_m = W_\delta\cdot(2m-1)^{-\frac{1}{2(m-1)}}$$

$$n_s = (2m-1)^{-\frac{2m-1}{2(m-1)}} \qquad (5.1.24a)$$

$$Re_s = Re.B_m.W_\delta.\delta^{-\frac{1}{2m-1}} \qquad (5.1.25)$$

$$\tau_w = -\tau_{\theta.r} = \frac{\alpha}{g}\cdot B_m^{\frac{2m-1}{m}}\left\{\frac{2aW_m}{\nu}\right\}^{-\frac{1}{m}}\cdot W_\delta^{\frac{m}{m}}\cdot\delta^{\frac{m}{m}} \qquad (5.1.26)$$

where W_δ and δ are obtained from eqa. (5.1.28) and (5.1.29).

Substituting these formulae into eq. (5.1.62), it becomes the following:

$$Nu_\delta Pr^{-1} = Y \cdot \frac{1 - \left(\frac{m-1}{m} \cdot \frac{C}{AD} + \frac{K_1}{m}\right) \cdot \cos\psi}{1 + (Pr-1) \cdot Z \cdot (Re.A.\delta)^{-\frac{1}{2m}}} \qquad (5.1.63)$$

where

$$Y = \frac{\alpha}{g} \cdot B_m^{\frac{2m-1}{m}} \cdot Re^{\frac{m-1}{m}} \cdot A^{\frac{m-1}{m}} \cdot \delta^{-\frac{1}{m}} \qquad (5.1.63a)$$

$$Z = \left(\frac{4809.8}{\alpha}\right)^{\frac{1}{2(2m-1)}} \cdot B_m^{-\frac{1}{2m}} \cdot \left\{1 + \frac{1}{2m}\left(\frac{C}{AD} - K_1\right)\cos\psi\right\} \qquad (5.1.63b)$$

5.1.2.4 Heat transfer coefficients for the uniform wall temperature in the circumferential direction

Nu_δ in the previous section is determined by the temperature difference between the inside tube wall and the surface of the boundary layer. This is still an imperfect way to describe heat transfer in single-phase flow and two Nusselt numbers are derived for correcting this procedure. One is the Nusselt number determined by the temperature difference between the inside tube wall and the centre of fluid (Nu_{ot}), the other is determined by the temperature difference between the inside tube wall and the mean temperature of the fluid ($N_{u_{mt}}$) with the uniform wall temperature in the circumferential direction.

(i) Derivation of Nu_{ot}

From Eq. (5.1.63)

$$q_w = \frac{Nu_\delta}{Pr \cdot Re} \cdot (Tw - T_\delta) \qquad (5.1.64)$$

T_δ is obtained from eq. (5.1.50) when ξ 1

$$T_\delta = T_c + \frac{1}{2}\cdot\left(\frac{A}{D}\right).S_c.\left(\frac{C}{AD} - 2\cos\psi\right) \qquad (5.1.65)$$

and the mean heat flux is obtained as follows:

$$q_{wm} = \frac{1}{2\pi}\int_0^{2\pi} q_w\, d\psi = \frac{1}{2} \qquad (5.1.66)$$

The term, $\{ 1 + \frac{1}{2m}\left(\frac{C}{AD} - K_1\right)\cos\psi \}$, of Z in eq. (5.1.63) has only a slight dependence on ψ. i.e. for $0<\psi<\pi$,

$$0.894 < \{ 1 + \frac{1}{2m}\left(\frac{C}{AD} - K_1\right)\cos\psi \} < 1.106$$

hence the mean value of Z is expressed

$$Z_m = \left(\frac{4809.8}{\alpha}\right)^{\frac{1}{2(2m-1)}} \cdot B_m^{-\frac{1}{2m}} \qquad (5.1.67)$$

where α is a coefficient and B_m is defined by eq. (5.1.24c).

Using eqs. (5.1.65) and (5.1.66), eq. (5.1.64) may be rewritten as:

$$q_w = M\left\{T_w - T_c - \frac{1}{2}\cdot\left(\frac{A}{D}\right)S_c\cdot\left(\frac{2m-1}{m}\cdot\frac{C}{AD} + \frac{K_1}{m}\right)\right\} = \frac{1}{2}$$

where

$$M = \frac{Y}{1 + (Pr-1)\cdot Z_m\cdot(R_e\cdot A\cdot\delta_o)^{-\frac{1}{2m}}} \qquad (5.1.68)$$

Therefore

$$T_w - T_c = \frac{1}{2M}\cdot\left\{1 + M\left(\frac{A}{D}\right)S_c\left(\frac{2m-1}{m}\cdot\frac{C}{AD} + \frac{K_1}{m}\right)\right\} \qquad (5.1.69)$$

Also, from eqs. (5.1.69) and (5.1.65) we obtain:

$$T_w - T_\delta = \frac{1}{2M}\{1 + M\cdot(\frac{A}{D})S_c(\frac{2m-1}{m}\cdot\frac{C}{AD} + \frac{K_1}{m})\}$$

$$-\frac{1}{2}(\frac{A}{D})\cdot S_c\cdot(\frac{C}{AD} - 2\cos\psi) \qquad (5.1.70)$$

The Nusselt number (Nu_{ot}) becomes

$$Nu_{ot} = Nu_\delta\cdot\frac{T_w-T_\delta}{T_w-T_c}$$

$$= Nu_\delta\{1 + \frac{2\cos - \frac{C}{AD}}{\frac{1}{M}\cdot(\frac{D}{A})\cdot\frac{1}{S_c} + (\frac{2m-1}{m}\cdot\frac{C}{AD} + \frac{K_1}{m})}\} \qquad (5.1.71)$$

(ii) Derivation of Nu_{mt}

The mixtured mean temperature (Tm) is defined

$$T_m = \frac{1}{\pi}\int_0^{2\pi}\int_0^1 T\cdot w\cdot\xi\cdot d\xi d\psi \qquad (5.1.72)$$

The distributions of temperature and the velocity in the axial direction are divided into two regions, one is the core region and the other the boundary layer. The thickness of the boundary layer can be used as the mean thickness (δ_o)

$$T_m = \frac{1}{\pi}\{\int_0^{2\pi}\int_0^{1-\delta_o} T\cdot w\cdot\xi d\xi d\psi + \int_0^{2\pi}\int_0^{\delta_o} T\cdot w\cdot d\eta\cdot d\psi\} \qquad (5.1.73)$$

Substituting eq. (5.1.10) for the velocity profile and eq. (5.1.50) for the temperature profile in the term for the core region and eq. (5.1.13) for the velocity profile and as below for the temperature profile in the term for the boundary layer into eq. (5.1.73)

$$\frac{T_w-T}{T_w-T_\delta} = \left(\frac{n}{\delta}\right)^{\frac{1}{2m-1}} \qquad (5.1.74)$$

The terms having magnitudes of an order less than δ_o^2 are neglected.

$$T_w-T_m = \frac{1}{2}\left(\frac{A}{D}\right)S_c\left(\frac{C}{AD}\right)\left(1+\frac{1}{m}\delta_o\right)+\frac{1}{2M}\left\{1+M\left(\frac{A}{D}\right)S_c\left(-\frac{1}{m}\cdot\frac{C}{AD}+\frac{K_1}{m}\right)\right\}$$

$$\times\left(1-\frac{2m-1}{m(2m+1)}\cdot\delta_o\right) \qquad (5.1.75)$$

Assuming that $\delta_o \ll 1$ in eq. (5.1.75), then the terms involving δ_o may be neglected.

$$T_w - T_m = \frac{1}{2}\left\{\frac{1}{M}+\left(\frac{A}{D}\right)S_c\left(\frac{m-1}{m}\cdot\frac{C}{AD}+\frac{K_1}{m}\right)\right\} \qquad (5.1.76)$$

The Nusselt number (Nu_{mt}) from eq. (5.1.76) is as follows:

$$Nu_{mt} = Nu_\delta\cdot\frac{T_w-T_\delta}{T_w-T_m} = Nu_\delta\left\{1+\frac{2\cos\psi}{\frac{1}{M}\left(\frac{D}{A}\right)S_c+\left(\frac{m-1}{m}\cdot\frac{C}{AD}+\frac{K_1}{m}\right)}\right\} \qquad (5.1.77)$$

The average Nusselt number of the whole tube ($Nu_{av.t}$) is derived by integration of eq. (5.1.77) with respect to ψ as follows:

$$Nu_{av.t} = \frac{1}{2\pi}\int_0^{2\pi} Nu_m\, d\psi$$

$$= Re.Pr.M\cdot\left\{1+M\cdot\left(\frac{A}{D}\right)\cdot S_c\cdot\left(\frac{m-1}{m}\cdot\frac{C}{AD}+\frac{K_1}{m}\right)\right\}^{-1} \qquad (5.1.78)$$

(iii) Evaluations of Nu_δ, Nu_{ot}, Nu_{mt} and $Nu_{av.t}$

According to Blasius's formula:

$$f_c = 0.316\ R_e^{-\frac{1}{4}},$$

$\delta = 0.316$ and $m = 4$ are substituted into eqs. (5.1.35), (5.1.36), (5.1.39) and (5.1.40), thus Nu_δ, Nu_{ot}, Nu_{mt} and $Nu_{av.t}$ can be evaluated as follows:

$$Nu_\delta = \frac{0.037 \cdot Pr \cdot (\frac{a}{R})^{-1.5} \cdot F^4}{1+2.346 \cdot (P_r-1) \cdot (\frac{a}{R})^{0.25} \cdot F^{-0.5}} (1 + 0.258 \cos\psi)$$

(5.1.79)

$$Nu_{ot} = Nu_\delta \left[1 + \frac{2 \cos\psi + 0.469}{\frac{1}{S_c}\{4.126 + 9.675 \cdot (P_r-1) \cdot F^{-0.5} \cdot (\frac{a}{R})^{0.25}\} - 0.727} \right]$$

(5.1.80)

$$Nu_{mt} = Nu_\delta \left[1 + \frac{2 \cos\psi}{\frac{1}{S_c}\{4.126 + 9.675 \cdot (P_r-1) \cdot F^{-0.5} \cdot (\frac{a}{R})^{0.25}\} - 0.258} \right]$$

(5.1.81)

$$Nu_{av.t} = \frac{Nu_\delta}{(1+0.258 \cos\psi)} \{1 - \frac{0.258\ S_c}{4.126 + 9.675 \cdot (P_r-1) F^{-0.5} \cdot (\frac{a}{R})^{0.25}}\}^{-1}$$

(5.1.82)

where $F = \{Re(\frac{a}{R})^2\}^{\frac{1}{5}}$.

When calculating these Nusselt numbers we assume A is unity and use δ_o obtained from eq. (5.1.39).

5.1.2.5 Heat transfer coefficients for uniform heat flux in the circumferential direction

The Nusselt number (Nu_δ) which is defined by the temperatures of the inside tube wall (T_w) and the surface of gas boundary layer (T_δ) can be defined as in eq. (5.1.63) when heat flux is uniform in the circumferential direction.

In this case, considering that $q_w = q_{wm}$, then we obtain from eqs. (5.1.64) and (5.1.66):

$$T_w - T_\delta = \frac{1}{2M} \cdot \frac{1}{\{1 - (\frac{m-1}{m} \cdot \frac{C}{AD} + \frac{K_1}{m}) \cos \psi\}} \qquad (5.1.83)$$

Substituting eq. (5.1.65) into eq. (5.1.83)

$$T_w - T_c = (\frac{A}{D}) S_c (\frac{C}{2AD} - \cos \psi) + \frac{1}{2M} \cdot \{1 - (\frac{m-1}{m} \cdot \frac{C}{AD} + \frac{K_1}{m}) \cos \psi\}^{-1}$$

(5.1.84)

The Nusselt number (Nu_{oh}) which is defined by the temperatures of the inside tube wall (Tw) and the centre of the fluid core (T_c) therefore becomes:

$$Nu_{oh} = Nu_\delta \cdot \frac{T_w - T_\delta}{T_w - T_c} = \frac{Nu_\delta}{1 - M(\frac{A}{D}) S_c (2 \cos\psi - \frac{C}{AD}) \{1 - (\frac{m-1}{m} \cdot \frac{C}{AD} + \frac{K_1}{m}) \cos \psi\}}$$

(5.1.85)

Assuming that $\delta_o \ll 1$, the average mixture temperature (T_m) is expressed as:

$$T_m = \frac{1}{\pi} \int_0^{2\pi} \int_0^1 T \cdot w \cdot \xi \cdot d\xi \cdot d\psi \qquad (5.1.86)$$

Eq. (5.1.50) for T and eq. (5.1.10) for W are substituted into eq. (5.1.86)

$$T_w - T_m = -\left(\frac{A}{D}\right).S_c.\cos\psi + \frac{1}{2M}\cdot\left\{1-\left(\frac{m-1}{m}\cdot\frac{C}{AD}+\frac{K_1}{m}\right)\cos\psi\right\}^{-1} \tag{5.1.87}$$

The Nusselt number (Nu_{mh}) which is defined by the temperature (Tw) and the average mixture temperature (Tm) becomes:

$$Nu_{mh} = Nu_\delta\cdot\frac{T_w - T_\delta}{T_w - T_n} = \frac{Nu_\delta}{1-2M\left(\frac{A}{D}\right)S_c\left\{1-\left(\frac{m-1}{m}\cdot\frac{C}{AD}+\frac{K_1}{m}\right)\cos\psi\right\}\cos\psi} \tag{5.1.88}$$

The average Nusselt number ($Nu_{av.h}$) is derived by averaging eq. (5.1.88) with respect to ψ as follows:

$$Nu_{av.h} = Re.Pr.M\,\frac{1}{2\pi}\int_0^{2\pi}\frac{\left\{1-\left(\frac{m-1}{m}\cdot\frac{C}{AD}+\frac{K_1}{m}\right)\cos\psi\right\}d\psi}{1-2M\left(\frac{A}{D}\right)S_c\left\{1-\left(\frac{m-1}{m}\cdot\frac{C}{AD}+\frac{K_1}{m}\right)\cos\psi\right\}\cos\psi} \tag{5.1.89}$$

These Nusselt numbers (Nu_{oh}, Nu_{mh}, $Nu_{av.h}$) become as follows, taking m = 4 and α = 0.316, as before:

$$Nu_{oh} = \frac{Nu_\delta.\ E}{E - S_c(0.130+0.587\cdot\cos\psi + 0.143\cdot\cos^2\psi)}$$

where

$$E = 1 + 2.346\cdot(Pr-1)\cdot\left\{Re\left(\frac{a}{R}\right)^2\right\}^{-\frac{1}{10}}\cdot\left(\frac{a}{R}\right)^{\frac{1}{4}} \tag{5.1.90}$$

$$Nu_{mh} = \frac{Nu_{\delta} \cdot E \ldots\ldots\ldots}{E - S_c(0.554\ \cos\psi + 0.143\ \cos^2\psi)} \qquad (5.1.91)$$

$$Nu_{av.h} = 0.037 \cdot F^{\frac{4}{5}} \cdot \left(\frac{a}{R}\right)^{\frac{-3}{2}} \cdot \frac{1}{2\pi} \int_0^{2\pi} \frac{(1 + 0.258\ \cos\ \psi)\ d\psi}{E - S_c(0.554\ \cos\psi + 0143\ \cos^2\psi)}$$

(5.1.92)

where

$$F = \{Re\left(\frac{a}{R}\right)^2\}^{\frac{1}{5}}$$

when calculating these Nusselt numbers, we assume that A is unity and δ_o is obtained from eq. (5.1.39).

5.1.2.6 Discussion and comparison of the theoretical analysis with the empirical results

Substituting eq. (5.1.36) into (5.1.50), the temperature profile in the core flow was derived. This was plotted together with the empirical results of Mori and Nakayama (24) and Hogg (29) in Fig. (5.1.7).

At S_c=1, the theoretical temperature profile is not in agreement with the empirical results. However taking S_c=0.585, which is evaluated from their empirical results, the theoretical profile agrees with their results.

The reason for the discrepancy at S_c=1 is thought to be firstly the assumption that heat flux is transferred only by secondary flow, and secondly the neglect of small terms involving δ_m in the analysis of the secondary flow.

Using S_c=0.585 and 1 for Coil C, the ratios between the Nusselt numbers (Nu_δ, Nu_{mt}, Nu_{ot}, Nu_{mh} and Nu_{oh}) and the mean Nusselt number (Nu_{av}) are shown in Fig. (5.1.8). These Nusselt numbers were derived as eqs. (5.1.79), (5.1.80), (5.1.81) and (5.1.82) with uniform wall temperature and as eqs. (5.1.90) and (5.1.91) with uniform heat flux.

As shown in the figure the heat transfer coefficient at the outer side is always the maximum, the inner is the minimum and the upper and lower sides have the average value. Two Nusselt numbers, Nu_{oh} and Nu_{mh}, at S_c=1 have values about six times greater on the other side than on the inner side. This proves that S_c=1 is not valid for the uniform heat flux case.

When S_c is taken as 0.585 all those Nusselt numbers have similarly shaped profiles. The ratio of heat transfer coefficient between the outer side and the inner side is in proportion to $(\frac{a}{R})^{0.345}$ as in eq. (4.2.9) in section (4.2.2.3). Since Pr has been taken as unity in this analysis S_c also determines the value of the ratio.

Fig. (5.1.9) shows a comparison between the theoretical and empirical results with similar results of a straight tube at Pr=1, S_c=0.585 and $\frac{a}{R}$ = 0.025(Coil C). Theoretical equations used are eq. (2.42) of Mori and Nakayama (24) and eqs. (5.1.82) and (5.1.92). The empirical formula is eq. (2.47) of Seban and McLaughlin (22) and applying to a straight tube. The two theoretical equations taken from the present work are in close agreement with other investigators.

From the figure and eqs. (5.1.82) and (5.1.92), in both cases of uniform wall temperature and of uniform heat flux, we have larger heat transfer coefficients than those for the straight pipe. The heat transfer coefficient of the uniform heat flux case is always about 10% greater than that of the uniform wall temperature case.

Fig. (5.1.10) shows the influence of Prandtl number on eqs. (5.1.82) and (5.1.92) and also shows another investigator's results.

From this figure, the values of the two equations are greater than that for a straight pipe in the range of Pr<2.0. The gap between the equations becomes wider in the range of Pr<0.8. Therefore these two equations are thought to be valid in the range of 0.8<Pr<2.0.

The reason for the growth of discrepancy outside this range is due to the use of the Taylor-Prandtl analogy for the flow model analysis in this section.

Figs. (5.1.11a) - (5.1.11c) show a comparison between the theoretical and the empirical heat transfer coefficients in the three coils (Coil A, B, C). The experimental results were taken under the uniform heat flux condition and are explained fully in section (4.2.2.3). The empirical heat transfer coefficients are determined by the temperature differences between the wall temperature and core centre temperature therefore this coefficient is defined on the same basis as the theoretical coefficient, h_{oh}.

Both theoretical and empirical results show that the heat transfer coefficient at the outer side is always greater than that of the inner side in all three coils. Also both types of results tend to have very similar profiles at $Re>4.5 \times 10^4$ and $(\frac{a}{R})>0.033$.

The heat transfer coefficients of the empirical results have greater values than those of the theoretical results in all three coils. At low Reynolds numbers this becomes especially noticeable as the gaps between the curves become wider.

The theoretical results have considerably lower values at small Reynolds number because of the value of S_c which is apparently smaller

than that found using empirical data in the present work (S_c = 0.585).

Fig. (5.1.12) shows the heat transfer coefficients at various S_c in the same conditions as case 3 ($R_e = 4.4 \times 10^4$) and case 4 ($R_e = 2.4 \times 10^4$) in Fig. (5.1.11b). At large Reynolds numbers the theoretical heat transfer coefficient (in this case h_{oh}) becomes identical in value to the empirical results at S_c = 0.63 for Coil C in case 3. At small Reynolds numbers, case 4, S_c is found to be 0.80.

This empirical method can only provide an approximation of S_c for the present work.

However Fig. (5.1.13) reported by Pratap (34) shows different temperature profiles in the core flow at different Dean numbers, which have a trend which is in agreement with our findings. From this figure the curve for a small Dean number (i.e. small Reynolds number) has a steeper slope than that of large numbers. Therefore, as S_c is related to this gradient, this would predict the value of S_c in case 4 in Fig. (5.1.12) being larger than that of case 3.

Fig. (5.1.14) shows the comparison between the theoretical average heat transfer coefficient taken from eqs. (5.1.82) and (5.1.92) and the empirical heat transfer coefficients at the outer and inner side in Coils A and C. The empirical results are shown fully in Fig. (4.2.16) in section (4.2.2.3). The theoretical results appear slightly lower than the empirical average but they are in good agreement. If the correction factor (S_c) was taken at precisely the theoretical value of h_{oh}, determined from ($T\overset{*}{w} - T^*_c$), it would agree sufficiently well with the experimental value.

The theoretical and experimental heat transfer coefficients at the inner side are always approximately one third of those at the outer side.

Above all, eqs. (5.1.82) and (5.1.92) depend on the correction factor strongly, so if a precise value of S_c can be found these equations are enough to describe closely the whole phenomena.

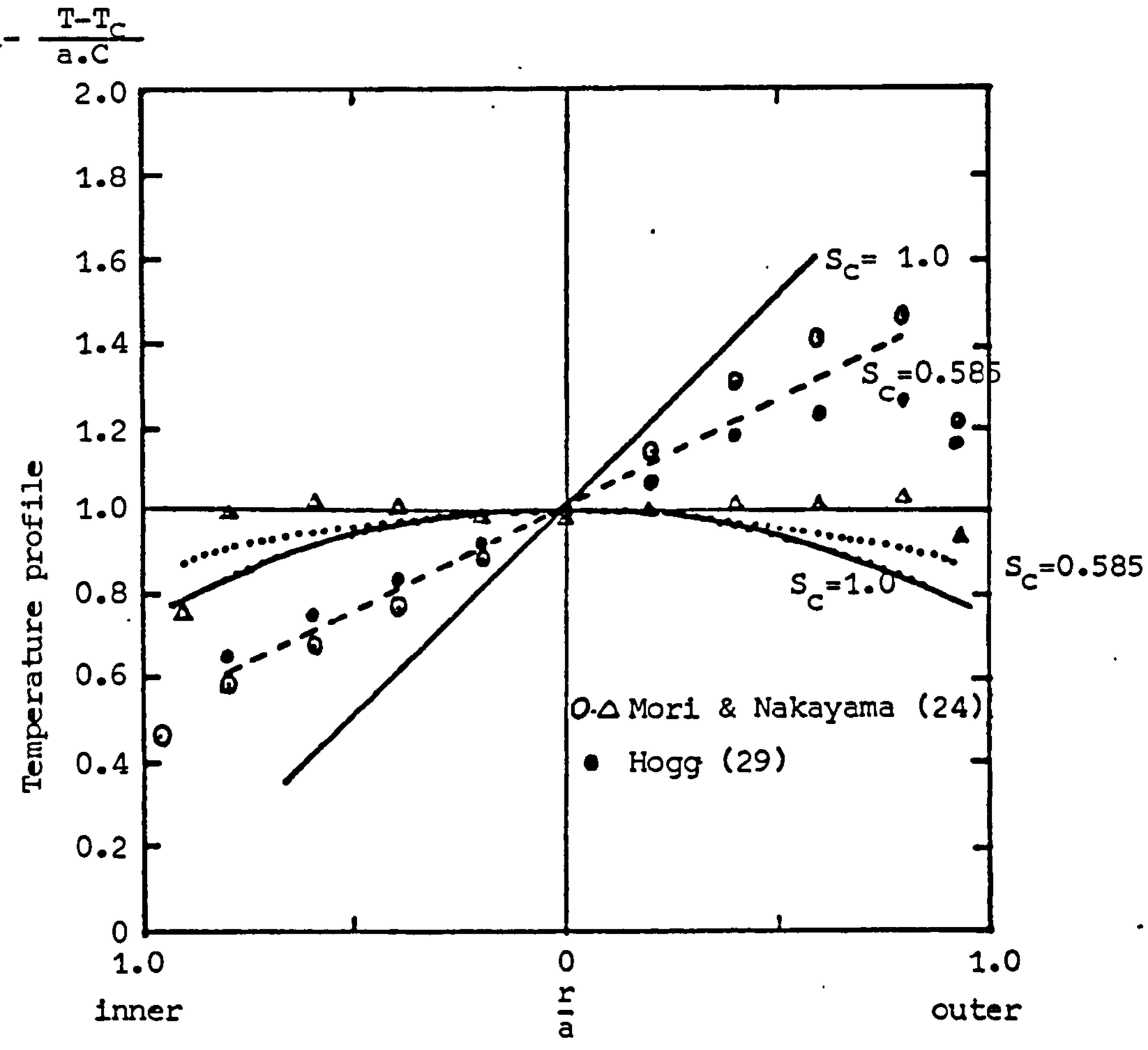


Fig. (5.1.7) Theoretical and empirical temperature profiles in the core flow. (S_c: correction factor)

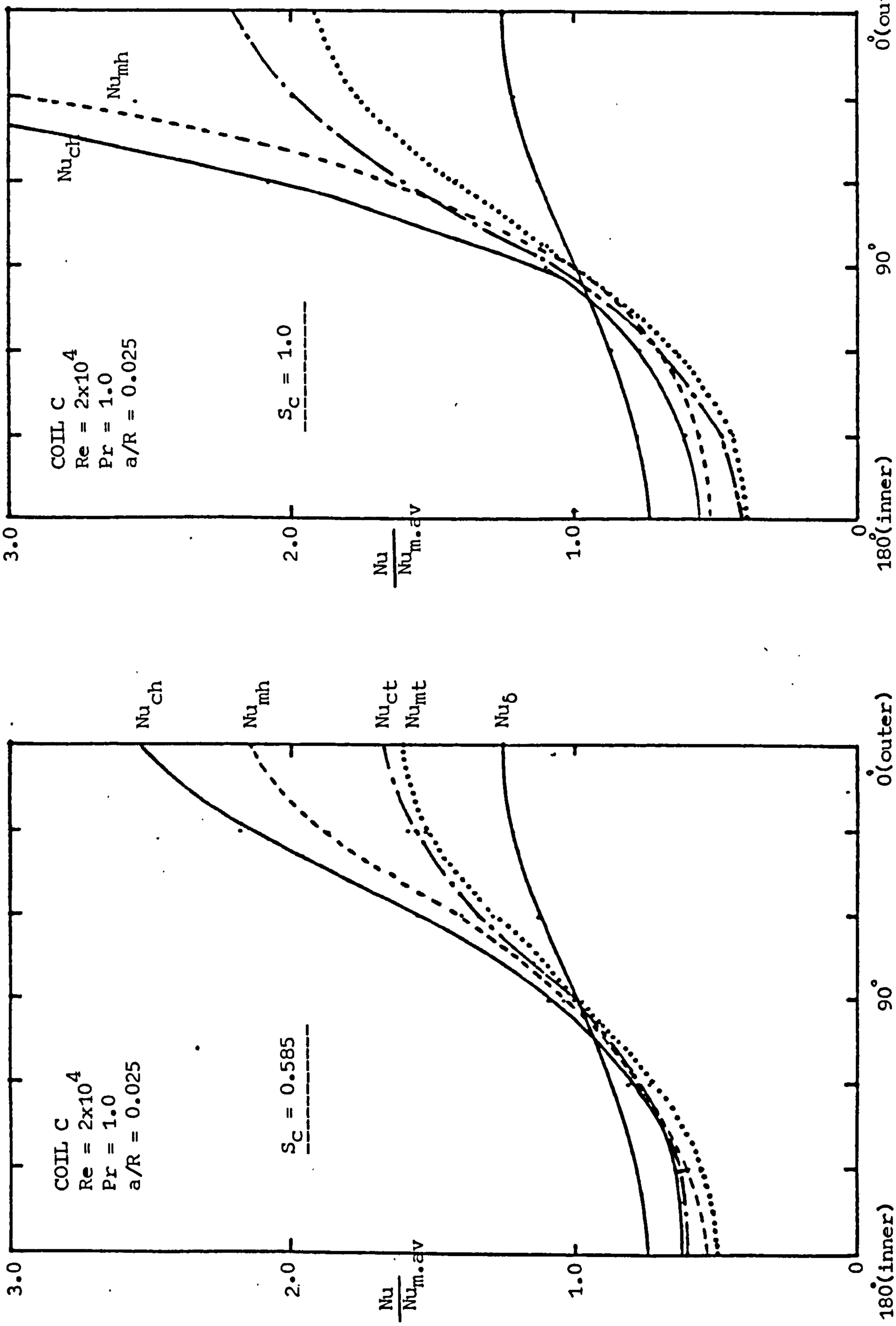


Fig. (5.1.8) Theretical Nusselt number ratios at S_c= 0.585 and at S_c= 1.0

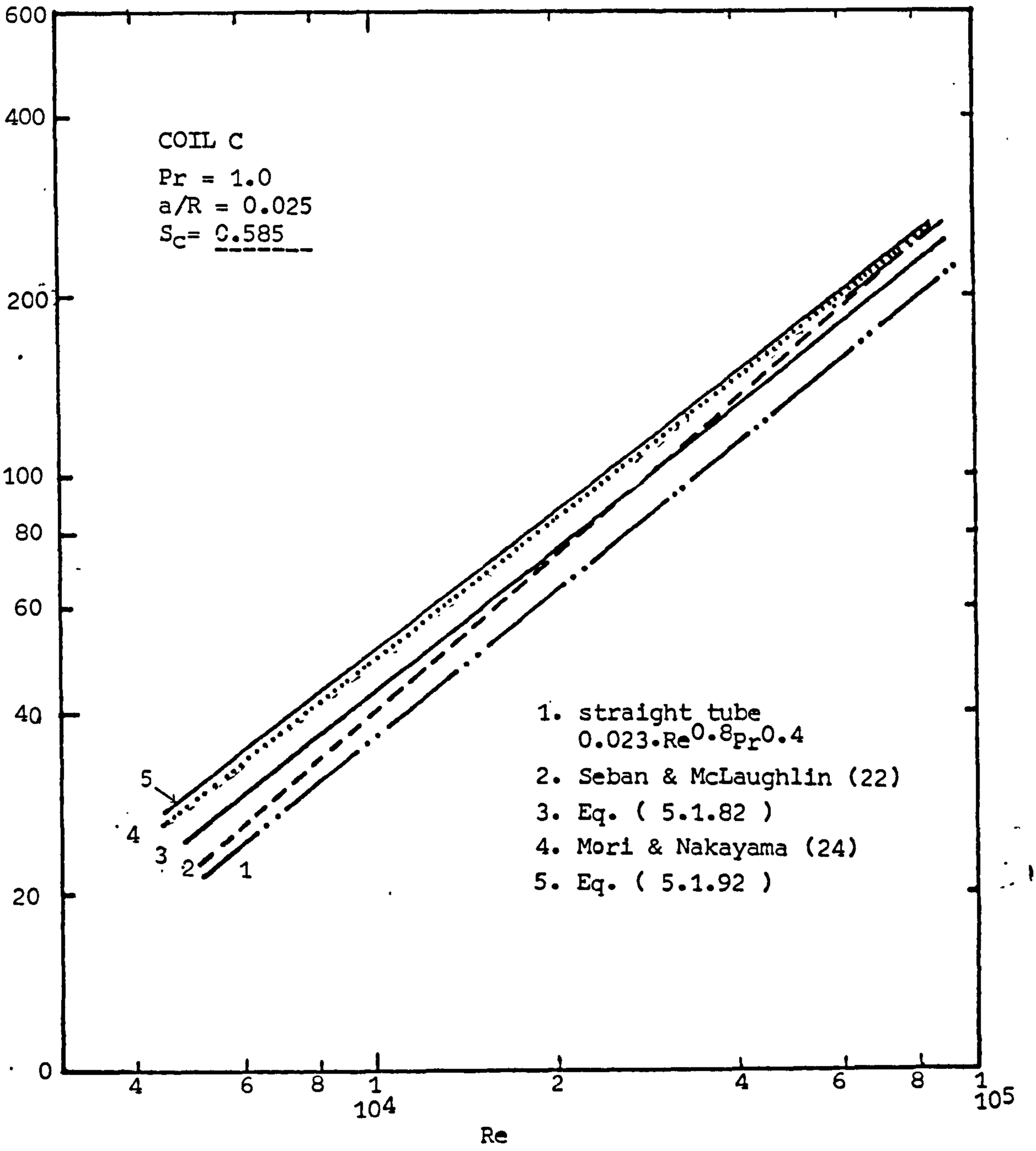


Fig. (5.1.9) Comparison of Nusselt numbers between theory and the other investigators'.

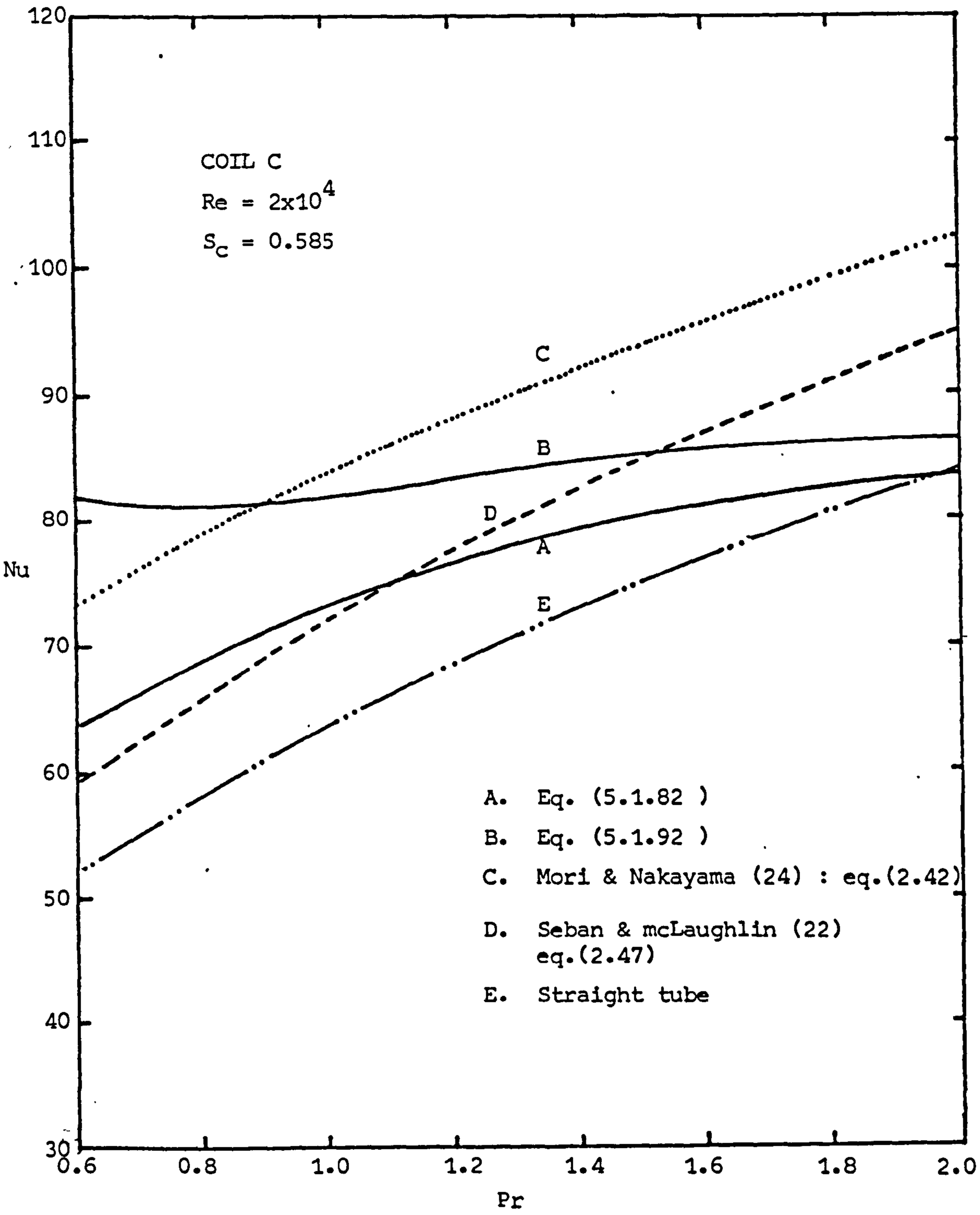


Fig. (5.1.10) Influence of Prandtl number on Nusselt numbers.

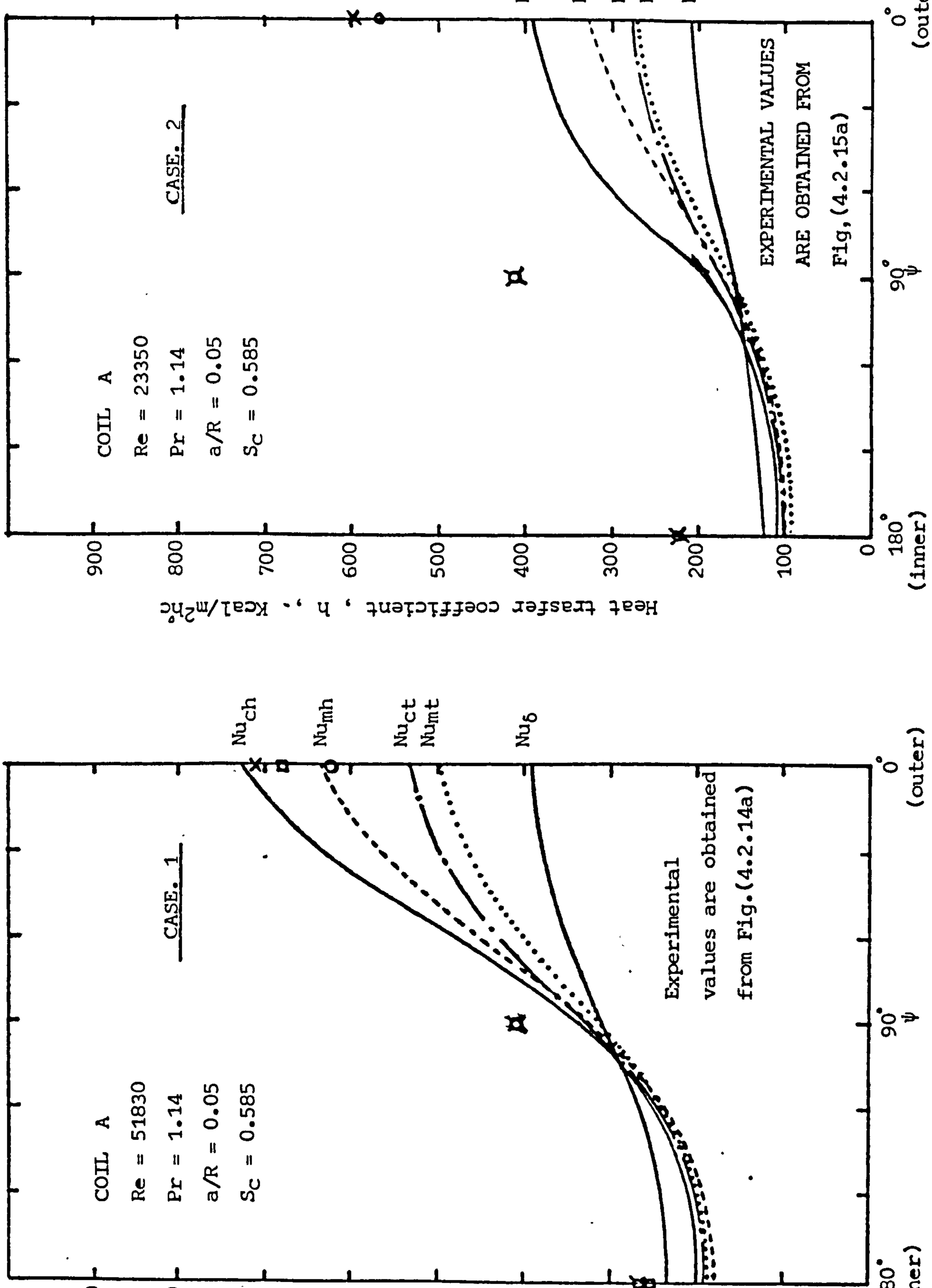


Fig. (5.1.11a) Comparison between the theoretical and empirical heat transfer coefficients (for COIL A)

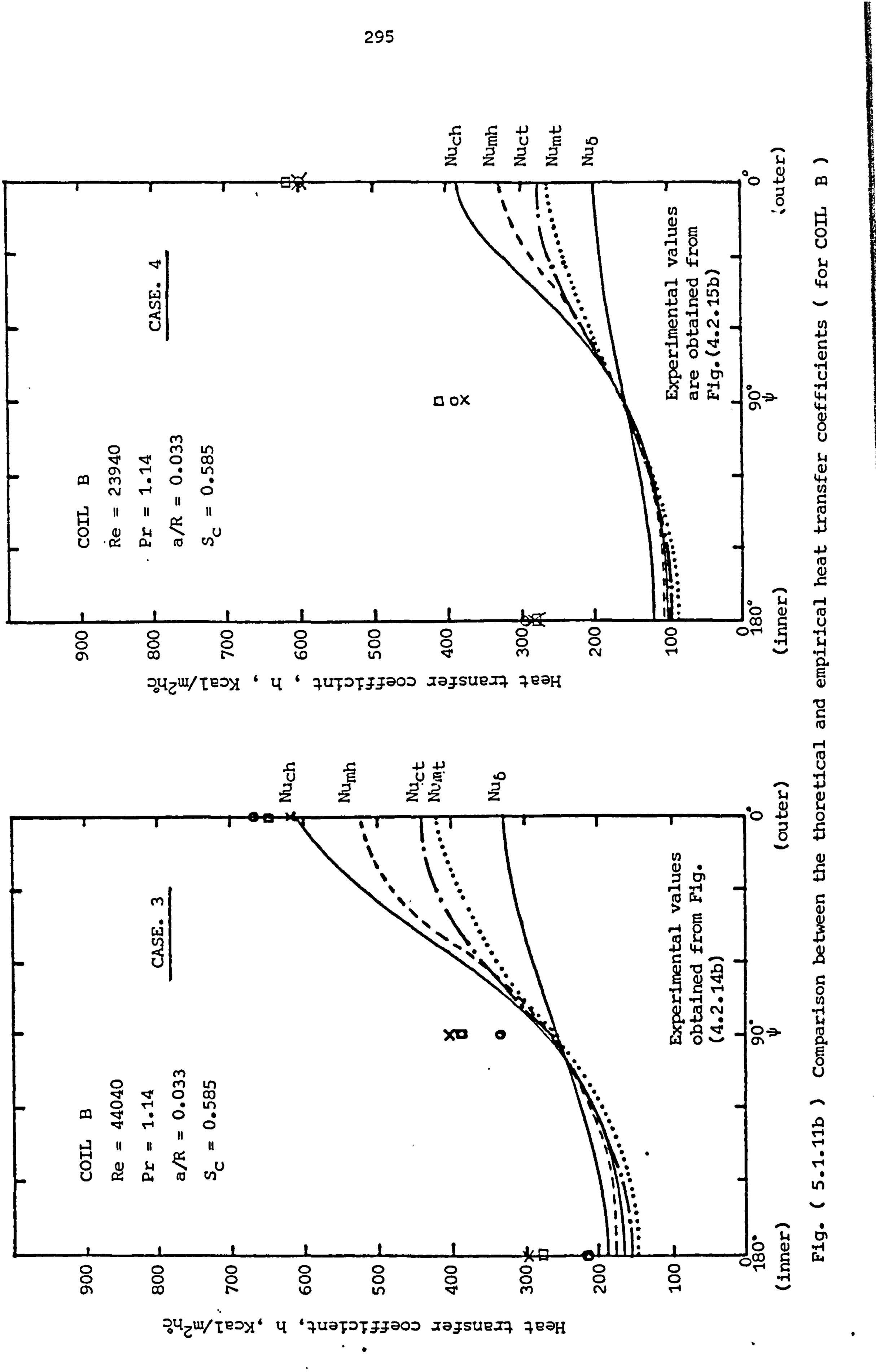


Fig. (5.1.11b) Comparison between the thoretical and empirical heat transfer coefficients (for COIL B)

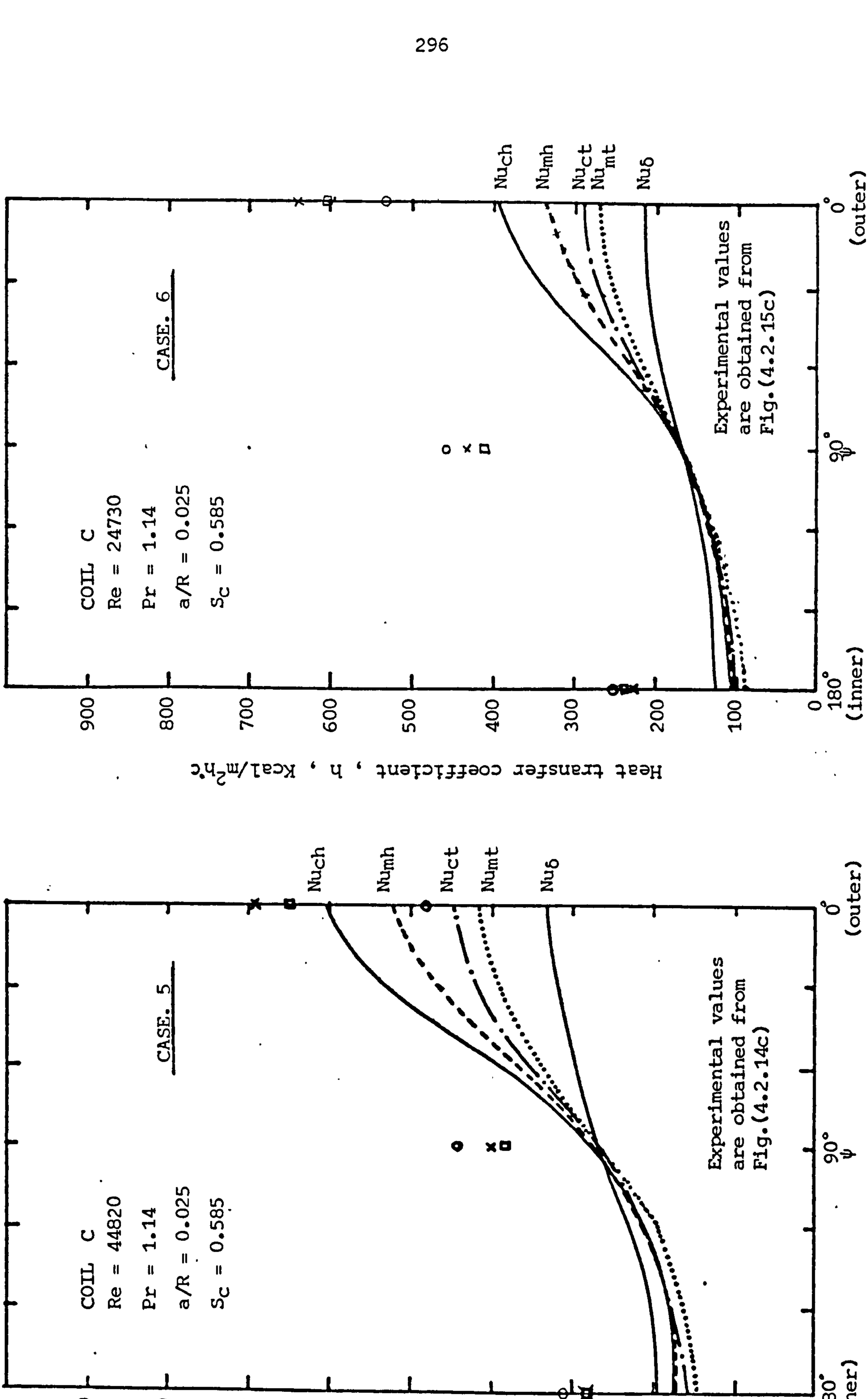
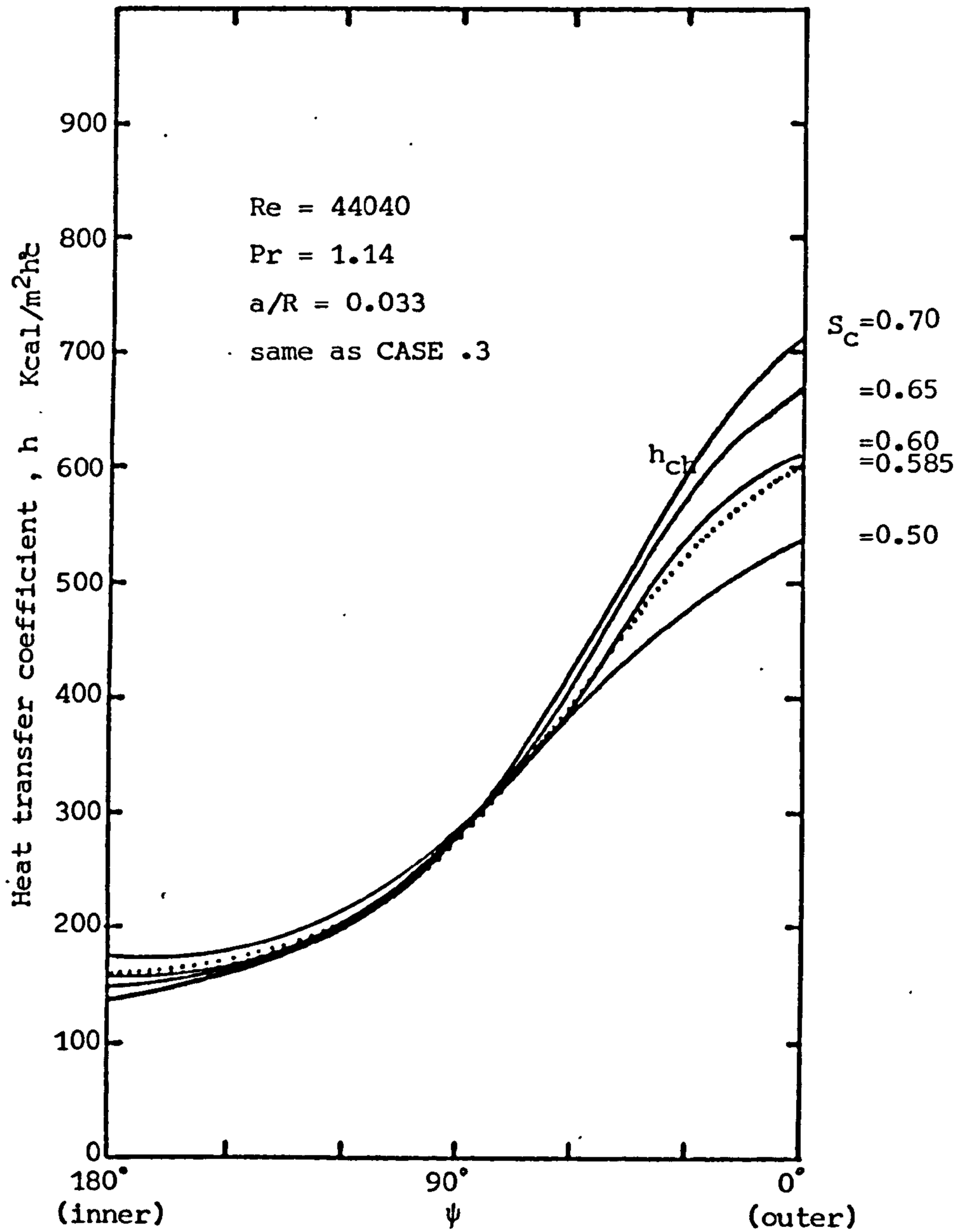


Fig. (5.1.11c) Comparison between the theoretical and empirical heat transfer coefficients (for COIL C)



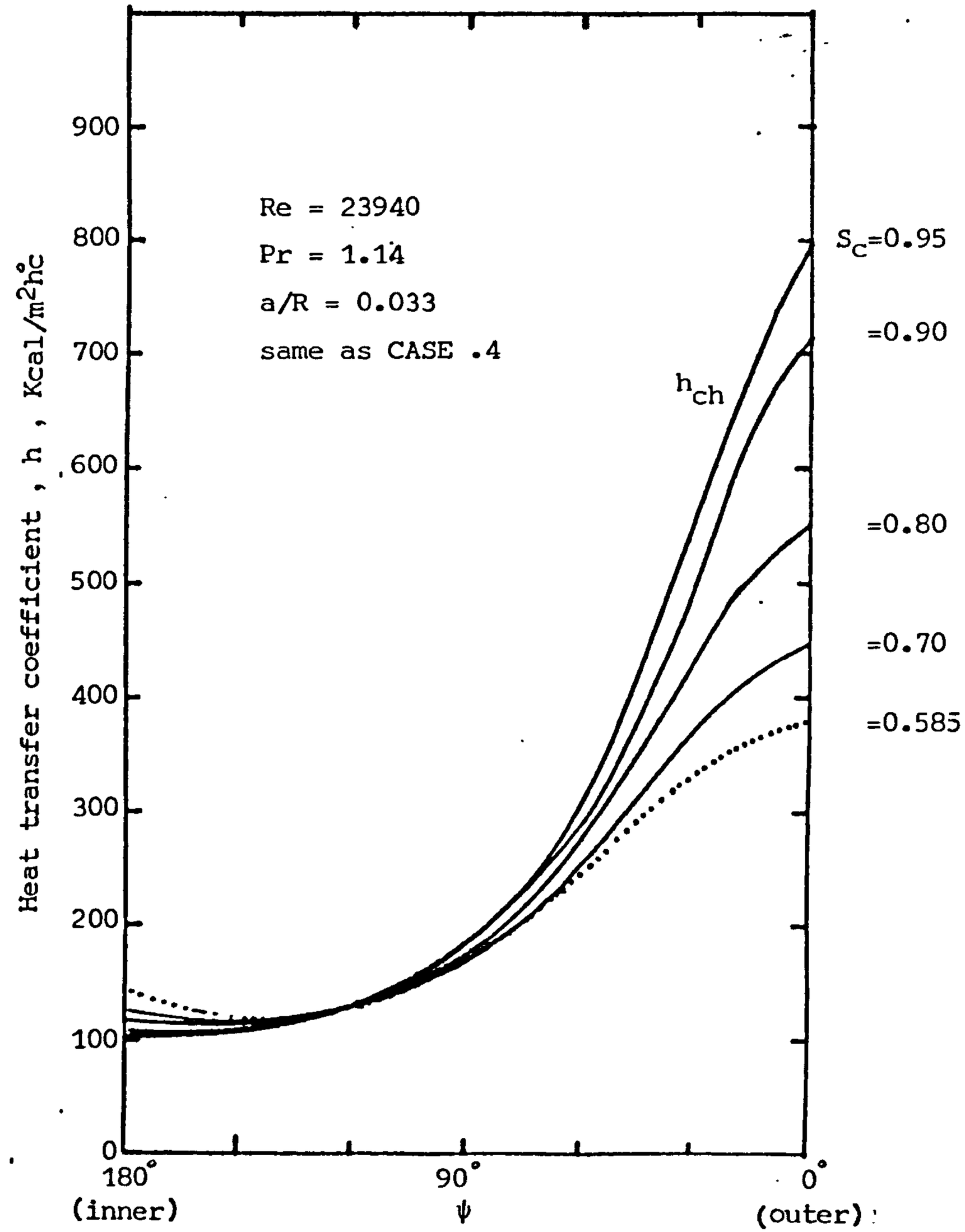


Fig. (5.1.12) Heat transfer coefficients at variuus S_c . . at Re = 44040 and Re = 23940.

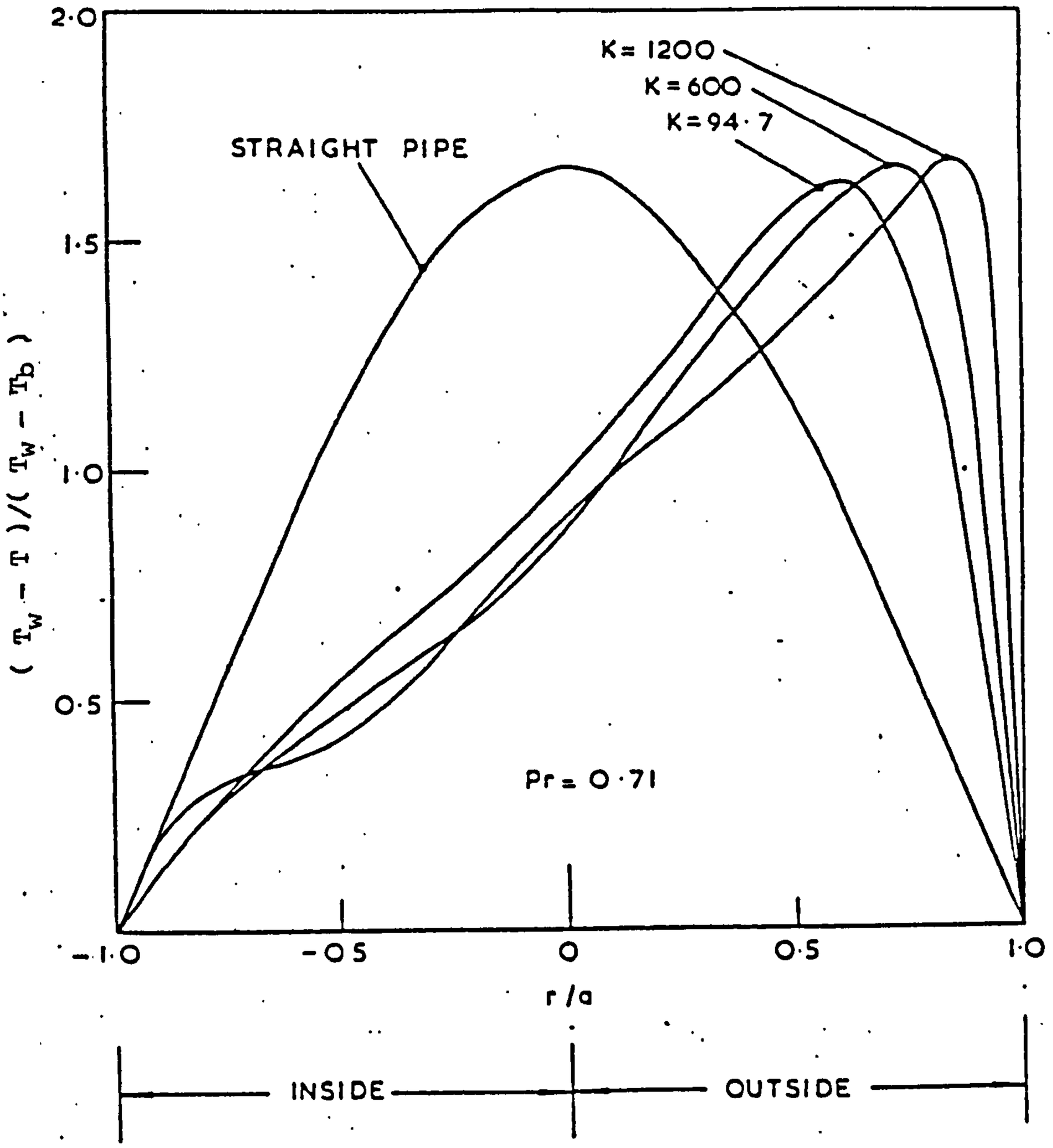


Fig. (5.1.13): Effect of Dean number on temperature profiles along plane AA. (horizontal plane) from Pratap (34).

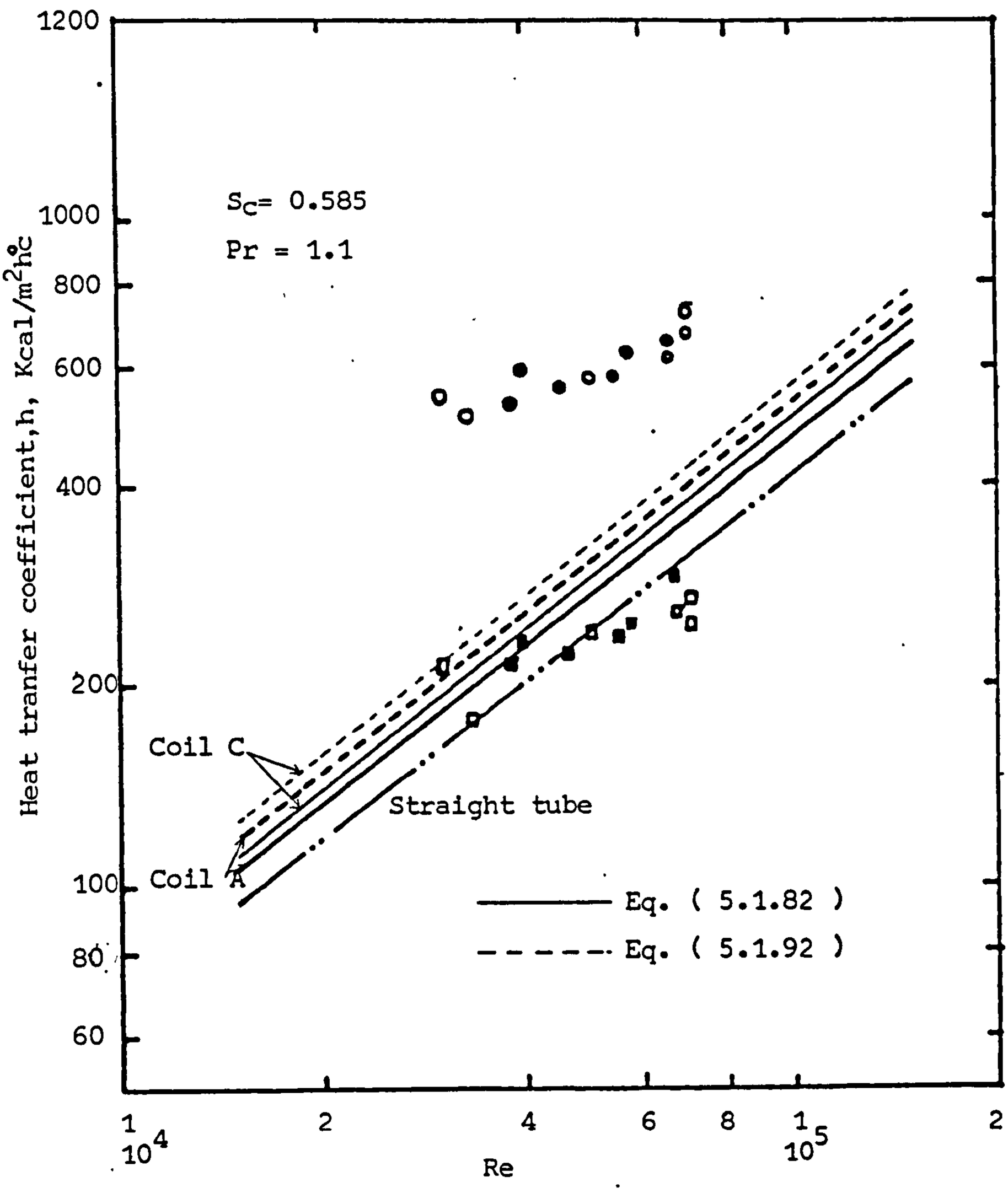


Fig. (5.1.14) : Comparison between the theoretical average heat transfer coefficient taken from eqs.(5.1.82) and (5.1.92) and empirical results at the inner and outer sides.(from Fig. (4.2.16)).

COIL A	COIL C	
○	●	outer
□	■	inner

5.2 Theoretical analysis of an annular two-phase flow

5.2.1 Introduction

Up to the present, flow mechanisms of two-phase flow in straight tubes have been studied empirically or theoretically by Lockhart-Martinelli (40), Levy (106), Wallis (87,107) and Hewitt and Hall-Taylor (81). However these investigators have not been able to explain fully any of the flow mechanisms occurring in two-phase flows.

In the case of two-phase flow in the coiled tube, empirical studies include Banerjee et al (39), Owhadi et al (47,64) and Kozeki et al (48, 53, 80). There are a few theoretical studies of the two-phase flow mechanisms in the coiled tubes but they do not adequately explain the mechanisms. Kozeki (48, 80) attempted a theoretical analysis of annular two-phase flow in coiled tubes, in which he divided the flow into a central gas core, a gas boundary layer and a liquid film.

The analysis described in this section is mainly based on the analysis put forward by Kozeki.

5.2.2 Model and Assumptions

In the case of the single-phase turbulent flow in the helically-coiled tube, the flow is divided into a central core and a boundary layer. The centrifugal force is assumed to dominate the turbulent diffusion in the central core. In the boundary layer, the local relationship between the velocity distribution and shearing stress is also assumed to be similar to that in the straight tube. These assumptions have been shown to explain these phenomena satisfactorily in sections (5.1.1) and (5.1.2).

This analytical method can be extended to annular two-phase flow.

The flow is divided into the central gas core, the gas boundary layer and liquid film as shown in Fig. (5.2.1).

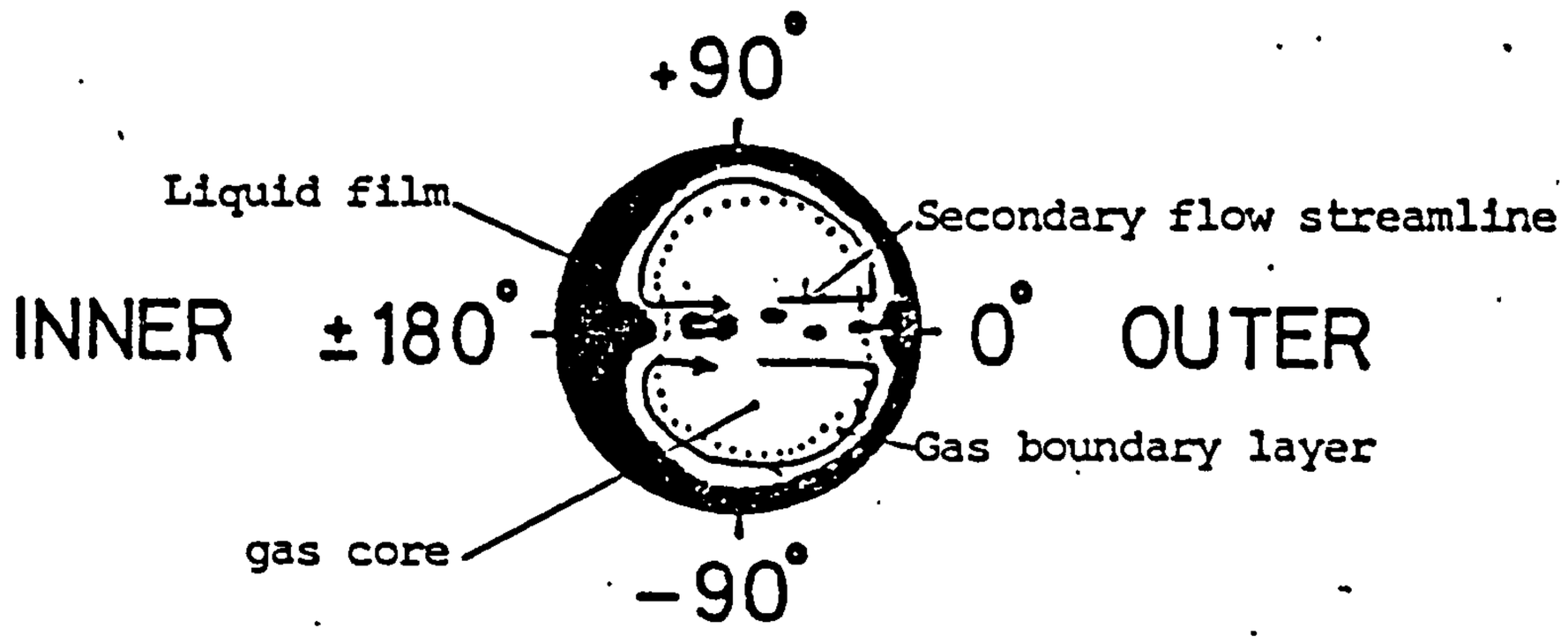


Fig. (5.2.1) : Model of annular two-phase flow.

In the gas core, the centrifugal force would dominate and cause the development of a secondary flow similar to that in the single-phase flow. In the liquid film a secondary flow would exist from the outer side to the inner side around the wall surface. Liquid droplets would be detached into the gas core at the inner side and, travel through the gas core by the centrifugal force, then coalesce with the water film at the outer side (see in section (4.3.3)).

In annular two-phase flow in a straight tube the droplets in the gas core are generated mainly by entrainment and disturbance waves and

meanwhile droplets are deposited by the droplet diffusion. Therefore the amounts of film flow rate and droplets in the gas core are balanced by the entrainment and deposition rates.

In the annular two-phase flow in the coiled tube, the droplets are entrained into the gas core as they would in a straight tube. The droplet deposition is effected strongly by the centrifugal force rather than droplet diffusion.

The entrainment phenomenon in the coiled tube has two contributing mechanisms. Firstly the top of the ruffled, wavy surface is sheared off from wave peak by the turbulent gas flow (including the phenomena of roll wave, wave undercut, bubble burst and liquid impingement)····· Ishii and Grolmes (89). Secondly entrainment occurs when liquid film becomes unsteady due to the force unbalance in the circumferential direction. In this section, the later phenomenon is thought to be the main feature.

For studying the above flow model, the following assumptions are also used:

1. The flow is an adiabatic fully developed annular turbulent two-phase flow.
2. The liquid film surface is unruffled, and irregularities at the point of entrainment are ignored. Also its thickness is very small compared with the tube radius.
3. The gas core flow is treated as single-phase flow ignoring the droplet carried in it and their momentum effect.
4. The thickness of the gas boundary layer is small enough compared with the tube radius.

5. The local friction factor on the gas-liquid interface given by Wallis (87) would be modified as follows:

$$f_i = \alpha_g (1 + b\delta_{fm}) \cdot Re_{gs}^{-\frac{1}{m}} \qquad (5.2.1)$$

6. The gas velocity is large enough compared with the liquid velocity. Also the circumferential velocity of the liquid is small enough compared with the velocity in axial direction.

7. The shearing stress in the axial direction on the interface is equal to that on the tube wall.

8. The gravity force is neglected.

9, The pressure distribution in the circumferential direction depends on the gas core flow and pressure in the radial direction in the liquid film is constant.

10. The relationship between local velocity distribution and the shear stress on the wall surface in the liquid film is the same as that for a straight tube.

11. The momentum in the circumferential direction in the liquid film is made up of the pressure gradient due to the secondary flow of the gas core, the liquid phase centrifugal force, the interfacial shear stress and the shear stress on the wall surface.

5.2.3 Analysis of the gas flow

In the gas core, although droplets exist in the flow, it is assumed to be a single-phase flow. The core is in contact with film surface which is assumed unruffled and whose thickness at each circumference is taken as the mean value at that point. The friction factor is uniformly constant around the surface. It is supposed that

the the velocity of the liquid (W_f) is very small compared with that of the gas flow.

.It follows, therefore, that the velocity distributions in the central gas core are the same as those obtained as in eq. (5.1.10),

$$U_g = D_t \cos \psi$$
$$V_g = -D_t \sin \psi$$
$$W_g = A_t \left(1 - \frac{C_t}{A_t D_t} \cos \psi\right) \qquad (5.2.2)$$

where C_t is a two-phase flow pressure gradient in the axial direction.

$$C_t = \frac{a}{R} \frac{\partial P}{\partial \theta} \qquad (5.2.3)$$

The values of A_t, C_t and D_t are unrelated to ψ and are derived by the same methods as in section (5.1.1).

Assuming that the velocity of liquid surface is very small, the velocity distributions of the gas boundary layer are obtained in the same way as eqs. (5.1.13) and (5.1.16)

$$W_g = W_{g\delta} \cdot \left(\frac{\eta_g}{\delta_g}\right)^{\frac{1}{2m-1}} \qquad (5.2.4)$$

$$V_g = -\frac{2m}{m-1} \cdot \frac{V_{g\delta}}{\delta_g} - \left\{\left(\frac{\eta_g}{\delta_g}\right)^{\frac{1}{2m-1}} - \left(\frac{\eta_g}{\delta_g}\right)\right\} \qquad (5.2.5)$$

The basic equations of the gas boundary layer are the same as eq. (5.1.11). Integrating eq. (5.1.11) with respect to η from 0 to δ_g, and substituting the shearing stresses (τ) at $\eta = 0$ obtains the following:

$$(\tau_{\theta.r})_{\eta_g=0} = C_t \cdot \delta_g + \frac{\partial}{\partial\psi}\int_o^{\delta_g} V_g W_g d\eta_g - W_{g\delta} \cdot \frac{\partial}{\partial\psi}\int_o^{\delta_g} v_g d\eta_g$$

$$P_{\delta_g} - P_{\eta_g=0} = \int_o^{\delta_g} (v_g^2 + \frac{a}{R} w_g^2 . \cos\psi)\, d\eta_g$$

$$(\tau_{\psi.r})_{\eta_g=0} = \int_o^{\delta_g} \frac{\partial P}{\partial\psi} d\eta_g + \frac{a}{R} \sin\psi \int_o^{\delta_g} w_g^2 d\eta_g + \frac{\partial}{\partial\psi}\int_o^{\delta_g} v_g^2 d\eta_g - V_{g\delta} \frac{\partial}{\partial\psi}\int_o^{\delta_g} v_g d\eta_g$$

(5.2.6)

Substituting eqs. (5.2.4) and (5.2.5) into eq. (5.2.6) and neglecting the small order terms, the shearing stresses become similar to eqs. (5.1.17) and (5.1.19).

$$(\tau_{\theta.r})_{\eta_g=o} = C_t\, \delta_g + \frac{4m(2m-1)}{(4m-1)(2m+1)} \{C_t(1-2\cdot\cos^2\psi) + A_t.D_t.\cos\psi\}$$

$$- (A_t.D_t - C_t.\cos\psi)\cos\psi \qquad (5.2.7)$$

$$(\tau_{\psi.r})_{\eta_g=o} = -\frac{2}{m+1}\cdot\frac{a}{R}\sin\psi.\, W_{g\delta}^2 .\delta_g + \frac{32m^2.D_t^2}{3(2m+1)(4m-1)}\cdot\frac{\sin\psi}{\delta_g}$$

$$x(2\cos\psi - \frac{\sin\psi}{\delta_g}.\frac{d\delta_g}{d\psi}) \qquad (5.2.8)$$

The value of V_g has a maximum in the layer, and in a similar relation to eq. (5.1.20), is given as follows:

$$(\frac{V_g}{W_g})_s = \frac{(\tau_{\psi.r})_{\eta=0}}{(\tau_{\theta.r})_{\eta=0}} = -\frac{4m\cdot V_{g\delta}}{(2m-1)\cdot\delta_g\cdot W_{g\delta}} \qquad (5.2.9)$$

and

$$(\dot{\tau}_{\psi.r})_{\eta=0} = \frac{4m.D_t.\sin\psi}{(2m-1)\delta_g(A_t - \frac{C_t}{D_t}\cos\psi)} \cdot (\tau_{\theta.r})_{\eta=0} \qquad (5.2.10)$$

The circumferential and axial direction components (Vg and Wg) in the gas boundary layer are denoted by V_{gs} and W_{gs} at $\eta=\eta_s$, the point where V_g reaches maximum and since $V_{gs} << W_{gs}$, therefore the resultant velocity (S_r) in a similar form to eq. (5.1.22), becomes:

$$S_r = (W_{gs}^2 + V_{gs}^2)^{\frac{1}{2}} \doteq W_{gs} \qquad (5.2.11)$$

Supposing that the relation between Sr and the interfacial shear stress is the same as that of the single-phase flow in the straight tube, then the $^{1}/_{(2m-1)}$ power law can be employed for S, therefore:

$$S = S_r \cdot \left(\frac{\eta}{\eta_s}\right)^{\frac{1}{2m-1}} \qquad (5.2.12)$$

and the mean velocity S_m is obtained from

$$\bar{S}_m = \int_0^1 2\xi \cdot S \cdot d\xi = B_m \cdot \eta_s^{\frac{1}{2m-1}} \cdot S_r \qquad (5.2.13)$$

where

$$B_m = \frac{(2m-1)^2}{m(4m-1)} \qquad (5.1.24c)$$

Then η_s is obtained from eqs. (5.2.4) and (5.2.5) as follows:

$$\eta_s = (2m-1)^{-\frac{2m-1}{2(m-1)}} \cdot \delta_g \qquad (5.2.14)$$

Also S_r is obtained from eqs. (5.2.4) and (5.2.14)

$$S_r = w_{g\delta}\,(2m-1)^{-\frac{1}{2(m-1)}} \qquad (5.2.15)$$

If we take an element of the tube length short as a straight pipe (as in section 5.1.1.2). From eq's (5.2.1.4) and (5.2.15), the mean velocity (S_m) at a point on the surface of the gas boundary layer is:

$$S_m = B_m \cdot w_{gm} \cdot w_{g\delta} \cdot \delta_g^{-\frac{1}{2m-1}} \qquad (5.2.16)$$

The Reynolds number and the friction factor in the supposed straight tube are the following:

$$Re_{gs} = \frac{2aS_m}{\nu_g}$$

$$f_i = \alpha_g(1 + b\delta_{fm})Re_{gs}^{-\frac{1}{m}} \qquad (5.2.17)$$

where $$\delta_{fm} = \frac{1}{2\pi}\int_0^{2\pi} \delta_f \, d\psi \qquad (5.2.18)$$

The shearing stress in the direction of the resultant velocity becomes:

$$\tau_s = -\frac{\tau_s^*}{\rho_g w_{gm}^2} = -\frac{f_i}{4}\cdot\frac{1}{2}\left(\frac{S_m}{w_{gm}}\right)^2$$

$$= -\frac{\alpha_g}{8}\cdot B_m^{2-\frac{1}{m}} \cdot Re_g^{-\frac{1}{m}} \cdot w_{g\delta}^{2-\frac{1}{m}} \cdot \delta_g^{-\frac{1}{m}} \cdot (1 + b\delta_{fm}) \qquad (5.2.19)$$

This is identical to the shear stress in the axial direction

$$(\tau_{\theta.r})_{\eta_g=0} = \tau_s \qquad (5.2.20)$$

Now $w_{g\delta}$ and δ_g are treated by the same procedure as the single-phase

flow and the small order terms are neglected.

$$w_{g\delta}^{2-\frac{1}{m}} = \{A_t(1 - \frac{C_t}{A_t D_t}\cos\psi)\}^{2-\frac{1}{m}}$$

$$\doteq A_t^{2-\frac{1}{m}}(1 - \frac{2m-1}{m}\cdot\frac{C_t}{A_t D_t}\cos\psi) \qquad (5.2.21)$$

$$\delta_g^{\frac{1}{m}} = \left\{\delta_{gm}(1 + K_1\cos\psi + \cdots)\right\}^{\frac{1}{m}} \doteq \delta_{gm}^{\frac{1}{m}}(1 - \frac{K_1}{m}\cos\psi) \qquad (5.2.22)$$

The same procedure as for single-phase flow in section (5.1.1) is followed by equating eqs. (5.2.8) - (5.2.10) and (5.2.20), and substituting eqs. (5.2.21) and (5.2.22) into them. Since the angle ψ is arbitrary, the average value of between 0 and ψ is taken. Then, if we neglect the small terms we obtain the following equations:

$$\frac{1}{2}C_t = -\frac{\alpha_g}{8}\cdot B_m \cdot Re_g \cdot A_t^{2-\frac{1}{m}} \cdot \delta_{gm}^{-\frac{1}{m}} \cdot (1 + b\delta_{fm}) \qquad (5.2.23)$$

$$\frac{6m-1}{(4m-1)(2m+1)}\cdot A_t\cdot D_t = -\frac{\alpha_g}{8} B_m \cdot Re_g^{2-\frac{1}{m}} \cdot A_t^{-\frac{1}{m}} \cdot \delta_{gm}^{2-\frac{1}{m}} \cdot (1+b\delta_{fm})(\frac{2m-1}{m}\cdot\frac{C_t}{A_t\cdot D_t} + \frac{K_1}{m})$$

(5.2.24)

$$(\frac{a}{R})(\frac{A_t}{D_t})^2 \cdot \alpha_{gm}^2 - \frac{16m^2}{3(4m-1)}\cdot K_1 + \frac{8m^2}{4m-1}\cdot\frac{C_t}{A_t\cdot D_t} = 0 \qquad (5.2.25)$$

$$(\frac{a}{R})(\frac{A_t}{D_t})^2\cdot\delta_{gm}^2\cdot(2K_1 - 3\frac{C_t}{A_t\cdot D_t}) + \frac{16m^2}{3(4m-1)}\cdot K_1(K_1 + \frac{C_t}{A_t\cdot D_t}) -$$

$$- \frac{2m(32m^2 + 2m - 3)}{3(4m-1)(2m-1)} = 0 \qquad (5.2.26)$$

From these relations, $\frac{C_t}{A_t\cdot D_t}$, K_1, $(\frac{a}{R})(\frac{A_t}{D_t})^2\cdot\delta_{gm}^2$ and C_t are obtained.

The value of A_t can be found approximately from the continuity conditions as the same as in the single-phase flow as follows:

$$A_t \doteqdot 1 + \frac{1}{m} \cdot \delta_{gm} \qquad (5.2.27)$$

In the case of $m = 4$ and $\alpha = 0.316$, these four equations (5.2.23)-(5.2.26) can be solved as:

$$\frac{C_t}{A_t D_t} = -0.469,$$

$$K_1 = 0.377,$$

$$\left(\frac{a}{R}\right)\left(\frac{A_t}{D_t}\right)^2 \cdot \delta_{gm}^2 = 6.147$$

$$C_t = -0.0617 \cdot Re_g^{\frac{1}{5}} \cdot A_t^{\frac{9}{5}} \cdot \left(\frac{a}{R}\right)^{\frac{1}{10}} \cdot (1 + b\delta_{gm})^{\frac{4}{5}} \qquad (5.2.28)$$

From eq. (5.2.28) the value of A_t is approximately unity, also δ_g (from eq. (5.2.22)) and D_t become as follows:

$$\delta_g = 0.327 \cdot Re_g^{-\frac{1}{5}} \left(\frac{a}{R}\right)^{\frac{1}{10}} (1 + b\delta_{gm})^{\frac{4}{5}} (1 + 0.377 \cos\psi)$$

$$D_t = 0.132 \cdot Re_g^{\frac{-1}{5}} \left(\frac{a}{R}\right)^{\frac{1}{10}} (1 + b\delta_{gm})^{\frac{4}{5}} \qquad (5.2.29)$$

5.2.4 Analysis of annular liquid flow

Since the liquid film flows in steady state conditions the basic eqs. (5.1.2) - (5.1.5) are applicable for the liquid film. However the real film thickness around the tube fluctuates and cannot be determined accurately.

Designating the liquid film thickness as δ_f, the velocity distributions of the axial and circumferencial directions (W_f and V_f) in the

liquid film can be expressed as follows:

$$w_f = w_{f\delta} \left(\frac{\eta_f}{\delta_f}\right)^{\frac{1}{2n-1}} \tag{5.2.30a}$$

$$v_f = v_{f\delta} \left(\frac{\eta_f}{\delta_f}\right)^{\frac{1}{2n-1}} \tag{5.2.30b}$$

The liquid phase contains a continuous circulating mechanism, which briefly is as follows: Droplets are entrained into the gas core at the inner side, travel through the gas core to the outer side and are deposited into the liquid film and travel back towards the inner side in the liquid film. The following formula can be obtained for mass continuity in the circumferential direction (ψ direction)

$$2\int_o^{\delta f} v_f \, d\eta_f = \frac{Q_o^* \cdot f(\psi)}{\gamma_f \cdot a \cdot w_{fm}} = Q_o \cdot f(\psi) \tag{5.2.31}$$

where Q_o^* is the liquid flow rate of the circumferential direction per unit axial length of the tube, $f(\psi)$ is the fraction of the liquid in the film and γ_f is the specific weight. The rest of the liquid is in the gas phase as droplets.

From eqs. (5.2.30b)and (5.2.31),

$$Q_o \cdot f(\psi) = \frac{2n-1}{n} \cdot \delta_f \cdot v_{f\delta} \tag{5.2.32}$$

We can use the same relationship between the resultant velocity and shearing stress at the tube wall as the single-phase flow in the straight tube. Then assuming that $V_{f\delta} << W_{f\delta}$, W_f can be taken to be identical to the resultant velocity, S_r.

The mean velocity in a supposed straight tube, S_{fm} (as in section (5.1.1.2))

$$S_{fm} = \int_0^1 2\xi w_f d\xi = B_n \cdot w_{f\delta} \cdot \delta_f^{-\frac{1}{2m-1}} \qquad (5.2.33)$$

where

$$\xi = \frac{r}{a} \qquad (5.1.4)$$

and

$$B_n = \frac{(2n-1)^2}{n(4n-1)} \qquad (5.2.33a)$$

The Reynolds number and the friction factor is:

$$Re_{fs} = \frac{2a \cdot S_{fm}}{\nu_f}$$

$$f_{fs} = \alpha_f \cdot Re_{fs}^{\frac{-1}{n}} \qquad (5.2.34)$$

Then, the shearing stress in the direction of the resultant velocity at the tube wall is obtained by:

$$(\tau_{\theta.r})_{\eta_f=0} = -\frac{\alpha_f}{8} \cdot B_n^{2-\frac{1}{n}} \cdot Re_f^{-\frac{1}{n}} \cdot w_{f\delta}^{2-\frac{1}{n}} \cdot \delta_f^{\frac{1}{n}} \qquad (5.2.35)$$

and also the shear stress in the circumferential direction is obtained approximately by the values of $V_{f\delta}$ and $W_{f\delta}$ at $n = \delta_f$ as follows:

$$(\tau_{\psi.r})_{n_f=0} = (\tau_{\theta.r})_{\eta_f=0} \cdot \frac{v_{f\delta}}{w_{f\delta}} \qquad (5.2.36)$$

The film thickness δ_f is thought to be $\frac{\delta_f}{a} << 1$, therefore the equation (5.1.11) for the single-phase flow can be used for the liquid film flow as follows:

$$-u_f \frac{\partial w_f}{\partial n_f} + V_f \frac{\partial w_f}{\partial \psi} = -C_t - \frac{\partial}{\partial n_f} \cdot \tau_{\theta.r}$$

$$-v_f^2 = \frac{a}{R} \cdot w_f^2 \cdot \cos\psi + \frac{\partial P}{\partial n_f}$$

$$-u_f \cdot \frac{\partial v_f}{\partial n_f} + v_f \cdot \frac{\partial v_f}{\partial \psi} - \frac{a}{R} \cdot w^2_f \cdot \sin\psi - \frac{\partial P}{\partial \psi} - \frac{\partial}{\partial n_f} \cdot \tau_{\psi.r} \qquad (5.2.37)$$

In order to simplify the analysis, the following assumptions are made:

$$\frac{\partial}{\partial n_f} \cdot \tau_{\theta.r} = 0 \quad \text{or} \quad (\tau_{\theta.r})_{n_f=0} = (\tau_{\theta.r})_{n_f=\delta_f} \qquad (5.2.38)$$

$$\frac{\partial P}{\partial n_f} = 0 \qquad (5.2.39)$$

The momentum equation of the circumferential direction in eq. (5.2.37) is integrated with respect to n_f from 0 to δ_f as follows:

$$\frac{a}{R} \sin\psi \int_o^{\delta_f} w_f^2 \, dn_f + \int_o^{\delta_f} \frac{\partial P}{\partial \psi} dn_f + \frac{\partial}{\partial \psi} \int_o^{\delta_f} v_f^2 dn_f - v_{f\delta} \frac{\partial}{\partial \psi} \int_o^{\delta_f} v_f \, dn_f$$

$$= (\tau_{\psi.r})_{n_f=0} - (\tau_{\psi.r})_{n_f=\delta_f} \qquad (5.2.40)$$

Neglecting the pressure gradient in the gas boundary layer and using eq. (5.1.7):

$$\int_o^{\delta_f} \frac{\partial P}{\partial \psi} \, dn_f = -\frac{\rho_g}{\rho_f} \cdot \left(\frac{w_{gm}}{w_{fm}}\right)^2 \cdot \frac{a}{R} \cdot w^2_{g\delta} \cdot \sin\psi \cdot \delta_f \qquad (5.2.41)$$

Substituting eqs. (5.2.29) and (5.2.30) into eq. (5.2.40), it becomes:

$$\frac{a}{R} \sin\psi \cdot \delta_f \left\{ \frac{2n-1}{2n+1} \cdot w_f^2 - \frac{\rho_g}{\rho_f} \left(\frac{w_{gm}}{w_{fm}}\right)^2 w^2_{g\delta} \right\} + \frac{2n-1}{2n(2n+1)} \cdot v_{f\delta} \times$$

$$\left\{ (2n-1)\delta_f \frac{\partial v_{f\delta}}{\partial \psi} - v_{f\delta} \cdot \frac{\partial \delta_f}{\partial \psi} \right\} = (\tau_{\psi.r})_{n_f=0} - (\tau_{\psi.r})_{n_f=\delta_f} \qquad (5.2.42)$$

The fraction of liquid in the liquid film and total liquid phase are obtained using the following equation:

$$(w_{fm})_{film} = \frac{1}{\pi}\int_0^{2\pi}\int_0^{\delta_f} \cdot w_f \cdot d\eta \cdot d\psi \qquad (5.2.43)$$

then, the fraction becomes

$$\frac{(w_{fm})_{film}}{w_{fm}} = \frac{2n-1}{2n\pi}\int_0^{2\pi} w_{f\delta} \cdot \delta_f \cdot d\psi \qquad (5.2.44)$$

The mean liquid film thickness is defined as

$$\delta_{fm} = \frac{1}{2\pi}\int_0^{2\pi} \delta_f \cdot d\psi \qquad (5.2.45)$$

5.2.4.1 Analysis for liquid film thickness

The analysis for the liquid film thickness is treated based on the results in sections (5.2.3) and (5.2.4).

From the assumption (7), eq. (5.2.20) and eq. (5.2.35) are equal:

$$(\tau_{\theta.r})_{\eta_g=0} = (\tau_{\theta.r})_{\eta_f=0}$$

$$\alpha_g B_m^{2-\frac{1}{m}} \cdot Re_g^{-\frac{1}{m}} \cdot w_{g\delta}^{2-\frac{1}{m}} \cdot \delta_g^{-\frac{1}{m}} \cdot (1 + b\delta_{fm}) \cdot \frac{\rho_g}{\rho_f} \left(\frac{w_{gm}}{w_{fm}}\right)^2$$

$$= \alpha_f \cdot B_n^{2-\frac{1}{n}} \cdot Re_f^{-\frac{1}{n}} \cdot w_{f\delta}^{2-\frac{1}{n}} \cdot \delta_f^{-\frac{1}{n}} \qquad (5.2.46)$$

From eq. (5.2.37)

$$(\tau_{\psi.r})_{\eta_f=0} = -\frac{\alpha_f}{8} \cdot B_n^{2-\frac{1}{n}} \cdot Re_f^{-\frac{1}{n}} \cdot w_{f\delta}^{2-\frac{1}{n}} \cdot \delta_f^{-\frac{1}{n}} \cdot \frac{v_{f\delta}}{w_{f\delta}} \qquad (5.2.47)$$

and from eqs. (5.2.10) and (5.2.20)

$$(\tau_{\psi} \cdot r)_{\eta_f = \delta_f} = \frac{\alpha_g}{8} \cdot B_m \cdot Re_g^{2-\frac{1}{m}} \cdot w_{f\delta}^{-\frac{1}{m}} \cdot \delta_g^{2-\frac{1}{m}} \cdot (1 + b\delta_{fm})^{-\frac{1}{m}}$$

$$\times \frac{4m \cdot v_{g\delta} \cdot \rho_g}{(2m-1) \cdot \delta_g \cdot w_g \cdot \rho_f} \cdot \left(\frac{w_{gm}}{w_{fm}}\right)^2 \qquad (5.2.48)$$

Substituting eqs. (5.2.47) and (5.2.48) into eq. (5.2.42)

$$\Gamma_{cent.} + \Gamma_{iner.} = -\frac{\alpha_g}{8} \cdot B_m^{2-\frac{1}{m}} \cdot Re_g^{-\frac{1}{m}} \cdot w_{g\delta}^{2-\frac{1}{m}} \cdot \delta_g^{-\frac{1}{m}} \cdot (1 + b\delta_{fm}) \cdot \frac{\rho_g}{\rho_f} \cdot \left(\frac{w_{gm}}{w_{fm}}\right)^2$$

$$\times \left\{ \frac{4m \cdot v_{g\delta}}{(2m-1) \cdot \delta_g \cdot w_g} + \frac{v_{f\delta}}{w_{f\delta}} \right\} \qquad (5.2.49)$$

where

$$\Gamma_{cent.} = \frac{a}{R} \sin \psi \cdot \delta_f \cdot \left\{ \frac{2n-1}{2n+1} \cdot w_{f\delta}^2 - \frac{\rho_g}{\rho_f} \cdot \left(\frac{w_{gm}}{w_{fm}}\right)^2 \cdot w_{g\delta}^2 \right\} \qquad (5.2.49a)$$

$$\Gamma_{iner.} = \frac{2n-1}{2n(2n+1)} \cdot v_{f\delta} \cdot \left\{ (2n-1) \cdot \delta_f \cdot \frac{dv_{f\delta}}{d\psi} - v_{f\delta} \cdot \frac{d\delta_f}{d\psi} \right\} \qquad (5.2.49b)$$

Subscriptions cent. and iner., are the centrifugal and inertia terms respectively.

The values of $\frac{dV_{f\delta}}{d\psi}$ and $\frac{d\delta_f}{d\psi}$ which comprise the inertia term are very small compared with the other terms, therefore the inertia term can be neglected.

Using eqs. (5.2.32) and (5.2.46), eq. (5.2.49) becomes the following lengthy formula:

$$F(\psi) = \frac{a}{R}\cdot\sin\psi\cdot\delta_f\cdot\left\{\frac{2n-1}{2n+1}\cdot J\cdot w_{g\delta}^{\frac{2n(2m-1)}{m(2n-1)}}\cdot\frac{\delta_f^{\frac{2}{2n-1}}}{\delta_g^{\frac{2n}{m(2n-1)}}} - \frac{\rho_g}{\rho_f}\left(\frac{w_{gm}}{w_{fm}}\right)^2\cdot w_{g\delta}^2\right\}$$

$$+\left(\tau_{\varphi\cdot r}\right)_{\eta_g=0}\cdot\left\{\frac{4m\cdot v_{g\delta}}{(2m-1)\cdot\delta_g\cdot w_{g\delta}} + \frac{n\cdot Q_o\cdot f\cdot\delta_g^{\frac{n}{m(2n-1)}}}{(2n-1)\cdot J\cdot w_{g\delta}^{\frac{n(2m-1)}{m(2n-1)}}\cdot\delta_f^{\frac{2n}{2n-1}}}\right\} = 0$$

(5.2.50)

where

$$J = \left[\frac{\alpha_g}{\alpha_f}\cdot B_m^{2-\frac{1}{m}}\cdot B_n^{\frac{1}{n}-2}\cdot Re_g^{-\frac{1}{m}}\cdot Re_f^{\frac{1}{n}}\cdot(1+b\delta_{fm})\cdot\frac{\rho_g}{\rho_f}\cdot\left(\frac{W_{gm}}{W_{fm}}\right)^2\right]^{\frac{2n}{2n-1}}$$

(5.2.50a)

The liquid film thickness $\delta_f(\psi)$ can be obtained from eq. (5.2.50) using eqs. (5.2.28) and (5.2.29).

Giving arbitrary value to Q_o initially and 1 to $f(\psi)$ and solving eq. (5.2.50) by an iterative process, the relation between $F(\psi)$ and $\delta(\psi)$ was determined. This function is presented as Fig. (5.2.2).

For the starting values of Q_o that are tried, it is possible to have either none, one or two values of $\delta(\psi)$ that satisfy $F(\psi) = 0$.

In the case of two δ_f's: the point $\delta_f = \delta_{f2}$, shown in Fig. (5.2.2), is in an unstable condition because the centrifugal force affected to the liquid phase is predominant. The point $\delta_f = \delta_{f1}$ is the stable condition because the shearing stress at the tube wall has a predominant effect in keeping the liquid film thickness constant.

In the case of ~~non~~ no solution δ_f: the liquid film does not exist, ~~the liquid~~

~~film does not exist~~, the liquid phase exists as droplets in the gas phase or as a disturbance wave.

In the case of one δ_f: the two forces in Fig. (5.2.2) are balanced and the liquid film exists, and this solution gives the correct values of δ_f.

If the solution of eq. (5.2.50) gives either none, or two results for Q_0, a more appropriate value of Q_0 is tried and the calculations are repeated. This iterative procedure is continued until a single solution for δ_f is obtained.

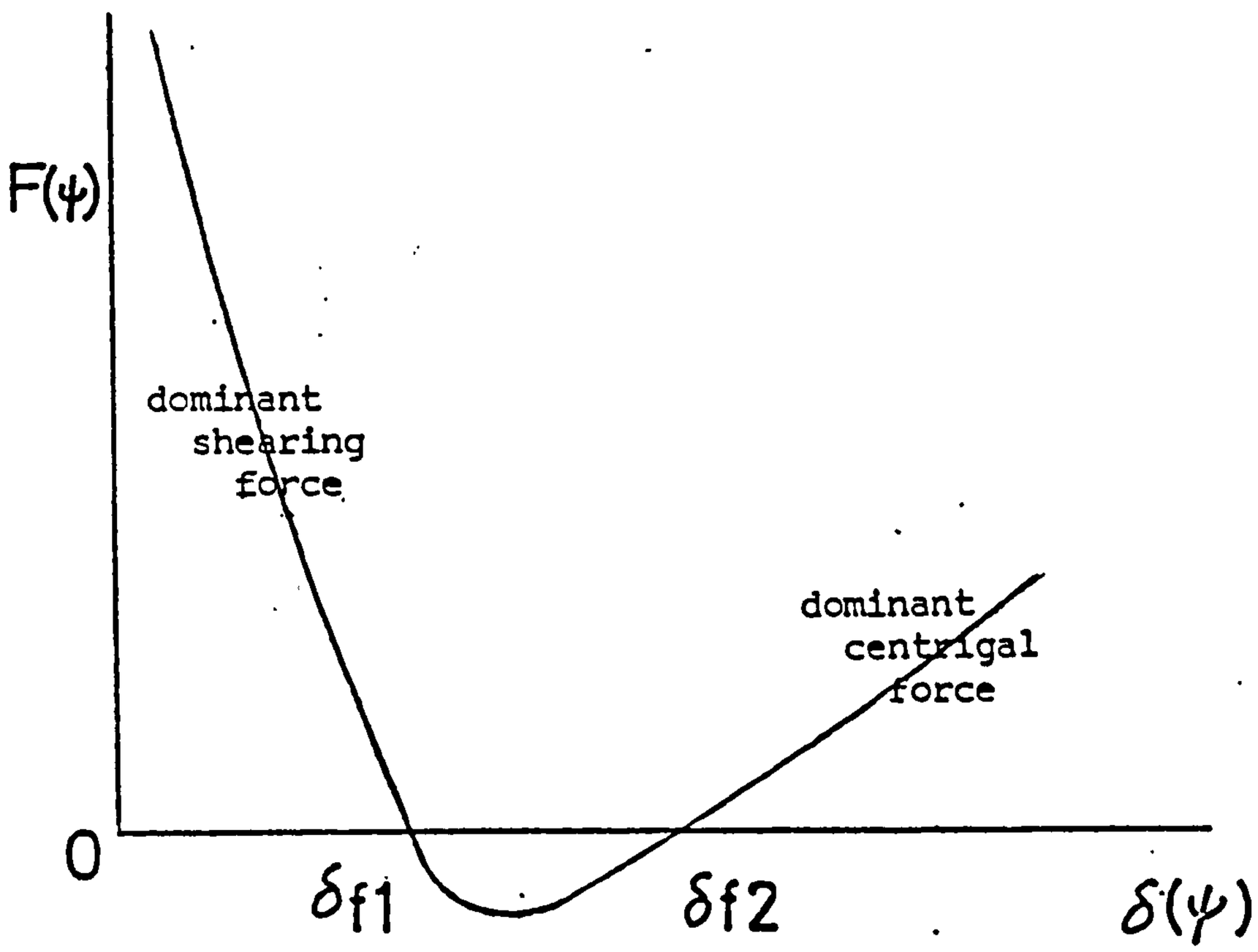


Fig.(5.2.2) Relation between $F(\psi)$ of eq.(5.2.50) and liquid film thickness.

The entrainment phenomenon increases at a small value of $f(\psi)$ and decreases (thickening the film thickness) at a large value of $f(\psi)$. Although in solving eq. (5.2.50) for the present data, a value of unity was always taken as entrainment did not occur.

In the case of m = n = 4 and $\alpha_g = \alpha_f = 0.316$, as in eqs. (5.2.28) and (5.2.29), eq. (5.2.50) becomes as follows:

$$F(\psi) = \sin\psi.\delta_f \left[1.070 \left\{ \frac{\delta_f(1+b.\delta_{fm})^{\frac{16}{5}} . Y_1}{Y_2.(1+0.377\cos\psi)} \right\}^{\frac{2}{7}} - 1 \right] + \frac{0.0277}{(1+0.469\cos\psi)^{5/4}} - \left[\frac{1.220\sin\psi(1+b\delta_{fm})^{4/5}}{Y_1.(1+0.377\cos\psi)^{5/4}} + 0.644.Q_o.f.\left(\frac{a}{R}\right)^{-\frac{1}{2}}. \frac{(1+b\delta_{fm})^{12/35}.Y_2^{1/7}.Y_3}{(1+0.377\cos\psi)^{3/28}.Y_1^{8/7}.\delta_f^{8/7}} \right] = 0 \quad (5.2.51)$$

where

$$Y_1 = \{ Re_g \left(\frac{a}{R}\right)^2 \}^{\frac{1}{5}}$$

$$Y_2 = \frac{\mu_f}{\mu_g} \left(\frac{\rho_g}{\rho_f}\right)^{\frac{1}{2}}$$

$$Y_3 = \frac{w^*_{fm}}{w^*_{gm}} \left(\frac{\rho_f}{\rho_g}\right)^{\frac{1}{2}} \quad (5.2.51a)$$

and μ is the viscosity.

This equation has four parameters, Y_1, Y_2, Y_3 and $Q^*_o \cdot f \cdot \left(\frac{a}{R}\right)^{-\frac{1}{2}}$ which relate to the film thickness in the coil.

Considering the relation between entrainment and Q_o (the liquid flow rate of the circumferential direction per unit axial length of the tube), the growth of the film thickness is limited when the gas flow rate is fixed. There are two reasons of this limitation, firstly when the film thickness its surface becomes ruffled and is sheared off into

the gas phase, secondly when the solution to $F(\psi) = 0$ does not exist due to a high entrainment rate and disturbance phenomena.

The flow rate in the circumferential direction from the inner side to the outer side is defined as $Q_o.f(\psi)$. The value $f(\psi)$ is unity unless entrainment occurs, and $0 < f(\psi) < 1$ if it does occur. The mean fraction of $f(\psi)$ must be obtained when entrainment occurs,

$$f_m = \frac{1}{2\pi} \int_o^{2\pi} f(\psi) \cdot d\psi \qquad (5.2.52)$$

This should be equal to the fraction which is obtained from eq. (5.2.44). The fraction decreases when Q_o^* is increasing. The value Q_o^* when both fractions are equal is thought to be the flow amount travelling from the inner to outer sides as droplets.

5.2.5 Discussion and comparison between the theoretical results and the empirical results

We substitute the value $b = 150$ into the interfacial friction factor formula (eq.(5.2.1), first proposed by Wallis (87.107)). Then substituting the result into eq. (5.2.51), the film thickness is evaluated using the calculation process described in section (5.2.3.1).

The calculations were started at the outer side ($\psi=0^{\circ}$) and carried out at intervals through 180° to the inner side ($\psi = 180^{\circ}$). Calculations were only necessary for 180° since the film thickness profile is assumed to be symmetrical (assumption (9) in section 5.2.2). The film thickness at the outer side must be evaluated at $\psi = 2^{\circ}$ instead of $\psi = 0^{\circ}$ because of the characteristics of the equation (5.2.51) and similarly that at the inner side is obtained at $\psi = 178^{\circ}$. The results are plotted in Figs. (5.2.3a) and (5.2.3b).

Fig. (5.2.3a) shows the film thickness profile of the air-water mixture in Coils A and C at atmospheric pressure. The flow rates used are the same flow conditions as shown previously (W_{gm} = 50.32 m/s, W_{fm} = 0.015 m/s) in Table (4.2.1) in section (4.3.3), i.e. high air - low water flow.

Fig. (5.2.3b) shows the film thickness profile at high air-high water flow conditions (W_{gm} = 50.32 m/s, W_{fm} = 0.04 m/s) in Coils A and C at the atmospheric pressure.

From these two figures, it is seen that the film tends to thicken at the inner and outer sides in both coils. Especially at High air - Low water flow, the film at the inner and outer sides becomes significantly thicker than at the upper and lower sides (at $\Psi = 90^{o}$). The film in the larger coil (Coil C) is thicker than in the smaller coil (Coil A) around the whole periphery the exception of the upper and lower sides where thicknesses are the same.

Figs. (5.2.4a) and (5.2.4b) show a comparison between the empirical results which were obtained by Whalley and Williams (88) and the theoretical results from eq. (5.2.51).

Fig. (5.2.4a) shows the film thickness profiles with a specific air velocity, W_{gm} = 29.3 m/s, and specific water velocity W_{fm}=0.045 m/s at 1.69 bars in $\frac{a}{R}$ = 0.0202 coil. Fig. (5.2.4b) shows the film profiles with the specific air velocity W_{gm} = 48.3 m/s, and specific water velocity, W_{fm} = 0.045 m/s at 1.69 bars in the same coil. Here Whalley and Williams (88) observed the fluctuations of film thickness with time. The $m_{0.02}$, $m_{0.1}$ and $m_{0.9}$ plots are values of the film thickness at a certain peripheral location which are exceeded for 2%, 10% and 90% of the time.

From these two comparisons empirical results with theory, the following features were observed:

(a) The empirical film profiles for the various m values are distributed in a wide range. The theoretical film profiles are based on the assumptions as in section (5.2.2) (i.e. smooth film surface, neglected the droplet ~~entrance~~ existence in the gas core and momentum effects, etc.). However these empirical and theoretical film profiles are of the similar shape, thus this theoretical work can explain the film profile phenomenon qualitatively.

(b) The theoretical results near the outer side ($\psi = 0^{o}$) and the inner side ($\psi = 180^{o}$) are less accurate due to the characteristic of the eq. (5.1.52) as already mentioned, but results of the empirical and theoretical in the range $30^{o} < \psi < 150^{o}$ are in good agreement.

(c) The theoretical results at the inner and outer sides show thicker profiles than those of the empirical results. If the liquid film becomes thick at the inner or outer sides in the real phenomenon, the film surface becomes rippled and is torn off as droplets into the gas core by the gas phase. Therefore the film thickness in the actual flow is limited. However the theoretical analysis does not allow for this entrainment phenomena in the formula of the film thickness.

Whalley and Williams (88) asserted that the entrainment rate does not exceed more than 30% of liquid flow rate. If this maximum entrainment rate is used in the theoretical analysis, the film profiles at the inner and outer are still thciker than the average film thickness of the empirical results.

(d) The liquid film flow rate Q_o from the outer side to inner side is equal to the entrainment rate from the inner side. Obviously the inner side becomes swollen immediately before each droplet is detached into the gas core. The entrainment rate is also referred to in feature (c).

We now extend to use the eq. (5.2.50) for the steam-water mixture flow at 2 bars and 40 bars at various steam quality. When applied to this type of profile, the equation is found to be even more realistic.

Fig. (5.2.5a) shows the film profiles at 2 bars and 2.713×10^5 Kg/m^2h for the total mass flow rate in the coil C. This condition is similar to the results of the present work.

On increasing the steam quality, the film profiles near the outer side increase in thickness but not significantly. Thick films lie at both the inner and outer sides. The empirical film profiles in this work are discussed fully in section (4.3.1) and (4.3.3).

From the wall temperature profiles, the position of the thinnest part of the film was thought to be at 30^o towards the outer side from the upper position. The thin film profiles for the upper half of the tube obtained in the present work were in good agreement with theoretical results obtained using eq. (5.2.50).

Fig. (5.2.5b) shows the film profile at the same flow rate as Fig. (5.2.5b) at 40 bars. The film thicknesses at the inner and outer sides have identical values to the case of 2 bars, except for the film thicknesses for 50~70% steam qualities at the upper side ($\psi = 90^o$). These become significantly thicker than for 2 bars. This phenomenon is explained firstly by the liquid film flow rate, Q_o, increasing secondly by the entrainment rate at the inner side which increases because it is proportional to the value of Q_o.

Up to the present no published work has reported that the entrainment rate at the inner side increases at high pressure and at low steam quality. Whalley et al (93) mentioned the surface tension of liquid phase decreased in the steam-water flow at high pressure (see Fig. (4.3.13)). However, the dependence of entrainment rate of surface tension has not been investigated fully.

Also, referring to investigation of the burnout mechanism which is described in section (4.3.5), this analysis is able to predict the burnout position. But, for a steam-water mixture this analysis is applicable only at low pressure (atmospheric to 20 bars) and large ρ_f/ρ_g conditions.

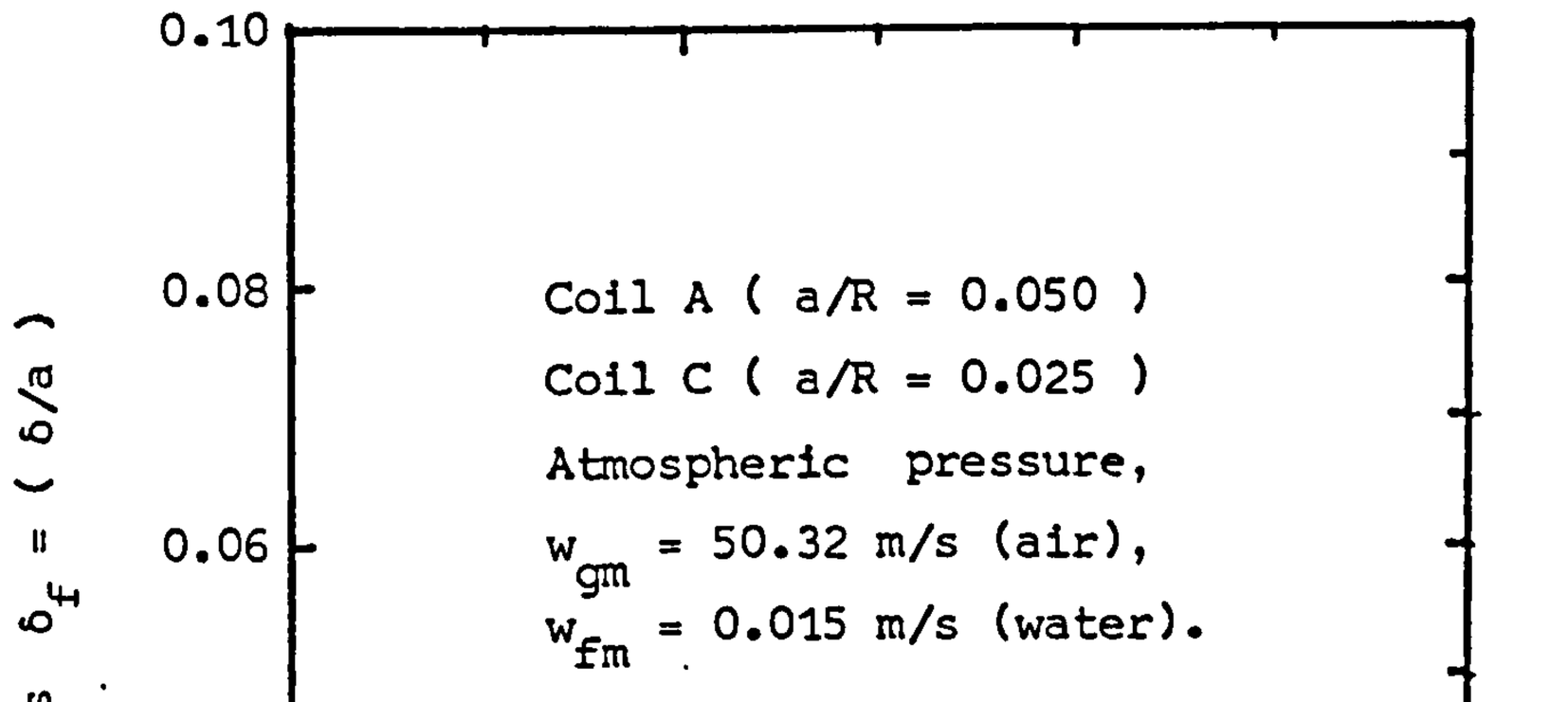


Fig. (5.2.3 a) : Liquid film profiles from eq.(5.2.51)
for air-water mixture in Coils A and C.
High air - low water flow in Table (4.2.1).

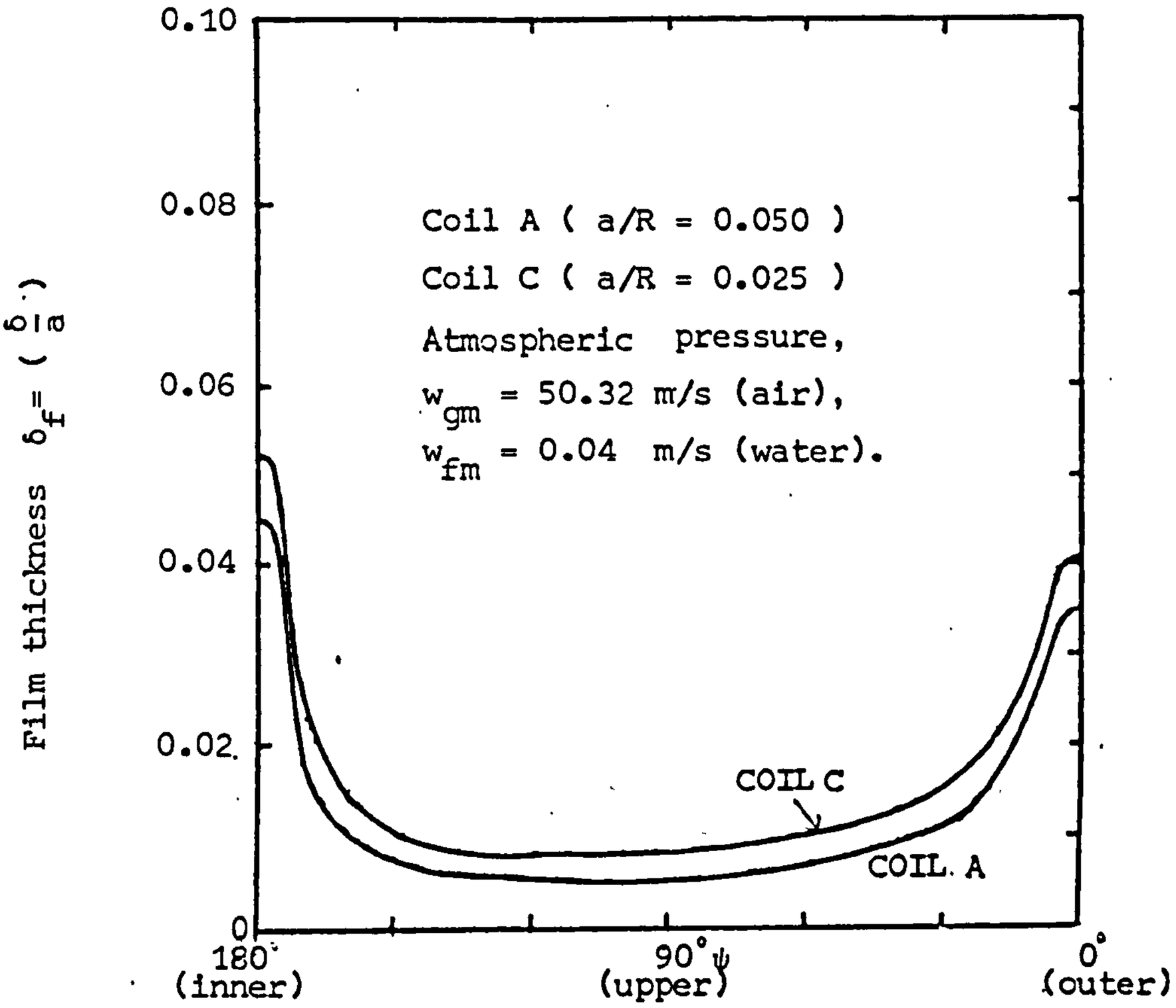


Fig. (5.2.3b) : Liquid film profiles from eq.(5.2.51)
for air-water mixture in Coils A and C.
High air - high water flow in Table(4.2.1).

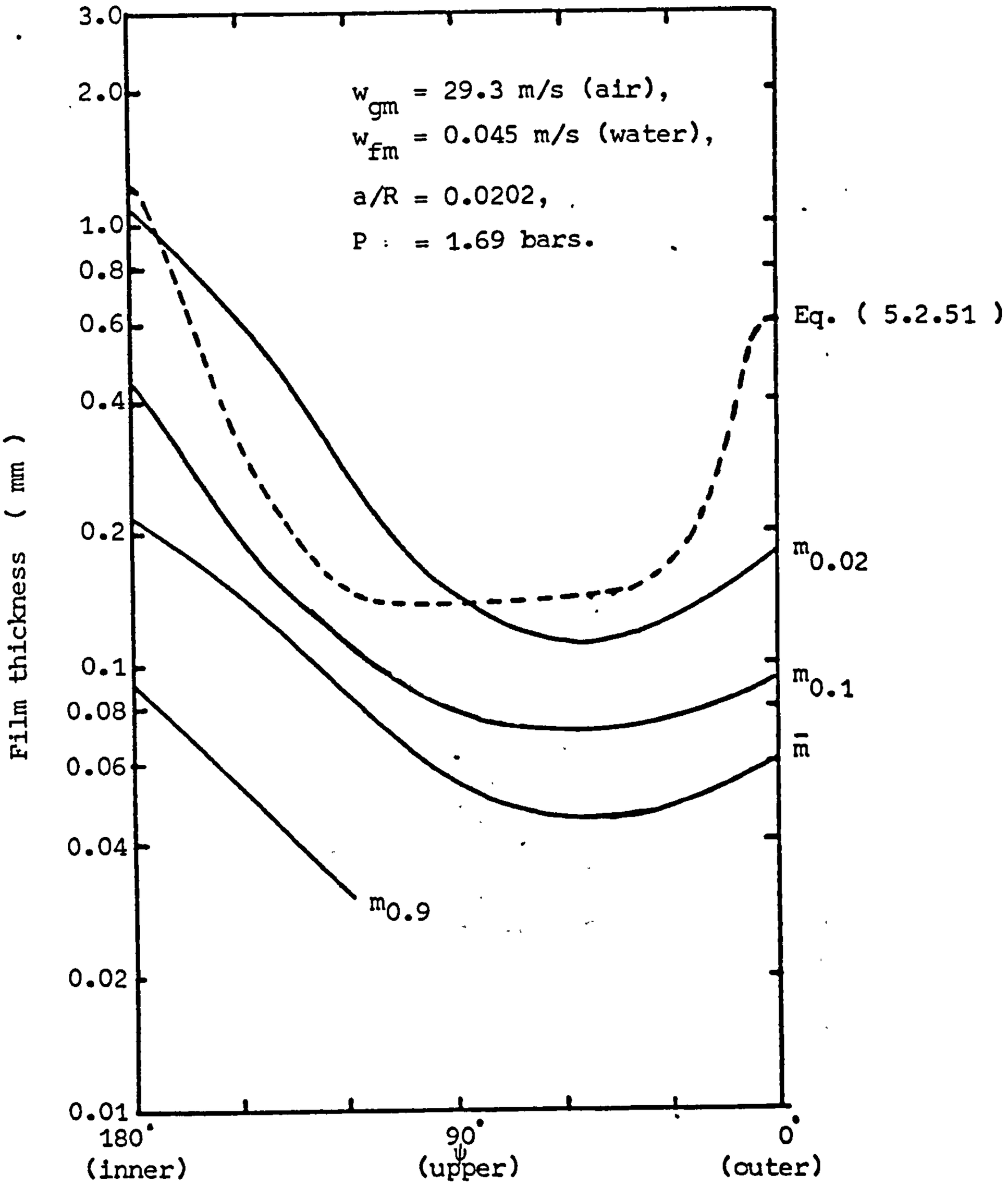


Fig. (5.2.4 a) : Comparison of liquid film profiles from eq. (5.2.51) with the experimental results of Whalley and Wiliams (88).

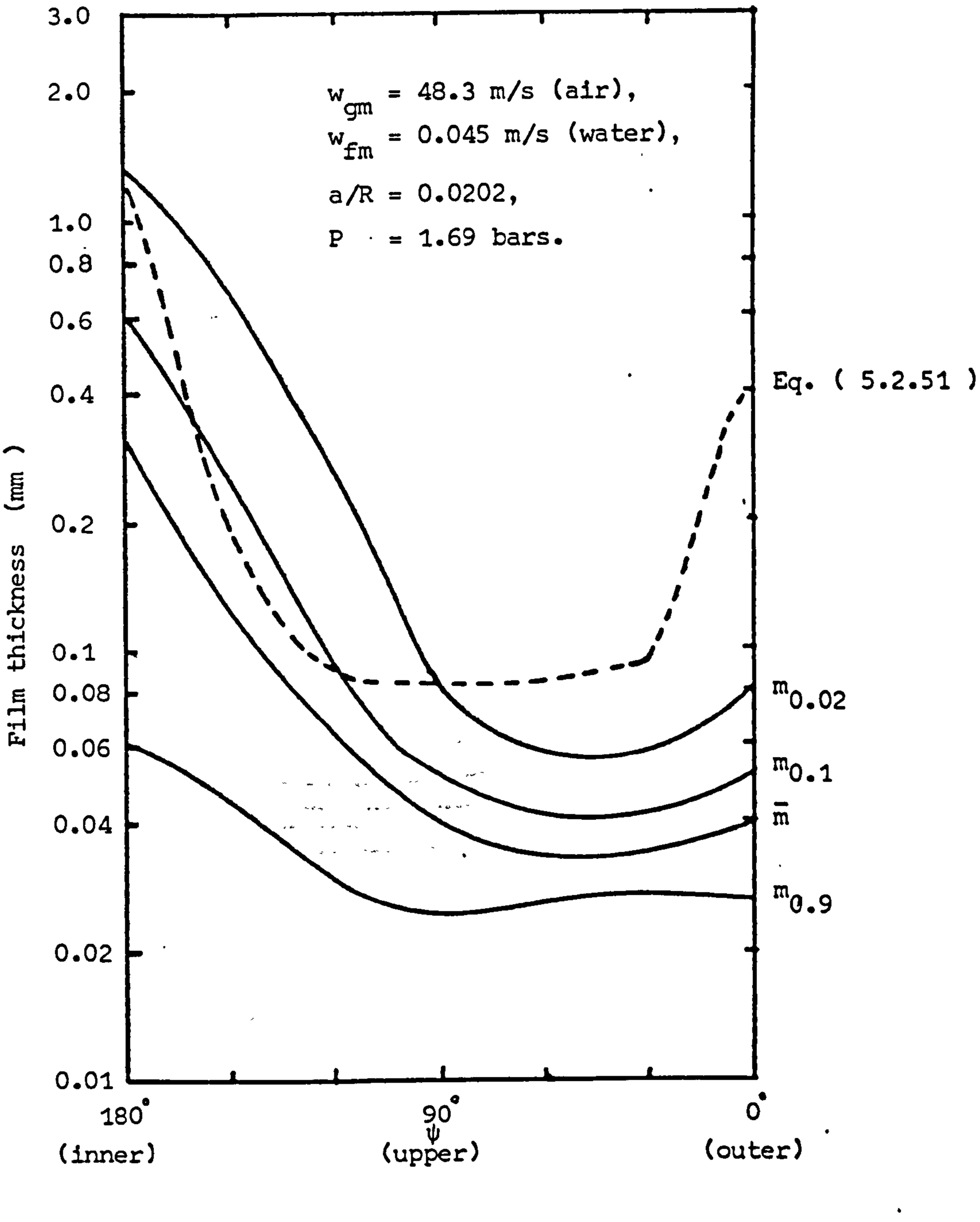


Fig. (5.2.4 b) : Comparison of liquid film profiles from eq.(5.2.51) with the experimentalresults of Whalley and Wilams (88).

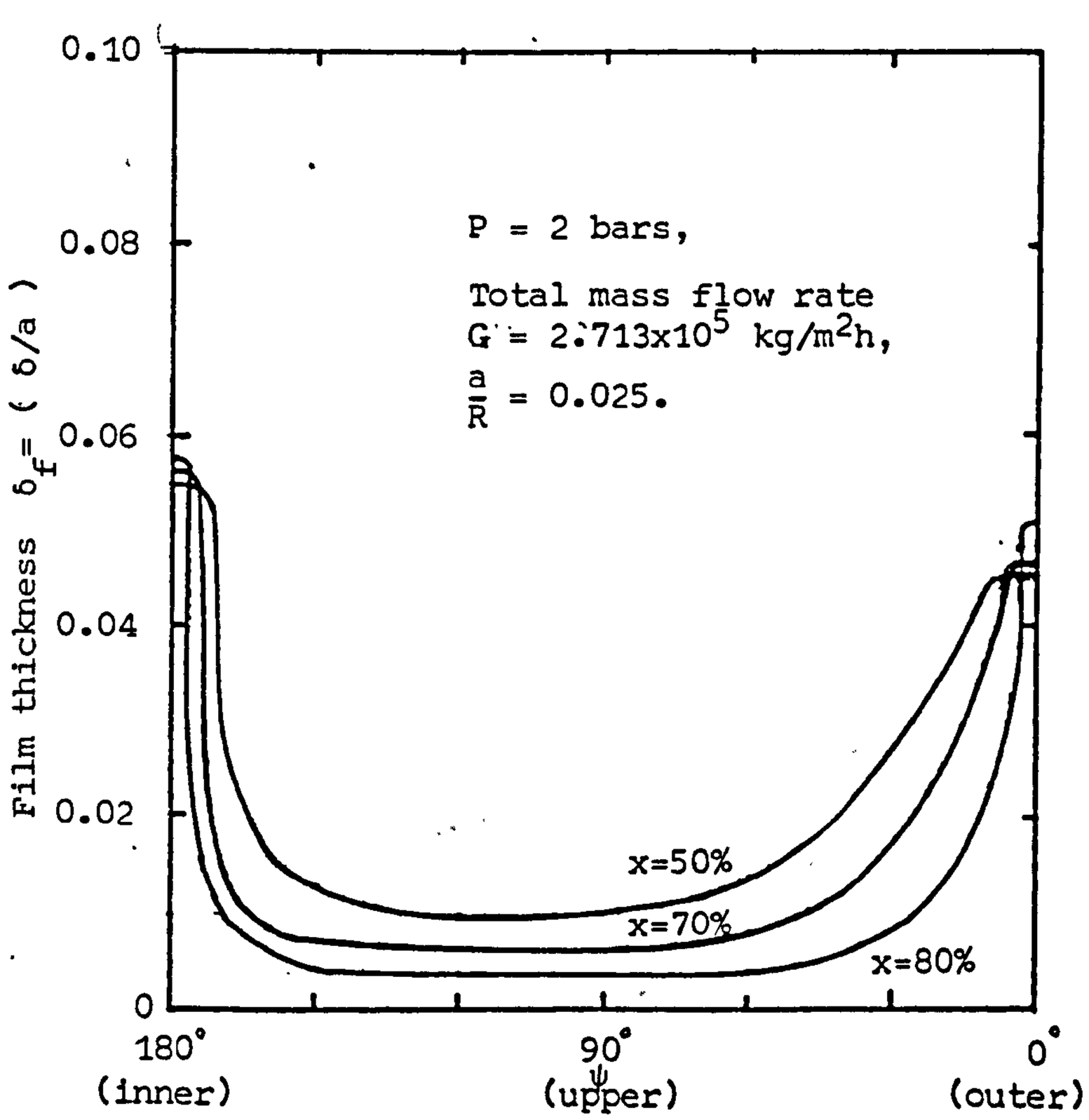


Fig. (5.2.5 a) : Liquid film profiles at various steam qualities and at 2 bars in Coil C.

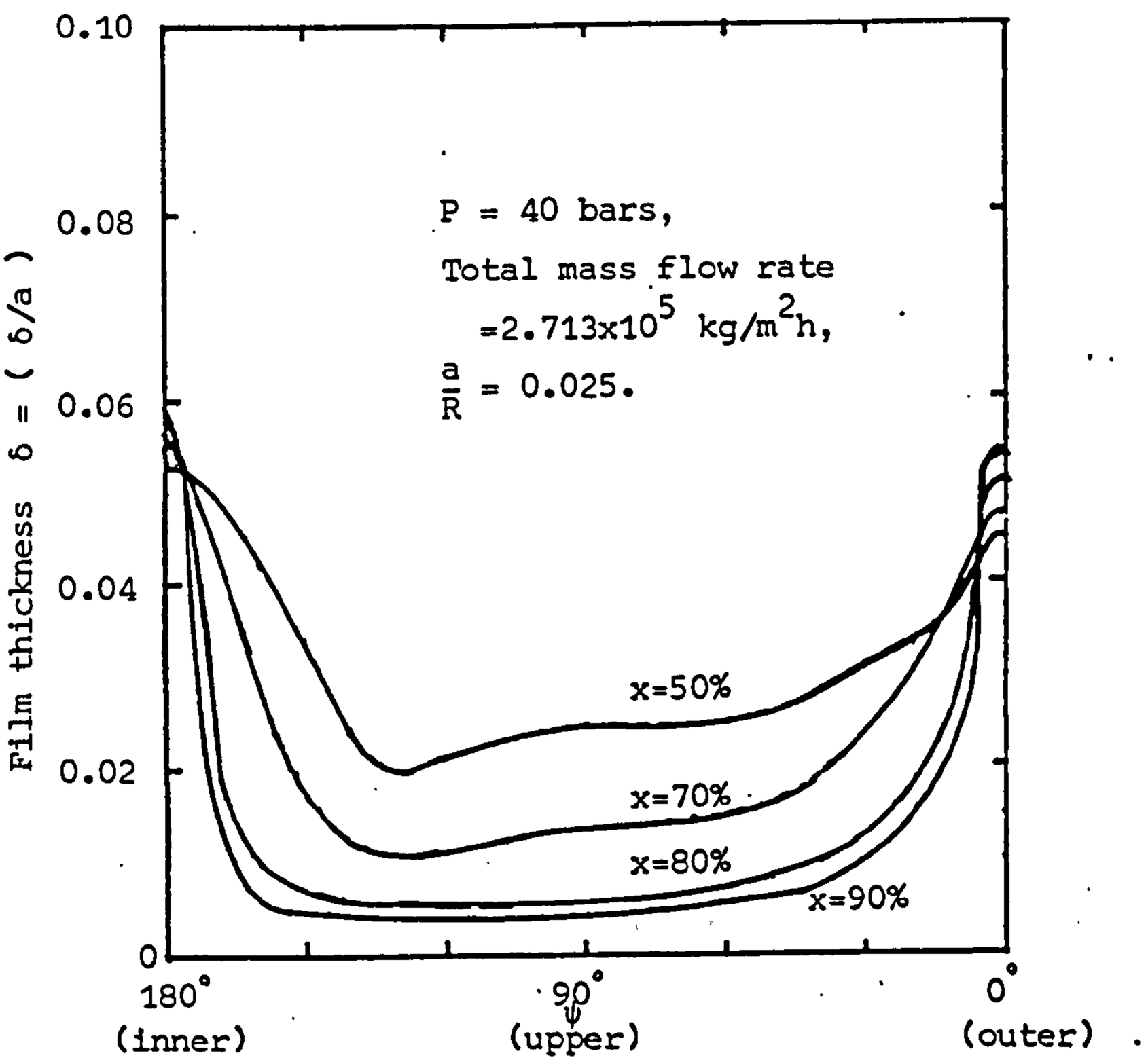


Fig. (5.2.5 b) : Liquid film profiles at various steam qualities and at 40 bars in Coil C.

5.3 Analysis of heat transfer in annular flow

From an examination of the results in section (4.3.4), the mechanism of the annular flow boiling heat transfer is thought to be convective boiling in the liquid film.

For proceeding with the theoretical analysis of the heat transfer coefficient, the following models and assumptions are used;

(a) In the boiling process, the liquid flow is accelerated; however in this section the liquid flow velocity is taken as constant.

(b) The liquid surface is smooth. The axial velocity ($W_{f\delta}$) at liquid film surface (δ_f) is derived in sections (5.2.3) and (5.2.4) and the shearing stress at the tube wall is obtained from eq. (5.2.35).

(c) The liquid surface temperature is constant at any cross section and it is at the saturated temperature of the liquid,

(d) The adiabatic film thickness and liquid velocity given by the eqs. (5.2.30) and (5.2.31) are valid for the heat addition case. Using the Taylor-Prandtl analogy (see section (5.1.2.2)), the liquid film is divided into the laminar sublayer and turbulent layer. The buffer layers are formulated as eq. (5.1.55)

$$\delta_b = \left(\frac{4809.8}{\alpha}\right)^{\frac{1}{2}} \cdot Re_s^{-\frac{2m-1}{2m}} \qquad (5.1.55)$$

The boiling heat transfer coefficient is obtained as follows:

(i) In the case of $\delta_f \leq \delta_b$,the liquid film that is formed is treated as a laminar sub-layer.

From eq. (5.1.57)

$$T_w - T_\delta = - Pr_f \cdot \frac{q_w}{\tau_w} \cdot W_{f\delta} \qquad (5.2.53)$$

The Nusselt number of the laminar sublayer is given by:

$$Nu_\delta = \frac{2a}{k_f} \cdot \frac{q_w^*}{T_w^* - T_\delta^*} = \frac{Re_f \cdot \tau_w}{w_{f\delta}} \qquad (5.2.54)$$

where k_f is the thermal conductivity.

(ii) In the case of $\delta_f > \delta_b$ the liquid film that is formed is treated as a turbulent layer.

From eq. (5.1.60)

$$T_w - T_\delta = - w_{f\delta} \cdot \frac{q_w}{\tau_w} \left\{1 + (Pr_f - 1) \cdot \left(\frac{\delta_b}{\delta_f}\right)^{\frac{1}{2n-1}}\right\} \qquad (5.2.55)$$

The Nusselt number is given by:

$$Nu_\delta = \frac{2a}{k_f} \cdot \frac{q_w^*}{T_w^* - T_\delta^*} = \frac{Re_f \cdot Pr_f \cdot \tau_w}{w_{f\delta}} \left\{1 + (Pr_f - 1) \left(\frac{\delta_b}{\delta_f}\right)^{\frac{1}{2n-1}}\right\}^{-1}$$

(5.2.56)

where

$$Re_f = \frac{2a \cdot w_{fm}}{\nu_f}$$

$$\tau_w = \frac{\alpha_f}{8} \cdot B_n^{2-\frac{1}{n}} \cdot Re_f^{-\frac{1}{n}} \cdot w_{f\delta}^{2-\frac{1}{n}} \cdot \delta_f^{-\frac{1}{n}}$$

δ_b is obtained from eq. (5.1.55)

$$Re_s = \frac{2a \cdot S_{fm}}{\nu_f}$$

$$S_{fm} = B_n \cdot W_{fm} \cdot W_{f\delta} \cdot \delta_f^{-\frac{1}{2n-1}} \qquad (5.2.57)$$

Substituting eq. (5.2.57) into eqs. (5.2.54) and (5.2.56), Nusselt numbers for both cases are given by the following:

In the case of $\delta_f \leq \delta_b$,

$$Nu_\delta = \frac{\alpha_f}{8} \cdot B_n^{2-\frac{1}{n}} \cdot Re_f^{1-\frac{1}{n}} \cdot w_{f\delta}^{1-\frac{1}{n}} \cdot \delta_f^{-\frac{1}{n}} \qquad (5.2.58)$$

In the case of $\delta_f > \delta_b$,

$$Nu_\delta = \frac{\alpha_f}{8} \cdot B_n^{2-\frac{1}{n}} \cdot Re_f^{1-\frac{1}{n}} \cdot w_{f\delta}^{1-\frac{1}{n}} \delta_f^{-\frac{1}{n}} Pr_f \cdot \{1 + (Pr_f - 1)(\frac{\delta_b}{\delta_f})^{\frac{1}{2n-1}}\}^{-1}$$

(5.2.59)

As the values of Prandtl number in a steam-water system for saturated water must be near to unity, these Nusselt numbers are only valid for a restricted number of instances.

Using $\alpha_f = 0.316$ and n = 4, eqs. (5.2.58) and (5.2.59) are now both given by the same formula, as follows:

$$N_{u_\delta} = 0.028\ Re_f^{\frac{3}{4}} \cdot w_{f\delta}^{\frac{3}{4}} \cdot \delta_f^{-\frac{1}{4}}$$

5.3.1 <u>Discussion and comparison between the theoretical results and the empirical results</u>

Using the film profile of the steamwater flow in Fig. (5.2.5a), the values of the parameters, (Re_f, $W_{f\delta}$, δ_f) of eq. (5.2.60) and the forced convective boiling heat transfer coefficients were evaluated. These are shown in Fig. (5.2.6a).

The experimental conditions were $2.713 \times 10^{5 Kg/m^2 h}$ of total flow rate with 7942 $^{Kcal}/m^2 h$ of heat flux at 2 bars in Coil C ($\frac{a}{R} = 0.025$). The figure is based on Fig. (4.3.17c) which shows the empirical two-

phase heat transfer coefficients in Coil C. The evaluated values of Nu_δ , Re_f, $W_{f\delta}$ and δ_f are shown in Table (A.2) and (A.3) in the Appendix.

From the figure, the heat transfer coefficient at the upper side has a greater value than that of the outer side in steam qualities greater than 30%. It becomes maximum about 70~80% of the steam and has about 25% higher value than the empirical results at their peaks. The heat transfer coefficients at the outer side have similar values to the upper side up to 40% steam quality and have about 50% greater values than those of the empirical results. However both the results show similar profiles within a 40% variation; hence eq. (5.2.60) can qualitatively explain the phenomena of the heat transfer coefficient in steam-water flow at 2 bars.

Eq. (5.2.60) is used for high pressure (20 bars) experimental results. Kozeki (48,53,80) investigated the heat transfer coefficient under the conditions of 1.95×10^6 Kg/m^2h of total flow rate, 20×10^4, 10×10^4 and 5×10^4 $Kcal/m^2h$ of heat flux at 20 Kg/m^2g in a coil with $\frac{a}{R} = 0.028$. His results are shown in Fig. (5.2.6b). This figure shows that the outer side has the largest heat transfer coefficient up to 90% steam quality and the upper side has a heat transfer coefficient at approximately a mean of the outer and inner side values.

From these two figures, the values of eq. (5.2.60) are affected by the terms $W_{f\delta}$ and δ_f. The film thickness, δ_f, is already discussed in section (5.2.3.2). The film at the upper side thickens at high steam pressure and at low steam quality (see Figs. (5.2.5a) and (5.2.5b)). However the film at the upper side becomes thin at low steam pressure

and low steam quality. Therefore the heat transfer coefficient obtained from eq. (5.2.60) is directly related to the film thickness (δ_f). The present theoretical analysis seems to be in agreement with the experimental results qualitatively. This means that the theory may be able to explain the phenomena to a certain extent. However the applicable range of this analysis will be limited to within the assumptions, that is, relatively low pressure and liquid Prandtl number about unity.

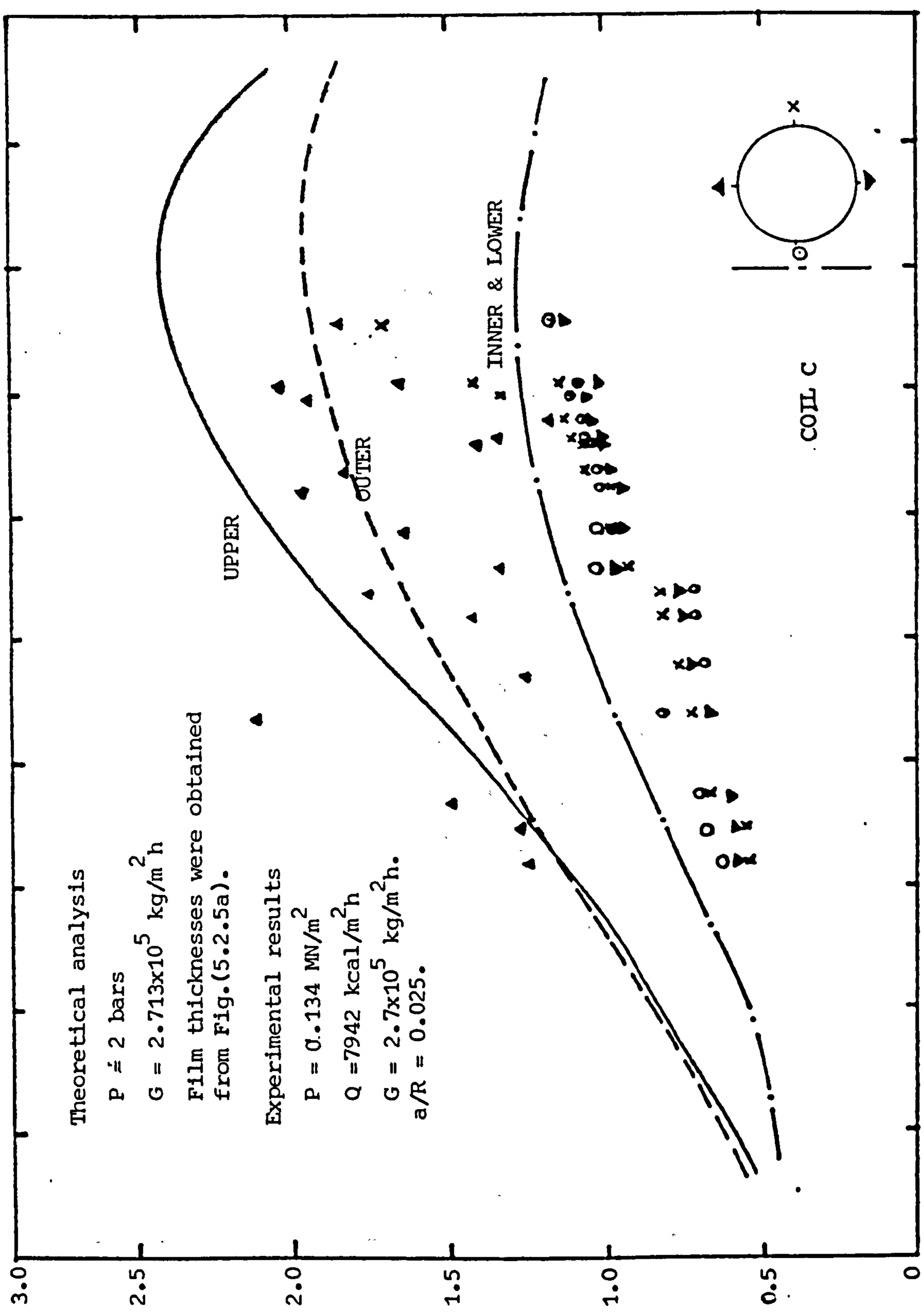


Fig.(5.2.6a) : Comparison of local heat transfer coefficient between the resuts from eq.(5.2.60) and the exprimental results (same as Fig. (4.3.17 c)) .

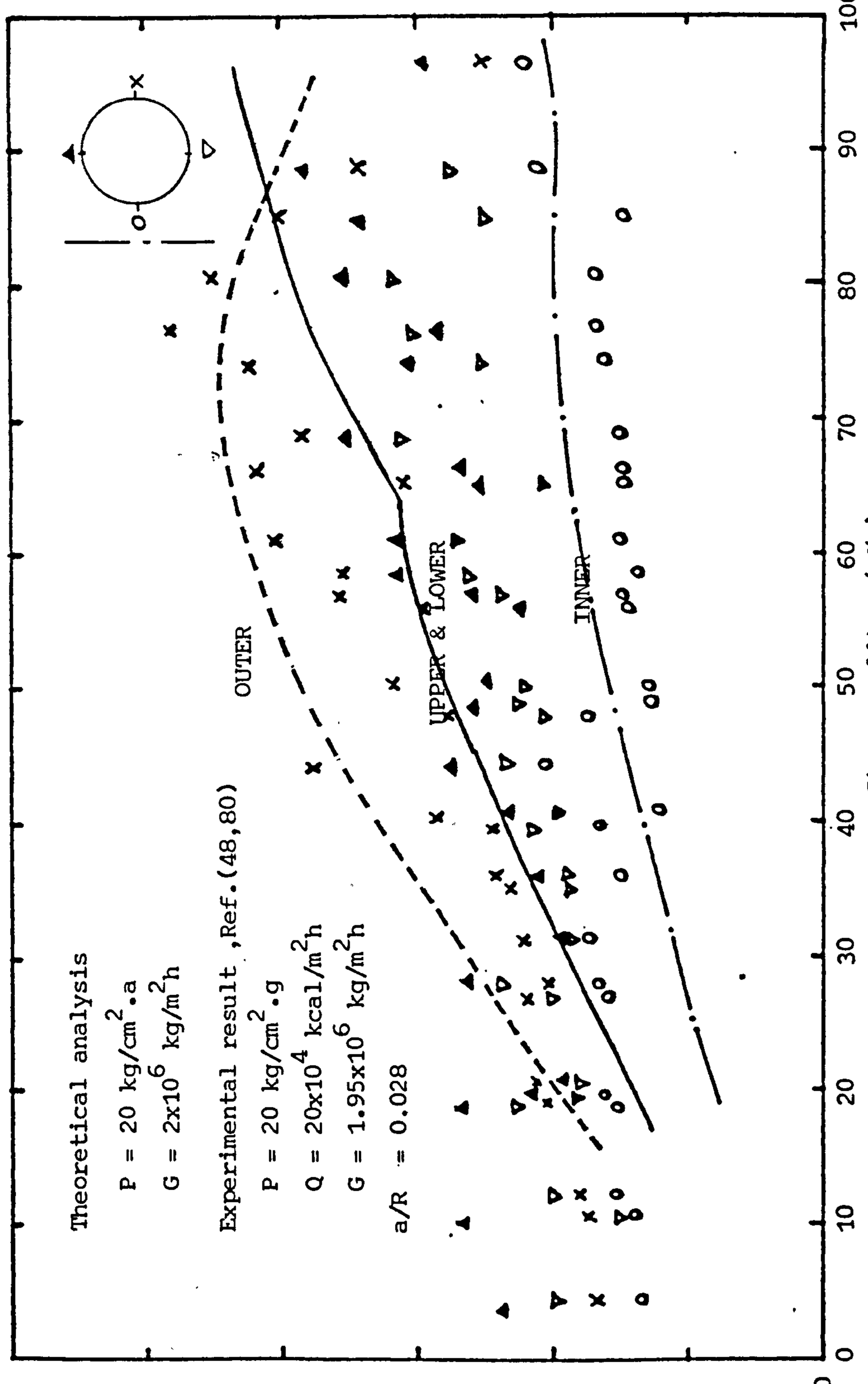


Fig.(5.2.6b) : Comparison of local heat transfer coefficients between the results from eq.(5.2.60) and the experimental results of Kozeki (48,80) at 20 bars.

5.4 Summary of the chapter

The purpose of the present work is to study the flow mechanisms of two-phase flow with heat transfer in the coiled tube. Chapter four explains the flow mechanisms using experimental results and this chapter derives a theoretical model to describe the flow mechanism.

The first two sections discuss turbulent single-phase flow and another two sections are for the two-phase flow. The following characteristic similarities and differences are found from the comparison made between the theoretical and empirical results.

(a) The friction factor of the single-phase flow in the coiled tube is derived as eq. (5.1.38). This is shown togetherwith other investigators' results and the present empirical results in Fig. (5.1.3). They are seen to be in good agreement.

(b)-(i) The heat transfer coefficients of single-phase flow in the coiled tube are described for the two cases of uniform wall temperature and uniform heat flux, when Prandtl number is near to unity. They are shown together with other investigators' formulae in Fig. (5.1.9) and agree with them.

The comparisons between the theoretical and empirical local heat transfer coefficients in three coils (Coils A, B, C) are shown in Figs. (5.1.11a) - (5.1.11c). They agree with each other qualitatively but they differ quantitatively. This difference is due to the magnitude of the correction factor (S_c) used, and difficulties in modelling the secondary flow force in the gas core.

(b)-(ii) The theoretical average heat transfer coefficients have slightly smaller values than those of the empirical results.

However they are thought to be in good agreement and that any discrepancies are quite small. (See in Fig. (5.1.14)).

(c) The formula for the liquid film profile in two-phase flow in the coiled tube is proposed as eq. (5.2.51). This is based on the listed assumptions, especially that the flow model is for a symmetrical pattern (see Fig. (5.2.1)). Referring to the sections (5.2.3.2) and (5.2.4.1), this flow model is valid up to 20 bars.

The theoretical results are compared with the empirical results obtained by Whalley and Williams (88) in Figs. (5.2.4a) and (5.2.4b). Both profiles are in good agreement in the range of circumferential angle, $30^{o} < \psi < 160^{o}$. The theoretical results show thciker film profiles at the outer side than the empirical results. This is due to the effects of entrainment rate and droplet density in the gas core.

The theoretical film profile in the steam-water flow for different steam qualities at 2 bars and 40 bars are shown in Figs. (5.2.5a) and (5.2.5b). It is shown that the film thickness at the whole periphery becomes large at high pressure and at low steam quality. In the actual phenomena the growth of the film thickness is thought to be limited by the interfacial shear stress, gravity, centrifugal forces, etc. We cannot assess the accuracy of the theory at high pressure and at low steam quality from the present work.

(d) The theoretical forced convection heat transfer coefficients in the circumferential direction in the annular flow are evaluated from eq. (5.2.60) at near Pr = 1. These values are shown in Fig. (5.2.6a) at 2 bars with the present empirical results and

Fig. (5.2.6b) at 20 bars with Kozeki's empirical results (48,80). The profiles of local heat transfer coefficients at four positions (the upper, outer, lower and inner sides) are in agreement with the empirical results. However the theoretical values are about 30∿50% larger than the empirical results at 2 bars and 20∿30% larger at 20 bars.

(e) From points (a) to (d), the present theoretical analyses are thought to be in good agreement with the empirical results throughout. However, the theoretical formula in this chapter may only be valid up to 20 bars.

C H A P T E R 6

CONCLUSIONS

The object of the present work is to investigate the flow behaviour and heat transfer mechanisms of a steam-water mixture in three different diameter helically coiled tubes. Before the two-phase flow was investigated, heat transfer data for water or steam single-phase flow and pressure drop data of steam flow were taken. These data were compared with both experimental and theoretical results from other researchers in Chapter Four.

In Chapter Five an attempt to describe mathematically the experimental results of the present work was done. From a study of these empirical results and a comparison between the theoretical and empirical results, several important points were deduced. The deductions are useful in the design of many applications of helically-coiled tubes such as steam generators or chemical reactors.

6.1 Conclusions of single-phase flow

Wall temperature profiles

In both the case of laminar water and turbulent steam flow, the wall temperatures at the inner sides of the tube had the largest values. This is obviously due to the presence of the secondary stream from the inner to the outer side.

In the laminar water flow, when the inner side closely approached the saturation temperature, it was then exceeded by the upper side temperature. Hence, the position of the highest temperature became the upper side. This phenomenon occurred because the buoyancy force prevailed over the secondary flow force and the body force in axial flow direction.

Friction factor and local heat transfer coefficient

The friction factor was derived mathematically as eq. (5.1.38) in section (5.1). The equation agrees with the theoretical and empirical results of other investigators.

The smallest diameter coil (Coil A) had the largest pressure drop but its differences in three coils were not significant.

Theoretical heat transfer coefficients were defined as eqs. (5.1.80)-(5.1.82) for the uniform wall temperature and as eqs. (5.1.90)-(5.1.92) for the uniform heat flux in section (5.1.2). The equations are accurate for a range of Pr around unity. The present experiments were done in the condition of uniform heat flux and eqs. (5.1.90) - (5.1.92) agree quantitatively with the results with Sc = 0.80 for Re = 24000 and with S_c = 0.63 for Re = 44040 (see Fig. (5.1.12)).

The ratio of heat transfer coefficient between the outer and inner sides were taken as in eq. (4.2.4) for laminar water flow and eq. (4.2.9) for turbulent steam flow. These formulae were related to the diameter ratio between the tube and coil (i.e. $\frac{a}{R}$).

In both cases of laminar water and turbulent steam flows, the outer side had the largest heat transfer coefficient and the inner side had the smallest.

6.2 Conclusions of two-phase flow

Wall temperature profiles

Throughout the investigation, it was found that the wall temperature at the upper side always had the largest value.

The temperature profiles at the outer side was affected when the coil diameter was changed, because the centrifugal forces acting on

the liquid film were different. However, this effect is not considered very significant.

Flow patterns

The flow patterns in the three coils were obtained for a steam-water mixture and are shown in Figs. (4.3.3a) - (4.3.3c).

The various flow regions shown in these figures were compared with the original Baker map and several differences were found. One particularly interesting feature was a wavy [illegible] flow region occupying a narrow strip between the annular and stratified flow regions.

The most important difference between the helically-coiled tube and equivalent straight tube is the entrainment rate. Its magnitude in the case of helically-coiled tube is always smaller because of the effect of the centrifugal force.

Pressure drop

Pressure drops in two-phase flow were plotted against the two-phase frictional multiplier, ϕ_{gtt}, using the Lockhart-Martinelli parameter. At $0.1 < X_{tt}$, the two-phase flow pressure drop had a similar profile to that for a straight tube; however for $X_{tt} < 0.1$ the two-phase flow pressure drops had 45% larger values than for a straight tube.

From Banerjee et al (39), Owhadi et al (47), Kozeki (53.80) and the present work, turbulent characteristics appeared in the liquid phase around $Re_f = 800 \sim 1000$.

Liquid film profiles

Theoretical film thickness was proposed as in eq. (5.2.51) in section (5.2) and theoretical film thicknesses were compared with the empirical results of Whalley and Wiliams (88). At large superficial liquid velocity, where the centrifugal force acting on the liquid seems to dominate, the film is thicker at the other side than at the inner side. At large superficial gas velocity, the centrifugal force acting on the gas phase is so strong that the liquid is thicker at the inner side. The liquid at the upper and lower side is thinner and seems to be almost the same thickness as that for the straight tube.

Both the case of theoretical and empirical liquid profiles are in good agreement in the angle range of $30 < \psi < 160^{o}$.

Heat transfer coefficient

The local heat transfer coefficients were obtained using the Chen correlation (96). The heat transfer coefficients at the upper side had the highest values and the inner and lower sides the lowest. Empirical formulae for the local heat transfer coefficients were proposed in the form of eq. (4.3.26) for the upper, eq. (4.3.27) for the outer and eq. (4.3.28) for the lower and inner sides. The average heat transfer coefficient was proposed as in eq. (4.3.29) for the range between the atmospheric pressure and 30 $^{Kg}/cm^{2}g$.

The theoretical heat transfer coefficient was derived as eq. (5.2.60) in section (5.3) using values of film thickness and liquid velocity at the liquid surface, the derivation only being valid for a range of Pr around unity.

The experimental results of Kozeki (48) and the present work were

compared with the theoretical results and they are found to be in good qualitative agreement.

Burnout phenomenon

For a given set of test conditions, the onset of burnout occurred successively at the upper, outer and lower and inner sides. While burnout occurred in the present experiments at three sides, burnout at the inner side was not observed, even at 90% steam quality.

The first appearance of burnout occurred at different distances from the tube entrance for each of three coils and varied with different mass flow rates and pressures.

The onset of burnout is caused by the transition to completely stratified flow and start of "film inversion" phenomenon.

A P P E N D I X

Fig. No.	Title
A.1	The supplemental terms for eqs. (2.40) and (2.41)
A.2	Calculated values using eq. (5.2.60) for Fig. (5.2.5a)
A.3	Calculated values using eq. (5.2.60) for Fig. (5.2.5b)
B.1	Steam flow rate - Reading of differential gauge
B.2	Water flow rate - Reading of rotameters
C.1	Calibration results of thermocouples
C.2	Thermal conductivity of the coil (INCONEL 600) - Temperatures
C.3	Calibration results of thermometers
C.4	Calibration results of differential pressure gauge ΔP_{12}
C.5	Calibration results of differential pressure gauge ΔP_{41}
C.6	Calibration results of pressure gauges
D.1	Diagram for the auxiliary wall temperature reading system
D.2	Differential operational amplifier
E.1∿3	Drawings of mixer

APPENDIX (A.1)

The terms of g_m, A, Δg_m and ΔN_u of equations (2.40) and (2.41) were defined by Mori and Nakayama (24) as follows:

$$g_m = \frac{2}{\pi R_e}\left[\int_{-\pi}^{\pi}\int_{0}^{1-\delta} g_1 w_1 \eta d\eta d\psi + \int_{-\pi}^{\pi}\int_{0}^{\delta} g_w(1-\xi)d\xi d\psi\right] \qquad (A.1)$$

where $g = \frac{Tw-t}{\tau a}$ (A.1.1)

τ : temperature gradient along the pipe axis

g_1 : value in the flow core region

a : pipe radius

$$W = \frac{Wa}{\nu} \qquad (A.1.2)$$

W : axial component of velocity

ν : kinematic viscosity

$$\eta = \frac{r}{a} \qquad (A.1.3)$$

r : co-ordinate in radial direction in the cross section.

ψ : circumferential co-ordinate in the cross section.

$$\xi : 1 - \eta = \frac{a-r}{a} \qquad (A.1.4)$$

For equation (2.41)

$$A: \log A = \frac{1}{m+1}\left[\frac{1}{4}\{(4m+7)\log(2m+1) + (4m-7)\log m - \log(6m-1) - 11\log(4m-1) - (8m-15)\log(2m-1) - 9\log 2\} + \log\alpha\right] - \log\beta \qquad (A.2)$$

$$\Delta g_m : \Delta g_m = \frac{4(6m-1)(4m-1)m(m-1)}{(2m+1)^2(2m-1)^3}\cdot\frac{\beta}{\alpha} \qquad (A.3)$$

$$\Delta N_u : \quad \Delta N_u = \frac{4m^2-2m-1}{m^2(2m+1)} \cdot \bar{\delta}_m \tag{A.4}$$

$$\text{where } \log \bar{\delta}_m = \frac{1}{m+1}\left[\frac{1}{4}\left[3m \log (2m+1) + (15m-1) \log (2m-1)\right.\right.$$

$$-(7m-4) \times \{\log m + \log (4m-1)\} - m \log (6m-1)$$

$$\left.\left.-9m \log 2\right] + m \log \alpha\right] \tag{A.4.1}$$

If the Blasius's resistance formula (shown below) is taken, terms of β, j and m become:

$$N_{us} = 0.038 \, Re^{3/4} \, Pr^{1/3}, \tag{A.5}$$

$$\beta = 0.038 \quad j = \frac{1}{3} \quad m = 4$$

Then if the conventional formula for a straight pipe is taken, terms of β, j and m become

$$N_{us} = 0.023 \, Re^{0.8} \, Pr^{0.4}, \tag{A.6}$$

$$\beta = 0.023 \quad j = 0.4 \quad m = 5.$$

TABLE (A.2)

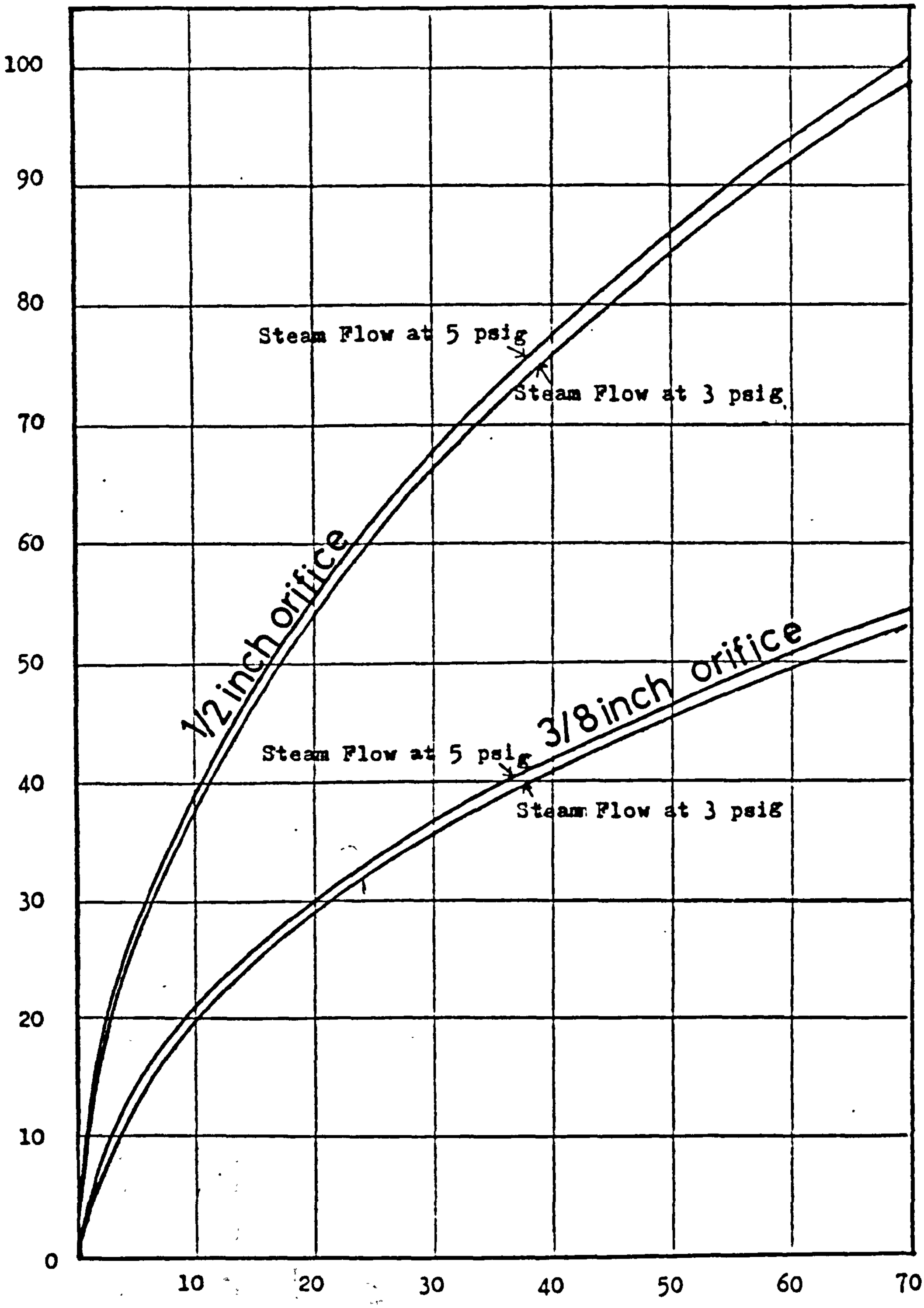
Calculated values using eq. (5.2.60) for Fig. (5.2.5a)

x	R_{ef}	ψ	$\omega_{f\delta}$	δ_f	N_δ	h_{TP}
%						
20	3360	2^o	14.32	0.040	202.12	8500
		90^o	10.79	0.018	199.5f	8390
		178^o	8.83	0.062	126.00	5300
30	2940	2^o	23.95	0.042	265.66	11180
		90^o	18.05	0.015	278.01	11170
		178^o	14.48	0.060	164.87	6940
40	2520	2^o	37.71	0.043	331.44	13940
		90^o	27.31	0.013	350.09	14730
		178^o	23.62	0.059	215.14	9050
50	2100	2^o	55.42	0.045	380.38	16000
		90^o	41.25	0.010	444.18	18690
		178^o	36.28	0.055	263.74	11100
60	1680	2^o	78.41	0.046	415.49	17480
		90^o	57.71	0.008	570.95	21500
		180^o	45.05	0.055	262.14	11030
70	1260	2^o	116.72	0.046	451.02	18970
		90^o	77.32	0.007	530.48	22320
		178^o	66.92	0.056	282.84	11900
80	840	2^o	180.80	0.051	450.40	18940
		90^o	108.23	0.004	580.37	24420
		178^o	106.80	0.057	295.75	12440
90	420	2^o	375.60	0.052	460.90	19390
		90^o	192.67	0.004	530.48	22320
		180^o	104.18	0.058	294.36	12400

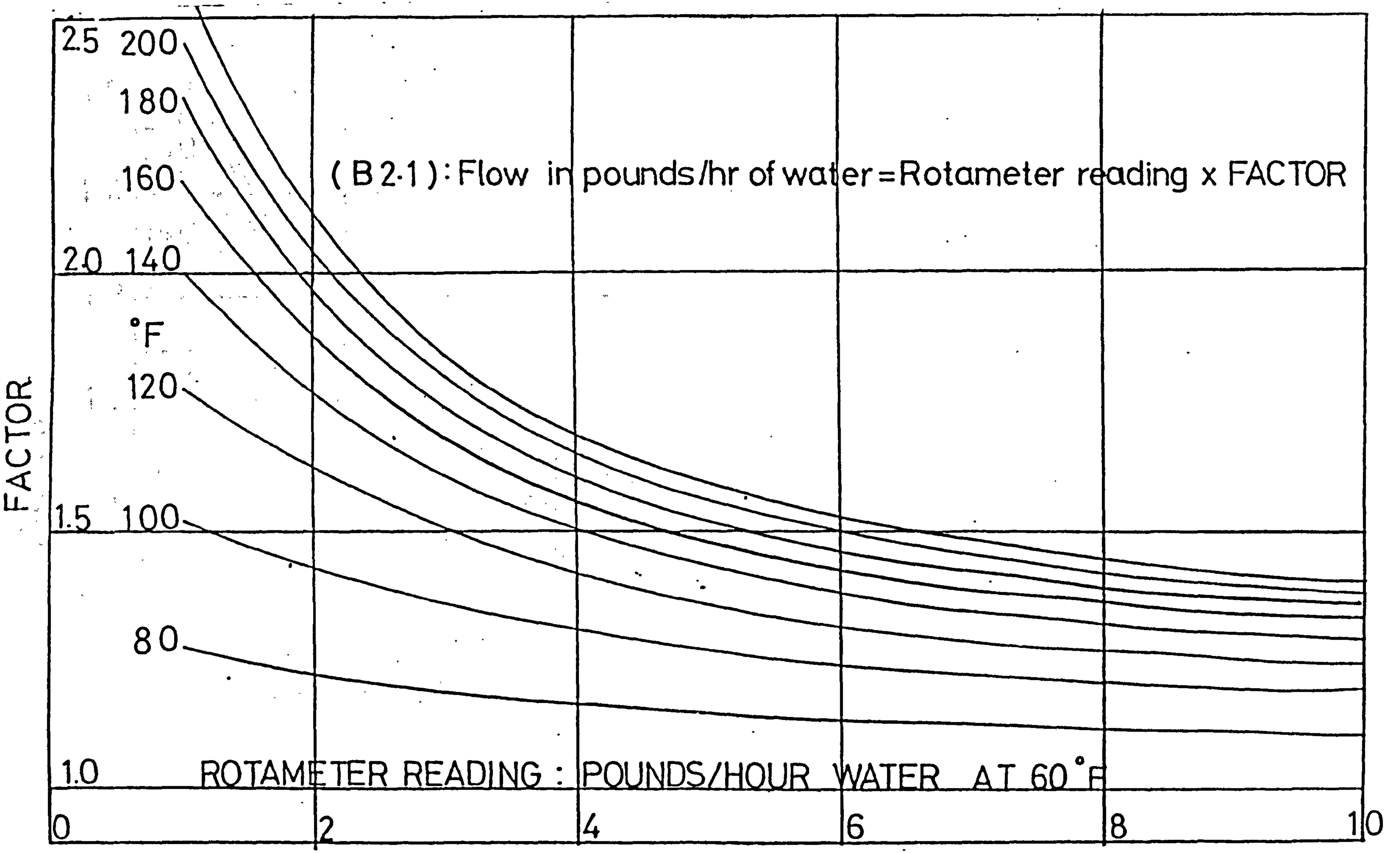
TABLE (A.3)

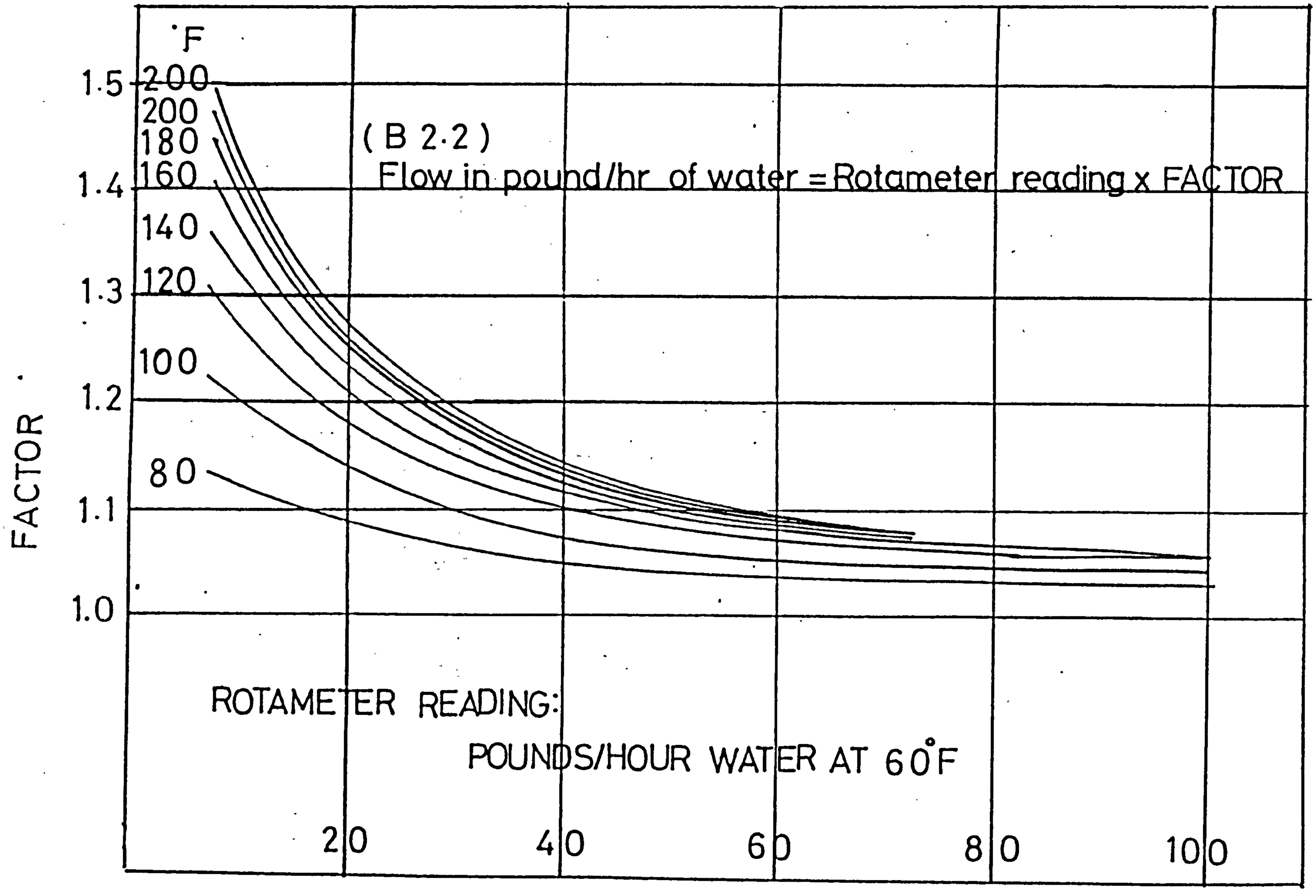
Calculated values using eq. (5.2.60) for Fig. (5.2.5b)

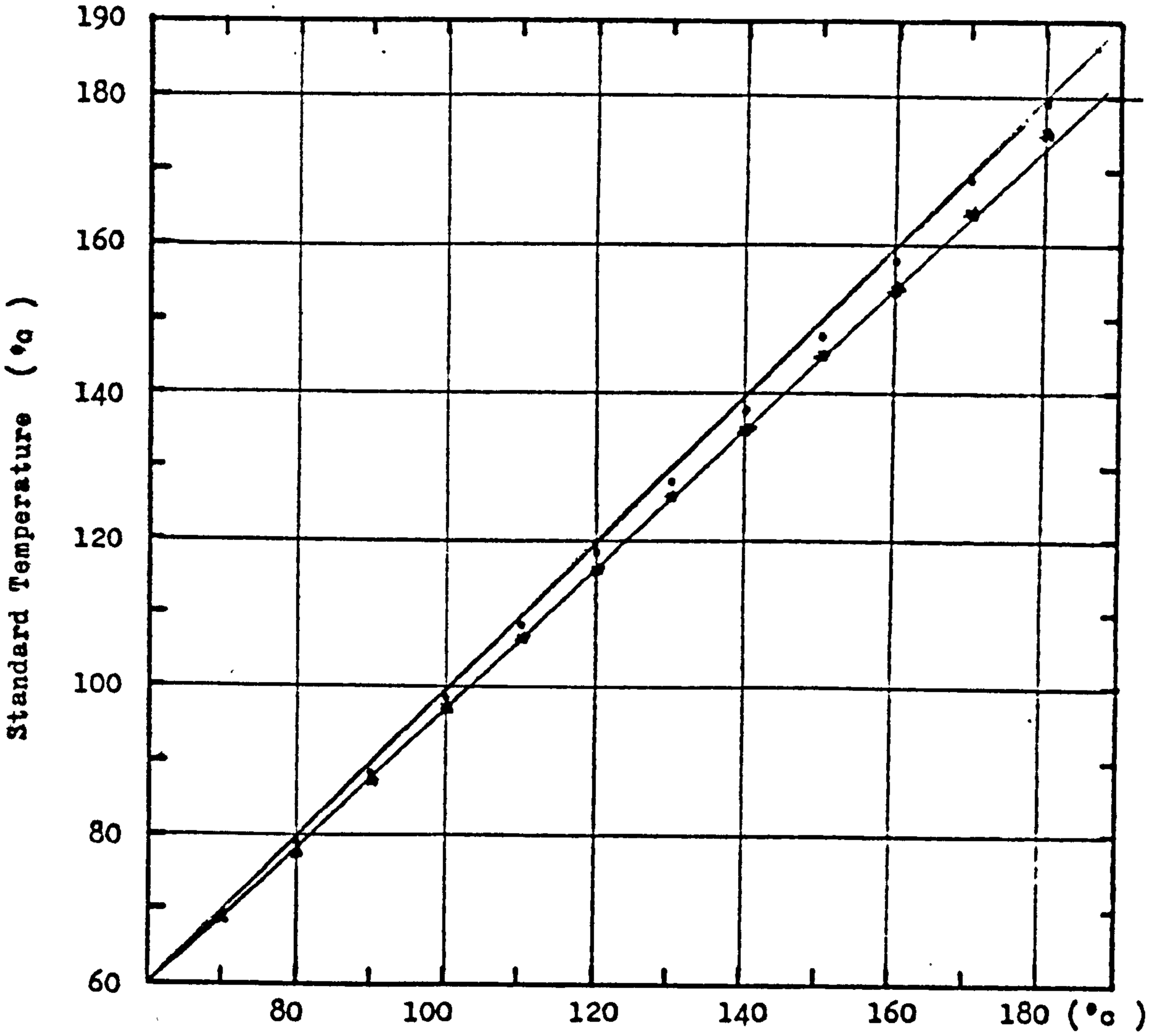
x	R_{ef}	ψ	$\omega_{f\delta}$	δ_f	N_δ	h_{TP}
%						
20	47781	2^o	5.55	0.011	992.1	39780
		90^o	4.24	0.019	717.8	28790
		178^o	2.72	0.043	416.7	16720
30	41808	2^o	9.30	0.011	1337.0	53610
		90^o	7.10	0.018	968.8	38860
		178^o	4.55	0.041	563.1	22580
40	35835	2^o	14.25	0.011	1656.0	66410
		90^o	10.87	0.017	1200.0	48120
		178^o	6.96	0.039	698.0	27990
50	29863	2^o	21.07	0.010	1945.0	77940
		90^o	16.06	0.016	1411.0	56540
		178^o	10.27	0.037	821.6	23960
60	23891	2^o	30.09	0.011	2116.0	84850
		90^o	22.84	0.017	1541.0	61790
		178^o	14.55	0.038	900.3	36090
70	17918	2^o	44.14	0.012	2209.0	88580
		90^o	30.63	0.010	1760.0	70580
		178^o	21.11	0.039	950.0	38100
80	11950	2^o	70.21	0.016	2176.0	87260
		90^o	43.14	0.006	1958.0	78520
		178^o	32.90	0.043	955.6	38320
90	5972	2^o	144.90	0.027	1941.0	77810
		90^o	74.05	0.003	2100.0	84180
		178^o	62.33	0.041	928.5	37240



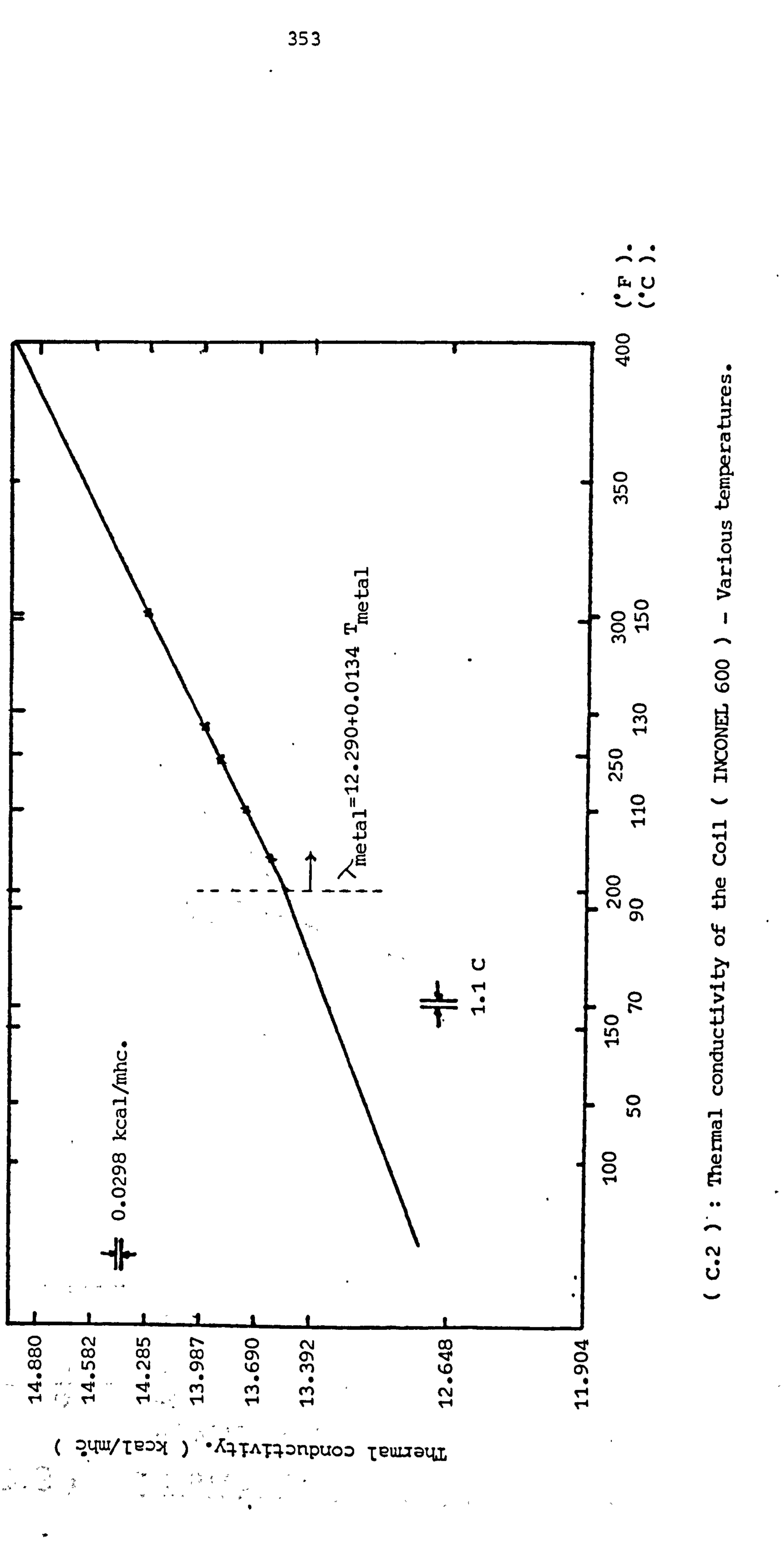
(B.1) : steam flow rate.

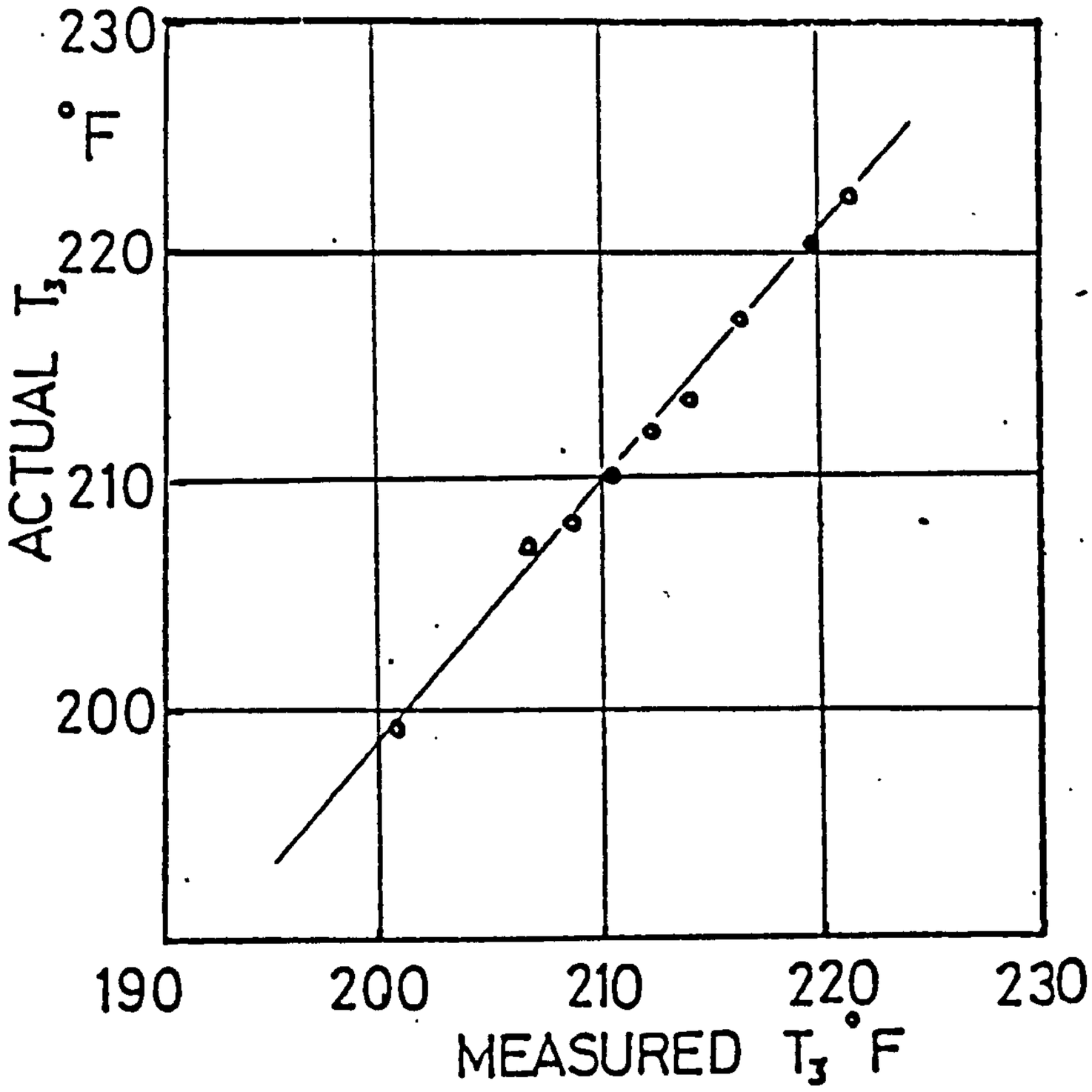

(B2-1): Flow in pounds/hr of water = Rotameter reading x FACTOR
FACTOR
25
20
1.5
1.0
200
180
160
140
120
100
80
°F
ROTAMETER READING : POUNDS/HOUR WATER AT 60°F
0
2
4
6
8
10

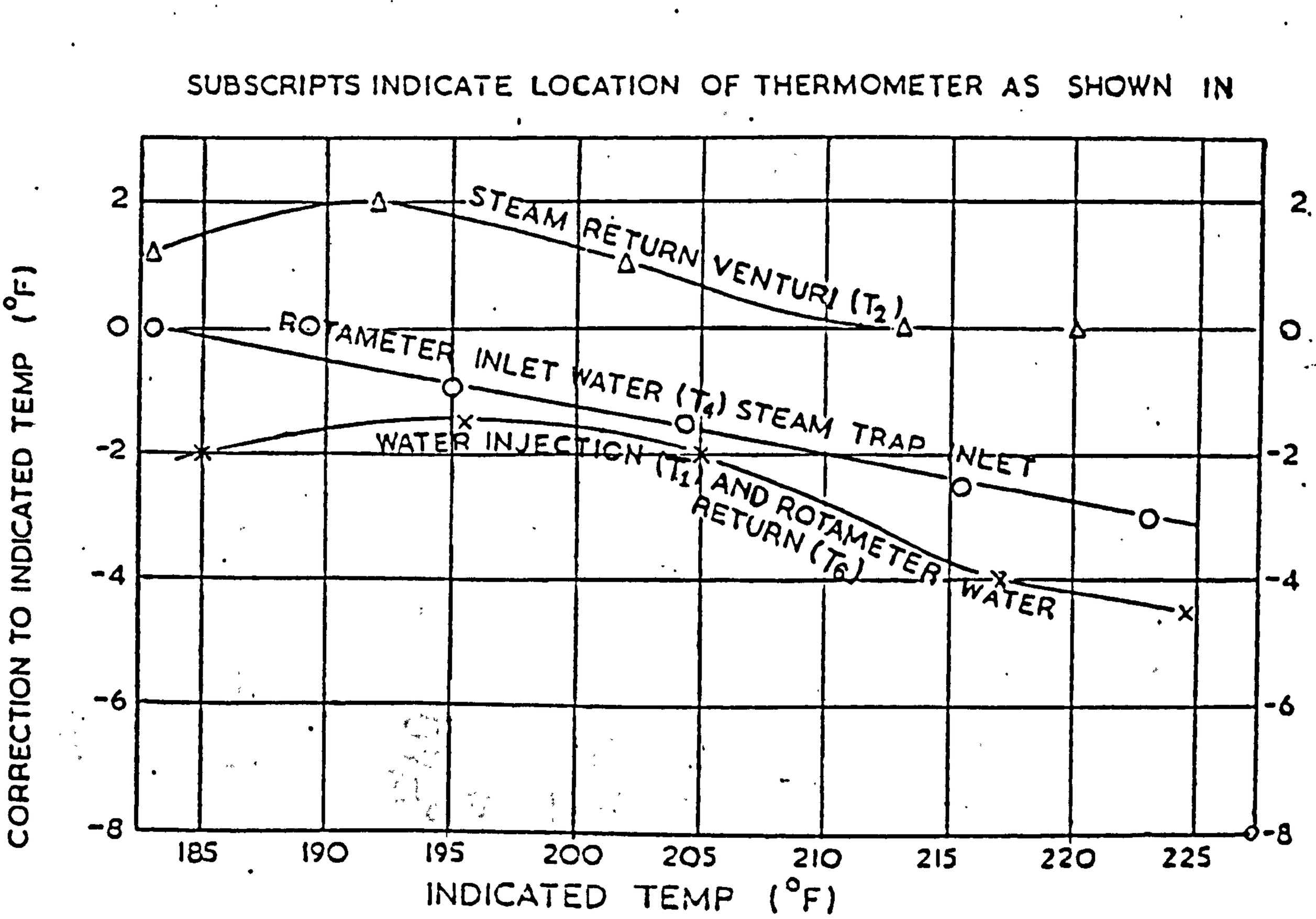

°F
200
200
180
160
140
120
100
80
1.5
1.4
1.3
1.2
1.1
1.0
FACTOR
(B 2·2)
Flow in pound/hr of water = Rotameter reading x FACTOR
ROTAMETER READING:
POUNDS/HOUR WATER AT 60°F
20
40
60
80
100



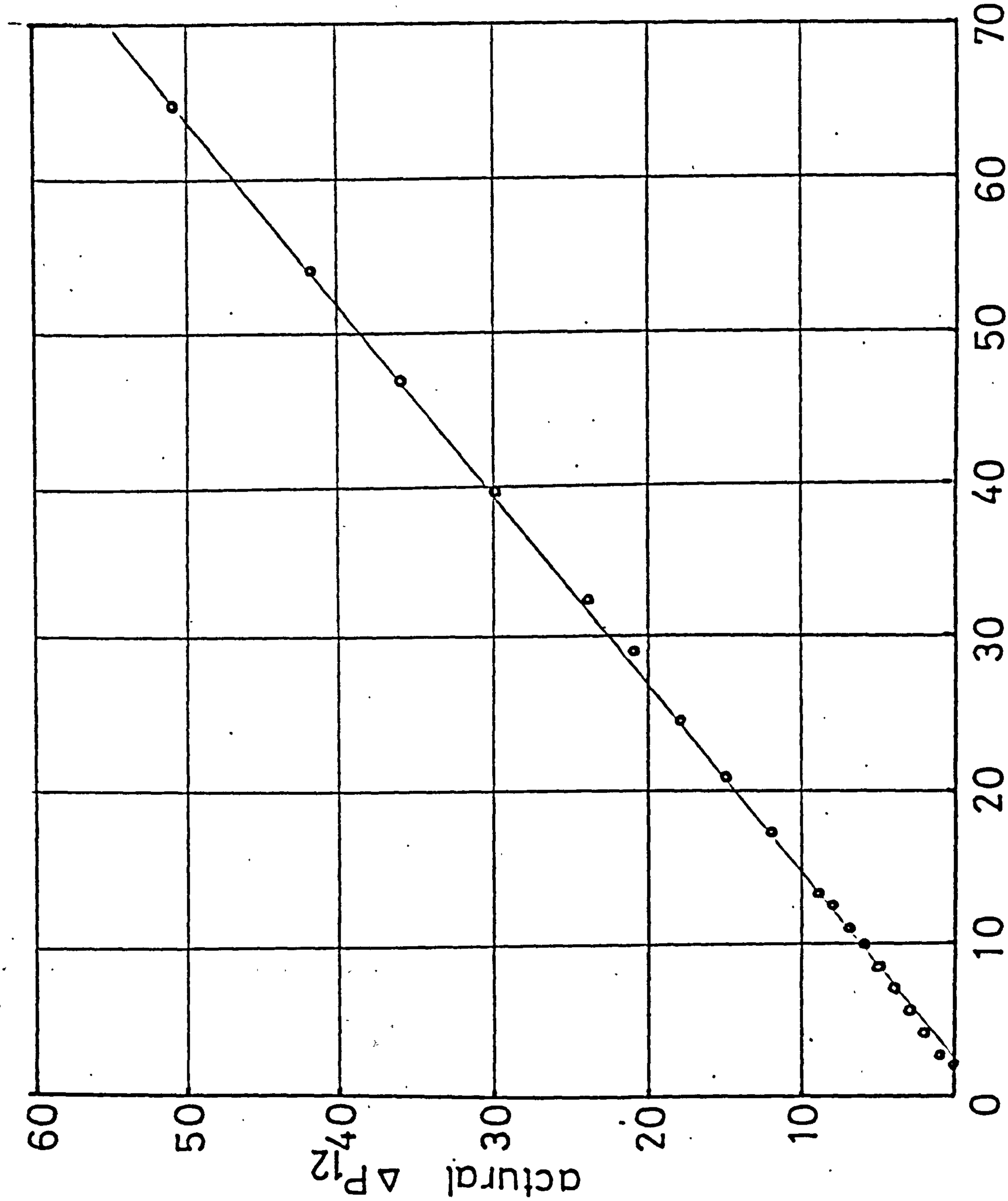
(C.1) : Calibration results of thermocouples.


Thermal conductivity. (kcal/mhc)
14.880
14.582
14.285
13.987
13.690
13.392
12.648
11.904
0.0298 kcal/mhc.
1.1 c
λ_{metal}=12.290+0.0134 T_{metal}
λ_{metal}
(C.2) : Thermal conductivity of the Coil (INCONEL 600) - Various temperatures.
50
70
90
110
100
150
200
250
300
350
400
130
150
T(°C)
T(°F)

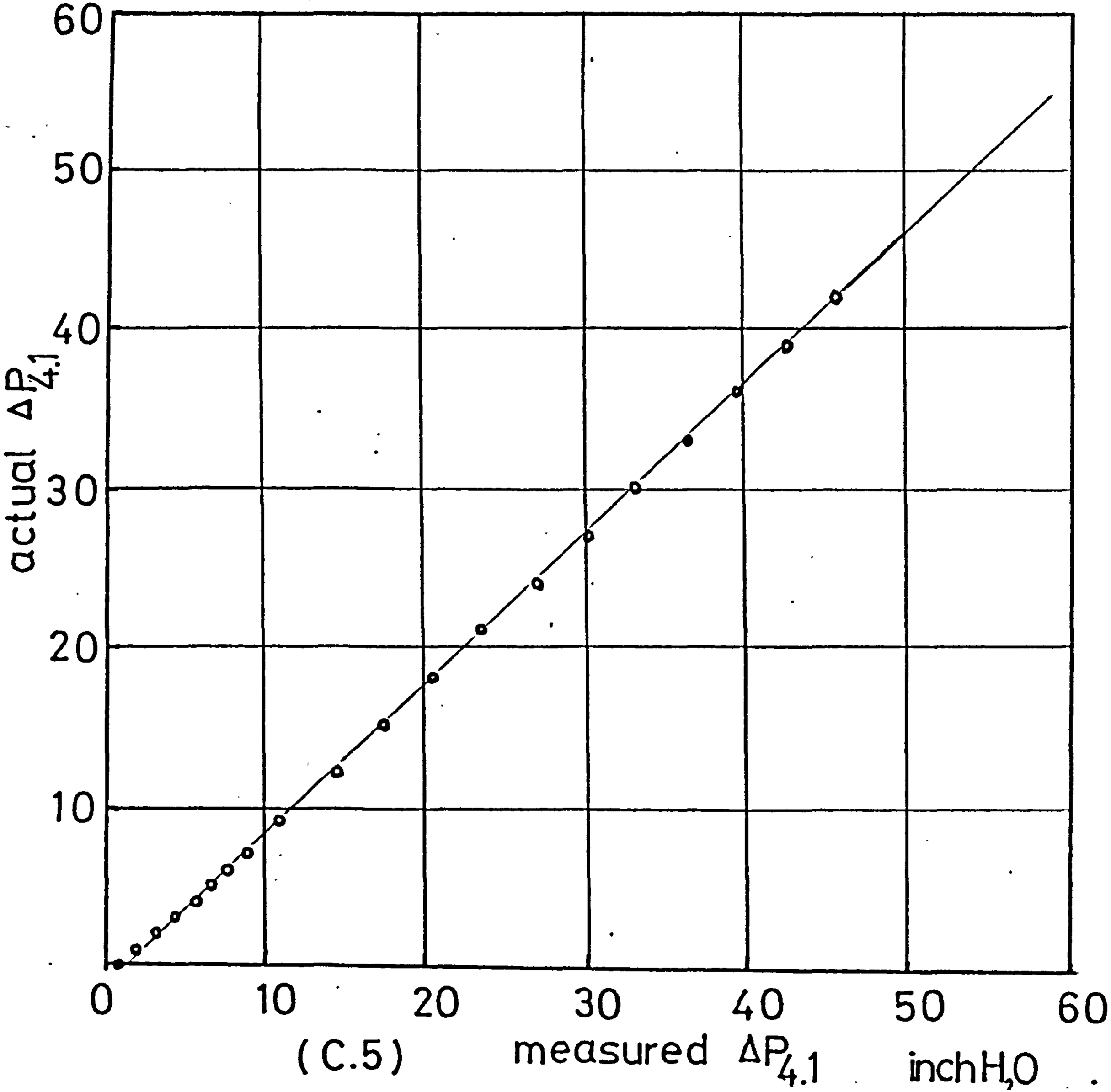




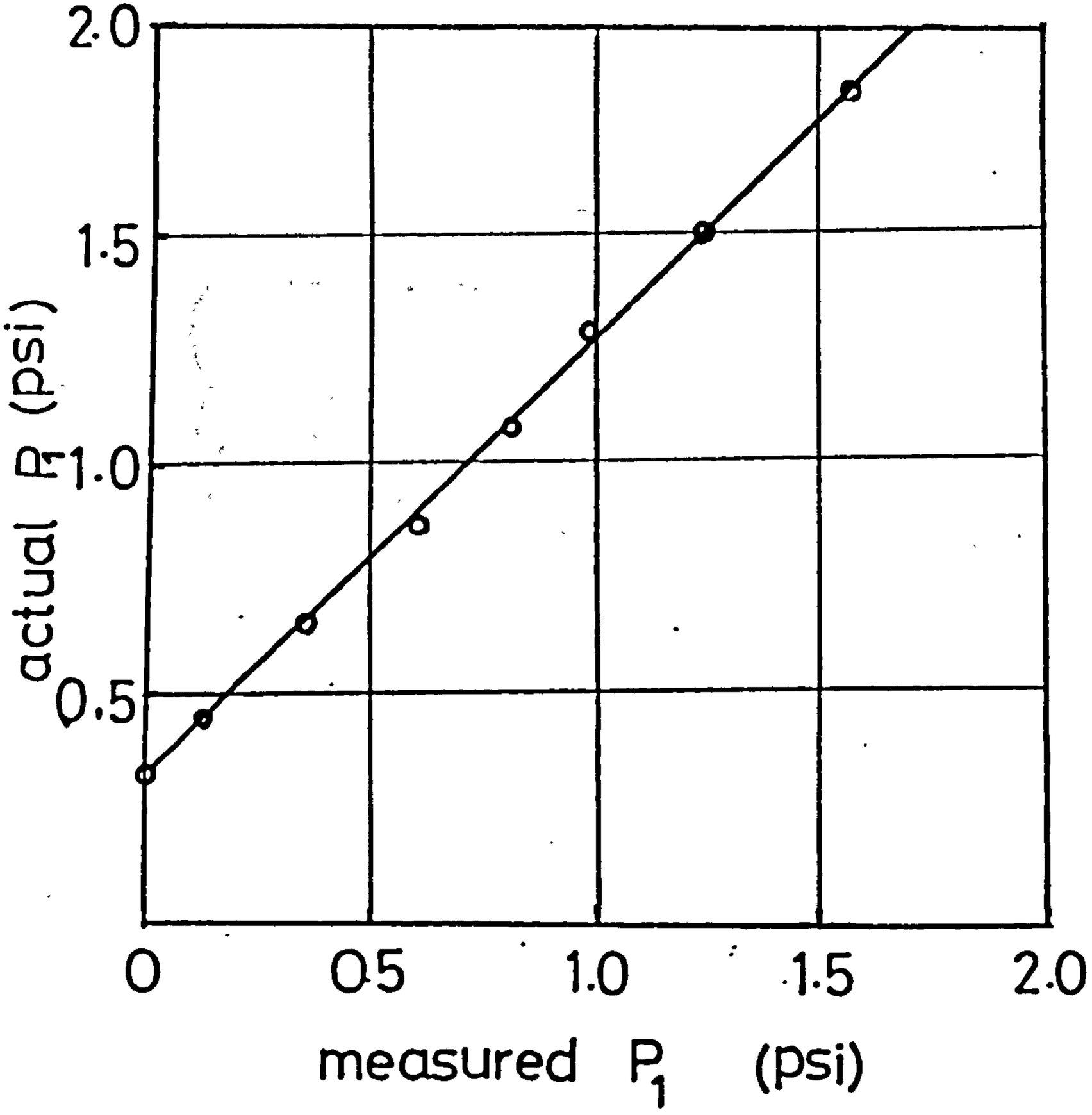
(C.3) THERMOMETER CORRECTION CHART

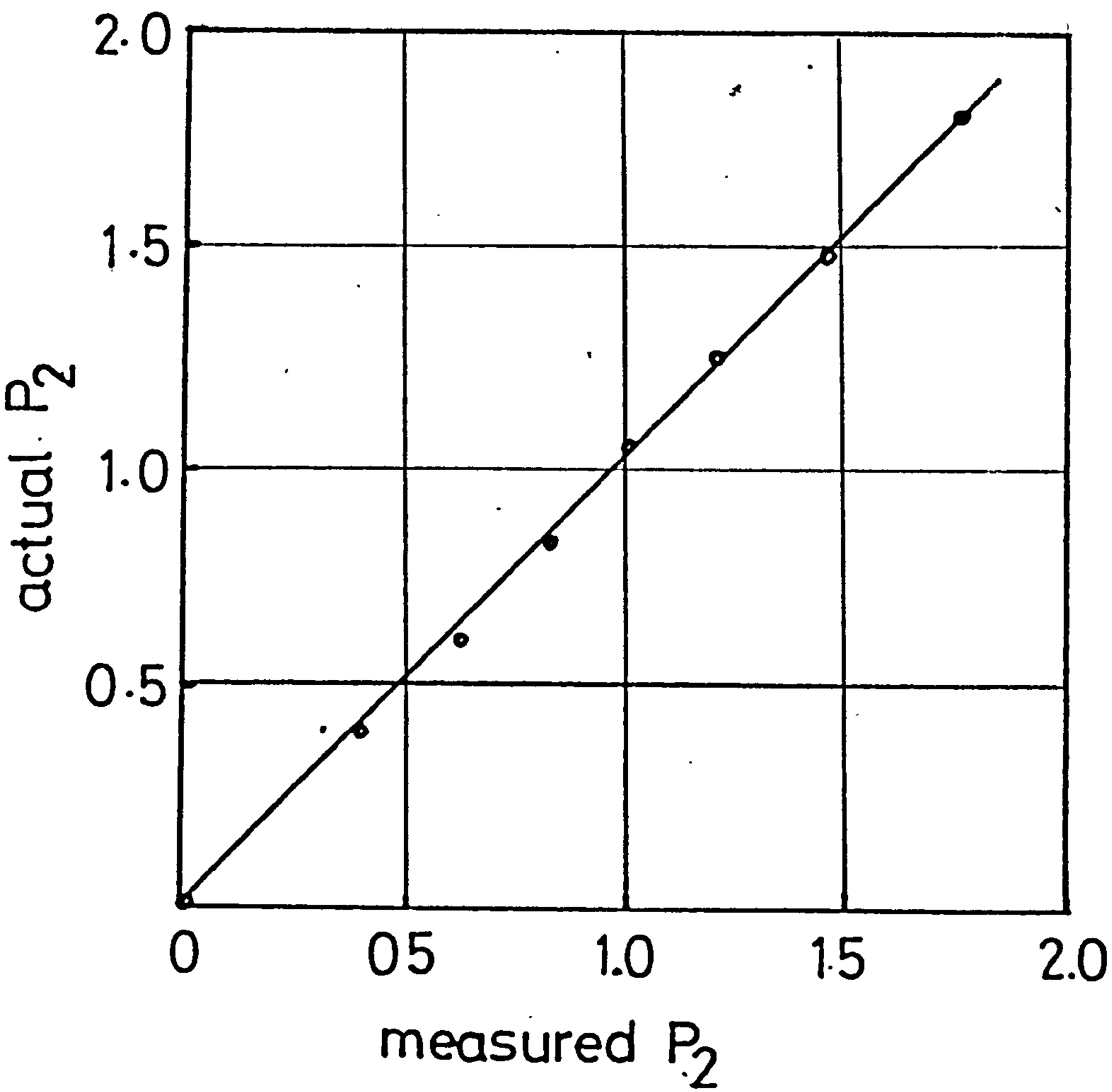

70
60
50
40
30
20
10
0
measured ΔP_{12} inch H_2O
actural ΔP_{12}
60
50
40
30
20
10
0

(C.4)

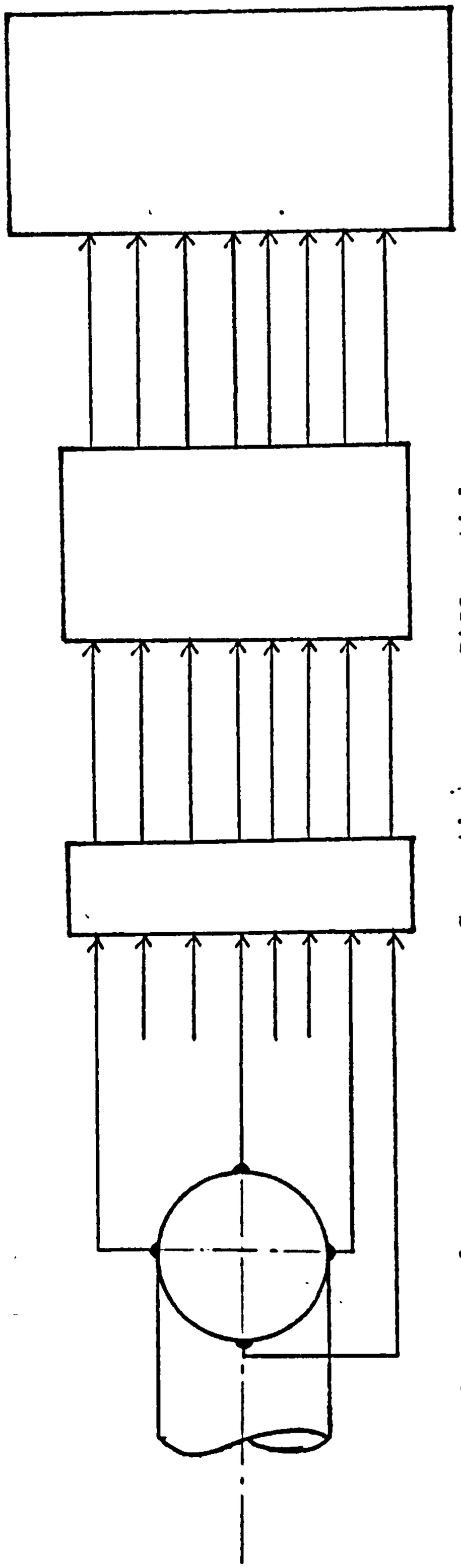

60
50
40
30
20
10
0
10
20
30
40
50
60
actual $\Delta P_{4.1}$
measured $\Delta P_{4.1}$
inch H_2O

(C.5)


2.0
1.5
1.0
0.5
0
0.5
1.0
1.5
2.0
actual P_1 (psi)
measured P_1 (psi)


2.0
1.5
1.0
0.5
0
0.5
1.0
1.5
2.0
actual P_2
measured P_2

357



Thermocouple on the tube surface.

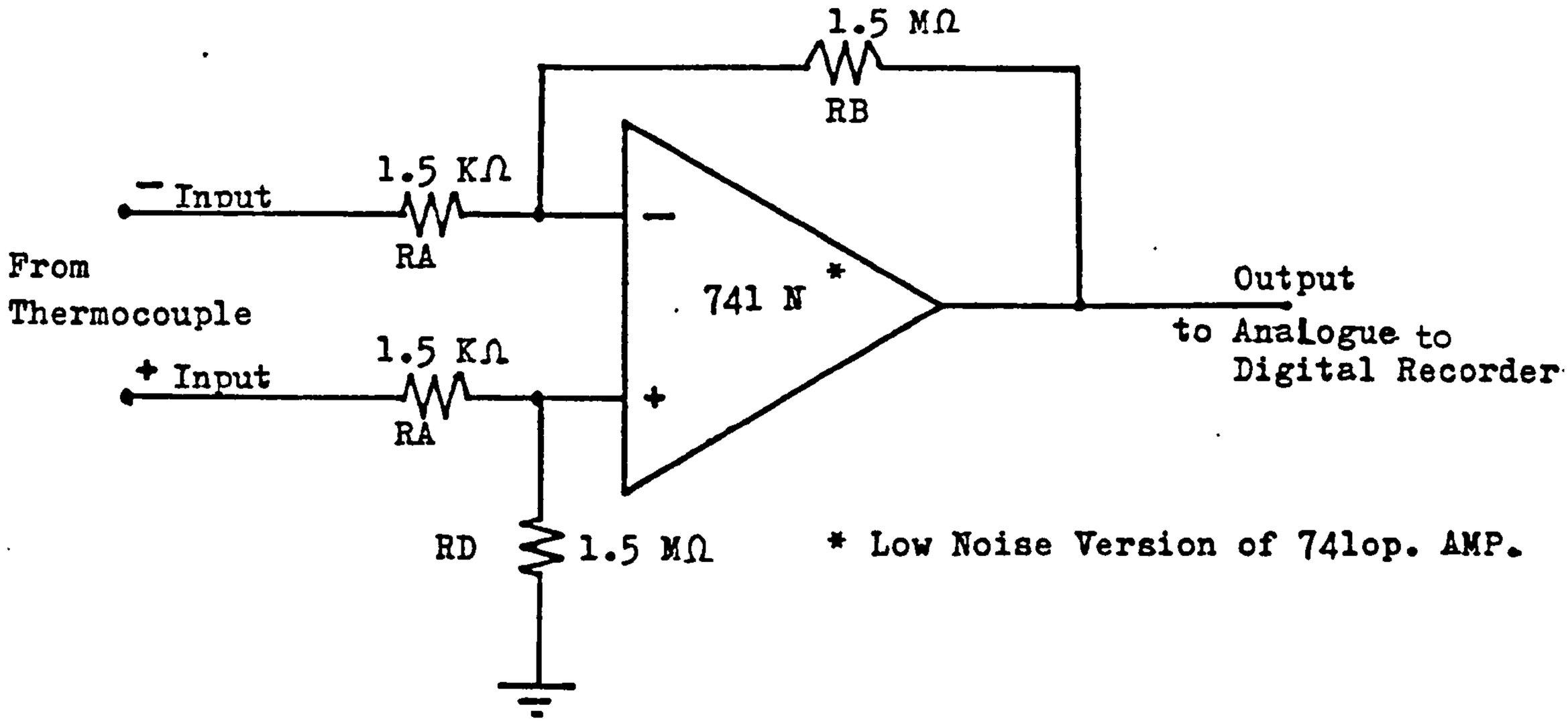
Connections (see Phot. (3.5)).

Differential operational amplifiers.

Analogue to digital converter and tape recorder (see (d.2) in Appendix).

(D.1) : Diagram for the auxially temperature readind system.

(D.2) : Eight Differential Operationel Amplifiers .



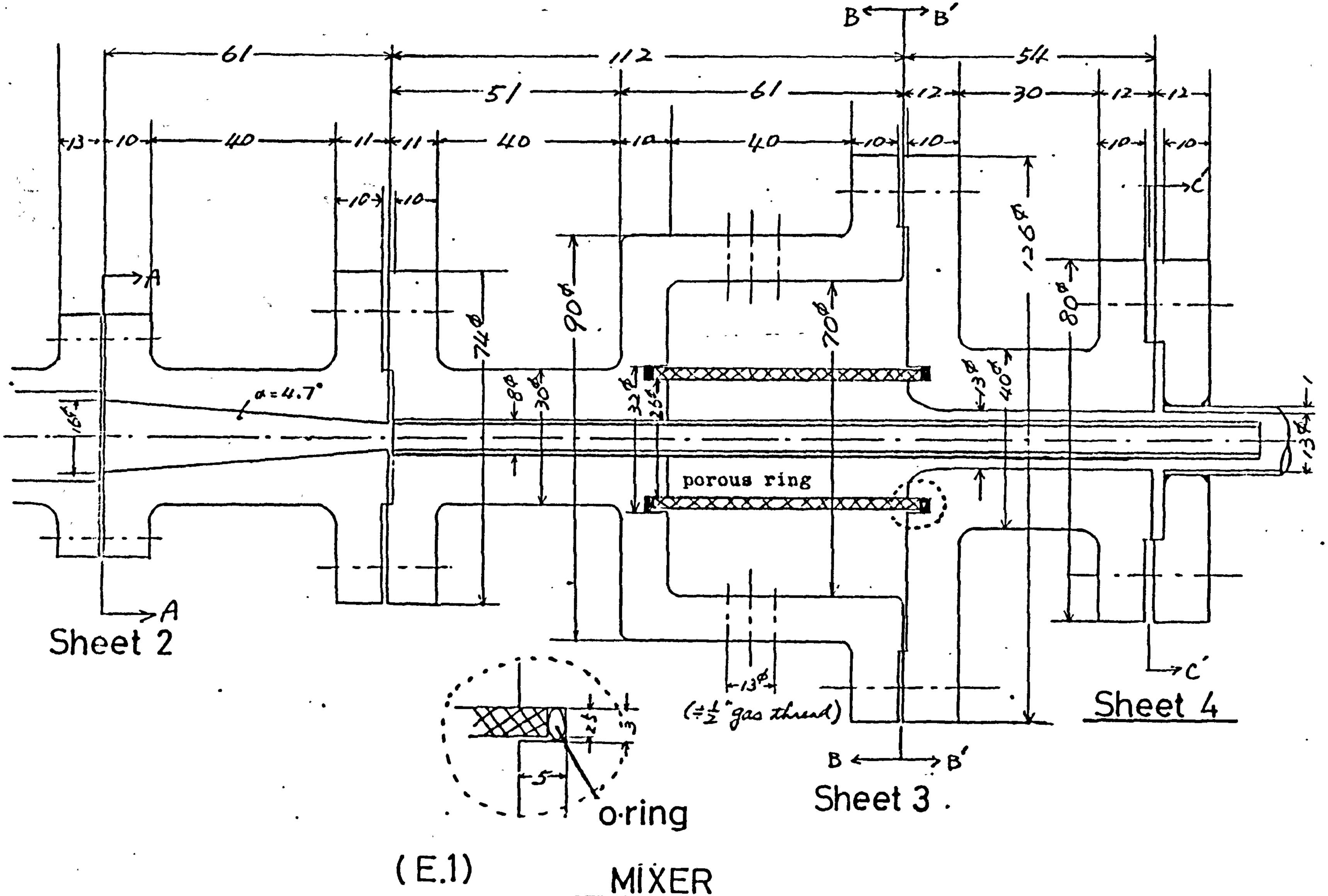
$$\text{Gain} = \frac{RB}{R1} \quad : \quad R1 = \text{Source Resistance} + RA$$

$$\text{Obtained Gain on Test} \quad \left(= \frac{\text{Output Voltage}}{\text{Input Voltage}} \right)$$

List of obtained Gains for the amplifiers.

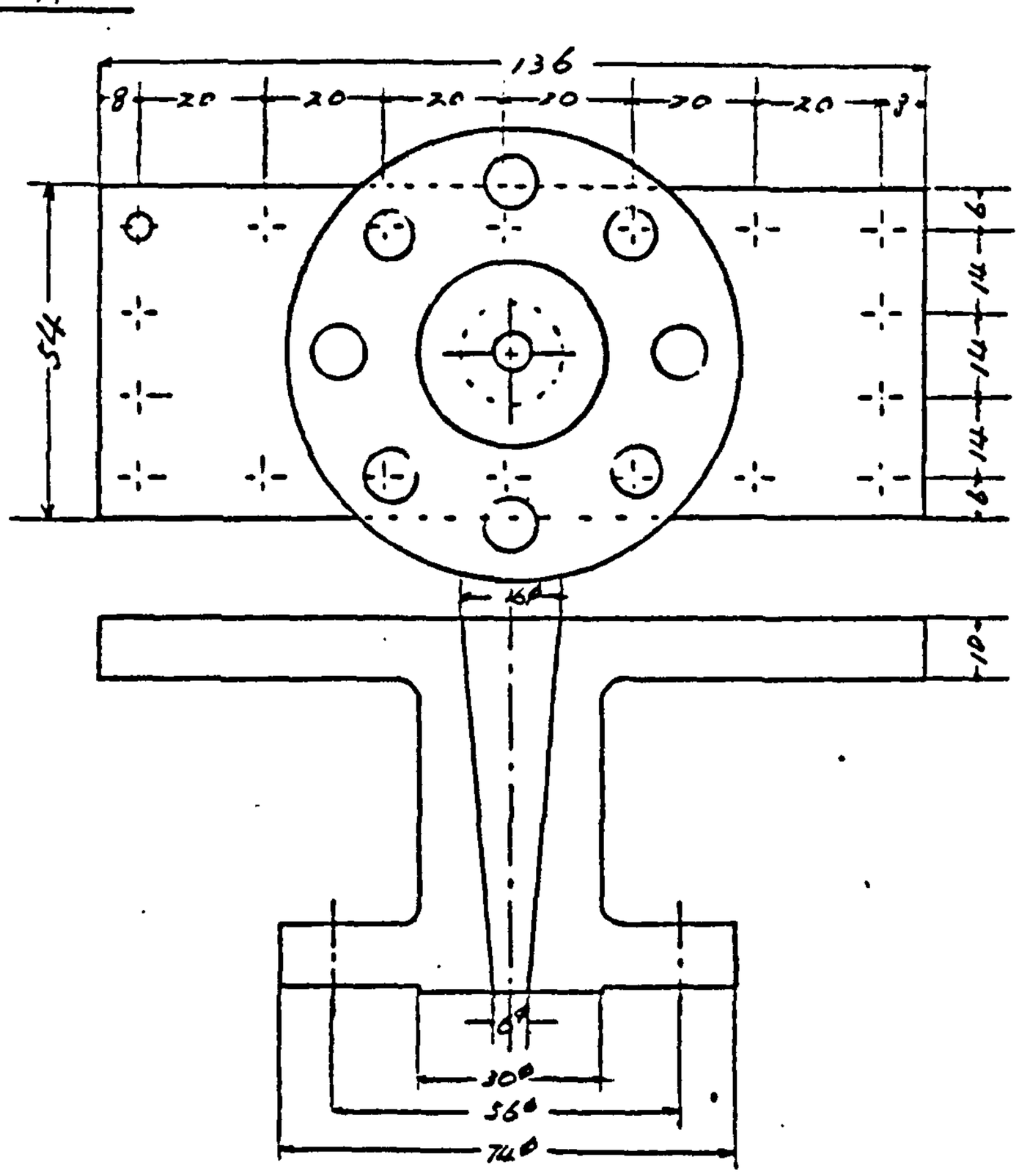
Channel	Gain
1.	905.8
2.	894.8
3.	879.8
4.	838.8
5.	883.7
6.	897.7
7.	843.2
8.	920.7

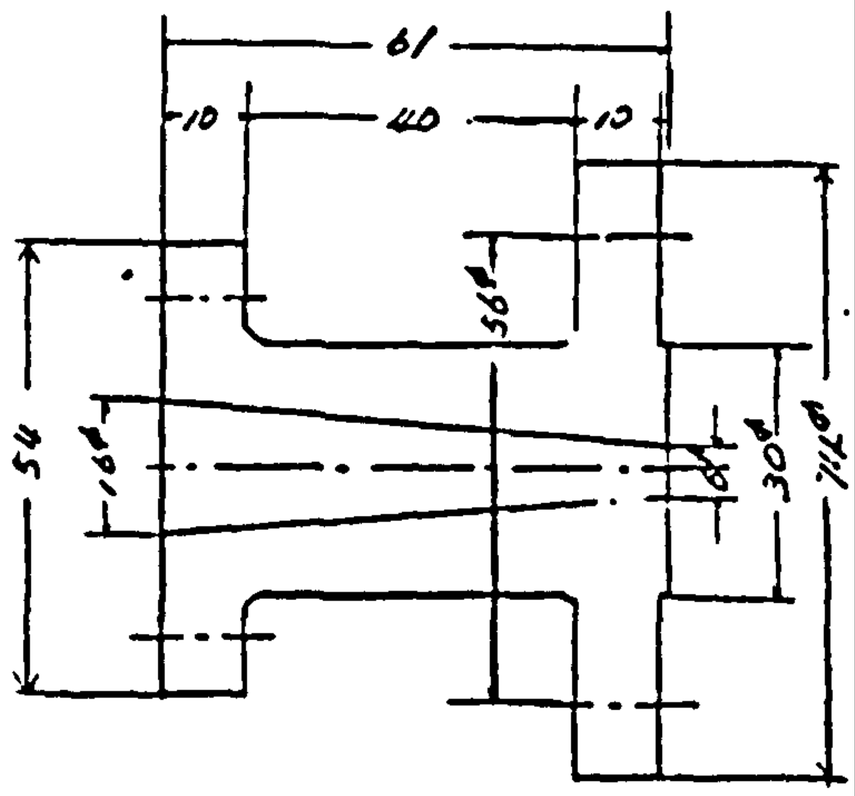
SCALE · M/M



(E.1) MIXER

A-A

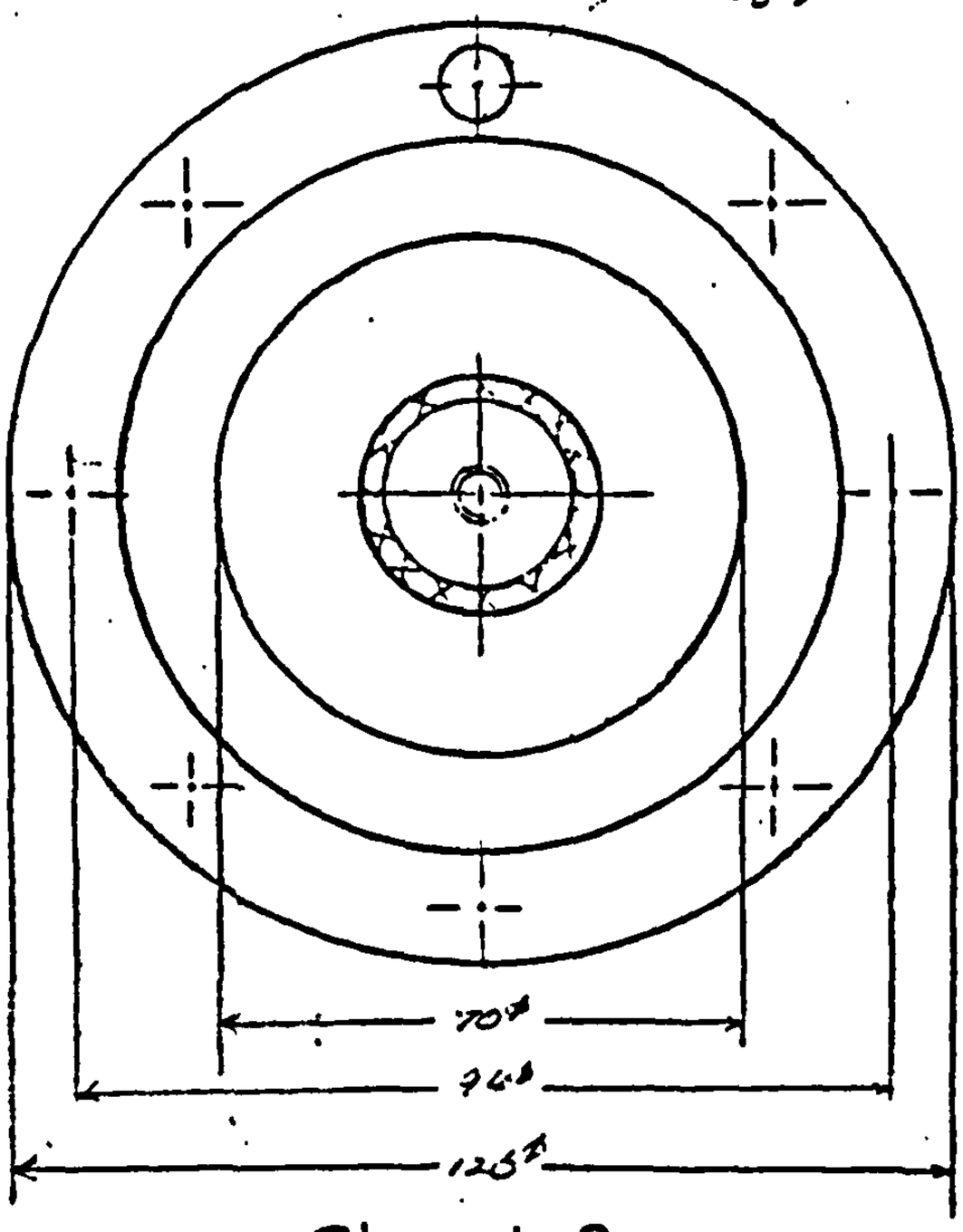




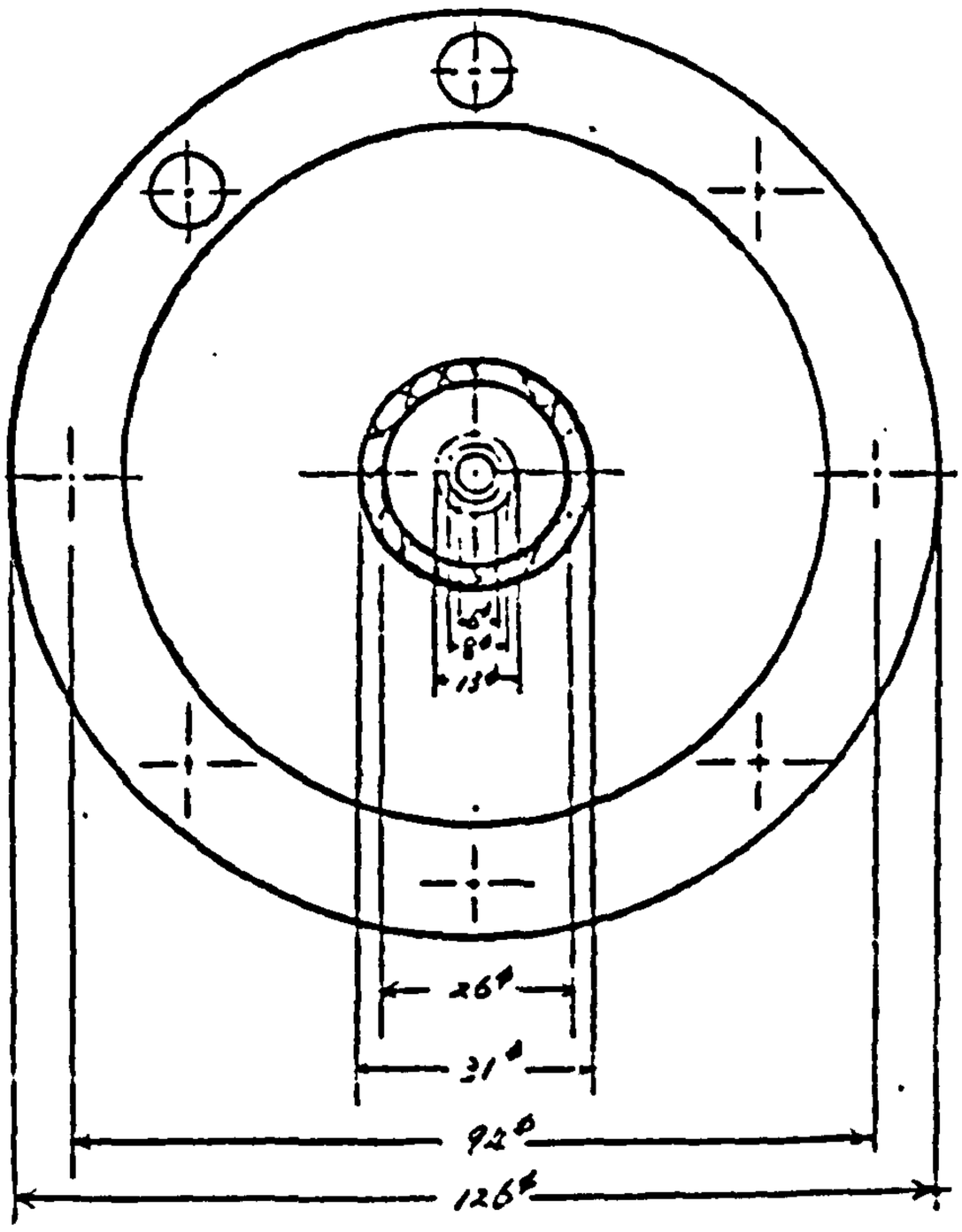
Sheet 2

B-B

10 Nos (3/8") x 8 Bolts.



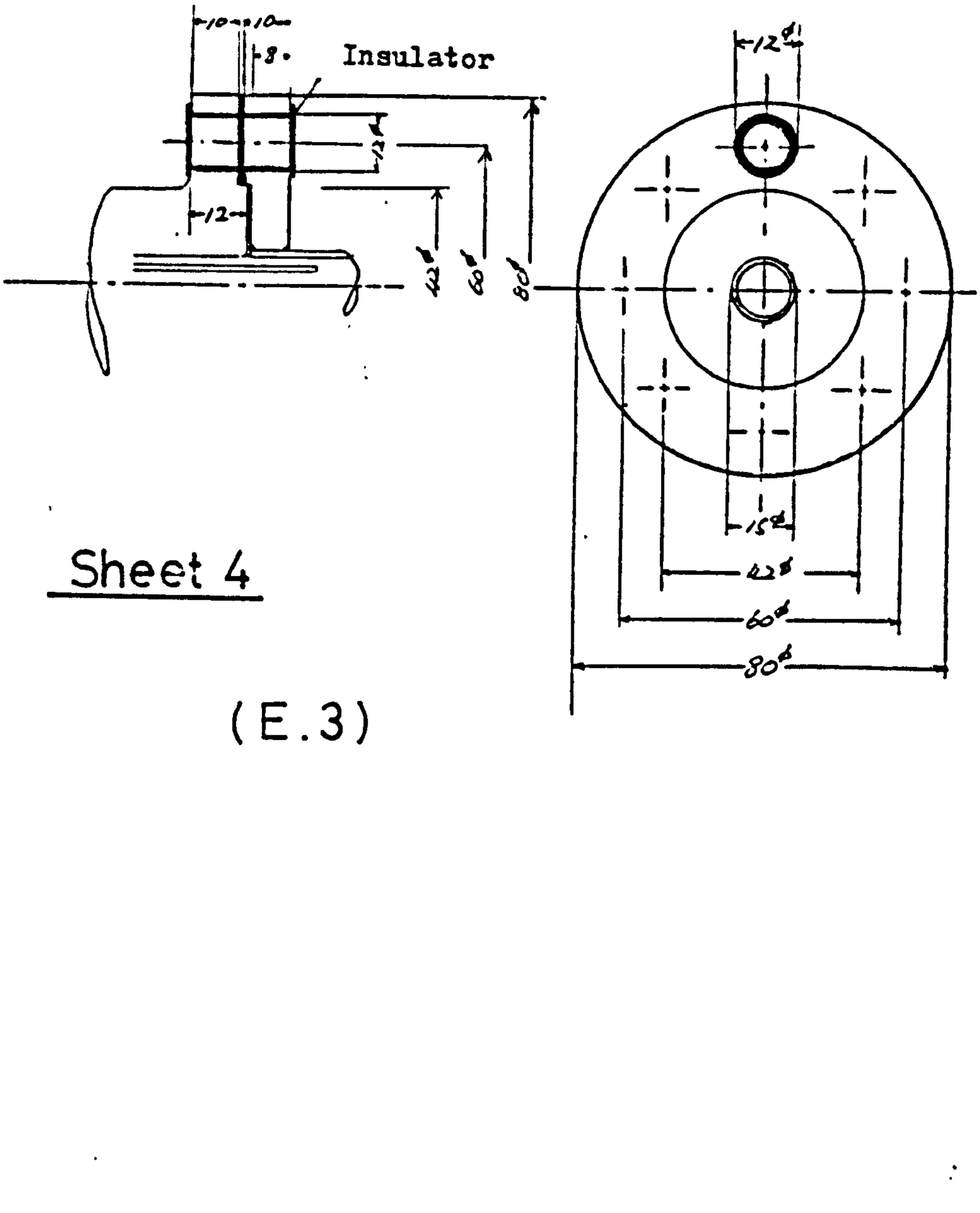
B'-B'



Sheet 3

C-C

C'-C'



Sheet 4

(E.3)

LIST OF REFERENCES

Abdelmessih, A.H., Fakhri, A., and Yin, S.T. (78-1974): "Hysteresis effects in incipient boiling superheat of Freon 11". 5th Int. Heat Transfer Conf. Tokyo, pp.165-169, B4.5.

Adler, M. (2-1934): "Flow in a curved tube". Z. ang. Mathematiks U Mechaniks, 14, 257.

Akagawa, K., Sekoguchi, T., and Ueda, M. (8-1971): "Study on a Gas-Liquid two-phase flow in a helically coiled tube", Bulletin of JSME. Vol.14, No.72.

Akiyama, M., and Cheng, K.C., (9-1971): "Boundary vorticity method for laminar forced convection heat transfer in curved pipes", Int. Journal of Heat and Mass Transfer, Vol.14, pp.1659.

Akiyama, M., and Cheng, K.C., (23-1972): "Laminar forced convection heat transfer in curved pipes with uniform wall temperature". Int. Journal Heat and Mass Transfer, Vol.15, pp.1426-1431.

Alves, G.E., (52-1954): "Co-current liquid-gas flow in a pipe-line contactor", Chem. Engng. Prog. Vol.50, No.9, pp.449-456, September.

Austin, L.R. (11-1971): "The development of viscous flow within helical coils". Ph.D. thesis, University of Utah, Utah.

Austin, L.R. and Seader, J.D. (18-1973): Fully developed viscous flow in coiled circular pipes". AICh.E. Journal, Vol.19, 1, pp.85-94.

Bailey, N.A., Collier, J.G. and Ralph, J.C. (71-1973): "Post Dryout heat transfer in nucleate and cryogenic equipment". ASME, 73-HT-16, pp.1-16.

Baker, O. (50-1954): "Design of pipe lines for simultaneous flow of oil and gas". Oil and Gas Journal, 26 July.

Banerjee, S., Rhodes, E., and Scott, D.S. (55-1967): "Film inversion of concurrent two-phase flow in helical coils". AIChE. Journal, Vol.13, No.1, pp.189-191.

Banerjee, S., Rhodes, E., and Scott, D.S. (39-1969): "Studies on concurrent gas-liquid flow in helically coiled tubes. I - Flow patterns, pressure drop and hold up". Canadian J. of Chemical Engng. Vol.47, pp.445-452, October.

Barna, S. (3-1962): "On secondary flow in stationary curved pipes". Quart. J. Mech. and Applied Math., Vol.16, pp.61-77.

Bell, K.J. and Owhadi, A. (65-1969-70): "Local heat transfer measurements during forced-convection boiling in a helically coiled tube". Proc. Inst. Mech. Engnrs. Vol.184, Pt.3C, pp.52-58.

Bennet, A.W., Hewitt, G.F., Kearsey, H.A., Keeys, R.K. and Lacey, P.M.C. (83-1965-66): "Flow visualisation studies of boiling at high pressure". Proc. Inst. Mech. Engnrs. Vol. 180, Pt. 3C.

Bishop, A.A., Sandberg, R.D., and Tong, L.S. (73-1965): "Forced convection heat transfer at high pressure after the critical heat flux". ASME 65-HT-31.

Boyce, B.E., Collier, J.G. and Levy, J. (42-1968): "Hold-up and pressure drop measurements in the two-phase flow of air-water mixtures in helical coils". Proc. Int. Symposium on Research in co-current Gas-Liquid flow. University of Waterloo, Ontario, Canada. pp.203-231, September.

British Standard 1042. (74-1964): "Methods for the measurement of fluid flow in pipes. Part I. Orifice plates, Nozzles and Venturic tubes".

Butterworth, D. and Pulling, D.J. (104-1972): "A visual study of mechanisms in horizontal, annular, air-water flow". UKAEA, AERE-M2556.

Butterworth, D. and Hewitt, G.F. (62-1977): "Two-phase flow and heat transfer". Harwell series. Oxford University Press. pp.203.

Carver, J.R., Kalarala, C.R. and Slotnik, J.S. (68-1964): "Heat transfer in coiled tubes with two-phase flow". U.S. Atomic Energy Commission. Research Report No. 4438.

Chen, J.C. (96-1963): "A correlation for boiling heat transfer to saturated fluids in convective flow". Paper presented to 6th National Heat Transfer Conf., Boston, 11-14 Aug., ASME reprint 63-HT-34.

Collier, J.G. and Wallis, G.B. (43-1967): "Two-phase flow and heat transfer". Notes for summer course held at Stanford University, Palo Alto, Calif. July, Vol.1, Ch.5.

Collier, J.G. (44-1972): "Convective Boiling and Condensation". McGraw-Hill. pp.36-37.

Coney, M.W.E. (86-1971): "The variation of liquid film thickness in horizontal two-phase flow". Central Electricity Research Laboratories. RD/L/N273/71.

Cumo, M., Farello, G.E., and Ferrani, G. (70-1972): "The influence of curvature in post dryout heat transfer". Int. Journal Heat and Mass Transfer, Vol.15, pp.2045-2062.

Dean, W.R. (1-1927): "Note on the motion of fluid in a curved pipe". Phil. Mag. 4, pp.208-223.

Dean, W.R. (14-1928): "The streamline motion of a fluid in a curved pipe". Phil.Mag.5, (30), pp.673-695.

de La Harpe, A., Lehongre, S., Mollard, J., and Johnnes, C. (66-1968): "Boiling heat transfer and pressure drop of liquid helium-I under forced circulation in a helically coiled tube". Advances in Cryogenic Engng. Proc. of the 1968 Cryogenic Engng. Conf. Vol.14, pp.170-177.

Detra, R.W. (31-1953): "The secondary flow in curved pipes". Mitt. aus den Institut fur Aerodynamik, E.T.H., Zurich, No.20.

Dittus, F.W., and Boelter, L.M.K. (97-1930): "Heat transfer in automobile radiators of the tubular type". Engineering 2 (13), pp.443-461.

Dravid, A.N., Smith, K.A., Merill, E.W., and Brian, P.L.T. (19-1971): "Effect of secondary fluid motion on laminar flows and heat transfer in helically coiled tube". AICh E. Journal, Vol.17, No.5, pp.1107.

Duchatelle, L., de Nucheze, L., and Robin, M.G. (67-1973): "Departure from nucleate boiling in helical tube of liquid metal heated steam generators". ASME, 73-HT-57.

Farmer, P.R. (46-1972): "Air-water mixtures flowing in helices. Part II: Pressure drop measurement". Central Electricity Research Laboratories. RD/L/N157/72.

Farmer, P.R (54-1972): "Air-water mixtures flowing in helices. Part III: Flow regimes". Central Electricity Research Laboratories. RD/L/N157/72.

Fisher, S.A. and Hopley, C.E. (60-1971): "Axial view studies of air-water mixtures flowing in a vertical 90^{0} bend and horizontal tube". Central Electricity Research Laboratories. RD/L/N266/71.

Foster, H.K. and Zeber, N. (98-1955): "Dynamics of vapour bubbles and boiling heat transfer". AIChE. Journal. Vol.11, No.4, pp.531-535.

Goldmann, K., Firstenberg, H., and Lombardi, C. (85-1961): "Burnout in turbulent flow - a droplet diffusion model". Trans. of ASME., Series C, 83-2(1961-5), pp.158-162.

Goldstein, S. (105-1957): "Modern Developments in Fluid Dynamics". pp.339, University Press, Oxford.

Hall-Taylor, N.S. and Nedderman, R.M. (94-1968): "The coalescence of disturbance waves in annular two-phase flow". Chem. Engng. Science, vol.22, pp.551-564.

Humphrey, J.A.C. (13-1977): "Flow in ducts with curvature and roughness". Ph.D. Thesis, London University, June 1977.

Hasson, D. (4-1955): "Research Correspondence, Vol.1, (1955) pp.57.

Howes, W.B. (10-1932): "Some sidelights of the heat transfer problem". Trans. Inst. of Chem. Engnrs. 10, pp.162.

Hawithorne, W.R. (30-1951): "Secondary circulation in fluid flow". Proceedings of the Royal Society, 206A, 374.

Heineman, J.B. (72-1960): "An experimental investigation of heat transfer to superheated steam in round and rectangular channels". U.S. Atomic Energy Commission, ANL-6213.

Hewitt, G.F. and Roberts, D.N. (84-1969): "Studies of two-phase flow patterns by simultaneous X-ray and flash photography". UKAEA. AERE-M2159.

Hewitt, G.F. (59-1969-70): "Disturbance waves in annular two-phase flow". Proc. Inst. Mech. Engnrs. Vol.184, Pt. 3C, pp.142-150.

Hewitt, G.F. and Hall-Taylor, N.S. (81-1970): "Annular two-phase flow". Pergamon Press, Oxford.

Hewitt, G.F. (82-1978): "Measurement of two-phase flow parameters". Academic Press, London.

Hogg, G.W. (29-1968): "The effect of secondary flow on point heat transfer coefficients for turbulent flow inside curved tubes". Ph.D. thesis, University of Idaho.

Hutchinson, P. and Whalley, P.B. (91-1973): "A possible characterisation of entrainment in annular flow". Chem. Engng. Science, 28, pp.974-5.

Ishida, K. (63-1977): "Annular flow boiling in helically-coiled tubes steam generator". MSc. Thesis, London University.

Ishii, A. and Grolmes, M.A. (89-1975): "Inception criteria for droplet entrainment in two-phase cocurrent film flow". AIChE. Journal, Vol.21, No.2., pp.308-318.

Ito, H. (25-1959): "Friction factors for turbulent flow in curved pipes". Journal of Basic Engng. Trans. ASME., 81, pp.123-134.

Ito, H. (6-1970): "Laminar flow in curved pipes". The Institute of High Speed Mechanics, Japan, Rep. No224, 22, pp.161-180.

Jaschke, D. (35-1925): "warmeubergang und Druckverlast in Rohrschlangen". Z. Ver. Dt. Ing. 69, 1526, Z.V.D.I. 24, 1.

Jens, W.H. and Lottes, P.A. (99-1951): "Analysis of heat transfer, burnout, pressure drop, and density data for high pressure water". US Atomic Energy Commission, ANL-4627.

Kalb, C.E. and Seader, J.D. (20-1972): "Heat and mass transfer phenomena for viscous flow in curved circular tubes". Int. J. Heat and Mass Transfer, Vol.15, pp.801-817.

Kalb, C.E. and Seader, J.D. (21-1974): "Fully developed heat transfer in curved circular tube with uniform wall temperature". AIChE. Journal, Vol.20, No.23, pp.340-346.

Katto, Y. (78-1976): "Dennetsu Gairon (Japanese) - an introduction to heat transfer". pp.93-99, Yokendo Press, Tokyo.

Kay, J.M. and Nedderman, R.M. (75-1974): "An introduction to fluid mechanics and heat transfer". 3rd Edition, Cambridge University Press, pp.68-73.

Kenning, D.B.R., Shock, R.A.W. and Poon, J.Y. (76-1974): "Local reductions in heat transfer due to buoyancy effects in upward turbulent flow". 5th Int. Heat Transfer Conf., Tokyo, NC4.3, pp.139-143.

Kooijman, J.M. and Lacey, P.M.C. (56-1968): Unpublished experiment. Exeter University.

Kozeki, M., Nariai, H., Furukawa, T., and Kurusu, K. (53-1970): "A study of helically-coiled tubes one-through steam generator". Bulletin of JSME., Vol.13, No.66, pp.1485-1494.

Kozeki, M. (48-1973): "Film thickness and flow boiling for two-phase annular flow in helically-coiled tube". Reactor Heat Transfer - Proc. of an International Meeting, Karlsruhe, pp.351-372.

Kozeki, M. (80-1973): "A study of two-phase behaviours and heat transfer in helically-coiled tube. (Japanese)" Mitsui Engineering and Shipbuilding Co. Ltd.

Kutateladze, S.S. and Bolishanski, V.M. (26-1966): "A concise encyclopedia of heat transfer". Pergamon Press, pp.114.

Lacey, P.M.C. (58-1970): "Two-phase flow in curved ducts". Paper presented at annual meeting of DECHEMA, Frankfurt/Main. June.

Levy, S. (106-1966): Prediction of two-phase annular flow with liquid entrainment. Int. J. Heat and Mass Transfer. Vol.9, pp.171-187.

Lis, J. and Strickland, J.A. (102-1970): "Local variations of heat transfer in a horizontal steam evaporator tube". 4th Int. Heat Transfer Conf., Paris, Paper B4.6.

Lockhart, R.W. and Martinelli, R.C. (40-1949): "Proposed correlation of data for isothermal two-phase two-component flow in pipes". Chem. Engng. Prog. 45(1), pp.39-48.

Maddock, C. (61-1973): "The structure of annular two-phase flow in bends". Ph.D. Thesis, Exeter University.

Martinelli, R.C. and Nelson, D.B. (45-1948): "Prediction of pressure drop during forced circulation boiling of water". Transaction ASME, 70, pp.695.

McConalogue, D.J. and Srivastava, R.S. (15-1968): "Motion of a fluid in a curved tube". Proc. Royal Society, 307A, pp.37-53.

Merkel, F. (36-1927): "Der grundlagen der warmenbertragung". pp.51. Leipzig: Steinkoph.

Miropolski, Z.L. and Pikus, V.Yu. (69-1969): "Critical boiling heat fluxes in curved channels". Heat Transfer Soviet Research. 1 (1), pp.74-79.

Mori, Y. and Hijikata, K. (79-1979): "Nagare to Netsu No Kogaku II (Japanese) - Engineering of fluid and heat". pp.109-110, Kyoritsu Shuppan. Co. Ltd., Tokyo.

Mori, Y. and Nakayama, W. (5-1965): "Study on forced convective heat transfer in curved pipes, (1st Report, Laminar region)". Int. J. Heat and Mass Transfer, vol.8, pp.67.

Mori, Y. and Nakayama, W. (24-1967): "Study on forced convective heat transfer in curved pipes, (2nd Report, Turbulent region)". Int. J. Heat and Mass Transfer, Vol.10, pp.37.

Olson, D.E. (12-1971): "Fluid mechanics relevant to respiratory flow with curved or elliptical tubes and bifurcating system". Ph.D. Thesis, London University.

Owhadi, A., Bell, K.J. and Crain, B. (64-1967): "Forced convection boiling inside helically-coiled tubes". Int. J. Heat and Mass Transfer, Vol.10, pp.397-401.

Owhadi, A., Bell, K.J. and Crain, B. (47-1968): "Forced convection boiling inside helically-coiled tubes". Int. J. Heat and Mass Transfer, Vol.11, pp.1779-93.

Paleev, I.I. and Filippovich, B.S. (92-1966): "Phenomena of liquid transfer in two-phase dispersed annular flow". Int. J. Heat and Mass Transfer, Vol.9, pp.1089-93.

Patanker, S.V., Pratap, V.S. and Spalding, D.B. (17-1974): "Prediction of laminar flow and heat transfer in helically-coiled pipes". J. Fluid Mechanics, 62, 3, pp.579.

Patanker, S.V., Pratap, V.S. and Spalding, D.B. (33-1975): "Prediction of turbulent flow in curved pipes". J. Fluid Mechanics, 67, 3, pp.595.

Pratap, V.S. (34-1975): "Flow and heat transfer in curved ducts". Ph.D. Thesis, London University.

Pratt, N.H. (37-1947): "The heat transfer in a reaction tank cooled by means of a coil". Transaction Institute Chem. Engnrs., 25, pp.163-180.

Rippel, G.R., Eidt, C.M. and Jordan, H.B. (41-1966): "Two-phase flow in a coiled tube - Pressure drop, hold-up and liquid phase axial mixing". I and EC process design and development, Vol.5, No.1, pp.32-39.

Robertson, J.M. (103-1972): "Dryout in horizontal hairpin waste-heat boiler tubes". 13th National Heat Transfer Conf., Denver, Colorado.

Rogers, G.F.C. and Mayhew, Y.R. (38-1964): "Heat Transfer and pressure loss in helically coiled tube with turbulent flow". Int. J. Heat and Mass Transfer, 7, pp.1207-16.

Raksenow, W.N. (95-1952): "A method of correlating heat transfer data for surface boiling of liquids". Transaction ASME, 74, 969.

Rowe, M. (32-1966): "Some secondary flow problems in fluid dynamics". Ph.D. Thesis, Cambridge University.

Ruffel, A.E. (49-1974): "The application of heat transfer and pressure drop data to the design of helical coil one-through boilers". Paper presented at Symp. on Multiphase flow systems. Inst. Chem. Engnrs., Strathclyde University, April 1974.

Schmidt, E. (27-1967): "Heat transfer and pressure loss in spiral coils". Chem. Engng. Tech., Vol.39, pp.781.

Schrock, V.E. and Grossman, L.M. (100-1959): "Forced convection boiling studies, final report on forced convection vaporization project". Lawrence Radiation Lab. Rep. No. TID-14632.

Scott, D.S. (51-1963): "Properties of concurrent gas-liquid flow". Adv. Chem. Engng., 4, pp.199-277.

Seban, R.A. and McLaughlin, E.F. (22-1963): "Heat transfer in tube coils with laminar and turbulent flows". Int. J. Heat and Mass Transfer, Vol.6, pp.387-95.

Shires, G.L. and Khauna, R.D. (57-1971): "Two-phase flow and heat transfer in helical coils". Heat Transfer and Fluid flow Research Symp., AEEW-M1023.

Srinivasan, P.S., Nandapurkar, S.S. and Holland, F.A. (28-1968): "Pressure drop and heat transfer in coils". Chem. Engnrs. Vol.218, pp.218.

Tatterson, P.F., Dallman, J.C. and Hanratty, T.J. (90-1977): "Drop sizes in annular gas-liquid flows". AIChE. Journal, Vol.23, No.1, pp.68-76.

Tong, L.S. (101-1965): "Boiling heat transfer and two-phase flow". John Wiley, New York.

Truesdell, L.C. (JR), and Adler, R.J. (16-1970): "Numerical treatment of fully-developed laminar flow in helically-coiled tubes". AIChE. Journal, Vol.16, 6, pp.1010.

Wallis, G.B. (107-1969): "One dimensional Two-phase flow". McGraw-Hill. p.320.

Wallis, G.B. (87-1970): "Annular two-phase flow. Part 1: Simple Theory, pp.59-72, Part 2: Additional effects, pp.73-82." J. of Basic Engng., Transaction ASME., March.

Whalley, P.B., Hutchinson, P., and Hewitt, G.F. (93-1974): "The calculation of critical heat flux in forced convection boiling". Int. Heat Transfer Conf., Tokyo. B 6.11, pp.290-4.

Whalley, P.B. and Williams, N.M. (88-1977): "Air-water two-phase flow in a helically coiled tube". Paper presented European Two-phase flow group, Grenoble, June.

White, C.M. (7-1929): "Streamline flow through curved pipes". Proc. Royal Society, 123A, pp.645-63.

* * *

(Abbreviations)

AERE : Atomic Energy Research Establishment
AIChE : American Institute of Chemical Engineers
ASME : American Society of Mechanical Engineers
JSME : Japanese Society of Mechanical Engineers
UKAEA : United Kingdom Atomic Energy Authority